

Photoswitchable Macromolecules: The Foundation of Photodynamic Block Copolymer Lithography

Zur Erlangung des akademischen Grades eines
DOKTORS DER NATURWISSENSCHAFTEN
(Dr. rer. nat.)

von der KIT-Fakultät für Chemie und Biowissenschaften
des Karlsruher Instituts für Technologie (KIT)

genehmigte

Dissertation

von

M.Sc. Linh Duy Thai

1. Referent: Prof. Dr. Patrick Théato
2. Referent: Prof. Dr. Hans-Achim Wagenknecht
3. Cotutelle-Referent: Prof. Dr. Christopher Barner-Kowollik

Tag der mündlichen Prüfung: 22.10.2024

"If we start tomorrow right now, no matter what comes next, we've won."

Rick Grimes, The Walking Dead

Declaration

This cotutelle PhD dissertation was conducted and written between July 2021 and July 2024 at the Institute of Nanotechnology (INT), Karlsruhe Institute of Technology (KIT) and at Queensland University of Technology (QUT) under the supervision of Prof. Dr. Patrick Théato (KIT) and Prof. Dr. Christopher Barner-Kowollik (QUT). Jun. Prof. Dr. Hatice Mutlu is the external co-supervisor.

I hereby confirm that I have prepared the work independently, used only the sources specified and have not made use of any unauthorized assistance from third parties. In particular, I have identified content taken verbatim or in essence from other works as such. I have read the statutes for safeguarding scientific practice at the Karlsruhe Institute of Technology (KIT). I also declare that I am not currently in any ongoing doctoral process and have not made any previous attempts at a doctorate. The submission and archiving of the primary data are ensured at the institute in accordance with paragraph A (6) of the KIT's rules for ensuring good scientific practice.

Karlsruhe, 04.09.2024

Linh Duy Thai

Abstract

The microphase separation of block copolymers leads to diverse thin-film nanostructures, such as spheres, cylinders, lamella and gyroids. Such thin-film nanostructures – typically on the scale of 10-100 nm – are of profound importance for applications such as microelectronics, catalysis and lithography. However, these conventional block copolymer morphologies are typically static once formed. In the current literature, manipulation of these nanostructures is often achieved via physical and chemical methods. Generally, a change in the volume fraction and/or the relative polarity between blocks is the driving force for a transition in morphology.

Given the remote and precise control enabled by light as an external stimulus, reversible switching between morphologies by light of a specific color is thus highly appealing. Therefore, inclusion of light-sensitive molecules into block copolymers is essential. One attractive class of photo-responsive entities are photoswitches. A photoswitch interacts with light to change its conformation and reverses by another color of light or via a thermal pathway. An ideal photoswitch should exhibit a large geometrical and/or polarity change upon irradiation. The former feature (i.e., large difference in geometry) is maximized only when photoswitches are installed as main-chain repeating units. This is particularly critical for the manipulation of block copolymer nanostructures. However, there is a critical lack of research focused on main-chain photoswitchable block copolymers despite a large library of photoswitches.

Herein, we establish the underpinning synthetic strategies for the integration of photoswitches into polymers and block copolymers as main-chain groups and as side-chain groups where applicable. We explore head-to-tail Acyclic Diene METathesis (ADMET), hydroxyl-yne click polymerization and a sequence-defined approach combining hydroxyl-yne click, protection/deprotection, and thiol-Michael click chemistries as synthetic tools. We demonstrate that photoswitchable polymers and block copolymers can be obtained efficiently via the developed strategies, successfully incorporating three different photoswitches, namely α -bisimine, hydrazone and spiropyran. We further show that solution photoisomerization of the embedded photoswitches is independent of the polymerization methods as well as dispersity of polymer chains. Furthermore, we found a general pathway to enhance the efficiency of solid-state photoisomerization (or photoswitching) – one of the key factors for light-induced morphological switching of block copolymer nanostructures, referred to herein as ‘photodynamic block copolymer lithography’. The current thesis thus introduces a chemical and synthetic foundation for the realization of advanced polymeric materials that have rarely been explored in the current literature. Finally, preliminary study on thin-film and bulk morphologies of selected photoswitchable block copolymers shows promising results,

providing guidance for our future endeavors towards realizing our vision of photodynamic block copolymer lithography.

Key words

Photoswitches • chromophore • bisimine • hydrazone • spiropyran • head-to-tail Acyclic Diene METathesis • cross-metathesis • hydroxyl-yne • thiol-Michael click chemistry • deprotection • polyaddition • step-growth polymerization • macro chain stopper • ARGET ATRP • post-modification • glass transition temperature • sequence-defined • main-chain • action plot • block copolymer • nanostructure • bulk morphology • thin-film • phase diagram • photoswitchable polymers • solid-state photoswitching • lithography • low dispersity • photoisomerization • kinetics.

Table of contents

Declaration	iv
Abstract	v
Key words.....	vi
Table of contents	vii
List of Tables	xi
List of Equations.....	xi
List of Figures.....	xi
List of Symbols and Abbreviations	xxv
Publications and Manuscripts included in this PhD research	xxvii
Conference Contributions	xxviii
Acknowledgements	xxix
Chapter 1: Introduction, Thesis Objectives and Thesis Outline	31
1.1. Introduction.....	31
1.2. Thesis objectives.....	33
1.3. Thesis outline	34
Chapter 2: Literature Review	36
2.1. Block copolymer nanostructures	36
2.2. Manipulation of block copolymer nanostructures	38
2.3. Photoswitches and their integration in material science	42
2.3.1. The Jablonski diagram	42
2.3.2. Examples of photoswitches.....	43
2.3.3. Integration of photoswitches into smart materials	48
2.4. Potential polymerization techniques for main-chain polymers.....	50
2.4.1. Acyclic Diene METathesis (ADMET) polymerization.....	50
2.4.2. Ring Opening Metathesis Polymerization (ROMP).....	51
2.4.3. Radical Ring Opening Polymerization (rROP)	52
2.4.4. X-yne click polymerization.....	53
2.5. Research gaps in photoswitchable block copolymers	54
Chapter 3: Exploring Head-to-tail ADMET and Hydroxyl-yne Click Polymerization for the Synthesis of α -bisimine-based Main-chain Block Copolymers	56
3.1. Head-to-tail ADMET polymerization	56
3.2. Hydroxyl-yne click polymerization	64
3.3. Concluding remarks	66
Chapter 4: Sequence-defined Main-chain Oligomers and Block Copolymers based on α - bisimine 67	
4.1. Synthesis of main-chain odd- and even-numbered sequences	68

4.2.	Functional group tolerance of the hydroxyl-yne click reaction	71
4.3.	Block copolymer synthesis	72
4.4.	Concluding remarks.....	73
Chapter 5:	Glass Transition Temperature and Solid-state Photoswitching Efficiency.....	75
5.1.	Correlation between glass transition temperature and photoswitching efficiency..	76
5.1.1.	Topological design and synthesis of the main-chain chromophore polymers	76
5.1.2.	Molecular flexibility is the key element for the photo-switching efficiency of solid-state polymers	79
5.2.	Modulation of glass transition temperature	81
5.3.	Concluding remarks.....	83
Chapter 6:	Photoisomerization of α -bisimine Main-chain Polymers	85
6.1.	Impact of polymerization techniques on the isomerization of α -bisimine based polymers.....	85
6.2.	Impact of dispersity and odd-even numbers of repeating units on isomerization kinetics	89
6.3.	Concluding remarks.....	90
Chapter 7:	Hydrazone-based Main-chain Polymers and Block Copolymers	91
7.1.	Hydrazone main-chain photoswitching polymers	91
7.1.1.	Design and Synthesis	92
7.1.2.	Photoisomerization study	95
7.1.3.	Effect of photoisomerization on solution and solid-state properties	97
7.1.4.	Concluding remarks.....	100
7.2.	Hydrazone main-chain block copolymer synthesis	101
7.2.1.	Synthesis route	101
7.2.2.	Photoisomerization and light responsive property of HO-[H] ₄ -OH	105
7.3.	Concluding remarks.....	106
Chapter 8:	Spiropyran-based Polymers and Block Copolymers	108
8.1.	Regioisomeric effect on the photo- and halochromism of main-chain spiropyran polymers.....	108
8.1.1.	Synthesis of SPs main-chain polymers	110
8.1.2.	Photo- and halochromism.....	112
8.1.3.	Concluding remarks.....	118
8.2.	Block copolymer with spiropyran as pendant groups	119
8.3.	Concluding remarks.....	122
Chapter 9:	Nanostructures of Photoswitchable Block Copolymers: Preliminary Study .	123
9.1.	Nanostructures of bisimine-based block copolymers	124
9.2.	Nanostructures of hydrazone-based block copolymer	126
9.3.	Concluding remarks.....	128
Chapter 10:	Conclusions and Outlook.....	129
10.1.	Conclusions	129
10.2.	Outlook	133

Chapter 11: Experimental Part.....	135
11.1. Instruments and Characterization	135
11.1.1. Nuclear Magnetic Resonance Spectroscopy (NMR)	135
11.1.2. Diffusion Ordered Spectroscopy	135
11.1.3. Flash column chromatography	135
11.1.4. Size Exclusion Chromatography (SEC)	136
11.1.5. Liquid Chromatography – Mass Spectrometry (LC-MS)	136
11.1.6. SEC-MS	137
11.1.7. UV-vis spectroscopy	137
11.1.8. Differential Scanning Calorimetry (DSC)	137
11.1.9. Thermogravimetric Analysis (TGA)	138
11.1.10. Dynamic Light Scattering	138
11.1.11. Small-Angle X-ray Scattering (SAXS)	138
11.1.12. Transmission Electron Microscopy (TEM)	138
11.1.13. Laser experiments	139
11.1.14. LED emission spectra	140
11.2. Chemicals	141
11.3. Information for Chapter 3	146
11.3.1. Synthesis of bisimine diol 1	146
11.3.2. Synthesis of bisimine mono-ol 2	147
11.3.3. Synthesis of bisimine monomer 3	148
11.3.4. ARGET ATRP synthesis of PS_nBr polymers	151
11.3.5. Post-polymerization modification of PS_nBr polymers	152
11.3.6. Synthesis of photoresponsive block copolymers	154
11.3.7. Synthesis of bisimine-diBr	157
11.3.8. Synthesis of Br-bisimine-OH	158
11.3.9. Synthesis of monomer M_{B1}	161
11.3.10. Synthesis of polymer P_{B1}	163
11.4. Information for Chapter 4	165
11.4.1. Synthesis protocol	165
11.4.2. NMR Spectra	188
11.5. Information for Chapter 5	262
11.5.1. Deconvolution of UV-vis spectra	262
11.5.2. Synthesis protocol	263
11.5.3. SEC traces	267
11.5.4. TGA thermograms	268
11.5.1. UV-vis spectrum of P_5	269
11.5.2. NMR spectra	269
11.6. Information for Chapter 6	275
11.7. Information for chapter 7	276

11.7.1.	Sample preparation for DSC measurement	276
11.7.2.	Action plot experiment	276
11.7.3.	Irradiation study of P _{h1} and P _{h2}	276
11.7.4.	TGA thermograms	279
11.7.5.	Photoswitching cycle	279
11.7.6.	Synthesis protocol	280
11.7.7.	NMR spectra	297
11.8.	Information for Chapter 8	327
11.8.1.	Photochromism study on main-chain polymers in DMAc and Toluene	327
11.8.2.	Halochromism investigated by NMR and SEC	327
11.8.3.	UV-vis spectra of P _{SP2} film	329
11.8.4.	Dynamic Light Scattering (DLS) spectra	330
11.8.5.	Synthesis Protocol	330
11.8.6.	NMR spectra	344
11.9.	Information for Chapter 9	376
11.9.1.	TEM investigation of BCP periodicity	376
11.9.2.	Spectra and Graphs	383
References	384
Curriculum Vitae (CV)	401

List of Tables

Table 3.1. Summary of results for block copolymer synthesis experiments	63
Table 8.1. M_n , Dispersity, and Optical properties of P_{SP1} , P_{SP2} , P_{SP3} and P_{SP4}	112
Table 9.1. Peak positions (expressed as q/q^*) of Bragg reflections for typical structures. ²⁸⁸	124
Table 11.1. List of chemicals used in this thesis. All chemicals and solvents were used without any further purification unless specified.....	141

List of Equations

Eq 11.1.....	135
Eq 11.2.....	139

List of Figures

Figure 1.1. Illustration of the ultimate goal of the project. Photodynamic block copolymer lithography refers to the alteration of block copolymer thin-film nanostructures upon illumination with light. Such transformation should ideally be observed in real-time via Transmission Electron Microscopy (TEM). However, the current thesis aims to establish the synthetic foundation for the preparation of photoswitchable block copolymers that can be employed to realize photodynamic block copolymer lithography.....	32
Figure 2.1. Theoretical phase diagram for linear AB dibCPs based on SCFT. L = Lamella, G = Gyroid, C = Hexagonally-Packed Cylinder (HPC), S = Body Centered Cubic (BCC). The phase diagram is adapted with permission from ref. ^{35,36} . Copyright © 2006 American Chemical Society.	37
Figure 2.2. Block copolymer blends can lead to alteration of the pristine nanostructure. Images were adapted from ref. ³⁹ with permissions. Copyright © 2014 American Chemical Society.	38
Figure 2.3. Dissimilarity of the block end group can drastically affect the nanostructure of block copolymer having the same degree of polymerization and composition. Images were adapted from ref. ⁴³ with permissions. Copyright © 2013 American Chemical Society.	38
Figure 2.4. Post-polymerization modification of pristine polymers via efficient chemistries can induce morphological transition owing to alteration in Flory-Huggins interaction parameter as well as volume fraction. Illustrations were adapted from ref. ^{44,45} with permissions. Copyright © 2022 American Chemical Society and © 2023 Royal Society of Chemistry.	39
Figure 2.5. Photo-induced cleavage of o-nitro benzyl ester located at a block junction led to a blend of two different polymers. Illustration adapted from ref. ⁴⁸ with permission.	40

Figure 2.6. Photoisomerization of azobenzene-containing block copolymer led to the reorientation of nanostructure. LPL: linearly polarized light. Illustration was adapted from ref. ⁴⁹ with permission. Copyright © 2006 American Chemical Society.	41
Figure 2.7. Jablonski diagram showing different electronic states and the relative energy levels as well as deactivation pathways. Radiative transitions are shown with vertical arrows while radiationless transitions are indicated by wavy arrows. The timescale or lifetime of each transition is also included.	42
Figure 2.8. Azobenzene photoswitches. Examples were adopted from refs. ⁵²⁻⁵⁶	43
Figure 2.9. (Left) Stilbene photoisomerization and side reactions. ⁶⁷⁻⁷⁰ (Right) Stiff Stilbene (SS) and Sterically hindered stiff stilbene (HSS). ⁷¹⁻⁷³	44
Figure 2.10. Overcrowded Alkenes (OAs): Photoswitches and Molecular Machine. ⁷⁶⁻⁷⁸	45
Figure 2.11. Indigoid photoswitches: Indigos, Thioindigos (TIs) and their derivatives. ^{82,85-90}	46
Figure 2.12. Imine photoswitches: (A) Proposed photoisomerization mechanism ⁹¹ and (B) examples. ⁹²⁻⁹⁴	46
Figure 2.13. Acyl and Arylhydrazone photoswitches. ^{99,105}	47
Figure 2.14. Spiropyran photoswitches. ^{107,112}	48
Figure 2.15. Integration of azobenzene ¹¹⁶ (A) and hydrazone ¹¹⁷ (B) into soft actuators. Images were adapted with permissions. Copyright © 2014 John Wiley and Sons.	48
Figure 2.16. Integration of spiropyran photoswitch into polymer for photopatterning ¹²⁵ (A) and photoswitchable wettability. ¹²¹ Images were adapted with permissions. Copyright © 2018, 2023 American Chemical Society.	49
Figure 2.17. Olefin metathesis: (A) mechanism ^{134,135} and (B) homopolymers, alternating polymers and head-to-tail polymers synthesized via Acyclic Diene METathesis (ADMET) polymerization.	50
Figure 2.18. General Mechanism of ROMP (A) and an example of ROMP of a stilbene-based cyclic monomer (B). ¹⁴⁶	51
Figure 2.19. Proposed mechanism of electro-redox-mediated metal-free ROMP.	51
Figure 2.20. Development in radical ring opening polymerization led to efficient cyclic monomer (B,C) with low ring-strain. ^{152,153} Illustration was adapted from ref. ¹⁵³	52
Figure 2.21. Typical X-yne click reactions, i.e., thiol-yne click, amino-yne click and hydroxyl-yne click, reported in the literature. ^{158,159}	53
Figure 2.22. Dynamic exchange reactions between a β -X- α,β -unsaturated carbonyl compounds with an X-type nucleophile (thiol, amine, phenol). Adapted from ref. ¹⁶⁰	53
 Figure 3.1. Synthesis of photoswitchable block copolymer via head-to-tail ADMET polymerization featuring main-chain α -bisimine photoswitch.	57
Figure 3.2. Synthesis of α-bisimine-based ADMET monomer. (A) Synthesis route for the monomer. (B) ¹ H NMR spectrum (500 MHz, CDCl ₃) of monomer 3 with assignment of important resonances. Reproduced from ref. ¹⁸⁸ with permission from the Royal Society of Chemistry.	57
Figure 3.3. Synthesis of macro-chain stopper based on polystyrene (PS). (A) Synthesis route. (B) Stacked ¹ H NMR spectra of polystyrene before (PS ₇₀ -Br) and after (PS ₇₀ -A2) end-group modification, respectively. (C) THF-SEC traces of pristine and modified polymers. (D) Summary of the molecular characterization for the PS _n Br synthesized via ARGET ATRP. ^(a) The dispersity \bar{D} was determined by THF-SEC; ^(b) Monomer conversion and percentage (%) of the Br-end group, respectively, were determined by ¹ H NMR spectroscopy. Reproduced from ref. ¹⁸⁸ with permission from the Royal Society of Chemistry.	58
Figure 3.4. Synthesis of photoswitchable block copolymers PS_n-[B]_x. (A-B) Comparative ¹ H NMR spectra (500 MHz, 32 scans, CDCl ₃). (C-E) THF-SEC traces of block copolymers PS _n -[B] _x with normalized RI detector response. M_n values and dispersity are reported in Table 3.1. Reproduced from ref. ¹⁸⁸ with permission from the Royal Society of Chemistry.	60
Figure 3.5. Chain extension with PEG-based macro chain stoppers. (A) ¹ H NMR spectrum of PEG ₄₆ -[B] ₂₀ in CDCl ₃ . THF-SEC traces of PEG ₄₆ -A1 (B) and PEG ₁₁₅ -A1 (C) macro chain stopper and mixture of the macro chain stopper and monomer 3 . Part of the results were adapted from ref. ¹⁸⁸ with permission from the Royal Society of Chemistry.	61

Figure 3.6. Synthesis of α -bisimine main-chain homopolymer via hydroxyl-yne click polymerization. (A) Synthesis scheme for monomer **M_{B1}** (up) and polymer **P_{B1}** (bottom). (B) Stacked ¹H NMR spectra (600 MHz, 32 scans, CDCl₃) of the monomer and the polymer. (C) DMAc-SEC traces of the resulting homopolymers synthesized under different polymerization conditions reported in the table shown in section (D). (D) Summary of the polymerization conditions for the homopolymer synthesis. Reproduced from ref.¹⁹⁵ with permission from American Chemical Society (ACS). 65

Figure 3.7. Photoswitching main-chain block copolymer synthesis via hydroxyl-yne click polymerization. (A) Reaction scheme. (B-C) THF-SEC traces of macro chain stoppers and block copolymer mixtures. 66

Figure S3.1. ¹ H NMR spectrum of bisimine diol 1 in MeOD.	146
Figure S3.2. ¹³ C NMR spectrum of bisimine diol 1 in MeOD.	147
Figure S3.3. ¹ H NMR spectrum of bisimine mono-ol 2 in CDCl ₃	148
Figure S3.4. ¹³ C NMR spectrum of bisimine mono-ol 2 in CDCl ₃	148
Figure S3.5. ¹ H NMR spectrum of bisimine monomer 3 in CDCl ₃	149
Figure S3.6. ¹³ C NMR spectrum of bisimine monomer 3 in CDCl ₃	150
Figure S3.7. COSY NMR spectrum of bisimine monomer 3 in CDCl ₃	150
Figure S3.8. ¹ H NMR spectrum of PS₇₀Br in CDCl ₃	151
Figure S3.9. ¹ H NMR spectrum of PS₁₁₅Br in CDCl ₃	152
Figure S3.10. ¹ H NMR spectrum of PS₂₃₀Br in CDCl ₃	152
Figure S3.11. ¹ H NMR spectrum of PS₇₀A2 in CDCl ₃	153
Figure S3.12. ¹ H NMR spectrum of PS₁₁₅A2 in CDCl ₃	153
Figure S3.13. ¹ H NMR spectrum of PS₂₃₀A2 in CDCl ₃	154
Figure S3.14. ¹ H NMR spectrum of PS₇₀[B]₅ in CDCl ₃	155
Figure S3.15. ¹ H NMR spectrum of PS₇₀[B]₈ in CDCl ₃	155
Figure S3.16. ¹ H NMR spectrum of PS₇₀[B]₃₄ in CDCl ₃	156
Figure S3.17. ¹ H NMR spectrum of PS₁₁₅[B]₁₀ in CDCl ₃	156
Figure S3.18. ¹ H NMR spectrum of PS₁₁₅[B]₃₆ in CDCl ₃	157
Figure S3.19. ¹ H NMR spectrum of PEG₄₆[B]₂₀ in CDCl ₃	157
Figure S3.20. ¹ H NMR spectrum of bisimine-diBr in CDCl ₃	158
Figure S3.21. ¹ H NMR spectrum of Br-Bisimine-OH in CDCl ₃	159
Figure S3.22. COSY NMR spectrum of Br-Bisimine-OH in CDCl ₃	160
Figure S3.23. ¹³ C NMR spectrum of Br-bisimine-OH in CDCl ₃	160
Figure S3.24. ¹ H NMR spectrum (600 MHz) of M_{B1} in CDCl ₃	161
Figure S3.25. COSY NMR spectrum of M_{B1} in CDCl ₃	162
Figure S3.26. ¹³ C NMR spectrum of M_{B1} in CDCl ₃	162
Figure S3.27. ¹ H NMR spectrum (600 MHz) of P_{B1} in CDCl ₃	163
Figure S3.28. COSY NMR spectrum of P_{B1} in CDCl ₃	164
Figure S3.29. ¹³ C NMR spectrum of P_{B1} in CDCl ₃	164

Figure 4.1. Synthetic strategy to obtain monodisperse α -bisimine main-chain oligomers with facile post-synthesis modification and perfect chain-end group fidelity. Synthesis route for odd-number (A) and even-number (B) homo-sequences of main-chain α -bisimines. Conditions for the hydroxyl-yne click reaction: **TBDMSO-[B]₁-yne** (2.1 eq), **HO-[B]₁-OH** (1.0 eq), DABCO base (20 mol% with respect to the hydroxy end-group) in anhydrous DCM (0.4 M). Identical conditions were employed for the even-number sequences. Deprotection of hydroxy group was carried out in TBAF solution (1.0 M in THF) for 30 minutes; (C) Synthesis of the graft sequence via thiol-Michael click reaction. 68

Figure 4.2. Chemical and macromolecular solution-state analysis confirms the successful synthesis and quantitative post-modification by thiol-Michael click reaction of the α -bisimine sequences. (A) Comparative ¹H NMR spectra (600 MHz, 32 scans, in CDCl₃) of a 3-mer sequence, **TBDMSO-[B]₃-OTBDMS** (in blue), and the

respective modified sequence, **TBDMSO-[B-SC₁₂]₃-OTBDMS** (in purple). The assignment of selected resonances was made via careful analysis of 1D and 2D NMR spectra (Experimental part, section 11.4). (B) THF-SEC for **TBDMSO-[B]_n-OTBDMS** (blue traces) and **TBDMSO-[B-SC₁₂]_n-OTBDMS** (purple traces), with *n* = 2-7. Note that the number of alkyl side chains (*n*) is less than that of α-bisimine units by one unit. The apparent molar mass was determined on the basis of polymethylmethacrylate (PMMA) calibration standard. (C) Number-averaged molar mass determined by ¹H NMR spectroscopy (*M_{n,NMR}*) and by THF-SEC (*M_{n,SEC}*). $\Delta M_n = M_{n,SEC} - M_{n,NMR}$, $\% \Delta M_n = \Delta M_n / M_{n,NMR} \times 100\%$ 69

Figure 4.3. Chemical compatibility enables the orthogonal incorporation of functional chain-ends. (A) Sectional stacked ¹H NMR spectra (600 MHz, 32 scans, in CDCl₃) of 2-mer sequences with functional end groups: **ene-[B]₂-OTBDMS** (orange curve), **YNE-[B]₂-OTBDMS** (red curve), **Acryl-[B]₂-OTBDMS** (blue curve). (B) THF-SEC traces for **ene-[B]₂-OTBDMS** (orange trace), **YNE-[B]₂-OTBDMS** (red trace), **Acryl-[B]₂-OTBDMS** (blue trace) sequences. *M_n* values were determined based on PMMA calibration standards. 71

Figure 4.4. Metal-free hydroxyl-yne click reaction as a potent ligation chemistry to generate block copolymers. (A) Synthesis of ABA triblock copolymers via the hydroxyl-yne click reaction between **PDMS-yne** (2.2 eq) and **HO-[B]_n-OH** (1.0 eq) under the catalysis of DABCO (20 mol%). (B) Stacked sectional ¹H NMR spectra (600 MHz, 32 scans, in CDCl₃) of **PDMS-yne** (black curve) and **PDMS-[B]₆-PDMS** ABA triblock copolymers (green curve). (C) THF-SEC traces of **PDMS-yne** (black trace) and the ABA triblock copolymers (odd sequenced one shown in the upper SEC traces and the even-ones at the bottom). *M_{n,SEC}* values were determined based on PMMA calibration standard. 72

Figure 4.5. AB diblock copolymers. (A) General structures of AB diblock copolymers with olefin (**PDMS-[B]₂-ene**) and (non-activated) alkyne end-groups (**PDMS-[B]₂-YNE**). (B) THF-SEC traces of **PDMS-[B]₂-ene** (left, green color) and **PDMS-[B]₂-YNE** (right, green color). *M_{n,SEC}* values were determined on the basis of PMMA calibration standards. 73

Figure S4.1. Synthesis route for odd-numbered sequences of main-chain α-bisimine, the thiol-Michael modified sequences, and ABA triblock copolymers.....	165
Figure S4.2. Synthetic route to even-numbered sequences, thiol-Michael-modified sequences and ABA triblock copolymers.....	173
Figure S4.3. Synthesis route to olefin-terminated 2-mer sequence and the AB diblock copolymer.....	179
Figure S4.4. Synthesis route for YNE-[B]₂-PDMS	183
Figure S4.5. Synthesis route to acrylate-terminated 2-mer sequence of α-bisimine.	186
Figure S4.6. ¹ H NMR (600 MHz, 32 scans) spectrum of HO-[B]₁-OH in CDCl ₃	188
Figure S4.7. Carbon-Proton Decoupled ¹³ C NMR (151 MHz) spectrum of HO-[B]₁-OH in CDCl ₃	188
Figure S4.8. COSY NMR spectrum of HO-[B]₁-OH in CDCl ₃	189
Figure S4.9. ¹ H NMR (600 MHz, 32 scans) spectrum of HO-[B]₁-OTBDMS in CDCl ₃	190
Figure S4.10. Carbon-Proton Decoupled ¹³ C NMR (151 MHz) spectrum of HO-[B]₁-OTBDMS in CDCl ₃	190
Figure S4.11. COSY NMR spectrum of HO-[B]₁-OTBDMS in CDCl ₃	191
Figure S4.12. ¹ H NMR (600 MHz, 32 scans) spectrum of TBDMSO-[B]₁-yne in CDCl ₃	192
Figure S4.13. Carbon-Proton Decoupled ¹³ C NMR (151 MHz) spectrum of TBDMSO-[B]₁-yne in CDCl ₃	192
Figure S4.14. COSY NMR spectrum of TBDMSO-[B]₁-yne in CDCl ₃	193
Figure S4.15. ¹ H NMR (600 MHz, 32 scans) spectrum of TBDMSO-[B]₃-OTBDMS in CDCl ₃	194
Figure S4.16. Carbon-Proton Decoupled ¹³ C NMR (151 MHz) spectrum of TBDMSO-[B]₃-OTBDMS in CDCl ₃	195
Figure S4.17. COSY NMR spectrum of TBDMSO-[B]₃-OTBDMS in CDCl ₃	196
Figure S4.18. ¹ H NMR (600 MHz, 32 scans) spectrum of HO-[B]₃-OH in CDCl ₃ , indicating that the protecting group (TBDMS) was completely cleaved.....	197
Figure S4.19. ¹ H NMR (600 MHz, 32 scans) spectrum of TBDMSO-[B]₅-OTBDMS in CDCl ₃	198
Figure S4.20. COSY NMR spectrum of TBDMSO-[B]₅-OTBDMS in CDCl ₃	199
Figure S4.21. Carbon-Proton Decoupled ¹³ C NMR (151 MHz) spectrum of TBDMSO-[B]₅-OTBDMS in CDCl ₃	200
Figure S4.22. ¹ H NMR (600 MHz, 32 scans) spectrum of HO-[B]₅-OH in CDCl ₃	201
Figure S4.23. ¹ H NMR (600 MHz, 32 scans) spectrum of TBDMSO-[B]₇-OTBDMS in CDCl ₃	202

Figure S4.24. COSY NMR spectrum of TBDMSO-[B]₇-OTBDMS in CDCl ₃	203
Figure S4.25. Carbon-Proton Decoupled ¹³ C NMR (151 MHz) spectrum of TBDMSO-[B]₇-OTBDMS in CDCl ₃	204
Figure S4.26. ¹ H NMR (600 MHz, 32 scans) spectrum of HO-[B]₇-OH in CDCl ₃	205
Figure S4.27. ¹ H NMR (600 MHz, 32 scans) spectrum of TBDMSO-[B-SC₁₂]₃-OTBDMS in CDCl ₃	206
Figure S4.28. COSY NMR spectrum of TBDMSO-[B-SC₁₂]₃-OTBDMS in CDCl ₃	207
Figure S4.29. Carbon-Proton Decoupled ¹³ C NMR (151 MHz) spectrum of TBDMSO-[B-SC₁₂]₃-OTBDMS in CDCl ₃	208
Figure S4.30. ¹ H NMR (600 MHz, 32 scans) spectrum of TBDMSO-[B-SC₁₂]₅-OTBDMS in CDCl ₃	209
Figure S4.31. COSY NMR spectrum of TBDMSO-[B-SC₁₂]₅-OTBDMS in CDCl ₃	210
Figure S4.32. Carbon-Proton Decoupled ¹³ C NMR (151 MHz) spectrum of TBDMSO-[B-SC₁₂]₅-OTBDMS in CDCl ₃	211
Figure S4.33. ¹ H NMR (600 MHz, 32 scans) spectrum of TBDMSO-[B-SC₁₂]₇-OTBDMS in CDCl ₃	212
Figure S4.34. COSY NMR spectrum of TBDMSO-[B-SC₁₂]₇-OTBDMS in CDCl ₃	213
Figure S4.35. Carbon-Proton Decoupled ¹³ C NMR (151 MHz) spectrum of TBDMSO-[B-SC₁₂]₇-OTBDMS in CDCl ₃	214
Figure S4.36. ¹ H NMR (600 MHz, 32 scans) spectrum of PDMS-yne in CDCl ₃	215
Figure S4.37. ¹ H NMR (600 MHz, 32 scans) spectrum of PDMS-[B]₃-PDMS in CDCl ₃	216
Figure S4.38. COSY NMR spectrum of PDMS-[B]₃-PDMS in CDCl ₃	217
Figure S4.39. ¹ H NMR (600 MHz, 32 scans) spectrum of PDMS-[B]₅-PDMS in CDCl ₃	218
Figure S4.40. COSY NMR spectrum of PDMS-[B]₅-PDMS in CDCl ₃	219
Figure S4.41. ¹ H NMR (600 MHz, 32 scans) spectrum of PDMS-[B]₇-PDMS in CDCl ₃	220
Figure S4.42. COSY NMR spectrum of PDMS-[B]₇-PDMS in CDCl ₃	221
Figure S4.43. ¹ H NMR (600 MHz, 32 scans) spectrum of TBDMSO-[B]₂-OTBDMS in CDCl ₃	222
Figure S4.44. COSY NMR spectrum of TBDMSO-[B]₂-OTBDMS in CDCl ₃	223
Figure S4.45. Carbon-Proton Decoupled ¹³ C NMR (151 MHz) spectrum of TBDMSO-[B]₂-OTBDMS in CDCl ₃	224
Figure S4.46. ¹ H NMR (600 MHz, 32 scans) spectrum of HO-[B]₂-OH in CDCl ₃	224
Figure S4.47. ¹ H NMR (600 MHz, 32 scans) spectrum of TBDMSO-[B]₄-OTBDMS in CDCl ₃	225
Figure S4.48. COSY NMR spectrum of TBDMSO-[B]₄-OTBDMS in CDCl ₃	226
Figure S4.49. Carbon-Proton Decoupled ¹³ C NMR (151 MHz) spectrum of TBDMSO-[B]₄-OTBDMS in CDCl ₃	227
Figure S4.50. ¹ H NMR (600 MHz, 32 scans) spectrum of HO-[B]₄-OH in CDCl ₃	228
Figure S4.51. ¹ H NMR (600 MHz, 32 scans) spectrum of TBDMSO-[B]₆-OTBDMS in CDCl ₃	229
Figure S4.52. COSY NMR spectrum of TBDMSO-[B]₆-OTBDMS in CDCl ₃	230
Figure S4.53. Carbon-Proton Decoupled ¹³ C NMR (151 MHz) spectrum of TBDMSO-[B]₆-OTBDMS in CDCl ₃	231
Figure S4.54. ¹ H NMR (600 MHz, 32 scans) spectrum of HO-[B]₆-OH in CDCl ₃	232
Figure S4.55. ¹ H NMR (600 MHz, 32 scans) spectrum of TBDMSO-[B-SC₁₂]₂-OTBDMS in CDCl ₃	233
Figure S4.56. ¹ H NMR (600 MHz, 32 scans) spectrum of TBDMSO-[B-SC₁₂]₄-OTBDMS in CDCl ₃	234
Figure S4.57. ¹ H NMR (600 MHz, 32 scans) spectrum of TBDMSO-[B-SC₁₂]₆-OTBDMS in CDCl ₃	235
Figure S4.58. ¹ H NMR (600 MHz, 32 scans) spectrum of PDMS-[B]₂-PDMS in CDCl ₃	236
Figure S4.59. COSY NMR spectrum of PDMS-[B]₂-PDMS in CDCl ₃	237
Figure S4.60. ¹ H NMR (600 MHz, 32 scans) spectrum of PDMS-[B]₄-PDMS in CDCl ₃	238
Figure S4.61. COSY NMR spectrum of PDMS-[B]₄-PDMS in CDCl ₃	239
Figure S4.62. ¹ H NMR (600 MHz, 32 scans) spectrum of PDMS-[B]₆-PDMS in CDCl ₃	240
Figure S4.63. COSY NMR spectrum of PDMS-[B]₆-PDMS in CDCl ₃	241
Figure S4.64. ¹ H NMR (600 MHz, 32 scans) spectrum of ene-[B]₁-Br in CDCl ₃	242
Figure S4.65. COSY NMR spectrum of ene-[B]₁-Br in CDCl ₃	242
Figure S4.66. Carbon-Proton Decoupled ¹³ C NMR (151 MHz) spectrum of ene-[B]₁-Br in CDCl ₃	243
Figure S4.67. ¹ H NMR (600 MHz, 32 scans) spectrum of ene-[B]₁-OH in CDCl ₃	243
Figure S4.68. COSY NMR spectrum of ene-[B]₁-OH in CDCl ₃	244
Figure S4.69. ¹ H NMR (600 MHz, 32 scans) spectrum of ene-[B]₂-OTBDMS in CDCl ₃	245
Figure S4.70. COSY NMR spectrum of ene-[B]₂-OTBDMS in CDCl ₃	245
Figure S4.71. Carbon-Proton Decoupled ¹³ C NMR (151 MHz) spectrum of ene-[B]₂-OTBDMS in CDCl ₃	246

Figure S4.72. ^1H NMR (600 MHz, 32 scans) spectrum of ene-[B]₂-OH in CDCl_3	246
Figure S4.73. ^1H NMR (600 MHz, 32 scans) spectrum of ene-[B]₂-PDMS in CDCl_3	247
Figure S4.74. COSY NMR spectrum of ene-[B]₂-PDMS in CDCl_3	248
Figure S4.75. ^1H NMR (600 MHz, 32 scans) spectrum of YNE-[B]₁-OTBDMS in CDCl_3	249
Figure S4.76. Carbon-Proton Decoupled ^{13}C NMR (151 MHz) spectrum of YNE-[B]₁-OTBDMS in CDCl_3	249
Figure S4.77. COSY NMR spectrum of YNE-[B]₁-OTBDMS in CDCl_3	250
Figure S4.78. ^1H NMR (600 MHz, 32 scans) spectrum of YNE-[B]₁-OH in CDCl_3	251
Figure S4.79. ^1H NMR (600 MHz, 32 scans) spectrum of YNE-[B]₂-OTBDMS in CDCl_3	252
Figure S4.80. COSY NMR spectrum of YNE-[B]₂-OTBDMS in CDCl_3	253
Figure S4.81. ^1H NMR (600 MHz, 32 scans) spectrum of YNE-[B]₂-OH in CDCl_3	254
Figure S4.82. ^1H NMR (600 MHz, 32 scans) spectrum of PDMS-[B]₂-YNE in CDCl_3	255
Figure S4.83. COSY NMR spectrum of YNE-[B]₂-PDMS in CDCl_3	256
Figure S4.84. ^1H NMR (600 MHz, 32 scans) spectrum of acryl-[B]₁-OH in CDCl_3	257
Figure S4.85. COSY NMR spectrum of acryl-[B]₁-OH in CDCl_3	258
Figure S4.86. Carbon-Proton Decoupled ^{13}C NMR (151 MHz) spectrum of acryl-[B]₁-OH in CDCl_3	259
Figure S4.87. ^1H NMR (600 MHz, 32 scans) spectrum of acryl-[B]₂-OTBDMS in CDCl_3	260
Figure S4.88. COSY NMR spectrum of acryl-[B]₂-OTBDMS in CDCl_3	261
Figure S4.89. Carbon-Proton Decoupled ^{13}C NMR (151 MHz) spectrum of acryl-[B]₂-OTBDMS in CDCl_3	261

Figure 5.1. (A) Structural design of photoswitchable polymers for solid-state applications. In the literature, random copolymerization is commonly reported, which has limitations such as statistical distribution of chromophores, mainly side-chain chromophores. In this work, the precise control of chromophore density and polymer topology, main-chain chromophores and facile synthesis protocol are key design highlights. Direct comparison of isomerization efficiency in solution and solid state of different polymer topologies is also enabled. (B) and (C) Synthetic route and structures of α -bisimine-based homopolymers **P₁**, **P₂**, **P₃** and **P₄**. Reproduced from ref.¹⁹³ with permission from American Chemical Society.77

Figure 5.2. Synthesis and Characterization of main-chain photoswitching polymers. (A) ^1H NMR spectra of 1-dodecane thiol (up), polymer **P₁** (middle) and **P₃** (bottom). The disappearance of the magnetic resonances associated with the protons corresponding to the acrylate (protons **a** and **b**) confirms the full conversion of the thiol-Michael reaction. (B) THF-SEC traces and normalized RI detector response of **P₁**-**P₄** (left: **P₁** and **P₃**, right: **P₂** and **P₄**). (C) Molar absorptivity of chromophore in **P₁**-**P₄**, recorded in THF at 20 °C via UV-vis absorbance. (D) Stacked differential scanning calorimetry (DSC) thermograms of **P₁**-**P₄**, recorded during the second heating cycle. Reproduced from ref.¹⁹³ with permission from American Chemical Society.78

Figure 5.3. Photoisomerization of α -bisimine in THF solution. (A) Illustration of forward and thermal back-isomerization of α -bisimine cores in the polymer backbone. (B) stacked ^1H NMR spectra obtained during irradiation studies in solution of **P₁** ($[\alpha\text{-bisimine}] = 0.84 \text{ mM}$), $\lambda = 310 \text{ nm}$, number of photons (N_p): $3.0 \cdot 10^{19}$, laser power: $(4.5 - 5.5) \pm 4.2\%$ mW. The NMR-based conversion was determined by comparison of integral values corresponding to resonances associated with each isomer. Stacked UV-vis spectra obtained during irradiation studies of **P₁** (C) and thermal back-isomerization of **P₁** (D) in THF ($[\alpha\text{-bisimine}] = 32.2 \text{ }\mu\text{M}$, $\lambda = 310 \text{ nm}$, laser power: $(4.5 - 5.5) \pm 3.5\%$ mW) at 20 °C. The number of photons was calculated from Equation S11.1 (Experimental part). (E) Wavelength-dependent photoconversion of the α -bisimine measured for **P₁** in THF. Reproduced from ref.¹⁹³ with permission from American Chemical Society.79

Figure 5.4. Correlation between solid-state photoswitching efficiency and glass transition temperature. (A) Results of irradiation studies (THF solutions and cast films, thickness close to 400-600 nm) monitored by ^1H NMR and UV-vis spectroscopy. Conditions: $\lambda = 310 \text{ nm}$, $N_p = 1.5 \cdot 10^{19}$, laser power: $(4.5 - 5.5) \pm 4.6\%$ mW, $T = 20 \text{ }^\circ\text{C}$. The NMR study was repeated twice with almost identical results. (B) Correlation between T_g of the polymers and the solid-state isomerization efficiency compared to solution. The solid-state/solution isomerization ratio was calculated from the UV-vis study in which the absorbance at the irradiation wavelength, i.e., 310 nm, was kept identical. Reproduced from ref.¹⁹³ with permission from American Chemical Society.80

Figure 5.5. Post-polymerization modification of polymer P_{B1} via thiol-Michael click reaction. (A) General reaction scheme. (B) Exemplified stack 1H NMR spectra of the parent (black line) and the post-modified polymer (orange line). (C) Stacked DSC thermograms of the parent polymer (P_{B1}) and the modified polymers (P_{B1-C4} , P_{B1-C12} , $P_{B1-C2OH}$, and $P_{B1-C2Boc}$). Conditions: 3 cycles of heating and cooling from -90 °C to 120 °C at 20 °C·min ⁻¹ heating rate in a nitrogen atmosphere. The plotted DSC curves are taken from the second heating cycle. Reproduced from ref. ¹⁹⁵ with permission from American Chemical Society.	81
Figure 5.6. DSC thermograms of the odd-numbered sequences (A) and even-numbered sequences (B). Black lines are for pristine oligomers and orange lines are for post-modified oligomers. Conditions: 3 cycles of heating and cooling from -90 °C to 90 °C, 10 °C·min ⁻¹ , under N ₂ atmosphere; (C) Odd-even effect on glass transition temperature (T_g) of unmodified sequences, TBDMSO-[B]_n-OTBDMS	82

Figure S5.1. Deconvolution of UV-vis spectrum of α -bisimine core for the determination of isomerization conversion	262
Figure S5.2. Synthesis route for polymer P_1 , P_2 and P_5	263
Figure S5.3. Thiol-Michael modification of polymer P_1 , P_2 with 1-dodecanethiol.	265
Figure S5.4. Thiol-Michael modification of polymer P_{B1} with different thiols catalyzed by an NHC catalyst	266
Figure S5.5. THF-SEC traces of pristine and post-310nm irradiated polymer films of P_1 - P_4	267
Figure S5.6. THF-SEC trace of non-chromophore polymer P_5	267
Figure S5.7. THF-SEC traces of parent polymer (P_{B1}) and the derived polymers. In this case, polymer P_{B1} was synthesized in large scale (800 mg) under optimized condition (0.4 M in DCM, 20 mol% DABCO, 2 hours).	268
Figure S5.8. TGA thermograms of polymer P_1 - P_4 . $T_{d,5\%}$ (Temperature at which 5% mass of polymer is lost): P_1 (301 °C), P_2 (317 °C), P_3 (265 °C), P_4 (270 °C).	268
Figure S5.9. TGA thermogram of parent polymer (P_{B1}) and its thiol-Michael-modified derivatives. $T_{d,5\%}$ (Temperature at which 5% mass of polymer is lost) is 277 °C for P_{B1} , 260 °C for $P_{B1-C2OH}$, 270 °C for P_{B1-C4} , 272 °C for P_{B1-C12} , 185 °C for $P_{B1-C2Boc}$	268
Figure S5.10. UV-vis absorption spectrum of polymer P_5 in THF.	269
Figure S5.11. 1H NMR spectrum (600 MHz, 32 scans) of P_1 in $CDCl_3$	269
Figure S5.12. 1H NMR spectrum (600 MHz, 32 scans) of P_2 in $CDCl_3$	270
Figure S5.13. 1H NMR spectrum (600 MHz, 32 scans) of P_3 in $CDCl_3$	270
Figure S5.14. 1H NMR spectrum (600 MHz, 32 scans) of P_4 in $CDCl_3$	271
Figure S5.15. 1H NMR spectrum of polymer P_5 in $CDCl_3$	271
Figure S5.16. Stacked 1H NMR spectra (600 MHz, 32 scans) of P_{B1-C4} and P_{B1} in $CDCl_3$	272
Figure S5.17. COSY NMR spectrum of P_{B1-C4} in $CDCl_3$	272
Figure S5.18. Stacked 1H NMR spectra (600 MHz, 32 scans) of P_{B1-C12} and P_{B1} in $CDCl_3$	273
Figure S5.19. Stacked 1H NMR spectra (600 MHz, 32 scans) of $P_{B1-C2OH}$ and P_{B1} in $CDCl_3$	273
Figure S5.20. Stacked 1H NMR spectra (600 MHz, 32 scans) of $P_{B1-C2Boc}$ and P_{B1} in $CDCl_3$	274
Figure S5.21. Stacked 1H NMR spectra (600 MHz, 32 scans) of P_{B1-TMS} and P_{B1} in $CDCl_3$	274

Figure 6.1. Forward and Back isomerization of α-bisimine in P_{B1}. (A) General isomerization of α -bisimine in solution. (B) Sectional 1H NMR spectra (recorded in CD_2Cl_2) of P_{B1} before and after irradiation with 310 nm laser beam, $P = 6.0$ - 6.2 mW. The resonances marked with (*) are for the isomer of α -bisimine. The polymer solution was first prepared in THF which was removed after irradiation and redissolved in CD_2Cl_2 for NMR measurement. (C) Stacked UV-vis absorption spectra of P_{B1} in THF ($2.3 \cdot 10^{-5}$ mol·L ⁻¹) irradiated with 310 nm. (D) Stacked UV-vis absorption spectrum of the post-310 nm irradiated P_{B1} solution in THF at 20 °C. It should be noted that prior to irradiation, the THF solvent was passed through a short basic aluminum oxide column to remove peroxides which can potentially cause undesirable side reactions upon UV exposure. Reproduced from ref. ¹⁹⁵ with permission from American Chemical Society.	86
--	----

Figure 6.2. Isomerization kinetics of P_{B1} and P_2 in THF solution. (A) Structural comparison of P_{B1} synthesized via head-to-tail hydroxyl-yne and P_2 synthesized via head-to-tail ADMET polymerization. Kinetic traces for the forward	
--	--

isomerization at 310 nm irradiation ($P = 6.0\text{--}6.2\text{ mW}$, up to $3.0 \cdot 10^{19}$ photons) for P_{B1} (B) and P_2 (C). Thermal reversion kinetic traces for P_{B1} (D) and P_2 (E) at $20\text{ }^\circ\text{C}$ in CD_2Cl_2 . The ratio of isomers was determined by ^1H NMR spectroscopy in CD_2Cl_2 . Samples were first prepared in purified THF for the irradiation and subsequently blow-dried, redissolved in CD_2Cl_2 for NMR measurements. Reproduced from ref.¹⁹⁵ with permission from American Chemical Society.....87

Figure 6.3. First and second-order fits of forward photoisomerization of α -bisimine in two similar polymers, P_{B1} and P_2 . Reproduced from ref.¹⁹⁵ with permission from American Chemical Society.88

Figure 6.4. The odd-even effect does not influence the photoisomerization in solution. (A) Forward photoisomerization of α -bisimine core in an odd-number and an even-number sequence in THF monitored by UV-vis spectroscopy. Conditions: Irradiation wavelength: 310 nm, laser power: $4.3\text{ mW} \pm 5.0\%$. The rate coefficients ($k_{f,310}$) were derived based on a first-order kinetic model. (B) Thermal back isomerization at $20\text{ }^\circ\text{C}$. The rate coefficients (k_b) were derived from a first-order kinetic model. Note that the k_b used here represents the average rate coefficient of $(E,Z) \rightarrow (Z,Z)$ (k_{b1}) and $(E,E) \rightarrow (Z,Z)$ (k_{b2}) back reversion. Reproduced from ref.¹⁹⁵ with permission from American Chemical Society.89

Figure 7.1. Design strategy for two main-chain hydrazone polymers, enabling opposite changes in hydrodynamic volume upon photoisomerization of the hydrazone core. The taxonomy of the rotor and stator is adapted from the work of Aprahamian and colleagues.²³⁹ Reproduced from ref.²⁴⁰ with permission from John Wiley and Sons.92

Figure 7.2. Synthesis of two hydrazone main-chain photoswitching homopolymers. Representation of the head-to-tail ADMET polymerization of two monomers, M_{h1} (A) and M_{h2} (D). Sectional stacked ^1H NMR spectra (in either CD_2Cl_2 or CDCl_3) of M_{h1} and M_{h2} and the resulting polymers, P_{h1} (B) and P_{h2} (D). SEC traces recorded in dimethylacetamide (DMAc) of P_{h1} (C) and P_{h2} (F). HG-II: Hoveyda-Grubbs 2nd generation catalyst. M_n represents the apparent number-averaged molar mass. Reproduced from ref.²⁴⁰ with permission from John Wiley and Sons.93

Figure 7.3. Photoisomerization study of P_{h1} and P_{h2} . Sectional stacked ^1H NMR spectra recorded in toluene- d_8 of polymer solutions, P_{h1} (A) and P_{h2} (B), irradiated with 410 nm laser (forward isomerization), followed by 365 nm laser (back isomerization). Photoisomerization kinetics of P_{h1} (C) and P_{h2} (D) were fitted with an exponential function. Reproduced from ref.²⁴⁰ with permission from John Wiley and Sons.....95

Figure 7.4. Wavelength-dependent Z/E-photoisomerization recorded in toluene- d_8 of hydrazone core in P_{h1} . Reproduced from ref.²⁴⁰ with permission from John Wiley and Sons. Details on sample preparation is provided in Experimental part, Section 11.7.2.....97

Figure 7.5. Effect of photoisomerization on properties of hydrazone-based main-chain polymers. DMAc-SEC traces recorded for P_{h1} (A) and P_{h2} (B) upon forward and back photoisomerization. (C) Stacked DSC curves for P_{h1} and P_{h2} before and after 410-nm irradiation. Reproduced from ref.²⁴⁰ with permission from John Wiley and Sons...98

Figure 7.6. Synthesis strategies for sequence-defined oligomers and block copolymers based on hydrazone photoswitch. (A) Application of hydroxyl-yne click reaction and TBAF-deprotection chemistry. (B) Employment of hydroxyl-yne and cross-metathesis.101

Figure 7.7. Sectional stacked ^1H NMR spectra (recorded in CDCl_3) of an oligomer, **TBDMSO-[H]₂-OTBDMS** before and after deprotection with TBAF solution. The mixture was purified via workup and flash column chromatography prior to NMR measurement.102

Figure 7.8. (A) DMAc-SEC traces of hydrazone-based oligomers and block copolymers. (B) Summary of molar mass determined from NMR and SEC. (C) THF-SEC traces and (D) summary of **HO-[H]₄-OH**, **PDMS-yne** and **PDMS-[H]₄-PDMS**.102

Figure 7.9. ^1H NMR spectra recorded in CDCl_3 with assignment of important resonances of **HO-[H]₄-OH**, **PDMS-yne** and **PDMS-[H]₄-PDMS**.103

Figure 7.10. DOSY spectrum of **PDMS-[H]₄-PDMS** in CDCl_3 . It is clear that there is a mixture of two different block copolymers, both of which contain hydrazone and PDMS segments. Experiment details are provided in Experimental part, Section 11.7.....105

Figure 7.11. Forward (A) and back photoisomerization of **HO-[H]₄-OH** oligomer in toluene- d_8 . (C,D) Molecular weight distribution of the DMAc-SEC traces of the pristine and irradiated **HO-[H]₄-OH** oligomer. Prior to SEC measurement, the oligomer solution was blown-dried and redissolved in DMAc.106

Figure S7.1. Molar absorptivity of polymer P_{h1} and P_{h2} in toluene solution at 25 °C.....	276
Figure S7.2. Irradiation experiment of polymer P_{h1} (A) and P_{h2} (B) solution in toluene solvent monitored by UV-vis spectroscopy at 25 °C. [photoswitch] = $(1.2-4.0) \cdot 10^{-5}$ M.....	277
Figure S7.3. DMac SEC traces recorded for pristine (Z)- P_{h1} and the corresponding irradiated polymer. The conversion was determined by ¹ H NMR spectroscopy. For SEC measurements, the samples were blow-dried to remove the solvent (toluene) and redissolved in DMac.....	277
Figure S7.4. ¹ H NMR (600 MHz) spectra of (88%Z)- P_{h1} in toluene-d ₈ under 410-nm irradiation, followed by darkness at r.t for 4 days.....	278
Figure S7.5. ¹ H NMR (600 MHz) spectra of (Z)- P_{h2} in toluene-d ₈ under 410-nm irradiation, followed by darkness at r.t for 4 days.....	278
Figure S7.6. Irradiation of polymer P_{h2} solution in DMac solvent monitored by UV-vis spectroscopy at 25 °C. [photoswitch] = $1.5 \cdot 10^{-5}$ M.....	278
Figure S7.7. TGA thermograms of P_{h1} (A) and P_{h2} (B). Conditions: heating from 30 °C to 800 °C, at 20 °C·min ⁻¹ , under N ₂ atmosphere.....	279
Figure S7.8. Solution photoisomerization cycles of (88%Z)- P_{h1} (left) and (Z)- P_{h2} (right). c = $(1.1-1.4) \cdot 10^{-5}$ M in toluene at 25 °C; Forward photoisomerization was triggered by irradiating with λ = 410 nm ($6.0 \cdot 10^{17}$ photons, P = 4.5 mW ± 13%); Back photoisomerization was performed at λ = 310 nm ($2.1 \cdot 10^{18}$ photons, P = 5.5 mW ± 6.0%).	279
Figure S7.9. Synthesis route to monomers M_{h1} (A) and M_{h2} (B) and the respective polymers, i.e., P_{h1} (A) and P_{h2} (B).	280
Figure S7.10. Synthesis of hydrazone-based oligomers via hydroxyl-yne click and TBAF deprotection.	287
Figure S7.11. Synthesis route for hydrazone-based oligomers and block copolymers via hydroxyl-yne click reaction and cross metathesis.....	291
Figure S7.12. ¹ H NMR (600 MHz, 16 scans) spectrum of compound 1 in CDCl ₃	297
Figure S7.13. ¹³ C NMR (151 MHz, 1024 scans) spectrum of compound 1 in CDCl ₃	298
Figure S7.14. ¹ H NMR (600 MHz, 16 scans) spectrum of compound 2 in CDCl ₃	298
Figure S7.15. ¹³ C NMR (151 MHz, 1024 scans) spectrum of compound 2 in CDCl ₃	299
Figure S7.16. ¹ H NMR (600 MHz, 16 scans) spectrum of compound 3 in CD ₂ Cl ₂	299
Figure S7.17. ¹³ C NMR (151 MHz, 1024 scans) spectrum of compound 3 in CD ₂ Cl ₂	300
Figure S7.18. ¹ H NMR (600 MHz, 16 scans) spectrum of compound 4 in CDCl ₃	300
Figure S7.19. ¹³ C NMR (151 MHz, 1024 scans) spectrum of compound 4 in CDCl ₃	301
Figure S7.20. ¹ H NMR (600 MHz, 16 scans) spectrum of monomer M_{h1} in CD ₂ Cl ₂	301
Figure S7.21. ¹³ C NMR (151 MHz, 1024 scans) spectrum of monomer M_{h1} in CD ₂ Cl ₂	302
Figure S7.22. ¹ H NMR (600 MHz, 32 scans) spectrum of polymer (Z)- P_{h1} in CD ₂ Cl ₂	302
Figure S7.23. ¹ H NMR (600 MHz, 16 scans) spectrum of compound 5 in CDCl ₃	303
Figure S7.24. ¹³ C NMR (151 MHz, 1024 scans) spectrum of compound 5 in CDCl ₃	303
Figure S7.25. ¹ H NMR (600 MHz, 16 scans) spectrum of compound 6 in CDCl ₃	304
Figure S7.26. ¹³ C NMR (151 MHz, 1024 scans) spectrum of compound 6 in CDCl ₃	304
Figure S7.27. ¹ H NMR (600 MHz, 16 scans) spectrum of monomer M_{h2} in CDCl ₃	305
Figure S7.28. ¹³ C NMR (151 MHz, 1024 scans) spectrum of monomer M_{h2} in CDCl ₃	305
Figure S7.29. ¹ H NMR (600 MHz, 32 scans) spectrum of polymer (Z)- P_{h2} CDCl ₃	306
Figure S7.30. ¹ H NMR spectrum of HO-C₁₆-OH in CDCl ₃	306
Figure S7.31. ¹³ C NMR spectrum of HO-C₁₆-OH in CDCl ₃	307
Figure S7.32. COSY NMR spectrum of HO-C₁₆-OH in CDCl ₃	307
Figure S7.33. ¹ H NMR spectrum of TBDMSO-C₆-OH in CDCl ₃	308
Figure S7.34. ¹³ C NMR spectrum of TBDMSO-C₆-OH in CDCl ₃	308
Figure S7.35. ¹ H NMR spectrum of TBDMSO-preH-1 in CDCl ₃	309
Figure S7.36. ¹³ C NMR spectrum of TBDMSO-preH-1 in CDCl ₃	309
Figure S7.37. COSY NMR spectrum of TBDMSO-preH-1 in CDCl ₃	310
Figure S7.38. ¹ H NMR spectrum of TBDMSO-[H]₁-COOH in CDCl ₃	310

Figure S7.39. ^{13}C NMR spectrum of TBDMSO-[H]₁-COOH in CDCl_3 .	311
Figure S7.40. ^1H NMR spectrum of HO-C₆-yne in CDCl_3 .	311
Figure S7.41. ^1H NMR spectrum of HO-C₆-yne in CDCl_3 .	311
Figure S7.42. ^1H NMR spectrum of TBDMSO-[H]₁-yne in CDCl_3 .	312
Figure S7.43. ^{13}C NMR spectrum of TBDMSO-[H]₁-yne in CDCl_3 .	312
Figure S7.44. ^1H NMR spectrum of TBDMSO-[H]₂-OTBDMS in CDCl_3 .	313
Figure S7.45. ^{13}C NMR spectrum of TBDMSO-[H]₂-OTBDMS in CDCl_3 .	313
Figure S7.46. ^1H NMR spectrum of ene-preH-1 in CDCl_3 .	314
Figure S7.47. ^{13}C NMR spectrum of ene-preH-1 in CDCl_3 .	314
Figure S7.48. ^1H NMR spectrum of ene-[H]₁-COOH in CDCl_3 .	315
Figure S7.49. ^{13}C NMR spectrum of ene-[H]₁-COOH in CDCl_3 .	315
Figure S7.50. ^1H NMR spectrum of ene-[H]₁-yne in CDCl_3 .	316
Figure S7.51. COSY NMR spectrum of ene-[H]₁-yne in CDCl_3 .	316
Figure S7.52. ^{13}C NMR spectrum of ene-[H]₁-yne in CDCl_3 .	317
Figure S7.53. ^1H NMR spectrum of ene-[H]₂-ene in CDCl_3 .	317
Figure S7.54. Sectional COSY NMR spectrum of ene-[H]₂-ene in CDCl_3 .	318
Figure S7.55. ^{13}C NMR spectrum of ene-[H]₂-ene in CDCl_3 .	319
Figure S7.56. ^1H NMR spectrum of HO-[H]₂-OH in CDCl_3 .	319
Figure S7.57. ^{13}C NMR spectrum of HO-[H]₂-OH in CDCl_3 .	320
Figure S7.58. COSY NMR spectrum of HO-[H]₂-OH in CDCl_3 .	320
Figure S7.59. ^1H NMR spectrum of ene-[H]₄-ene in CDCl_3 .	321
Figure S7.60. ^{13}C NMR spectrum of ene-[H]₄-ene in CDCl_3 .	321
Figure S7.61. COSY NMR spectrum of ene-[H]₄-ene in CDCl_3 .	322
Figure S7.62. ^1H NMR spectrum of HO-[H]₄-OH in CDCl_3 .	323
Figure S7.63. ^{13}C NMR spectrum of HO-[H]₄-OH in CDCl_3 .	323
Figure S7.64. COSY NMR spectrum of HO-[H]₄-OH in CDCl_3 .	324
Figure S7.65. ^1H NMR spectrum of PDMS-[H]₄-PDMS in CDCl_3 .	325
Figure S7.66. Sectional COSY NMR spectrum of PDMS-[H]₄-PDMS in CDCl_3 .	326

Figure 8.1. General structure of four isomeric main-chain homopolymers. Reproduced from ref. ²⁶² with permission from the Royal Society of Chemistry.	109
Figure 8.2. Synthesis of regio-isomeric main-chain homopolymers based on a spiropyran scaffold. (A1-D1). Sectional ^1H NMR spectra recorded in CDCl_3 with assignment of important resonances of monomers and the respective polymers. (A2-D2) DMAc-SEC traces of the four polymers. Reproduced from ref. ²⁶² with permission from the Royal Society of Chemistry.	111
Figure 8.3. Simplified mechanism of photo- and acid-induced ring-opening and isomerization of SPs. The (Z)-MC/MCH⁺ and (E)-MC/MCH⁺ can adopt other conformations via rotation around the α - and γ -bond. Details of the stimuli-responsive mechanism can be found in refs. ^{106,108,266-270} . Reproduced from ref. ²⁶² with permission from the Royal Society of Chemistry.	112
Figure 8.4. Photochromism of four spiropyran-based main-chain homopolymers investigated via UV-vis spectroscopy. (A-D) UV-vis spectra recorded for polymer solutions irradiated with 330 nm. The red dashed lines denote the spectra recorded post-330 nm irradiation; the purple solid lines represent the spectra recorded immediately after 330 nm irradiation; the green solid lines indicate the spectra recorded after 500 nm irradiation of the 330 nm irradiated solutions (E-H) Control experiments: the DCM solvent was first irradiated with 330 nm, after which the polymer solution was added. The laser power at 330 nm and 500 nm irradiation was kept at $6.5 \text{ mW} \pm 5.2\%$ and $8.5 \text{ mW} \pm 13\%$, respectively. (I-L) Plots of $A_{\text{MC}}/A_{\text{SP}}$ vs time for P_{SP1} , P_{SP2} , P_{SP3} and P_{SP4} , respectively. Note that the protonated form of MC (MCH⁺) also exists but is grouped into the 'MC' label in A_{MC} (i.e., absorbance of the opened form) for the sake of simplicity. The absorbance of the 'MC' label in this case (A_{MC}) corresponds to the λ_{max} of the colored species in the visible range, and the A_{SP} refers to the absorbance at λ_{max} of the respective spiropyran. The $A_{\text{MC}}/A_{\text{SP}}$ ratio is used instead of A_{MC} to factor in the concentration difference between experiments assuming $A_{\text{MC}}/A_{\text{SP}}$	

$\sim c_{MC}/c_{SP}$ with $\epsilon_{MC}/\epsilon_{SP} = \text{constant}$. The number of photons (N_p) was converted into time via Eq. 11.2. The gray areas in (J-L) highlight the actual photochromic response of polymer solutions upon 330 nm irradiation. Reproduced from ref.²⁶² with permission from the Royal Society of Chemistry. 113

Figure 8.5. Halochromism of P_{SP1} , P_{SP2} , P_{SP3} , P_{SP4} in DCM investigated by UV-vis spectroscopy. (A-D) TFA addition (1.0 eq), (E-H) MsOH addition (1.0 eq). Time until equilibration is indicated. Molar concentration of SP moiety: 100 – 150 μM . (I-N) Comparison of the kinetics among four polymers upon acid addition. Normalized absorbance was used in Figure 4M and N to enable a qualitative comparison of the response rate of the polymers toward TFA and MsOH acid. The A_{MCH^+}/A_{SP} ratio is used instead of A_{MCH^+} to factor in the concentration difference between experiments assuming $A_{MCH^+}/A_{SP} \sim c_{MCH^+}/c_{SP}$ with $\epsilon_{MCH^+}/\epsilon_{SP} = \text{constant}$. A_{MCH^+} refers to the absorbance (A) of the **MCH⁺** form at λ_{max} in the visible range, and A_{SP} refers to the absorbance of the pristine SP at λ_{max} . Reproduced from ref.²⁶² with permission from the Royal Society of Chemistry. 116

Figure 8.6. Synthesis route for oligomers and block copolymers decorated with nitro-spiropyran side groups. The approach constitutes a series of hydroxyl-yne click and TBAF-deprotection chemistries to grow the backbone, followed by thiol-Michael click and hydroxyl-yne click reactions to attach nitro-spiropyran as side groups. 119

Figure 8.7. Synthesis and characterization of spiropyran-based oligomer, TBDMSO-[SP-NO₂]₂-OTBDMS. (A) Stacked sectional ¹H NMR spectra recorded in CDCl₃. (B) THF-SEC traces of oligomeric sequences. (C) Summary of molar mass determined from NMR and SEC (based on a PMMA calibration). 120

Figure 8.8. UV-vis study of photoisomerization of TBDMSO-[SP-NO₂]₂-OTBDMS in THF ($c \sim 10^{-5}$ M). The oligomer solution was irradiated with a monochromatic wavelength of 365 nm ($P = 5.0$ mW) and UV-vis spectra were recorded at 1 s interval. 121

Figure 8.9. Synthesis of PDMS-[SP-NO₂]₄-PDMS block copolymer. (A) THF-SEC traces and (B) summary of molar mass determined by NMR and SEC. 122

Figure S8.1. UV-vis spectra recorded for P_{SP1} , P_{SP2} , P_{SP3} and P_{SP4} before and after 330 nm irradiation in either toluene or DMAc solvent. Molar concentrations are between 50 and 150 μM 327

Figure S8.2. ¹H NMR spectra (left) and DMAc-SEC traces (right) of P_{SP1} solution before and after addition of TFA (1.0 eq) and MsOH (1.0 eq). The MsOH-added solution was subsequently quenched with 2.0 eq Et₃N. As can be seen in the NMR spectrum of the Et₃N-quenched polymer solution (top, blue), a small degree of degradation (most likely hydrolysis) was observed (signals marked with an asterisk). The breakage of one bond in the main-chain can cause significant shift in the SEC traces. In addition, side reactions arising from the internal acrylate C-C double bonds (e.g., [2+2]-cyclization) and the damage of the chromophore can be excluded as there is no change in the corresponding resonances of the acrylate C-C double bonds and the chromophore in the Et₃N-quenched polymer solution and the pristine solution. 327

Figure S8.3. ¹H NMR spectra (left) and DMAc-SEC traces (right) of P_{SP2} solution before and after addition of TFA (1.0 eq) and MsOH (1.0 eq). The MsOH-added solution was subsequently quenched with 2.0 eq Et₃N. Insignificant damage was shown in the NMR spectrum of the Et₃N-quenched polymer solution and the corresponding SEC traces. 328

Figure S8.4. ¹H NMR spectra (left) and DMAc-SEC traces (right) of P_{SP3} solution before and after addition of TFA (1.0 eq) and MsOH (1.0 eq). The MsOH-added solution was subsequently quenched with 2.0 eq Et₃N. Significant degradation (due to hydrolysis of ester bonds) was observed in the MsOH-added solution. The NMR spectrum of the MsOH-added solution quenched with Et₃N (top, blue) also indicates significant degradation (resonances marked with an asterisk). The chromophore and the internal acrylate C-C double bonds remain intact as shown in the NMR spectrum (top, blue). 328

Figure S8.5. ¹H NMR spectra (left) and DMAc-SEC traces (right) of P_{SP4} solution before and after addition of TFA (1.0 eq) and MsOH (1.0 eq). The MsOH-added solution was subsequently quenched with 2.0 eq Et₃N. Both NMR spectrum and SEC traces confirm the resistance of the polymer solution against hydrolysis induced upon MsOH addition. 329

Figure S8.6. UV-vis spectra of P_{SP2} polymer film on a quart slide before and after 330 nm irradiation. The film was generated by spin-coating of the P_{SP2} solution (60 mg·mL⁻¹) in toluene and subsequently dried at reduced vacuum for 24h before the irradiation experiment (330 nm irradiation, $P = 6.5$ mW \pm 6.5%). 329

Figure S8.7. DLS size distribution (Volume%) recorded for four polymers after addition of MsOH (1.0 eq) acid in DCM at 25 °C. The polymer solutions were kept in the dark overnight before the measurement.	330
Figure S8.8. Synthesis route for M_{SP1} and P_{SP1}	330
Figure S8.9. Synthesis route for monomer M_{SP2} and polymer P_{SP2}	332
Figure S8.10. Synthesis route for M_{SP3} and P_{SP3}	334
Figure S8.11. Synthesis route for M_{SP4} and P_{SP4}	335
Figure S8.12. Synthesis of spiropyran-based oligomers.	337
Figure S8.13. Synthesis of block copolymers from PDMS and spiropyran.	342
Figure S8.14. ¹ H NMR spectrum (600 MHz, 16 scans) of compound 1 recorded in CDCl ₃	344
Figure S8.15. Sectional COSY spectrum of compound 1 recorded in CDCl ₃	345
Figure S8.16. ¹ H NMR spectrum (600 MHz, 16 scans) of SP1-diOH recorded in CDCl ₃	345
Figure S8.17. Sectional COSY spectrum of compound SP1-diOH recorded in CDCl ₃	346
Figure S8.18. ¹³ C (151 MHz) NMR spectrum of SP1-diOH in CDCl ₃	347
Figure S8.19. ¹ H NMR spectrum (600 MHz, 16 scans) of SP1-mOH recorded in CDCl ₃	347
Figure S8.20. COSY sectional spectrum of compound SP1-mOH recorded in CDCl ₃	348
Figure S8.21. ¹ H NMR spectrum (600 MHz, 16 scans) of M_{SP1} recorded in CDCl ₃	348
Figure S8.22. COSY sectional spectrum of compound M_{SP1} recorded in CDCl ₃	349
Figure S8.23. ¹³ C (151 MHz) NMR spectrum of M_{SP1} in CDCl ₃	349
Figure S8.24. ¹ H NMR spectrum (600 MHz, 32 scans) of P_{SP1} recorded in CDCl ₃	350
Figure S8.25. COSY sectional spectrum of compound P_{SP1} recorded in CDCl ₃	350
Figure S8.26. ¹ H NMR spectrum (600 MHz, 16 scans) of compound 2 recorded in CDCl ₃	351
Figure S8.27. ¹³ C (151 MHz) NMR spectrum of compound 2 in CDCl ₃	351
Figure S8.28. ¹ H NMR spectrum (600 MHz, 16 scans) of SP2-mOH recorded in CDCl ₃	352
Figure S8.29. COSY sectional spectrum of compound SP2-mOH recorded in CDCl ₃	352
Figure S8.30. ¹³ C (151 MHz) NMR spectrum of SP2-mOH in CDCl ₃	353
Figure S8.31. ¹ H NMR spectrum (600 MHz, 16 scans) of M_{SP2} recorded in CDCl ₃	353
Figure S8.32. COSY sectional spectrum of compound M_{SP2} recorded in CDCl ₃	354
Figure S8.33. ¹³ C (151 MHz) NMR spectrum of M_{SP2} in CDCl ₃	354
Figure S8.34. ¹ H NMR spectrum (600 MHz, 32 scans) of P_{SP2} recorded in CDCl ₃	355
Figure S8.35. COSY sectional spectrum of compound P_{SP2} recorded in CDCl ₃	355
Figure S8.36. ¹ H NMR spectrum (600 MHz, 16 scans) of SP3-diOH recorded in CDCl ₃	356
Figure S8.37. COSY sectional spectrum of compound SP3-diOH recorded in CDCl ₃	356
Figure S8.38. ¹ H NMR spectrum (600 MHz, 16 scans) of SP3-mOH recorded in CDCl ₃	357
Figure S8.39. COSY sectional spectrum of compound SP3-mOH recorded in CDCl ₃	357
Figure S8.40. ¹ H NMR spectrum (600 MHz, 16 scans) of M_{SP3} recorded in CDCl ₃	358
Figure S8.41. COSY sectional spectrum of compound M_{SP3} recorded in CDCl ₃	358
Figure S8.42. ¹³ C (151 MHz) NMR spectrum of M_{SP3} in CDCl ₃	359
Figure S8.43. ¹ H NMR spectrum (600 MHz, 32 scans) of P_{SP3} recorded in CDCl ₃	359
Figure S8.44. COSY sectional spectrum of compound P_{SP3} recorded in CDCl ₃	360
Figure S8.45. ¹ H NMR spectrum (600 MHz, 16 scans) of compound 3 recorded in CDCl ₃ . By-products are marked with a cross.	360
Figure S8.46. ¹³ C (151 MHz) NMR spectrum of compound 3 in CDCl ₃	361
Figure S8.47. ¹ H NMR spectrum (600 MHz, 16 scans) of SP4-mOH recorded in CDCl ₃	361
Figure S8.48. COSY sectional spectrum of compound SP4-mOH recorded in CDCl ₃	362
Figure S8.49. ¹³ C (151 MHz) NMR spectrum of SP4-mOH in CDCl ₃	362
Figure S8.50. ¹ H NMR spectrum (600 MHz, 16 scans) of M_{SP4} recorded in CDCl ₃	363
Figure S8.51. COSY sectional spectrum of compound M_{SP4} recorded in CDCl ₃	363
Figure S8.52. ¹³ C (151 MHz) NMR spectrum of M_{SP4} in CDCl ₃	364
Figure S8.53. ¹ H NMR spectrum (600 MHz, 32 scans) of P_{SP4} recorded in CDCl ₃	364
Figure S8.54. COSY sectional spectrum of compound P_{SP4} recorded in CDCl ₃	365
Figure S8.55. ¹ H NMR spectrum of HO-C₁₆-OTBDMS in CDCl ₃	365

Figure S8.56. ^{13}C NMR spectrum of HO-C₁₆-OTBDMS in CDCl_3	366
Figure S8.57. ^1H MR spectrum of yne-C₁₆-OTBDMS in CDCl_3	366
Figure S8.58. ^{13}C NMR spectrum of yne-C₁₆-OTBDMS in CDCl_3	366
Figure S8.59. ^1H NMR spectrum of HO-SP-NO₂ in CDCl_3	367
Figure S8.60. ^1H NMR spectrum of yne-SP-NO₂ in CDCl_3	367
Figure S8.61. COSY spectrum of yne-SP-NO₂ in CDCl_3	368
Figure S8.62. ^{13}C NMR spectrum of yne-SP-NO₂ in CDCl_3	368
Figure S8.63. ^1H NMR spectrum of TBDMSO-[EA]₂-OTBDMS in CDCl_3	369
Figure S8.64. COSY spectrum of TBDMSO-[EA]₂-OTBDMS in CDCl_3	369
Figure S8.65. ^{13}C NMR spectrum of TBDMSO-[EA]₂-OTBDMS in CDCl_3	370
Figure S8.66. ^1H NMR spectrum of TBDMSO-[OH]₂-OTBDMS in CDCl_3	370
Figure S8.67. COSY sectional spectrum of TBDMSO-[OH]₂-OTBDMS in CDCl_3	371
Figure S8.68. ^{13}C NMR spectrum of TBDMSO-[OH]₂-OTBDMS in CDCl_3	371
Figure S8.69. ^1H NMR spectrum of TBDMSO-[SP-NO₂]₂-OTBDMS in CDCl_3	372
Figure S8.70. ^{13}C NMR spectrum of TBDMSO-[SP-NO₂]₂-OTBDMS in CDCl_3	372
Figure S8.71. COSY NMR spectrum of TBDMSO-[SP-NO₂]₂-OTBDMS in CDCl_3	373
Figure S8.72. ^1H NMR spectrum of HO-[EA]₂-OH in CDCl_3	373
Figure S8.73. ^1H NMR spectrum of PDMS-[EA]₄-PDMS in CDCl_3	374
Figure S8.74. ^1H NMR spectrum of PDMS-[OH]₄-PDMS in CDCl_3	374
Figure S8.75. ^1H NMR spectrum of PDMS-[SP-NO₂]₄-PDMS in CDCl_3	375

Figure 9.1. SAXS profile of bisimine-Si hybrid block copolymers, PDMS-[B]_n-PDMS , $n = 3, 5, 7$. Details on the structure and synthesis can be found in Chapter 4.	125
Figure 9.2. Zoomed-in TEM image of PDMS-[B]₅-PDMS thin film on carbon substrate. The observed nanostructure can be lamella or out-of-plane cylinders. Full TEM micrographs of other bisimine-based block copolymers are provided in Experimental part, Section 9.5.2, Figure S9.1-S9.6.....	126
Figure 9.3. SAXS profiles of PDMS-[H]₄-PDMS block copolymer before and after irradiation. The SAXS samples were prepared from the same stock solution which was irradiated with LED lights: $\lambda_{\text{max}} = 400$ nm for forward photoisomerization and $\lambda_{\text{max}} = 365$ nm for back photoisomerization. Details on the synthesis and structure of the block copolymer were reported in chapter 7.....	127

Figure S9.1. TEM micrograph of the triblock copolymer samples PDMS-[B]₂-PDMS used to extract the periodicity from the power spectrum in Figure S9.7 . The bright spots are bubbles resulting from the sample preparation.	376
Figure S9.2. TEM micrograph of the triblock copolymer samples PDMS-[B]₃-PDMS used to extract the periodicity from the power spectrum in Figure S9.7	377
Figure S9.3. TEM micrograph of the triblock copolymer samples PDMS-[B]₄-PDMS used to extract the periodicity from the power spectrum in Figure S9.7	378
Figure S9.4. TEM micrograph of the triblock copolymer samples PDMS-[B]₅-PDMS used to extract the periodicity from the power spectrum in Figure S9.7	379
Figure S9.5. TEM micrograph of the triblock copolymer samples PDMS-[B]₆-PDMS used to extract the periodicity from the power spectrum in Figure S9.7	380
Figure S9.6. TEM micrograph of the triblock copolymer samples PDMS-[B]₇-PDMS used to extract the periodicity from the power spectrum in Figure S9.7	381
Figure S9.7. Power spectra of the triblock copolymers TEM micrographs. The red circles indicate the peak maxima used to extract the domain spacing of the phase separation.....	382
Figure S9.8. Stack sectional ^1H NMR spectra (in CDCl_3 or CD_2Cl_2) of PDMS-[H]₄-PDMS block copolymer before and after irradiation with LEDs. The solution was withdrawn from the same stock solution to ensure the homogeneity of the sample in SAXS measurements.	383

Figure S9.9. DSC thermogram of hydrazone oligomer, **HO-[H]₄-OH**. The curve was taken from the second heating cycle. 383

Figure 10.1. Synthesis of main-chain block copolymer via head-to-tail ADMET polymerization and hydroxyl-yne click polymerization. 129

Figure 10.2. The sequence-defined strategy to synthesize main-chain α -bismine oligomers and block copolymers. This approach relies on the hydroxyl-yne click and TBAF-deprotection chemistry. For hydrazone, The TBAF-deprotection step causes undesirable isomerization of the photoswitch. As a compromise, cross-metathesis reaction was used instead, in combination with hydroxyl-yne click reaction for hydrazone main-chain oligomers and block copolymer synthesis. 130

Figure 10.3. The strategy to enhance solid-state photoswitching efficiency. 131

Figure 10.4. Main-chain hydrazone-based polymers showed photomanipulatable hydrodynamic volume and glass transition temperature. In the context of block copolymer nanostructure, such changes in solution and solid-state properties are indicative of possible alternation of the volume fraction of the photoswitchable block upon irradiation. 131

Figure 10.5. Synthesis of spiropyran-based polymers. The photochromism of spiropyrans is generally strongly dependent on the identity of the substituents on the aromatic moieties. We learned that nitro-substituted spiropyrans are more efficient in terms of photochromism. As the dramatic polarity change is a more attractive feature of spiropyrans, the design of block copolymers bearing spiropyrans as pendant groups is more convenient in terms of synthesis. 132

Figure 10.6. For Si-based block copolymers, installing fluorinated groups into the organic block has been shown to be beneficial for the orientation of block copolymer thin-film nanostructures, especially lamella and cylinders.²⁰² For the photoswitchable hybrid block copolymers obtained in this thesis, post-modification is a facile and efficient approach to decorate fluorinated side chains to the photoswitchable block, balancing the surface tension (γ) between Si-based and the organic blocks. 133

List of Symbols and Abbreviations

Symbol / Abbreviation	Full notation
χ	Flory-Huggins interaction parameter
$\tau_{1/2}$	Thermal half-life
λ_{irr}	Irradiation wavelength
A	Absorbance
ADMET	Acyclic Diene METathesis
AFM	Atomic Force Microscopy
ARGET ATRP	Activators ReGenerated by Electron Transfer ATRP
ATRP	Atom Transfer Radical Polymerization
AzB	Azobenzene
BCC	Body-Centered Cubic
BCP	Block CoPolymer
Cy	Cyclohexane
\mathcal{D}	Dispersity
DABCO	1,4-Diazabicyclo(2.2.2)octan
DASAs	Donor–Acceptor Stenhouse Adducts
DBU	1,8-Diazabicyclo(5.4.0)undec-7-ene
DCC	N,N'-dicyclohexylcarbodiimide
DCM	Dichloromethane
DIAD	Dilsopropyl AzoDicarboxylate
DLS	Dynamic Light Scattering
DOSY	Diffusion Ordered Spectroscopy
DSC	Differential Scanning Calorimetry
EA	Ether Acrylate
EtOAc	Ethyl Acetate
f	Volume fraction
FCC	Face-Centered Cubic
GI-SAXS	Grazing-Incidence SAXS
Gyr	Gyroid
HCP	Hexagonally Closed Pack
HG-II	Hoveyda-Grubbs 2 nd generation catalyst
HI	Hemiindigo
HSS	Hindered Stiff Stilbene
HTI	Hemithioindigo
Lam	Lamella
LC-MS	Liquid Chromatography–Mass Spectrometry
LED	Light-Emitting Diode
MBP	methyl 2-bromopropionate
MC	Merocyanine

Me ₆ TREN	tris[2-(dimethylamino)ethyl]amine
M_n	Number-Averaged Molar Mass
M_p	Peak Molar Mass
MWD	Molecular Weight Distribution
N	Degree of polymerization
NHC	N-Heterocyclic carbene
NMR	Nuclear Magnetic Resonance
N_p	Number of photons
OA	Overcrowded Alkene
oNB	ortho-nitro benzyl
P	Light source power
PDMS	Polydimethylsiloxane
PEG	Polyethylene glycol
PI	Polyisoprene
PMMA	Poly(methyl methacrylate)
PS	Polystyrene
q^*	Principal Bragg reflection peak
RAFT	Reversible Addition–Fragmentation chain-Transfer polymerization
RDRP	Reversible-Deactivation Radical Polymerization
ROMP	Ring Opening Metathesis Polymerization
ROP	Ring Opening Polymerization
rROP	Radical Ring Opening Polymerization
SAXS	Small Angle X-ray Scattering
SCNPs	Single chain nanoparticles
SEC	Size-Exclusion Chromatography
Sn(EH) ₂	tin(II) 2-ethylhexanoate
SP	Spiropyran
SS	Stiff Stilbene
TBDMS-	<i>tert</i> -Butyldimethylsilyl-
TEM	Transmission Electron Microscopy
T_g	Glass transition temperature
TGA	Thermogravimetric analysis
T_m	Melting temperature
Tol	Toluene

Publications and Manuscripts included in this PhD research

1. *Photoswitchable block copolymers based on main-chain α -bisimines*

Thai, L. D.; Guimarães, T. R.; Spann, S.; Goldmann, A. S.; Golberg, D.; Mutlu, H.; Barner-Kowollik, C. *Polym. Chem.* **2022**, 13, 5625-5635.

Parts of this publication are included in **Chapter 3**.

2. *Molecular photoswitching of main-chain α -bisimines in solid-state polymers*

Thai, L. D.; Guimarães, T. R.; Chambers, L. C.; Kammerer, J. A.; Golberg, D.; Mutlu, H.; Barner-Kowollik, C. *J. Am. Chem. Soc.* **2023**, 145, 14748-14755.

Parts of this publication are included in **Chapter 5**.

3. *Main-chain macromolecular hydrazone photoswitches*

Thai, L. D.[⊥]; Fanelli, J.[⊥]; Munaweera, R.; O'Mara, M. L.; Barner-Kowollik, C.; Mutlu, H. *Angew. Chem. Int. Ed.* **2024**, 63, e202315887.

[⊥]co-first author

Parts of this publication are included in **Chapter 7**.

4. *Photo- and halochromism of spiropyran-based main-chain polymers*

Thai, L. D.; Kammerer, J. A.; Mutlu, H.; Barner-Kowollik, C. *Chem. Sci.* **2024**, 15, 3687-3697.

Parts of this publication are included in **Chapter 8**.

5. *Access to main-chain photoswitching polymers via hydroxyl-yne click polymerization*

Thai, L. D.; Kammerer, J. A.; Théato, P.; Mutlu, H.; Barner-Kowollik, C. *ACS Macro Lett.* **2024**, 13, 6, 681–687.

Parts of this publication are included in **Chapters 3, 5 and 6**.

6. *Sequence-defined main-chain photoswitchable macromolecules with odd-even effect controlled properties*

Thai, L. D.; Kammerer, J. A.; Golberg, D.; Mutlu, H.; Barner-Kowollik, C. *Chem* **2024**, in press.

Parts of this manuscript are included in **Chapters 4, 5, 6 and 9**.

Conference Contributions

Molecular photoswitching of main-chain α -bisimines in solid-state polymers

Thai, L. D.; Guimarães, T. R.; Chambers, L. C.; Kammerer, J. A.; Golberg, D.; Mutlu, H.; Barner-Kowollik, C., *Queensland Annual Chemistry Symposium* (QACS), November **2023**, Brisbane, Australia. (Best oral presentation)

Main-chain macromolecular hydrazone photoswitches

Thai, L. D.; Fanelli, J.; Munaweera, R.; O'Mara, M. L.; Barner-Kowollik, C.; Mutlu, H., *The 38th Australasian Polymer Symposium*, February **2024**, Auckland, New Zealand. (Oral presentation)

Access to main-chain photoswitching polymers via head-to-tail ADMET polymerization

Thai, L.D.; et al., *the 50th World Polymer Congress, IUPAC MACRO*, July **2024**, Warwick, UK. (Oral presentation)

Acknowledgements

It's summertime now in Europe. Sitting alone in a room located somewhere in Germany, more than 9300 km away from my hometown in Viet Nam, trying to write something but my head is empty. I wonder how things have started that led the way for me to become the person I am today. I was born and grew up with four other siblings in a small village in the south of Viet Nam. Not so long before I was born, my parents had migrated from their birthplace in the central region with the hope of finding new land to build a better life. I remember the old days when an old motorbike was the most expensive thing we had in our home, the old days when we grabbed some rice with sugar and peanuts for breakfast before getting ready for work and school, the old days when it rained so heavily that my father had to carry me to school on slippery, muddy roads full of potholes. Back then, going to school was not easy as most families were still struggling to make ends meet. I remember many of my childhood friends dropped out of school when they were just 12 or 15 years old. This was not because of their lack of desire for education but rather because of poverty and lack of support. My parents couldn't finish school due to the war back then. But they did not let that same fate happen to us. I feel grateful to my parents for their upbringing and their wholehearted support for more than 28 years. Seeing my parents working hard every day so that we could have a warm meal at home installed in me a sense of appreciation of things I have received and achieved in life. I would like to take this opportunity to thank Mom and Dad for your relentless love and support throughout my life journey. You have sacrificed so much so that I could have a better future, so that I could see the world outside.

Of course, this PhD journey would not have been possible if it were not for my principal supervisor, Prof. Christopher Barner-Kowollik. I thank you so much for giving me such a precious opportunity to explore and implement many research ideas within the scope of this project. In my wildest dream, I never thought I would be so motivated and driven by a PhD research topic. It was a mundane day in April 2020 during the Covid pandemic when I saw the advertisement about this PhD position. At the time, I had no idea what this project really was about, but still I sent my application anyway. Then came the interview and quickly after that came the offer. I couldn't describe how happy and thrilled I was because everything happened so fast, and I had no time to process that. In hindsight, it was my right decision to embark on this journey. Even if it wasn't, I still learned so much from you, intellectually and professionally. I also want to thank Jun. Prof. Hatice Mutlu for the intellectual support throughout my PhD journey, especially for the help I got when I first came to Germany. Many thanks to my colleagues for your day-to-day help and assistance over the last three years, without which it would not have been easy for me.

To my friends back home in Viet Nam and to my new friend(s) in Germany and Australia, I appreciate the friendship we have forged. My life becomes more fulfilling when I have you by

my side. The experience you and I have had together, bad or good, is always with me and always an inseparable part of my life. We all have differences, but we accept each other regardless of where we're from, what we do and who we love in life.

Thank you all for everything.

Chapter 1: Introduction, Thesis Objectives and Thesis Outline

1.1. Introduction

Compared to other types of polymers, block copolymers are unique on account of their ability to self-assemble into nanostructures in the bulk and thin films. Block copolymer nanostructures, such as spheres, cylinders, gyroids and lamella – typically in the range of 10-100 nm – are highly promising for diverse nanotechnology-based applications, most importantly for **block copolymer lithography** or **nanopatterning**.¹ Specifically, the periodically ordered thin-film nanopatterns generated from BCPs serve as templates which can be transferred to target substrates to fabricate nanostructured surfaces and devices. Such nano template transfer technology is vital in many commercial endeavors, such as the microelectronics industry.²

One of the research aims of BCPs is achieving BCP thin-film morphologies with smaller and smaller domain spacing, which would allow for the fabrication of ultra dense nanopatterned templates, critically important for the production of high performance microelectronic components.³ Until now, BCP nanostructures with sub-10 nm, sub-5 nm or even sub-2 nm have been reported by increasing block incompatibility via employing Si-based or fluorinated blocks as well as decreasing block length.⁴⁻⁹

However, conventional block copolymers nanostructures are static once formed, suggesting that it is very challenging to manipulate them, for example reversibly/irreversibly switching from one ordered structure to another ordered one. There is further substantial interest in the possibility to fine tune and manipulate BCP nanostructures by physical and chemical methods as well as using external stimuli. It is ideal to switch from one ordered to another ordered nanostructure or from a disordered state to an ordered nanostructure in one single substrate, allowing one to access different or even new nanostructured morphologies.

Polymers that change their behaviors and/or properties upon irradiation with light are termed photo- or light-responsive polymers, belonging to a broader class of soft materials, i.e., stimuli-responsive materials. Other stimuli, including heat,¹⁰ pH,¹¹ and vapor,¹² have also been adopted in stimuli-sensitive materials. However, it appears that light is the most intriguing and highly sought-after stimulus, as it offers traceless and contactless control with superior spatial and temporal resolution.¹³ The photo-response of light-sensitive moieties can be either irreversible (i.e., photocleavage, as seen for *o*-nitrobenzyl esters¹⁴) or reversible (e.g., photoisomerization, as seen for photoswitches¹⁵). Photoswitches are molecules that show reversible configurational change upon interaction with light of suitable wavelengths, mostly via photoisomerization and/or photocyclization. Besides the potentially large geometric

change, significant alterations in the physical and chemical properties of photoswitches can result from photoswitching.

In light of the desirable feature of light as an external trigger, incorporation of light-sensitive molecules – especially photoswitches – into block copolymers may be an excellent strategy for precisely and remotely controlling the self-assembly of block copolymers, introducing the concept of ‘Photodynamic Block Copolymer Lithography’. Establishing synthetic principles of photodynamic block copolymer nanolithography is the ultimate goal of the current thesis. Considering morphological transition, it is ideal to observe such transformation in real time via High-Resolution Transmission Electron Microscopy (HR-TEM). To the best of our knowledge, in-situ TEM has never been used to visualize in real time the morphology transformation of stimuli-responsive polymer thin films induced by light. This far-reaching aim will be explored via inter-group collaboration within our team at the Queensland University of Technology (QUT).

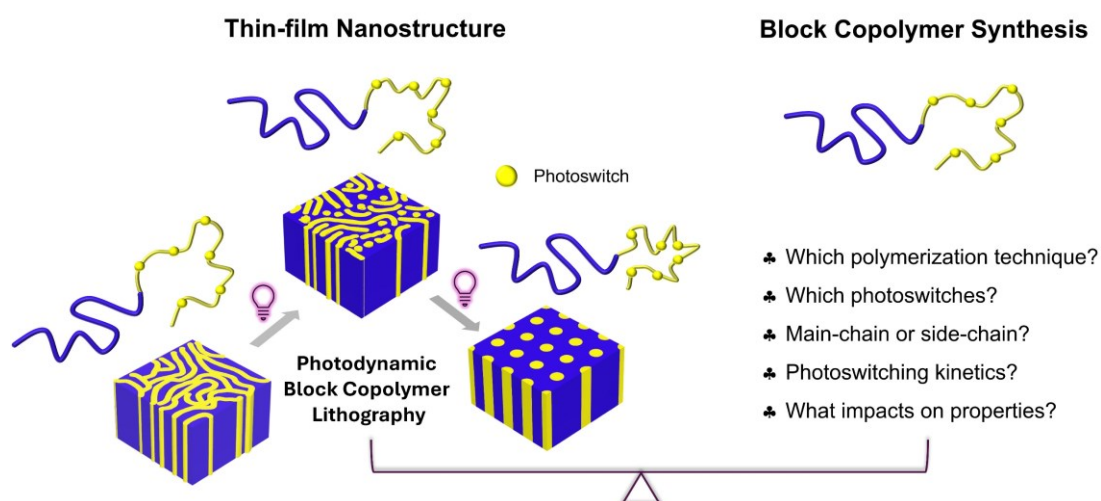


Figure 1.1. Illustration of the ultimate goal of the project. Photodynamic block copolymer lithography refers to the alteration of block copolymer thin-film nanostructures upon illumination with light. Such transformation should ideally be observed in real-time via Transmission Electron Microscopy (TEM). However, the current thesis aims to establish the synthetic foundation for the preparation of photoswitchable block copolymers that can be employed to realize photodynamic block copolymer lithography.

1.2. Thesis objectives

In order to realize the ultimate goal of establishing photodynamic block copolymer lithography, a toolbox of several synthetic aspects of photoswitchable block copolymers need to be addressed. Hence, the current thesis was conducted with the following key objectives in mind.

First, a review of literature is critical to understand and identify the current state and research gaps in the field of block copolymers (**Chapter 2**). Synthetically, main-chain photoswitchable polymers are scarcely explored compared to the side-chain design. There are also limited polymerization techniques to fabricate such polymers. Due to significantly larger geometrical difference among isomers, the main-chain feature is ideal and critically required in the context of the thesis. Therefore, **the second objective** is to explore and establish efficient synthetic methods to prepare main-chain photoswitchable polymers and block copolymers on the example of α -bisimine photoswitch (**Chapters 3 and 4**). **The third objective** concerns the solid-state photoisomerization efficiency of photoswitchable polymers (**Chapter 5**), which is one of the key factors to enable the photo-induced transformation of block copolymer thin film or bulk morphology. **The fourth objective** of the thesis aims to investigate potential effects of polymerization techniques as well as dispersity on the photoisomerization kinetics of the embedded photoswitch (**Chapter 6**). **The fifth objective** is to explore the possibilities to integrate other photoswitches other than α -bisimine into polymers (**Chapters 7 and 8**), which is important because each type of photoswitches has its own advantages and disadvantages. Establishing a small library of promising and diverse photoswitches provides more flexibility on the road towards photodynamic block copolymer lithography. **The sixth and final objective** is to investigate the bulk and/or thin-film morphology of the block copolymers successfully synthesized in the current thesis (**Chapter 9**). Insights into phase separation as well as arising problems assist the planning and strategy development for the next phase of the project.

1.3. Thesis outline

Chapter 2: Herein, common strategies used to manipulate block copolymer thin-film and bulk morphologies will be discussed. Following that the discussion transitions towards the integration of photoswitches into polymeric materials and block copolymers. Subsequently, research gaps in the realm of photoswitchable block copolymers for the manipulation of block copolymer morphologies will be explored. Analysis of these topics helps to assess the novelty of the thesis, which aims to establish strategies to effectively incorporate photoswitches into block copolymers, laying the foundations for photodynamic block copolymer lithography.

Chapter 3: To synthesize main-chain photoswitchable block copolymers, head-to-tail Acyclic Diene METathesis (ADMET) polymerization is initially chosen as the starting point. The model photoswitch was α -bisimine due its ease of synthesis and scalability. However, poor control over chain extension has been observed in this case. Subsequently, head-to-tail hydroxyl-yne click polymerization is further developed to prepare α -bisimine main-chain block copolymers. This specific variant of click chemistry offers key desirable features, including metal-free catalysis and fast reaction kinetics. Nevertheless, well-defined block copolymers are eluded. Consequently, a more potent strategy is required and reported later in chapter 4.

Chapter 4: Herein, a sequence-defined approach is introduced to prepare well-defined main-chain photoswitching oligomers and block copolymers on the example of α -bisimines. We harness the click-type nature of hydroxyl-yne reaction and deprotection chemistry to synthesize these macromolecules. The successful synthesis of block copolymers reported here encourages the inclusion of other photoswitches into block polymer, which is described in chapters 7 and 8.

Chapter 5: A general, yet simple efficient strategy to enhance the photoisomerization (or photoswitching) in the solid state is established herein. Since the final application of photoswitching block copolymers reported in the current thesis is for solid-state morphological switching, a high efficiency of the photoswitching in the solid state is therefore required.

Chapter 6: The chapter investigates the impact of polymerization techniques as well as dispersity on the solution (photo)isomerization kinetics of the α -bisimine photoswitch, particularly monitored via ^1H NMR and UV-vis spectroscopy.

Chapter 7: The chapter reports the synthesis and studies the photoisomerization of hydrazone-based main-chain homopolymers and block copolymers. Hydrazones are selected due to the high stability of the metastable isomers and visible light absorption feature. The *E/Z* photoisomerization of hydrazones leads to large geometrical changes and thus it is essential to incorporate them as main-chain repeating units. Head-to-tail ADMET polymerization and a sequence-defined approach are employed to prepare macromolecular hydrazone photoswitches. The impact of the photoisomerization on solution- and solid-state properties of the synthesized hydrazone-based homopolymers is also studied.

Chapter 1: Introduction, Thesis Objectives and Outline

Chapter 8: Herein, the impact of regioisomers on the photo- and halochromism of spiropyran main-chain homopolymers is assessed. In addition, we introduce a strategy to incorporate a spiropyran scaffold that offers higher photoswitching efficiency into block copolymer. The substantial change in polarity of spiropyran upon irradiation is attractive to remotely manipulate the Flory-Huggins interaction parameter of the resulting block copolymer.

Chapter 9: The chapter describes a preliminary study on the bulk and thin-film morphologies of photoswitchable block copolymers. The obtained results act as guidance for future plans and strategies to implement and develop photodynamic block copolymer lithography.

Chapter 2: Literature Review

Block Copolymers (BCPs) are a broad research topic in terms of their synthesis, characterization and application. The current chapter is strictly limited to exploring the fundamentals of block copolymer self-assembly in bulk or in thin films. This aspect is important to understand the strategies that have been employed in the literature to control and manipulate the morphology of BCPs. Before transitioning to photoswitchable BCPs, a brief introduction to photoswitches and their applications in soft materials will be given in order to highlight the great potential to transfer their photo-controllable properties to BCPs for photodynamic block copolymer lithography.

2.1. Block copolymer nanostructures

Block copolymers (BCPs) are a specific type of copolymer. The IUPAC definition states:¹⁶ “In the constituent macromolecules of a block copolymer, adjacent blocks are constitutionally different, i.e., adjacent blocks comprise constitutional units derived from different species of monomer or from the same species of monomer but with a different composition or sequence distribution of constitutional units.” Those distinct blocks are covalently connected and consequently the resulting block copolymers feature different properties compared to the corresponding statistical/random copolymers.

From a synthetic point of view, non-conjugated BCPs were initially synthesized via living polymerization techniques such as anionic and cationic polymerization.^{17,18} Later, with the advent of reversible-deactivation radical polymerization (RDRP) techniques, block copolymers preparation proceeded efficiently via, for example, Atom Transfer Radiation Polymerization (ATRP)¹⁹ or Reversible Addition-Fragmentation Chain Transfer (RAFT) polymerization.²⁰ In addition, block copolymers can be prepared via the combination of one of those methods with step growth polymerization techniques, e.g., ADMET (Acyclic Diene METathesis) or the use of click chemistry.^{21,22}

The unique feature of BCPs is perhaps the microphase separation between/among the constituting blocks that leads to various ordered nanostructures.²³⁻²⁵ These ordered nanostructures are typically spheres, cylinders, gyroids and lamella with domain size in the range of 10-100 nm. Uncommon morphologies also exist, such as hexagonally closed-packed spheres²⁶, and highly asymmetric lamella^{27,28}. Generally, there are three main prerequisites, according to Self-Consistent Mean Field theory (SCFT),²⁹ for AB-type diblock copolymers (diBCPs) to form microphase-separated morphologies: volume fraction f of each block, degree of polymerization N , i.e., number of repeating units or the chain length, and the degree of immiscibility between two blocks reflected through the so-called Flory-Huggins interaction parameter (χ). An illustration for the last requirement is the distinctive hydrophilic and hydrophobic nature of the two constituting blocks. The more chemically different the blocks

are, the more segregation is expected. The product of χN represents the segregation power and has to be larger than 10 for the formation of an ordered structure. The volume fraction f of each block affects the equilibrium morphology as depicted in Figure 2.1.

Block copolymer nanostructures (either in the bulk or thin film) are frequently characterized and analyzed by scattering techniques, such as Small Angle X-ray Scattering (SAXS),³⁰⁻³² and microscopic methods, including Transmission Electron Microscopy (TEM), Atomic Force Microscopy (AFM).³²⁻³⁴ However, theoretical aspects on the instrumentation and working principles of such techniques are not discussed in the current thesis. Rather, it is the synthesis aspects of block copolymers that is primarily explored.

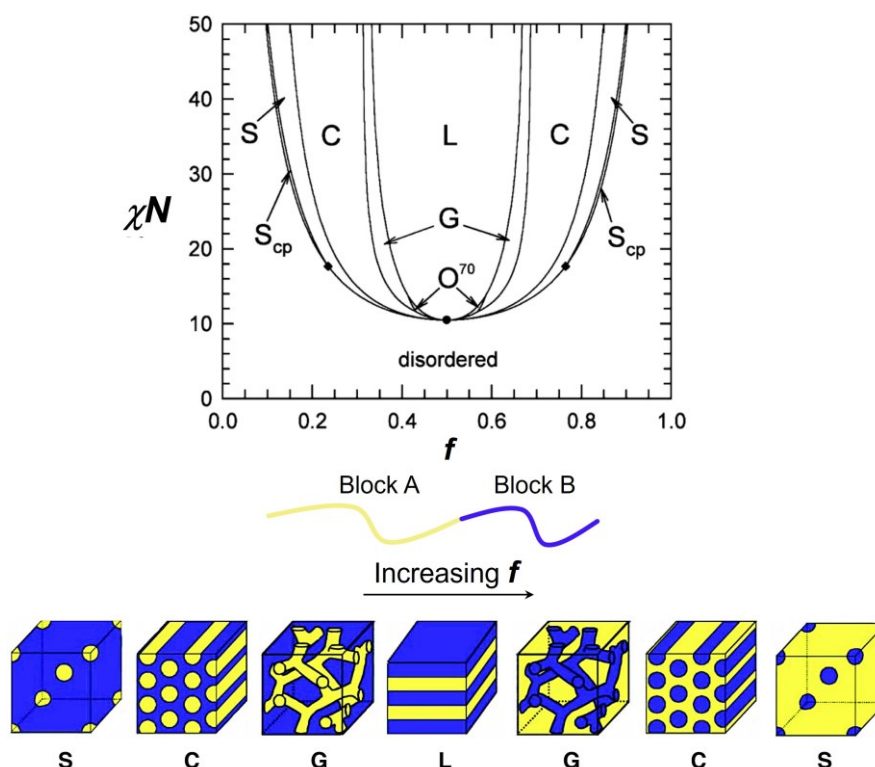


Figure 2.1. Theoretical phase diagram for linear AB diblock copolymers based on SCFT. L = Lamella, G = Gyroid, C = Hexagonally-Packed Cylinder (HPC), S = Body Centered Cubic (BCC). The phase diagram is adapted with permission from ref. ^{35,36}. Copyright © 2006 American Chemical Society.

Switching of the morphology of a non-conjugate BCP with a fixed degree of polymerization is possible, in principle, by altering the volume fraction and/or changing the polarity, e.g., hydrophobicity, of one block. In the context of the current research project, literature known approaches and strategies for controlling and manipulation of BCP nanostructures will be discussed in the next section. However, highly crystalline and conjugated BCPs, such as those based on alkylthiophene,³⁷ are not included in the discussion, because the synthetic route towards such BCPs is highly specialized and their microphase separated nanostructures are additionally strongly governed by crystallinity factors.³⁸

2.2. Manipulation of block copolymer nanostructures

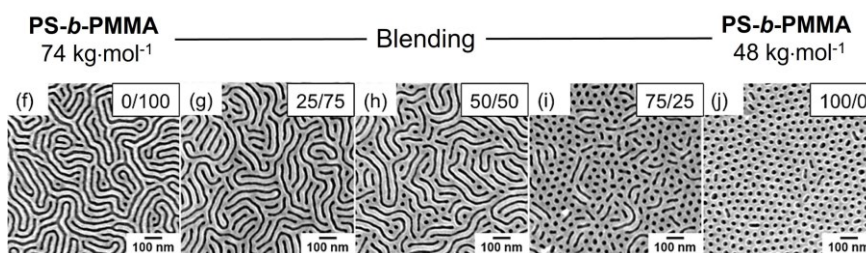


Figure 2.2. Block copolymer blends can lead to alteration of the pristine nanostructure. Images were adapted from ref.³⁹ with permissions. Copyright © 2014 American Chemical Society.

Blending BCPs with BCPs or with homopolymers is a physical method employed to manipulate BCP nanostructures.⁴⁰ In the work by Hashimoto *et al.*, mixtures of certain compositions of two lamella-forming polystyrene-*b*-polyisoprene (PS-*b*-PI) AB diBCPs having different chain length resulted in a cylinder morphology.⁴¹ Similarly, Black *et al.* studied binary mixtures of lamellar and cylindrical PS-*b*-PMMA BCPs, showing the lamella-to-cylinder transition when roughly 50 wt% of the cylindrical BCP was mixed with the lamellar BCP (Figure 2.2).³⁹ However, coexistence of these two thin-film morphologies was observed at unequal mixing ratios.³⁹ In addition, BCP and homopolymer binary blends (e.g., AB/A blends) were also examined.⁴² For AB/A blends, the chain length of the A homopolymer should not exceed that of the constituting block (A block) in order to prevent macrophase separation, allowing for the solubilization of the A homopolymer in the microdomain of the A block. In the ideal case, swelling of the A microdomain occurs, leading to change in volume fraction, and effectively change in morphology.⁴² Interestingly, the blending approach was used to access unconventional morphologies, such as highly unsymmetric lamella.^{27,28}

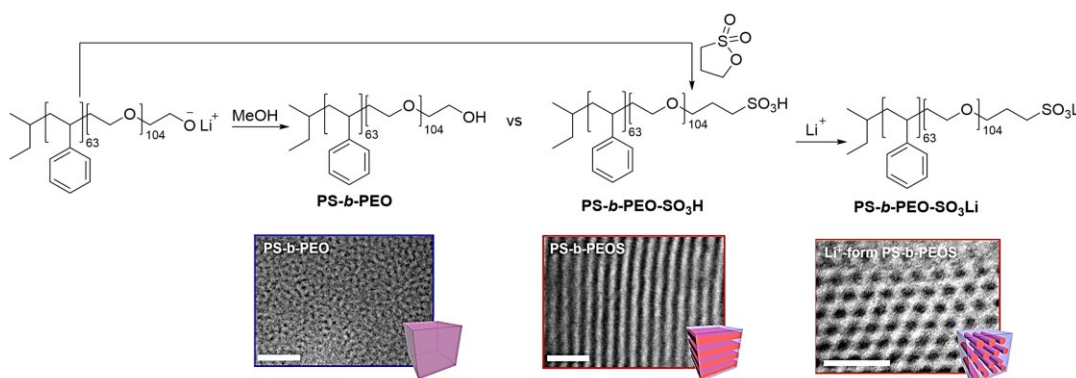


Figure 2.3. Dissimilarity of the block end group can drastically affect the nanostructure of block copolymer having the same degree of polymerization and composition. Images were adapted from ref.⁴³ with permissions. Copyright © 2013 American Chemical Society.

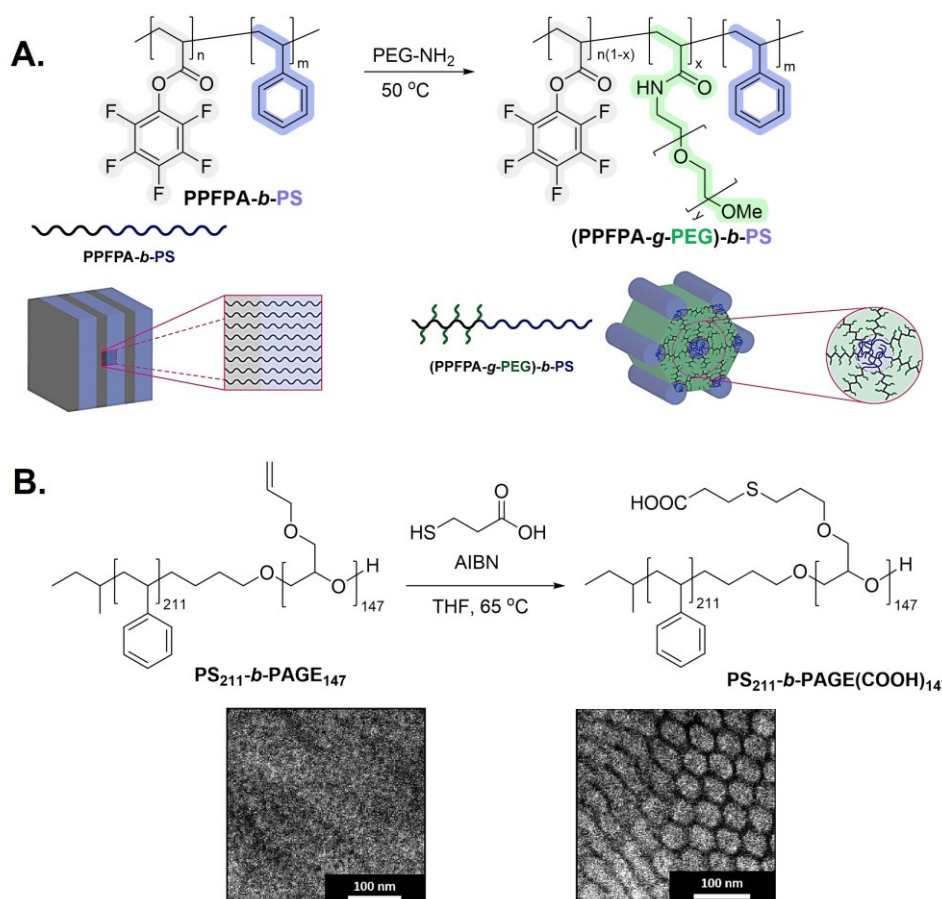


Figure 2.4. Post-polymerization modification of pristine polymers via efficient chemistries can induce morphological transition owing to alteration in Flory-Huggins interaction parameter as well as volume fraction. Illustrations were adapted from ref. ^{44,45} with permissions. Copyright © 2022 American Chemical Society and © 2023 Royal Society of Chemistry.

By changing the chemical nature of the end group, BCPs nanostructures can be altered as was demonstrated in the work reported by Park *et al.*⁴³ A parent diblock copolymer was synthesized via living polymerization, followed by quenching to obtain OH-terminated and SO₃H-terminated PS-*b*-PEG (polystyrene-*b*-polyethylene glycol) block copolymers (Figure 2.3). While the former BCP showed a poorly defined thin-film nanostructure, the latter exhibited a clear lamellar morphology. Further reaction of the SO₃H-end group with Li⁺ salt resulted in a BCP with hexagonally packed cylindrical morphology.⁴³ It can be inferred that changing the end group identity potentially has a key impact on the block compatibility (or the Flory-Huggins χ interaction parameter).

In a similar manner, the morphology of BCPs with modifiable pendant groups can also be manipulated via post-polymerization modification.^{44,45} For instance, a linear diblock copolymer containing activated pentafluoro phenyl (PFP) esters in one block was modified with different amounts of low M_n amine-terminated PEG (or PEO) due to the selective reaction between the amine and PFP groups (Figure 2.4A).⁴⁴ As a result, the bulk morphologies of the derived BCPs were different from the pristine BCP, which can be rationalized as the PEG chain is substantially polar as well as longer than the PFP ester groups, leading to a significant change in terms of hydrophilicity and volume fraction of the modified block. Other chemistries, such

as thiol-ene ligation,⁴⁵ were also applied to post-modify and tune the affinity among the parent blocks, affecting the χ parameter. It must be emphasized that such morphological transitions discussed above were observed in separate thin films or bulk samples corresponding to the parent and post-modified block copolymers.

In addition to physical blending and chemical changes, electric fields were employed to precisely tune BCP domain spacing.⁴⁶ For instance, Boker *et al.* applied a dc voltage up to 12.5 keV to block copolymer solutions (50-57 wt% in THF or toluene at room temperature) of PS-*b*-PI ($M_n \sim 50000 \text{ g}\cdot\text{mol}^{-1}$, $D < 1.03$) and observed a reversible change of approximately 6% in the lamellar spacing.⁴⁷ This was rationalized by the stretching of the PI block in solution under electric fields. However, it was only feasible to apply electric fields to BCP solutions rather than thin films in the reported work.

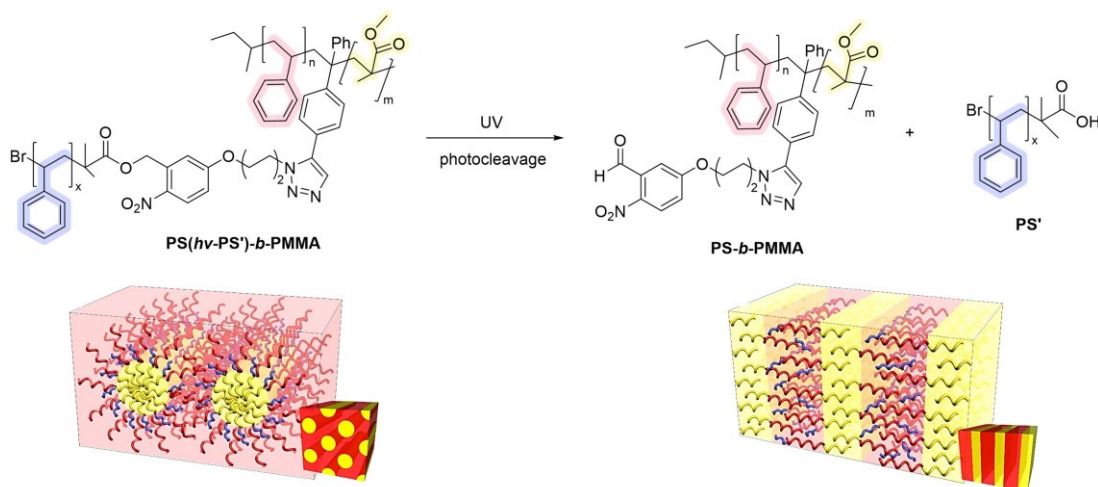


Figure 2.5. Photo-induced cleavage of *o*-nitro benzyl ester located at a block junction led to a blend of two different polymers. Illustration adapted from ref.⁴⁸ with permission.

Compared to physical methods and wet chemistry approaches, using light as an external stimulus appears more ideal. For instance, Kim *et al.* reported a milktoarm block copolymers containing two PS and one PMMA blocks of which a photocleavable *o*-nitrobenzyl (*o*NB) ester group was installed at one specific junction (Figure 2.5).⁴⁸ The original cylindrical morphology of the star BCP ($M_n = 24000 \text{ g}\cdot\text{mol}^{-1}$ for PMMA block, 22000 and 11000 $\text{g}\cdot\text{mol}^{-1}$ for two PS blocks, $D < 1.18$) transformed to lamellar nanostructures at the region irradiated with UV light as revealed by both Transmission Electron Microscopy (TEM) and Small-Angle X-ray Scattering (SAXS).⁴⁸ The light-induced cleavage of the *o*NB group resulted in a blend of linear diblock copolymer and homopolymer, inducing a morphology transition in a single substrate. However, while the use of light is advantageous in this work, the photoreaction is irreversible, and a very high temperature (230 °C) was applied during the irradiation to allow for the reorganization of BCP nanostructures.

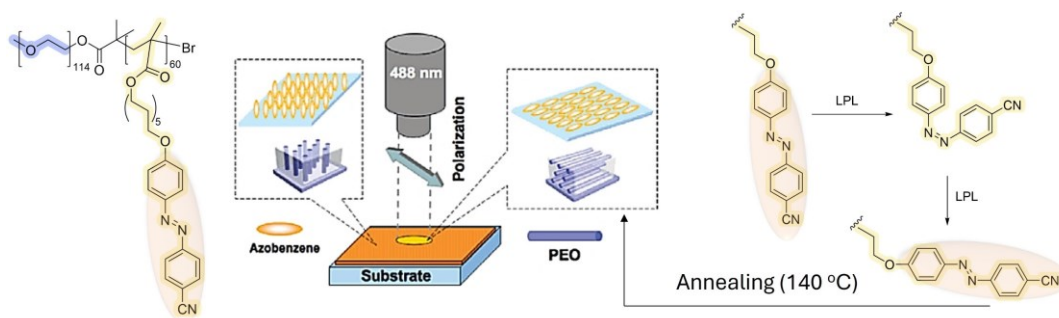


Figure 2.6. Photoisomerization of azobenzene-containing block copolymer led to the reorientation of nanostructure. LPL: linearly polarized light. Illustration was adapted from ref.⁴⁹ with permission. Copyright © 2006 American Chemical Society.

Another approach is to use reversibly photoisomerizable light-responsive moieties. Accordingly, Ikeda *et al.* incorporated azobenzene (AzB) photoswitch as a sidechain group in PEG-*b*-PMMA diBCP ($M_n = 34000 \text{ g}\cdot\text{mol}^{-1}$, $\bar{D} = 1.07$) and observed a change in the alignment (from vertical to horizontal) of the periodic array of cylinders upon irradiation with linearly polarized light (LPL) and the subsequent thermal annealing at 140°C .⁴⁹ Such interesting structural reorientation was explained by the reorientation of the liquid-crystalline AzB photoswitches under LPL irradiation, influencing the self-assembly of the BCP in its entirety.⁴⁹ However, the authors did not comment on the reversibility of the photocontrolled process. Another example is from the work of Meijer and colleagues.⁵⁰ Here, a photoswitchable material was prepared from a very low glass transition temperature (T_g) silicon-based oligomer functionalized with an azobenzene photoswitch at two chain ends. However, even though a photo-induced order-disorder transition was apparent in their work, such an oligomeric system is strictly not defined as a block copolymer and hence deemed less relevant. Nevertheless, the use of oligomers with a negative T_g eliminated the necessity of high annealing temperature.

From the exemplified strategies discussed above, it is clear that using light as the means to remotely manipulate BCP nanostructures is desirable. Specifically, inclusion of reversible photoswitchable moieties – such as azobenzenes – enables the non-destructive method for manipulation of block copolymer morphologies. However, in the realm of molecular photoswitches, azobenzenes are not the only examples. In the following section, a brief overview of selected photoswitches as well as their applications in photoresponsive materials will be given, demonstrating the significant potential of photoswitches for the realization of photoswitchable nanostructures of block copolymers, which however has rarely been harnessed.

2.3. Photoswitches and their integration in material science

2.3.1. The Jablonski diagram

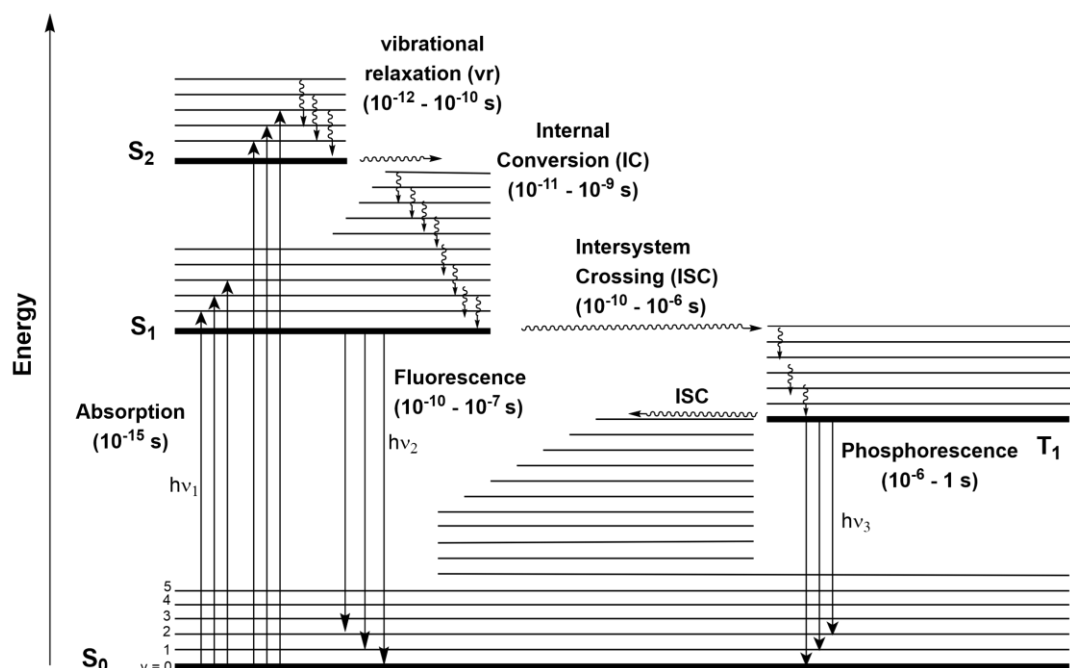


Figure 2.7. Jablonski diagram showing different electronic states and the relative energy levels as well as deactivation pathways. Radiative transitions are shown with vertical arrows while radiationless transitions are indicated by wavy arrows. The timescale or lifetime of each transition is also included.

Photochemical and photophysical processes involve the interaction between matter (e.g., atoms, inorganic/organic molecules) and photons. Upon illumination with photons of suitable energy, an organic molecule, e.g., a photoswitch, is excited to an excited state from which many possible deactivation pathways can take place in order to return to the stable ground state. Different electronic states and their relative energy levels (typically singlet (S_0 , S_1 , S_2 , etc.) and triplet (T_1 , T_2 , etc.)) as well as deactivation pathways are visualized in the Jablonski diagram.⁵¹ Accordingly, upon photon absorption (i.e., $S_n \leftarrow S_0$ excitation), the high-energy excited state species relaxes to its ground state via two main routes: radiative pathways and non-radiative pathways. The former pathways include emission of photons of lower energy (from the singlet state) and phosphorescence (emission of photons from the triplet state). The non-radiative processes include vibrational relaxation (vr), internal conversion (IC), intersystem crossing (ISC), and unimolecular chemical reactions (e.g., ionization, dissociation and isomerization). Note that these aforementioned deactivation pathways take place intramolecularly. The excited state species can also be deactivated or quenched intermolecularly.⁵¹

In the context of photoswitches, reversible isomerization and dissociation are the two main channels that enable the change in conformation of a photoswitch. Many organic molecules that contain delocalized double bonds in their structures – such as carbon-carbon (olefins), nitrogen-nitrogen (azo compounds), carbon-nitrogen (imines) double bonds – show *E/Z* or

cis/trans- photoisomerization due to a loss of stiffness of the double bond character in the excited state. In addition, the photoswitching process can occur via photobreakage of a hetero bond in a cyclic structure, e.g., spiro compounds, resulting in ring opening, as seen in spiropyrans.

In the below section, examples of photoswitches from the literature are selected based on those following an *E/Z*-photoisomerization and/or ring opening pathway.

2.3.2. Examples of photoswitches

2.3.2.1. Azobenzene and derivatives

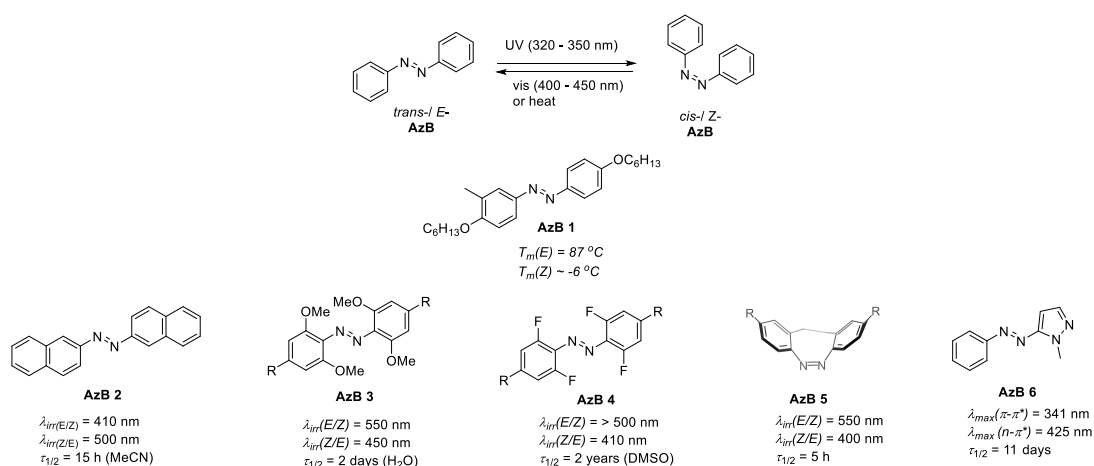


Figure 2.8. Azobenzene photoswitches. Examples were adopted from refs.⁵²⁻⁵⁶

Azobenzene (AzB) was synthetically first prepared in 1834⁵⁷ and subsequently commercially available for use as a popular dye. The popularity of azobenzene as a classic photoswitch started in 1937 when the *E/Z* photoisomerization of azobenzene was observed and reported.⁵⁸

The thermal characteristics, e.g., melting temperature (T_m), of several *trans*- and *cis*- isomers is often different. It was reported that the *cis*-form of an AzB compound has a negative T_m (approx. $-6\text{ }^{\circ}\text{C}$) (**AzB 1**, Figure 2.8), while the *trans*-isomer has a T_m of $87\text{ }^{\circ}\text{C}$, well above ambient temperature, making it possible to induce solid-to-liquid transition.⁸ It was explained that the presence of the symmetry-breaking methyl group on the phenyl ring of **AzB 1** drastically affects the molecular packing upon *E/Z*-photoisomerization, leading to light-induced solid-to-liquid transformation.⁵⁹ It is also possible to trigger such a transformation when the *trans*- and *cis*- isomers form an eutectic mixture, causing the transition temperature to drop well below room temperature.⁶⁰ The eutectic temperature of the irradiated mixture can further be reduced by mixing two or more pure *trans*-AzB derivatives with suitable ratios.⁶¹

trans-Azobenzenes are also responsive to linearly polarized light (LPL) due to their rod-like shape, a feature that was used to enhance the molecular orientation and crystallinity of AzBs in the solid state.^{62,63}

Further development has led to various derivatives of azobenzene with visible light absorption and tunable thermal half-lives. Several studies have highlighted intrinsic structural alterations, including tetra-*ortho*-chloro/fluoro substitution,^{64,65} heteroaryl,^{56,66} and bridged⁵⁵ designs, for modulation of electronic absorption (π - π^* and n - π^*) as well as thermal half-lives (from minutes to days) and photoisomerization performance of AzB system (Figure 2.8).

2.3.2.2. Stilbene and Stiff Stilbene (SS)

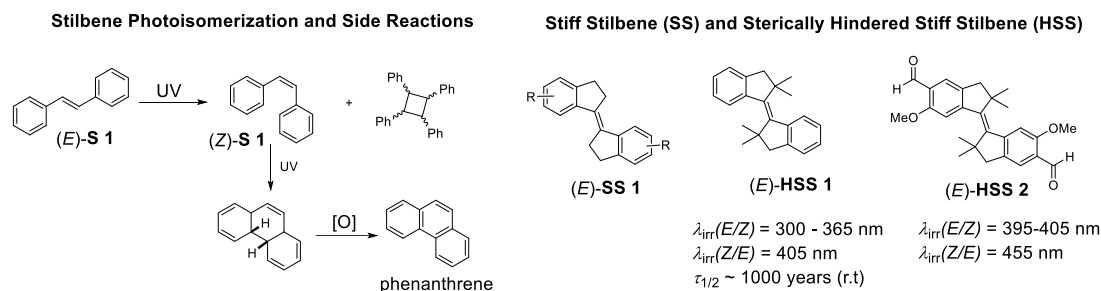


Figure 2.9. (Left) Stilbene photoisomerization and side reactions.⁶⁷⁻⁷⁰ (Right) Stiff Stilbene (SS) and Sterically hindered stiff stilbene (HSS).⁷¹⁻⁷³

In general terms, the *E/Z*-photoisomerization of stilbene occurs via rotation around the C-C double bond in the excited state.⁷⁴ Despite the structural similarity with AzBs, stilbene is prone to side reactions upon photoexcitation, such as electrocyclicization and photooxidation, as shown in Figure 2.9.⁶⁷⁻⁷⁰ This critically limits its use as a clean photoswitch.

An advanced version of stilbene – stiff stilbene (SS) – shows a lesser propensity for side reactions.⁷⁵ Ooyama and colleagues reported sterically hindered stiff stilbene (HSS) in which the sp^2 -C in the 5-membered ring of the SS is substituted with 2 methyl groups, making HSS more sterically congested than SS.⁷² The HSS molecule featured high isomer distribution ratios ($\sim 90\%$ *E* or *Z* isomer at the photostationary state (PSS) in both directions, i.e., *E/Z* and *Z/E* photoisomerization) and the photoisomerization was performed under aerobic conditions in a select solvents with no or insignificant photodegradation (Figure 2.9).⁷² A recent study by Feringa and coworkers explored the substituent effect that caused a red-shift in the UV-vis absorption of SS and HSS, enabling all visible light-induced forward and back switching ($\lambda_{irradiation} = 395 - 455 \text{ nm}$) (Figure 2.9).⁷¹

2.3.2.3. Overcrowded Alkenes

In addition to functioning as a photoswitch, overcrowded alkenes (OAs) are well-known as a molecular motor owing to their unidirectional 360° rotation around the C-C double bond, activated by light and heat, first reported by Feringa and colleagues in 1999.⁷⁶ The initial molecular design contained the two identical sterically crowded parts (“stator” and “rotor”) covalently linked in an out-of-plane fashion to the relatively short C-C double bond (Figure 2.10, right). In order to rotate in a full circle, the stator and the rotor must contain a chiral center next to the C-C double bond (Figure 2.9, right). Upon UV irradiation ($> 280 \text{ nm}$), *E/Z*-photoisomerization takes place, followed by thermal helical inversion to reach a relatively more stable *Z* isomer. Subsequently, further UV irradiation ($> 280 \text{ nm}$) triggers photoisomerization

to the metastable *E* isomer, which undergoes thermal helical inversion upon heating to more than 60 °C, reverting to the pristine *E* form (Figure 2.9, right).⁷⁶

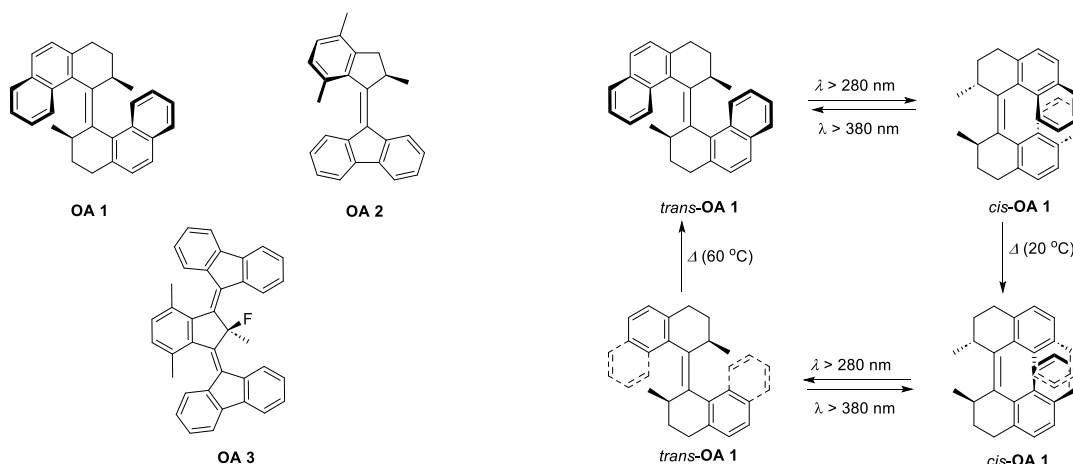


Figure 2.10. Overcrowded Alkenes (OAs): Photoswitches and Molecular Machine.⁷⁶⁻⁷⁸

Nine years after the report of the first generation molecular motor, Feringa and colleagues reported a second generation design, demonstrating that only one chiral rotor is sufficient to achieve unidirectional rotation (OA 2, Figure 2.10).⁷⁷ However, in 2015 Feringa and colleagues further demonstrated that the 360° rotary motion was achieved in a pseudo-symmetric system (“third generation”), implying there may be no strict chirality requirement to realize a molecular motor (e.g, OA 3, Figure 2.10).⁷⁸

2.3.2.4. Indigoids

Similar to azobenzenes, indigos are extremely well-known and extensively used in the dye and textile industry for centuries. However, unsubstituted indigos do not exhibit photoisomerization quenched by excited state proton transfer (ESPT) process.^{79,80} Early studies in the 1950s showed that double *N,N'*-alkylation of indigos released their photoswitchable characteristics (*E/Z* photoisomerization).⁸¹ Nonetheless, the role of *N,N'*-disubstituted indigos as photoswitches remained unattractive probably because of their extremely low thermal stability of the *Z*-isomer ($\tau_{1/2} \sim 5\text{s}$).^{81,82}

Nevertheless, recent studies by Hecht and colleagues have showcased opportunities to prolong the thermal half-lives of this class of photoswitches through modification of the electron-donating property of the nitrogen atom via versatile alkyl-, acyl-, or arylation chemistry.⁸² The most stable *Z*-isomer was observed for *N,N'*-diarylated indigos with $\tau_{1/2}$ up to 408 min at room temperature (indigo 3, Figure 2.11).⁸² The most attractive feature of this photoswitch is its red-shifted electronic absorption spectrum, with λ_{max} of the *E*-form in the orange-red color region (typically 600-650 nm).⁸³

Along with indigos, thioindigos (TIs) are an attractive all-visible responsive photoswitch.⁸⁴ In addition, derivatives of these two photowitches – hemiindigos (HIs) and hemithioindigos (HTIs) – have received growing research interest.⁸⁴

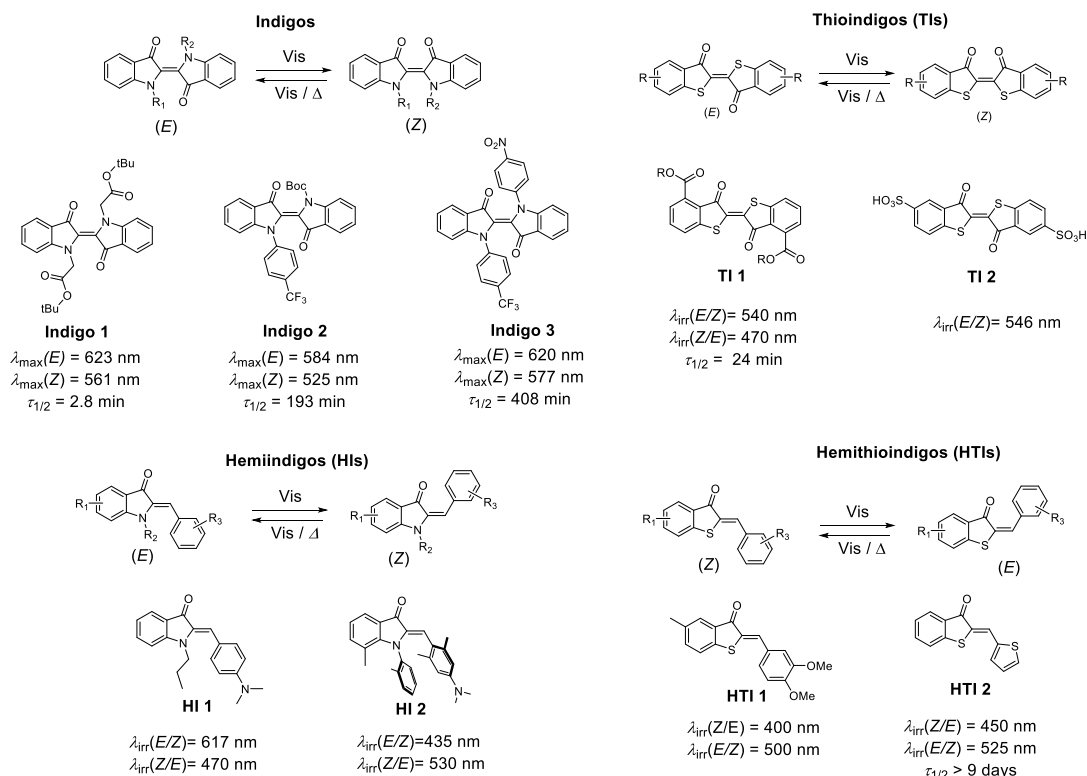


Figure 2.11. Indigoid photoswitches: Indigos, Thioindigos (TIs) and their derivatives.^{82,85-90}

2.3.2.5. Imines

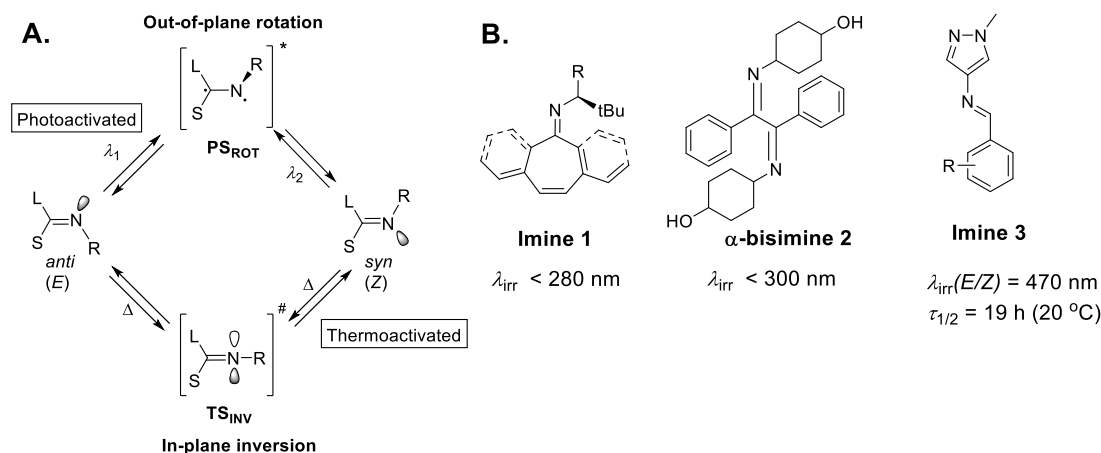


Figure 2.12. Imine photoswitches: (A) Proposed photoisomerization mechanism⁹¹ and (B) examples.⁹²⁻⁹⁴

Imines or Schiff bases are household names in coordination chemistry, where they are widely used as a ligand due to their capability to form complexes with metal ions.^{95,96} They are also known for their covalent dynamic chemistry, e.g., dynamic imine exchange reactions.⁹⁷ More importantly, imines can also undergo *E/Z*-photoisomerization,⁹¹ which is not surprising due to the structural similarity of the C-N with N-N and C-C double bonds. The general isomerization mechanism is presented in Figure 2.12.⁹¹ Notably, imine photoswitches can function as a molecular motor just like overcrowded alkenes when there is a stereogenic center located next to the imine nitrogen (e.g., **Imine 1**, Figure 2.12B).⁹⁸ Perhaps one critical drawback of imine photoswitch is that high energy photons ($\lambda > 250 \text{ nm}$) are required to activate the

photoswitching process.^{92,93} Still, very recently Greenfield *et al.* have reported a few visible light switchable aryl imines obtained from the condensation of aminopyrazole and benzaldehyde (**Imine 3**) with good photoswitching performance under 430 nm irradiation.⁹⁴

2.3.2.6. Hydrazones

Acyl and arylhydrazones show *E/Z* photoisomerization and have recently been exploited as outstanding photoswitch derivatives.⁹⁹⁻¹⁰⁴ Hydrazones are generally easy to synthesize, just like imines. Several hydrazone photoswitches, especially arylhydrazones, are classified as P-type photoswitches by virtue of their extremely stable metastable isomers, with thermal half-lives from years to hundreds or thousands of years (Figure 2.13).¹⁰² Compared to imines, UV-vis spectra of hydrazones are red-shifted and visible light, e.g., blue light, can be used for the forward photoswitching.

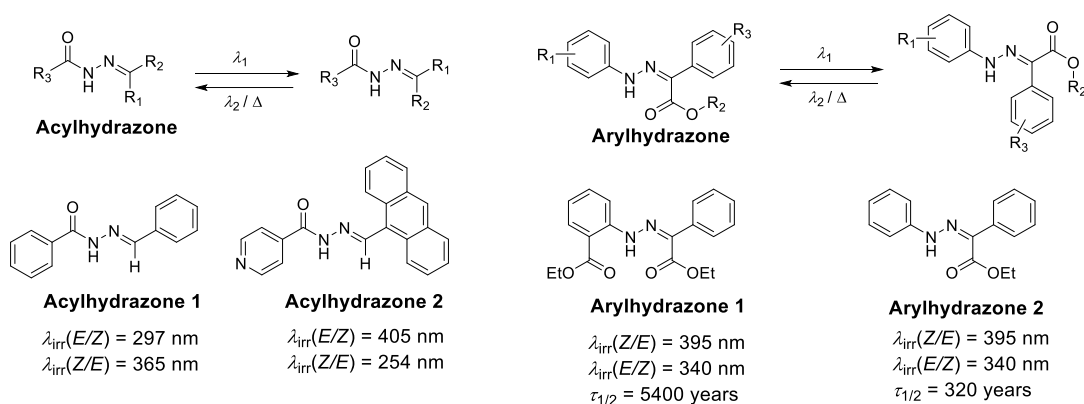


Figure 2.13. Acyl and Arylhydrazone photoswitches.^{99,105}

2.3.2.7. Spiropyrans

Spiropyrans (SPs) differ from other photoswitches discussed above in many ways. The general photoresponsive mechanism of these spiro compounds involves the ring-opening due to the UV-light labile spiro C-O bond, followed by thermal *Z/E* isomerization towards an extended π -conjugated form.¹⁰⁶⁻¹⁰⁸ The ring-closed form is non-planar, colorless and generally thermally stable, whereas the opened-form is intensively colored but unstable (Figure 2.14, top). In terms of polarity, the open-form is highly polar and zwitterionic and therefore referred to as merocyanine form (MC) while the closed-form is nonpolar.^{109,110} Reversion to the ring-closed structure (SP) usually occurs fast under thermal conditions or under visible light irradiation.¹¹¹ In a few cases, the opened state is the stable form due to the protonation of the MC form (MCH) (Figure 2.14, bottom).¹¹²

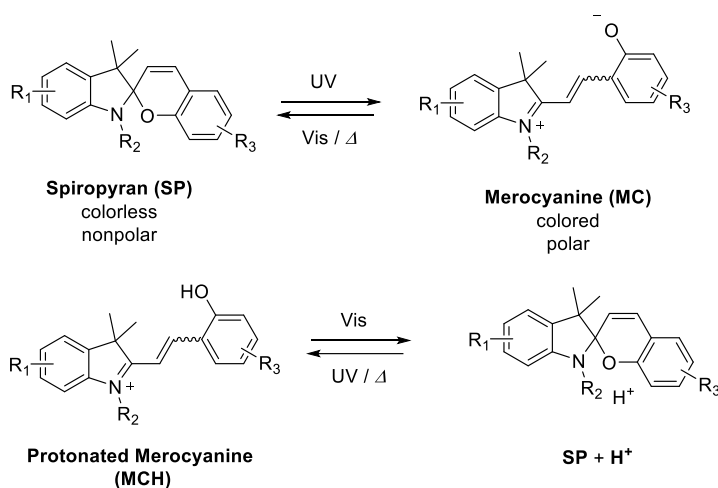


Figure 2.14. Spiropyran photoswitches.^{107,112}

The photoswitching of spiropyrans not only leads to a change in the geometry, but also causes a dramatic shift in the polarity as well as hydrophilicity. A problem with the MC form is its tendency to aggregate in nonpolar solvents.¹¹³ Besides being sensitive to light, the ring-closing and ring-opening switching can be triggered by other stimuli, including acid and temperature, making SPs a multi-stimuli responsive compound.¹⁰⁶

Alongside the above mentioned photoswitches, there are many more photoswitchable molecules, including diarylethenes¹¹⁴ and Donor–Acceptor Stenhouse Adducts (DASAs).¹¹⁵ However, for the sake of clarity and coherence as well as relevance, they are not included in the current section.

2.3.3. Integration of photoswitches into smart materials

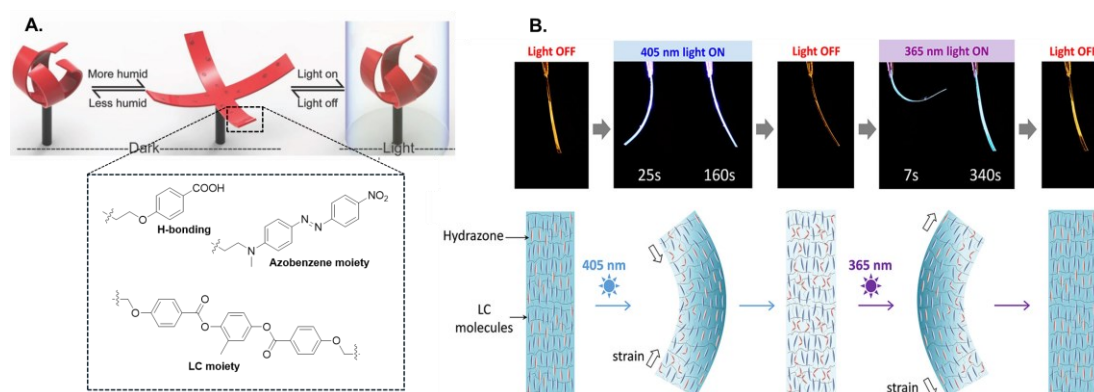


Figure 2.15. Integration of azobenzene¹¹⁶ (A) and hydrazone¹¹⁷ (B) into soft actuators. Images were adapted with permissions. Copyright © 2014 John Wiley and Sons.

Photoactuators rely on light as the energy supply to perform mechanical response. In the field of polymeric materials, soft photoactuators are constructed from conventional liquid crystalline elastomers or crosslinked liquid crystal polymer networks containing photoswitches. Photoswitches, such as azobenzenes^{116,118,119} and hydrazones,¹¹⁷ have successfully been integrated into actuators (Figure 2.15). Upon photoswitching, the change in the size and shape of the embedded photoswitches triggers the realignment of the liquid crystals, thus resulting

in mechanical output.¹¹⁹ Likewise, photo-controlled shape-changing and shape-memory materials were developed based on the *E/Z* photoisomerization of AzBs.¹²⁰⁻¹²³ Given the precise spatiotemporal control of light as an external stimulus, soft photoactuators are ideal candidates for advanced applications like artificial muscles and sensors.^{116,124}

Due to the distinct contrast in color of SP and the MC form, SPs have been incorporated in polymers for security printing as well as photopatterning with good photofatigue (Figure 2.16).¹²⁵ Furthermore, the MC form can selectively bind with some metal ions and therefore is harnessed to prepare photoresponsive polymers for sensor application.¹²⁶ Photoswitching polymers based on SPs have been applied as surface coating to switch wettability thanks to the intense change in the dipole moment upon photoswitching (Figure 2.16).^{127,128}

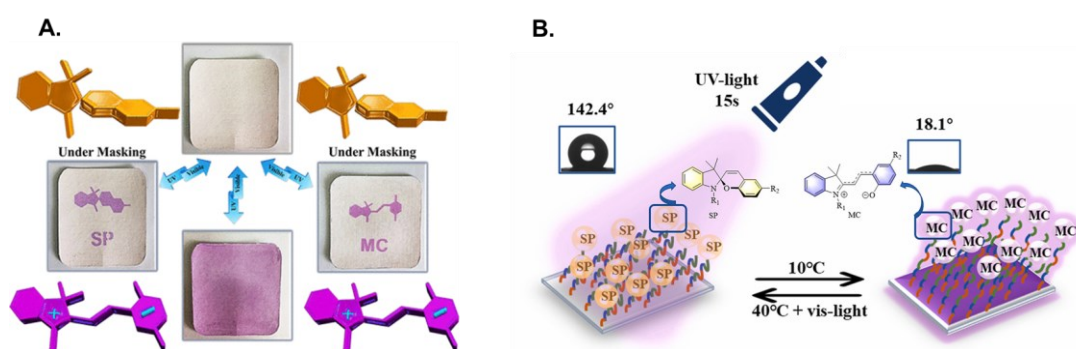


Figure 2.16. Integration of spiropyran photoswitch into polymer for photopatterning¹²⁵ (A) and photoswitchable wettability.¹²¹ Images were adapted with permissions. Copyright © 2018, 2023 American Chemical Society.

It was reported that the glass transition temperature (T_g) of polymers containing AzBs pendant groups can be switched by light due to the solid-to-liquid transition phenomenon of AzB molecules. The solid-to-liquid transition here is attractive for energy storage and self-healing applications.^{129,130} Also, photoswitchable adhesivity of siloxane-based materials was realized by exploiting such photo-induced transition.¹³¹ Photo-modulated glass transition temperatures were also achieved in hydrazone bearing homopolymers.¹³² In contrast to AzBs-based macromolecular systems, the photoswitching of hydrazone sidechains led to an increase in T_g . Due to the extremely long thermal half-lives of the arylhydrazone used, the change in T_g could be locked at different degree of photoisomerization.¹³²

Owing to the geometrical change induced by *E/Z* photoisomerization, installing photoswitches, e.g., imines, into polymer backbone is an effective approach to reversibly control the folding of the polymer chain, forming single chain nanoparticles (SCNPs).⁹³ In another example, the porosity and gas adsorption capability of porous organic frameworks was modulated by a light stimulus when chiral overcrowded alkenes are inserted into the framework backbone.¹³³ This is because the molecular motion of the main-chain photoswitch triggered by light irradiation facilitated the cooperative restructure of the constrained organic framework.¹³³ The main-chain feature is also important for the effective regulation of mechanical properties of soft materials, such as hydrogels, which was demonstrated by Truong, Barner-Kowollik and colleagues on the example of main-chain thioindigo photoswitches.⁸⁵ Synthetically, linear main-chain

photoswitchable polymers are not generally accessible via main stream reversible-deactivation radical polymerization (RDRP) techniques, e.g., ATRP and RAFT. As a result, establishing efficient polymerization techniques to synthetically access such polymers is critically important to maximize the photoswitchable geometry of photoswitches.

2.4. Potential polymerization techniques for main-chain polymers

2.4.1. Acyclic Diene METathesis (ADMET) polymerization

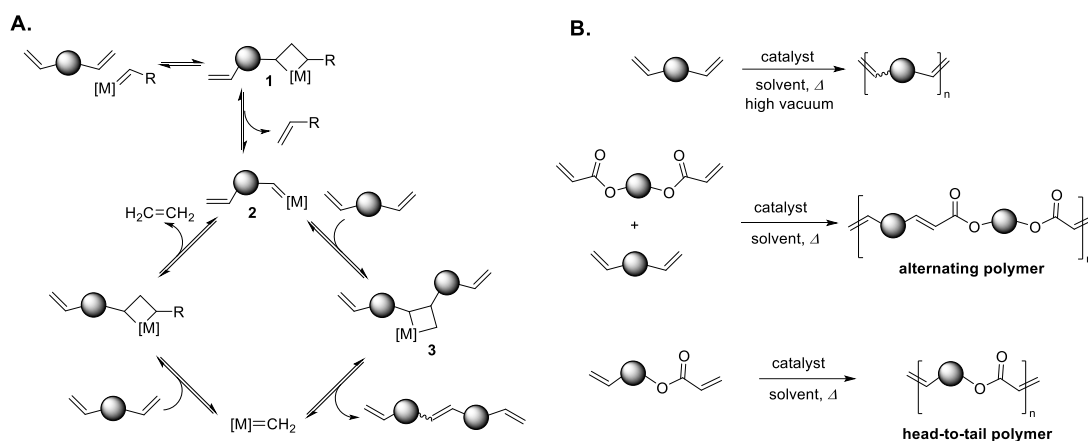


Figure 2.17. Olefin metathesis: (A) mechanism^{134,135} and (B) homopolymers, alternating polymers and head-to-tail polymers synthesized via Acyclic Diene METathesis (ADMET) polymerization.

Essentially, ADMET polymerization relies on the olefin metathesis catalyzed by a transition-metal complex catalyst, typically based on Ru and Mo.^{134,135} The general mechanism of olefin metathesis involves the coordination of the olefin to the metal center, forming metallacyclobutane intermediates **1**, **2** and **3** shown in Figure 2.17A.¹³⁴⁻¹³⁶ The successful reaction generates an internal alkene and releases ethylene gas as a byproduct. In polymer synthesis, a difunctional α,ω -olefin monomer is subjected to a homo-metathesis reaction catalyzed by a suitable catalyst. Typically, high vacuum and high temperature are applied to achieve high degree of polymerization.^{93,137,138} However, a small degree of olefin isomerization can happen in homo-metathesis.^{138,139} When electron-deficient dienes – such as those based on acrylates – and electron-rich dienes are mixed, a selective cross-metathesis reaction occurs upon catalyst addition, generating well-defined alternating polymers (Figure 2.17B).¹⁴⁰ For the head-to-tail ADMET polymerization, the monomer is designed to contain one olefin (α -) and one acrylate (ω -) handle at either end (Figure 2.17B).¹⁴¹ Thus, issues associated with stoichiometry are eliminated.

A desirable feature of ADMET polymerization is the possibility to control the sequence and spacing of functional groups. For instance, precise placement and high density of branch alkyl side chains in polyethylene was reported, allowing for the tuning of mechanical and thermal property of the resulting polymer.¹⁴² Furthermore, advanced materials with diverse functionality could also be achieved via post-modification to introduce functional groups, such as halogens, carboxylic acids and phosphonic acids.¹⁴³

In the context of photoswitchable polymers, ADMET polymerization was employed to prepare α -bisimine-based main-chain homopolymers while azobenzene-based homopolymers and block copolymers were synthesized via head-to-tail ADMET polymerization.^{93,144,145} As a result, the method is highly suitable for the initial synthesis of main-chain photoswitching polymers and block copolymers in the current thesis.

2.4.2. Ring Opening Metathesis Polymerization (ROMP)

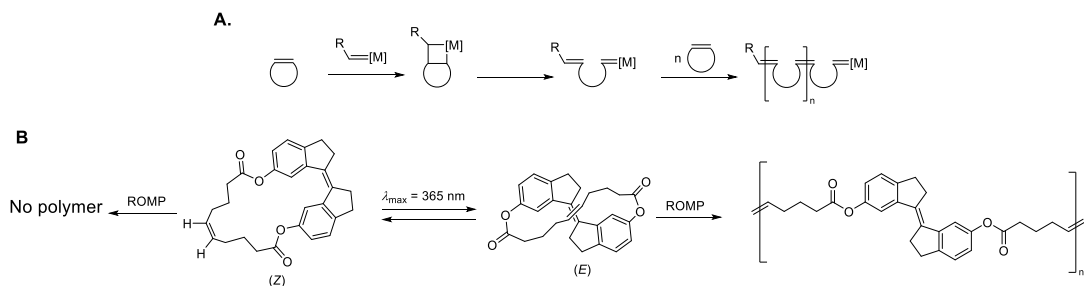


Figure 2.18. General Mechanism of ROMP (A) and an example of ROMP of a stilbene-based cyclic monomer (B).¹⁴⁶

Similar to ADMET polymerization, Ring-Opening Metathesis Polymerization (ROMP) is based on olefin metathesis.¹³⁵ However, instead of an acyclic monomer, cyclic olefins are used (Figure 2.18A). Polymers with low dispersity and controlled degree of polymerization and high chain-end fidelity can be synthesized under careful selection of catalyst and reaction conditions.^{147,148} However, the driving force of the polymerization is often due to the release of ring constraint, thus limiting the flexibility in monomer design. One strategy to enhance ring constraint is to employ photoswitch. Cui and colleagues synthesized a fairly large cyclic olefin bearing a (Z) -stiff stilbene and applied the Z/E -photoisomerization to make the monomer become strained, and thus reactive towards ROMP (Figure 2.18B).¹⁴⁶ This strategy not only enabled the polymerization but also afforded main-chain photoswitching polymers.

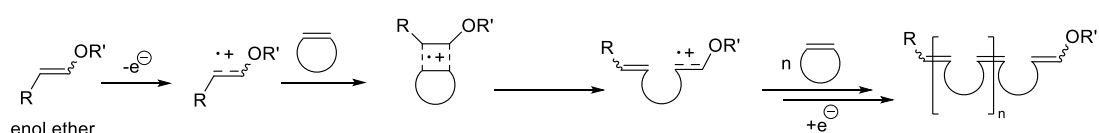


Figure 2.19. Proposed mechanism of electro-redox-mediated metal-free ROMP.

Additionally, advances in ROMP have led to the development of metal-free ROMP, allowing for a "greener" alternative to polymer synthesis.¹⁴⁹ In metal-free ROMP, an enol ether is used as initiator that decomposes by electrolysis into a cationic radical.¹⁵⁰ This radical is believed to interact with the cyclic monomer to form a cyclobutane radical complex. The polymer chain grows via the rapid ring opening of this complex, flowing by radical attack to another cyclic monomer (Figure 2.19). However, poor monomer solubility in the electrolyte medium is the critical drawback that curtails the synthesis of polymers with high monomer conversion. Another metal-free approach is to employ photoredox catalysis for the generation of enol ether radicals.¹⁵¹ This strategy allows one to use more diverse organic solvents as a polymerization medium, thus circumventing the solubility problem in the electrochemical approach.

Furthermore, the temporal and spatial control of light as a trigger makes this photochemical approach highly attractive.

2.4.3. Radical Ring Opening Polymerization (rROP)

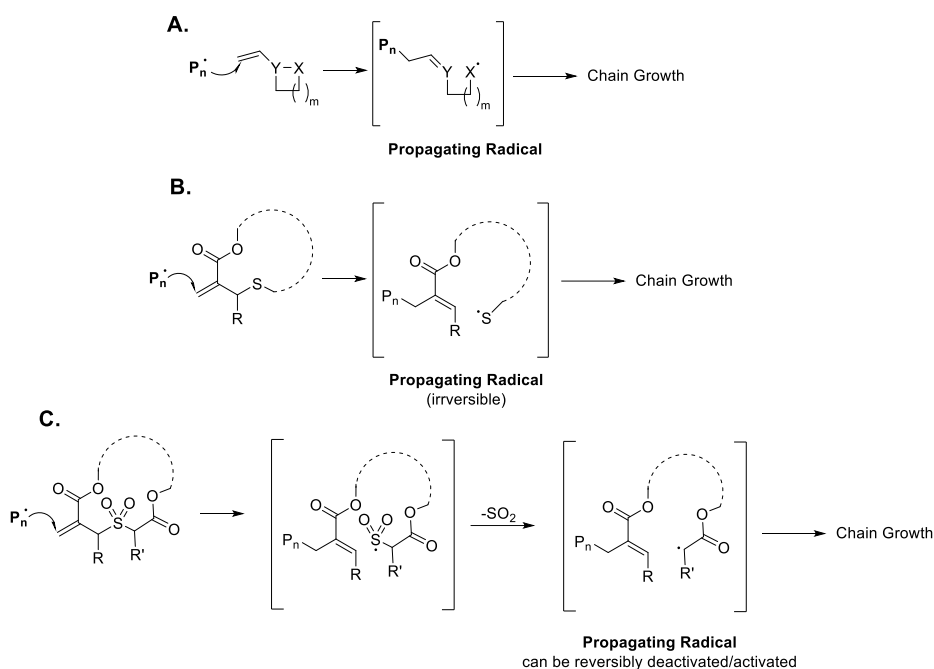


Figure 2.20. Development in radical ring opening polymerization led to efficient cyclic monomer (B,C) with low ring-strain.^{152,153} Illustration was adapted from ref.¹⁵³

In radical ring-opening polymerization (rROP), the cyclic monomer is designed to feature vinyl monomer type.¹⁵² The general mechanism involves the attack of propagating radical generated from an initiator to the cyclic monomer, extending the polymer chain. rROP technique benefits from both ring-opening polymerization and reversible deactivation radical polymerization (RDRP). However, in order to efficiently polymerize, the design of monomers in rROP must meet a set of criteria. Firstly, similar to RDRP, the monomer structure has to feature a radical acceptor, typically based on vinyl monomer. Secondly, high ring strain is required to favor the ring-opening mechanism. Thirdly, the ideal polymerization has to involve simultaneous ring-opening and isomerization mechanisms. Finally, the ring-opening step has to generate stabilized radical to ensure the efficient chain propagation.¹⁵² While such a radical technique has routinely been employed to prepare biodegradable polymeric materials,¹⁵² synthesis of main-chain photoswitching polymers via this route still remains critically challenging owing to the high ring constraint requirement.

However, recent pioneering studies have made the radical ring opening polymerization of cyclic monomers with large ring size possible (Figure 2.20 B,C). Essentially, the approach exploited the irreversible generation of thiyl or sulfonyl radicals from macrocyclic allylic sulfide monomers that could further involve in the chain growth (Figure 2.20B).^{154,155} To address the irreversible issue, Niu and colleagues developed a cyclic vinyl monomer motif bearing a sulfone group in close proximity to the vinyl group (Figure 2.20C).¹⁵³ The extrusion of sulfur

dioxide upon the ring opening step generates an alkyl radical that can reversibly be activated and deactivated, enabling the synthesis of block copolymer.¹⁵³ Via such monomer designs, short peptide sequences and bulky photolabile groups have successfully inserted into the polymer backbone.^{156,157} However, a large amount of comonomer, e.g., dimethyl acetamide (DMA), is frequently required to assist the polymerization and this inadvertently reduces the density of the active group.^{156,157} Although there is still substantial development required, success in employing this technique for synthesizing main-chain functional polymers is potentially profound in the long term.

2.4.4. X-yne click polymerization

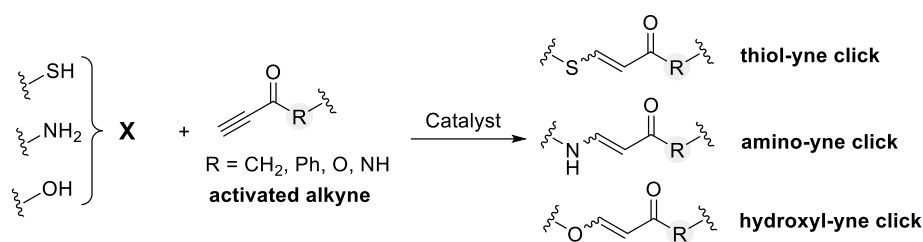
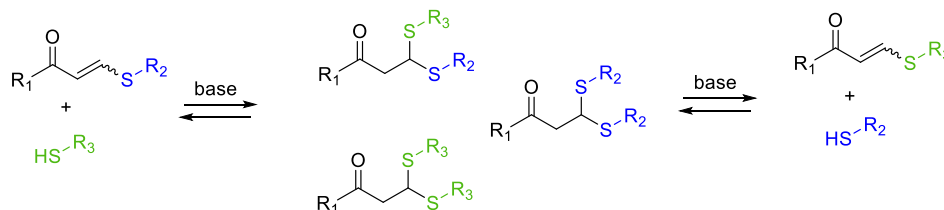
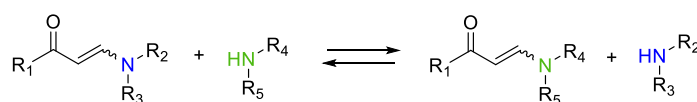


Figure 2.21. Typical X-yne click reactions, i.e., thiol-yne click, amino-yne click and hydroxyl-yne click, reported in the literature.^{158,159}

(A) Dynamic thiol exchange



(B) Dynamic amine exchange



(C) Dynamic phenol exchange

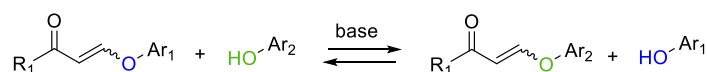


Figure 2.22. Dynamic exchange reactions between a β -X- α,β -unsaturated carbonyl compounds with an X-type nucleophile (thiol, amine, phenol). Adapted from ref.¹⁶⁰.

X-yne click reactions refer to the click reaction of a nucleophile, typically thiol, hydroxy and amine, with an activated alkyne catalyzed by an organobase (Figure 2.21).¹⁵⁸⁻¹⁵⁹ Such chemistries are extensively used in organic synthesis and have recently been emerged as a potent step-growth polymerization.¹⁶⁰ A few desirable characteristics of these techniques include metal-free catalysis, mild polymerization condition, fast reaction kinetics and post-modifiable double bonds.¹⁵⁸⁻¹⁶⁰ Polymers with advanced functionality and property, such as

aggregation-induced emission (AIE) and mechano-coloration, have been prepared via these reactions.^{161,162} Furthermore, polymers synthesized via X-yne click polymerization feature dynamic covalent bond exchange between the β -X- α,β -unsaturated carbonyl group and the respective X nucleophile (Figure 2.22), attractive for self-healing and covalent adaptable network (CAN) applications.¹⁶⁰ More importantly, polymer-polymer conjugation on an example of amino-yne click reaction has just recently been reported for the synthesis of block copolymers.¹⁶³ In light of these characteristics, integration of such X-yne click reactions in the synthesis of main-chain photoswitching polymers and block copolymers is therefore versatile and promising.

2.5. Research gaps in photoswitchable block copolymers

The research landscape of photoswitching BCPs appears to be dominated by azobenzene-based systems.¹⁶⁴⁻¹⁸⁰ Preparation and study of spiropyrans-based BCPs have occasionally been reported. Among the reported studies, the side-chain design of photoswitching BCPs is overwhelmingly dominant. However, investigation and manipulation of the solid-state nanostructures of such light-responsive BCPs remains critically scarce. There is only one study noted in section 2.2 in which the change in the orientation of the cylindrical morphology of azobenzene-based BCPs was reported.⁴⁹ The reported system is interesting yet not sufficiently profound in terms of enabling morphological transformations, likely because of the introduction of the azobenzene photoswitch as side-chain groups. As shown previously in section 2.3.2, the main-chain approach is essential to maximize the conformation and geometry change of the *E/Z*-isomerizable photoswitches, such as azobenzene, imine, overcrowded alkenes. The large change in geometry of the main-chain photoswitches may be effective to alter the volume fraction of the constituting block, hence influencing the equilibrium nanostructure of the photoswitching BCP, enabling the transition to another (order) nanostructure. For photoswitches that become drastically polar in the metastable state, such as spiropyrans, either main-chain or side-chain designs can, in theory, effectively lead to a profound change in the Flory-Huggins interaction parameter (χ) upon photoswitching.

Synthetically, access to main-chain linear polymers is generally not feasible via deactivation radical polymerization (RDRP) techniques.¹⁸¹ These techniques are often employed to synthesize side-chain functional polymers and block copolymers. However, recent advances in radical ring-opening polymerization allow for the main-chain incorporation of stimuli-responsive groups.^{153,156} Nevertheless, it is still critically challenging to install high density of main-chain reactive groups via such a radical route.¹⁸² On the other hand, some other polymerization techniques, e.g., (head-to-tail) Acyclic Diene METathesis (ADMET),^{93,145,183} Michael addition¹⁸⁴ and Ring-Opening METathesis Polymerization (ROMP),¹⁴⁶ have been employed to synthesize main-chain photoswitching polymers, limited to azobenzene,^{145,183,185} stiff stilbene¹⁴⁶ and α -bisimine.⁹³

Yet, to our best knowledge, few reports of main-chain BCPs, predominantly on the example of azobenzene, are found despite the large library of molecular photoswitches available in the literature,^{145,185} excluding block copolymer systems where only one photoswitch unit was installed at the block junction.^{178,186,187} Therefore, it is critically important to establish efficient synthetic tools for the preparation of well-defined and dense main-chain photoswitchable BCPs, paving the path toward photodynamic block copolymer lithography. This is the second objective of the thesis and will be discussed in the next two chapters (**Chapters 3 and 4**).

Chapter 3: Exploring Head-to-tail ADMET and Hydroxyl-yne Click Polymerization for the Synthesis of α -bisimine-based Main-chain Block Copolymersⁱ

3.1. Head-to-tail ADMET polymerization

Acyclic Diene METathesis (ADMET) polymerization relies on the metathesis reaction between two terminal olefin groups under the catalysis of transition metal-based complexes (e.g., Grubb's catalysts).¹³⁶ This technique was employed in our group to synthesize main-chain photoresponsive homopolymers based on α -bisimine photoswitch.⁹³ However, while α -bisimine photoswitches were successfully inserted into the polymer backbone, small degree of isomerization of the formed internal olefin bonds was observed, and high vacuum condition (200 mbar) as well as moderate reaction temperatures (65 – 85 °C) were required. On the one hand, it can be challenging to obtain block copolymers via this route due to the non-selective nature of the homo-metathesis reaction. On the other hand, head-to-tail ADMET polymerization exploits the highly selective cross-metathesis reaction, catalyzed by the Hoveyda-Grubbs 2nd generation catalyst (**HG-II**) under very mild reaction condition, between an α -acrylate and an ω -olefin to fabricate sequence-controlled main-chain polymers.¹⁴¹ Furthermore, block copolymers could be realized when a polymer with an acrylate end group (macro chain stopper) is in reaction mixture with the α,ω -monomer.¹⁴¹ This was also applied to synthesize azobenzene-based main-chain block copolymers.¹⁴⁵ Therefore, we initially chose this technique to test the feasibility to synthesize other photoswitching main-chain block copolymers. We selected α -bisimine as the model photoswitch considering its facile synthesis as well as its chemical compatibility with metathesis reaction. The general head-to-tail ADMET polymerization is depicted in Figure 3.1.

ⁱ Parts of this chapter were reproduced from Thai, L. D.; Guimarães, T. R.; Spann, S.; Goldmann, A. S.; Golberg, D.; Mutlu, H.; Barner-Kowollik, C. *Polym. Chem.* **2022**, 13, 5625-5635, and Thai, L. D.; Kammerer, J. A.; Théato, P.; Mutlu, H.; Barner-Kowollik, C. *ACS Macro Lett.* **2024**, 13, 6, 681–687, with permissions from the Royal Society of Chemistry and American Chemical Society.



Figure 3.1. Synthesis of photoswitchable block copolymer via head-to-tail ADMET polymerization featuring main-chain α -bisimine photoswitch.

Initially, we focused on the synthesis of non-symmetric α -acrylate/ ω -ene difunctional α -bisimine-based monomer (monomer **3**, Figure 3.2A). In parallel, non-commercially available macro chain stoppers with acrylate end group (**PS-A2**) were prepared via post-modification of the Br-end functionalized polystyrene (**PS-Br**) synthesized via Activators ReGenerated by Electron Transfer (ARGET) ATRP polymerization. For block copolymer synthesis, the resulting **PS-A2** or commercial acrylate-terminated polyethylene glycol (**PEG-A1**) was then mixed with α -bisimine-based monomer **3** in dichloromethane (DCM) solvent, followed by addition of **HG-II** catalyst at 40 °C.

3.1.1.1. Synthesis of α -bisimine ADMET monomer and macro chain stopper

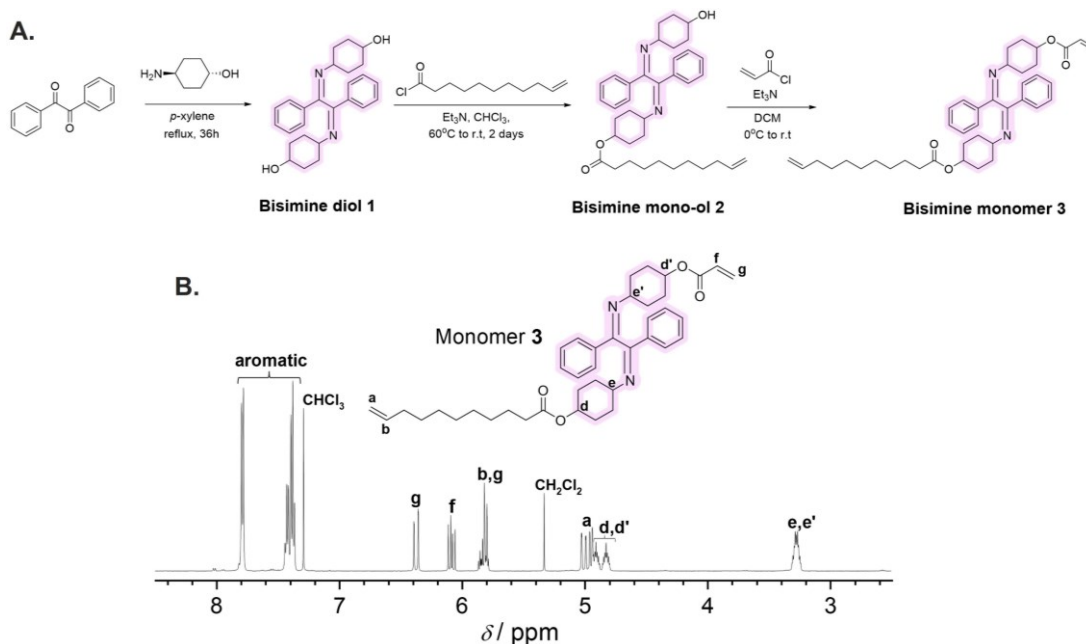


Figure 3.2. Synthesis of α -bisimine-based ADMET monomer. (A) Synthesis route for the monomer. (B) ^1H NMR spectrum (500 MHz, CDCl_3) of monomer **3** with assignment of important resonances. Reproduced from ref.¹⁸⁸ with permission from the Royal Society of Chemistry.

ADMET monomer **3** (^1H NMR spectrum depicted in Figure 3.2B) was successfully synthesized via a three-step protocol, including one condensation reaction and two consecutive esterification reactions (Figure 3.2A). Bisimine diol **1** was obtained on a gram-scale with good

yield (65 %) comparable with the reported value in the literature.⁹³ Purification of bisimine diol **1** was facile, only requiring washing with acetone. Interestingly, mono-ol **2** was directly obtained with 48% yield from the symmetric diol **1** without the need of protecting one of the two hydroxy groups beforehand. In addition, mono-ol **2** and monomer **3** were stable under the mildly acidic condition of the silica gel column in flash column chromatography. The proton NMR spectrum shown in Figure 3.2B confirms the successful synthesis of the ADMET monomer. The magnetic resonances associated with the acrylate (protons **g** and **f**), olefin (protons **a** and **b**) and the α -bisimine core (aromatic protons and proton **d**, **d'**, **e**, **e'**) are assigned in Figure 3.2B.

3.1.1.2. Synthesis of PS-based macro-chain stoppers

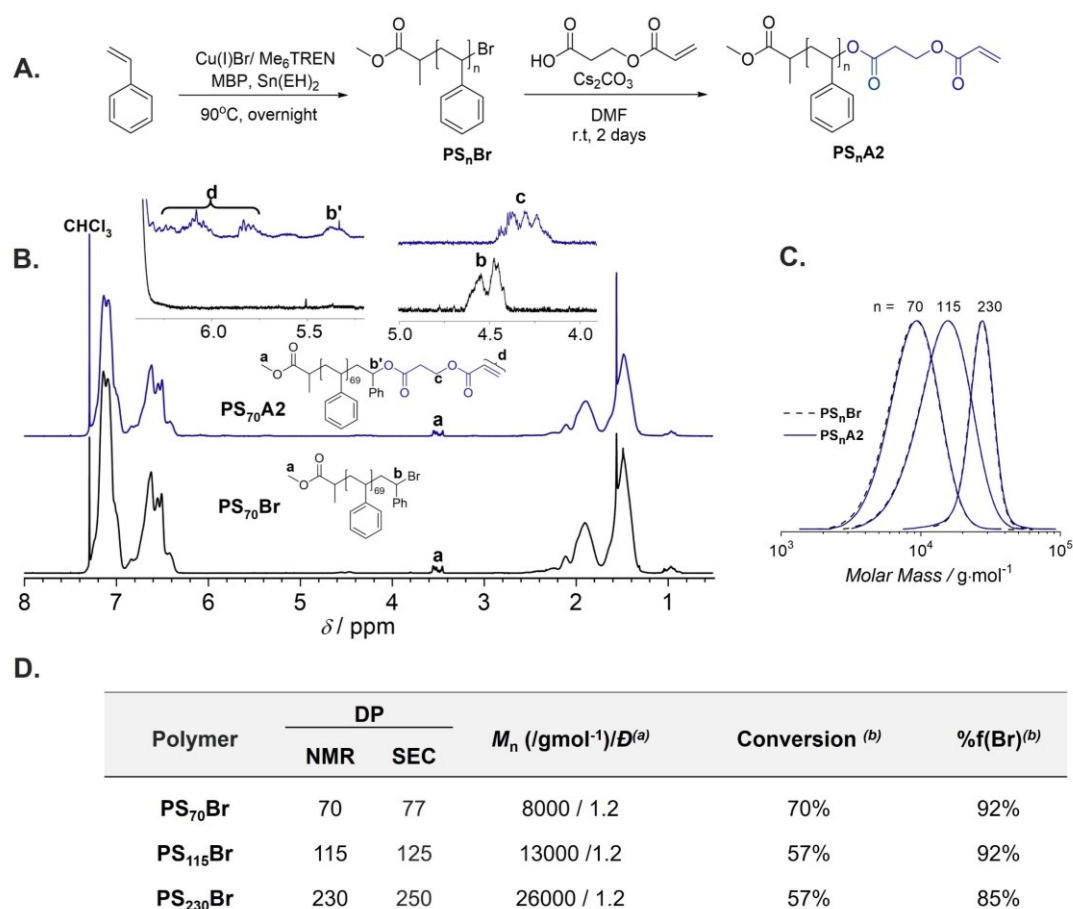


Figure 3.3. Synthesis of macro-chain stopper based on polystyrene (PS). (A) Synthesis route. (B) Stacked ¹H NMR spectra of polystyrene before (PS₇₀-Br) and after (PS₇₀-A2) end-group modification, respectively. (C) THF-SEC traces of pristine and modified polymers. (D) Summary of the molecular characterization for the PS_nBr synthesized via ARGET ATRP. ^(a)The dispersity \bar{D} was determined by THF-SEC; ^(b) Monomer conversion and percentage (%) of the Br-end group, respectively, were determined by ¹H NMR spectroscopy. Reproduced from ref.¹⁸⁸ with permission from the Royal Society of Chemistry.

The macro-chain stoppers were obtained via post-polymerization modification of the Br-end group of homopolymers that in turn were synthesized from ARGET ATRP (Figure 3.3A). Initially, we intended to use conventional ATRP for the synthesis of Br-capped homopolymers. However, a significant loss of the halide end group at a moderate monomer conversion was

encountered. In fact, the decrease of halide chain-end fidelity in traditional ATRP, due to an elimination reaction, has been reported before, especially for styrene-based polymers.^{189,190}

Given the significant importance of preserving the halide chain-end group for post-polymerization modification, ARGET ATRP was employed. Besides minimizing the undesirable elimination of the halide-end group, the amount of Cu(I) catalyst used in ARGET ATRP can be reduced to ppm levels.¹⁹⁰ Accordingly, a series of polystyrene derivatives (denoted **PS_nBr**, n indicates number of repeating unit) with high fidelity of the Br-end group (up to 92%) were synthesized (Figure 3.3D). Subsequently, acrylate chain-end polystyrenes (**PS_nA2**) were obtained via the transformation of the Br-end group of the respective homopolymers. ¹H NMR analysis (Figure 3.3B) confirmed the successful end-group modification by the disappearance of the magnetic resonance associated with proton **b** (indicating the presence of the Br-end group) and the appearance of new magnetic resonances associated with the acrylate-end group. Furthermore, Size Exclusion Chromatography (SEC) traces revealed no change in the molecular weight distribution of polymers upon the modification (Figure 3.3C and D).

3.1.1.3. Synthesis of photoresponsive block copolymers

Next, we prepared light responsive BCP via head-to-tail ADMET polymerization of monomer **3** and **PS_nA2** at different ratios (Figure 3.4). Preliminary experiments on ADMET homopolymerization of monomer **3** showed that 3 mol% (with respect to the acrylate group in monomer **3**) of **HG-II** catalyst was required for an efficient polymerization in DCM at 40 °C. Subsequently, these conditions were applied for the block copolymer synthesis attempts. To test the possibility of efficient chain extension of our system, three acrylate-end functionalized PS with different number average molecular weight (**PS₇₀A2**, **PS₁₁₅A2** and **PS₂₃₀A2** with M_n = 8000, 13000, and 26000 g·mol⁻¹, respectively) were employed as macro-chain stoppers in the head-to-tail ADMET polymerization of monomer **3**.

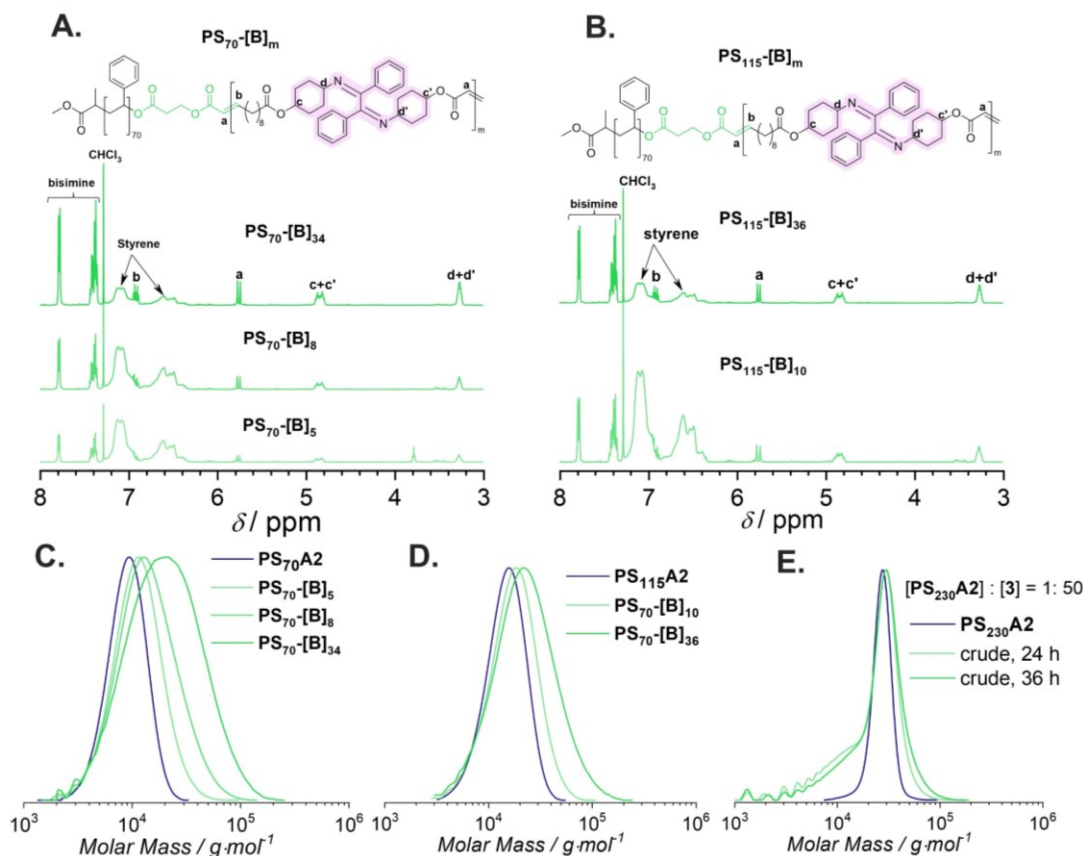


Figure 3.4. Synthesis of photoswitchable block copolymers $PS_n-[B]_x$. (A-B) Comparative 1H NMR spectra (500 MHz, 32 scans, $CDCl_3$). (C-E) THF-SEC traces of block copolymers $PS_n-[B]_x$ with normalized RI detector response. M_n values and dispersity are reported in Table 3.1. Reproduced from ref.¹⁸⁸ with permission from the Royal Society of Chemistry.

SEC traces of the purified block copolymers obtained from $PS_{70}A2$ show monomodal peaks with a good shift towards higher number-average molar mass (M_n), indicating the successful preparation of block copolymer ($PS_n-[B]_x$) (Figure 3.4C and Table 3.1). Both PS and α -bisimine segments are preserved after purification by precipitation in ice-cold MeOH (NMR spectra shown in Figure 3.4A,B). The shift towards higher M_n was also observed by varying the molar ratio between monomer **3** and $PS_{70}A2$ from 6 to 12, and to 50:1 (Figure 3.4C). However, a minor 'tailing' of SEC-traces was observed at higher molar ratios, indicating the presence of some unreacted PS. Monomodal SEC traces were also detected when $PS_{115}A2$ was employed as the macro-chain stopper (Figure 3.4D). However, in the case of $PS_{230}A2$ (1:50, with respect to the acrylate functional group), the SEC traces of the crude sample showed a predominant amount of ADMET homopolymer and unsatisfactory peak shift (Figure 3.4E). Possibly, for the high M_n value of PS_nA2 macro-chain stopper and the growing block copolymer, the coupling catalyzed by Hoveyda-Grubbs 2nd generation catalyst between the macro-chain stopper and the α -bisimine-based monomer/oligomer becomes ineffective. This may be associated with the coil conformation of the polymer in the respective solvent (i.e., CH_2Cl_2), leading to the acrylate-end group being hindered within the polymer chains, making it inaccessible to the Hoveyda-Grubbs 2nd generation catalyst. Such mechanism may also be

possible for low molecular PS-based systems (e.g. **PS₇₀A2**). Thus, head-to-tail ADMET polymerization may not be desirable for the synthesis of high M_n α -bisimine-based BCPs.

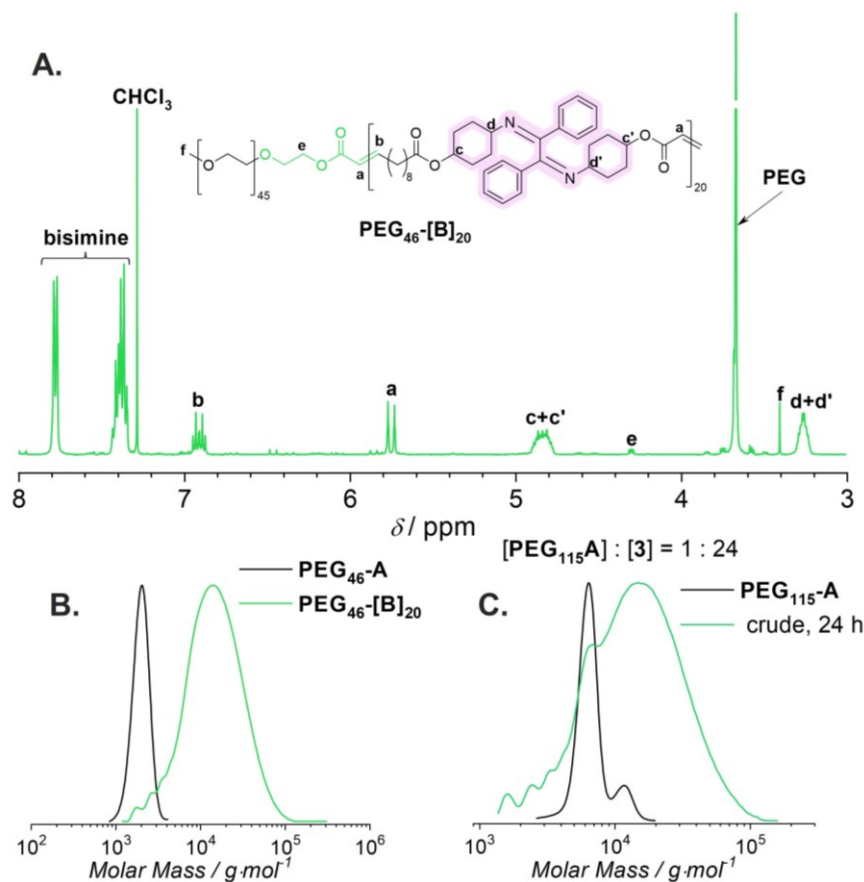


Figure 3.5. Chain extension with PEG-based macro chain stoppers. (A) ^1H NMR spectrum of $\text{PEG}_{46}\text{-[B]}_{20}$ in CDCl_3 . THF-SEC traces of $\text{PEG}_{46}\text{-A}$ (B) and $\text{PEG}_{115}\text{-A}$ (C) macro chain stopper and mixture of the macro chain stopper and monomer 3. Part of the results were adapted from ref.¹⁸⁸ with permission from the Royal Society of Chemistry.

Due to the selective cross-metathesis between the electron-deficient acrylate and electron-rich alkene, the internal C-C double bonds of the acrylate formed in the main-chain of the α -bisimine block of the resulting BCPs are evidenced by the multiplicities as well as chemical shifts of the corresponding protons (proton **a** at 5.7 ppm and proton **b** at 6.9 ppm, Figure 3.4A,B). Such functional groups can facilitate post-polymerization modification of the α -bisimine block, for example, via Michael reaction¹⁹¹ or azide-zwitterion cycloaddition,¹⁹² enabling the synthesis of tailor-made advanced macromolecular structures.

In addition to the nonpolar macro-chain stoppers (**PS₇₀A2** and **PS₁₁₅A2**), we also assessed a more polar macro-chain stopper, i.e., poly(ethylene glycol) methyl ether acrylate ($M_n = 2000$ g mol^{-1} , denoted as **PEG₄₆A1**). The same ADMET polymerization conditions (0.8 M in anhydrous CH_2Cl_2 , 40 $^\circ\text{C}$, overnight) were applied for the case of **PEG₄₆A1** macro chain stopper. The SEC traces of the resulting polymer shifted significantly compared to the initial macro-chain stopper, and the NMR spectrum shows the relevant magnetic resonances arising from PEG and the α -bisimine segments, indicating the successful chain extension (Figure

3.5A,B). However, chain extension with PEG of higher M_n (**PEG₁₁₅A1**, $M_n = 5000 \text{ g}\cdot\text{mol}^{-1}$) was not successful as evidenced by SEC traces shown in Figure 3.5C. Indeed, the latter emphasizes the great influence of polarity of the macro chain stopper on the outcome of chain extension in head-to-tail ADMET polymerization.

A summary of all the results discussed above is given in Table 3.1. A closer inspection of Table 3.1 indicates that the degree of polymerization (DP) for the ADMET block calculated from ^1H NMR spectroscopy and SEC are not in agreement with each other. The discrepancy becomes larger with higher ratios of ADMET monomer. Furthermore, the close examination of the SEC traces of BCPs generated from PS-based macro-chain stoppers (Figure 3.4C,D) suggests that the distributions in the lower molecular weight regions of those BCPs show rather incomplete shifts from those of the corresponding macro chain stoppers, especially in the case of **PS₁₁₅-[B]₃₆**, where the degree of polymerization is high.

Such minor 'tailing' of molecular weight distribution in addition to the variance between NMR-based and SEC-based degree of polymerization may be the indication of incomplete chain extension as discussed above. However, this may also be due to the backbone of the α -bisimine-based block. In other words, unlike the often-encountered saturated, aliphatic polymeric backbones, the main-chain of the bisimine block in our case constitutes bulky and rigid α -bisimine units (which also have cyclic rings in their structure) as well as acrylate internal C-C double bonds. Consequently, the interaction of the α -bisimine-based block with the stationary phase of the SEC column and the other block based on polystyrene will be markedly different from that of those saturated, aliphatic backbones. Thus, the use of conventional PS-/PMMA standard calibration curves can lead to relevant number average molecular weights of such BCPs.

Further, as a minor remark on the **PEG₄₆ADMET₂₀** BCP, the experimental degree of polymerization calculated from NMR (DP_{NMR}) is higher than the targeted theoretical value (Table 3.1). Still, the ^1H NMR spectrum recorded for the crude sample (i.e., before purification) showed a similar molar ratio compared to the designed one. Therefore, the higher DP_{NMR} for the purified BCP is apparently because of solubilization of the BCP with high content of PEG block in MeOH solvent (used to precipitate the polymer).

As concluding remarks, head-to-tail ADMET polymerization shows weak control over chain extension in the synthesis of α -bisimine main-chain block copolymers. The molar mass as well as the polarity of the macro chain stopper plays a significant role in polymerization. Therefore, it is necessary to find alternative methods to realize well-defined main-chain photoswitchable BCPs.

Table 3.1. Summary of results for block copolymer synthesis experiments

Entry	Block A (macro chain stopper)		Bisimine block			Block Copolymer	
	Name ^a	M_n /g·mol ^{-1 b} /Đ	DP			Name ^a	M_n /g·mol ^{-1 b} /Đ
			Theo	NMR ^c	SEC ^d		
1	PS ₇₀ A2	8000 / 1.2	6	5	3	PS ₇₀ -[B] ₅	10000 / 1.3
2			12	8	5	PS ₇₀ -[B] ₈	12000 / 1.5
3			50	34	11	PS ₇₀ -[B] ₃₄	15000 / 1.9
4	PS ₁₁₅ A2	13000 / 1.2	12	10	4	PS ₁₁₅ -[B] ₁₀	15000 / 1.3
5			50	36	9	PS ₁₁₅ -[B] ₃₆	18000 / 1.6
6	PS ₂₃₀ A2	26000 / 1.2	50	No chain extension/Mixture of BCP and significant amount of bisimine homopolymer			
7	PEG ₄₆ A1	2000 / 1.1	12	20	14	PEG ₄₆ -[B] ₂₀	11000/1.7
8	PEG ₁₁₅ A1	5000 / 1.1	No chain extension/Mixture of BCP and significant amount of bisimine homopolymer				

^(a) Subscript indicates degree of polymerization of purified BCPs, determined from ¹H NMR (500 MHz, CDCl₃, 32 scans). ^(b) for PS- and PEG-based polymers, M_n was derived from PS and PMMA calibration standard, respectively.

^(c) for purified BCPs, determined from ¹H NMR. ^(d) for purified BCPs, determined from THF-SEC.

3.2. Hydroxyl-yne click polymerization

In 2020, Tang and colleagues reported the efficient synthesis of alternating copolymers via hydroxyl-yne click polymerization technique.¹⁶¹ Two desirable advantages of this technique are the metal-free catalyst conditions and fast reaction kinetics due to the click nature of the X-yne chemistry.¹⁵⁹ However, application of this technique to the synthesis of photoswitching polymer has not been reported. Therefore, we are motivated to investigate the applicability of the hydroxyl-yne click reaction for the preparation of main-chain photoswitching homopolymers and block copolymers.

3.2.1.1. Homopolymer synthesis

We commence by discussing the design of the α -bisimine based monomer for the head-to-tail hydroxyl-yne polymerization. To our best knowledge, it is the first time that hydroxyl-yne polymerization is reported in a head-to-tail fashion. The primary alcohol and the activated alkyne groups, which are the essential functional groups, are placed at opposing ends of the monomer, making it an AB-type monomer (**M_{B1}** in Figure 3.6A). In comparison to the head-to-tail (AB-type) ADMET monomer featuring an α -bisimine that we have previously discussed in the section 3.1,¹⁸⁸ the structure of the former contains one C-S bond generated by the thiol-halide substitution reaction (compare Figure 3.B, the NMR trace shown up). Depending on the length of the functional thiol used as well as the alkyl halide, the spacing or density of the chromophore can readily be adjusted.

Head-to-tail homopolymerization of the hydroxyl-yne monomer (**M_{B1}**) is induced upon the addition of a catalytic amount (20 mol%) of the organobase, i.e., DABCO (1,4-diazabicyclo[2.2.2]octane), at ambient temperature.¹⁶¹ The influence of the solvent type and monomer concentration on the number-averaged molar mass (M_n) of the resulting polymers was studied. Accordingly, we selected dichloromethane (DCM) and tetrahydrofuran (THF) as solvents, and the molar concentration was set to either 0.4 M or 0.8 M (refer to Figure 3.6D). Surprisingly, a lower concentration of monomer (0.4 M) in DCM as the polymerization solvent gave the best result in terms of M_n ($M_n = 42500 \text{ g}\cdot\text{mol}^{-1}$, Figure 3.6C, D), a value that is more than twice as high as that for main-chain α -bisimine polymers synthesized via head-to-tail ADMET polymerization.¹⁹³

Usually for step-growth polymerization techniques, a highly concentrated solution of monomers (i.e., 1.0 M) and long reaction times are utilized to disfavor the intramolecular backbiting reaction, leading to the formation of linear polymers via intermolecular reactions.. Here, the hydroxyl-yne reaction as an X-yne click reaction^{159,163,194} has a very high driving force, rapidly taking place and achieving very high conversions (> 99%) within 2 h in a small-scale synthesis (100 – 200 mg) (Figure 3.6). The prolonged reaction times (24 h, Figure 3.6C, dotted line) do not enhance the M_n . We speculate that a lower concentration (0.4 M in our case) may help solubilize the growing polymer chains more efficiently during the polymerization. In fact, Tang *et al.* have also reported an optimal hydroxyl-yne polymerization

Chapter 3: head-to-tail ADMET and hydroxyl-yne click polymerization

of stimuli-inactive monomers in 0.4 M solution at ambient temperature.¹⁶¹ Furthermore, the head-to-tail design of our monomer eliminated the impact of non-ideal stoichiometry encountered for AA and BB monomer systems.

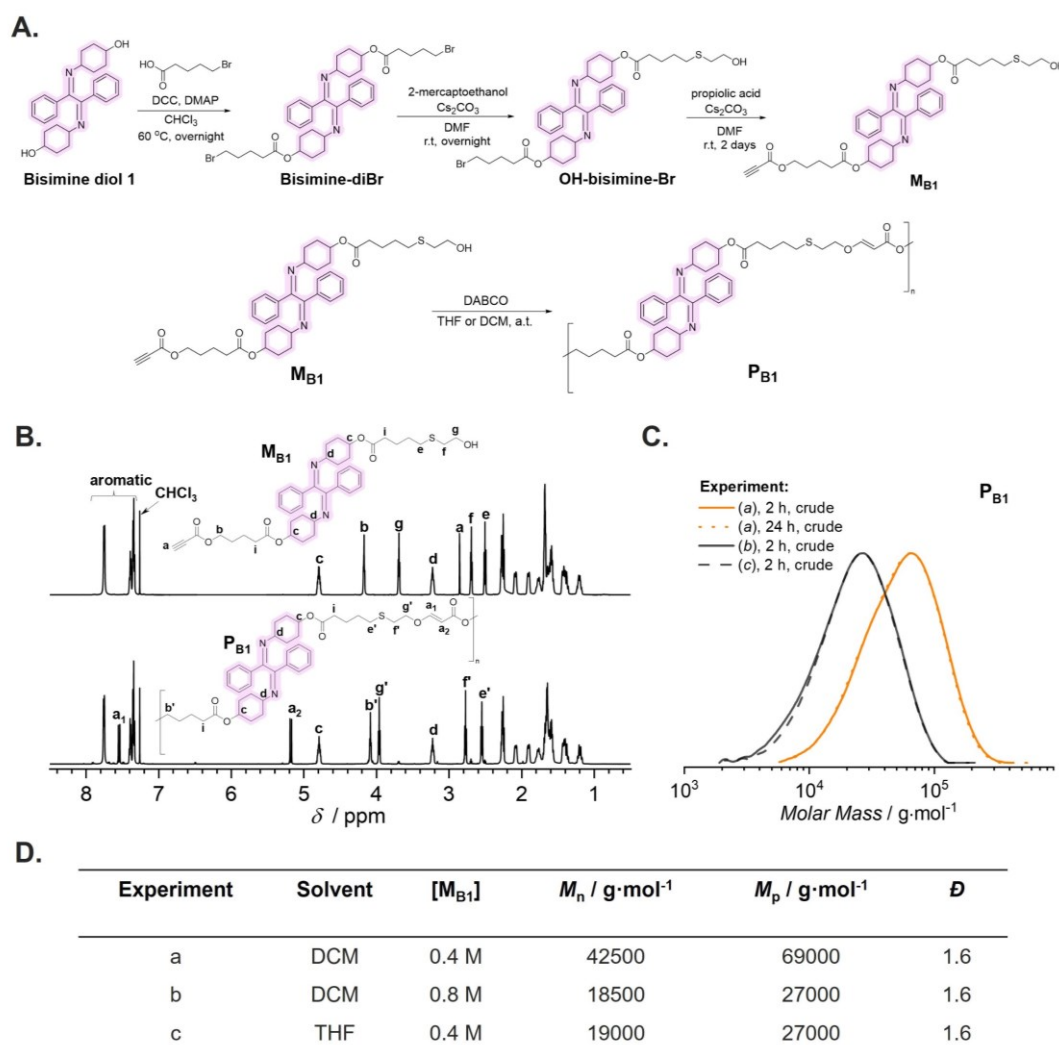


Figure 3.6. Synthesis of α -bisimine main-chain homopolymer via hydroxyl-yne click polymerization. (A) Synthesis scheme for monomer M_{B1} (up) and polymer P_{B1} (bottom). (B) Stacked ^1H NMR spectra (600 MHz, 32 scans, CDCl_3) of the monomer and the polymer. (C) DMS- d_6 SEC traces of the resulting homopolymers synthesized under different polymerization conditions reported in the table shown in section (D). (D) Summary of the polymerization conditions for the homopolymer synthesis. Reproduced from ref.¹⁹⁵ with permission from American Chemical Society (ACS).

The selective reaction between the hydroxy and the alkyne groups to form vinyl ether ester bonds (i.e., ether acrylate) is evidenced by the ^1H NMR spectrum recorded for the resulting polymer (Figure 3.6B, down). The magnetic resonances at 7.54 ppm (proton a_1) and 5.18 ppm (proton a_2 shown in Figure 3.6B) are associated with the internal acrylate protons, which is in line with literature.^{161,196,197} Furthermore, inspection of the NMR spectrum indicates no evidence of transesterification. More importantly, there was no impact on the α -bisimine core as revealed by the comparative NMR spectra of the monomer and polymer shown in Figure 3.6B. Thus, the technique features excellent control over the sequence of the α -bisimine photoswitches within the polymer chain.

3.2.1.2. Block copolymer synthesis

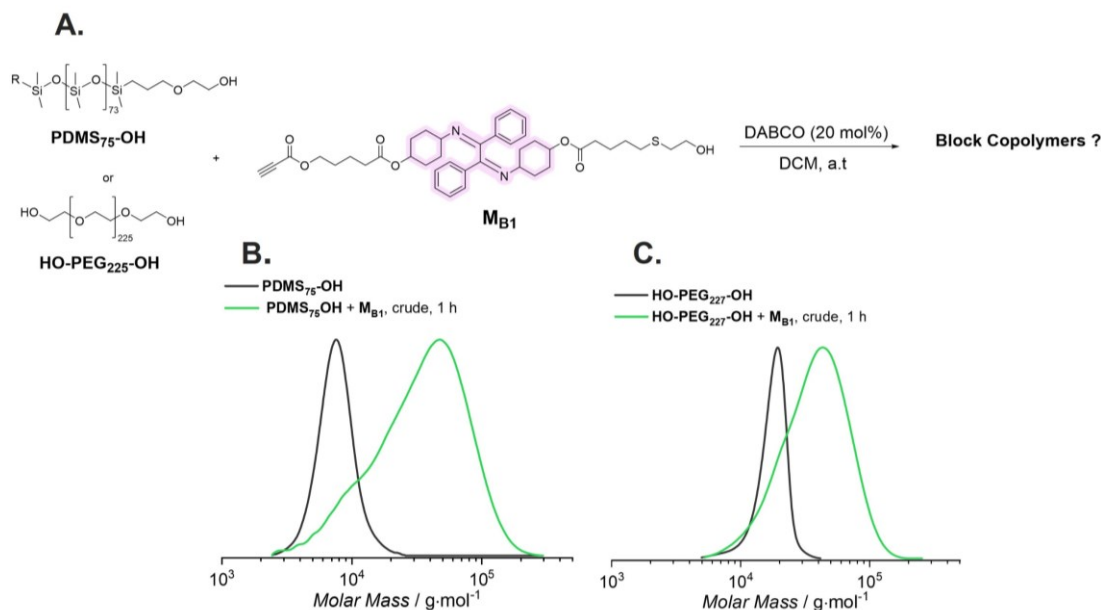


Figure 3.7. Photoswitching main-chain block copolymer synthesis via hydroxyl-yne click polymerization. (A) Reaction scheme. (B-C) THF-SEC traces of macro chain stoppers and block copolymer mixtures.

Given the efficient synthesis of α -bisimine main-chain homopolymer, we further apply the hydroxyl-yne click polymerization technique to prepare block copolymers depicted in Figure 3.7A. We utilized commercially available hydroxy-end functionalized homopolymer as macro chain stopper, i.e., hydroxy-terminated polydimethylsiloxane (**PDMS₇₅-OH**, $M_n \sim 5000 \text{ g}\cdot\text{mol}^{-1}$ in Figure 3.7B shown as black trace) and polyethylene glycol (**HO-PEG₂₂₇-OH**, $M_n = 10000 \text{ g}\cdot\text{mol}^{-1}$ in Figure 3.7C, black trace), respectively. However, the SEC traces recorded in THF for the crude polymerization reactions (green traces in Figure 3.7B and C, respectively) show the incomplete reaction of the macro chain stopper with the monomer **M_{B1}**, evidenced by the shoulder at low M_n corresponding to the macro chain stoppers.

3.3. Concluding remarks

In summary, while both polymerization techniques (i.e., ADMET and hydroxyl-yne), are efficient for main-chain α -bisimine homopolymer synthesis, a weak control over block copolymer synthesis via chain-extension of a macro chain stopper is encountered. In other words, neither the head-to-tail hydroxyl-yne click polymerization nor ADMET polymerization is ideal for the synthesis of photoswitching block copolymer. As a result, an alternative approach is required and this is explored in the next chapter.

Chapter 4: Sequence-defined Main-chain Oligomers and Block Copolymers based on α -bisimineⁱⁱ

In the previous chapter, we employed head-to-tail ADMET and hydroxyl-yne click polymerization techniques to synthesize main-chain photoswitching block copolymers. However, these two approaches are not desirable owing to their poor control over the chain extension, leading to a mixture of homopolymers and block copolymers. Furthermore, the dispersity (\mathcal{D}) of the obtained homo- and block copolymers is broad (mostly larger than 1.4). With regard to the block copolymers, including stimuli-responsive BCPs, dispersity affects their self-assembly.^{198,199} For example, diblock copolymers (diBCPs) with larger \mathcal{D} values may result in larger domain size of the resulting thin-film nanostructures.²⁰⁰ Therefore, achieving functional main-chain block copolymers with low dispersity is ideal.

A powerful approach to achieving monodisperse polymers is to use efficient, selective and orthogonal reactions in a stepwise and iterative manner to grow a polymer sequence with defined composition and topology.^{201,202} The obtained polymers are often referred to as sequence-defined polymers (SDPs).²⁰³ While powerful synthetic tools have been employed to deliver conventional (i.e., stimuli-non-active) synthetic macrostructures,^{204,205} sequence-defined main-chain stimuli-responsive polymers are still elusive.

In this chapter, we introduce the successful synthesis of sequence-defined main-chain homopolymers, graft polymers, and block copolymers, all containing α -bisimine repeating units in their main-chain. To synthesize the main-chain sequence with absolute chain-end group fidelity, we harness the hydroxyl-yne click reaction and deprotection chemistry. We further construct graft homo-sequences based on the as-synthesized homo-sequences by utilizing the *N*-heterocyclic carbene (NHC)-mediated thiol-Michael click reaction. We subsequently demonstrate the excellent functional group tolerance of the employed hydroxyl-yne click reaction towards olefins, acrylates and non-activated alkynes. Most importantly, main-chain photoswitching (hybrid) block copolymers with extremely low dispersity values (\mathcal{D} = 1.05-1.07) were synthesized and purified with ease by using the hydroxyl-yne click reaction as a ligation technique.

ⁱⁱ Parts of this chapter were reproduced from Thai, L. D.; Kammerer, J. A.; Golberg, D.; Mutlu, H.; Barner-Kowollik, C. *Chem* **2024**, *in press*, with permissions.

4.1. Synthesis of main-chain odd- and even-numbered sequences

We initially design two synthetic routes that allow for the realization of main-chain sequences with an even- and odd-number of α -bisimine photoswitches in parallel via the hydroxyl-yne chemistry (Figure 4.1A and C). For both designs, we use a heterofunctionalized α -bisimine monomer, **TBDMSO-[B]₁-yne**, with one hydroxy protected with a *tert*-butyldimethyl silyl (TBDMS) group (α -termini) and one activated alkyne (ω -termini). The selective protection of the hydroxy group in the α -bisimine monomer is essential to prevent polymerization during the reaction with other homofunctionalized dihydroxy-terminated monomers.

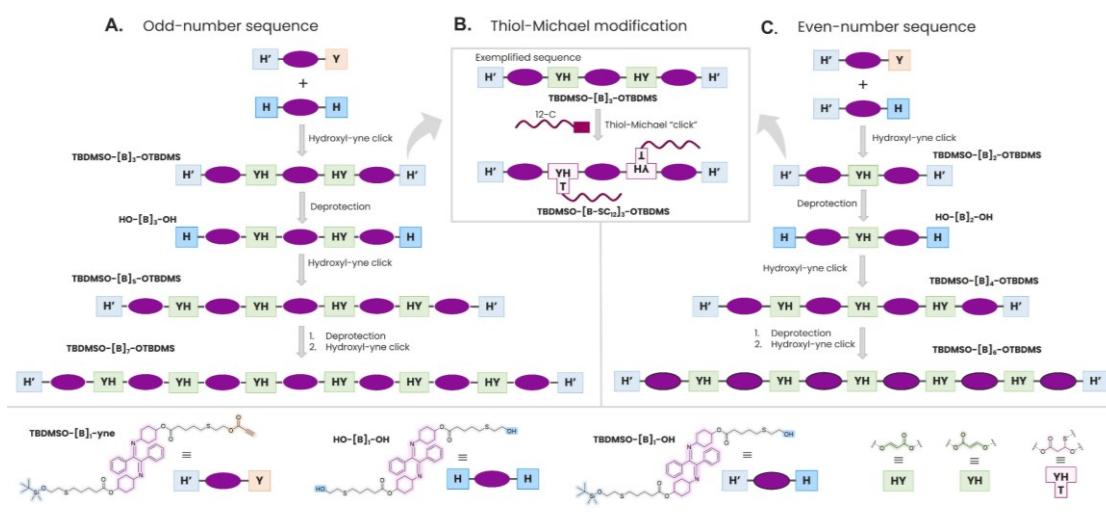


Figure 4.1. Synthetic strategy to obtain monodisperse α -bisimine main-chain oligomers with facile post-synthesis modification and perfect chain-end group fidelity. Synthesis route for odd-number (A) and even-number (B) homo-sequences of main-chain α -bisimines. Conditions for the hydroxyl-yne click reaction: **TBDMSO-[B]₁-yne** (2.1 eq), **HO-[B]₁-OH** (1.0 eq), DABCO base (20 mol% with respect to the hydroxy end-group) in anhydrous DCM (0.4 M). Identical conditions were employed for the even-number sequences. Deprotection of hydroxy group was carried out in TBAF solution (1.0 M in THF) for 30 minutes; (C) Synthesis of the graft sequence via thiol-Michael click reaction.

For the odd-numbered sequences, we employ a symmetrical homofunctionalized α -bisimine monomer, **HO-[B]₁-OH**, bearing two hydroxy groups at the two termini (Figure 4.1A). Upon addition of 20 mol% of DABCO as a base catalyst in anhydrous dichloromethane (DCM), the click reaction between the two monomers, **HO-[B]₁-OH** (1.0 eq) and **TBDMSO-[B]₁-yne** (2.1 eq), takes place, affording a monodisperse oligomer with three α -bisimine repeating units (**TBDMSO-[B]₃-OTBDMS**). The subsequent cleavage of the TBDMS protecting group in **TBDMSO-[B]₃-OTBDMS** with TBAF (tetra-*N*-butylammonium fluoride) solution generates **HO-[B]₃-OH** with two free hydroxy end-groups. The sequence of five α -bisimine photoswitches is obtained upon the hydroxyl-yne click reaction between **HO-[B]₃-OH** and **TBDMSO-[B]₁-yne**. The iterative cycle of hydroxyl-yne click followed by TBAF-deprotection is repeated until the desired α -bisimine repeating unit number is reached (Figure 4.1A). In a similar manner, the even-numbered sequence is synthesized by employing **TBDMSO-[B]₁-OH** and **TBDMSO-[B]₁-yne** monomers (Figure 4.1C).

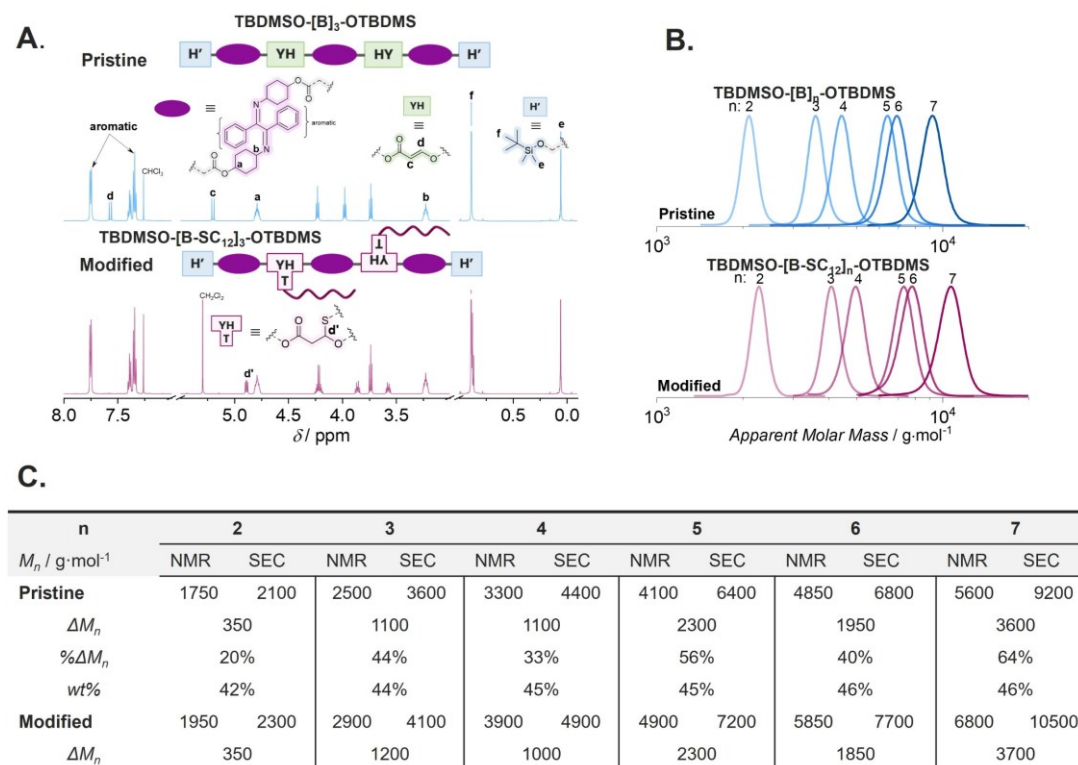


Figure 4.2. Chemical and macromolecular solution-state analysis confirms the successful synthesis and quantitative post-modification by thiol-Michael click reaction of the α -bisimine sequences. (A) Comparative ^1H NMR spectra (600 MHz, 32 scans, in CDCl_3) of a 3-mer sequence, **TBDMO-[B]₃-OTBDMS** (in blue), and the respective modified sequence, **TBDMO-[B-SC₁₂]₃-OTBDMS** (in purple). The assignment of selected resonances was made via careful analysis of 1D and 2D NMR spectra (Experimental part, section 11.4). (B) THF-SEC for **TBDMO-[B]_n-OTBDMS** (blue traces) and **TBDMO-[B-SC₁₂]_n-OTBDMS** (purple traces), with $n = 2-7$. Note that the number of alkyl side chains (n) is less than that of α -bisimine units by one unit. The apparent molar mass was determined on the basis of polymethylmethacrylate (PMMA) calibration standard. (C) Number-averaged molar mass determined by ^1H NMR spectroscopy ($M_{n,\text{NMR}}$) and by THF-SEC ($M_{n,\text{SEC}}$). $\Delta M_n = M_{n,\text{SEC}} - M_{n,\text{NMR}}$; % $\Delta M_n = \Delta M_n / M_{n,\text{NMR}} \times 100\%$.

Sequence-defined oligomers of 2 to 7 repeating units of α -bisimine were prepared (**TBDMO-[B]_n-OTBDMS**, $n = 2-7$). It should be noted that the length of the alkyl chain spacer in all monomers is identical (Figure 4.1). The TBDMS groups also act as the chain end-group which remains completely intact during the hydroxyl-yne click reaction, allowing for the precise determination of repeating unit number via ^1H NMR spectroscopy. The selective formation of *trans*-ether acrylate bonds is evidenced in the ^1H NMR spectra; the magnetic resonances of the respective protons ($\delta = 5.20$ ppm (proton **c**) and 7.56 ppm (proton **d**), Figure 4.2A, blue curve) match well with the literature-reported values.^{161,196,197,195} The SEC traces recorded in THF for these sequences clearly demonstrate their uniform molecular weight distribution (MWD) (Figure 4.2B).

Since the synthesized sequences contain internal ether acrylate bonds in their backbones, we exploit the thiol-Michael click reaction (in the presence of *N*-heterocyclic carbene (NHC) as the catalyst) to graft C₁₂-alkyl thiol on the oligomer backbone as side chains (**TBDMO-[B-SC₁₂]_n-OTBDMS**) (general synthesis scheme shown in Figure 4.1C) to afford comb-like macromolecular sequences. The comparative ^1H NMR spectra of pristine and post-modified oligomers (Figure 4.2A) show the complete disappearance (i.e., ~100% conversion) of

Chapter 4: Sequence-defined main-chain macromolecules based on α -bisimine

resonances associated with the unsaturated ether acrylate, accompanied by the appearance of new resonances (e.g., $\delta = 4.88$ ppm (proton **d'**)) due to the formation of C-S bonds (Figure 4.2A). The THF-SEC traces also indicate a noticeable increase in the hydrodynamic volume of the modified sequences, as expressed via the increase in the values of M_n (compare the SEC traces and M_n values shown in Figure 4.2B,C). These results confirm the successful and efficient post-polymerization functionalization of the sequence-defined macromolecules.

In work by Tang *et al.*,¹⁹⁶ the thiol-Michael reaction between hydroxyl-terminated thiols and the formed ether acrylates enabled the subsequent chain extension of the obtained (non-stimuli-responsive) sequence via hydroxyl-yne click reaction. Nonetheless, this strategy does not allow for the installation of main-chain reactive-groups (e.g., α -bisimine in our case). Here, our strategy combines the protection/deprotection chemistry and the hydroxyl-yne click reaction to initially synthesize linear sequenced-defined macromolecules decorated with main-chain photoswitches. The as-synthesized sequences can further be manipulated via a catalyst-mediated thiol-Michael reaction in just one step (i.e., post-synthesis modification), generating more complex structures, e.g., sequence-defined comb-like graft macromolecules.

Furthermore, close inspection of the data shown in Figure 4.2C reveals a mismatch between the M_n determined by ^1H NMR spectroscopy ($M_{n,\text{NMR}}$) and by SEC ($M_{n,\text{SEC}}$) for **TBMDSO-[B]_n-OTBDMS**. While the M_n values determined by NMR are identical to the theoretical values, the $M_{n,\text{SEC}}$ is always larger than the $M_{n,\text{NMR}}$. Since the calibration standard is based on poly(methylmethacrylate) (PMMA), the M_n determined here is related to the hydrodynamic volume of linear aliphatic polymer coils. However, the main-chain α -bisimine photoswitches and the TBDMS chain-end groups are non-linear and bulky moieties. In other words, the difference between $M_{n,\text{NMR}}$ and $M_{n,\text{SEC}}$ ($\Delta M_n = M_{n,\text{SEC}} - M_{n,\text{NMR}}$) observed here represents the substantial hydrodynamic volume contributed by the α -bisimine repeating units within the main-chain and the TBDMS end groups. Indeed, the ΔM_n values determined for the **TBMDSO-[B-SC₁₂]_n-OTBDMS** negligibly differ from those of the parent polymers (Figure 4.2C), strongly indicating that the cause of the $M_{n,\text{NMR}}-M_{n,\text{SEC}}$ difference originates from the non-linear and bulky groups.

4.2. Functional group tolerance of the hydroxyl-yne click reaction

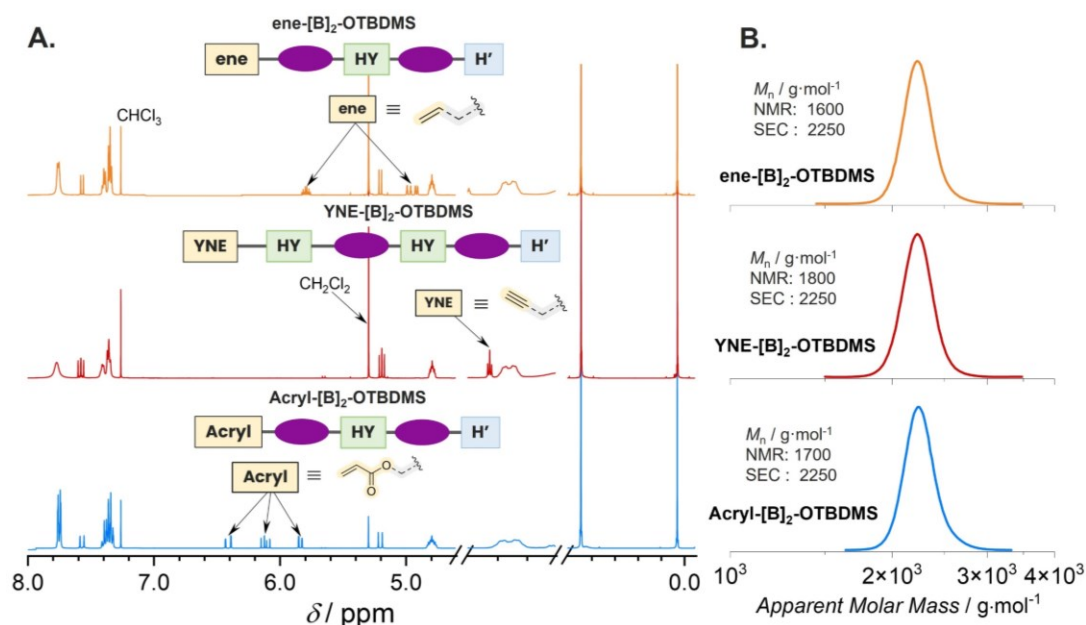


Figure 4.3. Chemical compatibility enables the orthogonal incorporation of functional chain-ends. (A) Sectional stacked ^1H NMR spectra (600 MHz, 32 scans, in CDCl_3) of 2-mer sequences with functional end groups: **ene-[B]₂-OTBDMS** (orange curve), **YNE-[B]₂-OTBDMS** (red curve), **Acryl-[B]₂-OTBDMS** (blue curve). (B) THF-SEC traces for **ene-[B]₂-OTBDMS** (orange trace), **YNE-[B]₂-OTBDMS** (red trace), **Acryl-[B]₂-OTBDMS** (blue trace) sequences. M_n values were determined based on PMMA calibration standards.

We further explore the tolerance of the hydroxyl-yne click reaction and the TBAF-deprotection towards other functional groups. Thus, in addition to the hydroxy- and TBDMS-terminated sequences, we design three 2-mer sequences, **ene-[B]₂-OTBDMS**, **YNE-[B]₂-OTBDMS**, **acryl-[B]₂-OTBDMS**, each containing two main-chain α -bisimine groups and functionalized with an end-group apart from hydroxy moiety, i.e., olefins, non-activated alkynes, and acrylates, respectively (NMR spectra and SEC traces are shown in Figure 4.3). The ^1H NMR spectra in Figure 4.3A unambiguously evidence the excellent functional group tolerance of our approach, in which the magnetic resonances corresponding to the respective reactive group ($\delta = 4.94$ and 5.78 ppm for olefin, $\delta = 1.95$ ppm for the non-activated alkyne, and $\delta = 5.83$, 6.11 , and 6.40 ppm for acrylate) remain chemically intact for each polymer sequence. Further, comparing the integral values of the magnetic resonances assigned to these end-groups (olefins, non-activated alkynes, and acrylates) with those of the α -bisimine (e.g., $\delta = 4.78$ ppm) confirms the quantitative end-group fidelity. These functional end-groups, i.e., olefin, acrylate, and non-activated alkyne, are crucial for other ligation chemistries, such as cross-metathesis²⁰⁶ and copper-catalyzed azide-alkyne cycloaddition (CuAAC).²⁰⁷ Thus, our herein reported method holds a key promise for combining other orthogonal ligation chemistries to further construct diverse monodisperse architectures, e.g., multiblock copolymers. Additionally, the M_n values determined from THF-SEC for these 2-mer sequences are identical (SEC traces are shown in Figure 4.3B), strongly suggesting the negligible impact of these end-groups, i.e., olefine, alkyne, and acrylate, which are small in size, on the hydrodynamic volume of the resulting sequences.

4.3. Block copolymer synthesis

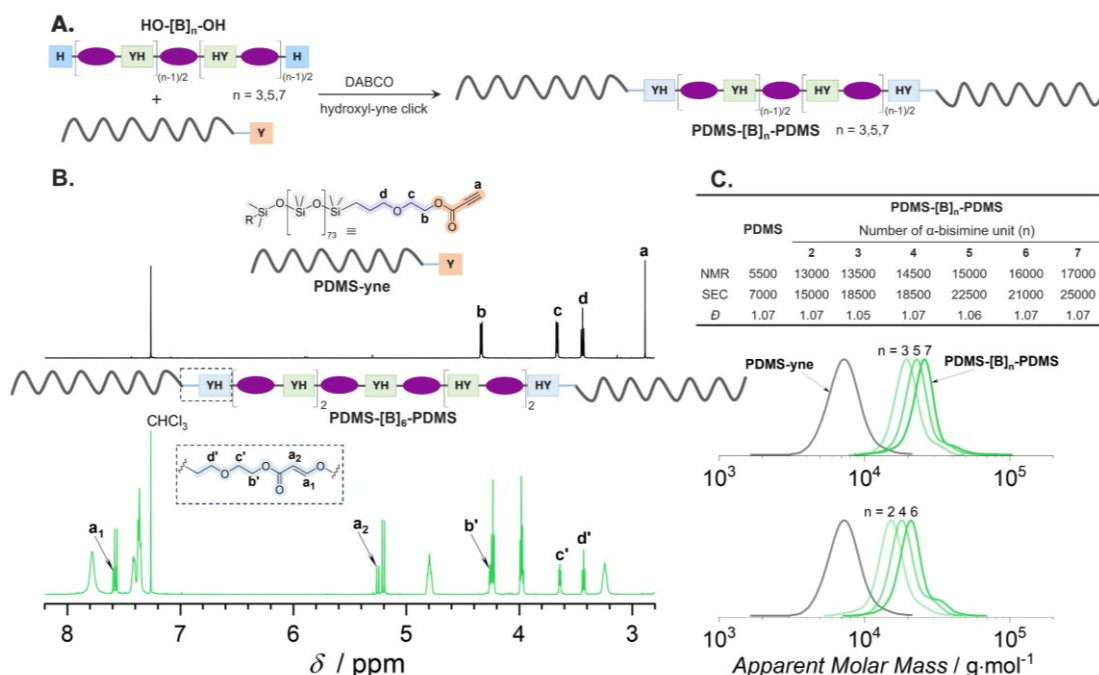


Figure 4.4. Metal-free hydroxyl-yne click reaction as a potent ligation chemistry to generate block copolymers. (A) Synthesis of ABA triblock copolymers via the hydroxyl-yne click reaction between **PDMS-yne** (2.2 eq) and **HO-[B]_n-OH** (1.0 eq) under the catalysis of DABCO (20 mol%). (B) Stacked sectional ¹H NMR spectra (600 MHz, 32 scans, in CDCl₃) of **PDMS-yne** (black curve) and **PDMS-[B]₆-PDMS** ABA triblock copolymers (green curve). (C) THF-SEC traces of **PDMS-yne** (black trace) and the ABA triblock copolymers (odd sequenced one shown in the upper SEC traces and the even-ones at the bottom). *M_{n,SEC}* values were determined based on PMMA calibration standard.

We have so far demonstrated the use of hydroxyl-yne click and TBAF-deprotection chemistry to synthesize monodisperse photoswitching oligomers with excellent functional groups tolerance. To further expand the application scope of such a click reaction, we next employ the hydroxyl-yne reaction as a ligation technique to synthesize photoswitching block copolymers, namely AB diblock and ABA triblock copolymers. We select a commercially available silicon-decorated polymer with a hydroxyl end-group, hydroxy-terminated poly(dimethylsiloxane) (**PDMS-OH**, *M_n* ~ 5500 g·mol⁻¹ (determined by ¹H NMR), \bar{D} = 1.07), to form the light-inactive block (A block). Inorganic-organic hybrid block copolymers are highly attractive, especially for lithography applications, due to the smaller domain size of thin-film nanostructures.^{199,208,209} Nevertheless, to our best knowledge, photoswitchable main-chain hybrid BCPs with very low dispersity values have not been reported.¹⁸⁷

Prior to block copolymers synthesis, we transformed the hydroxy end-group in **PDMS-OH** to the activated alkyne group (**PDMS-yne**). The α -bisimine block (B block) originates from the hydroxy-terminated sequences (**ene-[B]₂-OH**, **YNE-[B]₂-OH**, **HO-[B]_n-OH** with *n* = 2-7). We then ligated the sequences via DABCO-catalyzed hydroxyl-yne click reaction between **PDMS-yne** (A block) and the photoswitching block (B block), forming AB diblock (i.e., **ene-[B]₂-PDMS**, **YNE-[B]₂-PDMS**) and ABA (i.e., **PDMS-[B]_n-PDMS**, *n* = 2-7) triblock copolymers (Figure 4.4 and 4.5). The analysis of the ¹H NMR spectra of the obtained BCPs confirms the clean and complete ligation (Figure 4.4B).

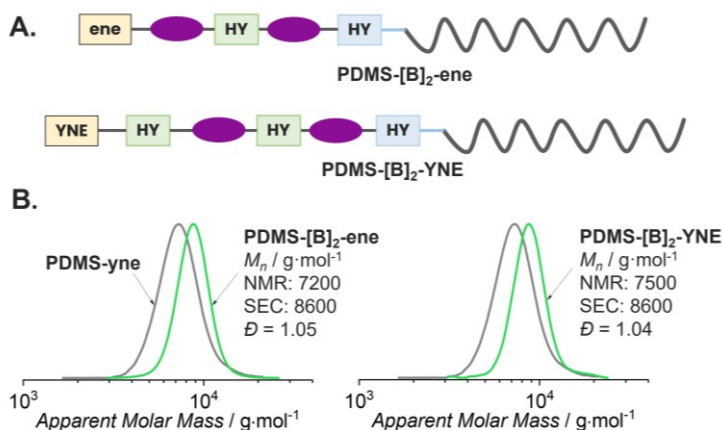


Figure 4.5. AB diblock copolymers. (A) General structures of AB diblock copolymers with olefin (**PDMS-[B]₂-ene**) and (non-activated) alkyne end-groups (**PDMS-[B]₂-YNE**). (B) THF-SEC traces of **PDMS-[B]₂-ene** (left, green color) and **PDMS-[B]₂-YNE** (right, green color). $M_{n,SEC}$ values were determined on the basis of PMMA calibration standards.

The integration of the magnetic resonances of the ether acrylate protons at block junctions (e.g., $\delta = 5.25$ ppm (proton **a**₂), Figure 4.4B) or the functional end-group in the case of AB diBCPs, allows to calculate the precise number of α -bisimine repeating units as well as the length of the PDMS block, matching exactly with the theoretical values. THF-SEC traces recorded for these BCPs unambiguously confirm the successful chain extension with \bar{D} values close to 1.05 and 1.07 (Figure 4.4C). Noticeably, while the AB diBCPs show a unimodal MWD (Figure 4.5B), a small shoulder peak at higher (apparent) molar mass appears in the SEC traces of the ABA triBCPs (Figure 4.4C). The shoulder peak becomes more noticeable in polymers with a larger number-averaged molar mass (M_n). This shoulder is not a result of incomplete chain extension but likely due to aggregation caused by the interchain interaction at high M_n values.^{210,211} Since the light-responsive block (α -bisimine block) is monodisperse, the \bar{D} values slightly above 1.0 are a result of the disperse PDMS-blocks and the high molecular weight shoulders due to agglomeration.^{210,211} More importantly, the facile and efficient synthesis of main-chain photoswitching block copolymers exemplified here highlights the metal-free hydroxyl-yne click reaction as a potent ligation technique to realize more advanced architectures, such as multi-block copolymers.

4.4. Concluding remarks

In conclusion, we introduce sequence-defined main-chain photoswitchable macromolecules with absolute chain end-group functionality via efficient organobase-catalyzed hydroxyl-yne click and TBAF-deprotection chemistries. We have also demonstrated the excellent compatibility of these chemistries toward other functional groups, i.e., olefins, acrylates and non-activated alkynes. In addition, the formation of internal ether acrylate bonds from the metal-free hydroxyl-yne click reaction allows for the post-modification functionalization of the sequence defined macromolecules via thiol-Michael chemistry, generating more complex sequence-defined light-responsive macromolecules in just one additional step. We further show the hydroxyl-yne click reaction as a powerful ligation technique for main-chain

Chapter 4: Sequence-defined main-chain macromolecules based on α -bisimine

photoswitchable AB and ABA block copolymer synthesis. We envisage that with this strategy, development of other photoswitching block copolymers, such as those based on hydrazone and spiropyran, is synthetically feasible, which will be reported in **Chapters 7 and 8**. More importantly, we have achieved the second objective of the current thesis by establishing the sequence-defined strategy to realize main-chain photoswitching block copolymers, at least on the example of α -bisimine photoswitch.

Chapter 5: Glass Transition Temperature and Solid-state Photoswitching Efficiencyⁱⁱⁱ

Alongside the successful synthesis of well-defined main-chain photoswitching block copolymers reported in Chapter 4, another important aspect of the “photodynamic block copolymer lithography” concept is the possibility to switch the solid-state (thin-film) block copolymer nanostructure. Hence, clean and efficient photoswitching, e.g., photoisomerization, in the solid state of the photo-sensitive block is essential and is the objective of this chapter.

While some chromophores, e.g., diarylethenes, respond relatively fast to irradiation in the solid state, the isomerization efficiency of other photoswitches, e.g., azobenzene, is significantly reduced in the solid state compared to solution.²¹² Possibly, the restricted movement of the chains is inflicted by intermolecular interactions of the chromophores, e.g., π - π stacking, contribute to the poor performance in the solid state.²¹³ Various strategies have been developed to address this issue.²¹⁴ In the realm of photoresponsive polymeric materials, for example, Weis *et al.* designed a homopolymer containing azobenzene side chains in which two methoxy groups were substituted on the phenyl rings of the chromophore, causing a distortion in its planarity, significantly reducing the intermolecular π - π stacking and enhancing solid-state isomerization.²¹⁵ Furthermore, the modification caused a red-shift in the optical absorption of the polymer, enabling photopatterning of the material with visible light ($\lambda_{\text{max}} = 625$ nm, $\lambda_{\text{max}} = 470$ nm).²¹⁵ The latter was particularly important for the full reversibility of the system as irradiation with red light reduced photobleaching compared to UV light irradiation. However, a chemical modification of the chromophore is not always possible as it requires fine-tuning for each type of chromophores and side reactions may occur.

In an alternative – yet often not explicitly mentioned – approach, chain spacers, e.g., alkyl chains of a sufficient length, or bulky groups, e.g., tetraphenylethene, have provided sufficient molecular mobility for photoswitching.²¹⁶ In a comparable manner, monomers containing photoactive groups were copolymerized with other monomers to diminish the intermolecular interaction among chromophores in the resulting copolymers (refer to Figure 5.1 A).²¹⁷ Notably, all approaches described thus far have been applied to side-chain photoswitches. While

ⁱⁱⁱ Parts of this chapter were reproduced from Thai, L. D.; Guimarães, T. R.; Chambers, L. C.; Kammerer, J. A.; Golberg, D.; Mutlu, H.; Barner-Kowollik, C. *J. Am. Chem. Soc.* **2023**, 145, 14748-14755 (with permission from the American Chemical Society), and Thai, L. D.; Kammerer, J. A.; Théato, P.; Mutlu, H.; Barner-Kowollik, C. *ACS Macro Lett.* **2024**, 13, 6, 681–687 (with permission from the American Chemical Society), and Thai, L. D.; Kammerer, J. A.; Golberg, D.; Mutlu, H.; Barner-Kowollik, C. *Chem* **2024**, *in press*, with permissions.

Chapter 5: Glass transition temperature and solid-state photoswitching efficiency

photoswitching polymers with main-chain photoswitches such as azobenzenes,^{218,219} have been explored, even fewer attempts to improve photoswitching efficiency have been made in these systems. In summary, despite these efforts and the general progress in solid-state photoswitching,^{214,220,221} studying solid-state photoisomerization or photoswitching still remains challenging and there is still a critical and consistent lack of efficiently photoswitching polymers.

In contrast to approaches described in the literature, we here employ linear structures with adjustable chromophore density and branched topologies to assist the photoisomerization of main-chain chromophore in the solid state (refer to Figure 5.1A). We again employ the head-to-tail ADMET polymerization to synthesize α -bisimine main-chain homopolymers, followed by post-polymerization modification using the thiol-Michael addition reaction to generate the branched architectures (refer to Figure 5.1B, C for general synthesis route and structures).

We will show that the different topologies do not affect isomerization in solution, whereas both an additional spacer within the main-chain and a branched topology significantly improve the isomerization efficiency in the solid state. The higher isomerization efficiency is inversely correlated with the glass transition temperature (T_g) of the polymers, reflecting the importance of molecular mobility of the chromophore for the isomerization efficiency.

5.1. Correlation between glass transition temperature and photoswitching efficiency

5.1.1. Topological design and synthesis of the main-chain chromophore polymers

We synthesized four different main-chain chromophore polymers via a head-to-tail ADMET polymerization with different topologies to systematically investigate the influence on the isomerization efficiency. The parent polymers are **P₁** and **P₂**, of which the latter contains an additional alkyl spacer. The head-to-tail ADMET polymerization not only allows the installation of the α -bisimine photoswitch into the backbone, but also creates possibilities for post-polymerization modification due to the formation of main-chain internal acrylate double bonds. By making use of the base-catalyzed thiol-Michael reaction of the electron-deficient internal acrylate double bonds, a precise placement of side chains to the pristine ADMET polymers was realized. Accordingly, polymers **P₁** and **P₂** were modified with a C₁₂-alkyl thiol to afford polymers **P₃** and **P₄**, respectively (refer to Figure 5.1B for general synthesis route). The modification conditions are mild, and the conversions are quantitative (~100% conversion, ¹H NMR spectra in Figure 5.2A). Critically, the chromophore remains intact as evidenced in the ¹H NMR spectra (Figure 5.2).

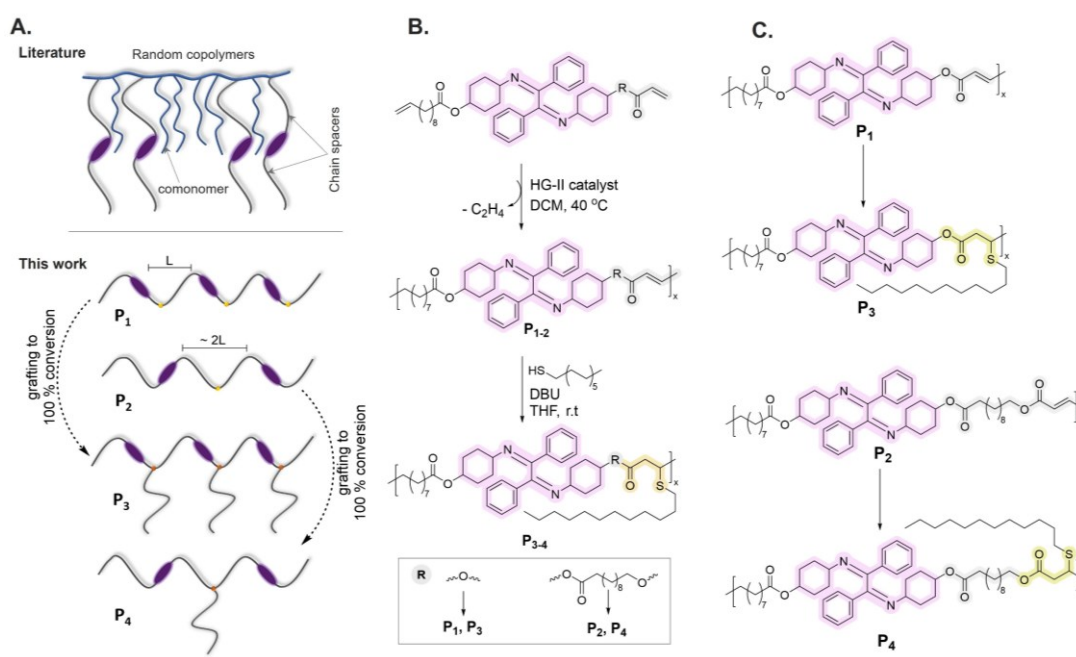


Figure 5.1. (A) Structural design of photoswitchable polymers for solid-state applications. In the literature, random copolymerization is commonly reported, which has limitations such as statistical distribution of chromophores, mainly side-chain chromophores. In this work, the precise control of chromophore density and polymer topology, main-chain chromophores and facile synthesis protocol are key design highlights. Direct comparison of isomerization efficiency in solution and solid state of different polymer topologies is also enabled. (B) and (C) Synthetic route and structures of α -bisimine-based homopolymers **P**₁, **P**₂, **P**₃ and **P**₄. Reproduced from ref.¹⁹³ with permission from the American Chemical Society.

To correlate the topology of the polymers with their photoswitching efficiency and physical properties, we initially characterize their molecular weight distributions, thermal properties and UV-vis absorptivity (Figure 5.2). Upon the modification, **P**₃ shows higher M_n compared to the pristine **P**₁, whereas M_n of **P**₄ is smaller than that of **P**₂ (Figure 5.2B). Such an opposite trend observed in **P**₄ may be linked to contraction of the polymer coil resulted from the combination of the longer alkyl chain in the backbone (compared to **P**₃) and the enhancement in the chain flexibility upon the thiol-Michael addition. Regarding the optical property, while there is no shift in the solution UV-vis absorption among the four polymers, the intensity of peak absorptivity at 251 nm decreases from **P**₁ to **P**₄ (Figure 5.2C). The disappearance of the internal acrylate bonds in **P**₃ and **P**₄ may be contributing to this observation. However, the UV-vis spectrum of the blank polymer (polymer **P**₅, refer to Experimental part, Section 11.5, Figure S5.10) featuring no α -bisimine groups, but internal acrylate double bonds in the backbone, showed almost no absorption in the 225-700 nm range. Thus, the internal acrylate double bonds likely do not contribute to the absorption of the chromophore. In fact, such optical behavior may be caused by the shrinkage in mass fraction of the chromophore (62 wt% in **P**₁, 47 wt% in **P**₂, 45 wt% in **P**₃, and 37 wt% in **P**₄).²²²

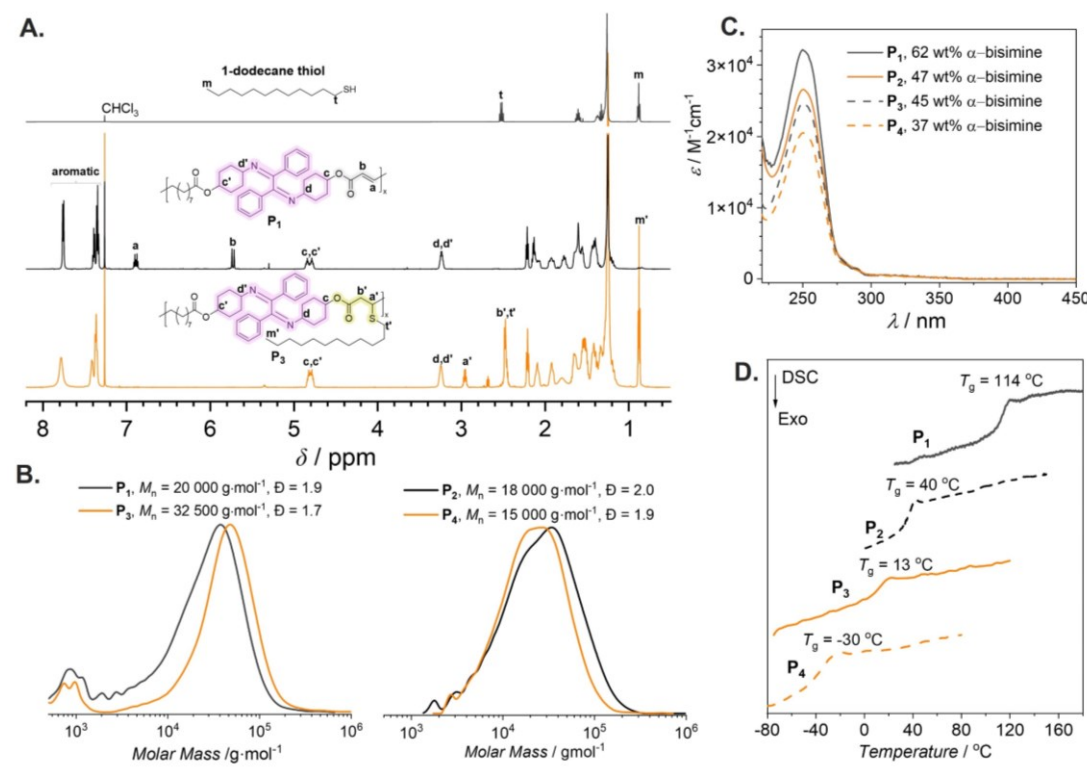


Figure 5.2. Synthesis and Characterization of main-chain photoswitching polymers. (A) ^1H NMR spectra of 1-dodecane thiol (up), polymer P_1 (middle) and P_3 (bottom). The disappearance of the magnetic resonances associated with the protons corresponding to the acrylate (protons a and b) confirms the full conversion of the thiol-Michael reaction. (B) THF-SEC traces and normalized RI detector response of P_1 - P_4 (left: P_1 and P_3 , right: P_2 and P_4). (C) Molar absorptivity of chromophore in P_1 - P_4 , recorded in THF at 20°C via UV-vis absorbance. (D) Stacked differential scanning calorimetry (DSC) thermograms of P_1 - P_4 , recorded during the second heating cycle. Reproduced from ref.¹⁹³ with permission from the American Chemical Society.

With regard to the thermal properties, thermogravimetric analysis (TGA) showed all polymers have good thermal stability with thermal degradation temperatures (i.e., temperatures of 5% mass loss, $T_{d,5\%}$) higher than 260°C (compare Figure S5.9 in section 11.5, Experimental part), with P_2 displaying the highest $T_{d,5\%}$ of 317°C . TGA data also suggest that thermal decomposition of the post-functionalized polymers P_3 and P_4 begins at approx. 260°C , almost 40°C lower than the unfunctionalized polymers (P_1 and P_2), consistent with the lower thermal stability of the introduced thio-ether bonds. The glass transition temperature (T_g) value is highest for P_1 (114°C), followed by P_2 (40°C) and P_3 (13°C), and P_4 shows the lowest T_g (-30°C) (Figure 5.2D). Interestingly, although the crystallization of alkyl side chains has been reported in the literature,²²³ it was not observed for our main-chain branched polymers. Possibly, the presence of the bulky chromophore in the backbone disturbs the crystallization.

The difference in T_g upon modification of chromophore density (62 wt% in P_1 vs 47 wt% in P_2) and polymer topology (P_1 vs P_3 , and P_2 vs P_4) can be primarily derived from the change in the degree of intermolecular interaction, e.g., π - π stacking, among the α -bisimine cores. For example, due to the relatively long length of the side chain in P_3 and P_4 , the chromophores are shielded from each other, lowering the degree of stacking. For non-chromophore containing polymers, the presence of alkyl side chains often results in lower thermal glass transition temperatures.²²⁴⁻²²⁶ Furthermore, the increased number of end-groups per chain^{227,228} and

weight percentage of low T_g components²²⁹ will also result in a lower T_g . In our case, all three factors likely contribute to a decreased T_g and increased molecular mobility following attachment of the flexible alkyl chains.

5.1.2. Molecular flexibility is the key element for the photo-switching efficiency of solid-state polymers

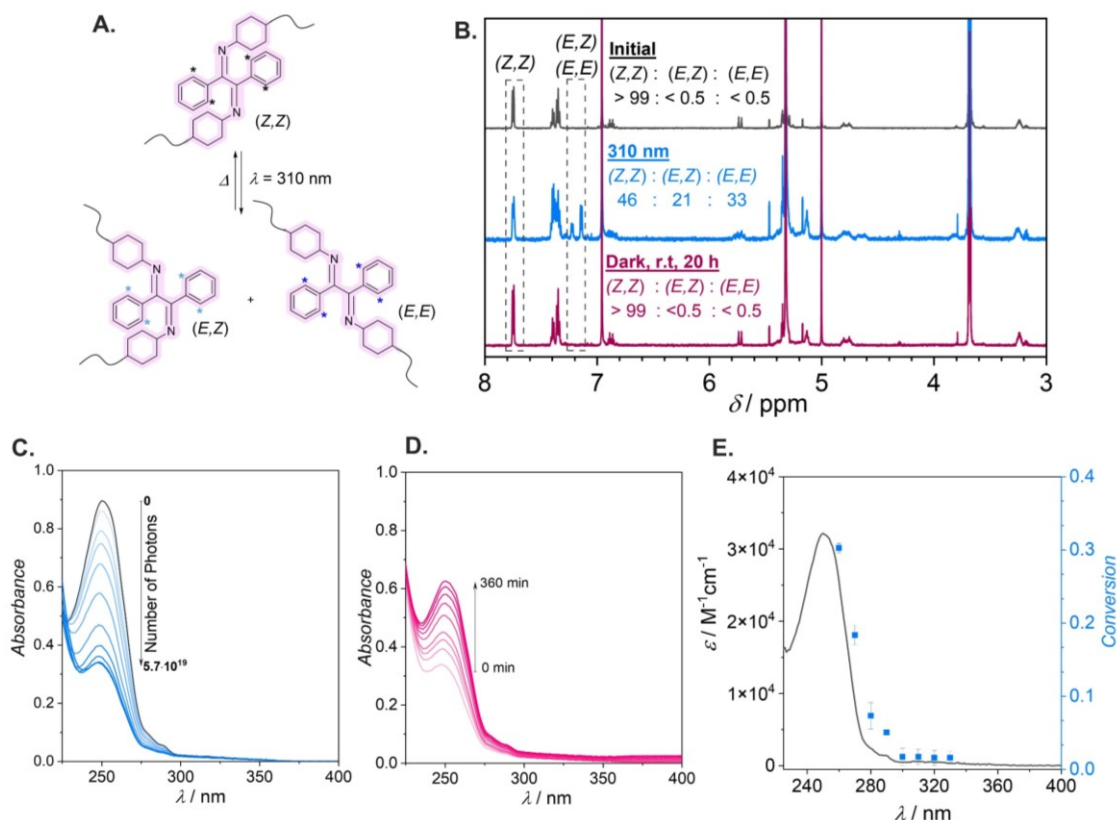


Figure 5.3. Photoisomerization of α -bisimine in THF solution. (A) Illustration of forward and thermal back-isomerization of α -bisimine cores in the polymer backbone. (B) stacked ^1H NMR spectra obtained during irradiation studies in solution of \mathbf{P}_1 ($[\alpha\text{-bisimine}] = 0.84$ mM), $\lambda = 310$ nm, number of photons (N_p): $3.0 \cdot 10^{19}$, laser power: $(4.5 - 5.5) \pm 4.2\%$ mW. The NMR-based conversion was determined by comparison of integral values corresponding to resonances associated with each isomer. Stacked UV-vis spectra obtained during irradiation studies of \mathbf{P}_1 (C) and thermal back-isomerization of \mathbf{P}_1 (D) in THF ($[\alpha\text{-bisimine}] = 32.2$ μM , $\lambda = 310$ nm, laser power: $(4.5 - 5.5) \pm 3.5\%$ mW) at 20°C . The number of photons was calculated from Equation S11.1 (Experimental part). (E) Wavelength-dependent photoconversion of the α -bisimine measured for \mathbf{P}_1 in THF. Reproduced from ref.¹⁹³ with permission from the American Chemical Society.

To demonstrate the applicability of ^1H NMR and UV-vis spectroscopy to monitor the photoisomerization of the α -bisimine chromophore, we first conducted laser experiments on polymer \mathbf{P}_1 in tetrahydrofuran (THF) solution (Figure 5.3B-D for exemplary NMR and UV-vis spectra of \mathbf{P}_1). Upon the irradiation with UV-light (310 nm, $3.0 \cdot 10^{19}$ photons, calculated from Eq. 11.2, Section 11.1, Experimental part), a mixture of metastable isomers, (E,Z) and (E,E), is formed (Figure 5.3A,B). Due to the isomerization, the maximum UV-Vis absorbance at 251 nm gradually decreased from 0.9 to 0.3 with an increasing number of photons without an additional absorption band appearing (Figure 5.3C). Thus, it can be inferred that both the (E,Z) and (E,E) isomers do not absorb UV light, implying the π - π delocalization is distorted upon the light-driven isomerization. The NMR and UV-vis spectroscopy results of the studies allow to

monitor not only the photoisomerization of the α -bisimine photoswitch, but also its thermal back-isomerization (Figure 5.3B-D), showing the reversibility of the isomerization. It should be noted that the molar concentration of the chromophore in both studies was different due to the concentration constraint for each method.

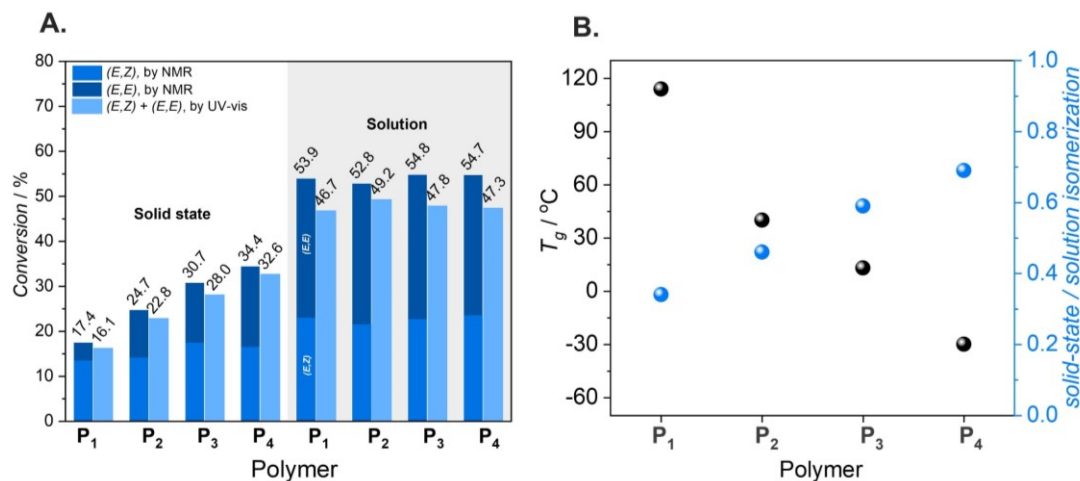


Figure 5.4. Correlation between solid-state photoswitching efficiency and glass transition temperature. (A) Results of irradiation studies (THF solutions and cast films, thickness close to 400-600 nm) monitored by ^1H NMR and UV-vis spectroscopy. Conditions: $\lambda = 310$ nm, $N_p = 1.5 \cdot 10^{19}$, laser power: $(4.5 - 5.5) \pm 4.6$ % mW, $T = 20$ °C. The NMR study was repeated twice with almost identical results. (B) Correlation between T_g of the polymers and the solid-state isomerization efficiency compared to solution. The solid-state/solution isomerization ratio was calculated from the UV-vis study in which the absorbance at the irradiation wavelength, i.e., 310 nm, was kept identical. Reproduced from ref.¹⁹³ with permission from the American Chemical Society.

Subsequently, we applied ^1H -NMR and UV-vis spectroscopy to quantify the photoisomerization of α -bisimines photoswitch for the four polymers in both solution (THF) and solid-state (spin-cast film) after the 310 nm irradiation with a fixed number of photons ($N_p = 1.5 \cdot 10^{19}$). From the NMR study, the isomerization reaches values between 53% and 55% in solution for all topologies, making the photoswitching efficiency in solution independent of the molecular design (Figure 5.4A). Despite the marked difference in chromophore concentration in the solution studies, the results from UV-vis spectroscopy (determined from deconvolution of UV-vis spectra, Figure S5.1, Section 11.5, Experimental part) also show a similar conversion for four polymers, compared to the NMR study (~48%, Figure 5.4A).

As discussed above, the alternation of polymer structures from linear to branched along with chromophore density has a critical impact on their thermal properties, i.e., T_g , and thus, molecular mobility. Whereas the photoisomerization of the four polymers in solution is independent of the topology, we anticipate an impact of the topology and molecular mobility on the isomerization efficiency of the α -bisimine in the solid-state. This is shown by the irradiation experiments carried out on spin-coated films while keeping the total dose of photons constant as well ($N_p = 1.5 \cdot 10^{19}$) (Figure 5.4A). Within the solid state, the conversion measured by ^1H NMR and UV-vis spectroscopy is consistently lower than that in solution for all four polymers (Figure 5.4A). However, unlike in solution, clear differences are observed among the four polymers. Polymer **P₄** reaches the highest isomerization efficiency (32%-34%), exceeding the lowest conversion observed for **P₁** by close to a factor of two (16%-17%). In addition, the

percentage of (*E,E*)-isomer is smaller than that of (*E,Z*)-isomer in the solid state, except for **P₄** (18.1% (*E,E*) vs 16.3% (*E,Z*)), whereas the opposite was observed in solution (Figure 5.4A). The longer spacing of chromophores in the **P₄** backbone, coupled with the shielding effect from the side chain explains the relatively high conversion observed in **P₄**, as the stacking of the α -bisimine chromophore is likely to be reduced, providing **P₄** with sufficient molecular mobility to efficiently isomerize. The photoswitching efficiency is inversely correlated with the T_g as visualized in Figure 5.4B, clearly illustrating the key role of molecular mobility for the photoisomerization efficiency in the solid state. The efficiency of photoswitching can be as high as 70% compared to the solution state (achieved in polymer **P₄**, Figure 5.4B).

In addition, to evaluate the dependence of isomerization efficiency on absorptivity at different wavelengths, we carried out an action plot study of polymer **P₁** in THF solution using a wavelength-tuneable laser system.²³⁰ The result (Figure 5.3E) reveals that the conversion is proportional to the absorptivity of the chromophore. Thus, with the same number of photons, we expect a higher population of metastable isomers, i.e., (*E,Z*) and (*E,E*), if shorter wavelength of irradiation is to be used instead of the 310-nm irradiation wavelength.

5.2. Modulation of glass transition temperature

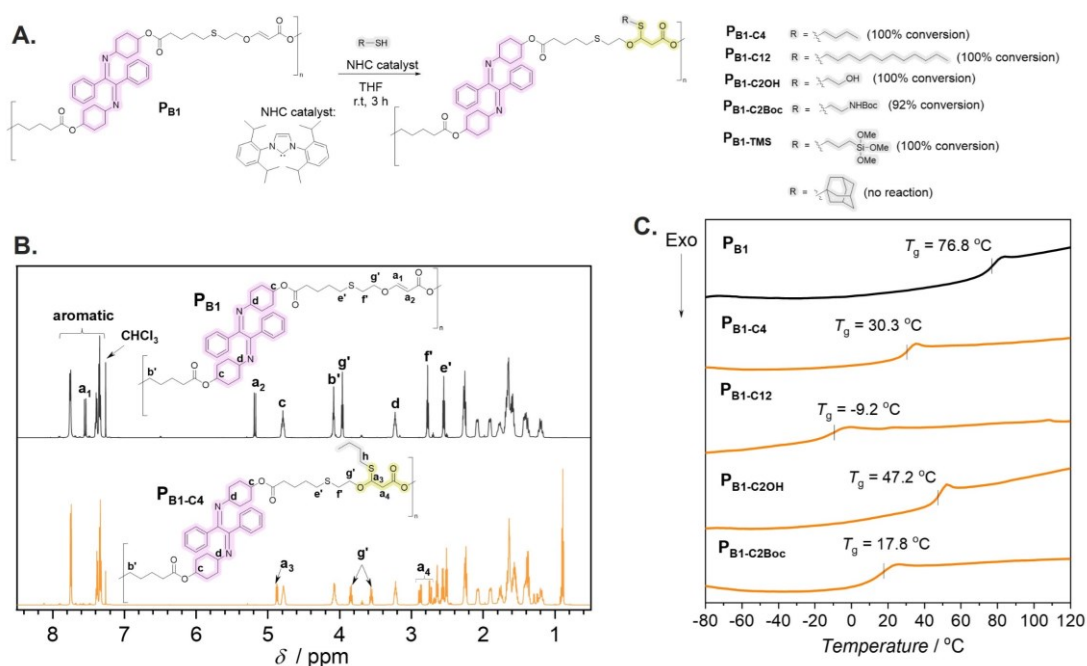


Figure 5.5. Post-polymerization modification of polymer **P_{B1} via thiol-Michael click reaction.** (A) General reaction scheme. (B) Exemplified stack ¹H NMR spectra of the parent (black line) and the post-modified polymer (orange line). (C) Stacked DSC thermograms of the parent polymer (**P_{B1}**) and the modified polymers (**P_{B1}-C₄**, **P_{B1}-C₁₂**, **P_{B1}-C_{2OH}**, and **P_{B1}-C_{2Boc}**). Conditions: 3 cycles of heating and cooling from -90 °C to 120 °C at 20 °C·min⁻¹ heating rate in a nitrogen atmosphere. The plotted DSC curves are taken from the second heating cycle. Reproduced from ref.¹⁹⁵ with permission from the American Chemical Society.

Delighted by the benefit of lowered T_g on the solid-state photoswitching, we are set on to apply the thiol-Michael modification to α -bisimine polymers synthesized via hydroxyl-yne click reaction to probe the change in T_g . As clearly shown in chapter 4, ether acrylates residing on the backbone of the α -bisimine homosequences underwent efficiently the thiol-Michael

reaction catalyzed by the NHC-catalyst. Therefore, we apply the same reaction condition to post-modify the polymer **P_{B1}** (reported in chapter 3) with different types of thiols depicted in Figure 5.5A. Upon the successful modification, the glass transition temperatures are recorded.

For the linear aliphatic thiols, a full conversion was achieved, whereas for the thiols containing bulky groups, such as adamantane and *tert*-butoxycarbonyl (Boc), the conversion was either neglectable or reduced (Figure 5.5A, Figure S5.16-S5.21, Section 11.5.2, Experimental part). ¹H NMR spectra clearly evidence the successful and selective reactions (resonances of related protons shown in Figure 5A, i.e., proton **a₃** (δ = 4.87 ppm), **a₄** (δ = 2.73 and 2.87 ppm), **g'** (δ = 3.55 and 3.84 ppm), which are in accordance with the values reported in literature¹⁹⁶ (refer to Figure 5.5B and Figure S5.16-S5.21, Experimental part, Section 11.5.2). There is no shift of the resonances in the aromatic region associated with the α -bisimine core, indicating that the photoswitch remains unaffected by the post-modification. We subsequently measured the T_g of the parent and modified polymers (Note to the reader: polymer **P_{B1-TMS}** is highly prone to hydrolysis and thus was excluded).

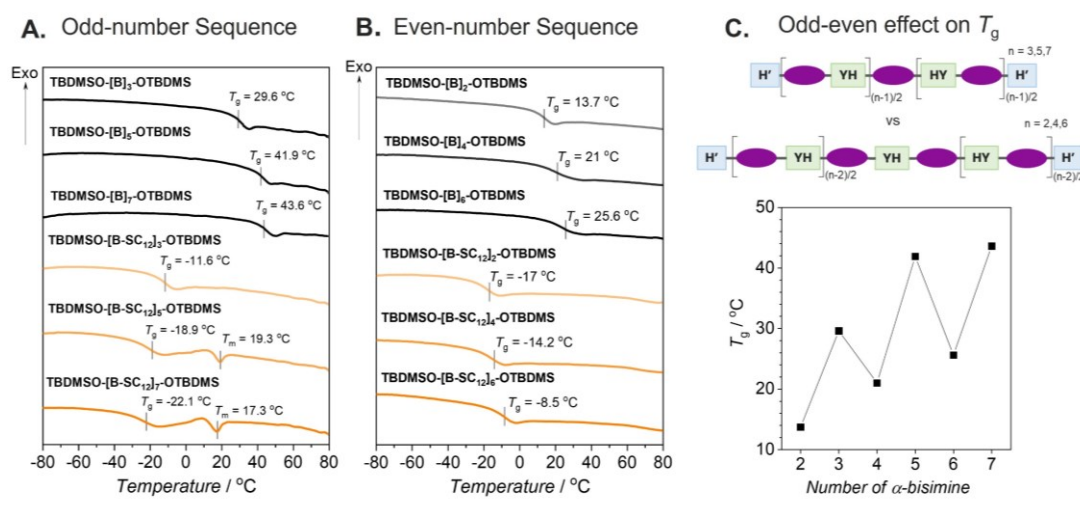


Figure 5.6. DSC thermograms of the odd-numbered sequences (A) and even-numbered sequences (B). Black lines are for pristine oligomers and orange lines are for post-modified oligomers. Conditions: 3 cycles of heating and cooling from -90 °C to 90 °C, 10 °C·min⁻¹, under N₂ atmosphere; (C) Odd-even effect on glass transition temperature (T_g) of unmodified sequences, TBDMO-[B]_n-OTBDMS.

Compared to the parent polymer (**P_{B1}**), all modified polymers displayed lower T_g value (Figure 5.5C). The polymer **P_{B1-C12}** modified with a C₁₂-alkyl thiol had the lowest T_g (-9.2 °C), followed by polymer **P_{B1-C2Boc}** with the bulky Boc group (17.8 °C). Clearly, the long aliphatic side chain gives rise to the most reduction in T_g of the modified polymer. With this in mind, we next measure the T_g of α -bisimine sequences (TBDMO-[B]_n-OTBDMS and TBDMO-[B-SC₁₂]_n-OTBDMS, n = 2-7, reported in chapter 4) to confirm this trend (Figure 5.6A,B). Expectedly, all the modified sequences display negative glass transition temperatures, in the range of -23 and -8 °C. To our surprise, however, there is additionally a melting endotherm (T_m ~ 17-19 °C) in the DSC curves of the modified odd-numbered sequences, TBDMO-[B-SC₁₂]_n-OTBDMS, n =

5 and 7. It is important to emphasize that this behavior is not observed for the post-modified even-numbered sequences nor the post-modified polydisperse homopolymers.

Further analysis of the pristine even- and odd-numbered α -bisimine sequences via DSC shows an interesting trend. While the T_g value of sequences with odd numbers (3, 5, and 7) of the photoswitch falls in the range of 29 – 44 °C, their even-numbered counterparts (2, 4, and 6) feature a significantly lower T_g by almost 20 °C (13-26 °C) (compare Figure 5.6A,B). The plot of T_g vs the number of α -bisimine units (Figure 5.6C) repeatedly shows a zig-zag pattern. It has been reported that the properties of organic materials, such as liquid crystals and (semi)crystalline polymers, oscillate in an alternating pattern associated with the odd and even number of the repeating unit, e.g., methylene groups (n_{CH_2}).²³¹⁻²³⁵ This phenomenon – known as the odd-even effect – has been studied since the end of the 19th century.²³⁵ Its main characteristic is that the solid-state physical properties (e.g., modulus and melting points) increase differently for odd and even n_{CH_2} , whereas the liquid state properties (e.g., boiling points in low molecular weight materials) generally increase linearly with n_{CH_2} .²³⁵ This effect has also been observed for precise sequence-defined macromolecules.²³⁶

Therefore, the alternation in the T_g observed in our case is attributed to the odd-even effect. Since the higher T_g values are observed for the odd-numbered sequences, we hypothesize that these sequences have stronger interchain interaction and higher packing density in the solid-state, leading to higher glass transition temperatures. Structurally, the odd-numbered sequences are perfectly symmetric, as the chain center falls onto the symmetric α -bisimine unit (Figure 5.6C). This may explain for the sidechain crystallization observed only for the C₁₂-grafted modified sequences of odd-number of α -bisimine units (refer to Figure 5.6A). For the even-numbered sequences, the chain center falls onto the ether acrylate, which is asymmetric. As a result, the odd-even effect can originate from the symmetry factor in our case. Indeed, it has been pointed out that molecular symmetry plays a critical role in the stability of liquid crystals in which more symmetric isomers exhibit a higher melting point.²³⁷ For photoswitching polymers, such odd-even effect can be utilized to effectively lower their T_g and increase chain flexibility, which is the relevant factor for the solid-state photoswitching efficiency.¹⁹³

5.3. Concluding remarks

In this chapter, we have developed a simple yet efficient strategy to enhance the solid-state photoisomerization of α -bisimine-based main-chain polymers. The reduction in T_g is clearly shown to be beneficial for the photoswitching efficiency in the solid state. Modulation of T_g is facile via thiol-Michael modification to graft alkyl side chains to the parent photoswitching polymer backbone. More importantly, the formation of internal acrylate and ether acrylate in polymers synthesized from head-to-tail ADMET and hydroxyl-yne click polymerization techniques, respectively, allows for such modifications. Thus, there are clear advantages of employing such chemistries, i.e., cross-metathesis, hydroxyl-yne click, and thiol-Michael click reaction, to synthesize and functionalize main-chain photoswitching polymers and block

Chapter 5: Glass transition temperature and solid-state photoswitching efficiency

copolymers. Furthermore, with the oligomers obtained via the sequence-defined approach, their glass transition temperatures are also affected by the odd-even effect. This provides another option to manipulate T_g without the need for post-modification. A high conversion of photoisomerization in the solid-state (e.g., thin films and the bulk) is strategically required for applications in photodynamic block copolymer lithography.

Chapter 6: Photoisomerization of α -bisimine Main-chain Polymers^{iv}

Investigation of photoisomerization kinetics in solution is important to evaluate the performance of the photoswitch covalently embedded in the polymer main-chain and constitutes one of the objectives in the current thesis. This also serves as benchmark for the photoisomerization in the solid state. So far, we have reported the synthesis of α -bisimine main-chain photoswitching polymers via two main pathways: head-to-tail ADMET polymerization and head-to-tail hydroxyl-yne click polymerization. The chemistries of these two methods are very different and this may affect the photoisomerization of the main-chain α -bisimine phoswitch. Furthermore, we have also harness the metal-free hydroxyl-yne click reaction and TBAF-deprotection chemistry to successfully synthesize monodisperse α -bisimine oligomers (**TBDMSO-[B]_n-OTBDMS**, $n = 2-7$) as well as well-defined block copolymers. Compared to the polydisperse main-chain polymers, such as **P₂** (from ADMET polymerization) and **P_{B1}** (from hydroxyl-yne click), the photoisomerization kinetics of the monodisperse oligomers may also be dissimilar, considering the dispersity factor. Moreover, between even-numbered and odd-numbered sequences of α -bisimine oligomers, we observed the contrast in their glass transition temperatures due to the odd-even effect. Whether the odd-even effect has an impact on the solution photoisomerization is also another concern.

In this chapter, we investigate and compare the forward and back isomerization kinetics of α -bisimine-based main-chain oligomers and polymers. We will address the following factors that may or may not affect the isomerization kinetics: polymerization techniques, dispersity, and even-odd numbers of α -bisimine repeating units.

6.1. Impact of polymerization techniques on the isomerization of α -bisimine based polymers

Firstly, we explored the solution isomerization of polymer **P_{B1}** obtained from hydroxyl-yne click polymerization (**Chapter 3**). THF is an ideal solvent for the solution photoisomerization of the α -bisimine photoswitch due to the excellent solubility of the constituting polymer in THF and its low UV cut-off wavelength. We use a monochromatic wavelength of 310 nm at a laser power of 6.0-6.2 mW and initially traced the photoisomerization via UV-vis spectroscopy. As shown in Figure 6.1C, the gradual decrease of the peak absorption corresponding to the (Z,Z)-

^{iv} Parts of this chapter were reproduced from Thai, L. D.; Kammerer, J. A.; Théato, P.; Mutlu, H.; Barner-Kowollik, C. *ACS Macro Lett.* **2024**, 13, 6, 681–687 (with permission from American Chemical Society), and Thai, L. D.; Kammerer, J. A.; Golberg, D.; Mutlu, H.; Barner-Kowollik, C. *Chem* **2024**, *in press*, with permissions.

Chapter 6: Photoisomerization of α -bisimine Main-chain Polymers

isomer upon 310 nm irradiation with different dose of photons indicated the photoisomerization to the (Z,E)- and (E,E)-form. Full recovery of the (Z,Z)-isomers was reached after approximately 6 h by thermal reversion at 20 °C (Figure 6.1D).

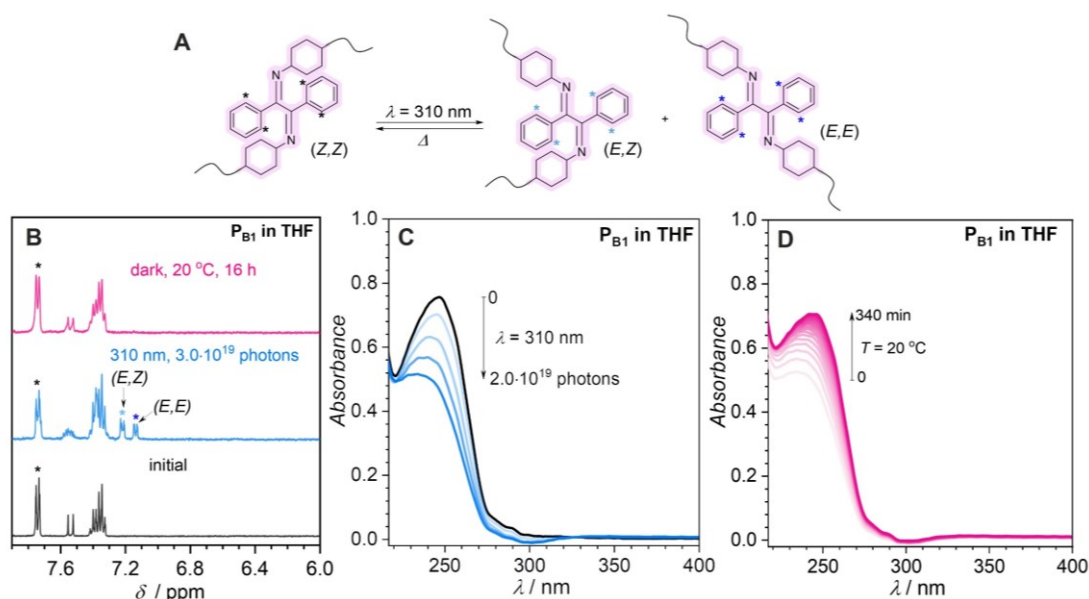


Figure 6.1. Forward and Back isomerization of α -bisimine in P_{B1} . (A) General isomerization of α -bisimine in solution. (B) Sectional ^1H NMR spectra (recorded in CD_2Cl_2) of P_{B1} before and after irradiation with 310 nm laser beam, $P = 6.0\text{--}6.2 \text{ mW}$. The resonances marked with (*) are for the isomer of α -bisimine. The polymer solution was first prepared in THF which was removed after irradiation and redissolved in CD_2Cl_2 for NMR measurement. (C) Stacked UV-vis absorption spectra of P_{B1} in THF ($2.3 \cdot 10^{-5} \text{ mol} \cdot \text{L}^{-1}$) irradiated with 310 nm. (D) Stacked UV-vis absorption spectrum of the post-310 nm irradiated P_{B1} solution in THF at 20 °C. It should be noted that prior to irradiation, the THF solvent was passed through a short basic aluminum oxide column to remove peroxides which can potentially cause undesirable side reactions upon UV exposure. Reproduced from ref.¹⁹⁵ with permission from American Chemical Society.

We next employed ^1H NMR spectroscopy to study the isomerization kinetics of the macromolecular photoswitches in depth. We calculated the ratio of the isomers from the integral values of the resonance associated with protons of the respective isomers (i.e., (Z,Z), (E,Z) and (E,E)) after a specific number of photons (up to $3.0 \cdot 10^{19}$ photons at 310 nm). An exemplary ^1H NMR spectrum is shown in Figure 6.1B. In accordance with the UV-vis measurements, the NMR result showed a full thermal back-switching process after 16 h at 20 °C when the resonances of the (E,Z) and (E,E) completely disappeared and those of the initial (Z,Z) isomer recovered (Figure 6.1B). Figure 6.2B displays the kinetic curves for the forward isomerization of the α -bisimine core in P_{B1} .

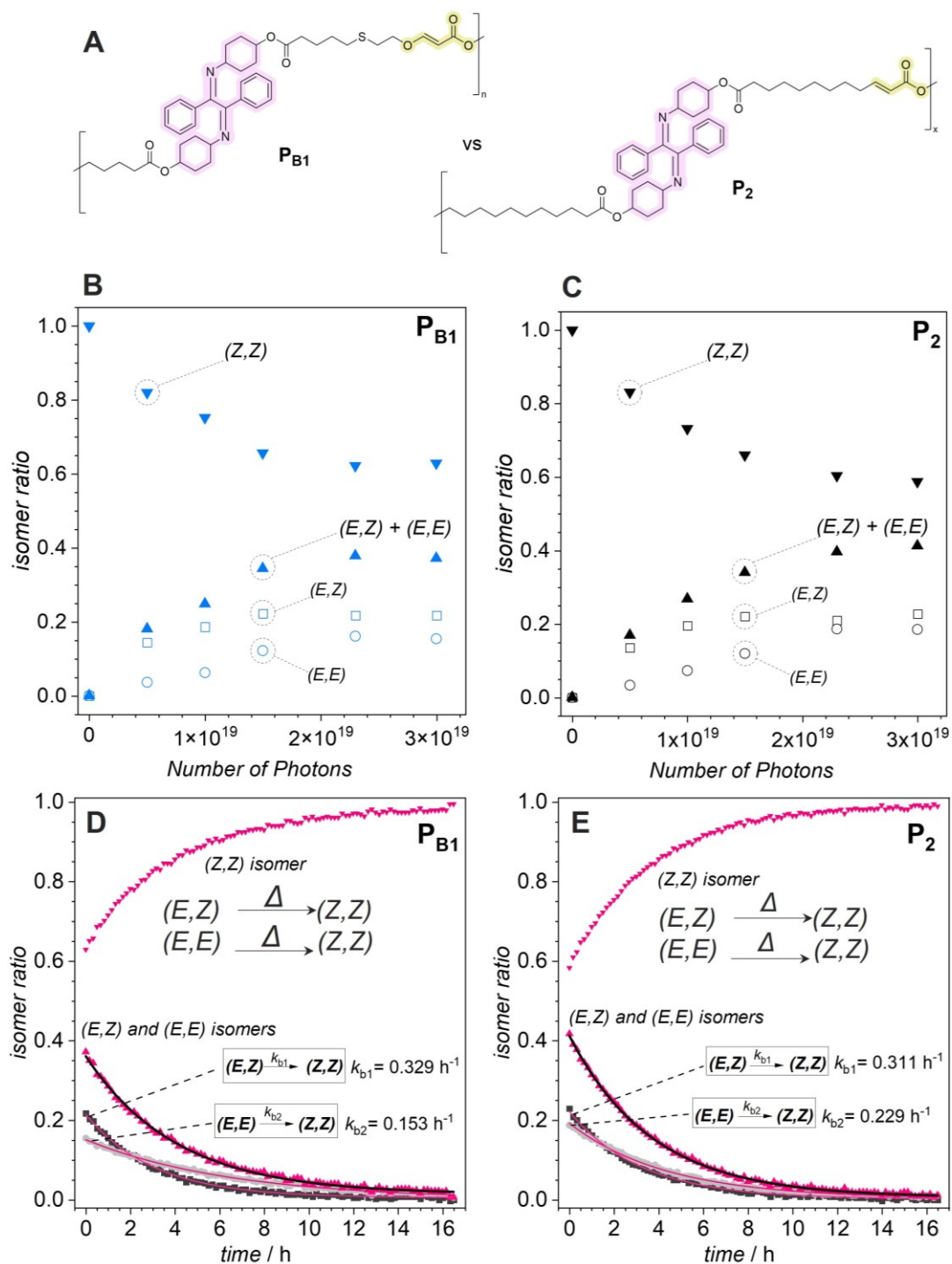


Figure 6.2. Isomerization kinetics of P_{B1} and P_2 in THF solution. (A) Structural comparison of P_{B1} synthesized via head-to-tail hydroxyl-yne and P_2 synthesized via head-to-tail ADMET polymerization. Kinetic traces for the forward isomerization at 310 nm irradiation ($P = 6.0$ – 6.2 mW, up to $3.0 \cdot 10^{19}$ photons) for P_{B1} (B) and P_2 (C). Thermal reversion kinetic traces for P_{B1} (D) and P_2 (E) at 20 °C in CD_2Cl_2 . The ratio of isomers was determined by 1H NMR spectroscopy in CD_2Cl_2 . Samples were first prepared in purified THF for the irradiation and subsequently blow-dried, redissolved in CD_2Cl_2 for NMR measurements. Reproduced from ref.¹⁹⁵ with permission from the American Chemical Society.

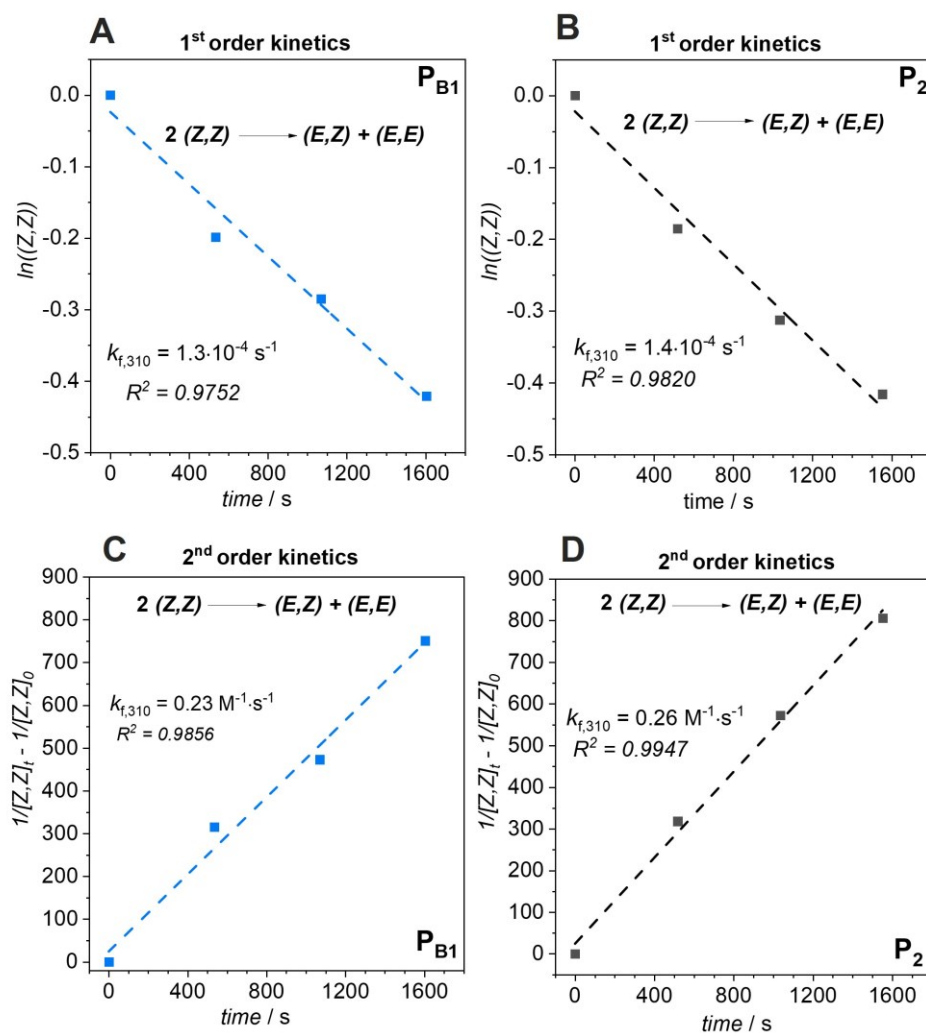


Figure 6.3. First and second-order fits of forward photoisomerization of α -bisimine in two similar polymers, P_{B1} and P_2 . Reproduced from ref.¹⁹⁵ with permission from the American Chemical Society.

To simplify the calculation of the rate coefficient ($k_{f,310}$), we assumed the direct conversion of the (Z,Z)-isomer to both (E,Z) and (E,E) isomers in the forward isomerization under 310 nm irradiation. Accordingly, we employed a first-order kinetic model for the analysis of the data. While this model describes the experimental data reasonably well ($k_{f,310} = 1.3 \cdot 10^{-4} \text{ s}^{-1}$, $R^2 = 0.9752$) (Figure 6.3A), the 2nd order kinetics provides a slightly better fit ($k_{f,310} = 0.23 \text{ M}^{-1} \cdot \text{s}^{-1}$, $R^2 = 0.9856$, Figure 6.3C), which implies that a more complex nature of the isomerization of the α -bisimine photoswitch might be operational. For the thermal reversion, the post-310 nm irradiated sample was kept in the dark at 20 °C and the ^1H NMR spectra were recorded at 10-minute intervals. The kinetic traces of the back isomerization were subsequently plotted (Figure 6.2D). We fitted the traces with 1st order kinetics and the results clearly pointed to the direct reversion of (E,Z)- and (E,E)- isomers to the (Z,Z)-isomer.

We subsequently explored whether there is any significant difference in the isomerization behavior of the main-chain α -bisimine core of polymers synthesized from hydroxyl-yne versus those previously obtained via the metal-based ADMET polymerization route. Thus, we conducted the isomerization kinetics study of the ADMET-derived polymer P_2 . A structural

comparison is shown in Figure 6.2A. We used identical irradiation conditions, i.e., irradiation wavelength ($\lambda = 310$ nm), laser power (6.0-6.2 mW), solvent (THF), and temperature (25 °C for forward and 20 °C for thermal back isomerization). The first-order (forward photoisomerization) kinetic coefficient of the ADMET polymer **P₂** differed only insignificantly by 10^{-5} s⁻¹ from the that of **P_{B1}** (compare, Figure 6.3A,B), within the error margin of the experiment. The thermal reversion traces are also similar to those of **P_{B1}** (compare Figure 6.2D,E). Thus, we conclude that the polymerization technique does not affect the performance of the α -bisimine photoswitch.

6.2. Impact of dispersity and odd-even numbers of repeating units on isomerization kinetics

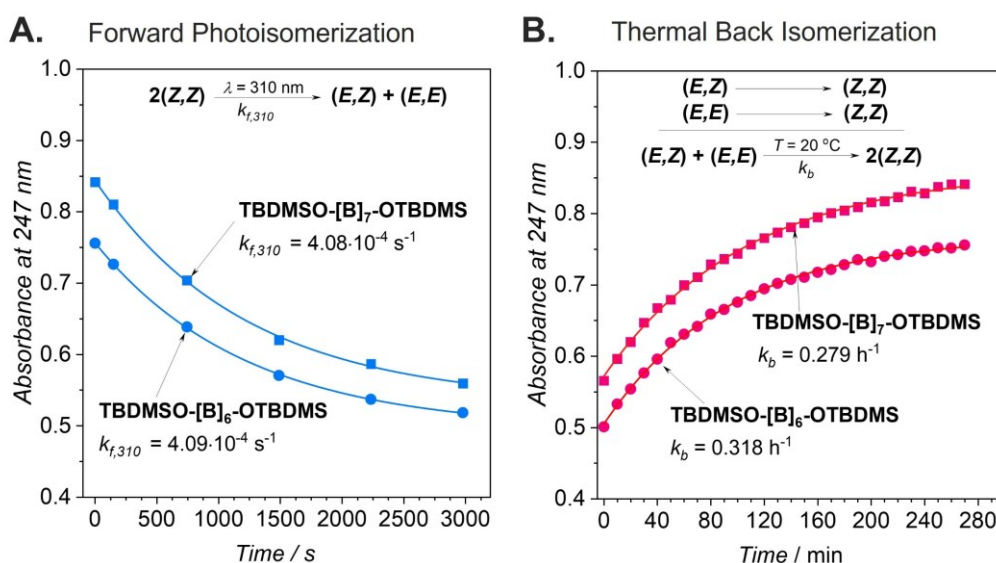


Figure 6.4. The odd-even effect does not influence the photoisomerization in solution. (A) Forward photoisomerization of α -bisimine core in an odd-number and an even-number sequence in THF monitored by UV-vis spectroscopy. Conditions: Irradiation wavelength: 310 nm, laser power: 4.3 mW \pm 5.0%. The rate coefficients ($k_{f,310}$) were derived based on a first-order kinetic model. (B) Thermal back isomerization at 20 °C. The rate coefficients (k_b) were derived from a first-order kinetic model. Note that the k_b used here represents the average rate coefficient of $(E,Z) \rightarrow (Z,Z)$ (k_{b1}) and $(E,E) \rightarrow (Z,Z)$ (k_{b2}) back reversion. Reproduced from ref.¹⁹⁵ with permission from the American Chemical Society.

Given the odd-even-effect-induced fluctuation in the T_g of the α -bisimine-based sequences reported in chapter 5, we questioned whether such an effect could influence the solution isomerization of the covalently installed α -bisimine core. Thus, we performed a kinetic study on the forward and thermal back isomerization of two sequences, **TBDMSO-[B]₇-OTBDMS** (odd number) and **TBDMSO-[B]₆-OTBDMS** (even number) (Figure 6.4).

The isomerization kinetics were monitored via UV-vis spectroscopy. For the forward isomerization, we irradiated the polymer solutions in THF solvent using the monochromatic wavelength of 310 nm (laser power P: 4.3 mW \pm 5.0%) and a UV-vis spectrum was recorded after irradiation with a specific number of photons (N_p). The number of photons can conveniently be converted to the irradiation time via Eq. 11.2 (Experimental part, Section 11.1). Subsequently, we traced the thermal back isomerization at 20 °C via accumulated UV-vis

spectra recorded for the post-310 nm-irradiated solutions. To compare the forward and back isomerization of these two odd- and even-numbered sequences, we plotted the absorbance recorded at 247 nm (corresponding to the absorption peak of the α -bisimine) against time (Figure 6.4).

For the photoisomerization at 310 nm, we again assume the direct conversion of the (Z,Z)-isomer to (Z,E) and (E,E) isomer with first order kinetics. The derived rate coefficients for both sequences (**TBDMSO-[B]₇-OTBDMS** and **TBDMSO-[B]₆-OTBDMS**) are the same, namely $4.08 \cdot 10^{-4} \text{ s}^{-1}$ and $4.09 \cdot 10^{-4} \text{ s}^{-1}$, respectively (Figure 6.4A). Although the values determined for the monodisperse sequence are almost three times higher than those for the polydisperse, we cannot ascribe such difference to the dispersity factor. It is because the laser power applied here is lower (4.5 mW vs 6.0-6.2 mW) and the photoisomerization of the α -bisimine photoswitch may also be dependent on the power of the light source.

Alternatively, the kinetic comparison between the monodisperse and polydisperse systems may be more accurate if we consider the thermal back isomerization at the same temperature (20 °C). For thermal back isomerization of the monodisperse oligomers, we employ a first order kinetic model, once more, to determine the rate coefficients. The results show that both sequences do not significantly differ from each other in terms of kinetics ($k_b = 0.279\text{-}0.318 \text{ h}^{-1}$ at 20 °C in THF) (Figure 6.4B). The rate coefficients of the thermal back isomerization are in good agreement with the value we previously determined for a polydisperse main-chain α -bisimine polymer ($k_b = 0.241\text{-}0.270 \text{ h}^{-1}$ at 20 °C in THF).¹⁹⁵ Therefore, these results clearly evidence the independence of the isomerization kinetics of α -bisimine photoswitches on the odd or even number of repeating units (i.e., main-chain α -bisimine) well as the dispersity of the constituting polymers/oligomers.

6.3. Concluding remarks

It is clear that there are no unfavorable outcomes of the polymerization methods on the solution isomerization kinetics of the embedded photoswitch, i.e. α -bisimine. The same conclusion can be made for the dispersity and odd-even numbers of α -bisimine repeating units. This is encouraging as there will be more flexibility in the selection of polymerization techniques suitable for the target photoswitch other than α -bisimine without compromising its photoswitching performance.

Chapter 7: Hydrazone-based Main-chain Polymers and Block Copolymers^v

In the previous chapters, we have focused on exploring and establishing synthetic pathways to achieve main-chain photoswitching homopolymers and block copolymers with α -bisimine as the model photoswitch. With the outlook toward photodynamic block copolymer lithography, the impact of the photoswitching process on the solution and solid-state properties of the photoswitchable polymers is a guiding principle for us. For instance, it was shown that the photoisomerization of the main-chain α -bisimine polymer led to a reduction in the apparent molar mass (or hydrodynamic volume), likely due to the enhanced polymer chain flexibility upon isomerization.⁹³ In the block copolymer context, such reduction may be indicative of change in the volume fraction of the photoswitchable block if α -bisimine is incorporated. However, the critical drawback associated with the α -bisimine previously reported and utilized in this thesis is probably the need of using high energy photons (≤ 310 nm).⁹³ On the other hand, many arylhydrazones are switchable in the blue color region and the metastable isomers exhibit very long thermal half-lives (up to thousands of years).¹⁰¹ However, they have rarely been integrated in linear main-chain polymers as well as block copolymers. Therefore, integration of hydrazone into polymer as main-chain repeating units is the objective of this chapter. In the first part of this chapter, we synthesize and study the photoswitching-induced property changes of main-chain homopolymers based on hydrazones. The next part of this chapter is devoted for block copolymer synthesis.

7.1. Hydrazone main-chain photoswitching polymers

We initially employed head-to-tail ADMET polymerization technique to realize main-chain photoswitching polymer derived from hydrazone photoswitch. For main-chain stimuli-responsive polymeric materials, the connection point where the stimuli-sensitive groups are covalently installed into the polymer backbone impacts the behavior of macromolecules. For example, Craig *et al.* reported three similar mechano-responsive elastomers derived from three main-chain spiropyran regioisomers.²³⁸ Their results demonstrated different colorimetric responses from the three elastic polymer films upon stretching.²³⁸ Inspired by these regiochemical effects, we are interested in exploring if – for instance – changes in hydrodynamic volume happen if the substitution position of the arm connecting the rotor of the

^v Parts of this chapter were reproduced from Thai, L. D.; Fanelli, J.; Munaweera, R.; O'Mara, M. L.; Barner-Kowollik, C.; Mutlu, H. *Angew. Chem. Int. Ed.* **2024**, 63, e202315887, with permission from John Wiley and Sons. Some parts of this chapter were included in Vertiefungspraktikum of M.Sc. Julian Fanelli, entitled: "Towards Photodynamic Block Copolymer Lithography Driven by Hydrazone-Based Photoswitches".

hydrazone photoswitch to the polymer main-chain is switched from one side to another (refer to Design 1 vs Design 2 in Figure 7.1).

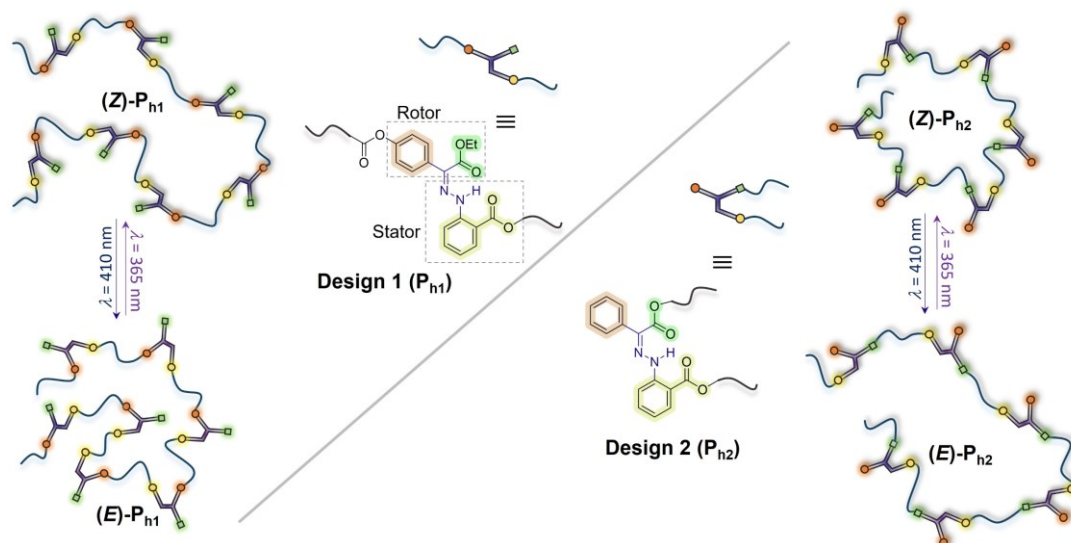


Figure 7.1. Design strategy for two main-chain hydrazone polymers, enabling opposite changes in hydrodynamic volume upon photoisomerization of the hydrazone core. The taxonomy of the rotor and stator is adapted from the work of Aprahamian and colleagues.²³⁹ Reproduced from ref.²⁴⁰ with permission from John Wiley and Sons.

7.1.1. Design and Synthesis

In both designs, i.e., polymer \mathbf{P}_{h1} and \mathbf{P}_{h2} , the stator (yellow phenyl ring in Figure 7.1) is *ortho*-substituted with the imine bond and with one of the two essential reactive handles for the ADMET polymerization (i.e., an acrylate). In design 1, i.e., \mathbf{P}_{h1} , the rotor is decorated with a phenyl ring that is substituted on the *para*-position with the polymerizable handle (i.e., the olefin) and the acetyl functional moiety, which acts as an *H*-bond acceptor. In design 2, i.e., \mathbf{P}_{h2} , the phenyl rotor is non-substituted and the functional group (i.e., the ester group shown in green in Figure 7.1), which serves as the *H*-bond acceptor, also provides the polymerizable functional unit (i.e., the olefin handle). The key design differences between the two polymers thus are (i) the position of one of the two arms connecting the rotor of the photoswitch to the backbone (Figure 7.1, Figure 7.2) and (ii) one additional ester group ($-\text{COOR}$) in the phenyl rotor of \mathbf{P}_{h1} (Figure 7.1, Figure 7.2).

Synthetically, the pure (Z)-isomer of \mathbf{M}_{h2} (denoted (Z)- \mathbf{M}_{h2}) was obtained without difficulty, whereas significantly more purification effort was needed to acquire the pure (Z)-configuration of \mathbf{M}_{h1} (denoted (Z)- \mathbf{M}_{h1}). However, we are also interested in investigating the effect of isomer mixtures in \mathbf{M}_{h1} (88% (Z)- and 12% (E)-isomers, denoted (88%Z)- \mathbf{M}_{h1}) on the final number-averaged molar mass (M_n) of the resulting polymers.

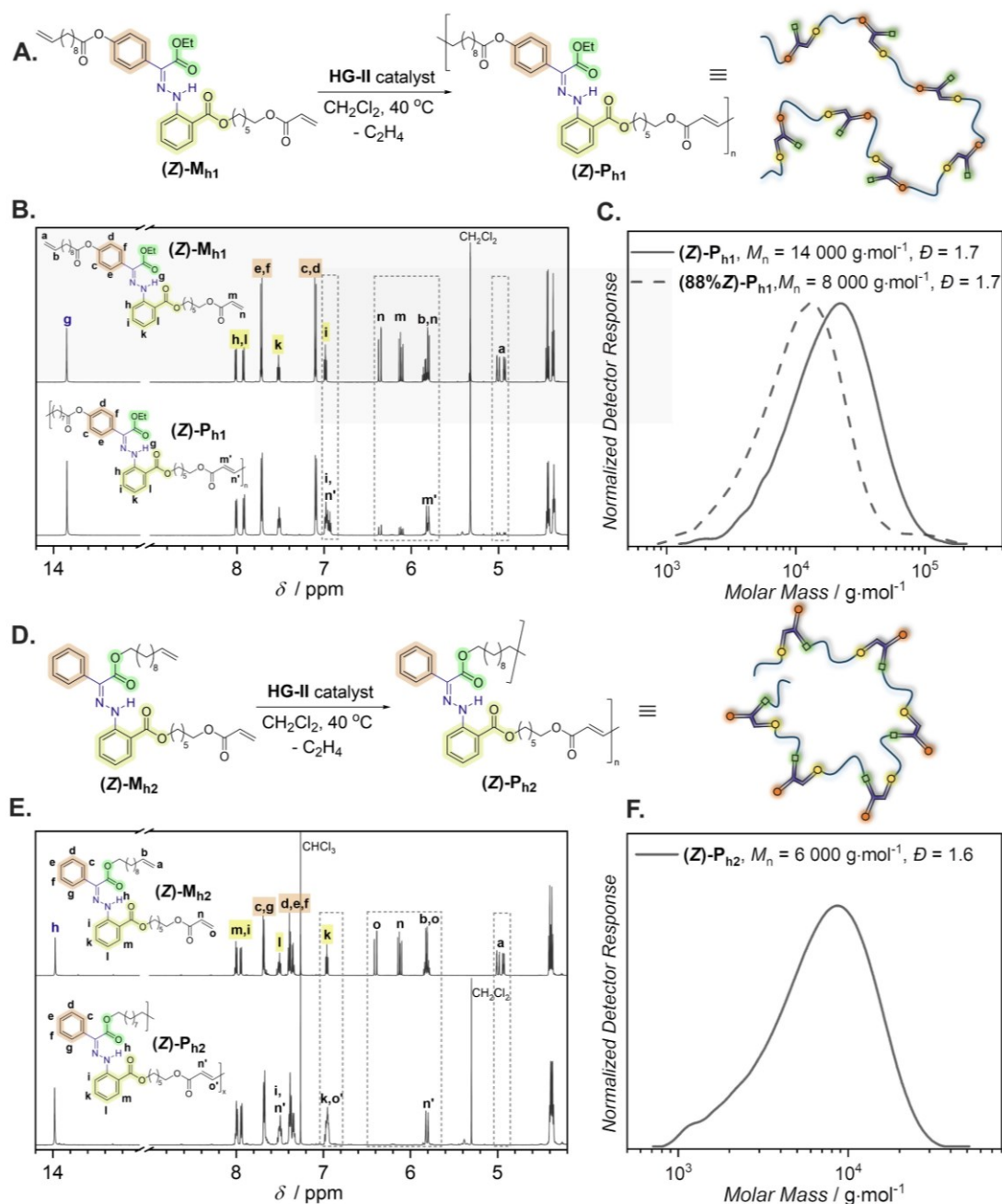


Figure 7.2. Synthesis of two hydrazone main-chain photoswitching homopolymers. Representation of the head-to-tail ADMET polymerization of two monomers, M_{h1} (A) and M_{h2} (D). Sectional stacked ^1H NMR spectra (in either CD_2Cl_2 or CDCl_3) of M_{h1} and M_{h2} and the resulting polymers, P_{h1} (B) and P_{h2} (E). SEC traces recorded in dimethylacetamide (DMAc) of P_{h1} (C) and P_{h2} (F). HG-II: Hoveyda-Grubbs 2nd generation catalyst. M_n represents the apparent number-averaged molar mass. Reproduced from ref.²⁴⁰ with permission from John Wiley and Sons.

To fabricate the main-chain photoswitchable polymers, we employed head-to-tail ADMET polymerization using a **HG-II** and dichloromethane (DCM) as the solvent.¹⁴⁰ The gradual disappearance of the magnetic resonances corresponding to the terminal alkene ($\delta = 4.96$ and 5.83 ppm) and acrylate groups ($\delta = 5.80$, 6.11 and 6.36 ppm) alongside the appearance of the internal acrylate bonds ($\delta = 5.81$ and 6.96 ppm) as indicated in Figure 7.2B,E confirms the high selectivity of the cross-metathesis polymerization. Despite the capability of hydrazones to form complexes with metal ions,²⁴¹ ADMET polymerization of the designed hydrazone

monomers proceeded smoothly under the catalysis of Ru-centered **HG-II**. As evidenced by the ^1H NMR spectra depicted in Figure 7.2B,E, there is no evident shift of the magnetic resonances associated with the hydrazone core, especially the resonances of the aromatic hydrogens, which are sensitive to complexation of the azomethine nitrogen to Ru.

We designed a hydrazone core featuring two ester groups in close proximity to the hydrazone hydrogen (highlighted as green and yellow in Figure 7.2A,D), which act as strong hydrogen acceptors. This, in turn, hindered access of the Ru-based **HG-II** catalyst to the photoswitchable core.²⁴² The apparent number average molecular weights, M_n , of the resulting polymers, **(Z)-P_{h1}**, **(88%Z)-P_{h1}** and **(Z)-P_{h2}** are close to 14000, 8000, and 6000 g·mol⁻¹ on the basis of a PMMA calibration, respectively (Figure 7.2). The M_n of **(Z)-P_{h1}** is comparable with the values reported for other main-chain photoresponsive polymers based on α -bisimine and azobenzene units.^{193,243} In contrast, with 12% of (*E*)-isomer in **(88%Z)-M_{h1}**, the M_n of the resulting polymer **((88%Z)-P_{h1})** is lower by almost 6000 g·mol⁻¹, compared to **(Z)-P_{h1}**. In the case of **(Z)-P_{h2}** (resulting from **(Z)-M_{h2}**), a smaller apparent M_n value is observed (6000 g·mol⁻¹). The more compact structure of the monomer **(Z)-M_{h2}** may lead to a reduction of the hydrodynamic volume of the resulting polymer **(Z)-P_{h2}**. Alternatively, the substitution of the alkenyl arm in the ester rotor (shown in green in Figure 7.2D) may bring the alkene and the acrylate groups residing in the stator in close proximity to each other, facilitating cyclization reactions and thus terminating the polymerization at lower M_n value. Thus, we hypothesize that the combination of these two factors may explain the lower M_n in the second design **((Z)-P_{h2})**. Nevertheless, the M_n values of these polymers are sufficient for performing the targeted photoisomerization studies.

With regard to the optical properties of **P_{h1}** and **P_{h2}**, it is surprising that there is no shift in the UV-vis absorption spectra of **(Z)-P_{h1}** and **(Z)-P_{h2}**, and the molar absorptivity of the two polymers are similar (approximately 21000 M⁻¹ cm⁻¹ at λ_{max} = 372 nm, refer to Figure S7.1, Experimental part, Section 11.7) and in agreement with the literature values for small molecule hydrazone structures.¹⁰¹ Due to the presence of the (*E*)-isomer (12%) in **(88%Z)-P_{h1}**, the absorption spectrum is blue-shifted (Figure S7.1, Experimental part, Section 11.7), as the (*E*)-isomer absorbs photons of higher energy than the (*Z*)-isomer.

7.1.2. Photoisomerization study

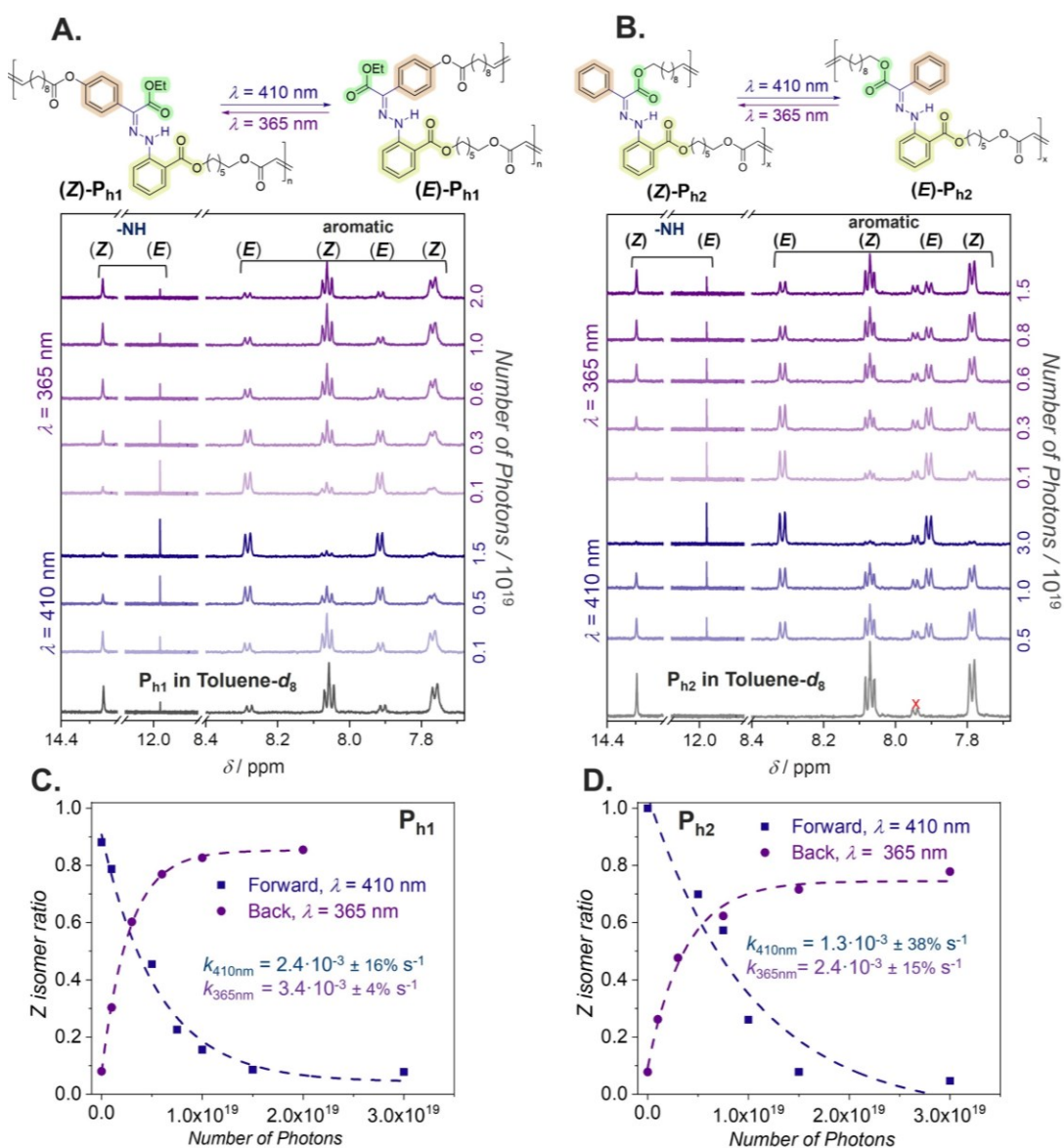


Figure 7.3. Photoisomerization study of P_{h1} and P_{h2}. Sectional stacked ¹H NMR spectra recorded in toluene-d₈ of polymer solutions, P_{h1} (A) and P_{h2} (B), irradiated with 410 nm laser (forward isomerization), followed by 365 nm laser (back isomerization). Photoisomerization kinetics of P_{h1} (C) and P_{h2} (D) were fitted with an exponential function. Reproduced from ref.²⁴⁰ with permission from John Wiley and Sons.

With the polymers in hand, we conducted photoisomerization studies of P_{h1} and P_{h2} in deuterated toluene (toluene-d₈) monitored by ¹H NMR spectroscopy. We selected (88%Z)-P_{h1} and (Z)-P_{h2} since the two polymers have comparable *M_n* values (i.e., close to 8000 g·mol⁻¹ for (88%Z)-P_{h1} and 6000 g·mol⁻¹ for (Z)-P_{h2}, respectively). We initially adapted the irradiation wavelengths previously employed in the literature.¹¹⁷ Accordingly, 410 nm and 365 nm were used for the forward and back photoisomerization, respectively, of the hydrazone core in P_{h1} and P_{h2}. As can be seen in Figure 7.3A,B (blue curves), upon irradiation with blue light ($\lambda = 410$ nm, laser power: 6.5 mW \pm 12.9%, up to 3.0 · 10¹⁹ photons) the magnetic resonances corresponding to the initial (Z)-hydrazone cores in both P_{h1} and P_{h2} decrease in intensity, accompanied by the emergence of new resonances associated with the (E)-isomer.

Chapter 7: Hydrazone-based Main-chain Polymers and Block Copolymers

Aprahamian and colleagues reported an extremely slow thermal back isomerization of the hydrazone cores similar to those in our study, with thermal half-lives up to 3400 years at 25 °C in dimethyl sulfoxide (DMSO).¹¹⁷ Indeed, we did not observe any signs of thermal back isomerization (confirmed by ¹H NMR spectroscopy, Figure S7.4-S7.5, Experimental part, Section 11.7) when our irradiated samples were kept in the dark for 4 days at ambient temperature. Therefore, the back isomerization is only possible with light irradiation (at 365 nm in the current study). Accordingly, the polymer solutions previously irradiated with 410 nm blue light were exposed to 365 nm laser-irradiation (laser power P: 5.0 mW ± 3.7%, up to 2.0·10¹⁹ photons). The ¹H NMR spectra of the reaction shown in Figure 7.3A,B (purple curves) clearly demonstrate the gradual recovery of the initial (Z)-isomer, confirming reversible photoisomerization. In both processes, no additional magnetic resonances aside from those of the isomers were observed in the ¹H NMR spectra, suggesting no side reactions and/or degradation of the irradiated polymers.

To quantify and compare the isomerization kinetics of **(88%Z)-P_{h1}** and **(Z)-P_{h2}** in toluene-*d*₈ at 25 °C, we plotted the isomerization conversion (determined via an NMR study) vs irradiation time. The number of photons (*N_p*) is converted to time by rearranging equation S11.1 (Experimental part, Section 11.1). The results reveal that polymer **(88%Z)-P_{h1}** isomerizes faster than polymer **(Z)-P_{h2}** in both the forward and back isomerization (compare Figure 7.3C,D). The associated rate coefficient of the forward isomerization at 410 nm (*k_{f,410nm}*) for **(88%Z)-P_{h1}** (2.4·10⁻³ s⁻¹) is almost twice as high as that for **(Z)-P_{h2}** (1.3·10⁻³ s⁻¹). For the back isomerization at 365 nm, the rate coefficients (*k_{b,365nm}*) are 3.4·10⁻³ s⁻¹ and 2.4·10⁻³ s⁻¹ for **(88%Z)-P_{h1}** and **(Z)-P_{h2}**, respectively.

Due to the fact that the power of the employed light source (6.5 mW ± 12.9% for 410 nm irradiation and 5.0 mW ± 3.7% for the 365 nm irradiation) are much lower than those employed in the literature,^{105,117} a direct comparison of the rate coefficients is challenging. At the photostationary state (PSS) during 410 nm irradiation, both polymers show a high Z-to-E isomerization conversion (~92% (E)-isomer for both **(88%Z)-P_{h1}** and **(Z)-P_{h2}**, Figure 7.3C,D). However, for the reversion process at 365 nm irradiation, while the PSS value for the (Z)-isomer in **(88%Z)-P_{h1}** is close to the initial ratio (85% (Z)-isomer at PSS 365 nm vs 88% (Z)-isomer initially), only around 80% of the (Z)-isomer in **(Z)-P_{h2}** is recovered. Data from UV-vis studies also agree with the NMR spectroscopic results even though we could not quantify the percentage of the (Z)- and (E)- isomers based on UV-vis spectra (Figure S7.2, Experimental part, Section 11.7). Changing the solvent from relatively non-polar toluene to aprotic polar dimethylacetamide (DMAc) does not appear to enhance the isomerization of the hydrazone core (Figure S7.6, Experimental part, Section 11.7), suggesting an insignificant contribution of solvent polarity on the photoisomerization efficiency of the studied photoswitch. In the literature, kinetic studies of small molecules similar to the hydrazone core in **(Z)-P_{h2}** also reported relatively low conversion for the back isomerization (75% - 86%).^{101,105} In our case, the steric effect inflicted by the *ortho*-substitution of the aliphatic backbone polymer chains connecting the rotor (ester group shown in green in Figure 7.2D) and the stator (phenyl group shown in

yellow in Figure 7.2D) of the hydrazone core in **(Z)-P_{h2}** may compromise the isomerization kinetics as well as the efficiency of the back isomerization.

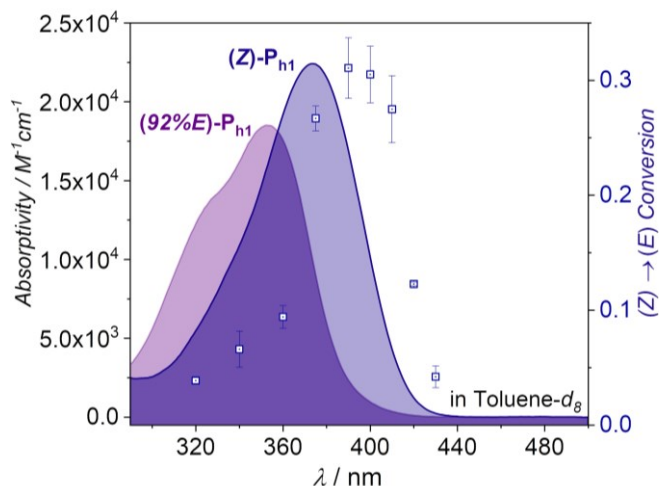


Figure 7.4. Wavelength-dependent Z/E-photoisomerization recorded in toluene- d_8 of hydrazone core in **P_{h1}**. Reproduced from ref.²⁴⁰ with permission from John Wiley and Sons. Details on sample preparation is provided in Experimental part, Section 11.7.2.

We further explore the reliance of the forward isomerization on the absorption wavelength of the hydrazone core, using polymer **(Z)-P_{h1}**. Specifically, the number of photons (N_p) was fixed at $2.5 \cdot 10^{18}$ and the molar concentration (0.8 mM) of the chromophore across the irradiation wavelength range (320 nm - 430 nm) was kept constant. The results collated in Figure 7.4 show the highest conversion at close to 390 nm. The shift of the highest conversion away from the maximum absorption peak of the initial (Z)-isomer – although a typical observation for nearly all studied photochemical processes²³⁰ – may partially be due to the spectral overlap between the (Z)- and (E)-isomers around the peak absorption at 375 nm (Figure 7.4), interfering with the forward isomerization in the overlapped region. As no difference in the absorption spectra between **(Z)-P_{h1}** and **(Z)-P_{h2}** is observed, we anticipate a similar action plot for **(Z)-P_{h2}**.

7.1.3. Effect of photoisomerization on solution and solid-state properties

Owing to the distinct geometrical difference of the two isomers, (Z) and (E), we believe the main-chain hydrazone photoswitch in the polymer backbone affects the hydrodynamic volume of the polymer during the photoisomerization. Further, the designs of **P_{h1}** and **P_{h2}** suggest that the position of the aliphatic arm in the rotary part of the hydrazone photoswitch in the two polymers (compare Figure 7.3, top part) are on opposite sides with respect to the C=N rotation axis. Thus, it appeared to be a viable hypothesis that the two polymers may feature antagonistic changes of their molecular weight distribution (MWD) upon photoisomerization.

To test the above hypothesis, we recorded and compared SEC traces of the pristine and irradiated polymer solutions ($\lambda = 410$ nm, followed by $\lambda = 365$ nm in toluene) of **P_{h1}** and **P_{h2}**.

Expectedly, Figure 7.5A,B demonstrates the antagonistic change of the apparent molecular weight distributions of P_{h1} and P_{h2} upon 410 nm laser irradiation. We have shown earlier in the NMR study (Figure 7.3) that there are no unfavorable reactions, e.g., intra-/intermolecular crosslink, or degradation, taking place during the photoisomerization. Therefore, the shift in the apparent molar mass of P_{h1} and P_{h2} upon photoisomerization is attributed to the hydrodynamic volume change of the polymers due to the altered packing density of polymer chains. To quantify these changes, we compared the apparent peak molar mass (M_p) after and before 410 nm irradiation ($\% \Delta M_p = (M_{p,410nm} - M_{p,pristine}) \cdot 100\% / M_{p,pristine}$). For polymer P_{h1} , a reduction of approx. 25% for **(Z)-P_{h1}** (with 13% (Z)- and 87% (E)-isomer at 410 nm PSS) (Figure S7.2, Experimental part, Section 11.7) and close to 22% for **(88%Z)-P_{h1}** (with 8% (Z)- and 92% (E)-isomer at 410 nm PSS) (Figure 7.5A) was observed. In contrast, polymer **(Z)-P_{h2}** displays a 20% increase in M_p after reaching the photostationary state (PSS) at 410 nm irradiation (with 8% (Z)- and 92% (E)-isomer) (Figure 7.5B). Upon back isomerization at 365 nm, the SEC traces of these polymers show a tendency to return to the initial distribution, however not completely (Figure 7.5A,B and Figure S7.3, Experimental part, Section 11.7).

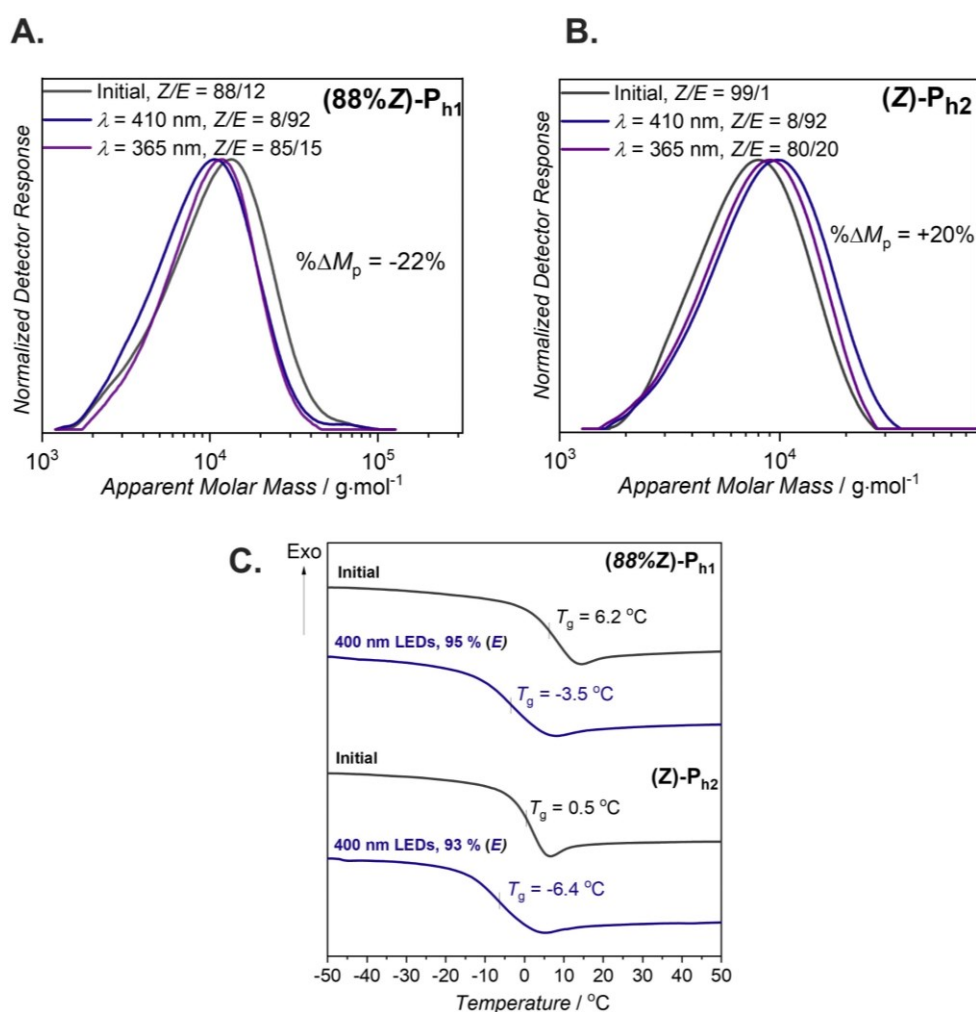


Figure 7.5. Effect of photoisomerization on properties of hydrazone-based main-chain polymers. DMac-SEC traces recorded for P_{h1} (A) and P_{h2} (B) upon forward and back photoisomerization. (C) Stacked DSC curves for P_{h1} and P_{h2} before and after 400-nm (LEDs) irradiation. Reproduced from ref.²⁴⁰ with permission from John Wiley and Sons.

These data demonstrate that by altering the substitution site of the main-chain arm, the behavior of a key macromolecular property, i.e., the hydrodynamic volume, can be manipulated. We submit that the properties of these materials in the solid-state, e.g., their glass transition temperature (T_g), are also affected by photoisomerization. It is well known that the T_g of a polymer can be critically influenced by *cis* and *trans* configurations in the polymer as the volume, chain stiffness and interchain cohesion of polymer chains are greatly affected via *cis* and *trans* configurations.^{243,244} In fact, Aprahamian and colleagues have illustrated a photomodulation of T_g on a series of polyacrylate- and polymethacrylate-based polymers bearing hydrazone side chains.¹³² In the current study, we investigate the role of photoisomerization on the resulting T_g of the reported main-chain polymers (**P_{h1}** and **P_{h2}**), employing DSC.

We initially examined the thermal stability of the studied polymers ((**88%Z**)-**P_{h1}** and (**Z**)-**P_{h2}**) using TGA. The temperature at which 5% mass is lost, $T_{d,5\%}$, is 298 °C for (**88%Z**)-**P_{h1}** and 302 °C (**Z**)-**P_{h2}** (Figure S7.7, Experimental part, Section 11.7), indicating the two polymers have excellent thermal stability despite their relatively low apparent average molar masses ($6000 < M_n < 8000 \text{ g}\cdot\text{mol}^{-1}$). These values, i.e., $T_{d,5\%}$, are similar to those reported for main-chain α -bisimine ADMET polymers.¹⁹³

We subsequently conducted DSC measurements of the pristine and irradiated polymers. The sample preparation conditions (i.e., solvent, temperature) were kept identical (refer to section 11.7, Experimental part for the detailed protocol). Solutions of (**88%Z**)-**P_{h1}** and (**Z**)-**P_{h2}** in DCM ($1.0 \text{ g}\cdot\text{L}^{-1}$) were irradiated with 400 nm LEDs (10 W) for 4 h (>93% Z-to-E conversion). It is important to emphasize that the pristine samples were prepared in a similar manner. Next, the pristine and irradiated samples (concentrated to $100 \text{ g}\cdot\text{L}^{-1}$ in DCM) were drop-cast in separate DSC pans, which were dried at 25 °C in high vacuum for 3 days prior to DSC measurement. The DSC thermograms depicted in Figure 7.5C show a T_g of 6.2 °C and 0.5 °C for the pristine (**88%Z**)-**P_{h1}** and (**Z**)-**P_{h2}**, respectively. The higher M_n and an additional ester group in (**88%Z**)-**P_{h1}** may explain the higher glass transition temperature (T_g) of (**88%Z**)-**P_{h1}**. Aprahamian and colleagues observed a lower T_g for side-chain hydrazone polymers with the longer aliphatic sidechain connected to the ester rotary part (highlighted in green in Figure 7.2D).¹³² Thus, a low T_g (0.5 °C) is not unexpected for (**88%Z**)-**P_{h1}**. Upon forward isomerization (>93% (E)-isomer at PSS, $\lambda_{irr,max} = 400 \text{ nm}$), both irradiated polymers show a decrease in T_g , i.e., a difference in T_g value (ΔT_g) before and after forward isomerization, of 9.7 °C for the irradiated (**88%Z**)-**P_{h1}** and a ΔT_g of 6.9 °C for the irradiated (**Z**)-**P_{h2}** (Figure 7.5C).

The observed ΔT_g is in contrast to the results reported earlier for the side-chain approach.¹³² In other words, when hydrazones are introduced as pendant groups, only one part (rotor or stator) of the photoswitch is connected to the polymer chain, leaving the other part unhindered. Consequently, this facilitates a tighter packing of the chromophores, i.e., hydrazones, which are of an aromatic nature upon forward isomerization (i.e., Z/E), leading to higher T_g .¹³² In our case, however, both stator and rotor of the photoswitch are tethered to the polymer backbone

through aliphatic carbon chains (C₆-C₁₁). As a result, the hydrazone photoswitches are surrounded by soft segments (i.e., aliphatic chains). In the case of **P_{h1}**, the structural change upon blue light irradiation enables these soft segments to closely pack. Further, there is no melting/crystallization process observed in the DSC thermograms (Figure 7.5C). Thus, the packing of such soft aliphatic chains driven by photoisomerization is the likely reason for the lower T_g (-3.5 °C) of the irradiated **P_{h1}**. In contrast, (**Z**)-**P_{h2}** resembles a polystyrene-type polymer with the phenyl rotary as the pendant group (the orange ring shown in Figure 7.2D, 7.3B). These groups can be considered as a part of the hard segment. Upon *Z/E* photoisomerization, the aggregation of these aromatic phenyl groups may be disturbed due to the polymer volume expansion, coupled with geometry of the resulting (*E*)-isomer disfavoring their tight packing. Consequently, these factors can be accountable for the negative T_g (-6.4 °C) of **P_{h2}** measured after forward isomerization.

7.1.4. Concluding remarks

We have realized the synthesis of main-chain hydrazone-based polymers (**P_{h1}** and **P_{h2}**) via head-to-tail ADMET polymerization, followed by a detailed photoisomerization study, including a photochemical action plot. By switching the substitution locations of the arm in the rotor of the hydrazone photoswitch, we demonstrate an antagonistic change in the hydrodynamic volume (between 20% and 25% changes in M_p) of the resulting polymers (**P_{h1}** and **P_{h2}**) upon forward photoisomerization. The photoisomerization behavior strongly affects the macroscopic physical properties of the polymers, particularly the reduction of T_g , thus implying a plasticizing effect. These findings are highly encouraging and promising signs for further inclusion of the arylhydrazones into block copolymers for the purpose of photo-manipulation of their nanostructures.

7.2. Hydrazone main-chain block copolymer synthesis

7.2.1. Synthesis route

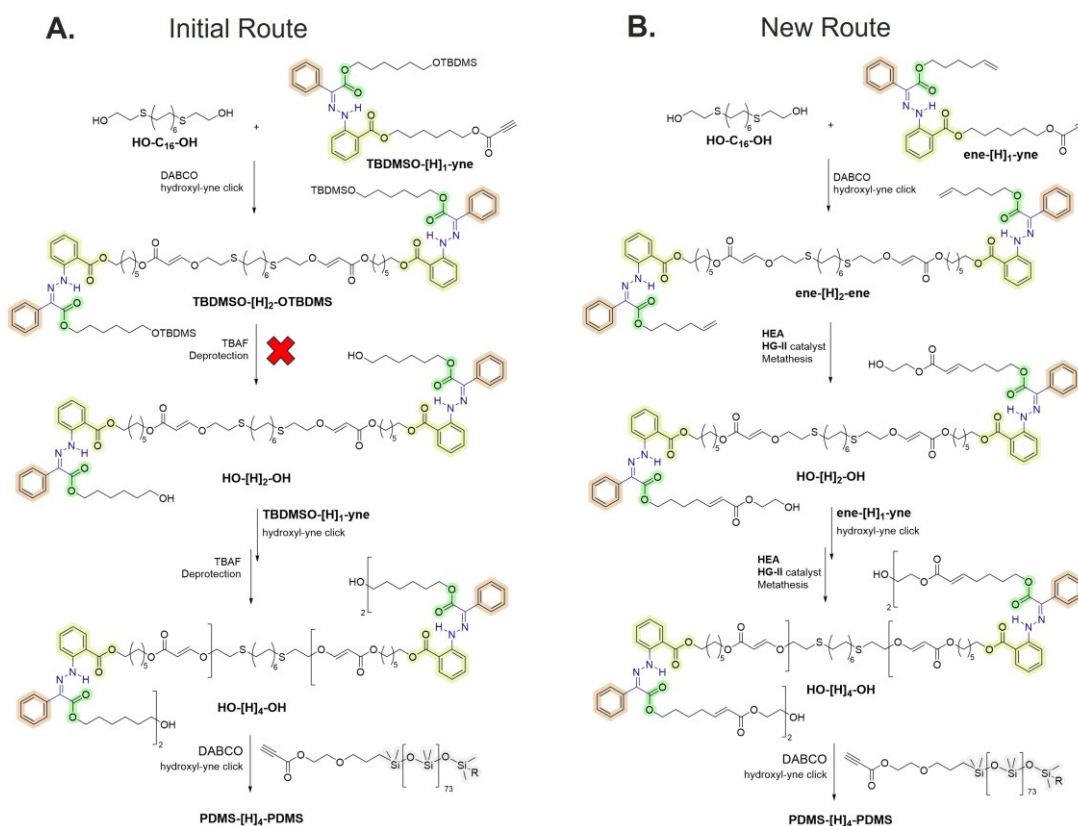


Figure 7.6. Synthesis strategies for sequence-defined oligomers and block copolymers based on hydrazone photoswitch. (A) Application of hydroxyl-yne click reaction and TBAF-deprotection chemistry. (B) Employment of hydroxyl-yne and cross-metathesis.

Based on the hydroxyl-yne click and TBAF-deprotection chemistries established in chapter 4, we initially adapted these chemistries to prepare hydrazone-based main-chain block copolymers (Figure 7.6A). Accordingly, a hydrazone monomer decorated with an activated alkyne and a TBMSO group, denoted **TBDMSO-[H]₁-yne**, was synthesized. This monomer was then reacted with a linear aliphatic monomer having two hydroxy end groups, denoted **HO-C₁₆-OH**, via hydroxyl-yne click reaction, yielding an oligomer with two hydrazone main-chain units and two TBDMSO groups, denoted **TBDMSO-[H]₂-OTBDMS** (Figure 7.6A). However, in the next step where the TBDMS protecting group was cleaved by TBAF solution, we observed an inefficient deprotection together with undesirable *Z/E* isomerization of the hydrazone core (compare NMR spectra in Figure 7.7). In other words, the deprotection step with TBAF is not compatible with hydrazone system and therefore cannot be used in further steps.

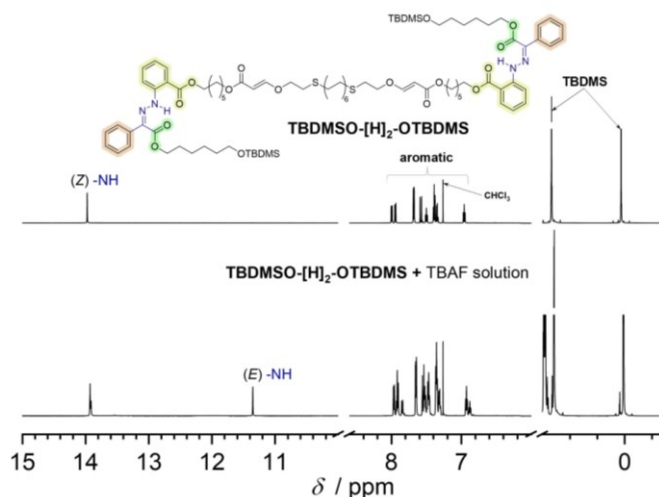


Figure 7.7. Sectional stacked ^1H NMR spectra (recorded in CDCl_3) of an oligomer, **TBDMOS-[H]₂-OTBDMS** before and after deprotection with TBAF solution. The mixture was purified via workup and flash column chromatography prior to NMR measurement.

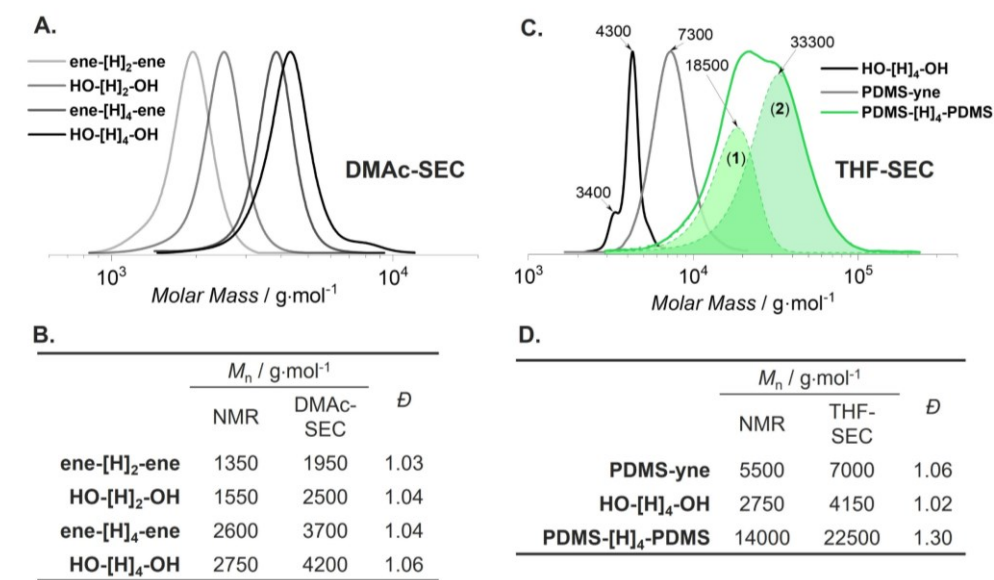


Figure 7.8. (A) DMAc-SEC traces of hydrazone-based oligomers and block copolymers. (B) Summary of molar mass determined from NMR and SEC. (C) THF-SEC traces and (D) summary of **HO-[H]₄-OH**, **PDMS-yne** and **PDMS-[H]₄-PDMS**.

Taking into consideration the excellent functional group compatibility of cross-metathesis reaction, we designed an alternative route, depicted in Figure 7.6B. In this new route, a hydrazone monomer equipped with an activated alkyne and an olefin functional group, denoted **yne-[H]₁-ene**, was synthesized. We showed in chapter 4 that the hydroxyl-yne click reaction does not chemically affect the olefin group. Thus, the reaction between **yne-[H]₁-ene** and **HO-C₁₆-OH** yielded an oligomer with two hydrazone main-chain units and two olefin end groups (Figure 7.6B). The olefin end groups were then reacted with an excess of hydroxy-terminated acrylate (2-hydroxyethyl acrylate, **HEA**) under the catalysis of **HG-II**.

The successful metathesis reaction was confirmed by NMR and SEC (Figure 7.8A and Figure S7.56, Experimental part, Section 11.7). The resulting oligomer, **HO-[H]₂-OH**, bearing two free

hydroxy end groups were subsequently used in the hydroxy-yne click reaction with **yne-[H]₁-ene**.

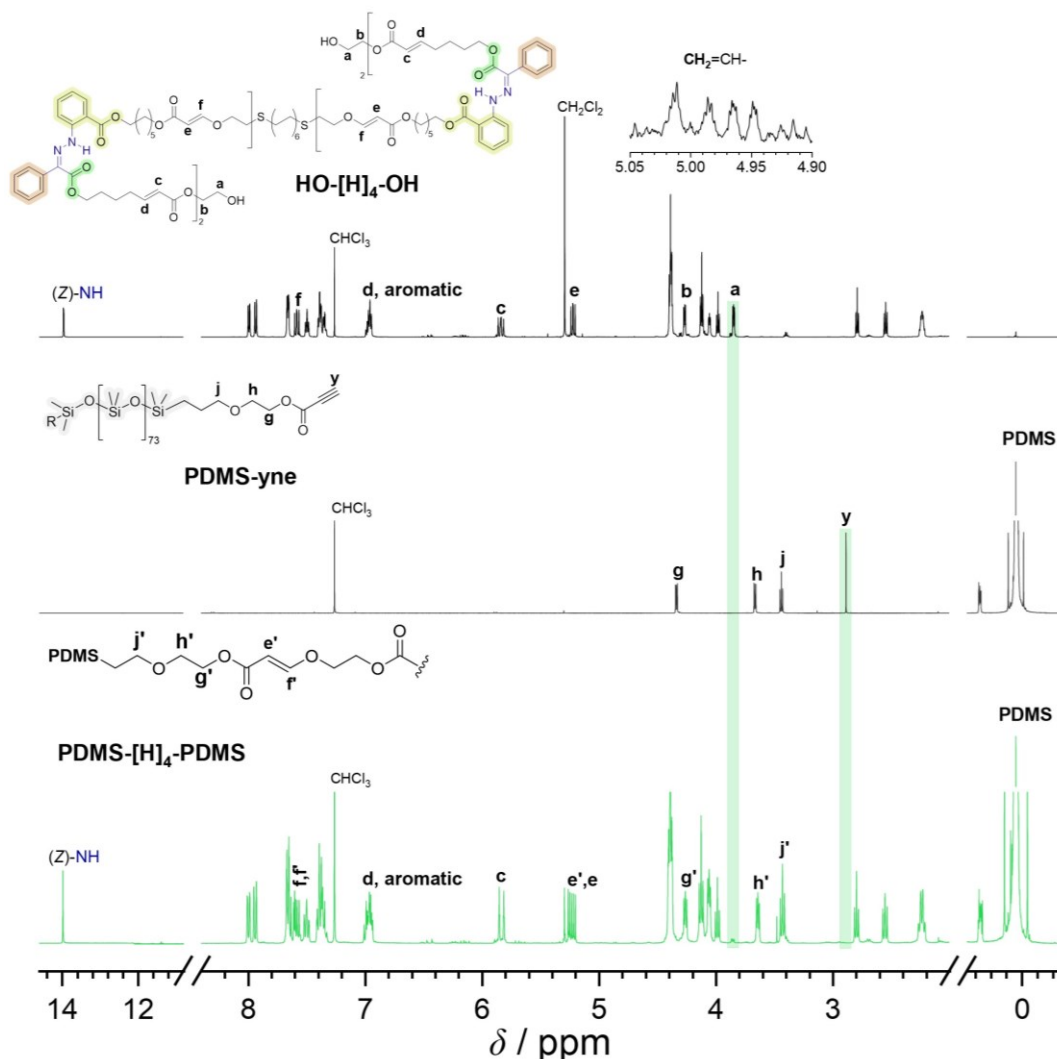


Figure 7.9. ¹H NMR spectra recorded in CDCl₃ with assignment of important resonances of **HO-[H]₄-OH**, **PDMS-yne** and **PDMS-[H]₄-PDMS**.

Hence, the alternation of hydroxyl-yne and cross-metathesis reaction allows for the growth in size of the hydrazone oligomer (SEC traces are shown in Figure 7.8A). Summary of number-average molar mass (M_n) is given in Figure 7.8B. It is noticeable that the M_n determined from SEC ($M_{n,SEC}$) is significantly larger than the $M_{n,NMR}$ which is the same as the theoretical value. Such difference likely arises from the non-linear and bulky hydrazone core, just as in the case of α -bisimine oligomers. Notably, the DMAc-SEC trace of the 4-mer sequence, **HO-[H]₄-OH**, shows a small shoulder at higher molar mass. This may originate from the solute-column interaction in the SEC column. When measured in THF-SEC, a shoulder at low M_n is much more prominent than the one at the higher M_n for **HO-[H]₄-OH** for (Figure 7.8C). One may argue that the presence of this low M_n oligomer is an indication of incomplete conversion in the metathesis step. Analysis of ¹H NMR spectrum of **HO-[H]₄-OH** shows less than 3% of unreacted olefin (at $\delta = 4.98$ ppm for $\underline{\text{CH}}_2=\text{CH}-$) (Figure 7.9, top). This also suggests that the

metathesis reaction may become less efficient when the oligomer becomes larger in size. However, this does not explain for the high M_n shoulder in both DMAc- and THF-SEC. An additional contribution may arise from the shuffling reaction during the **HG-II**-catalyzed cross-metathesis reaction.²⁴⁵⁻²⁴⁷ Potentially, a small fraction of the **HO-[H]₄-OH** oligomers undergo interchain cross-metathesis in an exchange manner, generating a small population of low M_n and high M_n species while keeping the number of internal acrylate bonds unchanged.

Although the obtained oligomer, **HO-[H]₄-OH**, is not perfect, it is still acceptable to use for the chain extension with **PDMS-yne** to synthesize block copolymers. The reaction condition is adapted from the α -bisimine-based block copolymer synthesis (in the presence of 20 mol% DABCO in DCM as a solvent). The resulting block copolymer was purified by flash column chromatography to remove the excess **PDMS-yne** homopolymer and the DABCO base. Unexpectedly, the SEC trace recorded in THF for the purified BCP, **PDMS-[H]₄-PDMS**, show a bimodal distribution, indicative of the existence of two polymers with different chain lengths. Analysis of the NMR spectra in Figure 7.9 shows roughly 7%-9% of unreacted end groups (i.e., hydroxy, $\delta = 3.85$ (proton **a**)). However, the SEC peak fitting by a Gaussian function shows a noticeable amount of the low M_n block copolymer (noted as BCP (1)) compared to the high M_n BCP (noted as BCP (2)) (Figure 7.8C). Furthermore, the $M_{n,SEC}$ determined for **PDMS-[H]₄-PDMS** is roughly 22500 g·mol⁻¹, which is more reasonable for a mixture of triblock copolymers rather than diblock and triblock copolymers. It should be emphasized that the term “triblock copolymer” used for **PDMS-[H]₄-PDMS** is strictly not correct. It is because the hydrazone block is separated by a linear aliphatic chain in the middle. Therefore, instead of an ABA triblock copolymer, AB-BA block copolymer is more accurate for **PDMS-[H]₄-PDMS**. The same argument can be made for the α -bisimine-based BCPs reported earlier in chapter 4. However, to keep it simple, we consider them as triblock copolymers.

To further characterize the BCP, Diffusion Ordered Spectroscopy (DOSY) was performed on **PDMS-[H]₄-PDMS** in CDCl₃. The DOSY spectrum (Figure 7.10) clearly shows the coexistence of two macromolecules, corresponding to species (1) and (2) as determined by SEC. Furthermore, both PDMS and hydrazone segments are presented in both macromolecules, meaning there is a mixture of two block copolymers rather than a blend of a homopolymer and a block copolymer. The higher M_n BCP (2) should have a smaller diffusion coefficient (D) value in the DOSY spectrum. Therefore, the derived D values for (1) and (2) are 1.60·10⁻¹⁰ m²s⁻¹ and 7.39·10⁻¹¹ m²s⁻¹, respectively. Even though the determination of M_n via D values has been reported in some works in the literature, most systems are for PMMA, PS and PEG-base polymers.^{248,249} However, the relative ratio of each species, (1) and (2), can be estimated based on their signal intensities in the DOSY spectrum: 64% of (2) and 36% of (1). The estimation from SEC is also similar, 60% of (2) and 40% of (1). Given the relatively high ratio of (1), incomplete conversion of the hydroxyl-yne reaction may not be sufficient to explain for the origin of the mixture formation. Rather, the contribution from the shuffling of cross-metathesis reaction discussed previously may now be more probable.

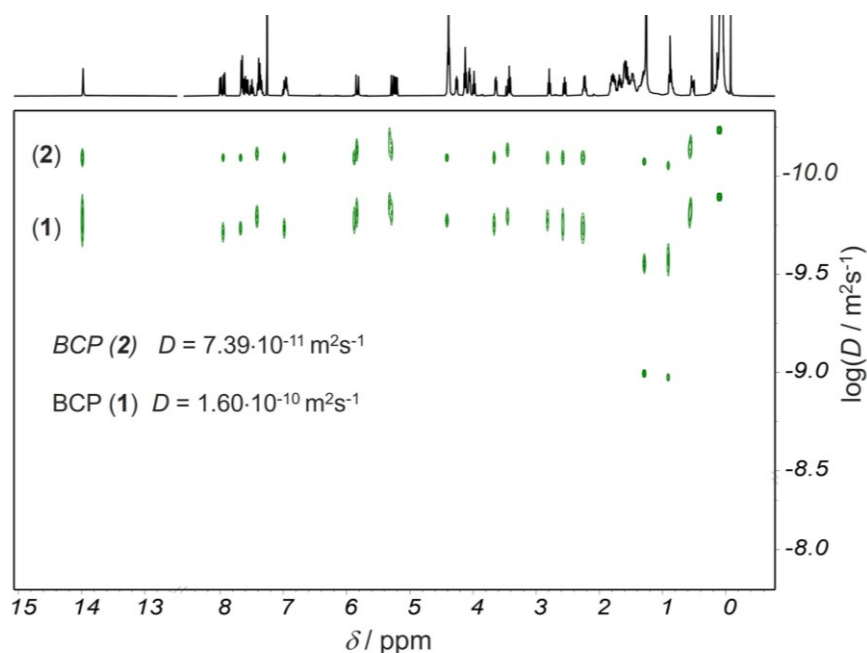


Figure 7.10. DOSY spectrum of **PDMS-[H]₄-PDMS** in CDCl_3 . It is clear that there is a mixture of two different block copolymers, both of which contain hydrazone and PDMS segments. Experiment details are provided in Experimental part, Section 11.7.

Regardless of the root cause, the impure block copolymer **PDMS-[H]₄-PDMS** obtained here will still be utilized for our purpose of photodynamic block copolymer lithography. It is the morphology transition triggered by light that is our interest even though the pristine morphology may be affected by block copolymer blend.

7.2.2. Photoisomerization and light responsive property of **HO-[H]₄-OH**

In Section 7.1, we have studied the photoisomerization kinetics and shown the change in the hydrodynamic volume of hydrazone-based main-chain polymer. Since the oligomer **HO-[H]₄-OH** is synthesized from a different approach (combination of hydroxyl-yne and metathesis), it is essential to study and confirm their photoisomerization as well as property change upon isomerization (e.g., hydrodynamic volume change).

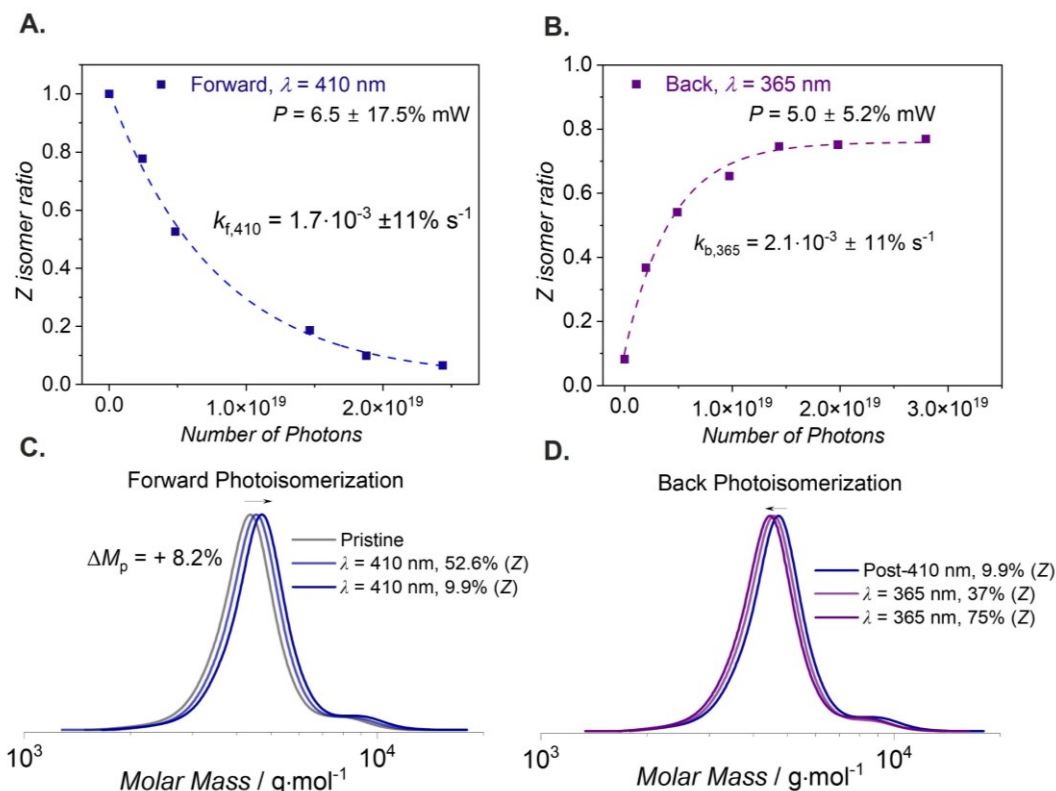


Figure 7.11. Forward (A) and back photoisomerization of **HO-[H]₄-OH** oligomer in toluene-*d*₈. (C,D) Molecular weight distribution of the DMAc-SEC traces of the pristine and irradiated **HO-[H]₄-OH** oligomer. Prior to SEC measurement, the oligomer solution was blown-dried and redissolved in DMAc.

For the photoisomerization study, we employed proton NMR spectroscopy to probe the kinetics of the forward and back isomerization of **HO-[H]₄-OH** (Figure 7.11A,B). Upon 410 nm-irradiation, a clean *Z/E* photoisomerization led to the formation of the *E* isomer. High ratio of the *E* isomer is observed at 410 nm PSS (~ 90% *E*-isomer). The back switching at 365 nm irradiation recovers 75% of the *Z*-isomer. We derived the rate constants for the forward ($k_{f,410}$) and back ($k_{b,365}$) photoisomerization with an exponential function, giving $k_{f,410} = 1.7 \cdot 10^{-3} \pm 11\% \text{ s}^{-1}$ and $k_{b,365} = 2.1 \cdot 10^{-3} \pm 11\% \text{ s}^{-1}$. These values are in good agreement with those determined for polymer **P_{h2}** (section 7.1.2) which contains the same main-chain hydrazone core.²⁴⁰ Furthermore, we also observed an increase ($\Delta M_p = 8.2\%$) in the peak molar mass of the 410 nm-irradiated oligomer and a reversion was observed in the back photoisomerization (Figure 7.11C, D), validating the reversibility of the process.

7.3. Concluding remarks

In this chapter, we have successfully incorporated hydrazone photoswitch into the polymer backbone via head-to-tail ADMET polymerization. Importantly, we demonstrate that by simply switching the attachment point connecting the photoswitch to the main-chain, the photo-induced change in hydrodynamic volume could be triggered in an opposite manner. Furthermore, the photoswitching led to a reduction in glass transition temperature by almost 10 °C. Following this, we have developed a synthetic route inspired by hydroxy-yne and cross-metathesis reaction to synthesize hydrazone main-chain block copolymers. Although the

Chapter 7: Hydrazone-based Main-chain Polymers and Block Copolymers

approach is not ideal to acquire well-defined block copolymers, the mixture of hydrazone-based block copolymers obtained here is still useful for the next step in our plan: photodynamic block copolymer lithography. In the end, photo-induced transition of block copolymer nanostructures is the ultimate goal.

Chapter 8: Spiropyran-based Polymers and Block Copolymers^{vi}

E/Z-photoisomerization leads to a significant change in the geometry of the molecular photoswitch. To modulate properties of photoswitching polymers based on such geometrical change, it is only effective to insert such *E/Z*-photoisomerizable molecules to the polymer backbone rather than as side-chain groups. This is clearly demonstrated in the last chapter with hydrazone photoswitch.²⁴⁰ For main-chain photoswitchable block copolymers, the photo-triggered shrinkage or expansion of the polymer coil in solution of the photoresponsive block may suggest an alteration in the volume fraction of that block. This in turn can induce a shift in the equilibrium of the block copolymer nanostructure, especially if the pristine nanostructure is close to the boundary of another phase.

However, this is not the only way to manipulate the morphology of block copolymers. Altering the polarity also greatly affects the interaction dynamics between two blocks, thus potentially resulting in the alteration of the Flory-Huggins interaction parameter (χ). Of the photoswitches shown in chapter 2, spiropyrans (SPs) are the ideal candidate for such manipulation. Thus, the objective of this chapter is to integrate SPs into polymers and block copolymers and study their photochromism.

Ideally, integration of SPs as main-chain repeating units can affect both the volume fraction and the hydrophilicity of the constituting block upon interaction with light. Furthermore, while SPs are sensitive to several external stimuli, their sensitivity towards a particular stimulus can intrinsically be contingent on the substitution pattern in their structures. Therefore, it is essential to gain insight into their behavior when included into polymeric materials. Hence, synthesis and study of main-chain spiropyran-based polymers are reported in the first part of this chapter. Subsequently, SP-based block copolymers will be synthesized and discussed in the second part of the chapter.

8.1. Regioisomeric effect on the photo- and halochromism of main-chain spiropyran polymers

Spiropyrans (SPs), typically containing a benzopyran (chromene) covalently connected to a heterocyclic moiety via the spiro-carbon (Figure 8.1), constitute a well-known and extensively studied class of multi-stimuli-responsive chemical structures.^{107,108,250} The ring-closed

^{vi} Parts of this chapter were reproduced from Thai, L. D.; Kammerer, J. A.; Mutlu, H.; Barner-Kowollik, C. *Chem. Sci.* **2024**, 15, 3687-3697, with permission from the Royal Society of Chemistry.

structure of SPs is normally the thermodynamically stable isomer, which can reversibly transform to the ring-opened form upon exposure to various stimuli, such as light irradiation, pH or mechanical force.^{108,250,251} The stimuli-responsive SP transformation is accompanied by a vivid color change (i.e., colorless to colored or vice versa) and a large polarity difference (i.e., apolar (hydrophobic) to polar/zwitterionic/merocyanine (hydrophilic) form or vice versa).

Most stimuli-responsive moieties are tethered directly to the polymer chain as either pendant groups – and to a far lesser extent – as main-chain active groups via ester and amide bonds.^{188,252-255} In the realm of SPs, the type of the substituents decorating the SPs, e.g., electron-withdrawing or electron-donating, has a potentially significant influence on the stimuli-sensitiveness of SPs-based polymers.²⁵⁶⁻²⁵⁸ However, the impact of ester groups located at different sites of SPs' aromatic moieties (regioisomers) has not been investigated. In fact – to our best knowledge – only two studies explore substituent location variations of the polymerizable group on the benzopyran moiety, leading to different levels of stretching-induced ring-opening and isomerization of the covalently embedded SP units.^{238,259} However, the SPs-based monomers were designed such that the SP moiety and the ester group of polymerizable handles were connected via a methylene group (-CH₂-) to the chromene moiety.^{238,259} Critically, the effect of these designs on the resulting photo- and pH-responsive properties was not explored. Interestingly, nitro-substituted SPs (**SP-NO₂**) have frequently been explored, most likely due to the resulting red-shifted electronic absorption and an enhanced quantum efficiency induced by the electron-withdrawing group.^{260,261} Remarkably, in the current literature, the electrochemical contribution of other groups, e.g., esters, is often ignored. However, tuning the properties of responsive macromolecular materials via subtle alterations of their chemical structures is undoubtedly a powerful avenue to establish varied property profiles with synthetic ease. Herein, we demonstrate such structural variations and their effect on the resulting material properties, opening a facile route to an advanced class of SP-containing responsive polymer systems, including photoresponsive BCPs.

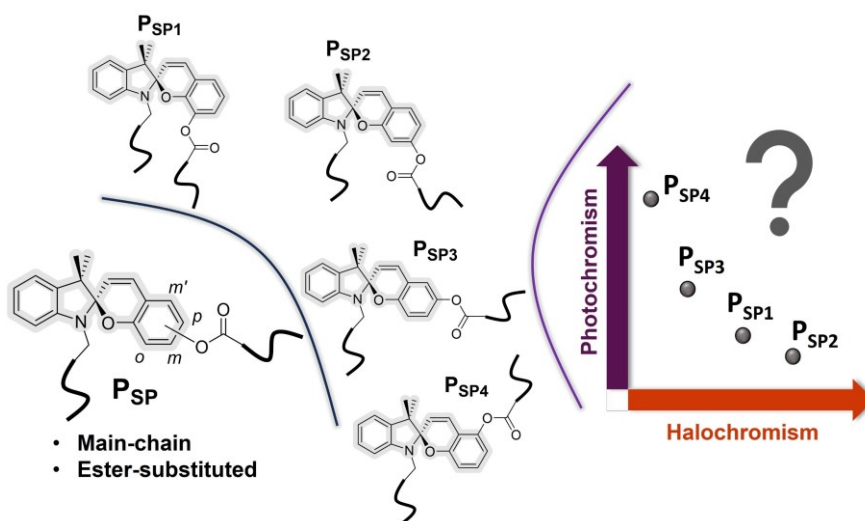


Figure 8.1. General structure of four isomeric main-chain homopolymers. Reproduced from ref.²⁶² with permission from the Royal Society of Chemistry.

We thus introduce the synthesis of four main-chain polymers (**P_{SP1}**, **P_{SP2}**, **P_{SP3}** and **P_{SP4}**) derived from four regioisomers of SPs via head-to-tail ADMET polymerization and investigate their photo- and acid-responsive properties (Figure 8.1). These polymers differ only in the substitution location on the SP's benzopyran (chromene) moiety (*o*-, *m*-, *p*- and *m'*- position, corresponding to **P_{SP1}**, **P_{SP2}**, **P_{SP3}** and **P_{SP4}**, respectively, refer to Figures 8.1 and 8.2) of the ester group (-OCOR, where R contains a polymerizable handle, inserting the chromophore into the polymer main-chain). Note that the benzopyran ring is substituted with the ester oxygen (-OCOR) rather than the carbonyl carbon (-COOR) of the ester group reported elsewhere for small structures.²⁶³ To our best knowledge, it is the first time that SPs bearing an ester group (-OOCR) substituted at either *m* or *m'* position (refer to Figure 8.2) are reported. The synthetic accessibility of all four substitution sites allows us to systematically study the influence of regio-isomers on the stimuli response of SPs. Interestingly, our results show that such minor structural differences have dramatic effects on the solution photo- and acid-responsiveness of the SP moieties of these polymers. Particularly, while **P_{SP1}** is relatively photo-inactive yet acid sensitive, the complete opposite behavior is observed for **P_{SP4}**.

8.1.1. Synthesis of SPs main-chain polymers

Initially, we designed four ADMET monomers, containing four spiropyran regioisomers as main-chain moieties. The handle containing the acrylate group is placed at the indoline nitrogen, while the phenyl ring of the chromene moiety is substituted with an ester group containing the olefin handle at one of the four sites, *o*-, *m*-, *p*- and *m'*-, yielding monomer **M_{SP1}**, **M_{SP2}**, **M_{SP3}** and **M_{SP4}**, respectively (Figure 8.2). The selective cross-metathesis using a Hoveyda-Grubbs 2nd generation catalyst (**HG-II**) between the acrylate and olefin functional groups affords the main-chain polymer **P_{SP1}**, **P_{SP2}**, **P_{SP3}** and **P_{SP4}** from the respective monomers. The sectional ¹H NMR spectra in Figure 8.2 unambiguously evidence the formation of the internal acrylate bond (proton resonances at $\delta \approx 5.75$ and 6.92 ppm) from the cross-metathesis, while leaving the SP chromophores chemically intact. The apparent number-average molar mass (M_n) of these polymers falls in the range of 7500 – 22000 g·mol⁻¹ (SEC traces and M_n are shown in Figure 8.2, bottom and Table 8.1), in line with other stimuli-responsive polymers synthesized via ADMET polymerization.^{145,193} Interestingly, during the polymerization, we observed gelation of the reaction mixture of **M_{SP2}** when dichloromethane (DCM) was used as solvent. The gelation could be prevented by using 1,2-dichlorobenzene (DCB) as solvent instead and obtaining polymer **P_{SP2}** (Figure 8.2B) successfully. Although the mechanism for the gelation of **M_{SP2}** in DCM solution is unclear, we speculate that the general structure of **M_{SP2}** with the ester group at the *m*-position of the benzopyran ring (Figure 8.2) might allow for a ligand-exchange reaction with the Ru-based **HG-II** catalyst which could gradually decompose in DCM solvent.²⁶⁴ On the basis of the observed M_n values of the four polymers (Table 8.1), the acrylate and the olefin handles in **P_{SP3}** are in an optimal orientation, enabling rapid polymerization and affording relatively high M_n compared to other three isomeric polymers. The

substitution-site dependence of M_n in ADMET polymerization is also observed in hydrazone-based main-chain polymers.²⁶⁵

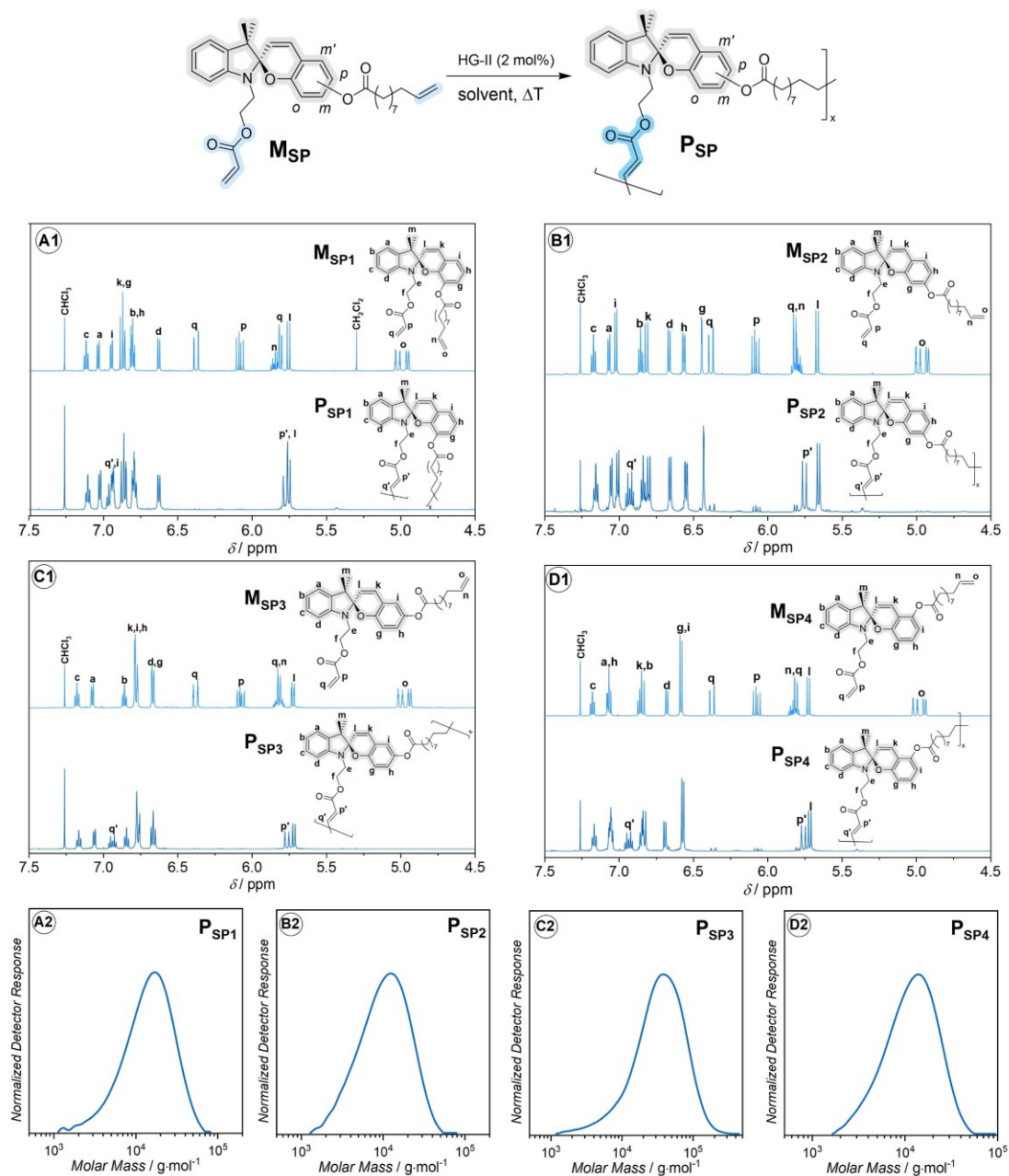


Figure 8.2. Synthesis of regio-isomeric main-chain homopolymers based on a spiropyran scaffold. (A1-D1). Sectional 1H NMR spectra recorded in $CDCl_3$ with assignment of important resonances of monomers and the respective polymers. (A2-D2) DMAc-SEC traces of the four polymers. Reproduced from ref.²⁶² with permission from the Royal Society of Chemistry.

With regard to the optical properties of the four polymers, there is insignificant difference in terms of the peak absorption band (λ_{max}) in DCM, corresponding to the π - π^* transition of the chromene moiety, close to the values reported for halogen- and ether-substituted SPs (λ_{max} = (297-299) nm, Table 8.1).²⁵⁶ The molar absorptivity of the SP chromophore at λ_{max} (i.e., ϵ_{max}) for P_{SP1} , P_{SP2} , P_{SP3} and P_{SP4} varies between $3700 M^{-1} \cdot cm^{-1}$ and $4700 M^{-1} \cdot cm^{-1}$, respectively (Table 8.1).

Table 8.1. M_n , Dispersity, and Optical properties of P_{SP1} , P_{SP2} , P_{SP3} and P_{SP4}

Polymer	M_n^a / $\text{g}\cdot\text{mol}^{-1}$	M_p^a / $\text{g}\cdot\text{mol}^{-1}$	\bar{D}^a	λ_{max}^b / nm	ϵ_{max}^b / $\text{M}^{-1}\cdot\text{cm}^{-1}$
P_{SP1}	11000	17000	1.6	297	4130
P_{SP2}	8000	12000	1.6	299	4630
P_{SP3}	22000	39000	1.9	299	3710
P_{SP4}	7500	10500	1.5	298	3850

^aDimethylacetamide (DMAc)-Size Exclusion Chromatography (SEC), on the basis of poly(methyl methacrylate) (PMMA) calibration. ^bin dichloromethane (DCM) at 25 °C.

8.1.2. Photo- and halochromism

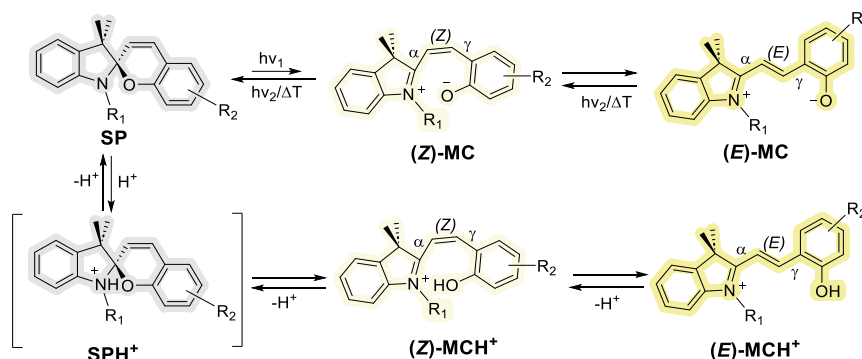


Figure 8.3. Simplified mechanism of photo- and acid-induced ring-opening and isomerization of SPs. The (Z)-MC/MCH⁺ and (E)-MC/MCH⁺ can adopt other conformations via rotation around the α - and γ -bond. Details of the stimuli-responsive mechanism can be found in refs.^{106,108,266-270}. Reproduced from ref.²⁶² with permission from the Royal Society of Chemistry.

Fundamentally, the closed- and open-conformation switching of SPs is a complex process, as there are several possible transient states, which have been subjected to careful experimental and theoretical investigation.^{108, 106,266-270} Briefly, the photo-induced transformation of SPs first takes place via the cleavage of the labile C-O spiro bond, followed by *E/Z*-isomerization around specific bonds (Figure 8.3) to form the merocyanine (MC) form (opened form).²⁶⁸ In the presence of a strong acid, the protonation of spiro oxygen and the subsequent isomerization generates thermally stable species (MCH⁺).²⁶⁸ However, probing the switching mechanism is not the main aim here. Instead, we explore the effect of the molecular design on the switching efficiency of SP main-chain polymers. Specifically, we reveal the effect of the location of the ester group on the chromene moiety on photo- and halochromism. We exploit the intense color difference between the spiropyran (closed-form, colorless) and the MC/MCH⁺ form (opened-form, colored), monitored by UV-vis spectroscopy, to compare the photo- and pH-responsive properties among P_{SP1} , P_{SP2} , P_{SP3} and P_{SP4} .

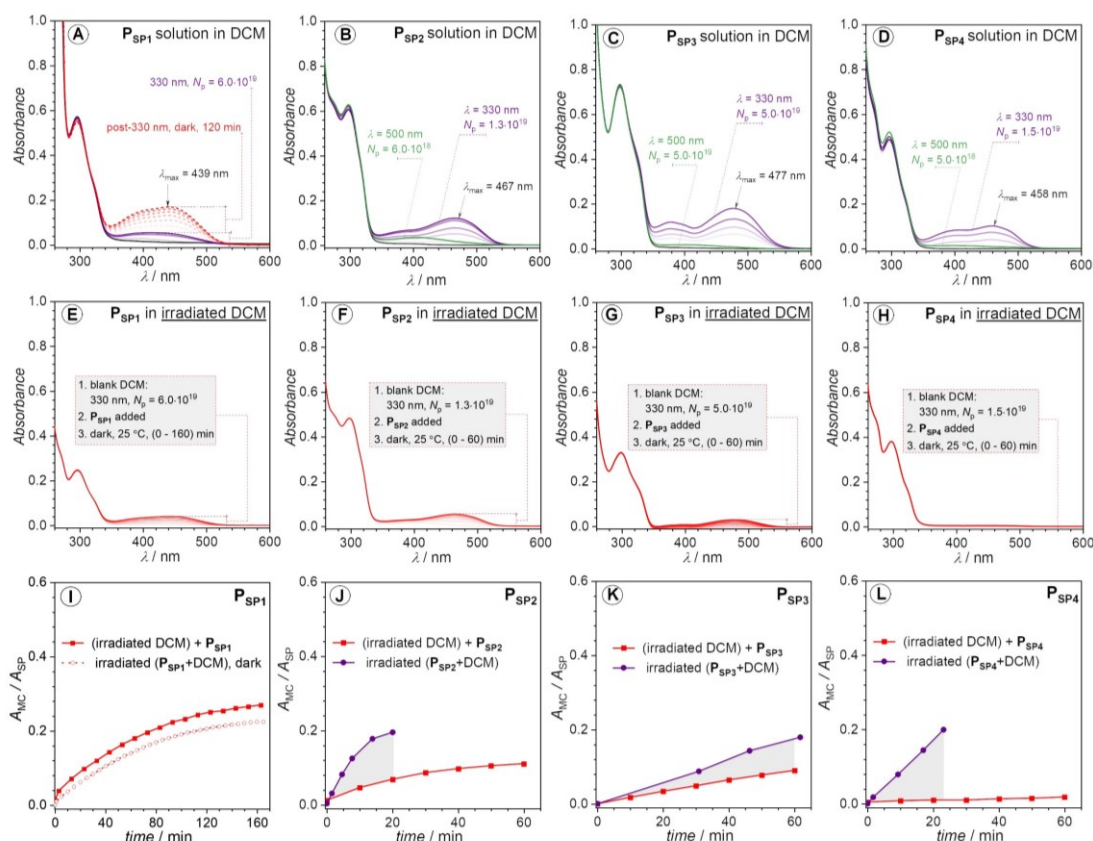


Figure 8.4. Photochromism of four spiropyran-based main-chain homopolymers investigated via UV-vis spectroscopy. (A-D) UV-vis spectra recorded for polymer solutions irradiated with 330 nm. The red dashed lines denote the spectra recorded post-330 nm irradiation; the purple solid lines represent the spectra recorded immediately after 330 nm irradiation; the green solid lines indicate the spectra recorded after 500 nm irradiation of the 330 nm irradiated solutions (E-H) Control experiments: the DCM solvent was first irradiated with 330 nm, after which the polymer solution was added. The laser power at 330 nm and 500 nm irradiation was kept at 6.5 mW ± 5.2% and 8.5 mW ± 13%, respectively. (I-L) Plots of A_{MC}/A_{SP} vs time for P_{SP1}, P_{SP2}, P_{SP3} and P_{SP4}, respectively. Note that the protonated form of MC (MCH⁺) also exists but is grouped into the 'MC' label in A_{MC} (i.e., absorbance of the opened form) for the sake of simplicity. The absorbance of the 'MC' label in this case (A_{MC}) corresponds to the λ_{max} of the colored species in the visible range, and the A_{SP} refers to the absorbance at λ_{max} of the respective spiropyran. The A_{MC}/A_{SP} ratio is used instead of A_{MC} to factor in the concentration difference between experiments assuming $A_{MC}/A_{SP} \sim C_{MC}/C_{SP}$ with $\epsilon_{MC}/\epsilon_{SP} = \text{constant}$. The number of photons (N_p) was converted into time via Eq. 11.2. The gray areas in (J-L) highlight the actual photochromic response of polymer solutions upon 330 nm irradiation. Reproduced from ref.²⁶² with permission from the Royal Society of Chemistry.

8.1.2.1. Photochromism

Initially, we conducted the irradiation of the four polymer solutions (50-150 μM) in dichloromethane (DCM) at ambient temperature (25 °C). We selected a monochromatic wavelength of 330 nm to minimize unfavorable side reactions, such as photodegradation. The UV-vis spectra in Figure 8.4 demonstrate the different photochromism of the investigated polymers. While there is almost no vivid color change of the P_{SP1} polymer solution unless when irradiated with relatively large number of photons (N_p) ($N_p = 6.0 \cdot 10^{19}$ photons) (Figure 8.4A). In contrast, the UV-vis spectra of P_{SP2}, P_{SP3} and P_{SP4} display new and strong absorption bands in the visible region (Figure 8.4B-D) upon irradiation. It is noticeable in the case of the latter polymers that in addition to an emerging absorption peak centered at around 458-477 nm, there is an absorption band lying at lower wavelengths close to 380-390 nm, suggesting the existence of at least two isomers of the opened form, e.g., (Z)- and (E)-isomers of MC.

Intriguingly, the color of the **P_{SP1}** solution in DCM gradually turned yellow in the dark after long time exposure to 330 nm irradiation ($N_p = 6.0 \cdot 10^{19}$ photons) (Figure 8.4A). We cannot exclude the solvent contributions, e.g., from DCM, to the photochromism of SPs, as frequently reported in the literature.²⁷¹⁻²⁷⁴ Nevertheless, it is worth noting that the pristine polymer solutions in DCM did not show any change in color at 25 °C in the dark, excluding solvatochromism as the root cause of the color change. However, to our surprise, the irradiation performed in other solvents, i.e., toluene and dimethylacetamide (DMAc), did not trigger a noticeable response from all four polymers (UV-vis spectra shown in Figure S8.1, Experimental part, Section 11.8). We chose toluene and DMAc alongside DCM as solvents for the irradiation study due to the good solubility of the polymers in these solvents which are of different polarity.

Protic solvents capable of forming H-bonds, such as methanol, can stabilize the merocyanine (MC) form, thus facilitating the photo-induced SP→MC conversion process.²⁷⁴ However, the four SP-based polymers reported in our work are hydrophobic and do not dissolve in such protic solvents. Toluene and DMAc do not possess H-bonding capabilities. Besides, DMAc can act as a Lewis base^{275,276} which may react with the opened form of spiropyran (merocyanine) induced by Lewis acid addition.²⁷⁷ However, it is not relevant to our case where no Lewis acid was added in the irradiation study. Even though DCM is not a protic solvent, its role as a very weak H-donor was previously reported,²⁷⁸ which may be a contributing factor to the color change observed for **P_{SP2}**, **P_{SP3}**, **P_{SP4}** under 330 nm irradiation in DCM. However, we cannot discard the possibility of UV-induced degradation of the halogenated solvents, e.g., CH₂Cl₂, CHCl₃, into halogen acids, e.g., HCl, that can cause the change in color of these polymer solutions owing to the generally acid-sensitive characteristics of SPs. For instance, Sommer and colleagues reported the *in-situ* generation of acid from DCM-*d*₂ and chloroform-*d* under sonication, which was responsible for the chromism of the reported SP-based polymers in the respective solvents.^{279,280}

To confirm the possible *in-situ* generation of halogen acid under UV-irradiation, we conducted control experiments in which only the blank DCM solvent was irradiated with an exact number of photons previously applied for each SP-based polymer solution, after which the stock polymer solution was rapidly added to the UV-exposed solvent. **P_{SP1}** in post-irradiated DCM shows a gradual increase in the visible absorption region ($\lambda_{max} = 439$ nm), which is identical with the irradiated **P_{SP1}** solution mentioned above (Figure 8.4A,E,I). Thus, the acid-induced ring-opening and isomerization observed for **P_{SP1}** takes place in the dark after 330 nm irradiation ($6.0 \cdot 10^{19}$ photons). In the case of **P_{SP2}** and **P_{SP3}**, the HCl formed *in-situ* also co-contributes to the color change (compare Figure 8.4B,C,F,G,J,K). In contrast, **P_{SP4}** appears to be barely affected in the irradiated blank solvent (Figure 8.4D,H,L). Therefore, these results allow to conclude that **P_{SP4}** is the most photo-active polymer, while **P_{SP1}** is insensitive to solution photo-irradiation. In other words, the substitution site of the ester group on the chromene moiety does indeed critically influence the photochromic properties of the main-chain polymers. It should be noted that the comparison made here is qualitative, yet

convincingly sufficient. Based on UV-vis spectra alone (Figure 8.4), we cannot quantify the ratio of the opened-form induced by irradiation. However, irradiation of higher concentrated solutions (close to 0.96 mM in DCM-*d*₂) with 330 nm laser light did not cause any change in the ¹H NMR spectra, probably due to the low efficiency of the photo-induced SP→MC transformation at higher concentrations (millimolar vs micromolar), also noted by Ballester and colleagues for a spiropyran compound in their study.²⁸¹

The colored state of the opened-form can be quenched via visible light irradiation ($\lambda = 500$ nm, $P = 8.5$ mW \pm 13%) (Figure 8.4B-D). Nevertheless, while the absorption at around 450-480 nm completely disappears under 500 nm irradiation (Figure 8.4B-D), the shoulder absorption band close to 390 nm persists. The incomplete visible light-induced colored to colorless reversion may be due to the stabilizing effect from either acidic protons or the solvent (DCM). In addition, we note the contribution of the polymer backbone to the thermal stability of the opened-form.²⁸² To avoid the impact from the *in-situ* forming acid (HCl), we performed the irradiation in thin films (solid-state) to expand the potential application scope of the polymers on the example of polymer **P_{SP2}**. Under similar irradiation condition ($\lambda = 330$ nm, $N_p = 1.5 \cdot 10^{19}$, $P = 6.5$ mW \pm 4.0%), the color of the polymer film on a quartz slide turned yellow, detectable with the naked eye. Indeed, the recorded UV-vis spectrum (Figure S8.6, Experimental part, Section 11.8) revealed a new broad absorption band in the visible region (up to 650 nm), suggesting SP→MC transformation in the solid state. However, the solid-state UV-vis spectrum of the MC is vastly different from the solution one, likely due to the intermolecular stacking of the formed MC species in the confined environment in the polymer film. Nevertheless, we have demonstrated the feasibility of solid-state photochromism of the SP-based polymer, i.e., **P_{SP2}**.

8.1.2.2. Halochromism

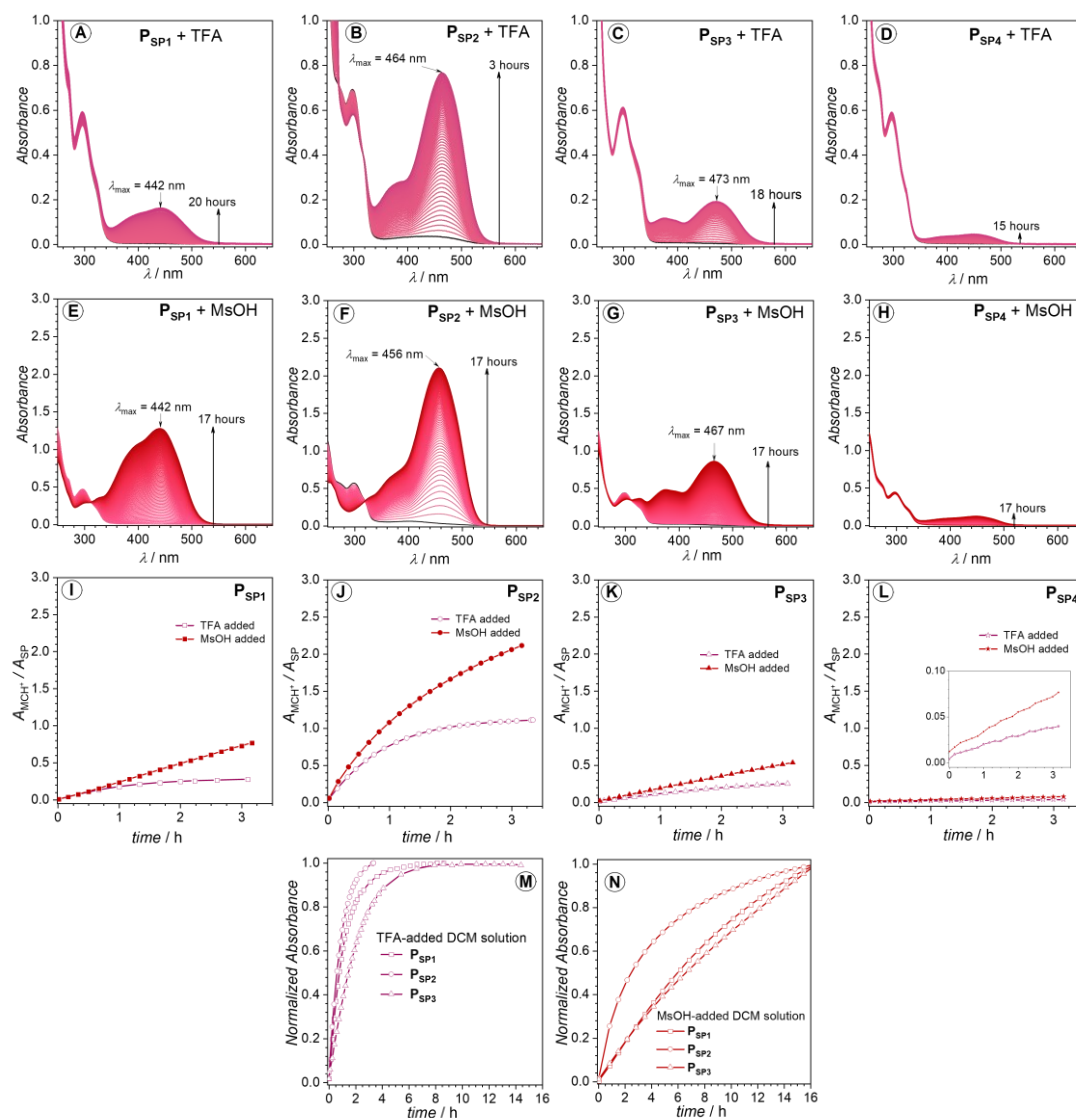


Figure 8.5. Halochromism of P_{SP1} , P_{SP2} , P_{SP3} , P_{SP4} in DCM investigated by UV-vis spectroscopy. (A-D) TFA addition (1.0 eq), (E-H) MsOH addition (1.0 eq). Time until equilibration is indicated. Molar concentration of SP moiety: 100 – 150 μM . (I-N) Comparison of the kinetics among four polymers upon acid addition. Normalized absorbance was used in Figure 4M and N to enable a qualitative comparison of the response rate of the polymers toward TFA and MsOH acid. The A_{MCH^+}/A_{SP} ratio is used instead of A_{MCH^+} to factor in the concentration difference between experiments assuming $A_{MCH^+}/A_{SP} \sim c_{MCH^+}/c_{SP}$ with $\epsilon_{MCH^+}/\epsilon_{SP} = \text{constant}$. A_{MCH^+} refers to the absorbance (A) of the MCH^+ form at λ_{max} in the visible range, and A_{SP} refers to the absorbance of the pristine SP at λ_{max} . Reproduced from ref.²⁶² with permission from the Royal Society of Chemistry.

The different responses of the polymers to the photogenerated acids indicate the strong effect of the molecular architecture on the halochromism of the main-chain polymers, which we systematically investigated with the addition of two acids with different pK_a (trifluoroacetic acid, CF_3COOH (TFA), $pK_a = 0.23$,²⁸³ methanesulfonic acid, $\text{CH}_3\text{SO}_3\text{H}$ (MsOH), $pK_a = -1.9$)²⁸⁴ to the polymer solutions in DCM. To avoid the acids affecting the polymer chain, such as cleavage of ester bonds, we added only 1.0 molar equivalent of either TFA or MsOH (with respect to the SP core) to the polymer solutions. The colorimetric response was monitored by UV-vis and ^1H NMR spectroscopy. As shown in Figure 8.5A-C, the solution of P_{SP2} swiftly changes color upon TFA addition, reaching an equilibrium within 3 hours. Equilibration of the

color changing process took significantly longer for **P_{SP1}** and **P_{SP3}**. The observed color change is due to the formation of **MCH⁺**.²⁶⁶ In contrast to **P_{SP1}**, **P_{SP2}**, and **P_{SP3}**, the **P_{SP4}** solution was hardly affected by TFA addition (Figure 8.5D), which is opposite to the strong photochromism of **P_{SP4}** discussed above.

Upon the addition of the stronger acid, i.e., MsOH ($pK_a = -1.9$)²⁸⁴, the change in absorbance is significantly larger than in the case of TFA addition, except for **P_{SP4}** which remains largely unaffected (compare Figure 8.5A-D and 8.5E-H). The absorption spectra of these **MCH⁺** species also feature a major absorption band within the 440-465 nm range and a shoulder at around 376-393 nm (Figure 8.5), indicating the existence of different stable isomers, e.g., (**Z**)- and (**E**)-**MCH⁺** (Figure 8.3). The varied sensitivity towards acids of these polymers is a strong indication of different pK_a values of the respective phenolate anions upon ester substitution of the chromene ring. To compare the kinetics of the halochromic processes for **P_{SP1}**, **P_{SP2}** and **P_{SP3}**, we qualitatively compared the curvature of the (normalized) absorbance (at λ_{max} of **MCH⁺**) vs time plot (Figure 8.5I-N). For both TFA ($pK_a = 0.23$)²⁸³ and MsOH ($pK_a = -1.9$)²⁸⁴ addition, **P_{SP2}** is the most responsive polymer, followed by **P_{SP1}** and **P_{SP3}** which show slightly different rates of response (Figure 8.5I-N).

If one compares the acid-induced and the photo-induced UV-vis spectra of **P_{SP2}** and **P_{SP3}** in DCM (Figure 8.4 and Figure 8.5), no prominent shift ((3-4) nm) in the peak and shoulder absorption in the visible region can be observed. For nitro-spirogyrans (**SP-NO₂**), a large spectral shift between the protonated **MC** (**MCH⁺**) and the **MC** form was reported.²⁸⁵ In the case of our ester-substituted main-chain SPs, the presence of the ester groups might bridge the electronic differences between the **MC** and **MCH⁺** forms. Alternatively, the H-bonding stabilization from the solvent, i.e., DCM, might equalize the spectral characteristics of the **MC** and **MCH⁺**.

To quantify the ratio of the **MCH⁺** species in each polymer, we replicated the study using more concentrated solutions (close to 0.97 mM of SP moiety in CD_2Cl_2) for ¹H NMR measurements. Accordingly, comparison of the integral values of protons **e** ($\delta \approx 4.25$ ppm) and **f** ($\delta \approx 3.25$ -3.60 ppm) in the closed-form (as shown in Figure 8.3 and Figure S8.2-S8.5, Experimental part, Section 11.8) with those in the opened-form gives the percentage of **MCH⁺** species (Figures S8.2-S8.5, Experimental part, Section 11.8). Approximately 50% of the spiropyran moieties in **P_{SP2}** transformed into the opened form (**MCH⁺**) upon addition of TFA (1.0 eq), twice as high as for **P_{SP3}** (25%) under identical conditions (Figure S8.3, S8.4, Experimental part, Section 11.8). Similar to **P_{SP3}**, the determined value for **P_{SP1}** is 29%, whereas only 9% was recorded for **P_{SP4}** (Figure S8.2 and S8.5, Experimental part, Section 11.8). The relative amount of **MCH⁺** increases further when MsOH is added instead: close to 75% of **MCH⁺** for **P_{SP1}**, **P_{SP2}** and **P_{SP3}** and only 10% for **P_{SP4}** (Figure S8.2-S8.5, Experimental part, Section 11.8). Interestingly, although the former polymers show the same ratio of **MCH⁺** species induced by MsOH addition at equilibrium, the absorbance or molar absorptivity of the **MCH⁺** in the case of **P_{SP2}** appears to be much higher than **P_{SP1}** and **P_{SP3}**. Thus, the ester-substitution pattern affects not only the

acid sensitivity of SPs, but also the molar absorptivity of the resulting **MCH⁺**. In addition, the highly polar nature of **MCH⁺** can lead to aggregation in solution at high conversion,²⁸⁶ as indicated by Dynamic Light Scattering (DLS) results for the MsOH-added polymer solutions (Figure S8.7, Experimental part, Section 11.8). Further, addition of 2.0 eq of triethyl amine (Et₃N) fully reverted the **MCH⁺** to the closed-form, as evidenced by ¹H NMR spectroscopy (Figure S8.2-S8.5, Experimental part, Section 11.8).

8.1.3. Concluding remarks

The experimental results discussed above clearly point to the significant role of the ester group substituted on the chromene ring beside the contribution from the solvent polarity. The most efficient photochromism is observed for **P_{SP4}**. However, such photochromic response is likely insufficient to trigger a desirably significant change in polarity between the closed- and opened-state of the SP core in **P_{SP4}**. As noted in section 8.1.1, nitro-substituted spiropyrans (**SP-NO₂**) are more efficient in this aspect and extensively used in the literature.^{260,261} Synthetically, it is more challenging to incorporate **SP-NO₂** into polymer backbone, especially into main-chain block copolymers synthesized via a sequence-defined approach. As the change in polarity is a more attractive feature than geometrical change of spiropyran photoswitch, we next utilize **SP-NO₂** as a pendant group in a sequence-defined block copolymer.

8.2. Block copolymer with spiropyran as pendant groups

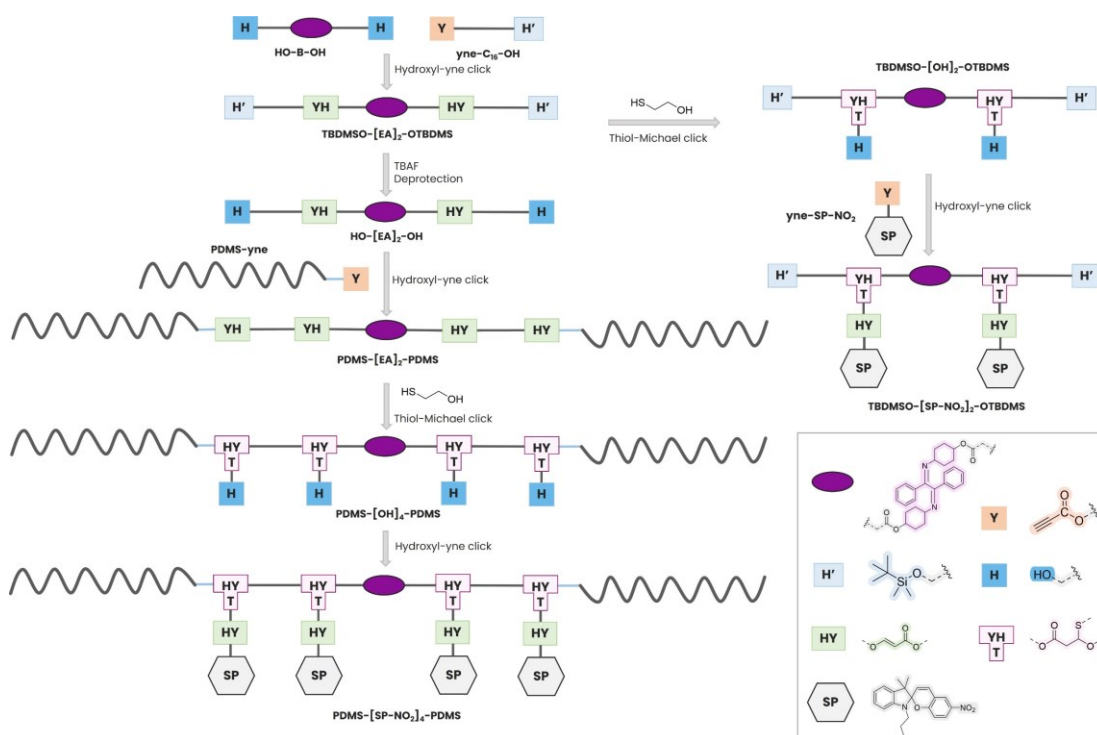


Figure 8.6. Synthesis route for oligomers and block copolymers decorated with nitro-spiropyran side groups. The approach constitutes a series of hydroxyl-yne click and TBAF-deprotection chemistries to grow the backbone, followed by thiol-Michael click and hydroxyl-yne click reactions to attach nitro-spiropyrans as side groups.

We commence by discussing the synthetic strategy to obtain spiropyran-based photoswitchable block copolymers (Figure 8.6). As the photoswitch is attached as a pendant group, we first synthesize a linear oligomer having functionalizable bonds (i.e., ether acrylate) via hydroxyl-yne click reaction and TBAF-deprotection chemistries. For the sake of purification (by flash column chromatography), we employ the dihydroxy-terminated α -bisimine monomer (**HO-[B]₁-OH**) reported earlier in chapter 4, owing to its strong UV absorption at 254 nm. In the end, there is only one α -bisimine group in the polymer backbone. A non-photochromic monomer bearing an activated alkyne (**yne**) and a protected hydroxy (**TBDMSO-**) end group, **yne-C₁₆-OTBDMS**, reacts with **HO-[B]₁-OH** via hydroxyl-yne click reaction, yielding an oligomer having two ether acrylate (**EA**) main-chain groups and two TBDMSO group at two ends, denoted **TBDMSO-[EA]₂-OTBDMS**. The chain extension is possible via TBAF-deprotection, followed by hydroxyl-yne click reaction. Upon reaching target number of EA bonds, the oligomer will be coupled with **PDMS-yne** (reported in chapter 4) via hydroxyl-yne click reaction to produce block copolymers (**PDMS-[EA]_n-PDMS**). The resulting macromolecule will be post-modified via thiol-Michael click reaction to functionalize a short sidechain with hydroxy end group (**PDMS-[OH]_n-PDMS** or **TBDMSO-[OH]_n-TBDMSO**). The nitro-spiropyran decorated with an activated alkyne (denoted **yne-SP-NO₂**) is subsequently tethered to the sidechain via hydroxyl-yne click reaction (Figure 8.6).

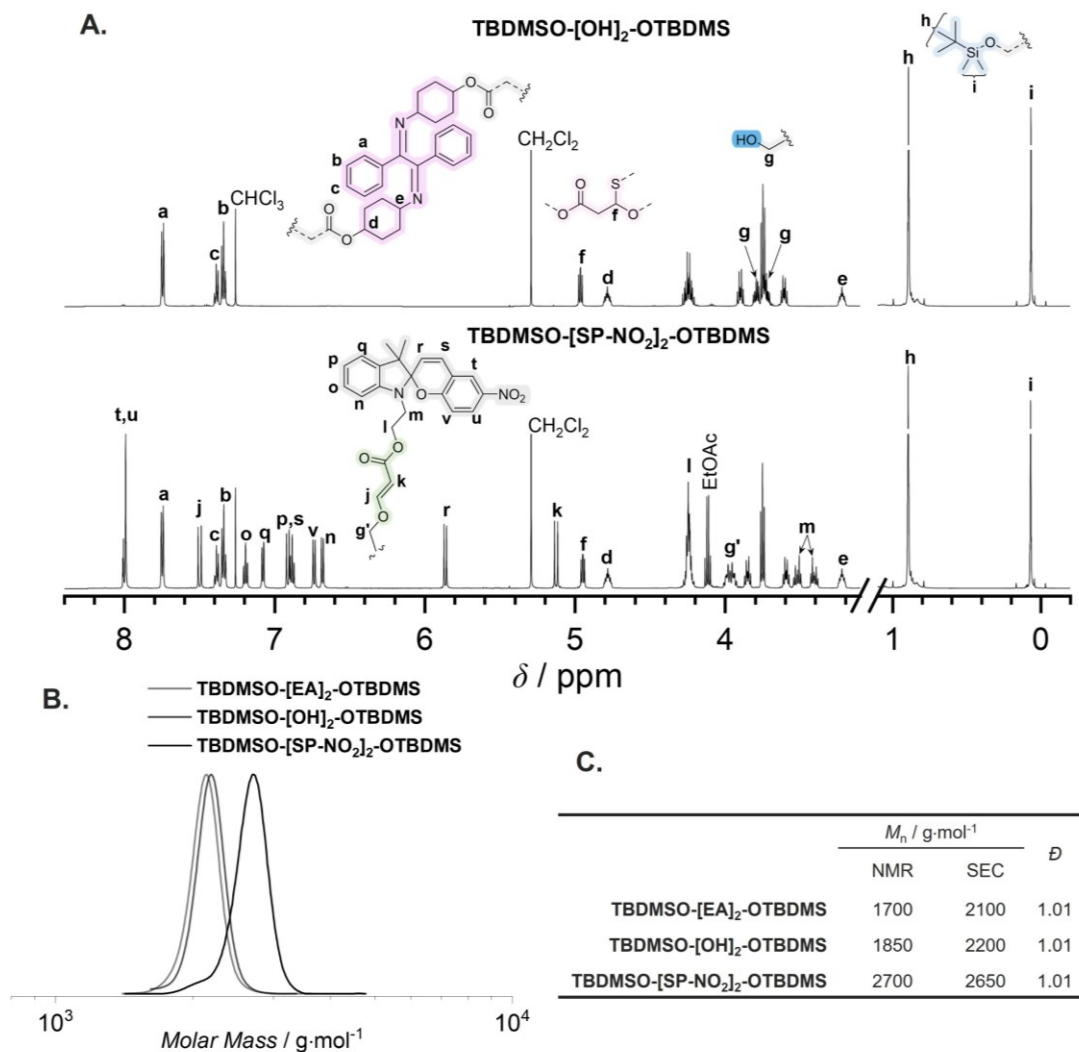


Figure 8.7. Synthesis and characterization of spiropyran-based oligomer, TBDMSO-[SP-NO₂]₂-OTBDMS. (A) Stacked sectional ¹H NMR spectra recorded in CDCl₃. (B) THF-SEC traces of oligomeric sequences. (C) Summary of molar mass determined from NMR and SEC (based on a PMMA calibration).

Prior to block copolymer synthesis, we investigated the possible impact of the α -bisimine group residing in the middle on the photoswitching of spiropyran. For this, we synthesized an oligomer bearing two **SP-NO₂** groups, **TBDMSO-[SP-NO₂]₂-OTBMS** (illustration is shown in Figure 8.6). THF-SEC and ¹H NMR spectra confirm the successful synthesis of this oligomer (Figure 8.7A,B). Specifically, the disappearance of the protons associated with the hydroxy pendant groups (protons **g**) and the appearance of new resonances (protons **g'**) evidence the 100% inclusion of the **SP-NO₂** as side groups (Figure 8.7A). The M_n value determined for **TBDMSO-[SP-NO₂]₂-OTBDMS** from SEC ($M_{n,SEC}$) is close to the theoretical value (or $M_{n,NMR}$) (Figure 8.7C). However, this is not the case for the precursors, **TBDMSO-[EA]₂-OTBDMS** and **TBDMSO-[OH]₂-OTBDMS**. Probably, such deviation is contributed by the bulky α -bisimine middle group, which becomes diminished at higher M_n when **SP-NO₂** is incorporated.

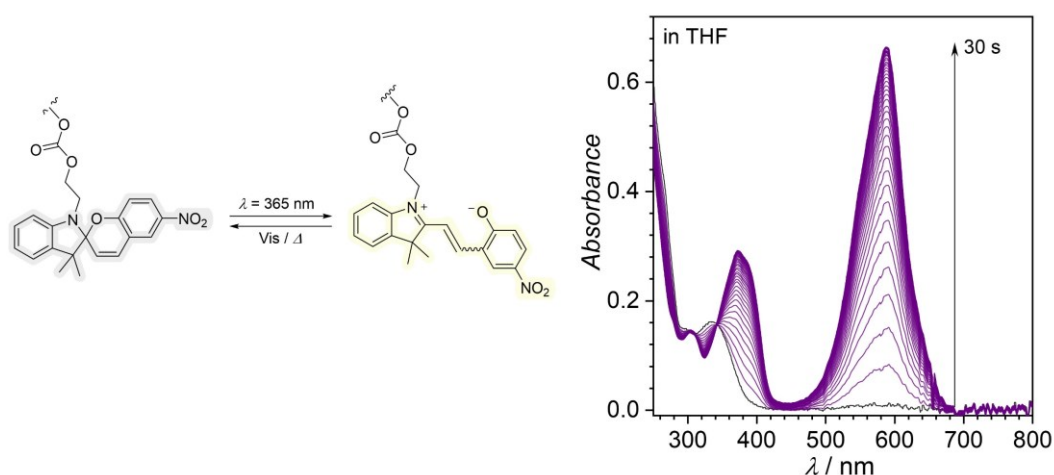


Figure 8.8. UV-vis study of photoisomerization of **TBDMSO-[SP-NO₂]₂-OTBDMS** in THF ($c \sim 10^{-5}\text{ M}$). The oligomer solution was irradiated with a monochromatic wavelength of 365 nm ($P = 5.0\text{ mW}$) and UV-vis spectra were recorded at 1 s interval.

We next performed the irradiation study on the obtained oligomer in THF solution. Accordingly, a diluted solution of **TBDMSO-[SP-NO₂]₂-OTBDMS** in THF was prepared in a quartz cuvette with a transparent bottom. A laser beam of 365 nm ($P = 5.0\text{ mW}$) was directed to the solution from the bottom of the quartz cuvette and the response of the oligomer was monitored via UV-vis spectroscopy. As shown in Figure 8.8, after just 30 s of irradiation, a profound spectral change is detected with a visible light absorbing species forming at $\lambda_{\text{max}} = 587\text{ nm}$, characteristic of the merocyanine form (MC).²⁸⁷ Thus, the presence of the α -bisimine photoswitch does not interfere with the photochromism of **SP-NO₂** photoswitch at 365 nm irradiation.

We next synthesize block copolymer, aiming to have four spiropyran units in one block. For preliminary study, this number is sufficient as a large number of **SP-NO₂** sidechains may increase the likelihood of aggregation and stacking of the MC form in the solid state. Figure 8.9 shows the THF-SEC traces of precursors and the resulting photoswitchable block copolymer (**PDMS-[SP-NO₂]₄-PDMS**). Similar to the oligomer synthesized previously, the $M_{n,\text{SEC}}$ matches well with the theoretical M_n (and $M_{n,\text{NMR}}$) for this block copolymer, confirming the success chain extension. The NMR spectra for all precursors and the block copolymer are provided in Experimental part, Section 11.8.

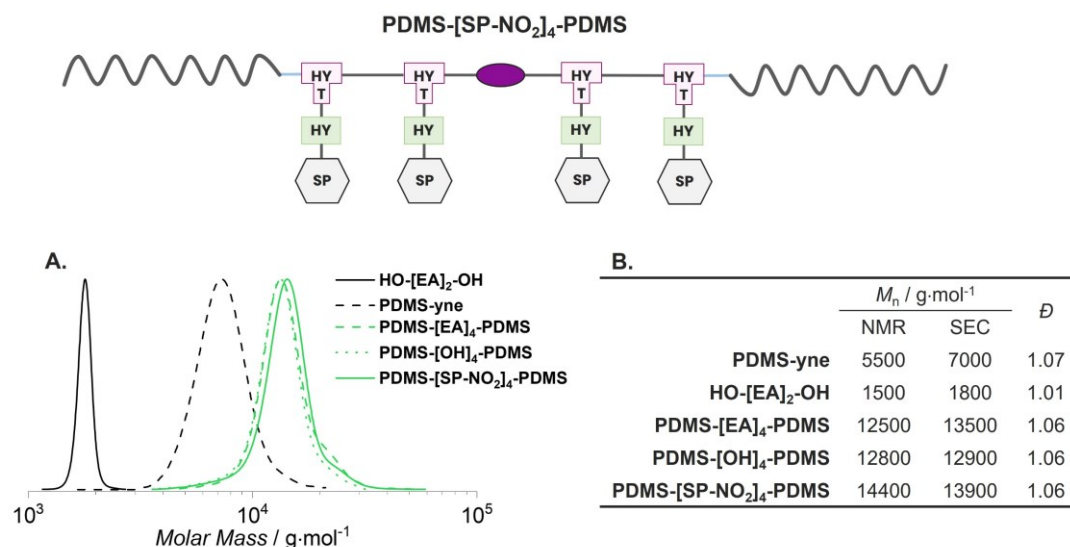


Figure 8.9. Synthesis of PDMS-[SP-NO₂]₄-PDMS block copolymer. (A) THF-SEC traces and (B) summary of molar mass determined by NMR and SEC.

8.3. Concluding remarks

In summary, we report the successful synthesis of four regio-isomeric main-chain homopolymers derived from spiropyran (**P_{SP1}**, **P_{SP2}**, **P_{SP3}**, **P_{SP4}**). We show the site-dependent photo- and halochromism of these polymers. Nevertheless, the photochromic response of these polymers is undesirably weak and hence not ideal to trigger a significant polarity switch upon irradiation. As a result, we resorted to a nitro-substituted spiropyran (**SP-NO₂**) which exhibits superior photoswitching in solution. However, the inclusion of this spiropyran as main-chain group in block copolymer is synthetically more challenging. As a compromise, a block copolymer consisting of four spiropyran units in the side chain of one block was synthesized via an efficient sequence-defined approach combined with post-synthesis modification.

Chapter 9: Nanostructures of Photoswitchable Block Copolymers: Preliminary Study^{vii}

Up to this point, the following objectives have been achieved: (1) identification of research gaps in the literature on the topic of block copolymer nanostructure manipulation (**Chapter 2**), (2) development of synthetic tools for the synthesis main-chain photoswitching macromolecules (**Chapter 3 and 4**), (3) strategies for enhancing the solid-state photoswitching (**Chapter 5**), (4) investigation of effects of polymerization techniques and dispersity on the solution photoisomerization kinetics of the covalently embedded photoswitch (**Chapter 6**), and (5) exploration of hydrazone as a potent main-chain photoswitch for the modulation of polymer properties (**Chapter 7**) , as well as inclusion of spiropyran to potentially exploit its photoswitchable polarity (**Chapter 8**). All of the five objectives listed above are essential for the final goal of photodynamic block copolymer lithography, which is all about switching the block copolymer thin-film nanostructures in-situ. Regarding block copolymer nanostructures, preliminary investigation of the bulk/ thin-film morphologies of photoswitchable block copolymers obtained so far is the sixth and final objective of this thesis and this provides information and feedback for upcoming plans and strategies.

Block copolymer morphologies can be characterized and/or observed in the bulk and/or in thin film. Bulk morphologies of BCPs are routinely identified by the Small Angle X-ray Scattering (SAXS) technique. The data obtained from SAXS show different Bragg reflection peaks for different ordered nanostructures. By comparing positions of the Bragg peaks (expressed as q/q^* , with q^* being the principal Bragg peak) in the SAXS profile with the calculated values, a specific morphology can be assigned.²⁸⁸ Typical nanostructures with positions of Bragg peaks are given in Table 9.1.²⁸⁸ On the other hand, microscopy techniques, such as TEM and AFM, are regularly employed to directly “observe” block copolymer thin film morphologies. However, in contrast to the bulk, thin-film nanostructures are sensitive to several factors, including film thickness, polymer/substrate (e.g., silicon wafer) and polymer/surface (such as air) interfacial energies. This may unfavorably lead to parallel (in-plane) orientation of the formed nanostructure or even a different morphology.²⁸⁹

^{vii} Parts of this chapter were reproduced from Thai, L. D.; Kammerer, J. A.; Golberg, D.; Mutlu, H.; Barner-Kowollik, C. *Chem* **2024**, *in press*, with permissions.

Table 9.1. Peak positions (expressed as q/q^*) of Bragg reflections for typical structures.²⁸⁸

Nanostructure	q/q^* ratio
Lamella (Lam)	1, 2, 3, 4, 5, 6...
Hexagonally Packed Cylinder (HPC)	$1, \sqrt{3}, \sqrt{4}, \sqrt{7}, \sqrt{9}, \sqrt{12}, \dots$
Body-Centered Cubic (BCC)	$1, \sqrt{2}, \sqrt{3}, \sqrt{4}, \sqrt{5}, \sqrt{6}, \dots$
Face-Centered Cubic (FCC)	$1, \sqrt{4/3}, \sqrt{8/3}, \sqrt{11/3}, \sqrt{12/3}, \sqrt{16/3}, \dots$
Gyroid (Gyr)	$1, \sqrt{4/3}, \sqrt{7/3}, \sqrt{8/3}, \sqrt{10/3}, \sqrt{11/3}, \dots$

In the following sections, SAXS and TEM are employed to examine the microphase separated structures of photoswitching block copolymer samples obtained in the previous chapters. Attempts to trigger the morphological transition are also included and discussed.

9.1. Nanostructures of bisimine-based block copolymers

We first investigated the bulk morphologies of α -bisimine-based block copolymers obtained from the sequence-defined approach reported in Chapter 4. We initially prepared SAXS samples from three BCPs having odd-number of α -bisimine photoswitch, i.e., **PDMS-[B]_n-PDMS**, $n = 3, 5, 7$. For the sake of self-assembly of block copolymers, annealing (either thermal or vapor annealing), is essential. For thermal annealing, the annealing temperature is usually 20-40 °C above the highest T_g or T_m of the constituting block. The PDMS block exhibits very low glass transition temperature, at around -120 °C as reported in the literature.²⁹⁰ From the DSC curves of the **TBDMS-[B]_n-OTBDMS** ($n = 2-7$) oligomers reported in Chapter 5 (Figure 5.6), the 7-mer sequence has the highest T_g of around 43 °C while the lowest T_g was observed for the 2-mer sequence. Therefore, it can be estimated that the T_g of the bisimine block in **PDMS-[B]_n-PDMS** series should be between 13 °C and 43 °C. Thus, prior to SAXS measurements, the **PDMS-[B]_n-PDMS** ($n = 3, 5, 7$) BCP samples were annealed at 60 °C overnight. The SAXS profiles for all three ABA triblock copolymers given in Figure 9.1 clearly show a microphase separation. Based on the position sequences of the Bragg peaks, the closest nanostructures for BCPs of 3, 5 and 7 bisimine units are most likely BCC, HCP and HCP, respectively. The microphase separation observed even for BCP with only three bisimine units is not surprising due to the strong chemical incompatibility between the PDMS block and the organic block. However, one may notice that some of the Bragg reflection peaks are absent in the SAXS patterns of **PDMS-[B]_n-PDMS**, probably due to symmetry factor.²⁸⁸

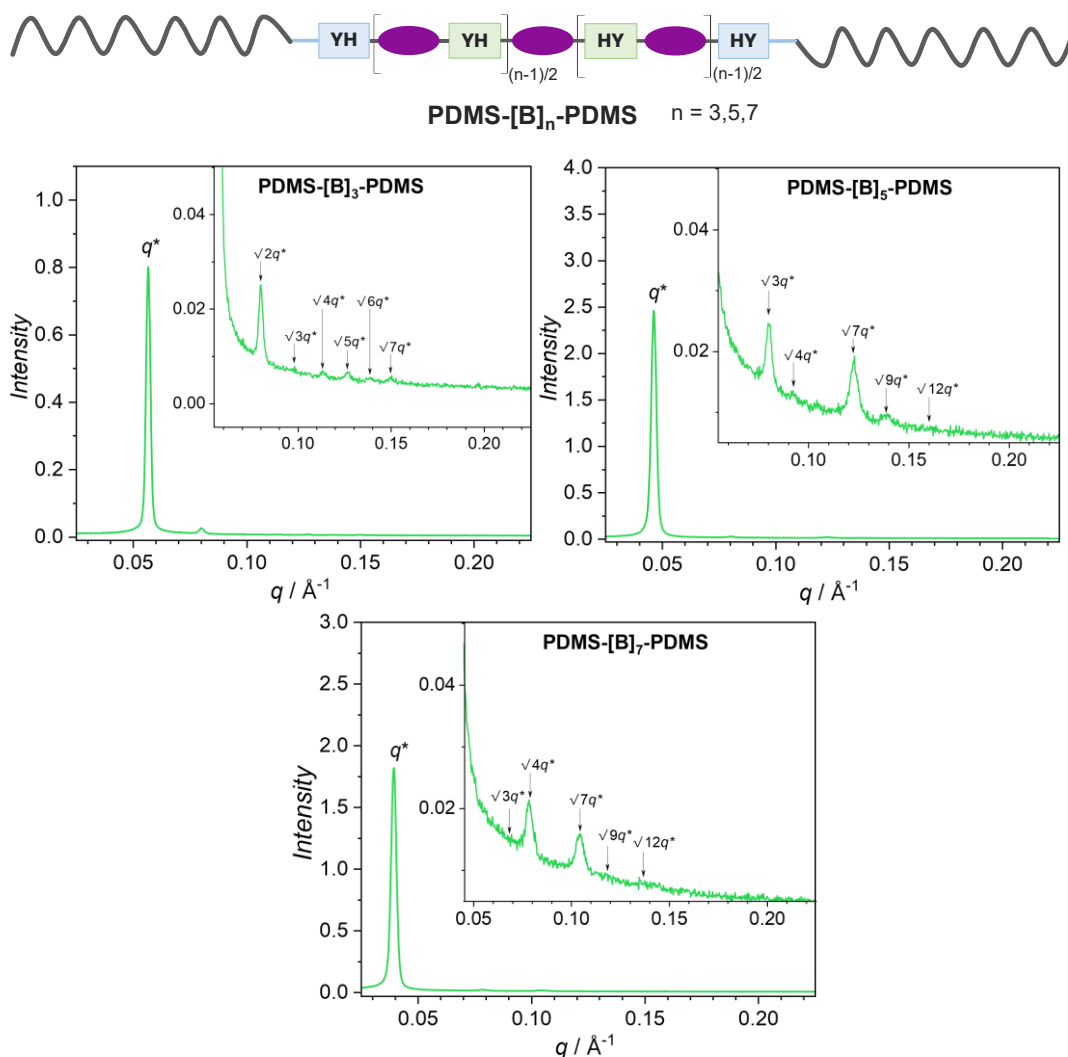


Figure 9.1. SAXS profile of bisimine-Si hybrid block copolymers, **PDMS-[B]_n-PDMS**, $n = 3, 5, 7$. Details on the structure and synthesis can be found in Chapter 4.

We further investigated the nanostructures of these three BCPs via TEM. As a preliminary study, thin films were drop-cast from the respective solution of **PDMS-[B]_n-PDMS** ($n = 3, 5, 7$) in chloroform onto carbon substrates. Due to the high electron density contrast between silicon- and carbon-based blocks, it does not require chemical staining prior to TEM imaging. This is especially critical for in-situ light-induced morphological transition investigated by TEM in the later stage of the project. TEM images of the photoswitchable block copolymers show ordered nanostructures as previously confirmed by SAXS (Figure S9.1-S9.6, Experimental part, Section 11.9). Nevertheless, due to the large difference in surface tension between the PDMS and α -bisimine-based blocks coupled with film thickness variations, different orientations and morphologies at different regions of the BCP thin films are unavoidable, making it challenging to determine the exact morphology. For instance, the TEM image of **PDMS-[B]₅-PDMS** shows a lamellar morphology while the SAXS result points to a cylindrical morphology (Figure 9.2). The apparent lamella observed here may be in fact resulted from the parallel orientation of the cylinders. Despite this, it is still possible to estimate the domain spacing (d) from both TEM and SAXS. Accordingly, the d values for **PBDMs-[B]_n-PDMS** ($n =$

3, 5, 7) are 12.4 nm, 16.3 nm, 18.9 nm, respectively. The results from SAXS are slightly smaller (10% - 16% difference): 11.1 nm (for $n = 3$), 13.6 nm (for $n = 5$) and 15.9 nm (for $n = 7$). The TEM thin-film morphologies for the even-numbered BCPs can be found in Experimental part, Section 11.9.

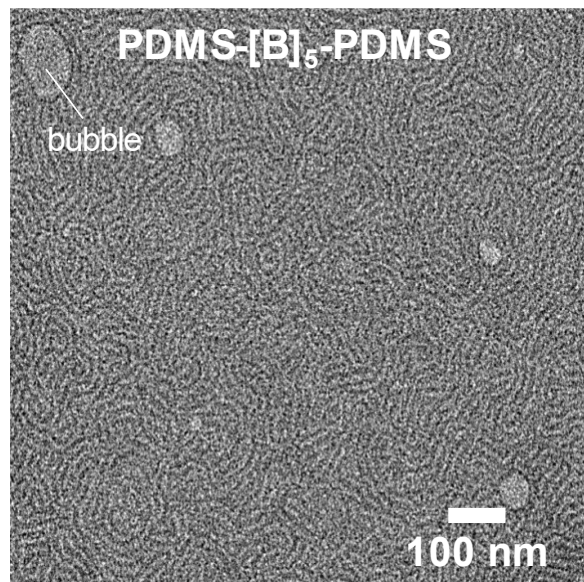


Figure 9.2. Zoomed-in TEM image of **PDMS-[B]₅-PDMS** thin film on carbon substrate. The observed nanostructure can be lamella or out-of-plane cylinders. Full TEM micrographs of other bisimine-based block copolymers are provided in Experimental part, Section 9.5.2, Figure S9.1-S9.6.

9.2. Nanostructures of hydrazone-based block copolymer

Subsequently, we studied the bulk morphology of hydrazone-based block copolymer, **PDMS-[H]₄-PDMS**, reported in chapter 7. It should be reiterated that this triblock copolymer is a mixture of two different block copolymers, both of which contain the photoresponsive hydrazone block and the PDMS block. The hydrazone block features a negative T_g at approximately -9.4 °C (determined via DSC measurement of the **HO-[H]₄-OH** oligomer, Figure S9.9, Experimental part, Section 11.9). Since both blocks (PDMS and hydrazone block) have glass transition temperature much lower than room temperature, the SAXS sample was left at room temperature prior to SAXS measurement. The SAXS profile of this block copolymer shows a strong principal peak (q^*) and a small but sharp reflection peak at $\sqrt{3}q^*$. Based on Table 9.1, possible morphologies are hexagonally packed cylinder (HPC) and body-centered cubic (BCC). The lack of other order peaks makes it challenging to assign the exact morphology. Since it is a blend of two block copolymers, a different morphology other than HPC and BCC may also be the case.

Compared to α -bisimine and spiropyran photoswitches, the hydrazone photoswitch has extremely long thermal half-life, from hundreds of years to thousands of years at room temperature.¹¹⁷ Therefore, we take this advantage to test the possibility of morphological change of the **PDMS-[H]₄-PDMS** block copolymer. For this, the same solution of the pristine polymer in dichloromethane was irradiated with a blue LED ($\lambda_{\text{max}} = 400 \text{ nm}$) to trigger the

forward photoisomerization. Upon reaching desired conversion (> 95%), part of the solution was withdrawn for SAXS sample preparation. The irradiated solution was subsequently irradiated with 365-nm LED to induce the back photoisomerization (~ 50% conversion), and another SAXS sample was prepared (NMR spectra shown in Figure S9.8, Experimental part, Section 11.9). Results in Figure 9.3 show the disappearance of the peak at $\sqrt{3}q^*$ while a weak and broad reflection at roughly $\sqrt{6}q^*$ emerges in the SAXS profile of the 400-nm irradiated sample. This peak becomes even weaker in the post-365nm irradiated sample (Figure 9.3, bottom). Although it is not conclusive of a morphological switching, it is promising to further investigate this BCP via TEM, which is in progress. However, similar to the α -bisimine based block copolymer, non-neutral interaction of the PDMS and photoswitchable block with the interfaces is highly likely and this can cause unreproducible and unreliable results in terms of morphologies.

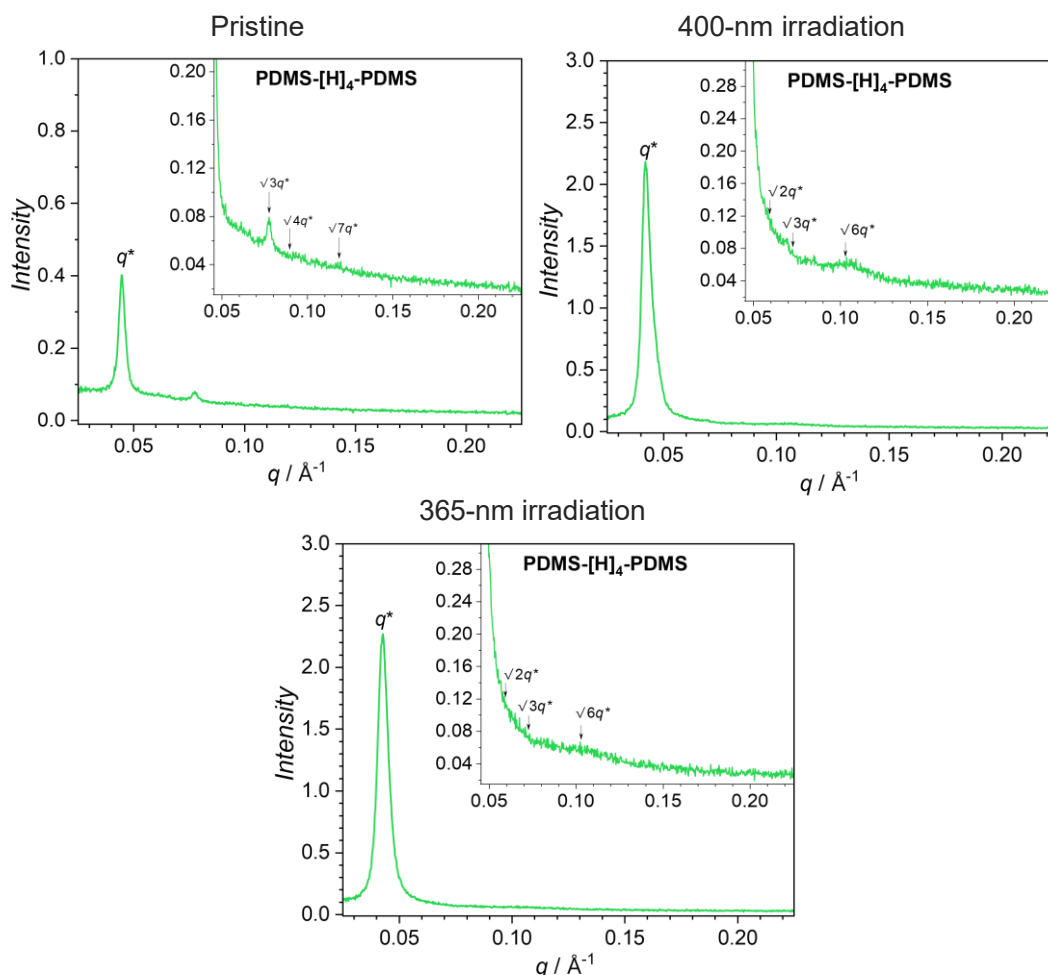


Figure 9.3. SAXS profiles of **PDMS-[H]₄-PDMS** block copolymer before and after irradiation. The SAXS samples were prepared from the same stock solution which was irradiated with LED lights: $\lambda_{\text{max}} = 400 \text{ nm}$ for forward photoisomerization and $\lambda_{\text{max}} = 365 \text{ nm}$ for back photoisomerization. Details on the synthesis and structure of the block copolymer were reported in chapter 7.

In order to eliminate the issues associated with interfacial energy, we envisage the chemical modification of the photoswitchable block to graft short, fluorinated side chains via thiol-

Michael click reaction between the main-chain (ether) acrylate bonds with commercially available fluorinated thiols. For hybrid block copolymers, the installation of fluorinated repeating units in the organic block helps lower its surface tension, balancing the interfacial energy between inorganic and organic blocks.^{208,291-293} As a result, perpendicular thin-film nanostructures can be achieved. We are also aware that such post-polymerization modification approach can alter the initial bulk and thin-film morphologies of the studied BCPs. However, in the end we are interested in the morphological switching induced by the photoisomerization of the organic block.

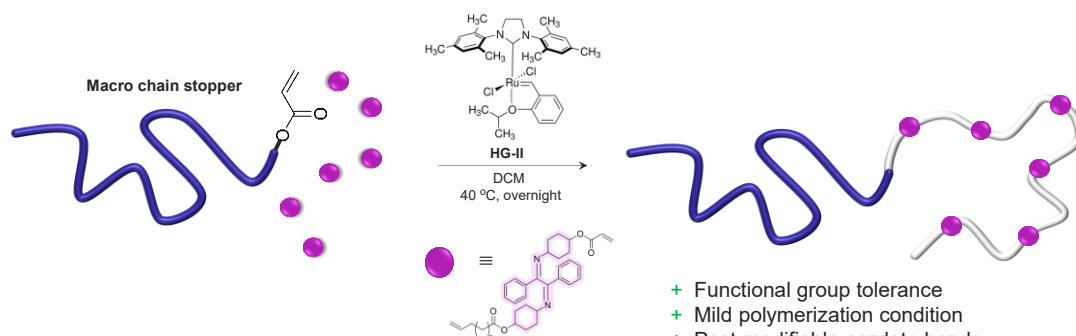
9.3. Concluding remarks

Herein, we have investigated the bulk and/or thin-film morphologies of α -bisimine and hydrazone-based block copolymers via SAXS and TEM. Although the morphological investigation is just in the starting phase, the results reported here are promising in that microphase separation is observed for these block copolymers. The current issue we are facing is the unmatched surface energy of the Si-based block and the photoswitchable block, leading to out-of-plane orientation of thin-film morphology. Nevertheless, we believe such an issue is manageable via chemical modification with fluorinated side chains in the future work. The preliminary study reported here lays the foundation towards dynamic block copolymer lithography – our final goal.

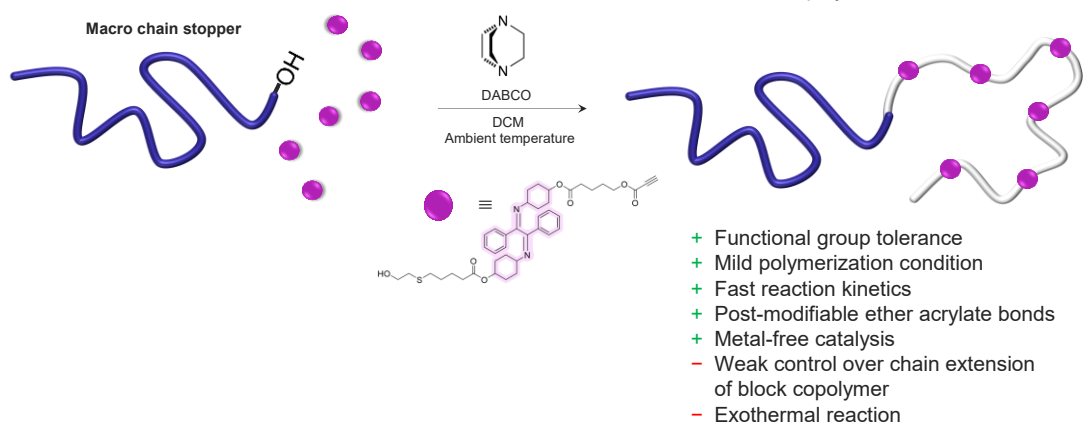
Chapter 10: Conclusions and Outlook

10.1. Conclusions

Head-to-tail Acyclic Diene METathesis (ADMET) polymerization



Head-to-tail hydroxyl-yne click polymerization



- + Functional group tolerance
- + Mild polymerization condition
- + Post-modifiable acrylate bonds
- Transition metal-based catalysis
- Weak control over chain extension of block copolymer

- + Functional group tolerance
- + Mild polymerization condition
- + Fast reaction kinetics
- + Post-modifiable ether acrylate bonds
- + Metal-free catalysis
- Weak control over chain extension of block copolymer
- Exothermal reaction

Figure 10.1. Synthesis of main-chain block copolymer via head-to-tail ADMET polymerization and hydroxyl-yne click polymerization.

In summary, we have had success in synthesizing homopolymers and block copolymers featuring (main-chain) photoswitches, namely α -bisimine, hydrazone and spiropyran. As a starting point, head-to-tail Acyclic Diene METathesis (ADMET) polymerization was employed to prepare main-chain photoswitchable homopolymers and to some extent block copolymers (Figure 10.1). The excellent chemical compatibility of this technique with all three photoswitches is greatly promising for the incorporation of other photoswitches as well as stimuli-responsive groups into the polymer backbone (**Chapters 3, 7, 8**). The main-chain design is emphasized owing to the potentially larger conformational changes upon *E/Z*-photoisomerization, which in turn can tremendously impact the solution and solid-state property.

In addition, we have also employed hydroxyl-yne click chemistry to synthesize photoswitchable main-chain polymers based on α -bisimine (**Chapter 3**). This polymerization

technique is desirable due to its extremely fast reaction kinetics as well as metal-free catalysis, while displaying good tolerance towards other functional groups, such as acrylates, olefins and unactivated alkyne (**Chapter 4**). However, the synthesis of block copolymer via this route is also challenging due to incomplete chain extension, similar to the case of head-to-tail ADMET polymerization (Figure 10.1).

Sequence-defined Approach for Block Copolymer Synthesis

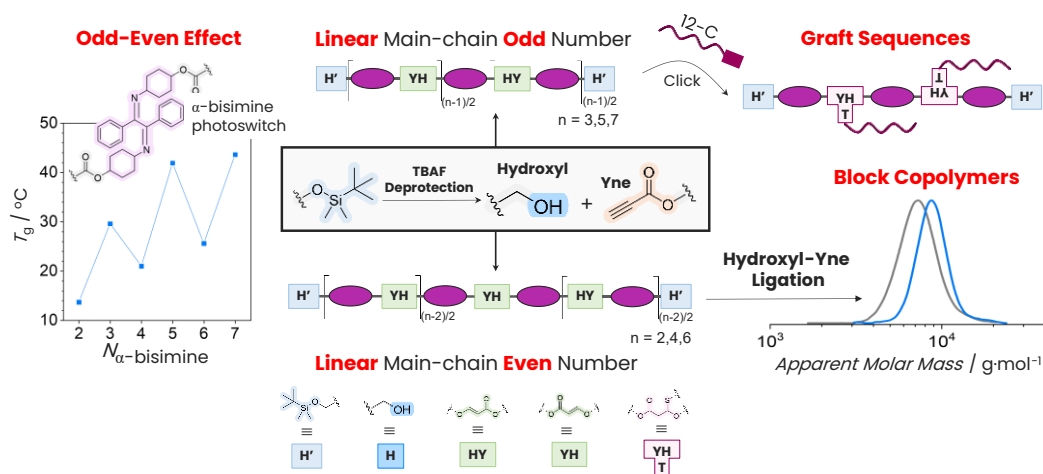


Figure 10.2. The sequence-defined strategy to synthesize main-chain α -bisimine oligomers and block copolymers. This approach relies on the hydroxyl-yne click and TBAF-deprotection chemistry. For hydrazone, the TBAF-deprotection step causes undesirable isomerization of the photoswitch. As a compromise, cross-metathesis reaction was used instead, in combination with hydroxyl-yne click reaction for hydrazone main-chain oligomers and block copolymer synthesis.

With the aim of photodynamic block copolymer lithography in mind, well-defined (main-chain) photoswitchable block copolymers are desirable. Therefore, we subsequently developed a sequence-defined strategy to synthesize such block copolymers via the combination of hydroxyl-yne click reaction and TBAF-deprotection chemistry (**Chapter 4**) (Figure 10.2). While this approach is applicable to α -bisimine and spiropyran, the TBAF-deprotection step caused unexpected isomerization of the hydrazone photoswitch. Alternatively, we combined hydroxyl-yne and metathesis chemistries to prepare main-chain hydrazone oligomers and block copolymer with acceptable results (**Chapter 7**).

We have also shown that the solution photoisomerization kinetics of α -bisimine and hydrazone-based polymers are not influenced by the polymerization techniques employed (**Chapter 6**), creating key flexibility in the choice of chemistries and polymerization techniques. However, the efficiency is often significantly diminished in the solid state, which is not ideal for solid-state applications, including photo-induced transition of thin-film and bulk morphology. We have next demonstrated an efficient strategy to lower the T_g of the photoswitchable block/homopolymer, greatly enhancing the photoisomerization performance in the solid state of main-chain α -bisimine photoswitch (**Chapter 5**) (Figure 10.3). This strategy is feasible on account of the thiol-Michael click reaction between the internal (ether) acrylates and the commercially available alkyl thiol. A lower T_g means better chain flexibility and less

intermolecular stacking of the embedded photoswitches, and thus benefits the solid-state photoswitching.

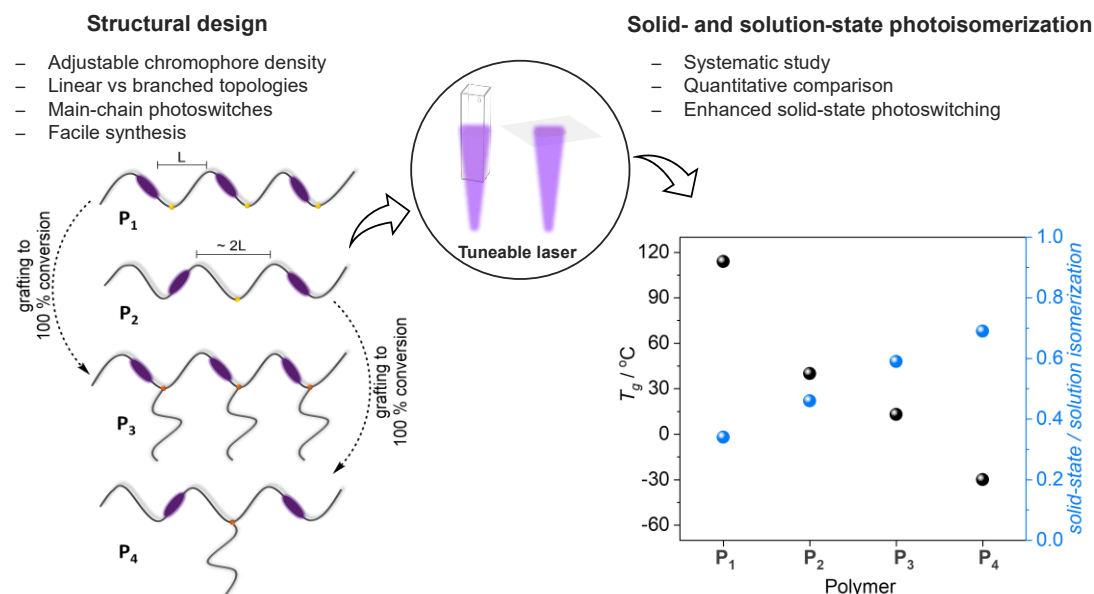


Figure 10.3. The strategy to enhance solid-state photoswitching efficiency.

For hydrazone-based main-chain system, changes in the hydrodynamic volume (as expressed via change in molar mass) and glass transition temperature were observed (**Chapter 7**) (Figure 10.4). The shift in size of the polymer coil in solution was a promising sign for a change in the volume fraction of the hydrazone-based block in the thin-film or bulk nanostructure. Compared to α -bisimine photoswitch, hydrazone is more advantageous taking into account the superior thermal stability of the isomer upon switching as well as its visible light-trigger photoisomerization. As there is no profound alteration of the polarity, the main-chain feature is a prerequisite for hydrazone and α -bisimine systems.

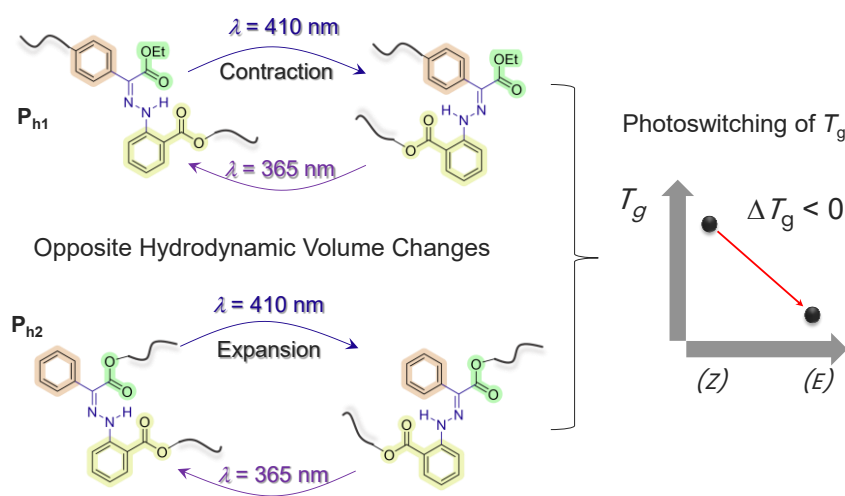


Figure 10.4. Main-chain hydrazone-based polymers showed photomanipulatable hydrodynamic volume and glass transition temperature. In the context of block copolymer nanostructure, such changes in solution and solid-state properties are indicative of possible alternation of the volume fraction of the photoswitchable block upon irradiation.

For spiropyran-based polymers, the photoswitchable polarity is the key attractive feature. Therefore, either the main-chain or side-chain design does not significantly affect the polarity change. We have learned that the efficiency of photo-triggered ring-opening and isomerization of spiropyrans is strongly affected by the substituents on the benzopyran moiety. Thus, nitro-substituted spiropyrans (**SP-NO₂**) are highly efficient in terms of photochromism. Therefore, we integrated this spiropyran scaffold as pendant groups to a block copolymer (**PDMS-[SP-NO₂]₄-PDMS**), installed via hydroxy-yne click chemistry, thiol-Michael ligation and TBAF-deprotection (**Chapter 8**) (Figure 10.5).

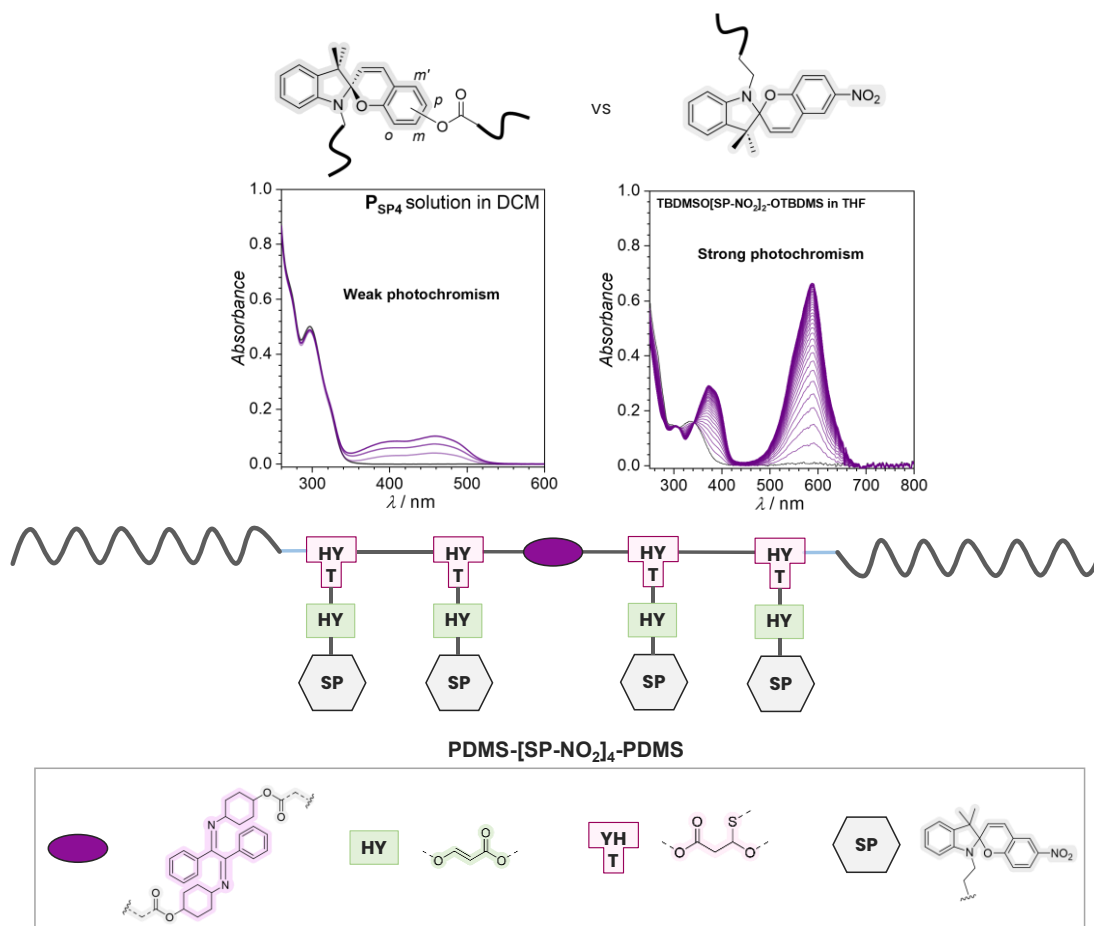


Figure 10.5. Synthesis of spiropyran-based polymers. The photochromism of spiropyrans is generally strongly dependent on the identity of the substituents on the aromatic moieties. We learned that nitro-substituted spiropyrans are more efficient in terms of photochromism. As the dramatic polarity change is a more attractive feature of spiropyrans, the design of block copolymers bearing spiropyrans as pendant groups is synthetically more convenient.

With the block copolymers synthesized via the sequence-defined approach in hands, we carried out a preliminary study to investigate their bulk and/or thin-film morphologies (**Chapter 9**). Due to the strong segregation of the Si-based block, clear nanostructures were observed even for block copolymers with only three α -bisimine units. Based on the SAXS results, there is a morphological difference between the block copolymer with 3 and 5 units of α -bisimine, which is promising sign for a transition of morphology upon photoswitching of α -bisimine. However, the orientation of thin-film morphologies of these hybrid block copolymers are strongly affected by the interfacial energy between the Si-based block and α -bisimine block,

which was indeed observed in our case. Therefore, this hurdle has to be overcome before attempting photoswitching of thin-film morphologies. Alternatively, we attempted to switch the bulk morphology of a hydrazone-based block copolymer, exploiting the long thermal half-life of the hydrazone isomer. While not assessed via an in-situ or ex-situ study, the SAXS profiles of the pristine and irradiated samples are slightly different from each other. Further investigation are being conducted in this regard.

In conclusion, the current thesis establishes a robust synthesis roadmap to acquire photoswitching polymers and block copolymers on three examples of photoswitches – α -bisimine, hydrazone and spiropyran. For photoswitches of which a potentially large geometrical change upon photoswitching is the dominant feature, e.g., hydrazone and α -bisimine, the main-chain design is critically important to maximize the potential for photo-modulation of material properties for advanced applications, including photodynamic block copolymer lithography.

10.2. Outlook

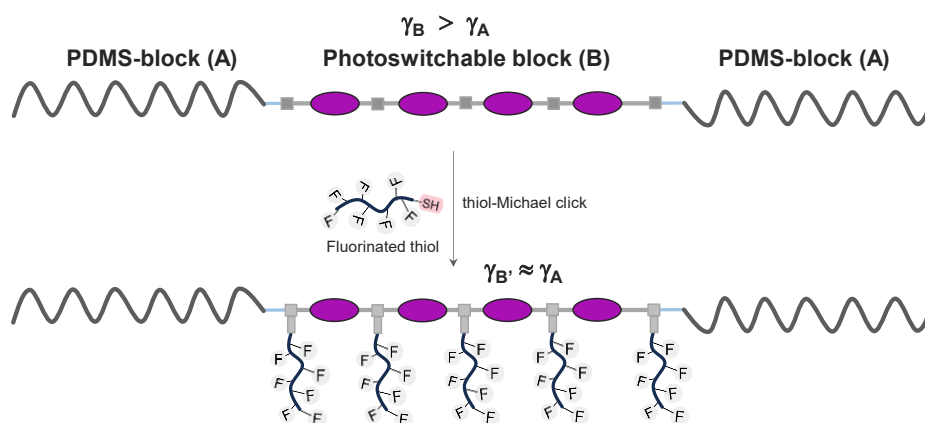


Figure 10.6. For Si-based block copolymers, installing fluorinated groups into the organic block has been shown to be beneficial for the orientation of block copolymer thin-film nanostructures, especially lamella and cylinders.²⁰² For the photoswitchable hybrid block copolymers obtained in this thesis, post-modification is a facile and efficient approach to decorate fluorinated side chains to the photoswitchable block, balancing the surface tension (γ) between Si-based and the organic blocks.

Aiming towards the goal of photodynamic block copolymer lithography, the following plans will be implemented in the near future. First, we aim to address the interfacial energy issue in PDMS-based block copolymers. We plan to perform post-synthesis modification of the pristine main-chain photoswitchable BCPs via thiol-Michael reaction with fluorinated alkyl thiol (Figure 10.6). The gap in surface energy between the PDMS block and the organic block is expected to be reduced owing to the hydrophobic nature of the fluorinated groups, thus counteracting the preferential interaction of one block with the interfaces.²⁰² We are aware that such modification may alter the block incompatibility (i.e., Flory-Huggins interaction parameter), which is, however, not detrimental to our final goal. Furthermore, the resulting glass transition temperatures of the post-modified block copolymers likely become lower or even negative, beneficial for solid-state photoswitching.

The second plan is to build a phase diagram of the hybrid ABA triblock copolymers based on α -bisimine and PDMS. With the synthetic method established here, it is facile to extend the length of the photoswitchable block and thus increase the volume fraction as well as the degree of polymerization (or length) of this organic block. We plan to employ SAXS to build the phase diagram. Furthermore, via the thiol-Michael reaction, the block copolymers can readily be modified with a fluorinated alkyl thiol chosen from the first plan mentioned above. Hence, a second phase diagram can be built. The phase diagram assists in the selection of a block copolymer of which the equilibrium nanostructure is close to the boundary of another phase. As a result, there is a higher chance to induce a phase transition upon irradiation of the block copolymer.

We also envisage the same plans for hydrazone-based main-chain block copolymers. However, it is important to find an alternative method to prepare such polymers in a more precise fashion. Instead of cross-metathesis reaction, other potential chemistries, such as alkyne-azide click reaction, may be considered in combination with hydroxyl-yne click reaction.

The next plan involves the utilization of the nitro-spiropyran-based block copolymers (**PDMS-[SP-NO₂]₄-PDMS**) reported in chapter 8. We are convinced that the photoswitchable polarity of this photoswitch is highly effective to manipulate the Flory-Huggins interaction parameter. However, due to the fast kinetics of the reversion reaction, it is more feasible to perform in-situ irradiation of the block copolymer film. To observe the morphological transition, we plan to employ Grazing-Incidence Small Angle X-ray Scattering (GI-SAXS). This technique allows the use of relatively thinner films compared to the conventional SAXS technique, allowing for a better penetration of the light beam into the sample. Depending on the obtained results, further chain extension of the spiropyran-based block is necessary.

We strongly believe that the plans proposed here are realistic and viable and the successful implementation of these plans makes the final goal of photodynamic block copolymer lithography within reach.

Chapter 11: Experimental Part

11.1. Instruments and Characterization

11.1.1. Nuclear Magnetic Resonance Spectroscopy (NMR)

Nuclear Magnetic Resonance (NMR) spectroscopy. ^1H and ^{13}C NMR spectra were recorded on either one of the following NMR spectrometers: a Bruker System AM 500 spectrometer, equipped with a PABBO BB-Probe or (5 mm), (^1H : 500 MHz, ^{13}C : 126 MHz), *Bruker* System 600 Ascend LH, equipped with a BBO-Probe (5 mm) with z-gradient (^1H : 600.13 MHz, ^{13}C 150.90 MHz), a *Bruker* Ultrashield 400, equipped with a QNP-Probe (5 mm) with z-gradient (^1H : 400 MHz, ^{13}C 100.66 MHz). The δ -scale was calibrated to the respective resonance of the solvent in which the sample was recorded.

11.1.2. Diffusion Ordered Spectroscopy

A ^1H -based Diffusion Ordered Spectroscopy (DOSY) NMR experiment was performed at 28 °C on a Bruker 400 Avance III HD spectrometer equipped with a BBO probe (5mm) with z-gradients (^1H : 400.16 MHz). The sample was prepared in CDCl_3 and the pulse sequence employed a longitudinal eddy current delay (LED) using bipolar gradients (Bruker ledbp2s) to compensate for eddy currents. The diffusion gradient length ($\delta/2$; p30) and diffusion delay (Δ ; d20) were optimized at 2000 μs and 0.15 s respectively. Gradient strength was linearly incremented from 2% at 0.963 Gcm^{-1} to 95% at 45.743 Gcm^{-1} in 24 steps. The pseudo-2d data was processed with TopSpin 3.6.5 and Dynamics Center 2.8.4). After Fourier transformation of the 1D spectra, the signal decay with respect to gradient strength G was fitted to:

$$f(G) = I_0 * e^{-D * G^2 * \gamma^2 * \delta^2 * (\Delta - \frac{\delta}{3})} * 10^4 \quad \text{Eq 11.1}$$

with the gyromagnetic ratio γ and the full signal intensity I_0 .

11.1.3. Flash column chromatography

Flash column chromatography was performed on an Interchim XS420+ flash chromatography system consisting of a SP-in-line filter 20- μm , an UV-VIS detector (200-800 nm) and a SofTA Model 400 ELSD (55 °C drift tube temperature, 25 °C spray chamber temperature, filter 5, EDR gain mode) connected via a flow splitter (Interchim Split ELSD F04590). The separations were performed using a Interchim dry load column (liquid injection) and a Interchim Puriflash Silica HP 30 μm column.

11.1.4. Size Exclusion Chromatography (SEC)

THF-SEC: The SEC measurements were conducted on a PSS SECurity² system consisting of a PSS SECurity Degasser, PSS SECurity TCC6000 Column Oven (35 °C), PSS SDV Column Set (8 x 150 mm 5 µm Precolumn, 8 x 300 mm 5 µm Analytical Columns, 100000 Å, 1000 Å and 100 Å) and an Agilent 1260 Infinity Isocratic Pump, Agilent 1260 Infinity Standard Autosampler, Agilent 1260 Infinity Diode Array and Multiple Wavelength Detector (A: 254 nm, B: 360 nm), Agilent 1260 Infinity Refractive Index Detector (35 °C). HPLC grade THF, stabilized with BHT, is used as eluent at a flow rate of 1 mL·min⁻¹. Narrow disperse linear poly(styrene) (M_n : 266 g·mol⁻¹ to 2.52·10⁶ g·mol⁻¹) and poly(methyl methacrylate) (M_n : 202 g·mol⁻¹ to 2.2·10⁶ g·mol⁻¹) standards (PSS ReadyCal) were used as calibrants. All samples were passed over 0.22 µm PTFE membrane filters. Molecular weight and dispersity analysis was performed in PSS WinGPC UniChrom software (version 8.2).

DMAc-SEC: The SEC measurements were conducted on a PSS SECurity² system consisting of a PSS SECurity Degasser, PSS SECurity TCC6000 Column Oven (60 °C), PSS GRAM Column Set (8x150 mm 10 µm Precolumn, 8x300 mm 10 µm Analytical Columns, 1000 Å, 1000 Å and 30 Å) and an Agilent 1260 Infinity Isocratic Pump, Agilent 1260 Infinity Standard Autosampler, Agilent 1260 Infinity Diode Array and Multiple Wavelength Detector (A: 254 nm, B: 360 nm), Agilent 1260 Infinity Refractive Index Detector (35 °C). HPLC grade DMAc, 0.01 M LiBr, is used as eluent at a flow rate of 1 mL·min⁻¹. Narrow disperse PS (M_n : 266 g·mol⁻¹ to 2.52·10⁶ g·mol⁻¹) and PMMA (M_n : 202 g·mol⁻¹ to 2.2·10⁶ g·mol⁻¹) standards (PSS ReadyCal) were used as calibrants. All samples were passed over 0.22 µm PTFE membrane filters. Molecular weight and dispersity analysis was performed in PSS WinGPC UniChrom software (version 8.2).

11.1.5. Liquid Chromatography – Mass Spectrometry (LC-MS)

LC-MS measurements were performed on an UltiMate 3000 UHPLC System (Dionex, Sunnyvale, CA, USA) consisting of a pump (LPG 3400SZ), autosampler (WPS 3000TSL) and a temperature-controlled column compartment (TCC 3000). Separation was performed on a C₁₈ HPLC column (Phenomenex Luna 5µm, 100 Å, 250 × 2.0 mm) operating at 40 °C. Water (containing 5 mmol·L⁻¹ ammonium acetate) and acetonitrile were used as eluents. A gradient of acetonitrile: H₂O, 5:95 to 100:0 (v/v) in 7 min at a flow rate of 0.40 mL·min⁻¹ was applied. The flow was split in a 9:1 ratio, where 90% of the eluent was directed through a DAD UV-detector (VWD 3400, Dionex) and 10% was infused into the electrospray source. Spectra were recorded on an LTQ Orbitrap Elite mass spectrometer (Thermo Fisher Scientific, San Jose, CA, USA) equipped with a HESI II probe. The instrument was calibrated in the m/z range 74–1822 using premixed calibration solutions (Thermo Scientific). A constant spray voltage of 3.5 kV, a dimensionless sheath gas, and a dimensionless auxiliary gas flow rate of 5 and 2 were applied, respectively. The capillary temperature was set to 300 °C, the S-lens RF level was set to 68, and the aux gas heater temperature was set to 100 °C.

11.1.6. SEC-MS

SEC-ESI-MS: Spectra were recorded on a Q Exactive Plus (Orbitrap) mass spectrometer (Thermo Fisher Scientific, San Jose, CA, USA) equipped with an HESI II probe. The instrument was calibrated in the m/z range 74-1822 using premixed calibration solutions (Thermo Scientific) and for the high mass mode in the m/z range of 600-8000 using ammonium hexafluorophosphate solution. A constant spray voltage of 3.5 kV, a dimensionless sheath gas flow rate of 10 and a dimensionless auxiliary gas flow rate 0 were applied, respectively. The capillary temperature was set to 320 °C, the S-lens RF level was set to 150, and the aux gas heater temperature was set to 125 °C. The Q Exactive was coupled to an UltiMate 3000 UHPLC System (Dionex, Sunnyvale, CA, USA) consisting of a pump (LPG 3400SD), autosampler (WPS 3000TSL), and a temperature-controlled column department (TCC 3000). Separation was performed on three mixed bead size exclusion chromatography columns (PSS, SDV micro columns 3 μ m 1000Å 4.6 x 250mm) with a precolumn (SDV micro precolumn 3 μ m 4.6x30 mm) operating at 30 °C. THF at a flow rate of 0.30 mL·min⁻¹ was used as eluent. The mass spectrometer was coupled to the column in parallel to an UV detector (VWD 3400, Dionex), and a RI-detector (RefractoMax520, ERC, Japan) in a setup described earlier.²⁹⁴ 0.27 mL·min⁻¹ of the eluent were directed through the UV and RI-detector and 30 μ L·min⁻¹ were infused into the electrospray source after post-column addition of a 50 μ M solution of sodium iodide in methanol at 20 μ L·min⁻¹ by a micro-flow HPLC syringe pump (Teledyne ISCO, Model 100DM). A 100 μ L aliquot of a polymer solution with a concentration of 2 mg·mL⁻¹ was injected into the SEC system.

11.1.7. UV-vis spectroscopy

UV-vis spectra were recorded on a Shimadzu UV-2700 spectrophotometer equipped with a CPS-100 electronic temperature control cell positioner. Solution samples were prepared in suitable solvents in quartz cuvettes (10 x 10 mm) (Hellma Analytics high precision cell cuvettes) at 20 °C or 25 °C. For solution study where THF was used as the solvent, THF was purified by passing through over aluminium oxide basic prior to sample preparation.

11.1.8. Differential Scanning Calorimetry (DSC)

Most **DSC measurements** were conducted using a Netzsch DSC 204 F1 Phoenix. Samples were sealed into Netzsch Al sample capsules. 3 cycles of heating/cooling ramps at scanning speed of either 20 °C·min⁻¹ or 10 °C·min⁻¹ were used. A nitrogen sample purge flow of 20 mL·min⁻¹ was employed. Glass transition temperatures were determined from the 2nd heating ramp. The data was analyzed using the TA Instruments Universal Analysis 2000 software (version 4.2E).

For DSC results reported in chapter 7 for hydrazone-based polymers, DSC analysis was performed on a Mettler Toledo STARe DSC system. Samples were heated under a N₂ flow

(30 mL·min⁻¹) from -100 °C to 90 °C at 20 °C ·min⁻¹ twice, and the glass transition temperature, i.e., T_g , was reported from the second heating scan.

11.1.9. Thermogravimetric Analysis (TGA)

Thermogravimetric Analysis (TGA) was performed on a STA 449 F3 Jupiter from Netzsch. Samples were analyzed in aluminium oxide pans at a heating rate of 20 °C·min⁻¹ from 30 °C to 800 °C under nitrogen atmosphere. The data was analysed using TA Instruments Universal Analysis 2000 software (version 4.2E).

11.1.10. Dynamic Light Scattering

Dynamic Light Scattering (DLS) measurements were performed on a Malvern Zetasizer Nano Z at 25 °C. A quartz cuvette (10 x 2 mm) was used for the experiment in DCM solvent.

11.1.11. Small-Angle X-ray Scattering (SAXS)

Small-Angle X-ray Scattering (SAXS) measurements were performed on a Xenocs Xeuss 2.0 system. Scattering data was collected using a Cu-K α ($\lambda = 1.542 \text{ \AA}$) microfocused tube source operating at 50 kV and 0.6 mA with a beam size of approximately 0.5 x 0.5 mm. SAXS data was collected on a Pilatus 1M detector at a sample-to-detector distance of 2501mm to give a q range of approximately 0.004 – 0.244 \AA^{-1} , where $q = 4\pi\sin\theta/\lambda$ is the magnitude of the scattering vector, 2θ is the scattering angle and λ is the wavelength of the incident beam. The sample to detector distances at the two detector distances were determined using the known lattice spacings in the scattering from silver behenate. Bulk samples were mounted on Kapton tape and were measured under vacuum. The measured scattering data was reduced to 1D scattering profiles by radial averaging.

11.1.12. Transmission Electron Microscopy (TEM)

Transmission electron microscopy (TEM) samples were prepared by dissolving the triblock copolymers (**PDMS-[B]_n-PDMS**, $n = 2-7$) with a concentration of 1 mg·mL⁻¹ in chloroform and depositing 2 μL of these solutions onto a carbon film TEM grid (4-6 nm film thickness). After drying in air, the samples were kept in vacuum for a few hours before imaging. Imaging was performed at 200 kV on a double aberration corrected JEOL NeoARM TEM equipped with a Gatan OneView Camera. To ensure comparability of the extracted periodicity, all micrographs were acquired at the same illumination angle and a defocus of 6 μm . This defocus enhanced the contrast of the phase separated structures and kept the spatial frequencies of the periodicity of all structures within the information limit. For the extraction of the periodicity, the images were binned by a factor of 2 in z and y direction and the 2D power spectra of the structures were calculated and radially averaged with a custom script²⁹⁵ that also corrected for slight distortions of the 2D power spectra, presumably due to the aberration correction. The periodicities of the structures were extracted from the peak maxima of the radial averaged power spectrum.

11.1.13. Laser experiments

All **laser experiments** were conducted using the apparatus shown in Figure S5.1.²³⁰. The light source was an OpoTek Opolette 355 OPO, producing 7 ns, 20 Hz pulses with a flattop spatial profile. The output beam was initially passed through a beam expander (-50 mm and 100 mm lens combination) to ensure it is sufficiently large to uniformly irradiate the entire sample volume. The beam then passes through an electronic shutter and directed upwards using a UV silica right angle prism. Finally, the beam enters the sample, suspended in a UV-vis holder (with a transparent bottom) or a glass vial, from below. The laser energy deposited into the sample was measured above the aluminum block/ UV-vis holder before and after experiments using a Coherent EnergyMax thermopile sensor (J-25MB-LE) to account for any power fluctuations during irradiation.

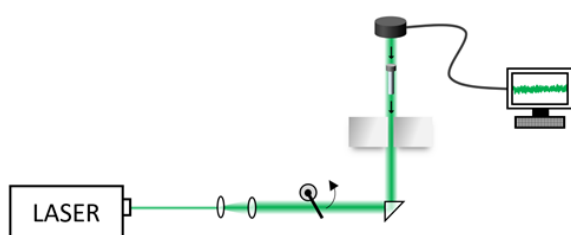


Figure S11.1. Schematic diagram of apparatus used for laser experiments.

Precise photon numbers were determined from the laser pulse energy using the following relation:

$$N_p = \frac{P\lambda t}{hc} \quad \text{Eq 11.2}$$

Where:

P (W): actual laser power passing through the substrate. $P = E_{\text{pulse}} f_{\text{rep}} T_{\lambda}$, where E_{pulse} is the pulse energy recorded above the sample holder (without sample container), f_{rep} is the laser repetition rate (20 Hz), and T_{λ} is the wavelength dependent transmission of the sample container (e.g., UV-vis cuvette or glass vial). For quartz cuvette used in the current thesis (Hellma Analytics), the transmission is 100%. For non-quartz sample containers, the T_{λ} value was first determined.

λ (m): wavelength of the incident radiation.

t (s): irradiation time.

h : Planck's constant ($6.626 \cdot 10^{-34}$ J·s).

c : speed of light ($\sim 3.0 \cdot 10^8$ m·s⁻¹).

11.1.14. LED emission spectra

LED emission spectra were recorded using an Ocean Insight Flame-T-UV-Vis spectrometer, with an active range of 200-850 nm and an integration time of 10 ms. LED output energies were recorded using a Thorlabs S401C thermopile sensor, with an active area of 100 mm² and a wavelength range of 190 nm – 20 μ m, connected to a Thorlabs PM400 energy meter console. The emitted power from each LED was measured for 60 seconds at a fixed distance from the sensor, after which the mean and standard deviation of the emission could be determined. LEDs were cooled during measurement to minimize any thermal effects on the emission power or sensor performance.

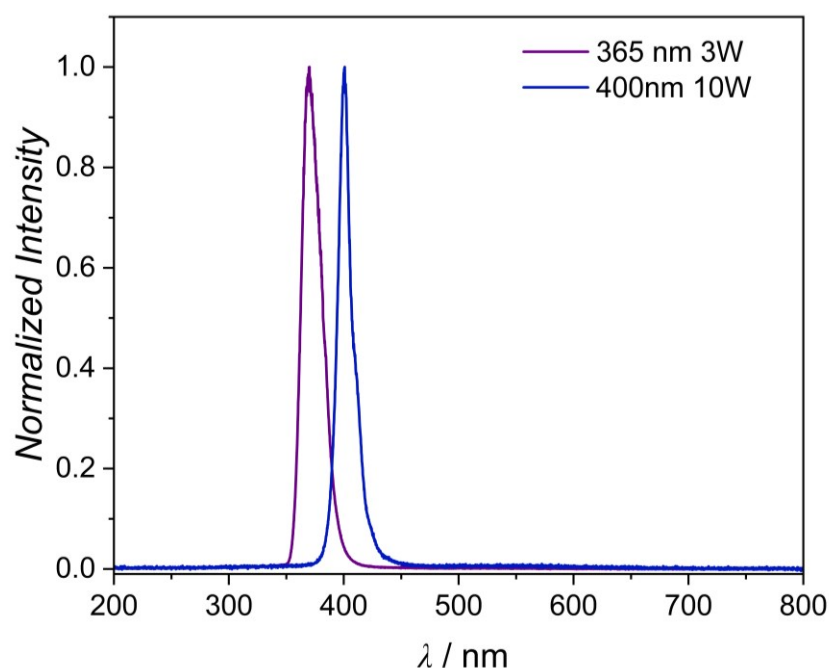
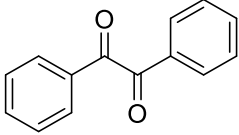
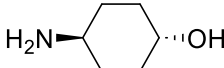
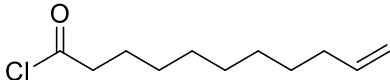
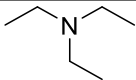
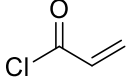
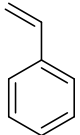
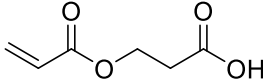
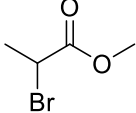
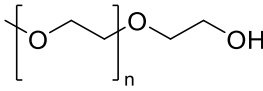
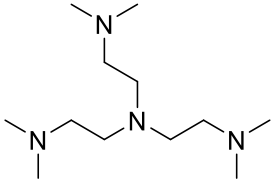
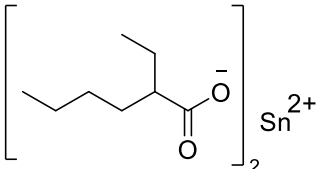


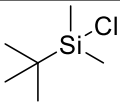
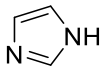
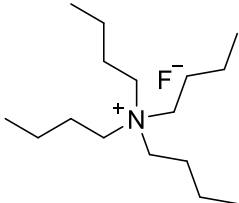
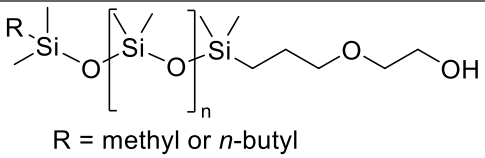
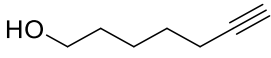
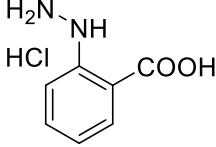
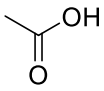
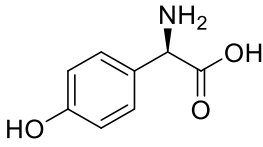
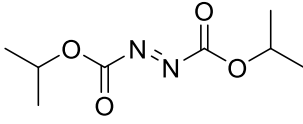
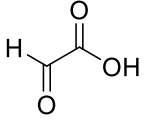
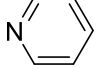
Figure S11.2. Emission spectra of 400-nm and 365-nm LEDs.

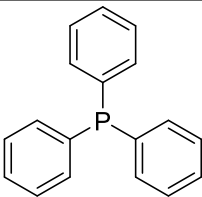
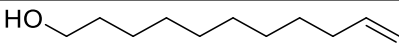
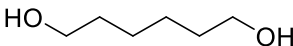
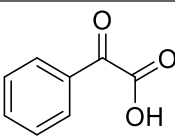
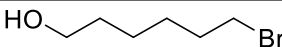
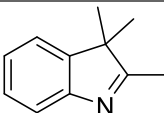
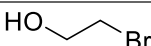
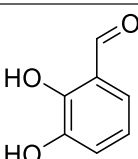
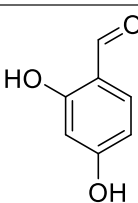
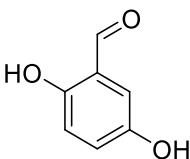
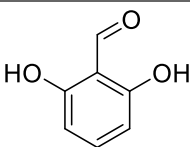
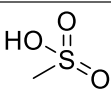
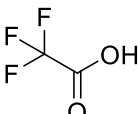
11.2. Chemicals

Table 11.1. List of chemicals used in this thesis. All chemicals and solvents were used without any further purification unless specified.

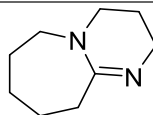
Name (Supplier, purity)	Chemical structure
Benzil (Alfa Aesar, 98%)	
<i>trans</i> -4-aminocyclohexanol (Apollo Scientific UK, 95%),	
10-undecenoyl chloride (TCI, 98%)	
triethylamine (Sigma Aldrich, 99.5%),	
acryloyl chloride (Sigma Aldrich, 97%)	
styrene (Sigma Aldrich, 99.9%),	
copper(I) bromide (Sigma Aldrich, 99.9%)	CuBr
2-carboxyethyl acrylate (Sigma Aldrich)	
methyl 2-bromopropionate (MBP) (Sigma Aldrich, 98%)	
polyethylene glycol methyl ether acrylate (Sigma Aldrich, $M_n = 2000 \text{ g}\cdot\text{mol}^{-1}$, PEG₄₆A1 , $M_n = 5000 \text{ g}\cdot\text{mol}^{-1}$, PEG₁₁₅A1)	
tris[2-(dimethylamino)ethyl]amine (Me ₆ TREN) (Sigma Aldrich, 97%)	
tin(II) 2-ethylhexanoate (Sn(EH) ₂) (Sigma Aldrich)	

Hoveyda-Grubbs catalyst 2 nd generation (HG-II , Sigma Aldrich, 97%)	
ethyl vinyl ether (Sigma Aldrich, >99%)	
5-bromovaleric acid (Merck, 97%)	
4-(dimethylamino)pyridine (DMAP) (Merck)	
N,N'-dicyclohexylcarbodiimide (DCC) (Merck)	
2-mercaptoethanol (Merck, 99%)	
1-butanethiol (Merck)	
1-dodecanethiol (Merck)	
(3-mercaptopropyl)trimethoxysilane (Merck)	
1-adamantanethiol (Merck)	
2-(boc-amino)ethanethiol (Merck)	
propionic acid (Merck, 95%)	
cesium carbonate (Merck and TCI)	Cs_2CO_3
1,4-diazabicyclo[2.2.2]octane (DABCO) (Merck)	
sodium sulfate anhydrous (Merck)	Na_2SO_4
1,3-bis(2,6-diisopropylphenyl)imidazol-2-ylidene (Combi-Blocks)	

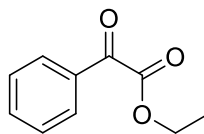
<i>tert</i> -Butyldimethylsilyl chloride (TBDMSCl) (Merck)	
imidazole (Merck)	
tetrabutylammonium fluoride (TBAF, 1M solution in THF) (Merck)	
poly(dimethylsiloxane), monohydroxy terminated (PDMS-OH , $M_n \sim 4670 \text{ g} \cdot \text{mol}^{-1}$) (Merck)	 R = methyl or <i>n</i> -butyl
6-heptyn-1-ol (Combi-Blocks)	
2-hydrazinobenzoic acid hydrochloride (97%, Combi-Blocks)	
acetic acid (glacial) (Thermo Fischer Scientific, >99%)	
copper (II) sulphate pentahydrate (VWR International, 98%)	$\text{CuSO}_4 \cdot 5\text{H}_2\text{O}$
<i>D</i> -4-hydroxyphenylglycine (98%, Sigma Aldrich)	
diisopropyl azodicarboxylate (DIAD) (98%, Sigma Aldrich) (DIAD) (Sigma Aldrich, 98%)	
glyoxylic acid solution (Sigma Aldrich, 50%)	
pyridine (Sigma Aldrich, >99%)	
thionyl chloride (Sigma Aldrich, 99%)	SOCl_2

triphenylphosphine (Ph ₃ P) (Sigma Aldrich, >95%)	
10-undecen-1-ol (Sigma Aldrich, 98%)	
1,6-hexanediol (Sigma Aldrich, 99%)	
benzoylformic acid (Combi-Blocks, 97%)	
6-bromo-1-hexanol (Sigma-Aldrich)	
2,3,3-trimethylindolenine (Sigma-Aldrich)	
2-bromoethanol (Sigma-Aldrich)	
2,3-dihydroxybenzaldehyde (Combi-Blocks)	
2,4-dihydroxybenzaldehyde (Combi-Blocks)	
2,5-dihydroxybenzaldehyde (Combi-Blocks)	
2,6-dihydroxybenzaldehyde (Combi-Blocks)	
methanesulfonic acid (MsOH) (Sigma-Aldrich)	
trifluoroacetic acid (TFA) (Alfa Aesar)	
Magnesium sulfate anhydrous (Merck)	MgSO ₄

1,8-Diazabicyclo(5.4.0)undec-7-ene (DBU)
(Merck)



ethyl benzoylformate (Combi-Blocks)



11.3. Information for Chapter 3

11.3.1. Synthesis of bisimine diol 1

Bisimine diol **1** was synthesized based on the protocol described in the literature.⁹³ Under inert atmosphere, benzil (20 g, 0.095 mol, 1.0 eq.) and *trans*-4-aminocyclohexanol (23 g, 0.20 mol, 2.1 eq.) was added to 60 mL of degassed *p*-xylene. The reaction was carried out under reflux condition for 48 h. Upon completion, the reaction mixture was cooled to ambient temperature and acetone was added. After 30 min of stirring, the mixture was filtered and washed 3 times with acetone to obtain α -bisimine diol **1** (25 g, white or yellow powder/solid, 65% yield).

¹H NMR (500 MHz, methanol-*d*₄) δ / ppm: 7.76 – 7.70 (m, 4H, H_{Ar}), 7.49 – 7.36 (m, 6H, H_{Ar}), 3.63 – 3.52 (m, 2H, -CH_{cyclic}-OH), 3.23 – 3.12 (m, 2H, -CH_{cyclic}-N=C), 2.07 – 1.96 (m, 2H), 1.85 – 1.71 (m, 4H), 1.66 – 1.52 (m, 4H), 1.41 – 1.30 (m, 2H), 1.28 – 1.16 (m, 2H), 1.04 – 0.90 (m, 2H). **¹³C NMR** (126 MHz, Methanol-*d*₄) δ / ppm: 165.2 (C=N-C, 2C), 138.0 (C_{Ar}-C=N, 2C), 132.2 (CH_{Ar}, 2C), 129.8 (4CH_{Ar}), 128.8 (CH_{Ar}, 4C), 70.3 (CH_{cyclic}-OH, 2C), 63.8 (CH_{cyclic}-N=C-, 2C), 34 (CH₂_{cyclic}, 2C), 33.9 (CH₂_{cyclic}, 2C), 33.0 (CH₂_{cyclic}, 2C), 31.7 (CH₂_{cyclic}, 2C). **HR-MS (ESI)**: calculated *m/z* for C₂₆H₃₃N₂O₂ [M+H]⁺ = 405.2537, found: 405.2531

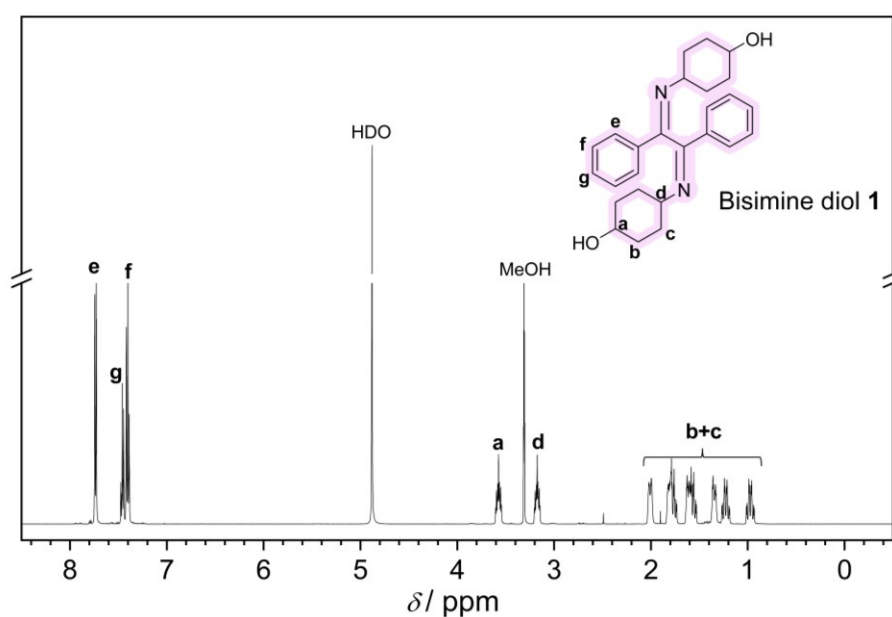


Figure S3.1. ¹H NMR spectrum of bisimine diol **1** in MeOD.

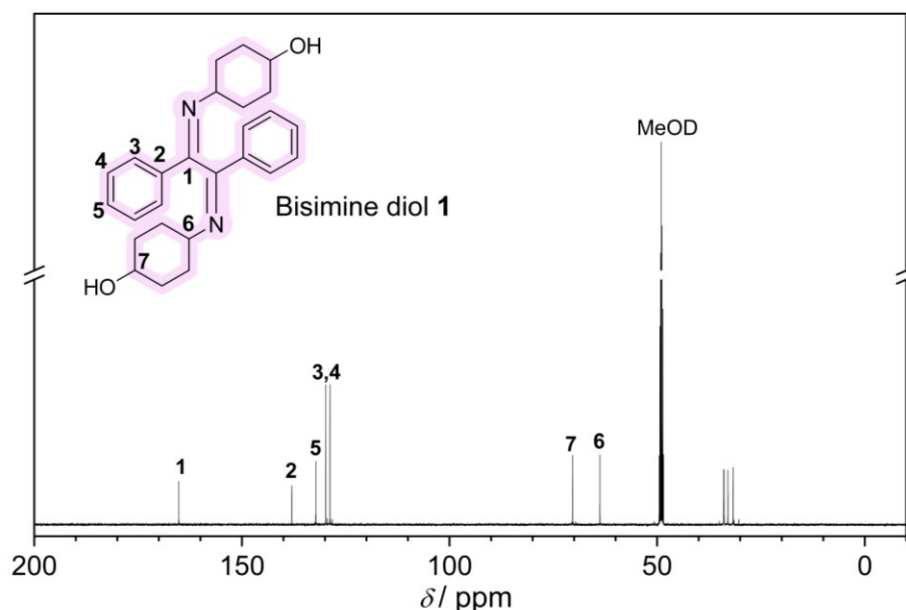


Figure S3.2. ^{13}C NMR spectrum of bisimine diol **1** in MeOD.

11.3.2. Synthesis of bisimine mono-ol **2**

Bisimine diol **1** (4.0 g, 9.9 mmol, 1.1 eq) and triethyl amine (Et_3N) (1.24 mL, 8.9 mmol, 1.0 eq) was dissolved in 120 mL of chloroform at 60 °C. Upon dissolution, the heat was turned off and a solution of 10-undecenoyl chloride (1.41 mL, 9.9 mmol, 1.0 eq) in 10 mL chloroform (1.0 M) was added in a dropwise manner to the previous solution. The reaction was stopped after 36 h. Upon completion, the mixture was washed with water and brine. The organic layer was dried over Na_2SO_4 , and the solvent was removed under reduced pressure. The residue was purified by flash column chromatography (EtOAc/n-hexane, 1:1, v/v) to obtain 2.7 g mono-ol **2** (48% yield) as yellow viscous oil.

^1H NMR (500 MHz, chloroform- d) δ / ppm 7.82 – 7.68 (m, 4H, HAr), 7.45 – 7.28 (m, 6H, HAr), 5.87 – 5.72 (m, 1H, $\text{CH}_2=\text{CH}-$), 5.02 – 4.87 (m, 2H, $\text{CH}_2=\text{CH}-$), 4.85 – 4.73 (m, 1H, $\text{CH}_{\text{cyclic}}-\text{C}(\text{O})\text{O}-$), 3.71 – 3.60 (m, 1H, $\text{CH}_{\text{cyclic}}-\text{OH}$), 3.28 – 3.13 (m, 2H, $\text{CH}_{\text{cyclic}}-\text{N}=\text{C}-$), 2.22 (t, $J = 7.6$ Hz, 2H, $-\text{CH}_2-\text{C}(\text{O})\text{O}-$), 2.13 – 1.99 (m, 4H), 1.95 – 1.82 (m, 2H), 1.82 – 1.70 (m, 2H), 1.64 – 1.51 (m, 6H), 1.46 – 1.02 (m, 16H). ^{13}C NMR (126 MHz, CDCl_3) δ / ppm: 173.43 ($\text{C}(\text{O})\text{O}-$, 1C), 163.22 & 163.17 ($\text{C}=\text{N}$, 2C), 139.24 ($-\text{CH}=\text{CH}_2$, 1C), 136.97 & 136.91 ($\text{C}_{\text{Ar}}-\text{C}=\text{N}-$, 2C), 130.79 & 130.74 (CH_{Ar} , 2C), 128.68 (CH_{Ar} , 4C), 127.73 & 127.68 (CH_{Ar} , 4C), 114.25 ($-\text{CH}=\text{CH}_2$, 1C), 71.83 ($\text{CH}-\text{OC}(\text{O})$, 1C), 69.89 ($-\text{CH}-\text{OH}$, 1C), 62.00 & 61.50 ($-\text{CH}-\text{N}=\text{C}$, 2C), 34.75 ($\text{C}_{\alpha}\text{H}_2-\text{C}(\text{O})-\text{O}-$, 1C), 33.86 ($\text{CH}_2-\text{CH}=\text{CH}_2$, 1C), 33.30 & 33.20 ($\text{CH}_2_{\text{cyclic}}$, 2C), 31.96 & 31.46 ($\text{CH}_2_{\text{cyclic}}$, 2C), 30.78 & 30.35 ($\text{CH}_2_{\text{cyclic}}$, 2C), 29.34 & 29.25 ($\text{CH}_2_{\text{cyclic}}$, 2C), 29.13 & 29.11 ($\text{CH}_2_{\text{aliphatic}}$, 4C),

28.94 (CH₂_{aliphatic}, 1C), 25.12 (C_βH₂, 1C). **HR-MS (ESI)**: calculated m/z for C₃₇H₅₁N₂O₃ [M+H⁺] = 571.3895, found: 571.3887.

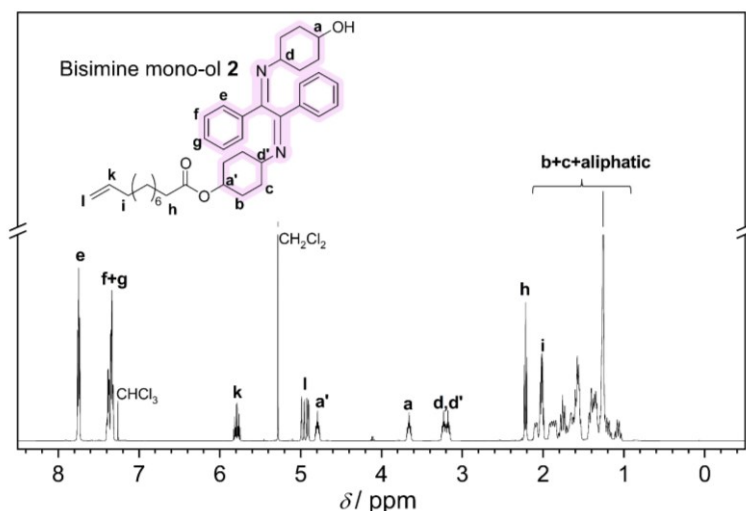


Figure S3.3. ¹H NMR spectrum of bisimine mono-ol **2** in CDCl₃.

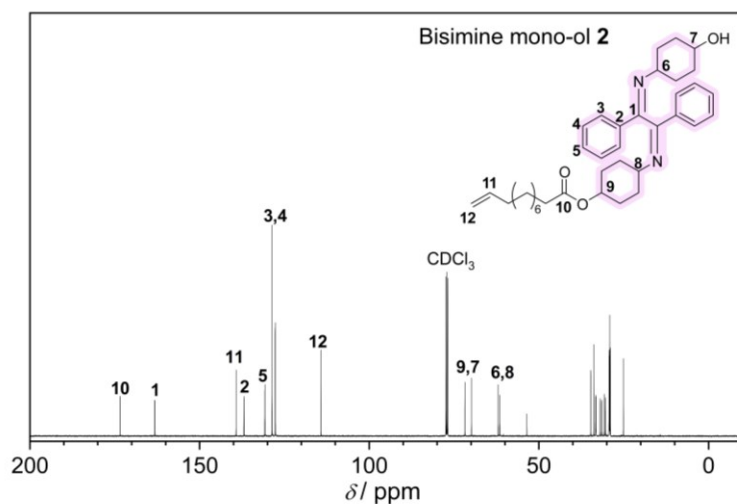


Figure S3.4. ¹³C NMR spectrum of bisimine mono-ol **2** in CDCl₃.

11.3.3. Synthesis of bisimine monomer **3**

Mono-ol **2** (2.0 g, 3.50 mmol, 1 eq) and Et₃N (0.73 mL, 5.26 mmol, 1.5 eq) were dissolved in 7.0 mL of dichloromethane. After the solution reached 0 °C, acryloyl chloride (0.42 mL, 5.3 mmol, 1.5 eq) in 5.3 mL dichloromethane was slowly added. The temperature was maintained at 0 °C for about 1 hour before being allowed to reach ambient temperature. After 24 h, the mixture was diluted in dichloromethane and washed with brine. The organic layer was then dried with Na₂SO₄ and the solvent was removed under reduced pressure. The residue was purified by flash column chromatography (EtOAc/n-Hexane, 1:9, v/v) to obtain 1.7 g monomer **3** (78% yield) as yellow viscous oil.

^1H NMR (500 MHz, Chloroform- d) δ /ppm 7.81 – 7.71 (m, 4H, H_{Ar}), 7.44 – 7.30 (m, 6H, H_{Ar}), 6.34 (dd, $J = 17.3, 1.6$ Hz, 1H, $\text{CH}_2=\text{CH}-\text{COO}$), 6.05 (dd, $J = 17.3, 10.5$ Hz, 1H, $\text{CH}_2=\text{CH}-\text{COO}$), 5.85 – 5.73 (m, 2H, $\text{CH}_2=\text{CH}-\text{C}(\text{O})\text{O}$ & $\text{CH}_2=\text{CH}-\text{CH}_2-$), 5.01 – 4.84 (m, 3H, $\text{CH}_2=\text{CH}-\text{CH}_2-$ & $\text{CH}_{\text{cyclic}}-\text{acrylate}$), 4.79 (m, 1H, $\text{CH}_{\text{cyclic}}-\text{OC}(\text{O})\text{R}$), 3.30 – 3.19 (m, 2H, $\text{CH}_{\text{cyclic}}-\text{N}=\text{C}-$), 2.22 (t, $J = 7.6$ Hz, 2H, $-\text{CH}_2-\text{C}(\text{O})\text{O}$), 2.18 – 1.86 (m, 6H), 1.84 – 1.72 (m, 2H), 1.70 – 1.51 (m, 6H), 1.51 – 1.15 (m, 16H). **^{13}C NMR** (126 MHz, CDCl_3) δ /ppm: 173.47 ($-\text{CH}_2-\text{C}(\text{O})\text{O}$, 1C), 165.77 ($\text{CH}_2=\text{CH}-\text{C}(\text{O})\text{O}$, 1C), 163.28 & 163.23 ($\text{C}=\text{N}$, 2C), 139.30 ($-\text{CH}_2-\text{CH}=\text{CH}_2$, 1C), 136.95 ($-\text{N}=\text{C}-\text{C}_{\text{Ar}}$, 2C), 130.85 (CH_{Ar} , 2C), 130.48 ($(-\text{CH}_2=\text{CH}-\text{C}(\text{O})\text{O})$, 1C), 129.05 ($\text{CH}_2=\text{CH}-\text{C}(\text{O})\text{O}-$, 1C), 128.74 (CH_{Ar} , 4C), 127.76 (CH_{Ar} , 4C), 114.28 ($\text{CH}_2=\text{CH}-\text{CH}_2-$, 1C), 72.27 & 71.82 ($-\text{CH}_{\text{cyclic}}-\text{C}(\text{O})\text{OR}$, 2C), 61.53 & 61.45 ($-\text{CH}_{\text{cyclic}}-\text{N}=\text{C}$, 2C), 34.79 ($-\text{C}_{\alpha}\text{H}_2-\text{C}(\text{O})\text{O}-$, 1C), 33.91 ($-\text{CH}_2-\text{CH}=\text{CH}_2$, 1C), 31.54 & 31.48 ($\text{CH}_2_{\text{cyclic}}$, 2C), 30.40 & 30.35 ($\text{CH}_2_{\text{cyclic}}$, 2C), 29.39 ($\text{CH}_2_{\text{cyclic}}$, 2C), 29.30 ($\text{CH}_2_{\text{cyclic}}$, 2C), 29.18 & 29.16 ($\text{CH}_2_{\text{aliphatic}}$, 4C), 29.00 ($\text{CH}_2_{\text{aliphatic}}$, 1C), 25.17 ($-\text{C}_{\beta}\text{H}_2$, aliphatic, 1C). **HR-MS (ESI)**: calculated m/z for $\text{C}_{40}\text{H}_{53}\text{N}_2\text{O}_4$ $[\text{M}+\text{H}^+]$ = 625.4000, found: 625.3991.

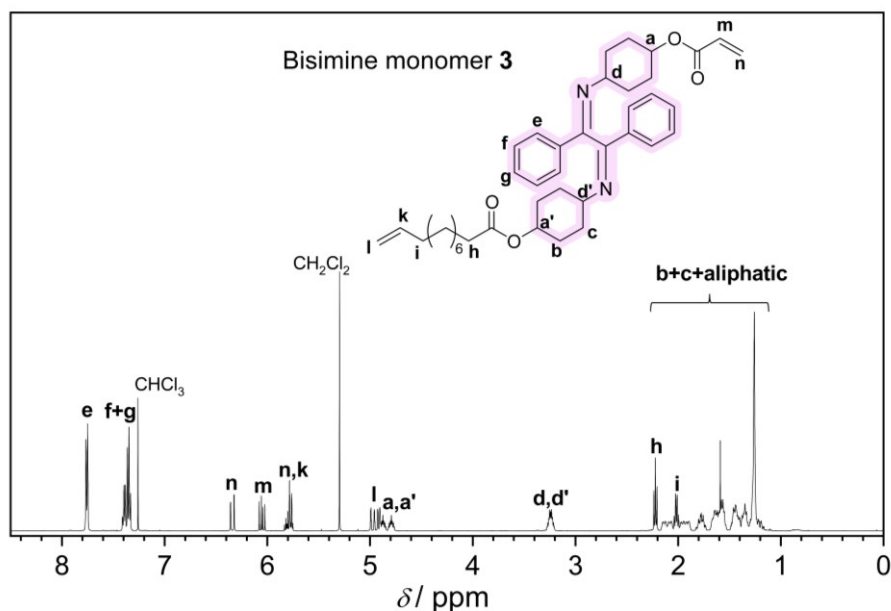


Figure S3.5. ^1H NMR spectrum of bisimine monomer **3** in CDCl_3 .

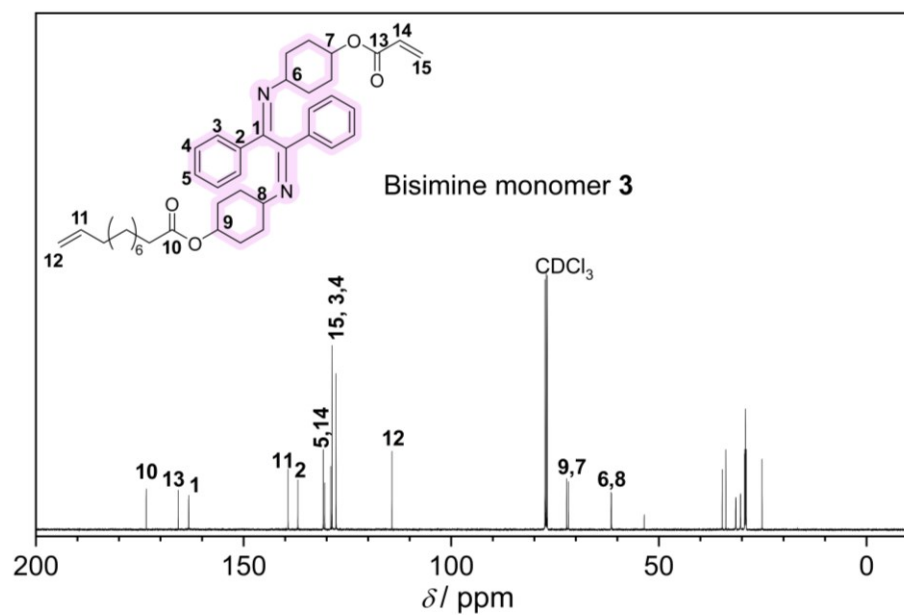


Figure S3.6. ^{13}C NMR spectrum of bisimine monomer **3** in CDCl_3 .

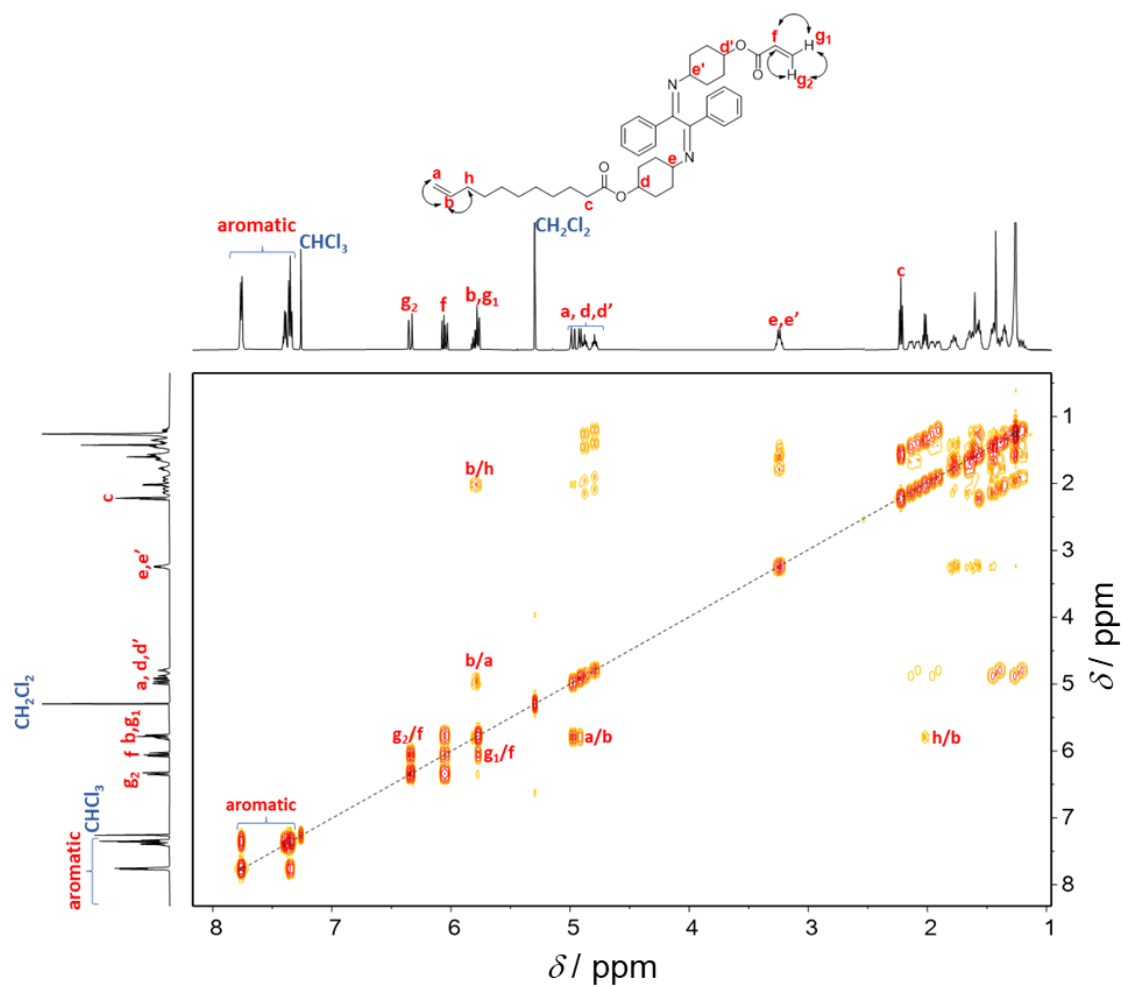


Figure S3.7. COSY NMR spectrum of bisimine monomer **3** in CDCl_3 .

11.3.4. ARGET ATRP synthesis of PS_nBr polymers

The synthesis protocol was adopted from the literature.¹⁹⁰ Copper bromide (Cu(I)Br) was purified by a procedure described in the literature.²⁹⁶ Styrene (St) and methyl 2-bromopropionate (MBP) was injected into a 25 mL-Schlenk tube charged with a magnetic stirring bar and subsequently percolated with N_2 (g). Meanwhile, a solution of Cu(I)Br , tris[2-(dimethylamino)ethyl]amine (Me_6TREN), and tin(II) 2-ethylhexanoate (Sn(EH)_2) in styrene was percolated with N_2 in a separated flask. Subsequently, the solution was injected to the previous Schlenk tube under N_2 atmosphere. The reaction commenced when the Schlenk tube was immersed in a preheated oil bath at 90 °C. The reaction was stopped when the desired monomer conversion was reached as assessed by ^1H NMR spectroscopy. During the synthesis of **PS₇₀Br**, **PS₁₁₅Br** and **PS₂₃₀Br**, the final $[\text{St}]/[\text{MBP}]$ ratios were 100, 200 and 400, respectively. In all cases, the molar ratios of Sn(EH)_2 and Me_6TREN to MBP were both 0.1 and the molar ratio of Cu(I)Br to styrene was 50 ppm. After the reaction finished, the solution was diluted in THF and passed through a short neutral alumina column to remove the Cu(I) complex. The solvent was subsequently removed under reduced pressure. The residue was dissolved in THF and precipitated in cold MeOH, filtered and dried under vacuum at 40 °C to obtain the desired polymer.

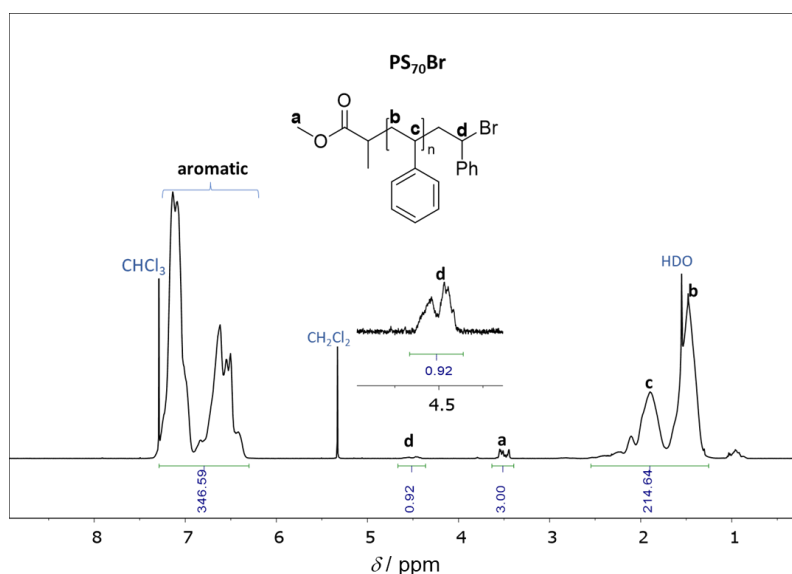


Figure S3.8. ^1H NMR spectrum of **PS₇₀Br** in CDCl_3 .

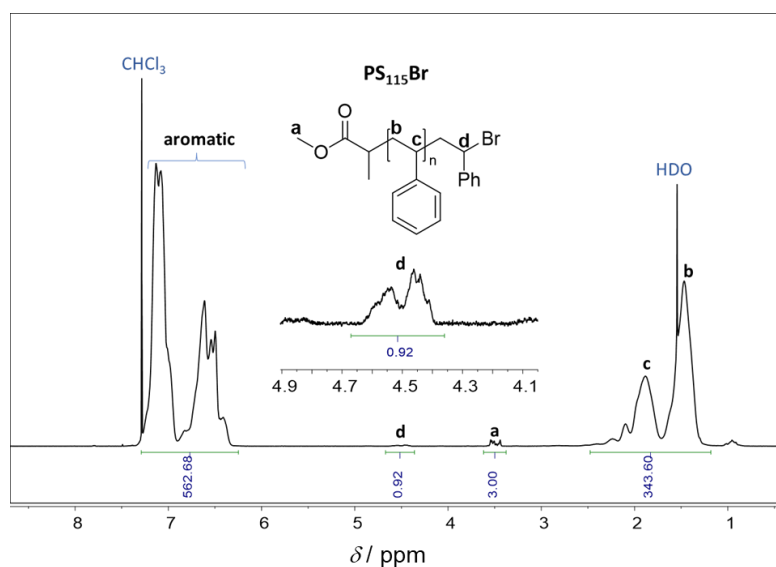


Figure S3.9. ^1H NMR spectrum of **PS₁₁₅Br** in CDCl_3 .

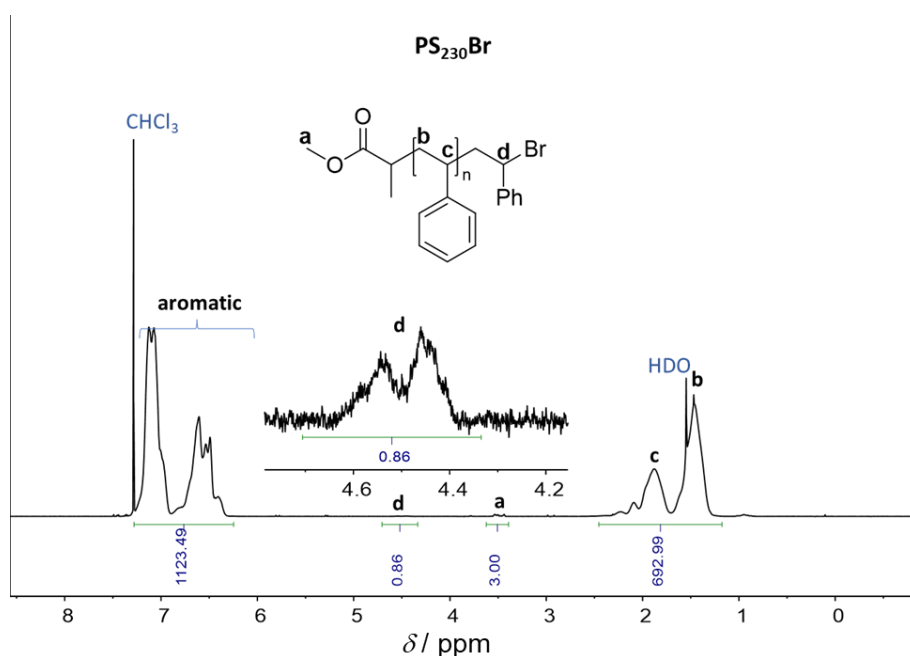


Figure S3.10. ^1H NMR spectrum of **PS₂₃₀Br** in CDCl_3 .

11.3.5. Post-polymerization modification of **PS_nBr** polymers

In a typical experiment, 2-carboxyethyl acrylate (68 μL , 0.57 mmol, 4.0 eq) was dissolved in DMF, followed by the addition of Cs_2CO_3 (93 mg, 0.29 mmol, 2.0 eq). Subsequently, **PS₇₀Br** (1000 mg, 0.14 mmol, 1.0 eq) was added slowly to the mixture. The reaction was carried out at ambient temperature for 48 h. Upon completion, the reaction solution was diluted in ethyl acetate and was washed with water (3 times). The organic phase was dried with MgSO_4 and the solvent was evaporated under reduced pressure. Subsequently, the residue was dissolved in THF and precipitated in cold MeOH, followed by filtration and vacuum drying at 40 $^\circ\text{C}$ to obtain the product as white powder.

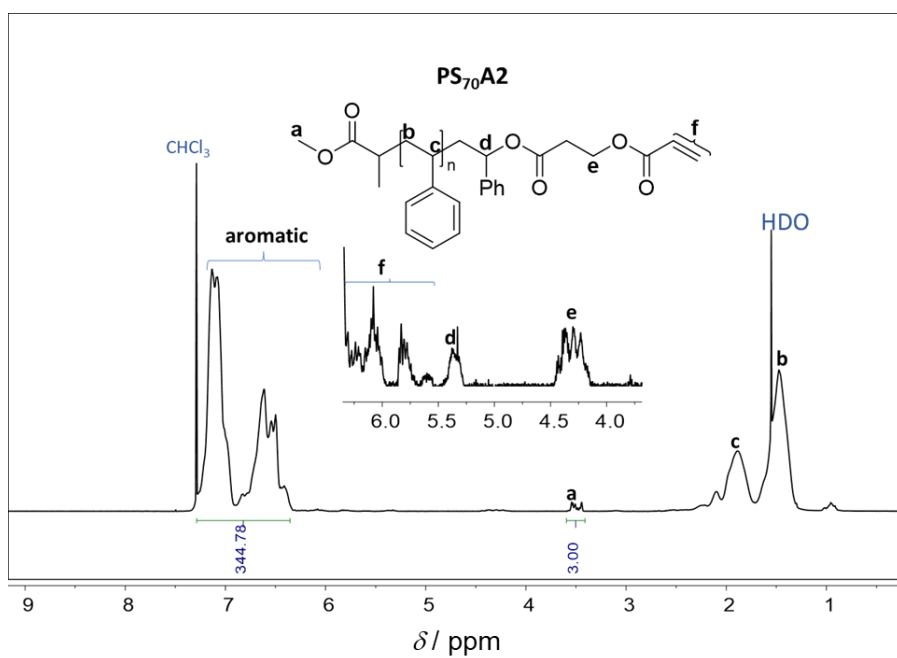


Figure S3.11. ¹H NMR spectrum of **PS₇₀A2** in CDCl₃.

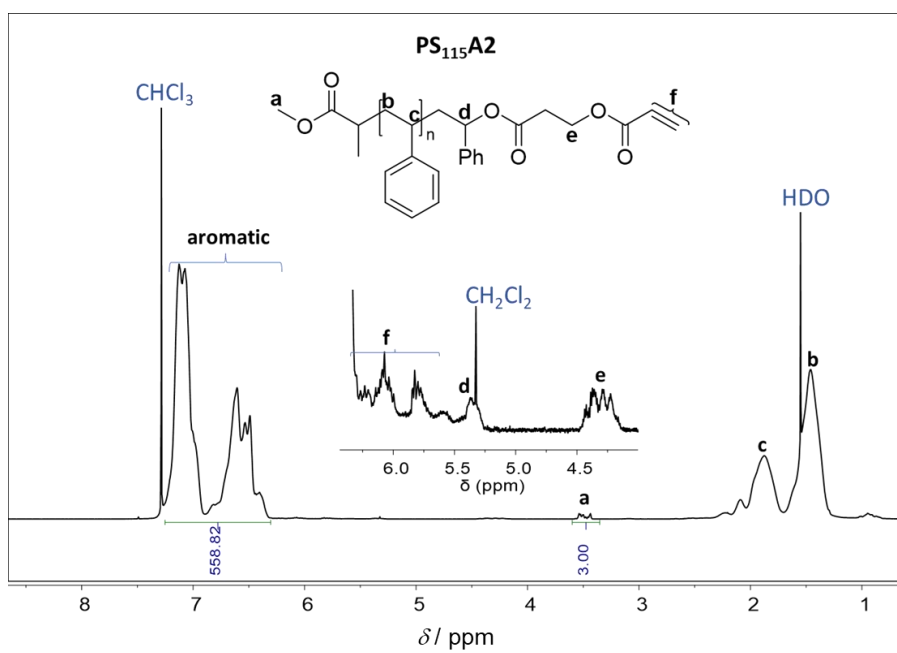


Figure S3.12. ¹H NMR spectrum of **PS₁₁₅A2** in CDCl₃.

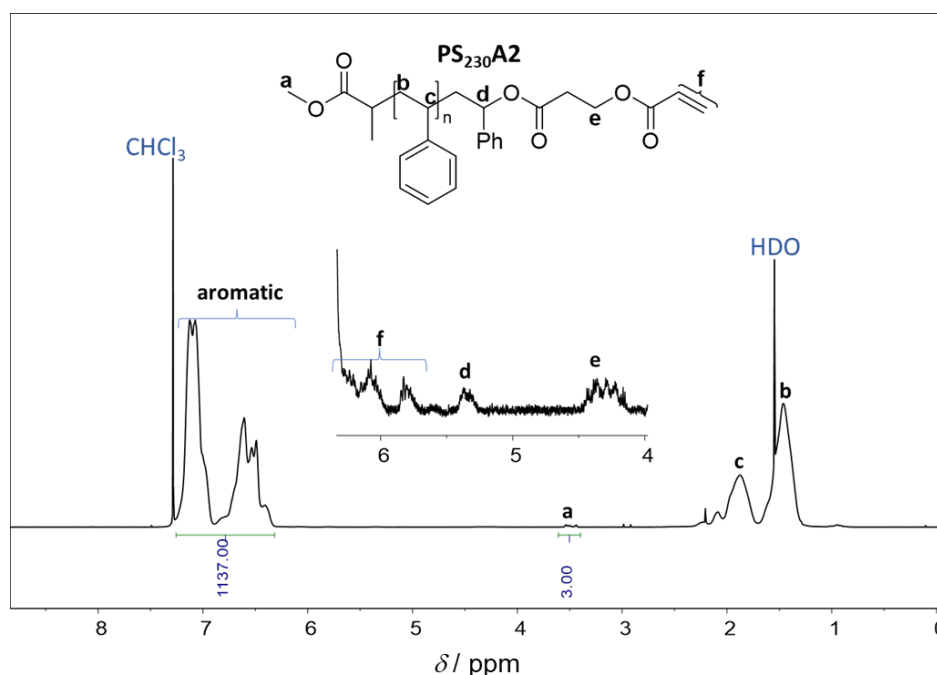


Figure S3.13. ^1H NMR spectrum of $\text{PS}_{230}\text{A2}$ in CDCl_3 .

11.3.6. Synthesis of photoresponsive block copolymers

Bisimine monomer **3** (0.5 M) and macro-chain stopper ($\text{PS}_n\text{A2}$ or $\text{PEG}_{46}\text{A1}$) were dissolved in dichloromethane in a Schlenk tube. The designed degree of polymerization in the ADMET block was calculated based on the molar ratio of the monomer and the acrylate functional group of the macro-chain stopper. Subsequently, Hoveyda-Grubbs (2nd generation) catalyst (3 mol%, with respect to the mole the monomer **3**) was added and the reaction mixture was immersed in a preheated oil bath at 40 °C. The valve of the Schlenk tube was gently opened from time to time to release the generated ethylene gas. After 3 h, another batch of the catalyst (3 mol%) was added. The conversion was monitored by ^1H NMR spectroscopy and SEC. Ethyl vinyl ether was added 30 min before the reaction was stopped to quench the catalyst. The reaction mixture was subsequently precipitated in methanol, followed by centrifugation and vacuum drying at 40 °C.

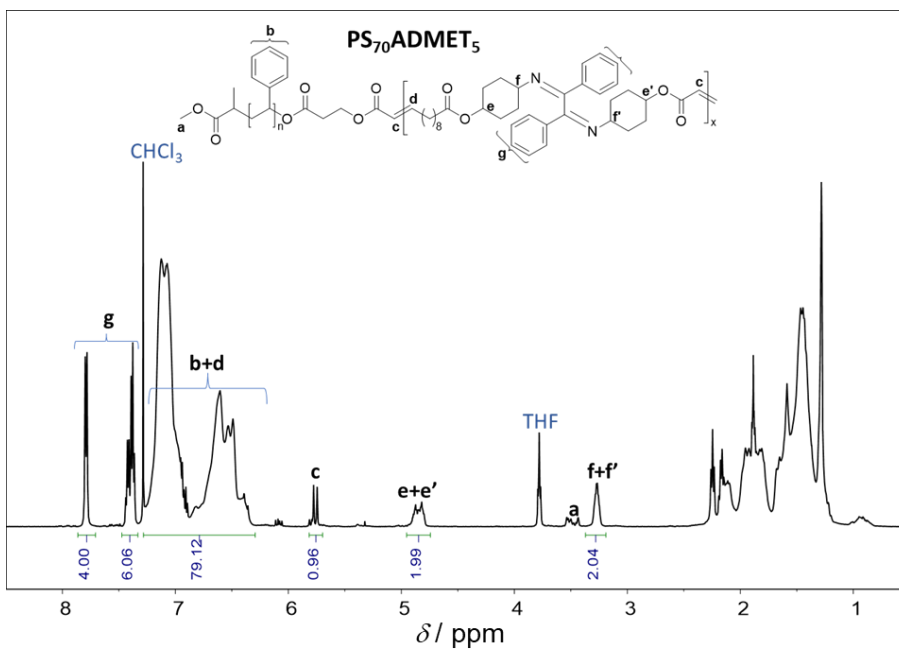


Figure S3.14. ¹H NMR spectrum of **PS₇₀[B]₅** in CDCl₃.

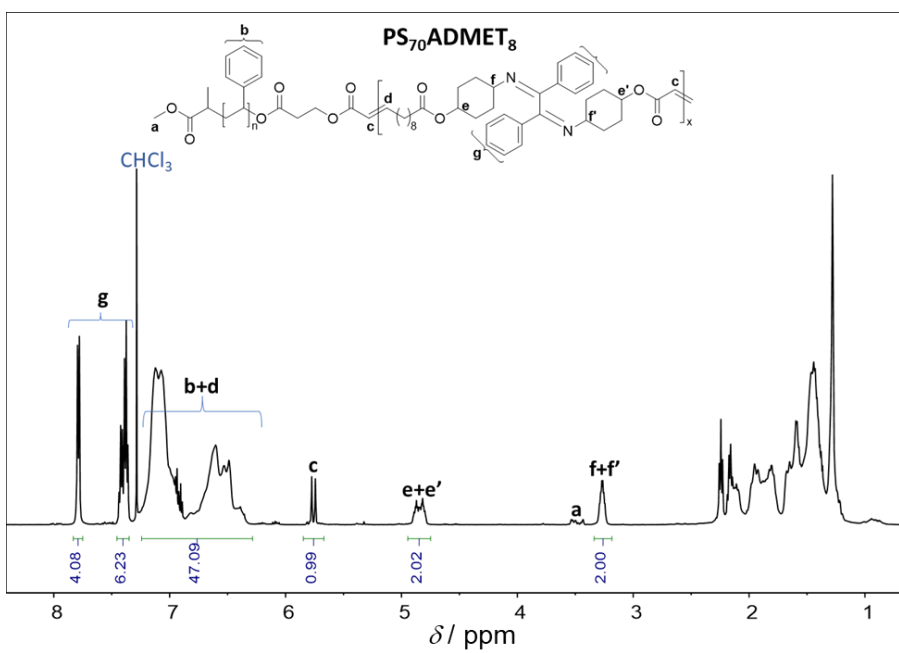


Figure S3.15. ¹H NMR spectrum of **PS₇₀[B]₈** in CDCl₃.

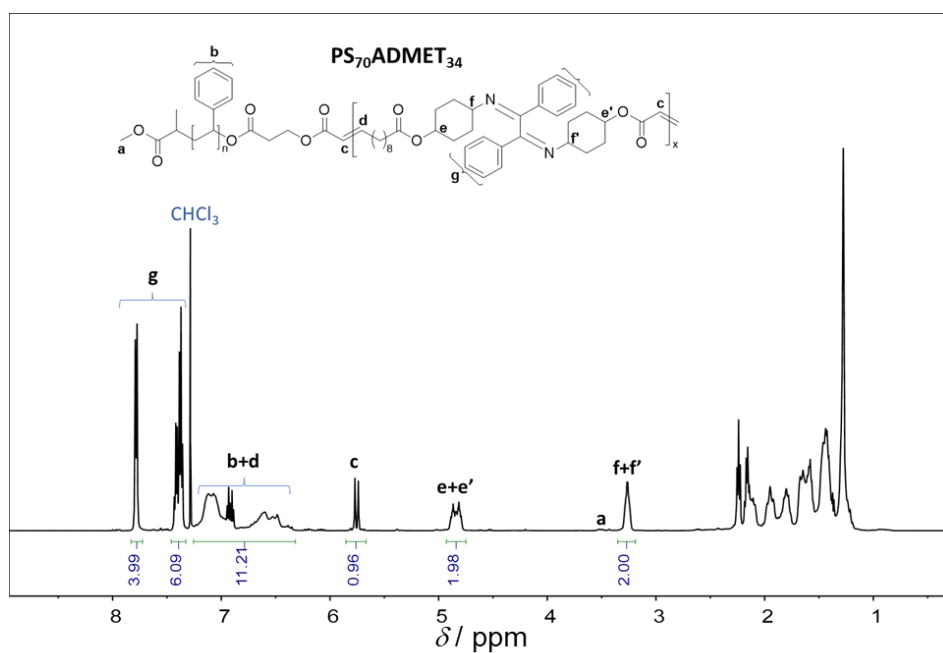


Figure S3.16. ¹H NMR spectrum of **PS₇₀[B]₃₄** in CDCl₃.

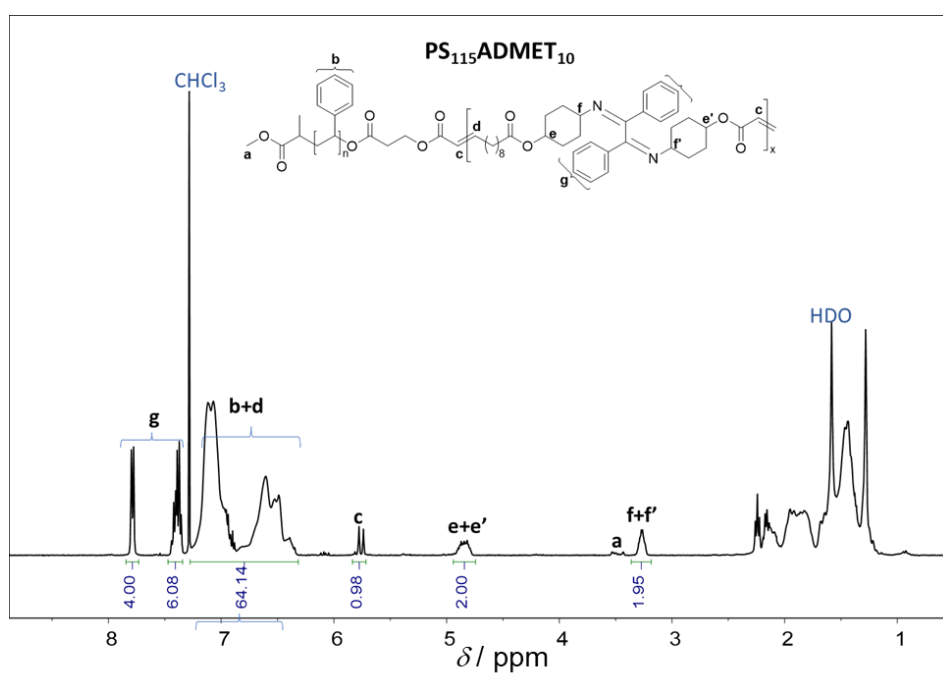


Figure S3.17. ¹H NMR spectrum of **PS₁₁₅[B]₁₀** in CDCl₃.

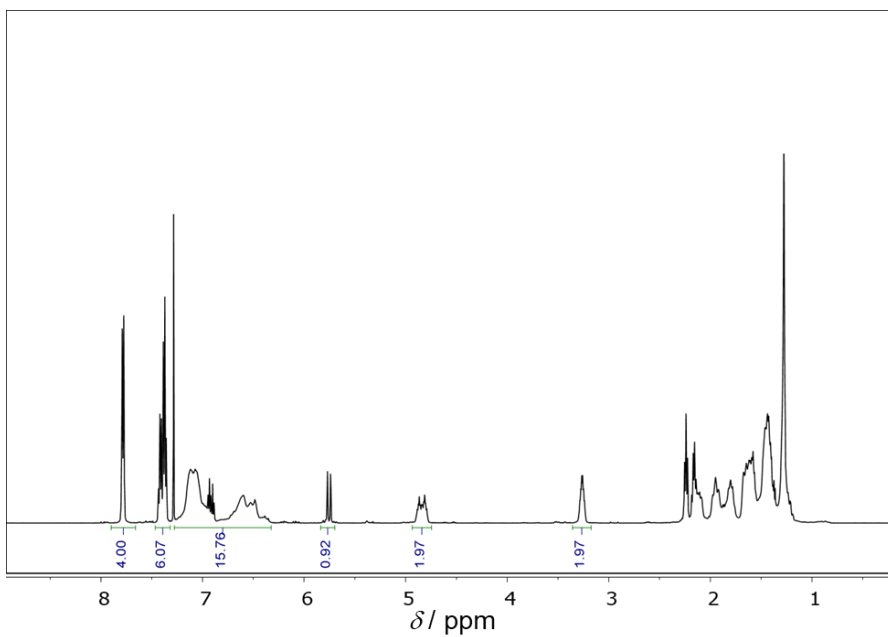


Figure S3.18. ^1H NMR spectrum of $\text{PS}_{115}[\text{B}]_{36}$ in CDCl_3 .

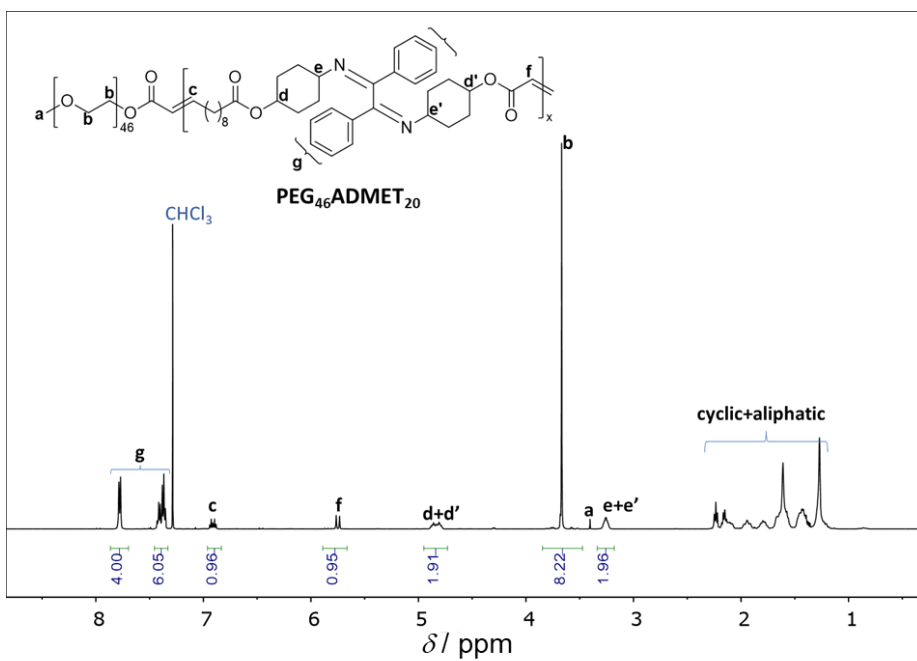
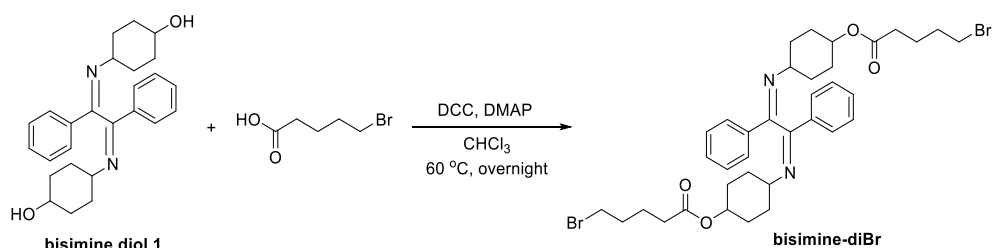


Figure S3.19. ^1H NMR spectrum of $\text{PEG}_{46}[\text{B}]_{20}$ in CDCl_3 .

11.3.7. Synthesis of bisimine-diBr



Bisimine diol **1** (2000 mg, 4.94 mmol, 1.0 eq), 5-bromovaleric acid (2685 mg, 14.8 mmol, 3.0 eq), and DMAP (121 mg, 20 mol%) were dissolved in CHCl_3 (70 mL) at 60 °C. Subsequently, DCC (3160 mg, 15.3 mmol, 3.1 eq) was added to the mixture. The reaction was run overnight. Upon completion, the precipitate was filtered out and the reaction solution was concentrated. The residue was purified by flash column chromatography with ethyl acetate (EtOAc) and cyclohexane (Cy) as eluents (EtOAc: Cy = 1/9, v/v). The product was obtained as sticky oil at 40 °C (95% yield).

$^1\text{H NMR}$ (600 MHz, CDCl_3) δ 7.77 – 7.72 (m, 4H), 7.41 – 7.33 (m, 6H), 4.80 (tt, J = 10.2, 4.2 Hz, 2H), 3.39 (t, J = 6.6 Hz, 4H), 3.23 (tt, J = 9.2, 3.8 Hz, 2H), 2.28 (t, J = 7.3 Hz, 4H), 2.12 – 2.05 (m, 2H), 1.94 – 1.83 (m, 6H), 1.80 – 1.71 (m, 6H), 1.56 (s, 4H), 1.48 – 1.36 (m, 4H), 1.21 (tdd, J = 12.5, 10.2, 3.8 Hz, 2H). **LC-MS**: calculated m/z for $\text{C}_{36}\text{H}_{47}\text{Br}_2\text{N}_2\text{O}_4^+$ $[\text{M}+\text{H}^+] = 731.1877$, found 731.1868.

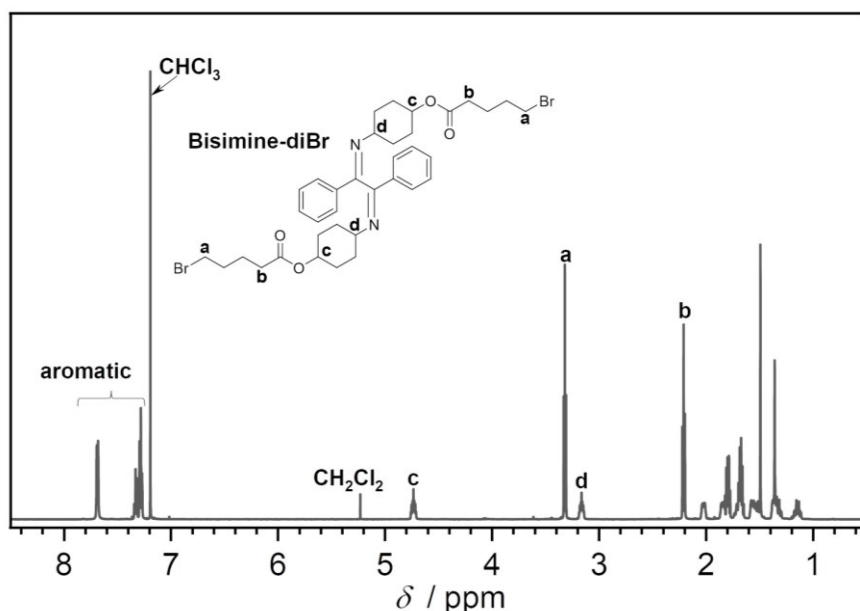
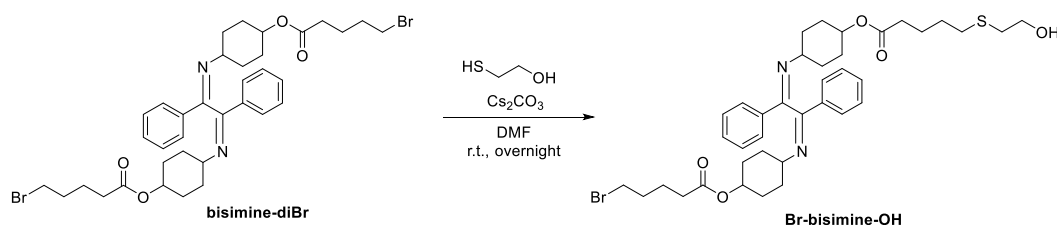


Figure S3.20. $^1\text{H NMR}$ spectrum of *bisimine-diBr* in CDCl_3 .

11.3.8. Synthesis of Br-bisimine-OH



Bisimine-diBr (2000 mg, 2.70 mmol, 1.0 eq) and 2-mercaptoethanol (0.19 mL, 1.0 eq) were dissolved in DMF (5.4 mL) at room temperature. Cesium carbonate (Cs_2CO_3) (446 mg, 1.35 mmol, 0.5 eq) was added in portion-wise manner to the solution. The reaction was run overnight. Upon completion, the mixture was diluted with EtOAc and extracted with water/brine (3 times) to remove DMF and salts. The EtOAc phase was then dried over Na_2SO_4 , filtered

and concentrated. The residue was purified by flash column chromatography (EtOAc:Cy = 1/99:80/20, v/v), yielding the product as pale yellow sticky oil (35% yield).

¹H NMR (600 MHz, CDCl₃) δ 7.75 (d, J = 7.6 Hz, 4H), 7.42 – 7.31 (m, 6H), 4.79 (ddtd, J = 10.5, 8.5, 4.2, 2.8 Hz, 2H), 3.69 (q, J = 5.7 Hz, 2H), 3.37 (t, J = 6.6 Hz, 2H), 3.23 (ddt, J = 13.6, 9.3, 3.8 Hz, 2H), 2.69 (t, J = 6.0 Hz, 2H), 2.52 – 2.48 (m, 2H), 2.26 (dt, J = 9.0, 7.3 Hz, 4H), 2.12 – 2.04 (m, 2H), 1.93 – 1.82 (m, 4H), 1.82 – 1.54 (m, 12H), 1.41 (s, 4H), 1.27 – 1.15 (m, 2H). **¹³C NMR** (151 MHz, CDCl₃) δ 172.87, 172.66, 171.25, 163.26, 136.78, 130.93, 128.74, 127.77, 77.37, 77.16, 76.95, 72.11, 72.02, 61.46, 61.43, 60.49, 60.39, 35.34, 34.16, 33.69, 33.11, 32.03, 31.43, 31.33, 30.30, 29.14, 29.12, 27.01, 24.19, 23.65, 21.15. **LC-MS**: calculated m/z for C₃₈H₅₂BrN₂O₅S⁺ [M+H⁺] = 727.2775, 729.2755, 728.2809, 730.2788; found 727.2770, 729.2754, 728.2801, 730.2777.

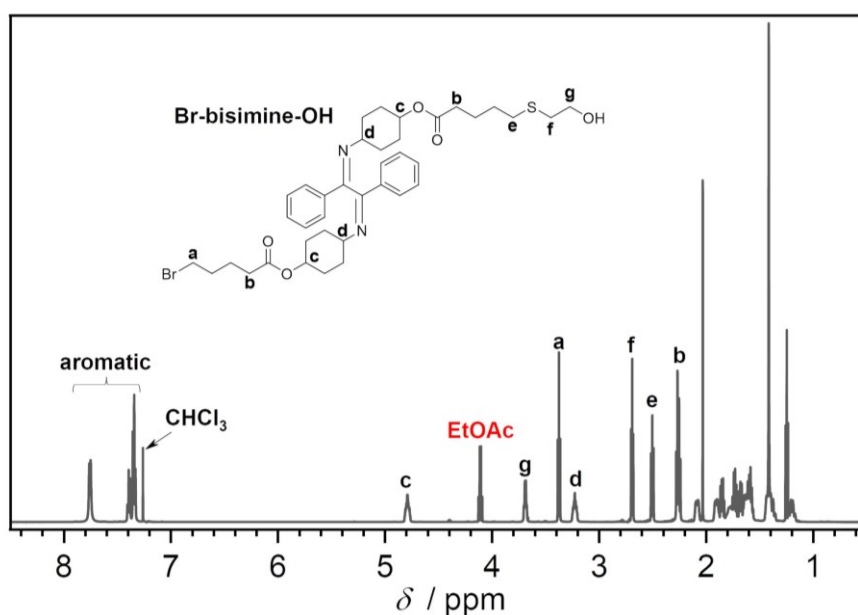


Figure S3.21. ¹H NMR spectrum of **Br-Bisimine-OH** in CDCl₃.

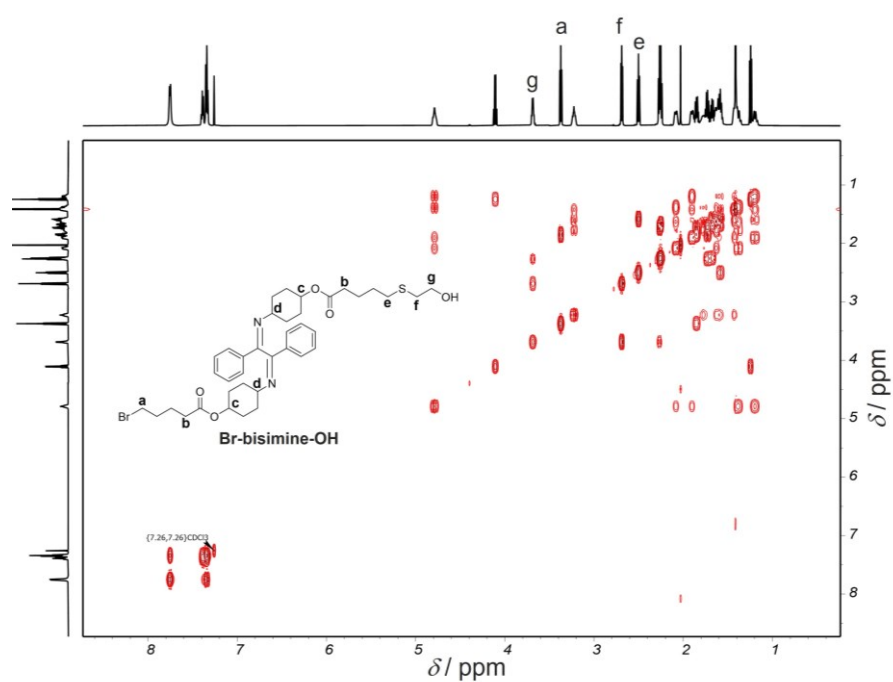


Figure S3.22. COSY NMR spectrum of **Br-Bisimine-OH** in CDCl_3 .

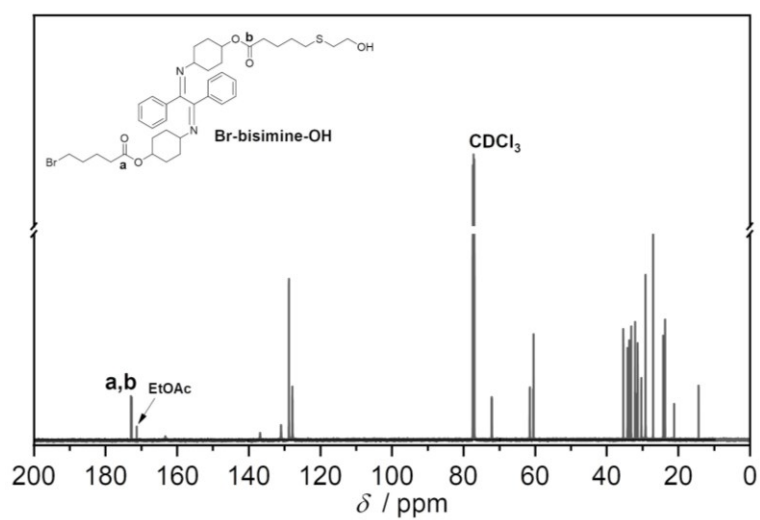
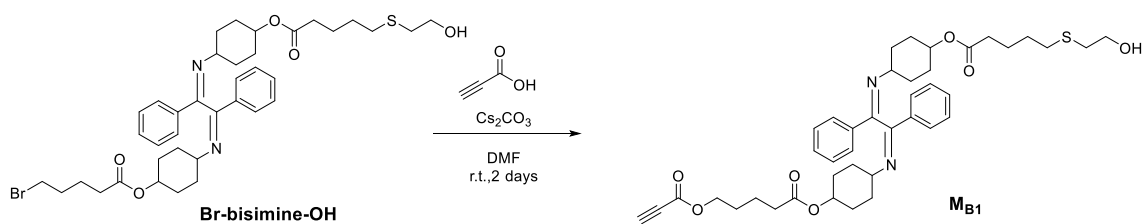


Figure S3.23. ^{13}C NMR spectrum of **Br-bisimine-OH** in CDCl_3 .

11.3.9. Synthesis of monomer **M_{B1}**



Br-bisimine-OH (660 mg, 0.9 mmol, 1.0 eq) and propiolic acid (0.11 mL, 2.0 eq) were dissolved in DMF (1.8 mL) at room temperature. Cesium carbonate (Cs_2CO_3) (294 mg, 0.9 mmol, 1.0 eq) was added to the solution. The reaction was run for 2 days. Upon completion, the mixture was diluted with EtOAc (100 mL) and extracted with water/brine (3 times) to remove DMF and salts. The EtOAc phase was then dried over Na_2SO_4 , filtered and concentrated. The residue was purified by flash column chromatography (EtOAc:Cy = 1/99:30/70, v/v), yielding the product as yellow sticky oil (77% yield). NMR spectra are provided in Section 7.

^1H NMR (600 MHz, CDCl_3) δ 7.75 (d, J = 7.6 Hz, 4H), 7.42 – 7.33 (m, 6H), 4.83 – 4.75 (m, 2H), 4.17 (h, J = 2.6 Hz, 2H), 3.69 (t, J = 5.9 Hz, 2H), 3.23 (dp, J = 13.1, 3.9 Hz, 2H), 2.86 – 2.84 (m, 1H), 2.69 (tt, J = 6.1, 1.9 Hz, 2H), 2.50 (t, J = 7.3 Hz, 2H), 2.32 – 2.23 (m, 4H), 2.08 (dt, J = 13.2, 4.4 Hz, 2H), 1.94 – 1.86 (m, 2H), 1.77 (d, J = 12.3 Hz, 2H), 1.72 – 1.54 (m, 12H), 1.47 – 1.35 (m, 4H), 1.26 – 1.15 (m, 2H). **^{13}C NMR** (151 MHz, CDCl_3) δ 172.87, 172.64, 163.22, 152.80, 136.84, 130.90, 128.75, 127.76, 77.37, 77.35, 77.16, 77.14, 76.95, 76.92, 74.82, 74.75, 72.11, 72.04, 65.86, 61.46, 61.43, 60.39, 35.35, 34.17, 34.06, 31.46, 31.43, 31.33, 30.31, 29.15, 29.11, 27.80, 24.20, 21.45. **LC-MS**: calculated m/z for $\text{C}_{41}\text{H}_{53}\text{N}_2\text{O}_7\text{S}^+$ [$\text{M}+\text{H}^+$] = 717.3568, found 717.3560.

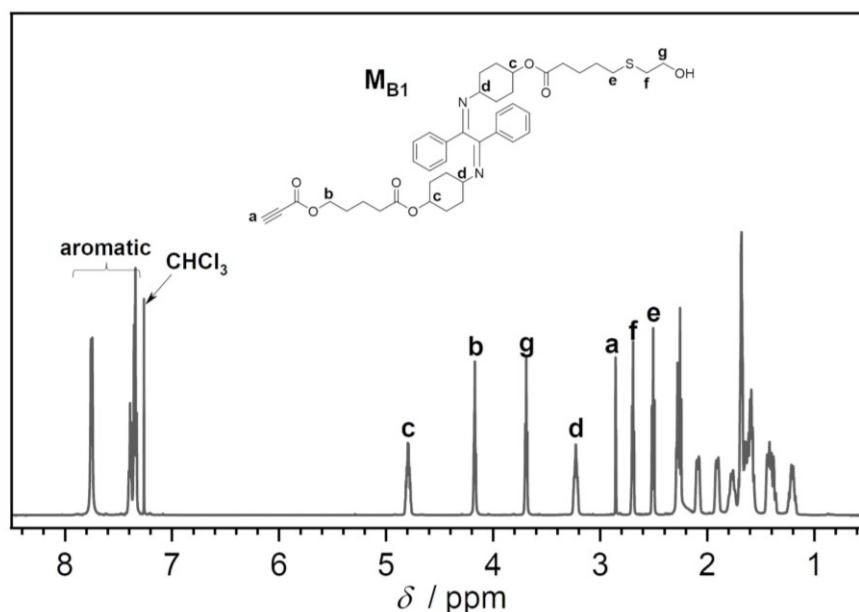


Figure S3.24. ^1H NMR spectrum (600 MHz) of **M_{B1}** in CDCl_3 .

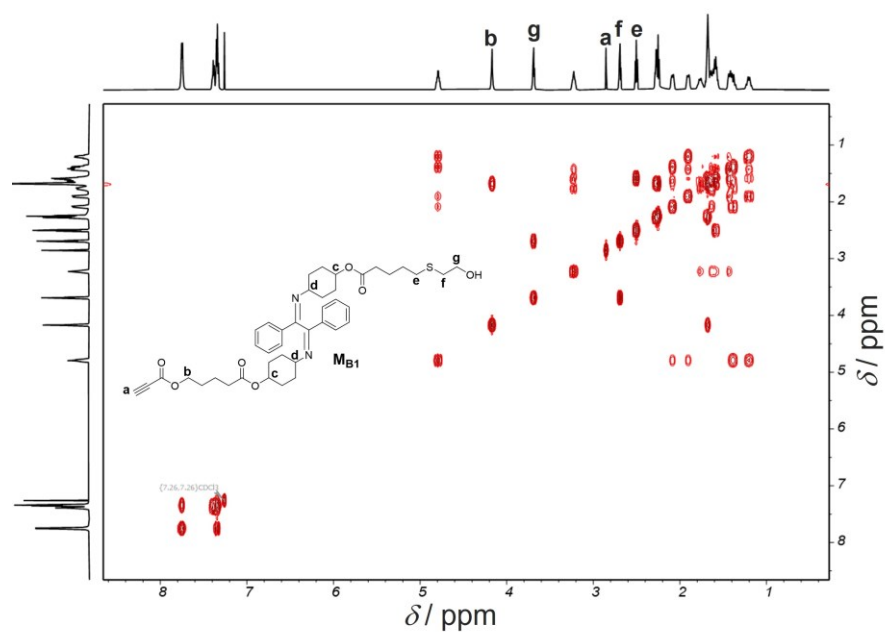


Figure S3.25. COSY NMR spectrum of M_{B1} in $CDCl_3$.

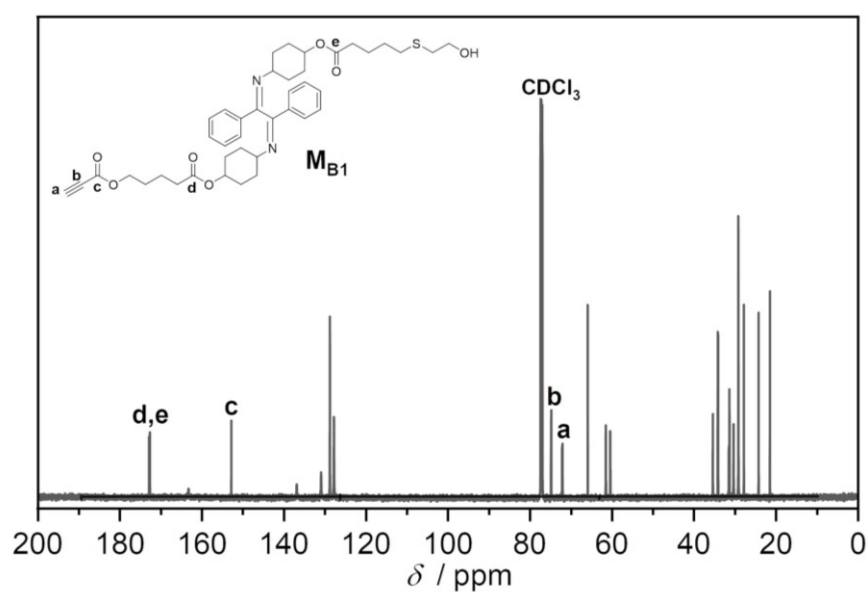
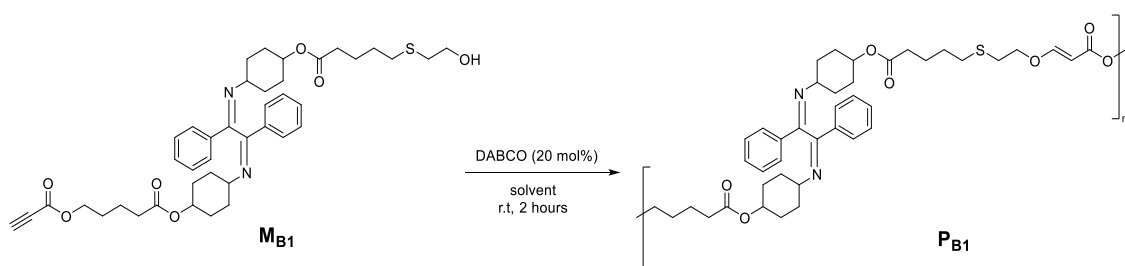


Figure S3.26. ^{13}C NMR spectrum of M_{B1} in $CDCl_3$.

11.3.10. Synthesis of polymer P_{B1}



General protocol: Monomer M_{B1} (100-150 mg) was dissolved in a chosen solvent (either DCM or THF, 0.4 M or 0.8 M). Following that, DABCO (20 mol%) was quickly added to the solution. Note that the reaction is exothermic. The reaction was carried out for 2 hours and then a small amount of sample was taken for SEC measurement. After 24 hours, sample was taken again for SEC measurement.

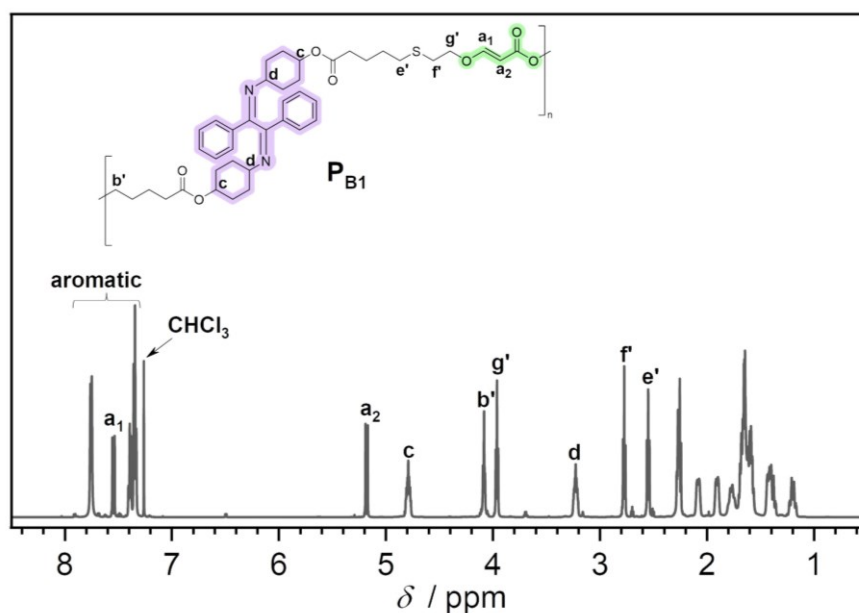


Figure S3.27. 1H NMR spectrum (600 MHz) of P_{B1} in $CDCl_3$.

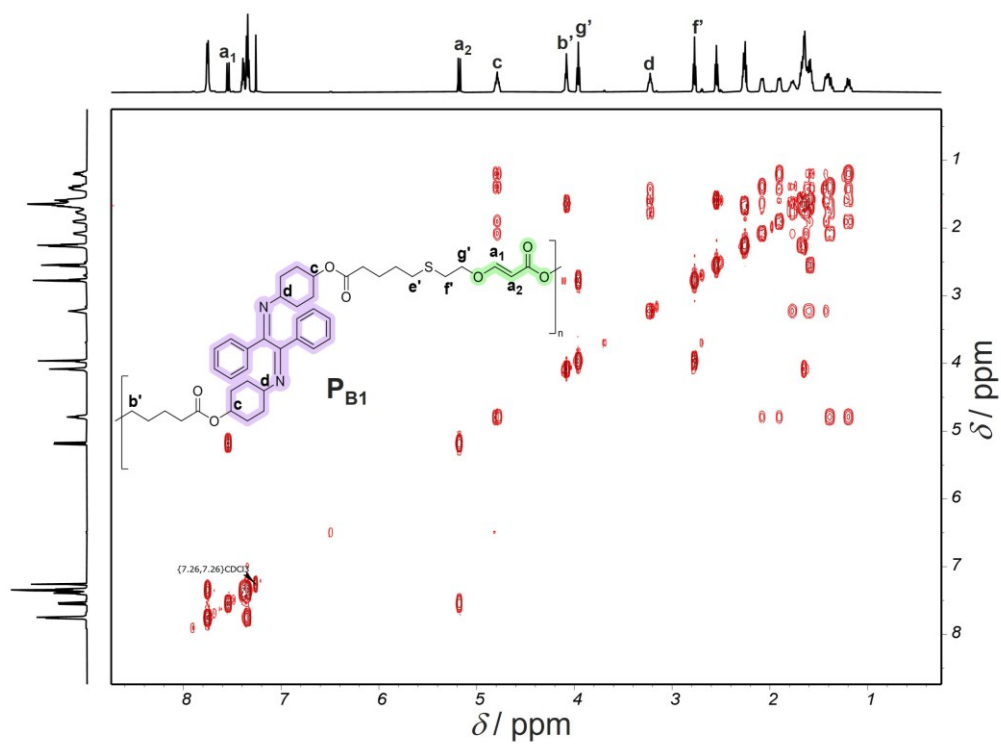


Figure S3.28. COSY NMR spectrum of P_{B1} in $CDCl_3$.

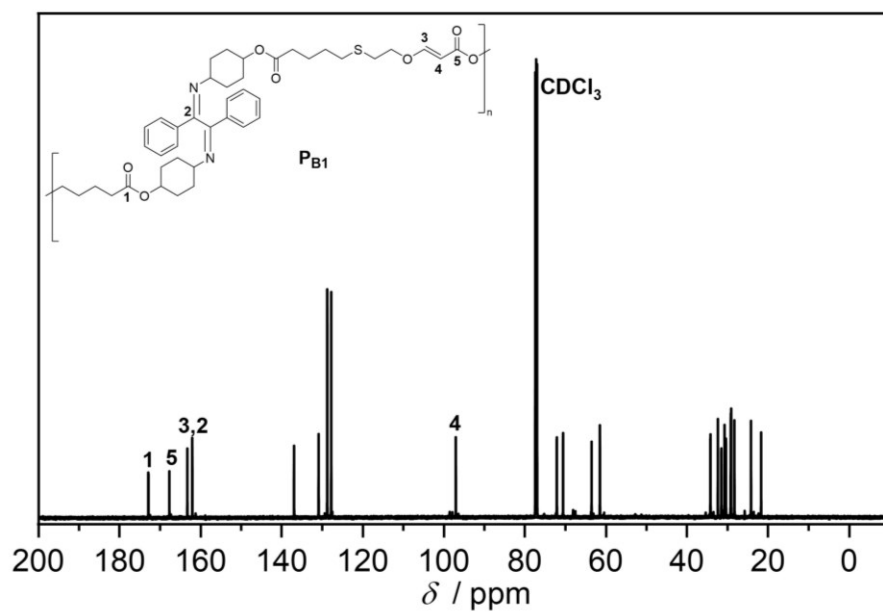


Figure S3.29. ^{13}C NMR spectrum of P_{B1} in $CDCl_3$.

11.4. Information for Chapter 4

11.4.1. Synthesis protocol

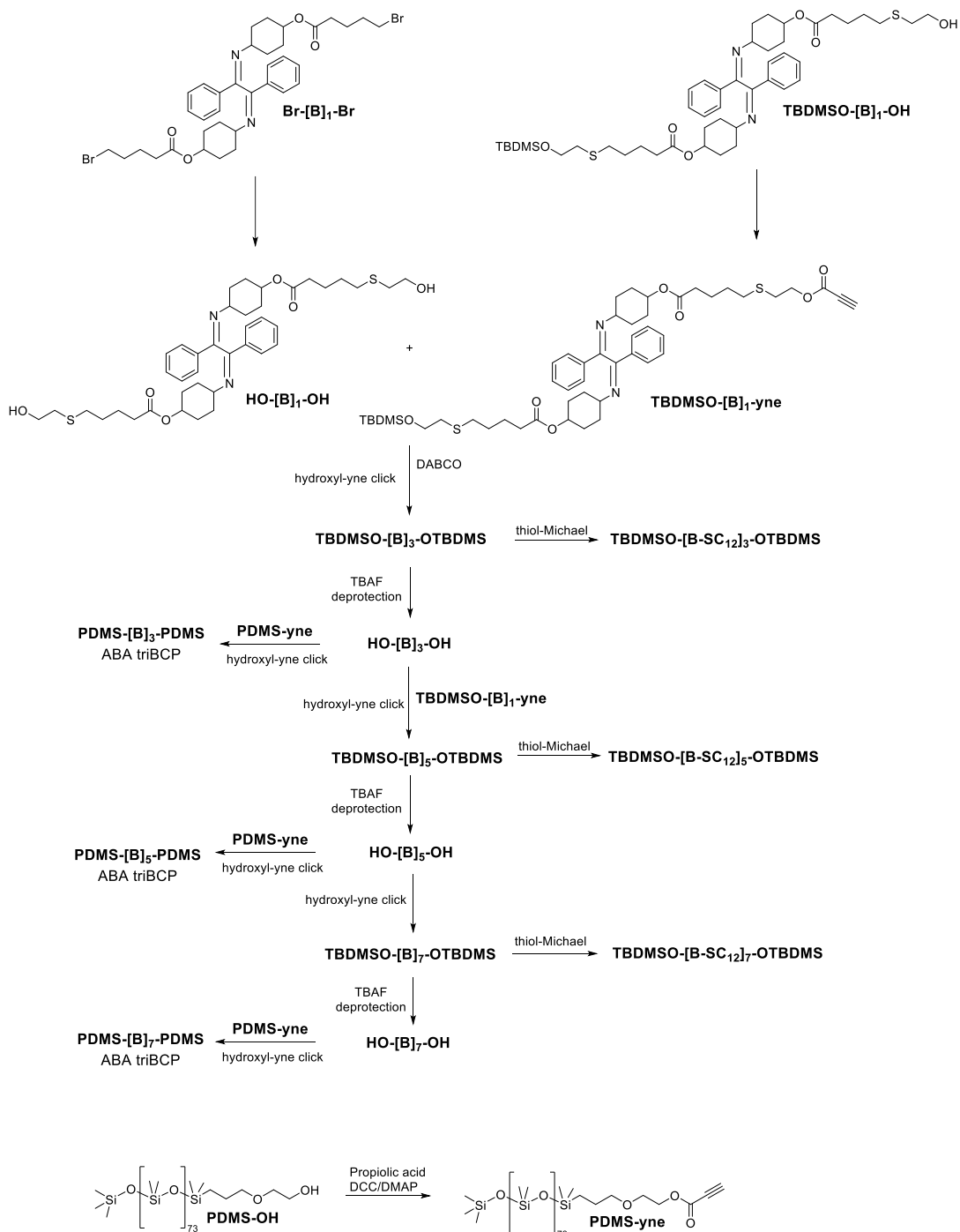
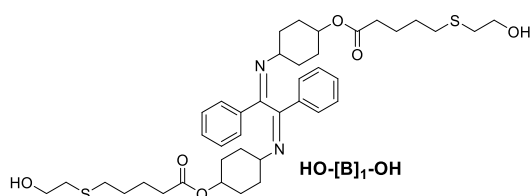


Figure S4.1. Synthesis route for odd-numbered sequences of main-chain α -bisimine, the thiol-Michael modified sequences, and ABA triblock copolymers.

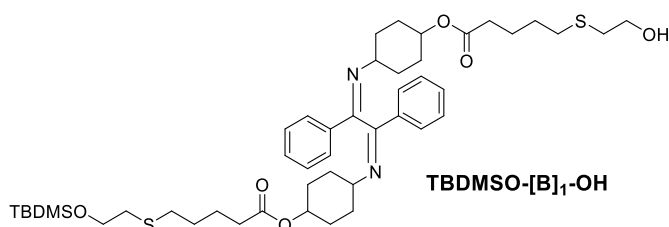
11.4.1.1. Synthesis of HO-[B]₁-OH



Br-[B]₁-Br (reported in chapter 3)¹⁹⁵ (15 g, 20.5 mmol, 1.0 eq) and 2-mercaptoethanol (4.3 mL, 3.0 eq) were dissolved in DMF (40 mL) at room temperature. Subsequently, Cs₂CO₃ (10 g, 1.5 eq) was added to the solution. The resulting mixture was stirred overnight. Upon completion, the reaction mixture was diluted in ethyl acetate (EtOAc) (250 mL) and was washed with water and brine (3 times) to remove DMF and salts. The organic phase (EtOAc) was then dried with Na₂SO₄ and concentrated under reduced pressure. The crude was purified via flash column chromatography (EtOAc:cyclohexane (Cy), 20/80 to 99/1, v/v), yielding 13 g sticky oil as product (87% purification yield).

¹H NMR (600 MHz, CDCl₃) δ 7.77 – 7.72 (m, 4H), 7.41 – 7.29 (m, 6H), 4.78 (tt, *J* = 10.2, 4.2 Hz, 2H), 3.68 (t, *J* = 6.0 Hz, 4H), 3.21 (tt, *J* = 9.6, 3.9 Hz, 2H), 2.68 (t, *J* = 6.1 Hz, 4H), 2.49 (t, *J* = 7.2 Hz, 4H), 2.24 (t, *J* = 7.3 Hz, 4H), 2.11 – 2.04 (m, 2H), 1.93 – 1.85 (m, 2H), 1.76 (tdd, *J* = 13.0, 9.7, 3.6 Hz, 2H), 1.71 – 1.53 (m, 12H), 1.45 – 1.33 (m, 4H), 1.19 (tdd, *J* = 12.4, 10.3, 3.8 Hz, 2H). **¹³C NMR** (151 MHz, CDCl₃) δ 173.45, 172.89, 163.26, 136.80, 130.84, 128.69, 127.70, 77.37, 77.16, 76.95, 72.03, 61.42, 60.49, 60.42, 35.24, 34.13, 31.41, 31.32, 30.28, 29.09, 24.15. **LC-MS**: calculated *m/z* for C₄₀H₅₇N₂O₆S₂⁺ [*M*+*H*⁺] = 725.3653, found 725.3648.

11.4.1.2. Synthesis of TBDMSO-[B]₁-OH

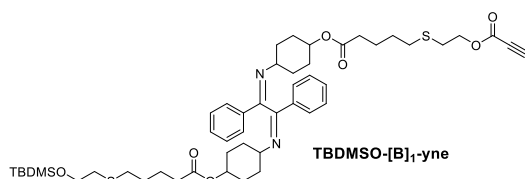


HO-[B]₁-OH (10 g, 13.8 mmol, 1.0 eq) and imidazole (2.8 g, 41.4 mmol, 3 eq) were dissolved in dry DMF (28 mL). Next, TBDMSO (2.1 g, 13.8 mmol, 1.0 eq) was added in a portion-wise manner to the reaction solution. After 4 h of reaction, the mixture was diluted in EtOAc (200 mL) and extracted with water and brine (3 times). The organic phase was dried with Na₂SO₄ and concentrated at reduced pressure. The residue was purified via flash column chromatography (EtOAc: Cy, 1:99-80:20, v/v). The product was obtained as an oil (~ 4 g, 34% yield).

¹H NMR (600 MHz, CDCl₃) δ 7.78 – 7.69 (m, 4H), 7.41 – 7.29 (m, 6H), 4.82 – 4.74 (m, 2H), 3.76 – 3.64 (m, 4H), 3.21 (ddt, *J* = 9.4, 6.9, 3.5 Hz, 2H), 2.67 (q, *J* = 5.8 Hz, 2H), 2.60 (qd, *J* = 5.8, 2.4 Hz, 2H), 2.56 – 2.46 (m, 4H), 2.24 (tt, *J* = 7.3, 3.6 Hz, 4H), 2.08 (dt, *J* = 14.3, 4.7 Hz, 2H), 1.94 – 1.85 (m, 2H), 1.75 (tdd, *J* = 12.9, 8.6, 3.5 Hz, 2H), 1.70 – 1.53 (m, 12H), 1.45 – 1.33 (m, 4H), 1.26 – 1.14 (m, 2H), 0.90 – 0.84 (m, 9H), 0.08 – 0.01 (m, 6H). **¹³C NMR** (151 MHz, CDCl₃) δ 172.86, 172.81, 163.20, 163.18, 136.86, 130.78, 128.65, 127.68, 77.38, 77.35, 77.16, 77.14, 76.95, 76.93, 72.00, 71.94, 63.45, 61.39, 60.42, 60.37, 35.29, 35.24, 34.44, 34.20, 34.12, 32.21, 31.42, 31.32, 31.30, 30.28, 29.25, 29.10, 29.07, 26.06, 25.97, 24.20,

24.15, 18.37, -5.21. **LC-MS**: calculated m/z for $C_{46}H_{71}N_2O_6S_2Si^+$ $[M+H]^+$ = 839.4518, found 839.4504.

11.4.1.3. Synthesis of TBDMSO-[B]₁-yne

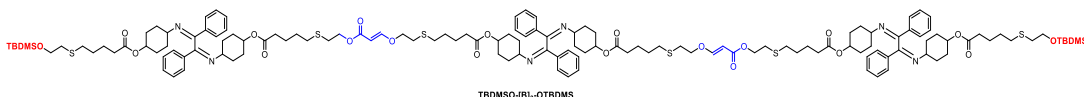


TBDMSO-[B]₁-OH (2.0 g, 2.38 mmol, 1.0 eq) and propiolic acid (0.3 mL, 4.77 mmol, 2.0 eq) were dissolved in $CHCl_3$ (2.5 mL). A mixture of DCC (984 mg, 4.77 mmol, 2.0 eq) and DMAP (29 mg, 0.24 mmol, 10 mol%) in 3 mL $CHCl_3$

was added slowly to the reaction mixture over 10 minutes. The reaction was stopped after 3 h. The crude was purified immediately via flash column chromatography (EtOAc:Cy, 1:99-50:50, v/v), yielding a pale yellow oil as product (1.5 g, 70%).

¹H NMR (600 MHz, $CDCl_3$) δ 7.72 – 7.67 (m, 4H), 7.35 – 7.25 (m, 6H), 4.74 (dddd, J = 10.3, 6.2, 4.2, 2.1 Hz, 2H), 4.25 (t, J = 7.0 Hz, 2H), 3.68 (t, J = 7.1 Hz, 2H), 3.18 (tt, J = 9.5, 3.9 Hz, 2H), 2.84 (s, 1H), 2.69 (t, J = 7.0 Hz, 2H), 2.55 (t, J = 7.1 Hz, 2H), 2.49 (dt, J = 10.3, 7.2 Hz, 4H), 2.20 (td, J = 7.4, 5.3 Hz, 4H), 2.07 – 1.99 (m, 2H), 1.85 (dd, J = 13.1, 4.4 Hz, 2H), 1.71 (tdd, J = 13.0, 9.5, 3.6 Hz, 2H), 1.66 – 1.50 (m, 12H), 1.37 (s, 4H), 1.21 – 1.10 (m, 2H), 0.83 (s, 9H), 0.00 (s, 6H). **¹³C NMR** (101 MHz, $CDCl_3$) δ 172.90, 172.82, 163.21, 152.47, 136.91, 130.82, 128.71, 127.72, 77.48, 77.36, 77.16, 76.84, 75.30, 74.52, 72.05, 71.99, 65.19, 63.49, 61.44, 53.54, 34.49, 34.25, 34.16, 32.27, 32.04, 31.48, 30.35, 30.05, 29.30, 29.13, 29.02, 24.25, 24.15, 18.43, -5.16. **LC-MS**: calculated m/z for $C_{49}H_{71}N_2O_7S_2Si^+$ $[M+H]^+$ = 891.4467, found 891.4452.

11.4.1.4. Synthesis of TBDMSO-[B]₃-OTBDMS

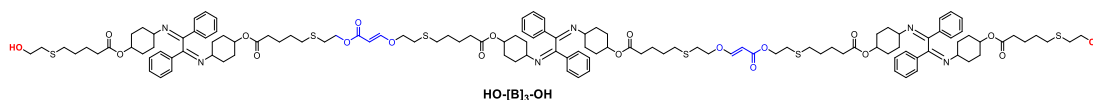


HO-[B]₁-OH (300 mg, 0.41 mmol, 1.0 eq) and **TBDMSO-[B]₁-yne** (774 mg, 0.87 mmol, 2.1 eq) were dissolved in dichloromethane (DCM) (2.2 mL). DABCO (18.6 mg, 0.165 mmol, 20 mol% with respect to the OH functional group) was quickly added to the reaction solution. The reaction was stopped after 30 minutes. The crude mixture was immediately purified via flash column chromatography (EtOAc:Cy, 1:99-80:20, v/v), yielding 900 mg product (87% purification yield).

¹H NMR (600 MHz, $CDCl_3$) δ 7.79 – 7.70 (m, 12H), 7.57 (s, 12H), 7.42 – 7.32 (m, 18H), 5.20 (s, 2H), 4.79 (tt, J = 9.8, 4.2 Hz, 6H), 4.23 (t, J = 7.1 Hz, 4H), 3.98 (t, J = 6.7 Hz, 4H), 3.73 (t, J = 7.2 Hz, 4H), 3.22 (tt, J = 9.6, 4.0 Hz, 6H), 2.78 (t, J = 6.7 Hz, 4H), 2.72 (t, J = 7.0 Hz, 4H), 2.61 (t, J = 7.1 Hz, 4H), 2.58 – 2.51 (m, 12H), 2.25 (ddt, J = 9.8, 4.5, 2.3 Hz, 12H), 2.11 – 2.05 (m, 6H), 1.94 – 1.86 (m, 6H), 1.81 – 1.72 (m, 6H), 1.71 – 1.52 (m, 26H), 1.46 – 1.35 (m, 12H), 1.20 (qd, J = 12.8, 3.8 Hz, 6H), 0.88 (d, J = 0.8 Hz, 18H), 0.05 (d, J = 0.8 Hz, 12H). **¹³C NMR** (151 MHz, $CDCl_3$) δ 172.93, 172.88, 172.83, 167.41, 163.25, 162.40, 136.94, 130.86, 128.74,

127.76, 96.75, 77.37, 77.16, 76.95, 72.09, 72.05, 72.02, 70.66, 63.52, 63.00, 61.47, 34.52, 34.28, 34.22, 34.17, 32.38, 32.29, 31.99, 31.51, 30.72, 30.37, 29.33, 29.17, 29.15, 29.10, 29.08, 27.04, 26.04, 24.28, 24.22, 24.17, 18.45, -5.13. **SEC-ESI-MS**: calculated m/z for $C_{138}H_{196}K_2N_6O_{20}S_6Si_2^{2+}$ $[M+2K^+] = 1292.0832$, found 1292.1051.

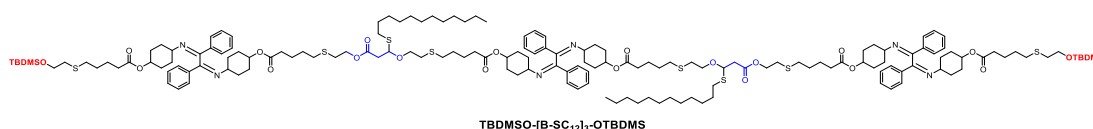
11.4.1.5. Synthesis of HO-[B]₃-OH



TBAF 1M solution (4.8 mL, 15 eq) was added to **TBDMSO-[B]₃-OTBDMS** (800 mg, 0.32 mmol, 1.0 eq) and the resulting solution was stirred at ambient temperature for 30 minutes. The reaction mixture was subsequently diluted in DCM and extracted with water (2 times). The organic phase was then dried with Na₂SO₄, and concentrated at reduced pressure. The residue was purified via flash column chromatography (DCM:EtOAc, 100% DCM to 50% DCM), yielding the product (600 mg, 83% purification yield).

¹H NMR (600 MHz, CDCl₃) δ 7.77 – 7.72 (m, 12H), 7.57 (d, $J = 12.6$ Hz, 2H), 7.41 – 7.31 (m, 18H), 5.20 (d, $J = 12.6$ Hz, 2H), 4.83 – 4.75 (m, 6H), 4.23 (t, $J = 7.0$ Hz, 4H), 3.97 (t, $J = 6.7$ Hz, 4H), 3.69 (q, $J = 5.8$ Hz, 4H), 3.22 (tt, $J = 9.6, 3.8$ Hz, 6H), 2.77 (t, $J = 6.7$ Hz, 4H), 2.75 – 2.67 (m, 8H), 2.54 (td, $J = 7.2, 2.6$ Hz, 8H), 2.50 (t, $J = 7.2$ Hz, 4H), 2.28 – 2.23 (m, 12H), 2.11 – 2.04 (m, 6H), 1.90 (dd, $J = 13.3, 4.6$ Hz, 6H), 1.76 (tdd, $J = 13.0, 9.5, 3.6$ Hz, 6H), 1.71 – 1.54 (m, 36H), 1.45 – 1.34 (m, 12H), 1.24 – 1.15 (m, 6H). **SEC-ESI-MS**: calculated m/z for $C_{126}H_{168}KN_6O_{20}S_6^+$ $[M+K^+] = 2317.0303$, found 2317.0536.

Synthesis of TBDMSO-[B-SC₁₂]₃-OTBDMS

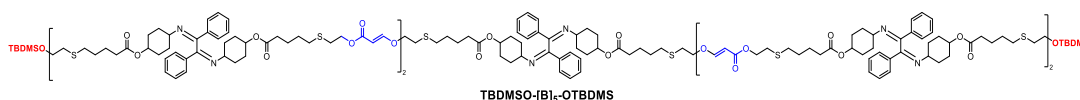


TBDMSO-[B]₃-OTBDMS (100 mg, 0.08 mmol of ether acrylate, 1.0 eq) and 1-dodecanethiol (0.19 mL, 10 eq) were dissolved in THF (0.16 mL). The NHC catalyst, 1,3-bis(2,6-diisopropylphenyl)imidazol-2-ylidene, (3.0 mg, 10 mol%) was then added. A crude NMR was recorded after 3 h of reaction to check the conversion (100% conversion). Upon completion, the reaction mixture was diluted in DCM and washed with saturated NaHCO₃ solution (2 times). The residue was concentrated and then precipitated in methanol to obtain pure product (90% purification yield). Note that the number of the alkyl side chain is less than that of α -bisimine units by one unit.

¹H NMR (600 MHz, CDCl₃) δ 7.77 – 7.73 (m, 12H), 7.41 – 7.32 (m, 18H), 4.89 (dd, $J = 8.2, 5.6$ Hz, 2H), 4.79 (tdd, $J = 9.4, 7.7, 3.9$ Hz, 6H), 4.27 – 4.16 (m, 4H), 3.86 (dt, $J = 9.7, 6.9$ Hz, 2H), 3.73 (t, $J = 7.1$ Hz, 4H), 3.57 (dt, $J = 9.7, 6.7$ Hz, 2H), 3.23 (ddt, $J = 13.6, 9.3, 3.9$ Hz, 6H), 2.91 (dd, $J = 15.4, 8.2$ Hz, 2H), 2.76 (dd, $J = 15.4, 5.6$ Hz, 2H), 2.71 (t, $J = 7.0$ Hz, 4H), 2.65

(td, $J = 6.7, 1.8$ Hz, 4H), 2.61 (t, $J = 7.1$ Hz, 4H), 2.59 – 2.50 (m, 16H), 2.27 – 2.22 (m, 12H), 2.12 – 2.04 (m, 6H), 1.94 – 1.87 (m, 7H), 1.81 – 1.72 (m, 7H), 1.71 – 1.53 (m, 36H), 1.39 (dddd, $J = 31.5, 18.9, 9.7, 5.1$ Hz, 16H), 1.31 – 1.15 (m, 40H), 0.90 – 0.85 (m, 24H), 0.05 (s, 12H). ^{13}C NMR (151 MHz, CDCl_3) δ 172.94, 172.88, 172.85, 169.78, 163.26, 136.96, 130.85, 128.74, 127.76, 81.52, 77.37, 77.16, 76.95, 72.08, 72.05, 72.03, 67.36, 63.76, 63.53, 61.48, 53.56, 41.98, 39.37, 34.53, 34.29, 34.24, 34.20, 32.30, 32.25, 32.05, 32.01, 31.53, 31.45, 30.48, 30.38, 30.16, 29.79, 29.76, 29.74, 29.72, 29.67, 29.65, 29.48, 29.35, 29.34, 29.30, 29.21, 29.18, 29.16, 29.10, 28.00, 26.04, 24.29, 24.26, 24.21, 22.82, 18.46, 14.27, 14.25, -5.13.

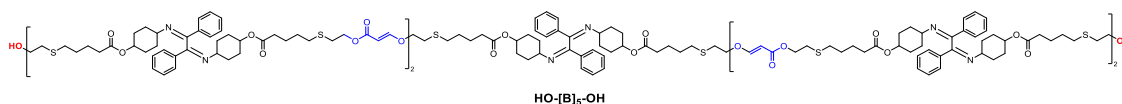
11.4.1.6. Synthesis of TBDMSO-[B]₅-OTBDMS



The synthesis protocol for **TBDMSO-[B]₅-OTBDMS** is similar to that for **TBDMSO-[B]₃-OTBDMS**. Accordingly, **HO-[B]₃-OH** (1.0 eq) reacts with **TBDMSO-[B]₁-yne** (2.1 eq) upon addition of 20 mol% of DABCO base in DCM (0.4 M) for 30 minutes. The crude mixture was purified via column chromatography (DCM:EtOAc, 100% DCM to 20% DCM) (87% purification yield).

^1H NMR (600 MHz, CDCl_3) δ 7.77 – 7.73 (m, 20H), 7.57 (d, $J = 12.6$ Hz, 4H), 7.42 – 7.31 (m, 30H), 5.20 (d, $J = 12.6$ Hz, 4H), 4.79 (tt, $J = 9.8, 4.2$ Hz, 10H), 4.23 (t, $J = 7.0$ Hz, 8H), 3.97 (t, $J = 6.7$ Hz, 8H), 3.73 (t, $J = 7.1$ Hz, 4H), 3.22 (tt, $J = 9.6, 3.9$ Hz, 10H), 2.78 (t, $J = 6.7$ Hz, 8H), 2.72 (t, $J = 7.0$ Hz, 8H), 2.61 (t, $J = 7.1$ Hz, 4H), 2.57 – 2.51 (m, 20H), 2.25 (ddd, $J = 9.7, 5.8, 2.2$ Hz, 20H), 2.08 (dq, $J = 9.1, 4.5$ Hz, 10H), 1.90 (dt, $J = 13.4, 4.6$ Hz, 10H), 1.81 – 1.72 (m, 10H), 1.71 – 1.54 (m, 50H), 1.46 – 1.34 (m, 20H), 1.20 (tdd, $J = 12.7, 10.1, 3.8$ Hz, 10H), 0.88 (s, 18H), 0.05 (s, 12H). ^{13}C NMR (151 MHz, CDCl_3) δ 172.82, 172.77, 172.72, 167.30, 163.14, 162.29, 136.82, 130.75, 128.62, 127.64, 96.63, 77.26, 77.05, 76.84, 71.98, 71.94, 71.90, 70.55, 63.41, 62.88, 61.35, 34.40, 34.17, 34.10, 34.06, 32.26, 32.18, 31.88, 31.39, 30.61, 30.26, 29.22, 29.06, 29.04, 28.99, 28.96, 25.93, 24.17, 24.11, 24.06, 18.34, -5.24. **SEC-ESI-MS**: calculated m/z for $\text{C}_{224}\text{H}_{308}\text{K}_2\text{N}_{10}\text{O}_{34}\text{S}_{10}\text{Si}_2^{2+}$ [$\text{M}+2\text{K}^+$] = 2068.9378, found 2068.9540.

11.4.1.7. Synthesis of HO-[B]₅-OH

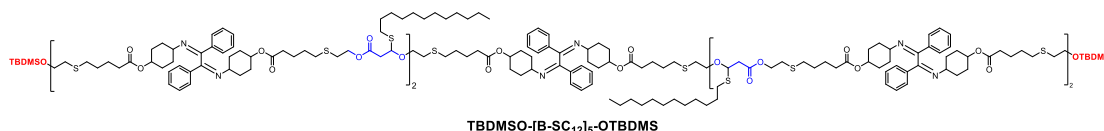


The deprotection protocol is similar to that for **HO-[B]₃-OH**. Accordingly, TBAF 1M solution (15 eq) was added to **TBDMSO-[B]₅-OTBDMS** (1.0 eq) and the resulting solution was stirred at ambient temperature for 30 minutes. The reaction mixture was then diluted in DCM and extracted with water (2 times). The organic phase was subsequently dried with Na_2SO_4 and

concentrated at reduced pressure. The residue was purified via flash column chromatography (DCM:EtOAc, 100% DCM to 20% DCM) to obtain the product (80% purification yield).

¹H NMR (600 MHz, CDCl₃) δ 7.77 – 7.72 (m, 20H), 7.56 (d, J = 12.6 Hz, 4H), 7.41 – 7.31 (m, 30H), 5.20 (d, J = 12.6 Hz, 4H), 4.78 (ddt, J = 11.0, 7.9, 4.1 Hz, 10H), 4.22 (t, J = 7.0 Hz, 8H), 3.97 (t, J = 6.7 Hz, 8H), 3.69 (t, J = 6.0 Hz, 4H), 3.22 (ddt, J = 13.6, 9.3, 3.9 Hz, 10H), 2.77 (t, J = 6.7 Hz, 8H), 2.72 (t, J = 7.0 Hz, 8H), 2.69 (t, J = 6.0 Hz, 4H), 2.54 (td, J = 7.2, 2.6 Hz, 16H), 2.50 (t, J = 7.2 Hz, 4H), 2.28 – 2.22 (m, 20H), 2.11 – 2.04 (m, 10H), 1.91 (dt, J = 13.4, 4.1 Hz, 10H), 1.76 (tdd, J = 13.1, 9.6, 3.4 Hz, 10H), 1.72 – 1.54 (m, 60H), 1.40 (dddd, J = 22.9, 15.7, 7.5, 3.3 Hz, 20H), 1.24 – 1.16 (m, 10H). **¹³C NMR** (151 MHz, CDCl₃) δ 172.78, 172.73, 167.31, 163.15, 162.30, 136.81, 130.75, 128.62, 127.64, 96.63, 77.27, 77.06, 76.85, 71.98, 71.94, 70.56, 62.89, 61.35, 60.29, 53.45, 35.26, 34.10, 34.08, 34.06, 32.26, 31.87, 31.39, 31.23, 30.61, 30.26, 29.06, 29.04, 28.98, 28.96, 24.11, 24.05. **SEC-ESI-MS**: calculated m/z for C₂₁₂H₂₈₀K₂N₁₀O₃₄S₁₀²⁺ [M+2K⁺] = 1954.8513, found 1954.8740.

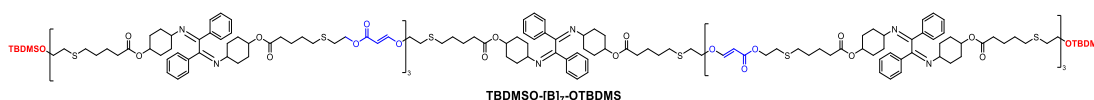
11.4.1.8. Synthesis of TBDMSO-[B-SC₁₂]₅-OTBDMS



The synthesis protocol is similar to that for **TBDMSO-[B-SC₁₂]₃-OTBDMS**. Accordingly, **TBDMSO-[B]₅-OTBDMS** (1.0 eq of ether acrylate bond) and 1-dodecanethiol (10 eq) were dissolved in THF (0.5M of ether acrylate bonds). The NHC catalyst, 1,3-bis(2,6-diisopropylphenyl)imidazol-2-ylidene, (10 mol%) was added. A crude NMR was recorded after 3 h of reaction to determine the conversion (close to 100% conversion). Upon completion, the reaction mixture was diluted in DCM and washed with saturated NaHCO₃ solution (2 times). The residue was concentrated and then precipitated in methanol to obtain pure product (85% purification yield).

¹H NMR (600 MHz, CDCl₃) δ 7.77 – 7.72 (m, 20H), 7.40 – 7.30 (m, 30H), 4.88 (dd, J = 8.2, 5.6 Hz, 4H), 4.78 (ddt, J = 10.3, 6.5, 3.1 Hz, 10H), 4.26 – 4.16 (m, 8H), 3.85 (dt, J = 9.7, 6.8 Hz, 4H), 3.73 (t, J = 7.1 Hz, 4H), 3.57 (dt, J = 9.7, 6.7 Hz, 4H), 3.22 (ddt, J = 13.7, 9.2, 3.9 Hz, 10H), 2.90 (dd, J = 15.4, 8.3 Hz, 4H), 2.76 (dd, J = 15.5, 5.6 Hz, 4H), 2.71 (t, J = 7.0 Hz, 8H), 2.68 – 2.63 (m, 10H), 2.62 – 2.48 (m, 36H), 2.24 (ddd, J = 9.1, 5.2, 2.1 Hz, 20H), 2.10 – 2.04 (m, 10H), 1.90 (dd, J = 13.2, 4.5 Hz, 10H), 1.76 (tdd, J = 13.1, 9.7, 3.6 Hz, 10H), 1.70 – 1.53 (m, 50H), 1.45 – 1.33 (m, 30H), 1.26 (dd, J = 9.0, 4.2 Hz, 84H), 0.89 – 0.85 (m, 30H), 0.05 (s, 12H). **¹³C NMR** (151 MHz, CDCl₃) δ 172.90, 172.85, 172.81, 169.75, 163.23, 136.93, 130.82, 128.70, 127.73, 81.49, 77.37, 77.16, 76.95, 72.05, 72.02, 72.00, 67.34, 63.73, 63.50, 61.44, 41.95, 39.33, 34.50, 34.26, 34.21, 34.16, 32.27, 32.22, 32.01, 31.98, 31.50, 31.42, 30.45, 30.35, 30.13, 29.76, 29.73, 29.71, 29.69, 29.64, 29.62, 29.45, 29.34, 29.32, 29.30, 29.24, 29.18, 29.14, 29.07, 28.63, 28.49, 27.97, 26.02, 24.79, 24.76, 24.26, 24.23, 24.18, 22.79, 18.43, 14.24, 14.23, -5.15.

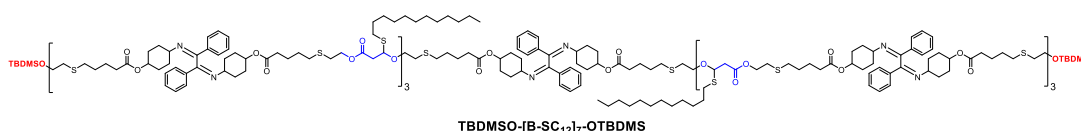
11.4.1.9. Synthesis of TBDMSO-[B]₇-OTBDMS



The synthesis protocol for **TBDMSO-[B]₇-OTBDMS** is similar to that for **TBDMSO-[B]₃-OTBDMS** and **TBDMSO-[B]₅-OTBDMS**. Accordingly, **HO-[B]₅-OH** (1.0 eq) reacts with **TBDMSO-[B]₁-yne** (2.1 eq) upon addition of 20 mol% of DABCO base in DCM (0.4 M) for 30 minutes. The crude mixture was purified via column chromatography (DCM:EtOAc, 100% DCM to 0% DCM) (90% purification yield).

¹H NMR (600 MHz, CDCl₃) δ 7.77 – 7.72 (m, 28H), 7.57 (d, J = 12.6 Hz, 6H), 7.42 – 7.31 (m, 42H), 5.20 (d, J = 12.6 Hz, 6H), 4.78 (td, J = 9.6, 4.5 Hz, 14H), 4.23 (t, J = 7.0 Hz, 12H), 3.97 (t, J = 6.7 Hz, 12H), 3.73 (t, J = 7.1 Hz, 4H), 3.22 (tt, J = 9.7, 3.9 Hz, 14H), 2.78 (t, J = 6.7 Hz, 12H), 2.72 (t, J = 7.0 Hz, 12H), 2.61 (t, J = 7.1 Hz, 4H), 2.55 (td, J = 7.2, 2.5 Hz, 28H), 2.25 (tt, J = 7.5, 2.2 Hz, 28H), 2.12 – 2.03 (m, 14H), 1.90 (dt, J = 9.2, 5.3 Hz, 14H), 1.76 (tdd, J = 13.1, 9.6, 3.6 Hz, 14H), 1.71 – 1.54 (m, 84H), 1.40 (ddt, J = 22.2, 12.5, 6.6 Hz, 28H), 1.20 (tdd, J = 12.7, 10.1, 3.8 Hz, 14H), 0.88 (s, 18H), 0.05 (s, 12H). **¹³C NMR** (151 MHz, CDCl₃) δ 172.93, 172.87, 172.82, 167.40, 163.24, 162.40, 136.94, 130.85, 128.73, 127.75, 96.74, 77.37, 77.16, 76.95, 72.09, 72.05, 72.02, 70.66, 63.51, 62.99, 61.46, 53.55, 34.51, 34.28, 34.21, 34.17, 32.37, 32.29, 31.99, 31.56, 31.51, 30.72, 30.37, 30.31, 29.32, 29.17, 29.15, 29.10, 29.07, 26.03, 24.27, 24.22, 24.16, 18.45, -5.14. **SEC-ESI-MS**: calculated m/z for C₃₁₀H₄₂₀K₂N₁₄O₄₈S₁₄Si₂²⁺ [M+2K⁺] = 2845.7924, found 2845.8198.

11.4.1.10. Synthesis of TBDMSO-[B-SC₁₂]₇-OTBDMS

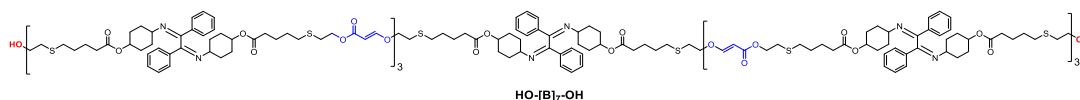


The synthesis protocol is similar to that for **TBDMSO-[B-SC₁₂]₅-OTBDMS**. Accordingly, **TBDMSO-[B]₇-OTBDMS** (1.0 eq of ether acrylate bond) and 1-dodecanethiol (10 eq) were dissolved in THF (0.5M of ether acrylate bonds). The NHC catalyst, 1,3-bis(2,6-diisopropylphenyl)imidazol-2-ylidene, (10 mol%) was added. A crude NMR was recorded after 3 h of reaction to determine the conversion (close 100% conversion). Upon completion, the reaction mixture was diluted in DCM and washed with saturated NaHCO₃ solution (2 times). The residue was concentrated and then precipitated in methanol to obtain pure product.

¹H NMR (600 MHz, CDCl₃) δ 7.76 – 7.73 (m, 28H), 7.40 – 7.31 (m, 42H), 4.88 (dd, J = 8.2, 5.6 Hz, 6H), 4.78 (dp, J = 14.1, 4.3 Hz, 14H), 4.26 – 4.16 (m, 12H), 3.85 (dt, J = 9.7, 6.8 Hz, 6H), 3.73 (t, J = 7.1 Hz, 4H), 3.57 (dt, J = 9.7, 6.7 Hz, 6H), 3.22 (ddt, J = 13.7, 9.3, 3.9 Hz, 14H), 2.90 (dd, J = 15.5, 8.3 Hz, 6H), 2.76 (dd, J = 15.4, 5.6 Hz, 6H), 2.70 (t, J = 7.0 Hz, 12H), 2.68 – 2.62 (m, 14H), 2.61 – 2.48 (m, 60H), 2.24 (td, J = 7.3, 2.4 Hz, 28H), 2.11 – 2.04 (m, 14H), 1.89 (dt, J = 13.4, 4.5 Hz, 14H), 1.76 (tdd, J = 13.1, 9.8, 3.6 Hz, 18H), 1.70 – 1.53 (m,

64H), 1.44 – 1.33 (m, 40H), 1.30 – 1.15 (m, 120H), 0.89 – 0.85 (m, 36H), 0.05 (s, 12H). ^{13}C NMR (151 MHz, CDCl_3) δ 172.88, 172.83, 172.79, 169.73, 163.22, 136.93, 130.81, 128.69, 127.72, 81.48, 77.37, 77.16, 76.95, 72.04, 72.01, 71.99, 67.33, 63.72, 63.50, 61.43, 41.94, 39.32, 34.49, 34.25, 34.20, 34.16, 32.26, 32.21, 32.01, 31.97, 31.89, 31.49, 31.41, 30.44, 30.41, 30.35, 30.29, 30.13, 29.79, 29.75, 29.75, 29.73, 29.70, 29.69, 29.64, 29.62, 29.44, 29.34, 29.31, 29.30, 29.24, 29.17, 29.14, 29.06, 28.63, 28.48, 27.96, 26.01, 24.79, 24.75, 24.22, 24.17, 22.78, 14.24, 14.22, -5.16.

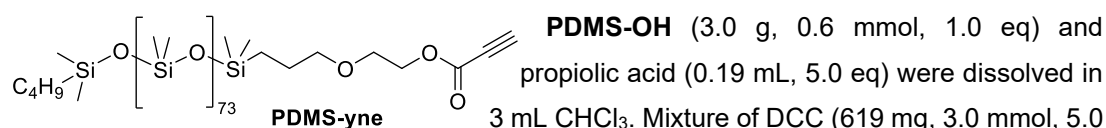
11.4.1.11. Synthesis of HO-[B]₇-OH



The deprotection protocol is similar to that for HO-[B]₃-OH and HO-[B]₅-OH. Accordingly, TBAF 1 M solution (15 eq) was added to TBDMSO-[B]₇-OTBDMS (1.0 eq) and the resulting solution was stirred at ambient temperature for 30 minutes. The reaction mixture was then diluted in DCM and extracted with water (2 times). The organic phase was subsequently dried with Na_2SO_4 and concentrated at reduced pressure. The residue was purified via flash column chromatography (DCM:EtOAc, 100% DCM to 0% DCM) to obtain the product.

^1H NMR (600 MHz, CDCl_3) δ 7.86 – 7.67 (m, 28H), 7.57 (dd, J = 12.5, 0.6 Hz, 6H), 7.44 – 7.32 (m, 42H), 5.20 (d, J = 12.6 Hz, 6H), 4.79 (q, J = 8.5 Hz, 14H), 4.23 (td, J = 7.0, 0.8 Hz, 12H), 3.98 (t, J = 6.7 Hz, 12H), 3.70 (q, J = 5.7 Hz, 4H), 3.28 – 3.18 (m, 14H), 2.78 (t, J = 6.7 Hz, 12H), 2.75 – 2.69 (m, 16H), 2.55 (td, J = 7.2, 2.8 Hz, 28H), 2.51 (t, J = 7.2 Hz, 4H), 2.26 (tt, J = 7.5, 2.0 Hz, 28H), 2.12 – 2.06 (m, 14H), 1.94 – 1.88 (m, 14H), 1.84 – 1.73 (m, 14H), 1.72 – 1.55 (m, 80H), 1.46 – 1.35 (m, 28H), 1.20 (q, J = 12.0 Hz, 14H).

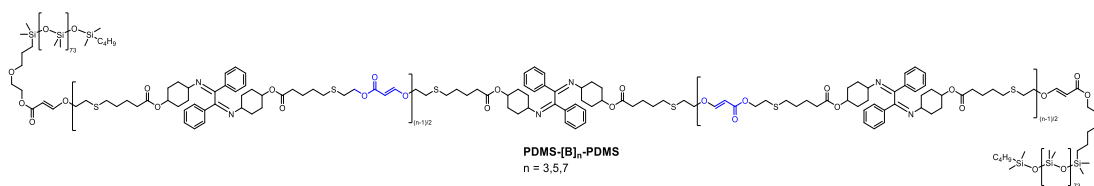
11.4.1.12. Synthesis of PDMS-yne



PDMS-OH (3.0 g, 0.6 mmol, 1.0 eq) and propionic acid (0.19 mL, 5.0 eq) were dissolved in 3 mL CHCl_3 . Mixture of DCC (619 mg, 3.0 mmol, 5.0 eq) and DMAP (7.3 mg, 10 mol%) in CHCl_3 (3 mL) was added slowly over 15 minutes to the reaction. After 3 h, the crude mixture was passed through a short SiO_2 column three times with DCM as the eluent to purify the product (70% purification yield).

^1H NMR (600 MHz, CDCl_3) δ 4.35 – 4.32 (m, 2H), 3.67 – 3.65 (m, 2H), 3.44 (t, J = 7.0 Hz, 2H), 2.88 (s, 1H), 1.65 – 1.59 (m, 2H), 1.35 – 1.28 (m, 4H), 0.90 – 0.86 (m, 3H), 0.55 – 0.51 (m, 4H), 0.09 – 0.06 (s, $-\text{[Si(CH}_3)_2\text{-O]}_n-$).

11.4.1.13. Synthesis of PDMS-[B]_n-PDMS triBCPs, n = 3,5,7



General protocol: HO-[B]_n-OH (n = 3,5,7) (1.0 eq) and PDMS-**yne** (2.2 eq) were dissolved in DCM (0.02 M). Subsequently, DABCO base (20 mol%) was added to the reaction mixture. After 30 minutes, a small amount of the reaction mixture was taken for THF-SEC measurement. Upon confirmation of successful block copolymer formation, the mixture was purified via flash column chromatography (DCM:EtOAc, 100% DCM to 50% DCM) to obtain pure block copolymers.

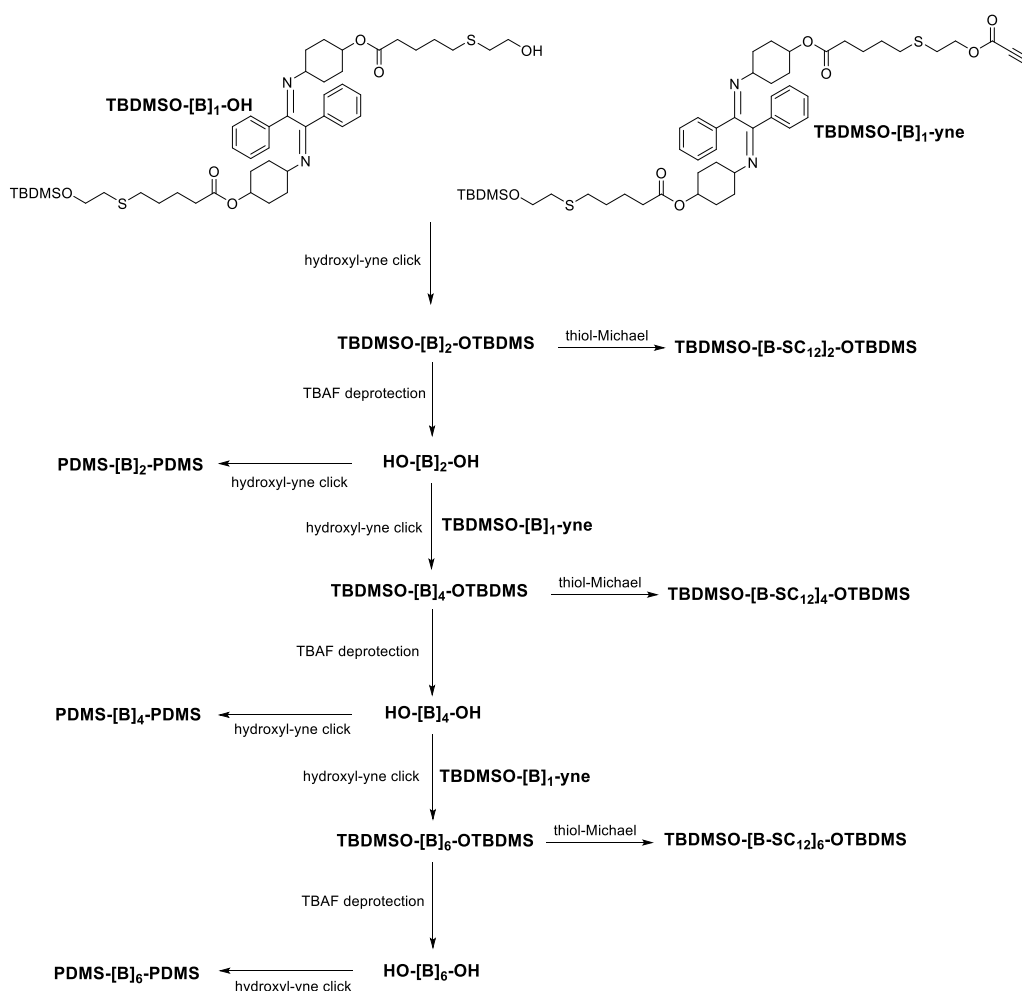
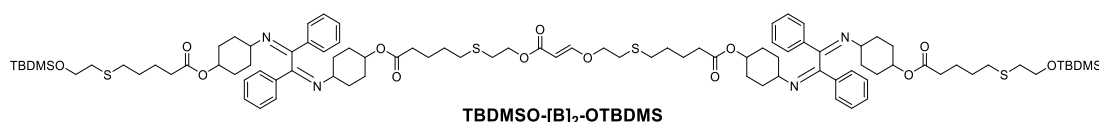


Figure S4.2. Synthetic route to even-numbered sequences, thiol-Michael-modified sequences and ABA triblock copolymers.

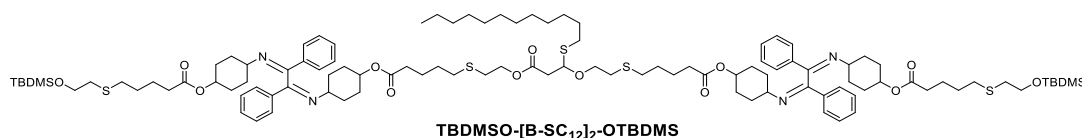
11.4.1.14. Synthesis of TBDMSO-[B]₂-OTBDMS



TBDMSO-[B]₁-OH (400 mg, 0.48 mmol, 1.0 eq) and **TBDMSO-[B]₁-yne** (467 mg, 0.52 mmol, 1.1 eq) were dissolved in dichloromethane (DCM) (1.2 mL). DABCO (10.7 mg, 20 mol%) was quickly added to the reaction solution. The reaction was stopped after 30 minutes. The crude mixture was immediately modified via flash column chromatography (EtOAc: Cy, 1:99-80:20, v/v), yielding 720 mg product (87% purification yield). NMR spectra are provided in section 4.

¹H NMR (600 MHz, CDCl₃) δ 7.77 – 7.72 (m, 8H), 7.57 (d, J = 12.6 Hz, 1H), 7.41 – 7.31 (m, 12H), 5.20 (d, J = 12.6 Hz, 1H), 4.83 – 4.75 (m, 4H), 4.23 (t, J = 7.0 Hz, 2H), 3.97 (t, J = 6.7 Hz, 2H), 3.73 (t, J = 7.1 Hz, 4H), 3.22 (tt, J = 9.5, 3.8 Hz, 4H), 2.78 (t, J = 6.7 Hz, 2H), 2.72 (t, J = 7.0 Hz, 2H), 2.60 (t, J = 7.1 Hz, 4H), 2.54 (dt, J = 9.6, 7.2 Hz, 8H), 2.25 (dtd, J = 7.4, 4.5, 2.3 Hz, 8H), 2.12 – 2.04 (m, 4H), 1.94 – 1.86 (m, 4H), 1.81 – 1.72 (m, 4H), 1.71 – 1.54 (m, 24H), 1.46 – 1.34 (m, 8H), 1.20 (tdd, J = 13.3, 11.2, 3.8 Hz, 4H), 0.88 (s, 18H), 0.05 (s, 12H).
¹³C NMR (151 MHz, CDCl₃) δ 172.92, 172.86, 172.81, 167.40, 163.26, 162.39, 136.89, 130.90, 128.74, 127.77, 96.74, 77.37, 77.16, 76.95, 72.06, 71.99, 70.66, 63.51, 62.99, 61.47, 53.55, 34.51, 34.27, 34.20, 34.16, 32.36, 32.28, 31.98, 31.48, 30.71, 30.34, 29.32, 29.15, 29.09, 29.07, 26.03, 24.27, 24.21, 24.16, 18.44, -5.15.

11.4.1.15. Synthesis of TBDMSO-[B-SC₁₂]₂-OTBDMS

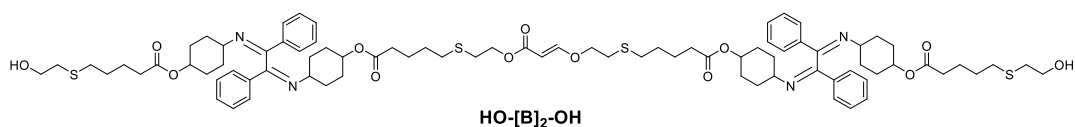


TBDMSO-[B]₂-OTBDMS (100 mg, 0.06 mmol, 1.0 eq of ether acrylate bond) and 1-dodecanethiol (117 μ L mL, 10 eq) were dissolved in THF (0.14 mL). The NHC catalyst, 1,3-bis(2,6-diisopropylphenyl)imidazol-2-ylidene, (2.3 mg, mol%) was subsequently added. A crude NMR was taken after 3 h of reaction to check the conversion (100% conversion). Upon completion, the reaction mixture was diluted in DCM and washed with saturated NaHCO₃ solution (2 times). The residue was concentrated and then precipitated in methanol to obtain pure product (88% purification yield). Note that the number of the alky side chain is less than that of α -bisimine unit by one unit. NMR spectra are provided in section 4.

¹H NMR (600 MHz, CDCl₃) δ 7.95 – 7.65 (br, 8H), 7.49 – 7.31 (m, 12H), 4.89 (dd, J = 8.2, 5.6 Hz, 1H), 4.83 – 4.75 (m, 4H), 4.27 – 4.18 (m, 2H), 3.86 (dt, J = 9.6, 6.8 Hz, 1H), 3.77 – 3.71 (m, 6H), 3.57 (dt, J = 9.7, 6.7 Hz, 1H), 3.30 – 3.17 (m, 4H), 2.91 (dd, J = 15.4, 8.2 Hz, 1H), 2.76 (dd, J = 15.5, 5.6 Hz, 1H), 2.71 (t, J = 7.0 Hz, 2H), 2.65 (td, J = 6.7, 1.8 Hz, 2H), 2.61 (t, J = 7.1 Hz, 4H), 2.58 – 2.50 (m, 10H), 2.25 (td, J = 7.3, 1.7 Hz, 8H), 2.12 – 2.06 (m, 4H), 1.94 – 1.88 (m, 4H), 1.71 – 1.52 (m, 26H), 1.39 (dddd, J = 34.2, 23.9, 10.8, 4.2 Hz, 10H), 1.25 (s,

22H), 0.88 (s, 21H), 0.05 (d, $J = 0.6$ Hz, 12H). ^{13}C NMR (151 MHz, CDCl_3) δ 172.78, 172.73, 172.69, 169.65, 163.18, 136.73, 128.68, 127.72, 124.77, 81.39, 77.28, 77.07, 76.86, 71.85, 67.97, 67.24, 63.63, 63.40, 61.39, 41.86, 39.24, 34.40, 34.15, 34.11, 34.06, 32.17, 32.12, 31.92, 31.88, 31.32, 30.35, 30.19, 30.04, 29.66, 29.64, 29.61, 29.54, 29.52, 29.35, 29.24, 29.22, 29.21, 29.17, 29.08, 29.05, 28.97, 28.92, 27.87, 25.92, 25.82, 24.16, 24.13, 24.08, 23.78, 22.69, 18.34, 14.15, 14.13, -5.25.

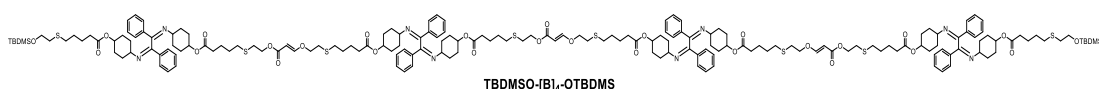
11.4.1.16. Synthesis of HO-[B]₂-OH



TBAF 1M solution (5.2 mL, 15 eq) was added to **TBDMSO-[B]₂-OTBDMS** (600 mg, 0.35 mmol, 1.0 eq) and the resulting solution was stirred at ambient temperature for 30 minutes. The reaction mixture was subsequently diluted in DCM and extracted with water (2 times). The organic phase was then dried with Na_2SO_4 and concentrated at reduced pressure. The residue was purified via flash column chromatography (DCM:EtOAc, 100% DCM to 50% DCM), yielding the product (450 mg, 86% purification yield).

^1H NMR (600 MHz, CDCl_3) δ 7.75 (d, $J = 7.6$ Hz, 8H), 7.57 (d, $J = 12.6$ Hz, 1H), 7.44 – 7.30 (m, 12H), 5.20 (d, $J = 12.6$ Hz, 1H), 4.79 (s, 4H), 4.23 (t, $J = 7.0$ Hz, 2H), 3.98 (t, $J = 6.7$ Hz, 2H), 3.74 – 3.64 (m, 4H), 3.27 – 3.18 (m, 4H), 2.78 (t, $J = 6.6$ Hz, 2H), 2.71 (dt, $J = 12.4$, 6.5 Hz, 6H), 2.58 – 2.47 (m, 8H), 2.26 (dd, $J = 8.7$, 5.8 Hz, 8H), 2.07 (t, $J = 16.0$ Hz, 4H), 1.91 (d, $J = 12.6$ Hz, 4H), 1.77 (s, 4H), 1.71 – 1.51 (m, 24H), 1.47 – 1.34 (m, 8H), 1.20 (q, $J = 11.5$ Hz, 4H). **LC-MS**: calculated m/z for $\text{C}_{83}\text{H}_{113}\text{N}_4\text{O}_{13}\text{S}_4^+$ [$\text{M}+\text{H}^+$] = 1501.7182, found 1501.7194.

11.4.1.17. Synthesis of TBDMSO-[B]₄-OTBDMS

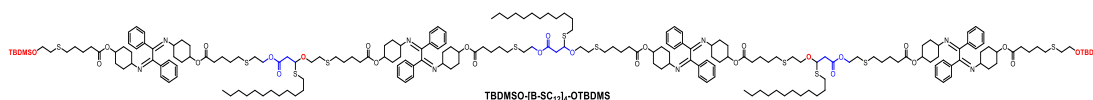


The synthesis protocol for **TBDMSO-[B]₄-OTBDMS** is similar to that for **TBDMSO-[B]₂-OTBDMS**. Accordingly, **HO-[B]₂-OH** (1.0 eq) reacts with **TBDMSO-[B]₁-yne** (2.1 eq) upon addition of 20 mol% of DABCO base in DCM (0.4 M) for 30 minutes. The crude mixture was purified via column chromatography (DCM:EtOAc, 100% DCM to 20% DCM).

^1H NMR (600 MHz, CDCl_3) δ 7.77 – 7.72 (m, 16H), 7.57 (d, $J = 12.6$ Hz, 3H), 7.41 – 7.31 (m, 24H), 5.20 (d, $J = 12.6$ Hz, 3H), 4.83 – 4.75 (m, 8H), 4.23 (t, $J = 7.0$ Hz, 6H), 3.97 (t, $J = 6.7$ Hz, 6H), 3.73 (t, $J = 7.1$ Hz, 4H), 3.22 (tt, $J = 9.5$, 3.8 Hz, 8H), 2.78 (t, $J = 6.7$ Hz, 6H), 2.72 (t, $J = 7.0$ Hz, 6H), 2.60 (t, $J = 7.1$ Hz, 4H), 2.54 (dt, $J = 9.6$, 7.2 Hz, 16H), 2.25 (dtd, $J = 7.4$, 4.5, 2.3 Hz, 16H), 2.12 – 2.04 (m, 8H), 1.94 – 1.86 (m, 8H), 1.81 – 1.72 (m, 8H), 1.71 – 1.54 (m,

48H), 1.46 – 1.34 (m, 16H), 1.20 (tdd, $J = 13.3, 11.2, 3.8$ Hz, 8H), 0.88 (s, 18H), 0.05 (s, 12H). ^{13}C NMR (151 MHz, CDCl_3) δ 172.85, 172.80, 172.75, 167.33, 163.17, 162.34, 136.85, 130.80, 128.67, 127.69, 96.68, 77.37, 77.16, 76.95, 72.01, 71.97, 71.94, 70.62, 63.46, 62.94, 61.40, 53.53, 34.45, 34.21, 34.15, 34.10, 32.30, 32.22, 31.98, 31.92, 31.50, 31.43, 30.65, 30.30, 29.26, 29.10, 29.08, 29.03, 29.01, 25.98, 24.21, 24.15, 24.10, 18.38, -5.19.

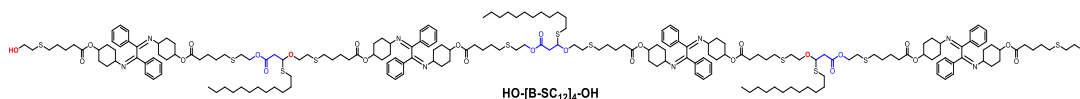
11.4.1.18. Synthesis of TBDMSO-[B-SC₁₂]₄-OTBDMS



TBDMSO-[B]₄-OTBDMS (1.0 eq of ether acrylate bond) and 1-dodecanethiol (10 eq) were dissolved in THF (0.5 M). The NHC catalyst, 1,3-bis(2,6-diisopropylphenyl)imidazol-2-ylidene, (10 mol%) was then added. A crude NMR was taken after 3 h of reaction to check the conversion (100% conversion). Upon completion, the reaction mixture was diluted in DCM and washed with saturated NaHCO_3 solution (2 times). The residue was concentrated and subsequently precipitated in methanol to obtain pure product. Note that the number of the alky side chain is less than that of α -bisimine by one unit.

^1H NMR (600 MHz, CDCl_3) δ 7.84 – 7.67 (m, 16H), 7.44 – 7.29 (m, 24H), 4.88 (dd, $J = 8.2, 5.6$ Hz, 3H), 4.82 – 4.74 (m, 8H), 4.26 – 4.16 (m, 6H), 3.85 (dt, $J = 9.7, 6.8$ Hz, 3H), 3.73 (td, $J = 6.9, 1.5$ Hz, 6H), 3.57 (dt, $J = 9.7, 6.7$ Hz, 3H), 3.27 – 3.19 (m, 8H), 2.90 (dd, $J = 15.4, 8.3$ Hz, 3H), 2.76 (dd, $J = 15.4, 5.6$ Hz, 3H), 2.71 (t, $J = 7.0$ Hz, 6H), 2.65 (td, $J = 6.8, 1.8$ Hz, 6H), 2.60 (t, $J = 7.1$ Hz, 4H), 2.58 – 2.48 (m, 20H), 2.24 (ddd, $J = 9.1, 5.1, 2.2$ Hz, 16H), 2.11 – 2.04 (m, 8H), 1.93 – 1.87 (m, 8H), 1.84 – 1.71 (m, 8H), 1.70 – 1.51 (m, 40H), 1.45 – 1.31 (m, 20H), 1.31 – 1.14 (m, 72H), 0.87 (d, $J = 7.3$ Hz, 27H), 0.05 (s, 12H). ^{13}C NMR (151 MHz, CDCl_3) δ 172.77, 172.73, 172.69, 169.66, 163.18, 136.73, 128.68, 127.71, 124.77, 81.40, 77.28, 77.07, 76.86, 71.85, 67.97, 67.24, 63.63, 63.40, 61.39, 41.86, 39.24, 34.40, 34.15, 34.11, 34.06, 32.17, 32.12, 31.92, 31.87, 31.32, 30.38, 30.19, 30.04, 29.66, 29.64, 29.61, 29.54, 29.52, 29.35, 29.24, 29.22, 29.21, 29.17, 29.08, 29.05, 28.97, 28.92, 27.87, 25.92, 25.82, 24.16, 24.13, 24.08, 23.79, 22.69, 18.34, 14.15, 14.13, -5.25.

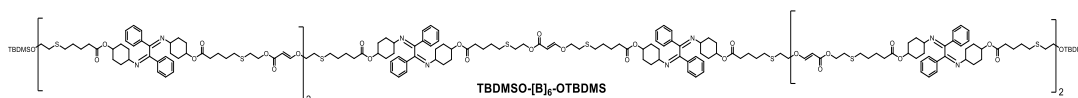
11.4.1.19. Synthesis of HO-[B]₄-OH



The deprotection protocol is similar to that for **HO-[B]₂-OH**. Accordingly, TBAF 1M solution (15 eq) was added to **TBDMSO-[B]₄-OTBDMS** (1.0 eq) and the resulting solution was stirred at ambient temperature for 30 minutes. The reaction mixture was subsequently diluted in DCM and extracted with water (2 times). The organic phase was then dried with Na_2SO_4 and concentrated at reduced pressure. The residue was purified via flash column chromatography (DCM:EtOAc, 100% DCM to 20% DCM) to obtain the product (89% purification yield).

¹H NMR (600 MHz, CDCl₃) δ 7.77 – 7.70 (m, 16H), 7.56 (d, J = 12.6 Hz, 3H), 7.40 – 7.30 (m, 24H), 5.19 (d, J = 12.6 Hz, 3H), 4.78 (dp, J = 14.3, 4.3 Hz, 8H), 4.22 (t, J = 7.0 Hz, 6H), 3.97 (t, J = 6.7 Hz, 6H), 3.68 (q, J = 5.6 Hz, 4H), 3.22 (ddt, J = 13.6, 9.3, 3.9 Hz, 8H), 2.77 (t, J = 6.7 Hz, 6H), 2.71 (t, J = 7.0 Hz, 6H), 2.68 (t, J = 6.0 Hz, 4H), 2.54 (td, J = 7.2, 2.6 Hz, 12H), 2.50 (t, J = 7.2 Hz, 4H), 2.24 (td, J = 7.3, 2.4 Hz, 16H), 2.10 – 2.04 (m, 8H), 1.92 – 1.87 (m, 8H), 1.76 (tdd, J = 13.1, 9.8, 3.4 Hz, 8H), 1.70 – 1.54 (m, 48H), 1.45 – 1.34 (m, 16H), 1.23 – 1.15 (m, 8H).

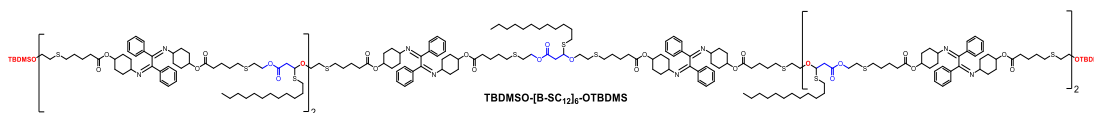
11.4.1.20. Synthesis of TBDMSO-[B]₆-OTBDMS



The synthesis protocol for **TBDMSO-[B]₆-OTBDMS** is similar to that for **TBDMSO-[B]₂-OTBDMS** and **TBDMSO-[B]₄-OTBDMS**. Accordingly, **HO-[B]₄-OH** (1.0 eq) reacts with **TBDMSO-[B]₁-yne** (2.1 eq) upon addition of 20 mol% of DABCO base in DCM (0.4 M) for 30 minutes. The crude mixture was purified via column chromatography (DCM:EtOAc, 100% DCM to 0% DCM) (87% purification yield).

¹H NMR (600 MHz, CDCl₃) δ 7.76 – 7.71 (m, 24H), 7.56 (d, J = 12.6 Hz, 5H), 7.41 – 7.29 (m, 36H), 5.19 (d, J = 12.6 Hz, 5H), 4.78 (tt, J = 9.6, 4.1 Hz, 12H), 4.22 (t, J = 7.0 Hz, 10H), 3.97 (t, J = 6.7 Hz, 10H), 3.72 (t, J = 7.1 Hz, 4H), 3.22 (tt, J = 9.7, 3.9 Hz, 12H), 2.77 (t, J = 6.7 Hz, 10H), 2.71 (t, J = 7.0 Hz, 10H), 2.60 (t, J = 7.1 Hz, 4H), 2.54 (td, J = 7.2, 2.4 Hz, 24H), 2.24 (tt, J = 7.5, 2.2 Hz, 24H), 2.11 – 2.05 (m, 12H), 1.93 – 1.86 (m, 12H), 1.80 – 1.72 (m, 12H), 1.71 – 1.53 (m, 72H), 1.45 – 1.33 (m, 24H), 1.27 – 1.14 (m, 12H), 0.87 (s, 18H), 0.04 (s, 12H).
¹³C NMR (151 MHz, CDCl₃) δ 172.85, 172.80, 172.75, 167.33, 163.18, 162.34, 136.84, 130.82, 128.67, 127.70, 96.68, 77.37, 77.16, 76.95, 72.01, 71.97, 71.94, 70.62, 63.46, 62.94, 61.40, 53.53, 34.45, 34.21, 34.15, 34.10, 32.30, 32.22, 31.98, 31.92, 31.43, 30.65, 30.30, 29.26, 29.10, 29.08, 29.03, 29.01, 25.98, 24.21, 24.15, 24.10, 18.39, -5.19.

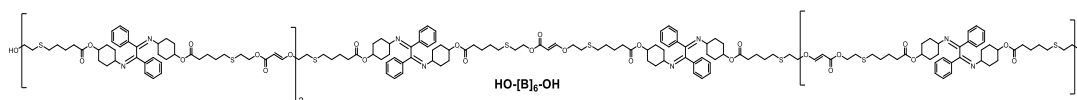
11.4.1.21. Synthesis of TBDMSO-[B-SC₁₂]₆-OTBDMS



TBDMSO-[B]₆-OTBDMS (1.0 eq of ether acrylate bond) and 1-dodecanethiol (10 eq) were dissolved in THF (0.5 M). The NHC catalyst, 1,3-bis(2,6-diisopropylphenyl)imidazol-2-ylidene, (10 mol%) was subsequently added. A crude NMR was recorded after 3 h of reaction to determine the conversion (close to 100% conversion). Upon completion, the reaction mixture was diluted in DCM and washed with saturated NaHCO₃ solution (2 times). The residue was concentrated and then precipitated in methanol to obtain pure product (90% purification yield). Note that the number of the alky side chain is less than that of α -bisimino units by one unit.

¹H NMR (600 MHz, CDCl₃) δ 7.82 – 7.70 (m, 24H), 7.44 – 7.29 (m, 36H), 4.88 (dd, J = 8.2, 5.7 Hz, 5H), 4.83 – 4.75 (m, 12H), 4.26 – 4.17 (m, 10H), 3.85 (dt, J = 9.7, 6.8 Hz, 5H), 3.73 (td, J = 6.9, 2.1 Hz, 6H), 3.57 (dt, J = 9.7, 6.7 Hz, 5H), 3.23 (tt, J = 9.3, 3.5 Hz, 12H), 2.90 (dd, J = 15.4, 8.3 Hz, 5H), 2.76 (dd, J = 15.4, 5.6 Hz, 5H), 2.71 (t, J = 7.0 Hz, 10H), 2.69 – 2.63 (m, 14H), 2.60 (t, J = 7.1 Hz, 4H), 2.58 – 2.48 (m, 36H), 2.24 (td, J = 7.5, 2.8 Hz, 24H), 2.11 – 2.05 (m, 12H), 1.93 – 1.87 (m, 12H), 1.78 (s, 12H), 1.70 – 1.52 (m, 72H), 1.38 (dddd, J = 26.5, 14.0, 9.2, 4.4 Hz, 38H), 1.30 – 1.12 (m, 90H), 0.89 – 0.85 (m, 33H), 0.05 (s, 12H). **¹³C NMR** (151 MHz, CDCl₃) δ 172.78, 172.73, 172.69, 169.65, 163.11, 136.72, 130.88, 128.69, 127.74, 127.72, 81.39, 77.27, 77.06, 76.85, 71.84, 67.97, 67.24, 63.63, 63.40, 61.40, 41.85, 39.24, 34.40, 34.15, 34.11, 34.06, 32.18, 32.12, 31.92, 31.88, 31.33, 30.36, 30.18, 30.04, 29.66, 29.64, 29.61, 29.60, 29.54, 29.53, 29.35, 29.24, 29.23, 29.21, 29.08, 29.05, 28.98, 28.92, 28.54, 28.39, 27.87, 25.92, 24.66, 24.16, 24.13, 24.08, 22.69, 18.33, 14.15, 14.13, 14.07, - 5.25.

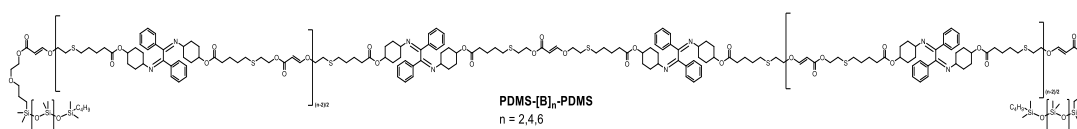
11.4.1.22. Synthesis of HO-[B]₆-OH



The deprotection protocol is similar to that for **HO-[B]₄-OH**. Accordingly, TBAF 1M solution (15 eq) was added to **TBDMSO-[B]₆-OTBDMS** (1.0 eq) and the resulting solution was stirred at ambient temperature for 30 minutes. The reaction mixture was subsequently diluted in DCM and extracted with water (2 times). The organic phase was then dried with Na₂SO₄ and concentrated at reduced pressure. The residue was purified via flash column chromatography (DCM:EtOAc, 100% DCM to 0% DCM) to obtain the product (85% purification yield).

¹H NMR (600 MHz, CDCl₃) δ 7.77 – 7.71 (m, 24H), 7.56 (d, J = 12.6 Hz, 5H), 7.40 – 7.29 (m, 36H), 5.19 (d, J = 12.6 Hz, 5H), 4.78 (tt, J = 10.3, 3.9 Hz, 12H), 4.22 (t, J = 7.0 Hz, 10H), 3.97 (t, J = 6.7 Hz, 10H), 3.68 (q, J = 5.4 Hz, 4H), 3.22 (tt, J = 9.7, 3.9 Hz, 12H), 2.76 (t, J = 6.7 Hz, 10H), 2.71 (t, J = 7.0 Hz, 10H), 2.68 (t, J = 6.0 Hz, 4H), 2.53 (td, J = 7.2, 2.6 Hz, 20H), 2.49 (t, J = 7.2 Hz, 4H), 2.24 (td, J = 7.3, 2.3 Hz, 24H), 2.07 (dd, J = 12.6, 4.4 Hz, 12H), 1.90 (dt, J = 12.7, 4.7 Hz, 12H), 1.76 (tdd, J = 13.2, 9.8, 3.4 Hz, 12H), 1.70 – 1.53 (m, 72H), 1.46 – 1.34 (m, 24H), 1.22 – 1.15 (m, 12H). **¹³C NMR** (151 MHz, CDCl₃) δ 172.76, 172.71, 167.29, 163.14, 162.29, 136.79, 130.76, 128.62, 127.64, 96.62, 77.33, 77.11, 76.90, 71.97, 71.95, 71.93, 70.57, 62.89, 61.34, 60.35, 53.48, 35.21, 34.09, 34.08, 34.05, 32.24, 31.92, 31.86, 31.45, 31.38, 31.26, 30.60, 30.24, 29.05, 29.03, 28.97, 28.95, 24.10, 24.05.

11.4.1.23. Synthesis of PDMS-[B]_n-PDMS triBCPs, n = 2,4,6



HO-[B]_n-OH ($n = 2,4,6$) (1.0 eq) and **PDMS-yne** (2.2 eq) were dissolved in DCM (0.02 M). Subsequently, DABCO base (20 mol% with respect to the OH functional end-group) was added to the reaction mixture. After 30 minutes, a small amount of the reaction mixture was taken for THF-SEC measurement. Upon confirmation of successful block copolymer formation, the mixture was purified via flash column chromatography (DCM:EtOAc, 100% DCM to 50% DCM) to obtain pure block copolymers.

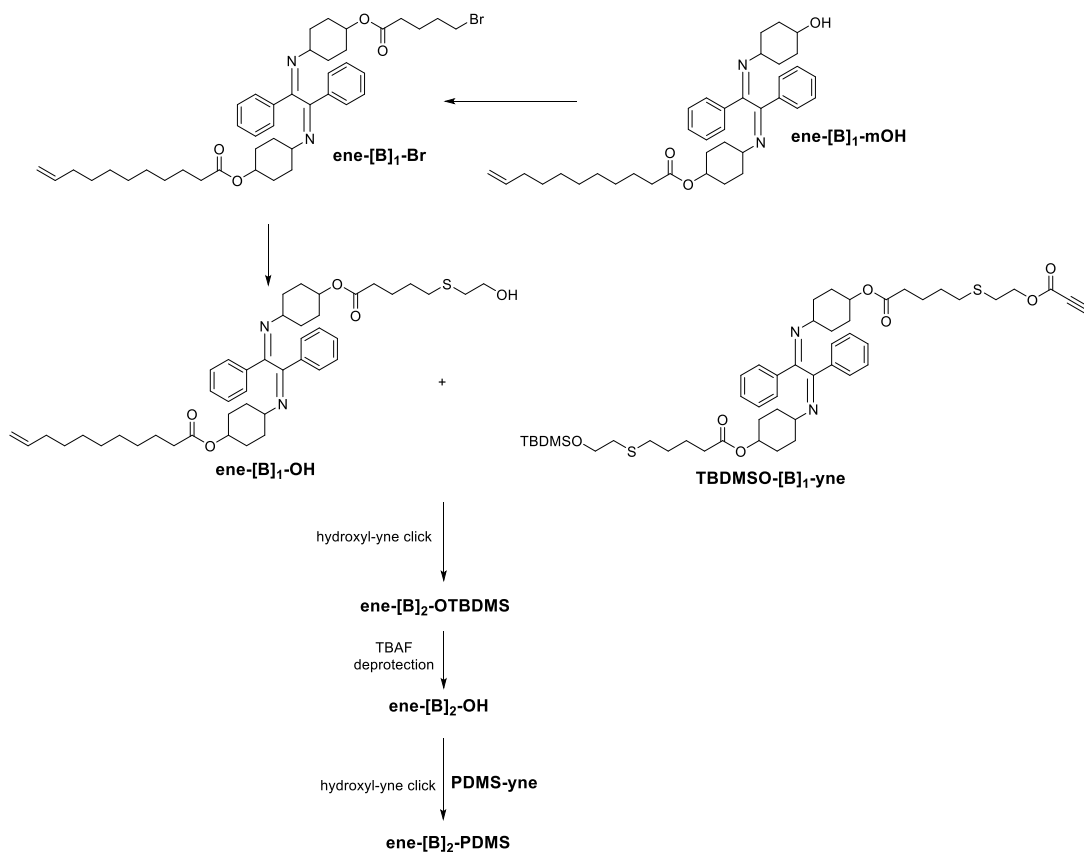
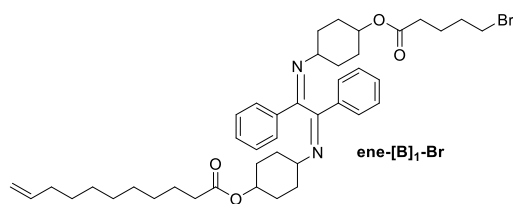


Figure S4.3. Synthesis route to olefin-terminated 2-mer sequence and the AB diblock copolymer.

Synthesis of ene-[B]₁-Br

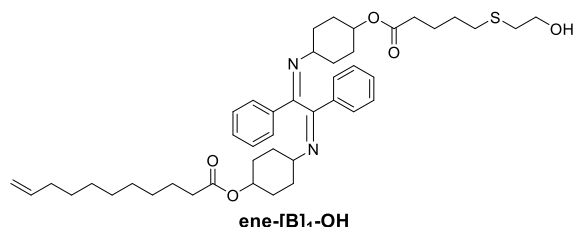


The synthesis of compound **ene-[B]₁-mOH** was reported in our previous work.¹⁸⁸ Compound **ene-[B]₁-mOH** (2800 mg, 4.9 mmol, 1.0 eq) and 5-Bromovaleric acid (1330 mg, 7.4 mmol, 1.5 eq) were dissolved in CHCl_3 (10 mL). Next, DCC (1530 mg, 7.4 mmol, 1.5 eq) and DMAP (120 mg, 10 mol%) were added to solution and the resulting mixture was heated to 50 °C. The reaction was stopped after 20 h. Upon completion, the crude was purified via flash column chromatography (EtOAc: Cy, 100% Cy to 20% Cy), yielding the product as sticky oil (3000 mg, 83% purification yield).

¹H NMR (600 MHz, CDCl_3) δ 7.75 (dt, $J = 7.2, 1.4$ Hz, 4H), 7.42 – 7.32 (m, 6H), 5.79 (ddt, $J = 16.9, 10.2, 6.7$ Hz, 1H), 5.01 – 4.88 (m, 2H), 4.80 (ddt, $J = 14.5, 9.3, 4.4$ Hz, 2H), 3.39 (t, $J = 6.6$ Hz, 2H), 3.27 – 3.19 (m, 2H), 2.28 (t, $J = 7.3$ Hz, 2H), 2.22 (t, $J = 7.5$ Hz, 2H), 2.12 – 2.06

(m, 2H), 2.04 – 2.00 (m, 2H), 1.93 – 1.83 (m, 4H), 1.80 – 1.70 (m, 4H), 1.66 – 1.54 (m, 8H), 1.41 – 1.32 (m, 6H), 1.29 – 1.16 (m, 8H). **¹³C NMR** (151 MHz, CDCl₃) δ 173.42, 172.65, 163.26, 163.18, 139.26, 136.92, 130.83, 128.71, 127.74, 114.26, 77.37, 77.16, 76.95, 72.15, 71.79, 61.48, 61.42, 53.54, 34.76, 33.87, 33.70, 33.11, 32.05, 31.51, 31.47, 30.37, 30.35, 29.35, 29.27, 29.15, 29.13, 28.97, 25.14, 23.67, 23.62, 23.60.

11.4.1.24. Synthesis of ene-[B]₁-OH

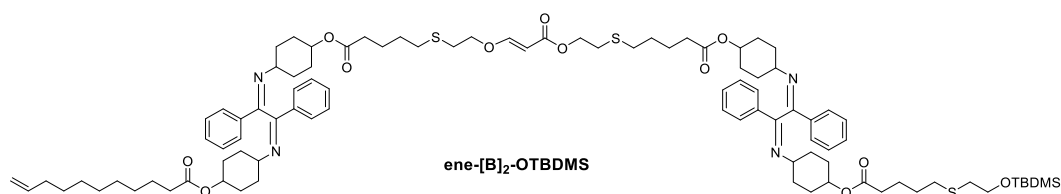


Compound **ene-[B]₁-Br** (1500 mg, 2.0 mmol, 1.0 eq) and 2-mercaptoethanol (0.29 mL, 2.0 eq) were dissolved in DMF (4 mL). Subsequently, Cs₂CO₃ (666 mg) was added to the reaction mixture. The reaction was run overnight at ambient temperature.

Upon completion, the mixture was diluted in EtOAc and extracted with water and brine (3 times). The organic phase was dried with Na₂SO₄ and concentrated at reduced pressure at 40 °C. The residue was further by flash column chromatography (EtOAc: Cy, 100% Cy to 20% Cy). The product was obtained as a palely yellow sticky oil.

¹H NMR (600 MHz, CDCl₃) δ 7.77 – 7.64 (m, 4H), 7.33 (dt, J = 30.7, 7.4 Hz, 6H), 5.75 (ddt, J = 16.9, 10.1, 6.7 Hz, 1H), 4.98 – 4.83 (m, 2H), 4.75 (dddd, J = 10.7, 8.9, 3.7, 2.1 Hz, 2H), 3.65 (q, J = 5.1 Hz, 2H), 3.19 (tt, J = 9.2, 3.7 Hz, 2H), 2.66 (t, J = 6.0 Hz, 2H), 2.46 (t, J = 7.2 Hz, 2H), 2.21 (t, J = 7.3 Hz, 2H), 2.17 (t, J = 7.5 Hz, 2H), 2.07 – 2.01 (m, 2H), 1.99 – 1.95 (m, 2H), 1.89 – 1.83 (m, 2H), 1.74 (m, 2H), 1.67 – 1.48 (m, 10H), 1.42 – 1.27 (m, 6H), 1.25 – 1.11 (m, 10H). **¹³C NMR** (151 MHz, CDCl₃) δ 173.33, 172.76, 139.18, 130.85, 128.69, 127.69, 114.15, 77.25, 77.04, 76.82, 71.91, 71.63, 61.42, 60.23, 53.44, 35.30, 34.66, 34.07, 33.78, 31.34, 31.21, 30.20, 29.26, 29.17, 29.06, 29.03, 28.87, 25.04, 24.10. **LC-MS**: calculated m/z for C₄₄H₆₃N₂O₅S⁺ [$M+H^+$] = 731.4453, found 731.4451.

11.4.1.25. Synthesis of ene-[B]₂-OTBDMS

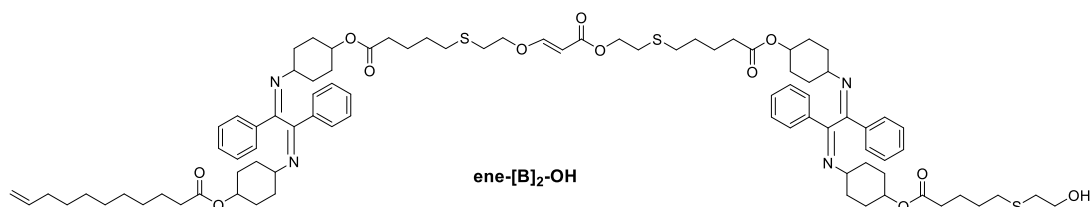


ene-[B]₁-OH (154 mg, 0.21 mmol, 1.0 eq) and **TBDMSO-[B]₁-yne** (197 mg, 0.22 mmol, 1.05 eq) were dissolved in dichloromethane (DCM) (0.6 mL). DABCO (5.0 mg, 20 mol%) was quickly added to the reaction solution. The reaction was stopped after 30 minutes. The crude mixture was immediately purified via flash column chromatography (EtOAc: Cy, 1:99-80:20, v/v), yielding 290 mg product (85% purification yield).

¹H NMR (600 MHz, CDCl₃) δ 7.76 (d, J = 7.7 Hz, 8H), 7.57 (d, J = 12.6 Hz, 1H), 7.42 – 7.32 (m, 12H), 5.79 (ddt, J = 16.9, 10.2, 6.7 Hz, 1H), 5.20 (d, J = 12.6 Hz, 1H), 5.01 – 4.88 (m, 2H),

4.79 (ddt, $J = 14.5, 10.0, 4.3$ Hz, 4H), 4.23 (t, $J = 7.0$ Hz, 2H), 3.98 (t, $J = 6.7$ Hz, 2H), 3.73 (t, $J = 7.1$ Hz, 2H), 3.23 (tt, $J = 8.5, 3.6$ Hz, 4H), 2.78 (t, $J = 6.7$ Hz, 2H), 2.72 (t, $J = 7.0$ Hz, 2H), 2.61 (t, $J = 7.1$ Hz, 2H), 2.58 – 2.51 (m, 6H), 2.25 (dtd, $J = 7.5, 4.7, 2.4$ Hz, 6H), 2.22 (t, $J = 7.5$ Hz, 2H), 2.11 – 2.05 (m, 4H), 2.04 – 1.99 (m, 2H), 1.94 – 1.87 (m, 4H), 1.77 (d, $J = 11.9$ Hz, 4H), 1.71 – 1.53 (m, 22H), 1.46 – 1.32 (m, 10H), 1.29 – 1.16 (m, 12H), 0.88 (s, 9H), 0.05 (s, 6H).

11.4.1.26. Synthesis of ene-[B]₂-OH

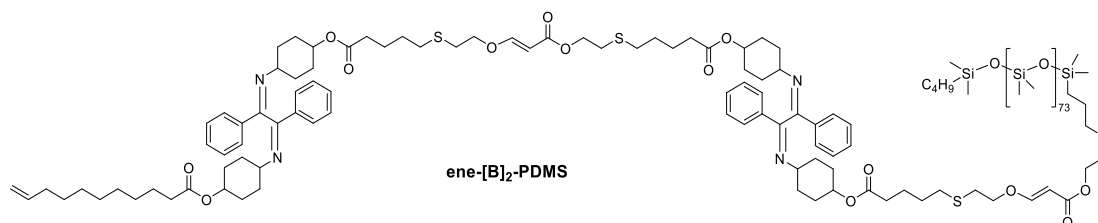


TBAF 1M solution in THF (1.1 mL, 7.0 eq) was added to **ene-[B]₂-OTBDMS** (264 mg, 0.163 mmol, 1.0 eq) and the resulting solution was stirred at ambient temperature for 30 minutes. The reaction mixture was subsequently diluted in DCM and extracted with water (2 times). The organic phase was then dried with Na₂SO₄ and concentrated at reduced pressure. The residue was purified via flash column chromatography (DCM:EtOAc, 100% DCM to 50% DCM), yielding the product (200 mg, 81% purification yield).

¹H NMR (600 MHz, CDCl₃) δ 7.78 – 7.71 (m, 8H), 7.57 (d, $J = 12.6$ Hz, 1H), 7.41 – 7.31 (m, 12H), 5.78 (ddt, $J = 16.9, 10.2, 6.7$ Hz, 1H), 5.20 (d, $J = 12.7$ Hz, 1H), 5.00 – 4.88 (m, 2H), 4.83 – 4.75 (m, 4H), 4.23 (t, $J = 7.0$ Hz, 2H), 3.97 (t, $J = 6.7$ Hz, 2H), 3.69 (q, $J = 5.8$ Hz, 2H), 3.22 (tt, $J = 9.6, 3.9$ Hz, 4H), 2.77 (t, $J = 6.7$ Hz, 2H), 2.72 (t, $J = 7.0$ Hz, 2H), 2.69 (t, $J = 6.0$ Hz, 2H), 2.54 (td, $J = 7.2, 2.7$ Hz, 4H), 2.50 (t, $J = 7.2$ Hz, 2H), 2.27 – 2.23 (m, 6H), 2.21 (t, $J = 7.5$ Hz, 2H), 2.12 – 2.05 (m, 4H), 2.04 – 1.99 (m, 2H), 1.94 – 1.87 (m, 4H), 1.81 – 1.52 (m, 26H), 1.46 – 1.31 (m, 10H), 1.29 – 1.15 (m, 12H). **¹³C NMR** (151 MHz, CDCl₃) δ 173.34, 172.77, 172.73, 167.31, 163.14, 162.30, 139.17, 136.79, 130.77, 128.63, 127.65, 114.16, 96.63, 77.28, 77.07, 76.86, 71.98, 71.96, 71.93, 71.69, 70.56, 62.89, 61.40, 61.36, 60.29, 53.45, 35.26, 34.66, 34.10, 34.08, 34.06, 33.77, 32.26, 31.93, 31.87, 31.38, 31.24, 30.61, 30.25, 29.36,

29.25, 29.17, 29.05, 29.02, 28.98, 28.96, 28.86, 25.04, 24.11, 24.05. **LC-MS**: calculated m/z for $C_{87}H_{119}N_4O_{12}S_3^+$ $[M+H^+] = 1507.7982$, found 1507.7992.

11.4.1.27. Synthesis of ene-[B]₂-PDMS AB diblock copolymer



Compound **ene-[B]₂-OH** (1.0 eq) and **PDMS-yne** (1.2 eq) were dissolved in DCM (0.02 M). Subsequently, DABCO base (20 mol%) was added to the reaction mixture. After 30 minutes, a small amount of the reaction mixture was taken for THF-SEC measurement. Upon confirmation of successful block copolymer formation, the mixture was purified via flash column chromatography (DCM:EtOAc, 100% DCM to 50% DCM) to obtain pure block copolymers.

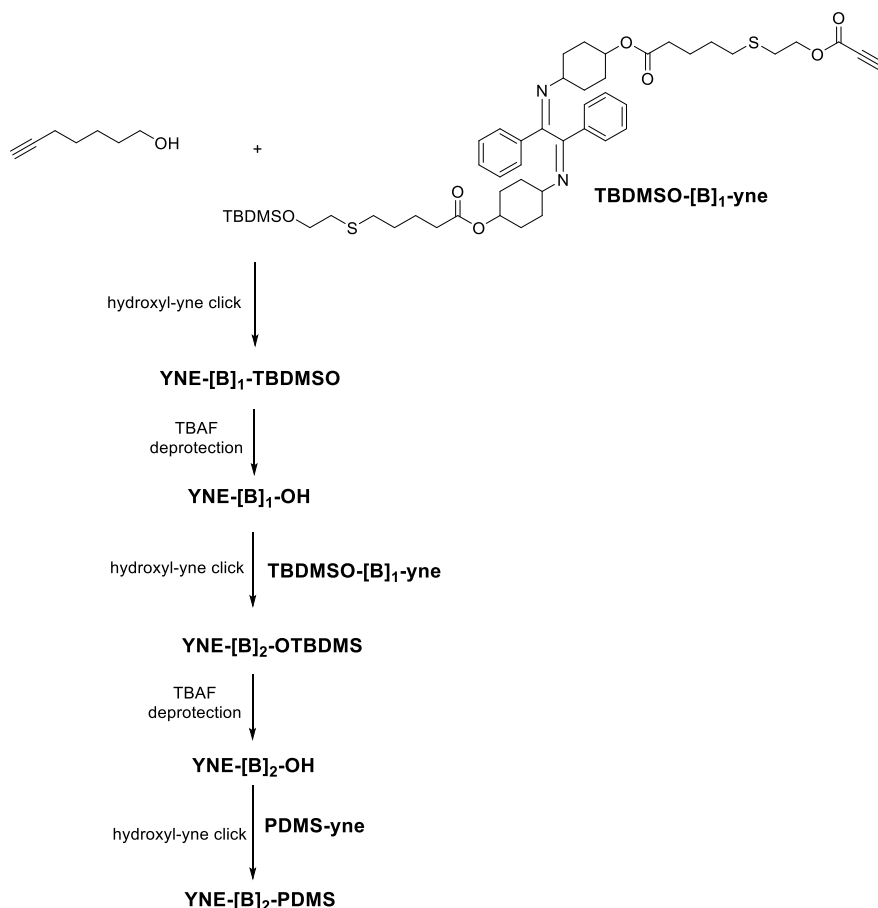
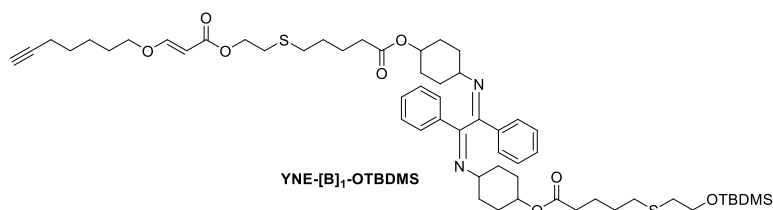


Figure S4.4. Synthesis route for YNE-[B]₂-PDMS.

11.4.1.28. Synthesis of YNE-[B]₁-OTBDMS



Compound TBDMSO-[B]₁-yne (190 mg, 0.213 mmol, 1.0 eq) and 6-heptyn-1-ol (26.3 mg, 0.234 mmol, 1.1 eq) were

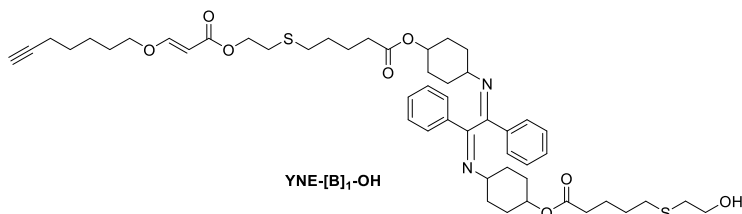
dissolved in dichloromethane (DCM) (0.6 mL). DABCO (5.0 mg, 20 mol%) was quickly added to the reaction solution. The reaction was stopped after 30 minutes. The crude mixture was immediately modified via flash column chromatography (EtOAc:Cy, 1:99-80:20, v/v), yielding 167 mg product (78% purification yield).

¹H NMR (600 MHz, CDCl₃) δ 7.83 – 7.67 (m, 4H), 7.58 (d, J = 12.6 Hz, 1H), 7.41 – 7.30 (m, 6H), 5.17 (d, J = 12.6 Hz, 1H), 4.78 (tt, J = 10.1, 4.2 Hz, 2H), 4.22 (t, J = 7.0 Hz, 2H), 3.83 (t, J = 6.5 Hz, 2H), 3.72 (t, J = 7.1 Hz, 2H), 3.22 (tt, J = 9.6, 3.8 Hz, 2H), 2.71 (t, J = 7.0 Hz, 2H), 2.60 (t, J = 7.1 Hz, 2H), 2.53 (dt, J = 8.2, 7.2 Hz, 4H), 2.24 (td, J = 7.3, 2.5 Hz, 4H), 2.19 (td, J = 6.8, 2.6 Hz, 2H), 2.07 (dd, J = 12.8, 4.7 Hz, 2H), 1.94 (t, J = 2.6 Hz, 1H), 1.92 – 1.86 (m, 2H), 1.81 – 1.47 (m, 20H), 1.44 – 1.33 (m, 4H), 1.25 – 1.14 (m, 2H), 0.87 (s, 9H), 0.04 (s, 6H).

¹³C NMR (151 MHz, CDCl₃) δ 172.86, 172.81, 167.64, 163.18, 162.98, 136.87, 130.81, 128.68, 127.71, 96.05, 84.15, 77.37, 77.16, 76.94, 71.98, 71.95, 70.98, 68.66, 63.47, 62.91, 61.41,

53.52, 34.46, 34.22, 34.16, 32.23, 31.94, 31.45, 30.69, 30.31, 29.27, 29.11, 29.09, 29.05, 28.43, 28.05, 25.99, 24.97, 24.22, 24.17, 18.40, 18.36, -5.18. **LC-MS**: calculated m/z for $C_{56}H_{83}N_2O_8S_2Si^+$ $[M+H]^+ = 1003.5355$, found 1003.5349.

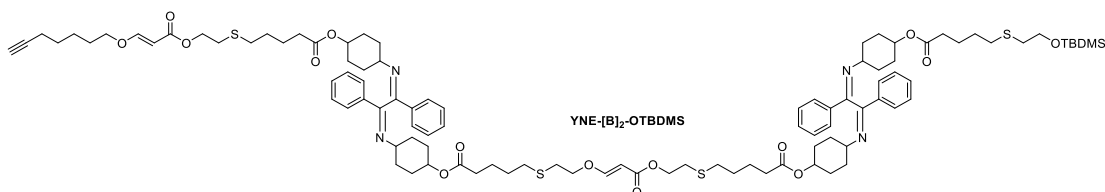
11.4.1.29. Synthesis of YNE-[B]₁-OH



TBAF 1M solution in THF (0.88 mL, 8.0 eq) was added to **YNE-[B]₁-OTBDMS** (111 mg, 0.11 mmol, 1.0 eq) and the resulting solution was

stirred at ambient temperature for 30 minutes. The reaction mixture was subsequently diluted in DCM and extracted with water (2 times). The organic phase was then dried with Na_2SO_4 and concentrated at reduced pressure. The residue was purified via flash column chromatography (DCM:EtOAc, 100% DCM to 50% DCM), yielding the product (96 mg, 96% purification yield). **¹H NMR** (600 MHz, $CDCl_3$) δ 7.86 – 7.67 (m, 4H), 7.59 (d, $J = 12.6$ Hz, 1H), 7.47 – 7.31 (m, 6H), 5.18 (d, $J = 12.6$ Hz, 1H), 4.79 (tq, $J = 9.5, 3.5$ Hz, 2H), 4.23 (t, $J = 7.0$ Hz, 2H), 3.85 (t, $J = 6.5$ Hz, 2H), 3.69 (q, $J = 5.2$ Hz, 2H), 3.32 – 3.17 (m, 2H), 2.72 (t, $J = 7.0$ Hz, 2H), 2.70 (t, $J = 6.0$ Hz, 2H), 2.55 (t, $J = 7.2$ Hz, 2H), 2.51 (t, $J = 7.2$ Hz, 2H), 2.25 (td, $J = 7.3, 3.4$ Hz, 4H), 2.21 (td, $J = 6.9, 2.6$ Hz, 2H), 2.12 – 2.06 (m, 2H), 1.95 (t, $J = 2.6$ Hz, 1H), 1.93 – 1.88 (m, 2H), 1.85 – 1.75 (m, 2H), 1.75 – 1.48 (m, 18H), 1.46 – 1.34 (m, 4H), 1.23 – 1.15 (m, 2H). **LC-MS**: calculated m/z for $C_{50}H_{69}N_2O_8S_2^+$ $[M+H]^+ = 889.4490$, found 889.4488.

11.4.1.30. Synthesis of YNE-[B]₂-OTBDMS

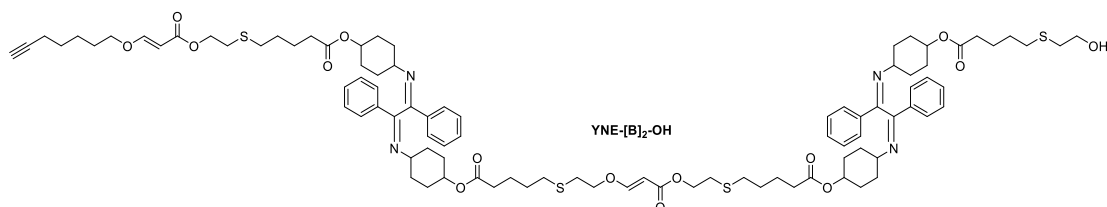


Compound **YNE-[B]₁-OH** (73 mg, 0.082 mmol, 1.0 eq) and **TBDMSO-[B]₁-yne** (80.5 mg, 0.090 mmol, 1.1 eq) were dissolved in dichloromethane (DCM) (0.2 mL). DABCO (1.8 mg, 20 mol%) was quickly added to the reaction solution. The reaction was stopped after 30 minutes. The crude mixture was immediately modified via flash column chromatography (EtOAc:Cy, 1:99-80:20, v/v), yielding 140 mg product (93% purification yield).

¹H NMR (600 MHz, $CDCl_3$) δ 7.77 (s, 8H), 7.59 (d, $J = 12.8$ Hz, 1H), 7.57 (d, $J = 12.7$ Hz, 1H), 7.45 – 7.32 (m, 12H), 5.20 (d, $J = 12.2$ Hz, 2H), 4.83 – 4.75 (m, 4H), 4.23 (t, $J = 7.0$ Hz, 4H), 3.98 (t, $J = 6.7$ Hz, 2H), 3.84 (t, $J = 6.5$ Hz, 2H), 3.73 (dd, $J = 7.4, 6.8$ Hz, 2H), 3.30 – 3.18 (m, 4H), 2.78 (t, $J = 6.7$ Hz, 2H), 2.72 (td, $J = 7.0, 1.2$ Hz, 4H), 2.61 (t, $J = 7.1$ Hz, 2H), 2.57 – 2.51 (m, 8H), 2.25 (tt, $J = 7.5, 2.4$ Hz, 8H), 2.20 (td, $J = 6.9, 2.7$ Hz, 2H), 2.12 – 2.05 (m, 4H), 1.95 (t, $J = 2.6$ Hz, 1H), 1.90 (dd, $J = 13.6, 4.6$ Hz, 4H), 1.86 – 1.75 (m, 4H), 1.75 – 1.47 (m, 30H), 1.46 – 1.35 (m, 8H), 1.23 – 1.15 (m, 4H), 0.88 (s, 9H), 0.05 (s, 6H). **¹³C NMR** (151 MHz, $CDCl_3$)

δ 172.89, 172.84, 172.79, 167.71, 167.41, 163.04, 162.40, 136.87, 130.81, 128.68, 127.71, 96.74, 96.09, 84.22, 77.37, 77.16, 76.95, 71.86, 71.05, 70.66, 68.68, 63.51, 62.99, 62.95, 61.56, 53.55, 34.52, 34.26, 34.20, 34.15, 32.37, 32.29, 31.99, 30.74, 30.73, 30.72, 29.32, 29.15, 29.10, 29.07, 28.49, 28.11, 25.02, 24.27, 24.21, 24.15, 18.45, 18.41, -5.14.

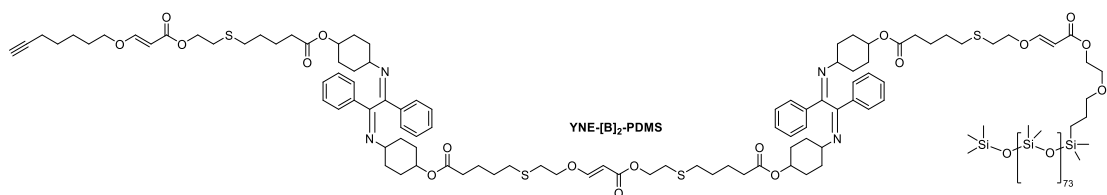
11.4.1.31. Synthesis of YNE-[B]₂-OH



TBAF 1M solution (0.51 mL, 7.5 eq) was added to **YNE-[B]₂-OTBDMS** (120 mg, 0.067 mmol, 1.0 eq) and the resulting solution was stirred at ambient temperature for 30 minutes. The reaction mixture was subsequently diluted in DCM and extracted with water (2 times). The organic phase was then dried with Na₂SO₄ and concentrated at reduced pressure. The residue was purified via flash column chromatography (DCM:EtOAc, 100% DCM to 50% DCM), yielding the product (100 mg, 89% purification yield).

¹H NMR (600 MHz, CDCl₃) δ 7.81 – 7.69 (m, 8H), 7.57 (dd, J = 13.5, 12.6 Hz, 2H), 7.42 – 7.30 (m, 12H), 5.18 (t, J = 12.4 Hz, 2H), 4.78 (tdq, J = 6.4, 4.2, 2.1 Hz, 4H), 4.22 (t, J = 7.0 Hz, 4H), 3.97 (t, J = 6.7 Hz, 2H), 3.84 (t, J = 6.5 Hz, 2H), 3.68 (q, J = 5.3 Hz, 2H), 3.22 (tt, J = 9.3, 3.8 Hz, 4H), 2.77 (t, J = 6.7 Hz, 2H), 2.71 (t, J = 6.8 Hz, 4H), 2.68 (t, J = 6.0 Hz, 2H), 2.57 – 2.52 (m, 6H), 2.50 (t, J = 7.2 Hz, 2H), 2.24 (td, J = 7.4, 2.5 Hz, 8H), 2.19 (td, J = 6.9, 2.6 Hz, 2H), 2.11 – 2.04 (m, 4H), 1.94 (t, J = 2.6 Hz, 1H), 1.93 – 1.87 (m, 4H), 1.84 – 1.74 (m, 4H), 1.74 – 1.46 (m, 30H), 1.45 – 1.33 (m, 8H), 1.22 – 1.14 (m, 4H). **LC-MS**: calculated m/z for C₉₃H₁₂₅N₄O₁₅S₄⁺ [M+H⁺] = 1666.8053, found 1666.8063.

11.4.1.32. Synthesis of YNE-[B]₂-PDMS



Compound **YNE-[B]₂-OH** (1.0 eq) and **PDMS-yne** (1.2 eq) were dissolved in DCM (0.02 M). Subsequently, DABCO base (20 mol%) was added to the reaction mixture. After 30 minutes, a small amount of the reaction mixture was taken for THF-SEC measurement. Upon confirmation of successful block copolymer formation, the mixture was purified via flash

column chromatography (DCM:EtOAc, 100% DCM to 50% DCM) to obtained pure block copolymers.

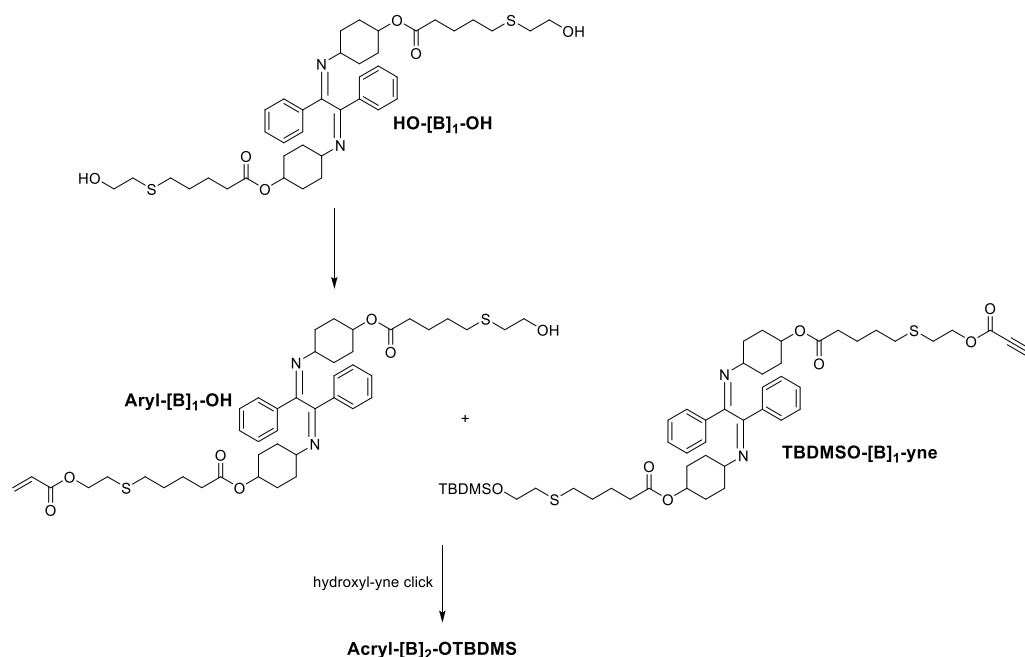
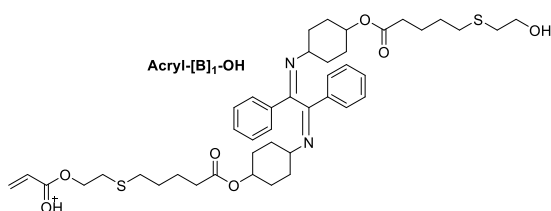


Figure S4.5. Synthesis route to acrylate-terminated 2-mer sequence of α -bisimine.

11.4.1.33. Synthesis of Acryl-[B]₁-OH



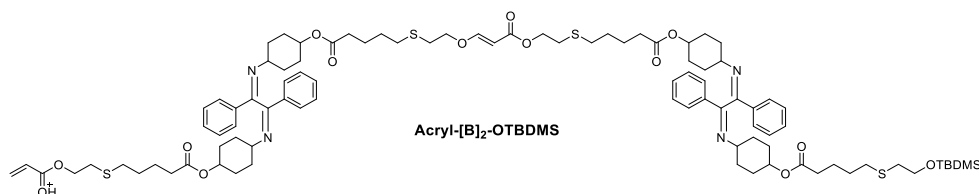
Compound **HO-[B]₁-OH** (2700 mg, 3.72 mmol, 1.0 eq) and triethylamine (TEA) (0.55 mL, 1.0 eq) were dissolved in dry DCM at 0 °C. Acryloyl chloride (0.3 mL, 1.0 eq) was injected into the stirring solution. The

reaction was stopped after 3 h. The crude was diluted in DCM and extracted with water and brine (3 times). The organic phase was dried with Na_2SO_4 and concentrated at reduced pressure at 40 °C. The residue was purified by flash column chromatography (EtOAc:Cy, 100% Cy to 30% Cy). The product was obtained as sticky oil (570 mg, 20% purification yield).

¹H NMR (600 MHz, CDCl_3) δ 7.78 – 7.70 (m, 4H), 7.41 – 7.31 (m, 6H), 6.40 (dd, J = 17.3, 1.4 Hz, 1H), 6.10 (dd, J = 17.3, 10.4 Hz, 1H), 5.83 (dd, J = 10.5, 1.4 Hz, 1H), 4.79 (dtd, J = 10.2, 5.3, 2.4 Hz, 2H), 4.27 (t, J = 7.0 Hz, 2H), 3.69 (t, J = 6.0 Hz, 2H), 3.22 (tt, J = 9.6, 3.9 Hz, 2H), 2.74 (t, J = 7.0 Hz, 2H), 2.69 (t, J = 6.0 Hz, 2H), 2.55 (t, J = 7.2 Hz, 2H), 2.50 (t, J = 7.3 Hz, 2H), 2.25 (td, J = 7.3, 1.3 Hz, 4H), 2.07 (ddd, J = 11.9, 5.2, 2.8 Hz, 2H), 1.90 (ddt, J = 12.9, 4.9, 2.7 Hz, 2H), 1.76 (tdd, J = 13.0, 9.2, 3.2 Hz, 2H), 1.71 – 1.53 (m, 12H), 1.46 – 1.33 (m, 4H), 1.20 (tdd, J = 12.4, 10.2, 3.8 Hz, 2H). **¹³C NMR** (151 MHz, CDCl_3) δ 172.86, 166.01, 163.23, 136.89, 131.24, 130.83, 128.70, 128.28, 127.72, 77.37, 77.16, 76.95, 72.05, 72.03, 63.70, 61.43, 60.38, 53.54, 35.34, 34.18, 34.16, 32.01, 31.47, 31.32, 30.48, 30.33, 29.14,

29.12, 29.05, 24.19, 24.18. **LC-MS**: calculated m/z for $C_{43}H_{59}N_2O_7S_2^+$ $[M+H]^+$ = 779.3746, found 779.3757.

11.4.1.34. Synthesis of Acryl-[B]₂-OTBDMS



Acryl-[B]₁-OH (106 mg, 0.136 mmol, 1.0 eq) and **TBDMSO-[B]₁-yne** (127.6 mg, 0.143 mmol, 1.05 eq) were dissolved in dichloromethane (DCM) (0.34 mL). DABCO (3.2 mg, 20 mol%) was quickly added to the reaction solution. The reaction was stopped after 30 minutes. The crude mixture was immediately modified via flash column chromatography (EtOAc:Cy, 1:99-80:20, v/v), yielding 200 mg product (88% purification yield).

¹H NMR (400 MHz, CDCl₃) δ 7.79 – 7.71 (m, 8H), 7.57 (d, J = 12.7 Hz, 1H), 7.44 – 7.30 (m, 12H), 6.41 (dd, J = 17.3, 1.4 Hz, 1H), 6.11 (dd, J = 17.3, 10.4 Hz, 1H), 5.83 (dd, J = 10.5, 1.4 Hz, 1H), 5.20 (d, J = 12.6 Hz, 1H), 4.79 (tt, J = 9.8, 4.2 Hz, 4H), 4.28 (t, J = 7.0 Hz, 2H), 4.23 (t, J = 7.0 Hz, 2H), 3.98 (t, J = 6.7 Hz, 2H), 3.73 (t, J = 7.1 Hz, 2H), 3.22 (tt, J = 9.6, 3.9 Hz, 4H), 2.75 (tt, J = 11.2, 6.8 Hz, 6H), 2.61 (t, J = 7.1 Hz, 2H), 2.58 – 2.50 (m, 8H), 2.29 – 2.20 (m, 8H), 2.13 – 2.05 (m, 4H), 1.96 – 1.86 (m, 4H), 1.83 – 1.53 (m, 28H), 1.47 – 1.32 (m, 8H), 1.27 – 1.14 (m, 4H), 0.88 (s, 9H), 0.05 (s, 6H). **¹³C NMR** (101 MHz, CDCl₃) δ 172.94, 172.88, 172.84, 167.42, 166.04, 163.25, 162.40, 136.95, 136.94, 131.27, 130.85, 128.73, 128.32, 127.75, 96.75, 77.48, 77.36, 77.16, 76.84, 72.10, 72.06, 72.03, 70.67, 63.73, 63.52, 63.00, 61.47, 34.52, 34.29, 34.22, 34.18, 32.38, 32.30, 32.05, 32.00, 31.52, 30.72, 30.52, 30.38, 29.33, 29.17, 29.11, 29.09, 26.04, 24.29, 24.22, 24.17, 18.46, -5.13. **LC-MS**: calculated m/z for $C_{92}H_{129}N_4O_{14}S_4^+$ $[M+H]^+$ = 1669.8152, found 1669.8167.

11.4.2. NMR Spectra

11.4.2.1. HO-[B]₁-OH

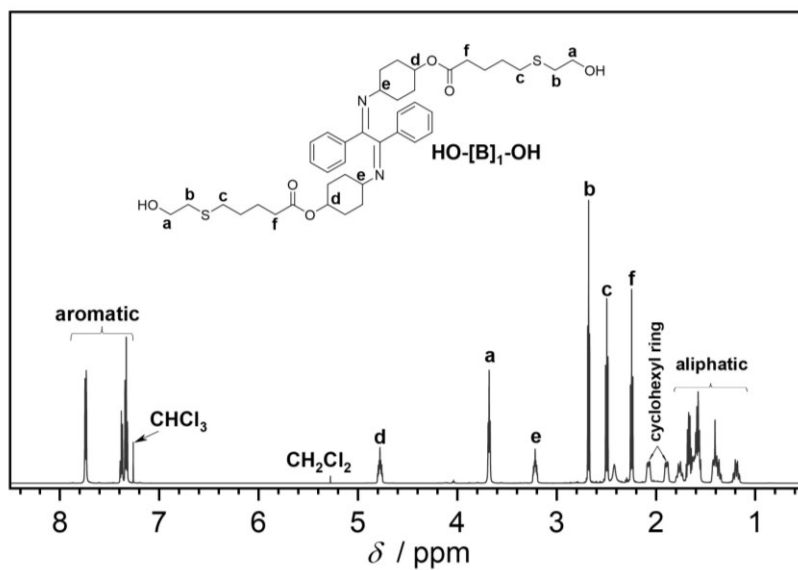


Figure S4.6. ¹H NMR (600 MHz, 32 scans) spectrum of HO-[B]₁-OH in CDCl₃.

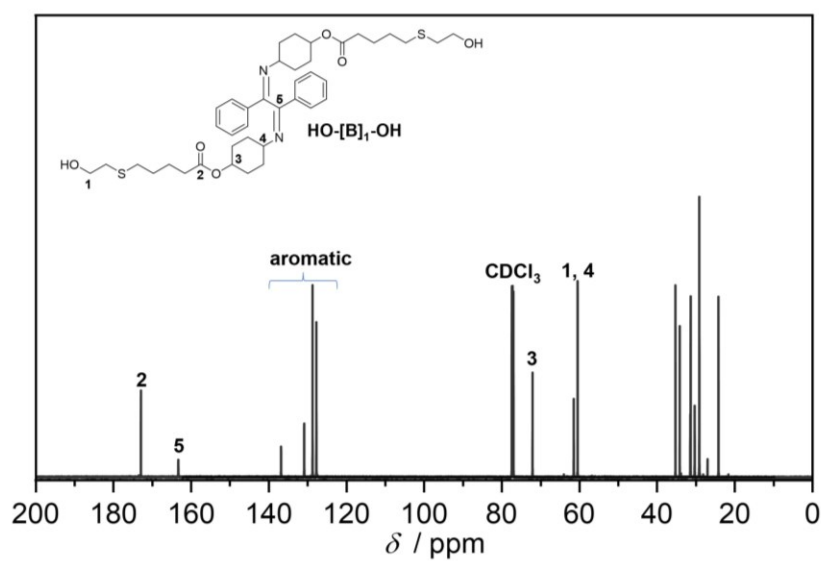


Figure S4.7. Carbon-Proton Decoupled ¹³C NMR (151 MHz) spectrum of HO-[B]₁-OH in CDCl₃.

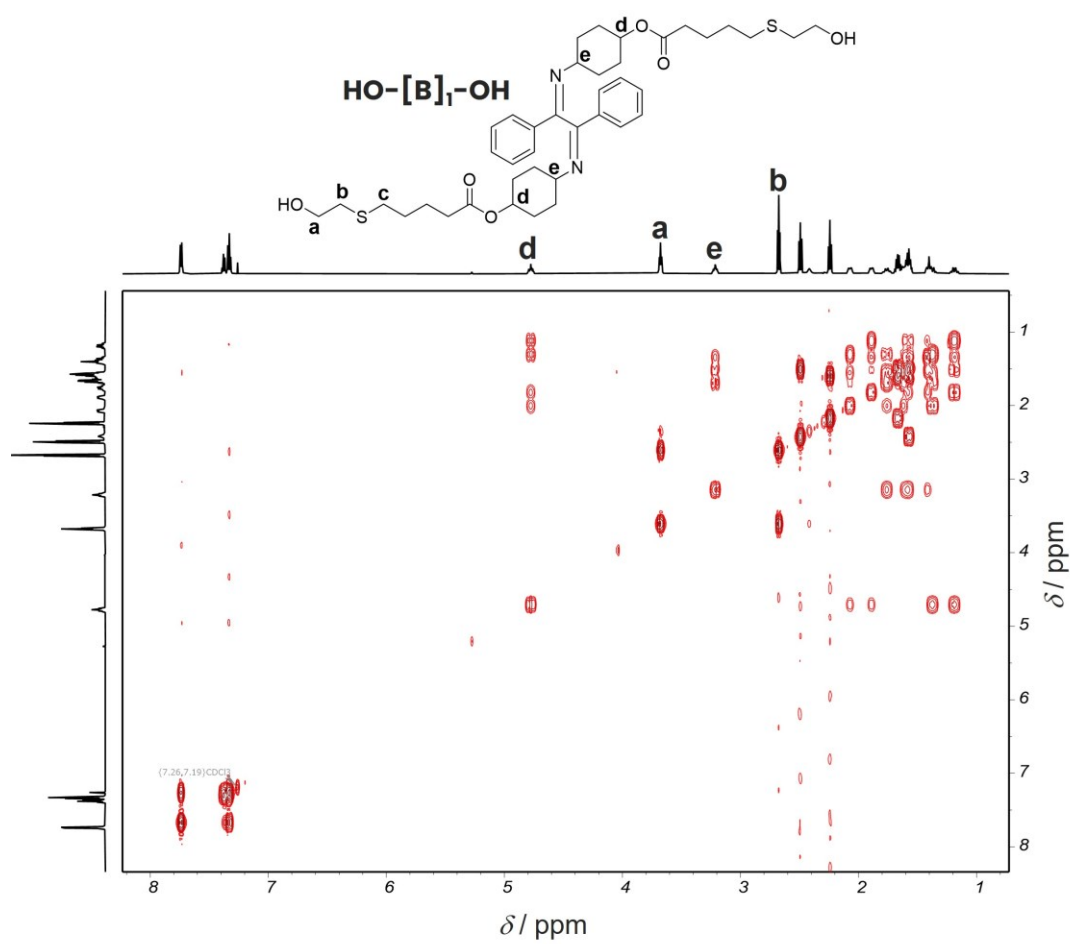


Figure S4.8. COSY NMR spectrum of **HO-[B]₁-OH** in CDCl_3 .

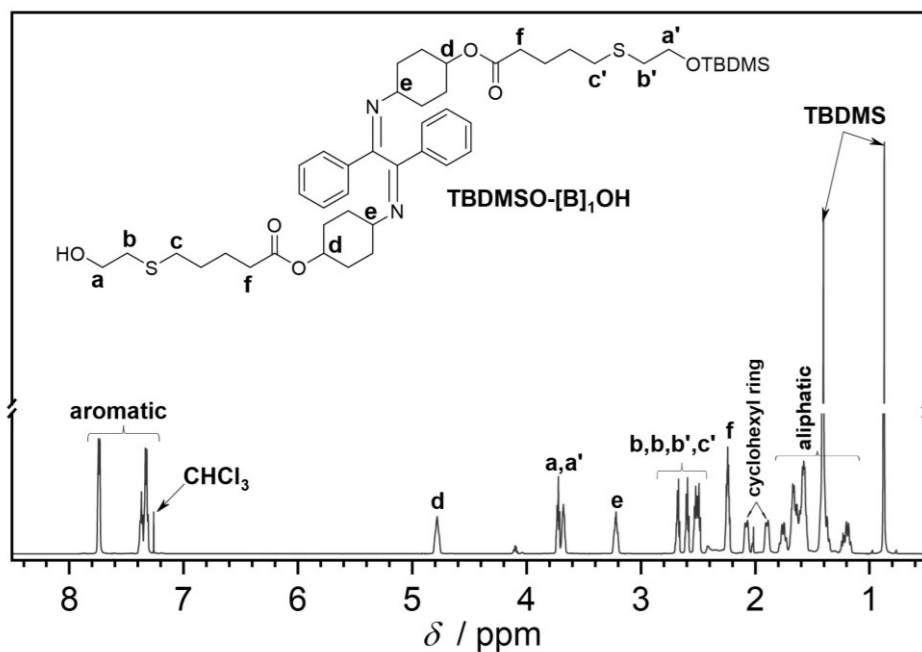
11.4.2.2. TBDMSO-[B]₁-OH

Figure S4.9. ¹H NMR (600 MHz, 32 scans) spectrum of HO-[B]₁-OTBDMS in CDCl₃.

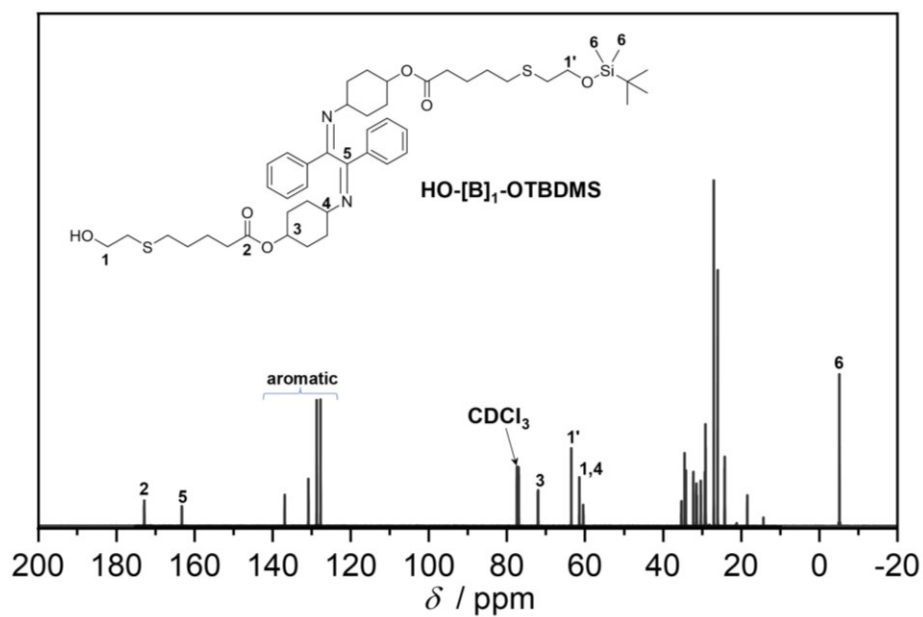


Figure S4.10. Carbon-Proton Decoupled ¹³C NMR (151 MHz) spectrum of HO-[B]₁-OTBDMS in CDCl₃.

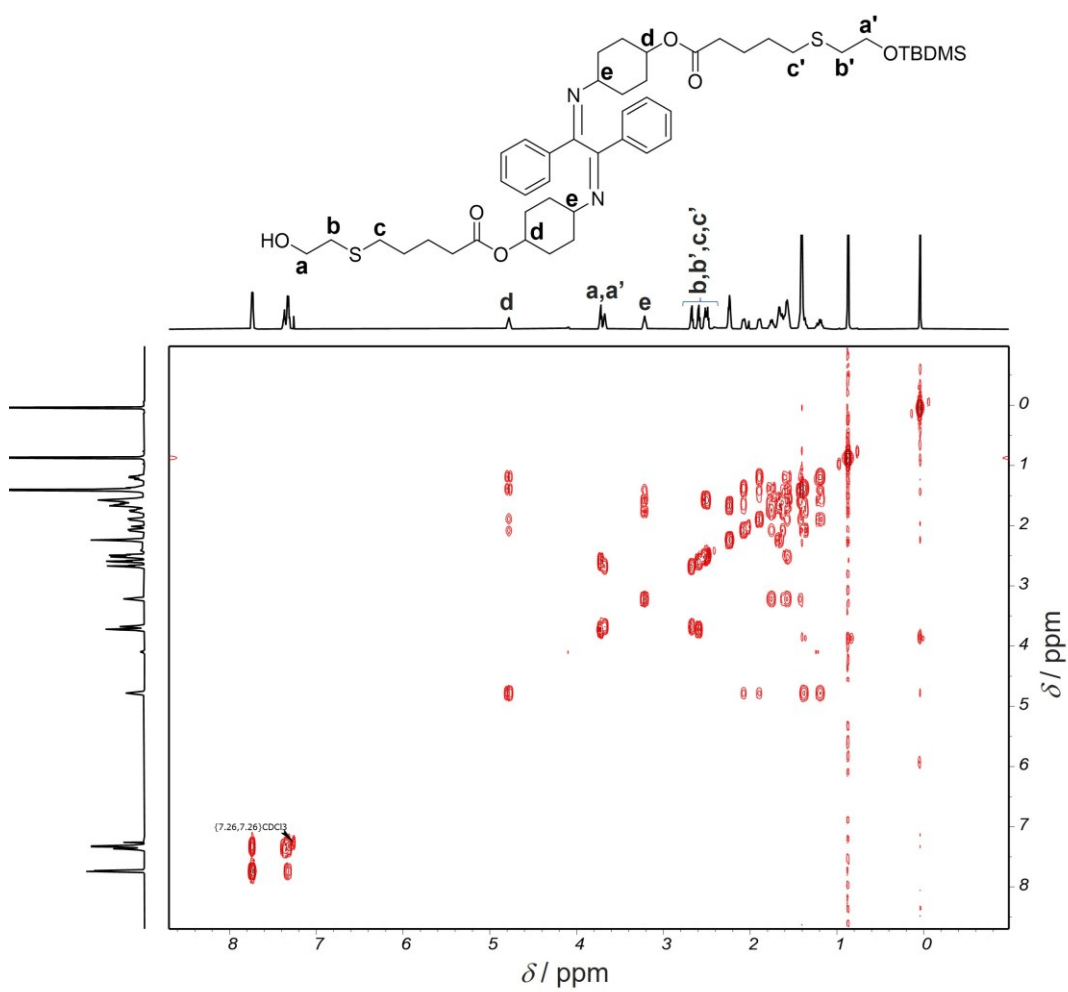


Figure S4.11. COSY NMR spectrum of *HO-[B]₁-OTBDMS* in CDCl₃.

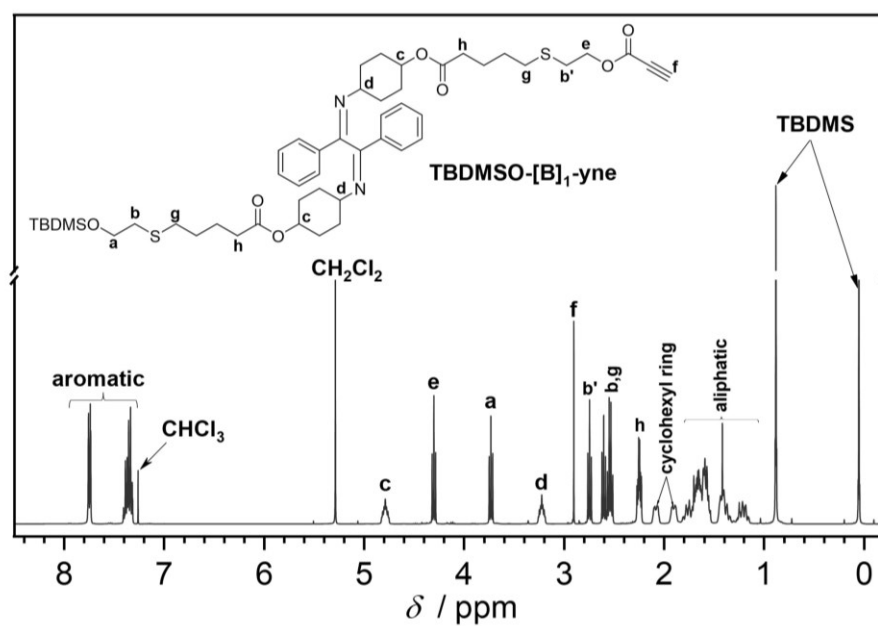
11.4.2.3. TBDMSO-[B]₁-yne

Figure S4.12. ¹H NMR (600 MHz, 32 scans) spectrum of TBDMSO-[B]₁-yne in CDCl₃.

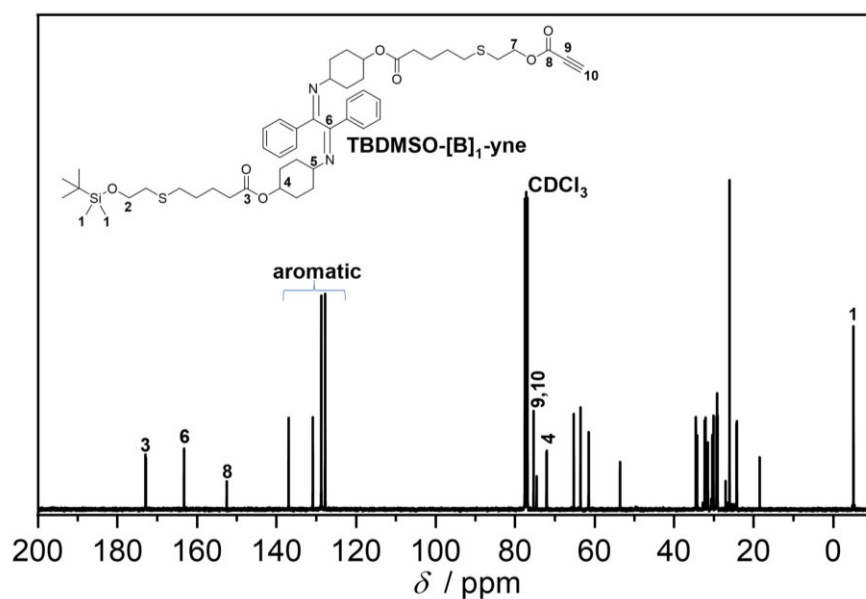


Figure S4.13. Carbon-Proton Decoupled ¹³C NMR (151 MHz) spectrum of TBDMSO-[B]₁-yne in CDCl₃.

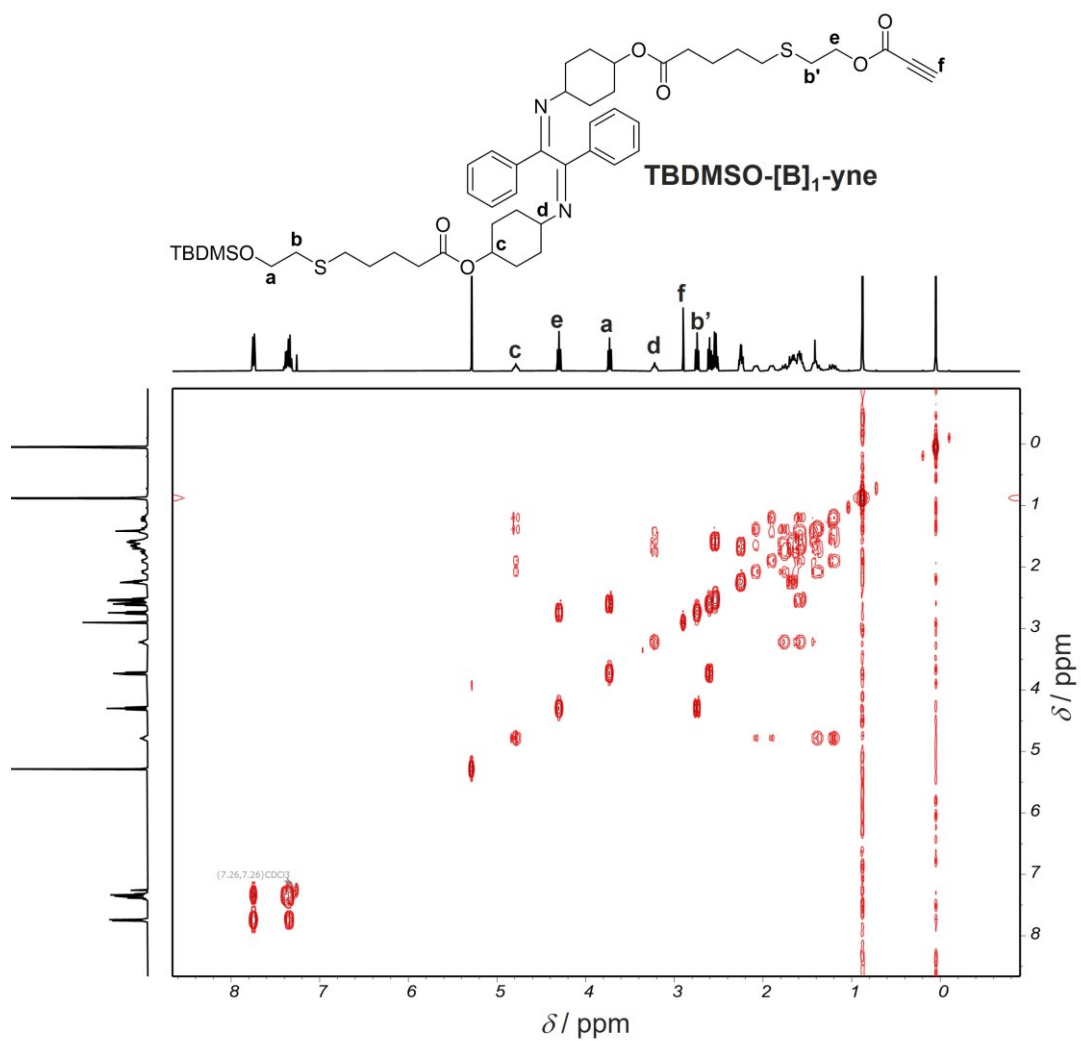


Figure S4.14. COSY NMR spectrum of **TBDMSO-[B]₁-yne** in CDCl₃.

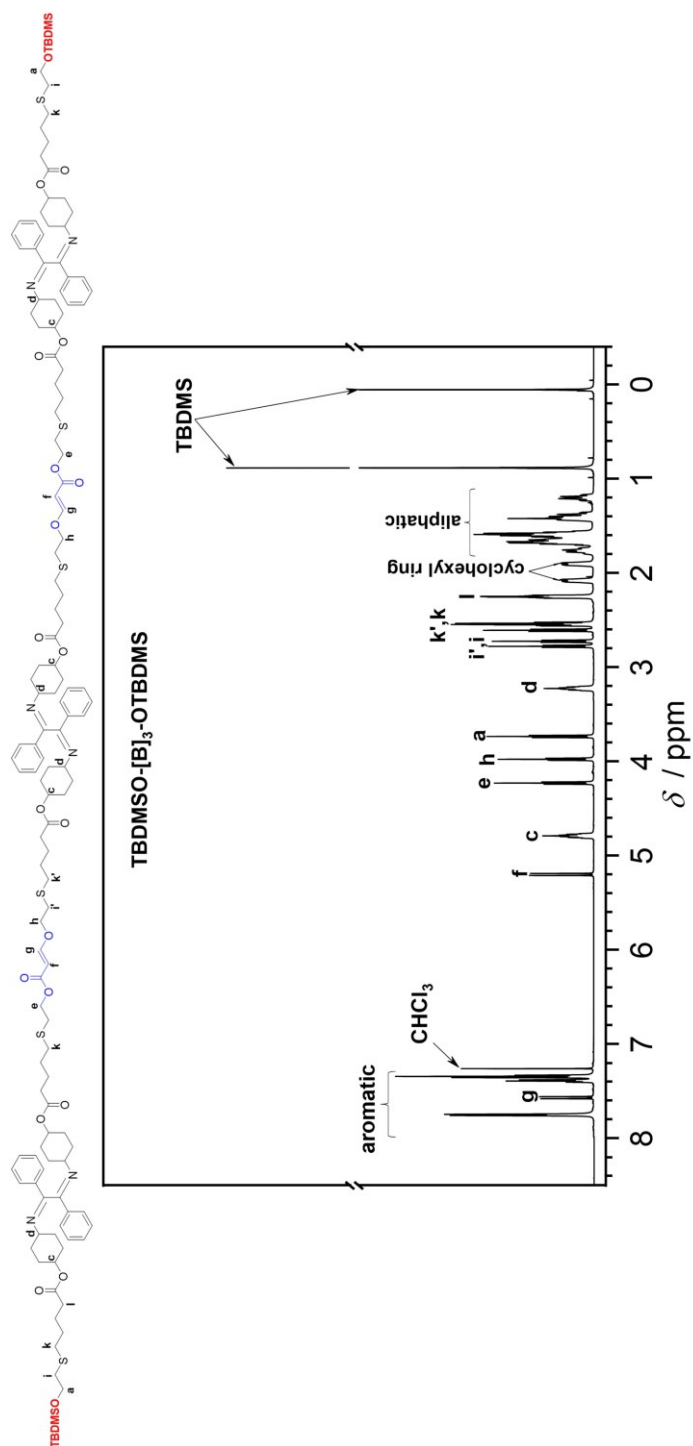
11.4.2.4. TBDMSO-[B]₃-OTBDMS

Figure S4.15. ¹H NMR (600 MHz, 32 scans) spectrum of TBDMSO-[B]₃-OTBDMS in CDCl₃.

196

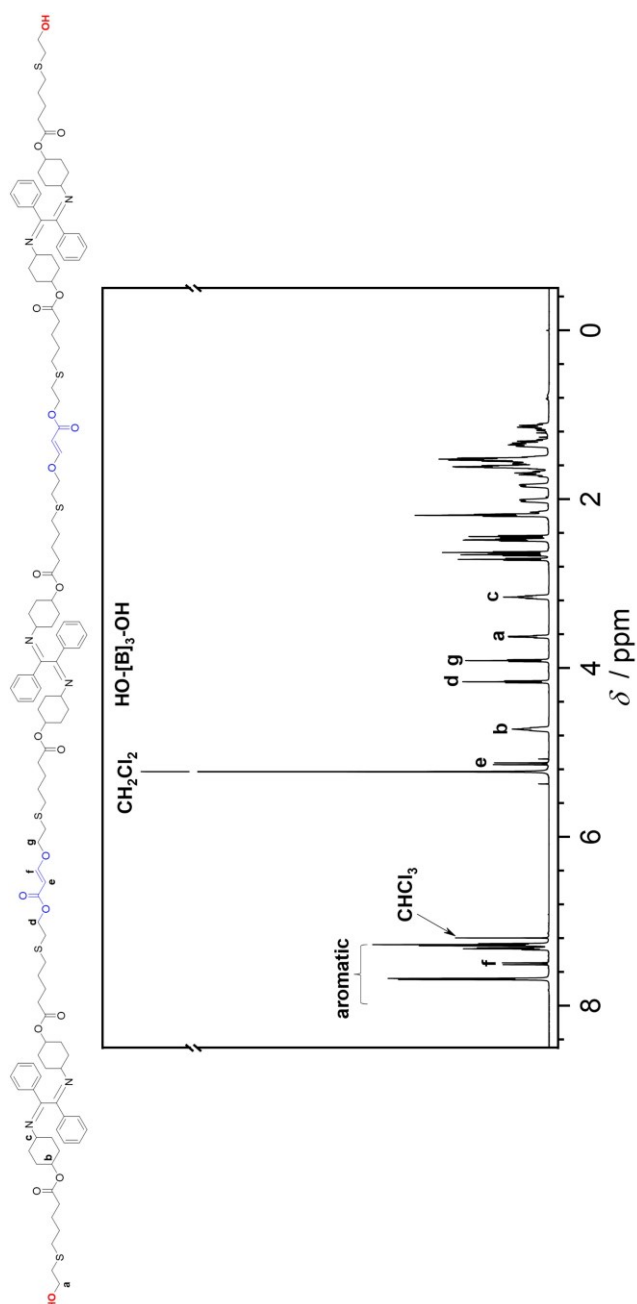
11.4.2.5. HO-[B]₃-OH

Figure S4.18. ¹H NMR (600 MHz, 32 scans) spectrum of HO-[B]₃-OH in CDCl₃, indicating that the protecting group (TBDMS) was completely cleaved.

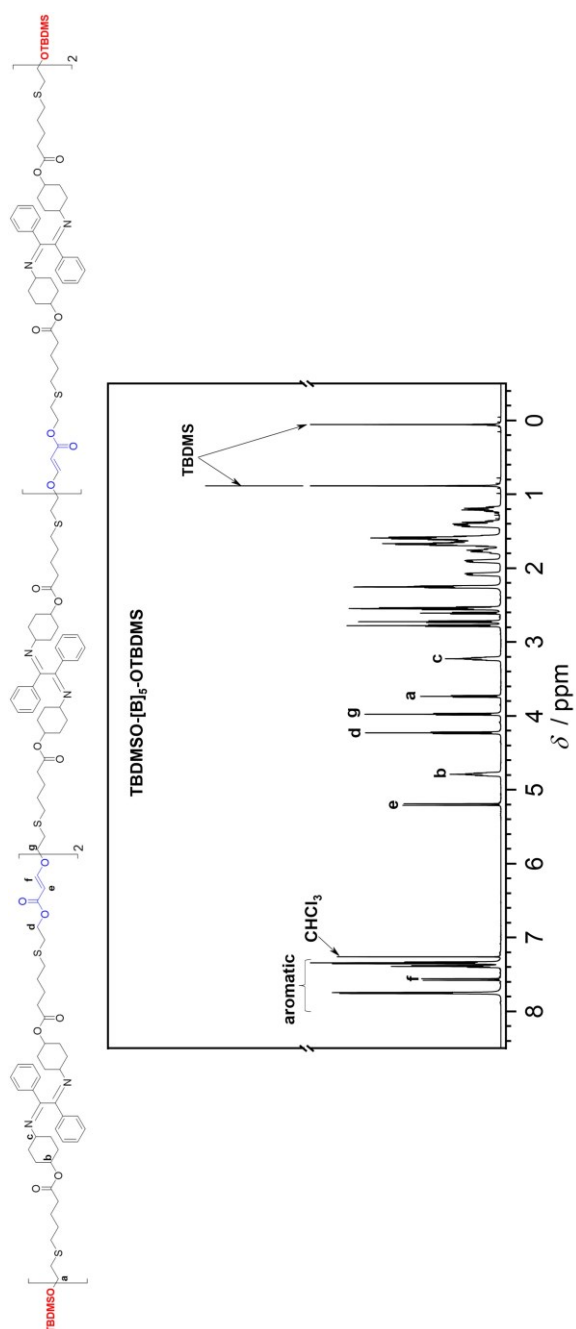
11.4.2.6. TBDMSO-[B]₅-OTBDMS

Figure S4.19. ¹H NMR (600 MHz, 32 scans) spectrum of TBDMSO-[B]₅-OTBDMS in CDCl₃.

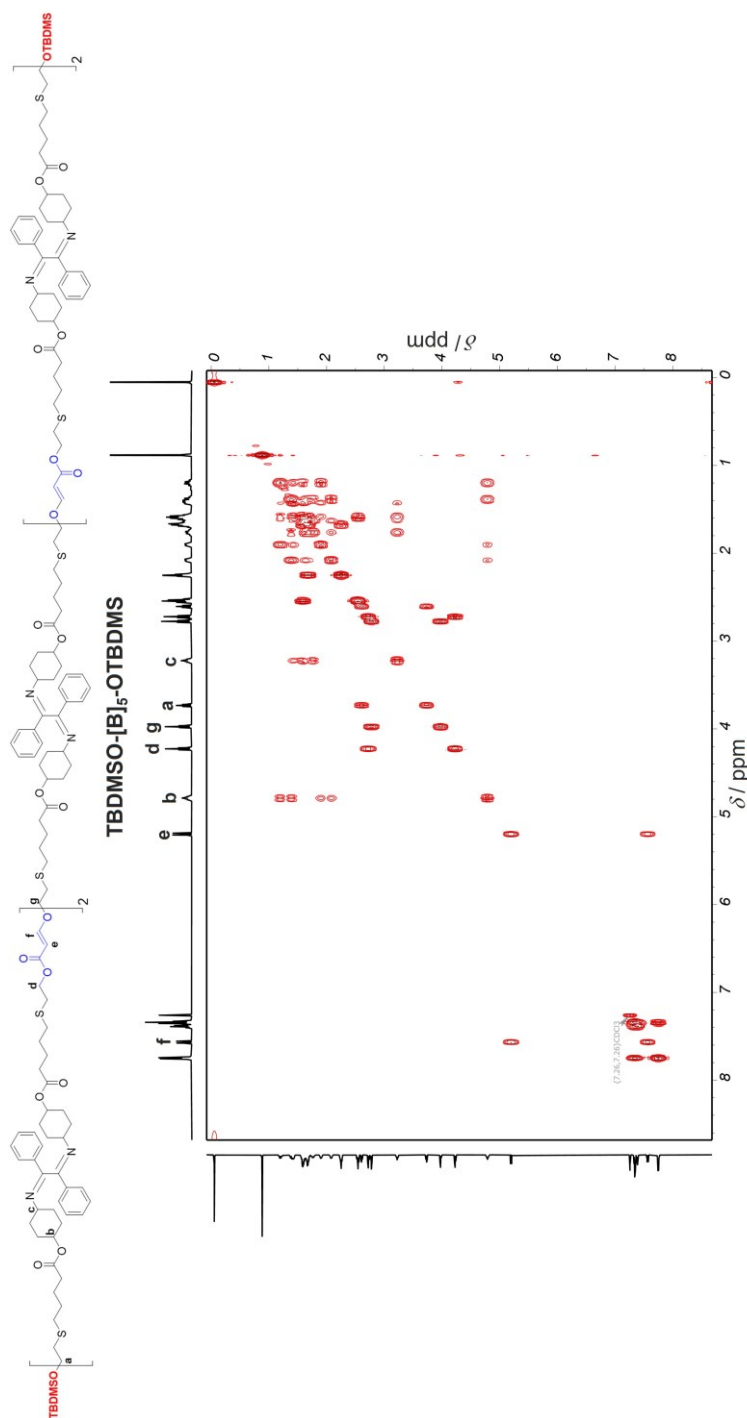


Figure S4.20. COSY NMR spectrum of **TBDMSO-[B]₅-OTBDMS** in CDCl₃.

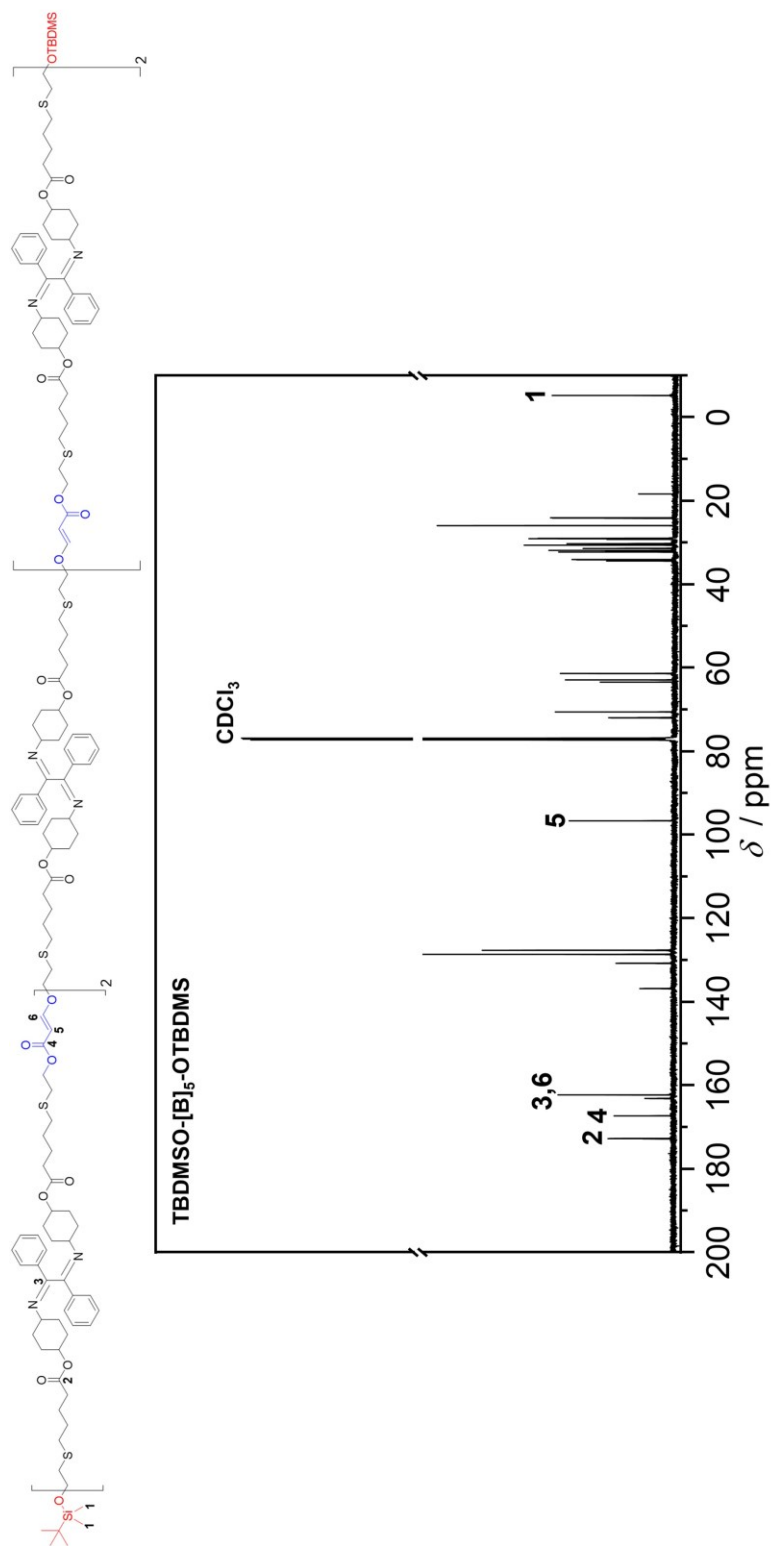


Figure S4.21. Carbon-Proton Decoupled ¹³C NMR (151 MHz) spectrum of **TBDMSO-[B]₅-OTBDMS** in CDCl₃.

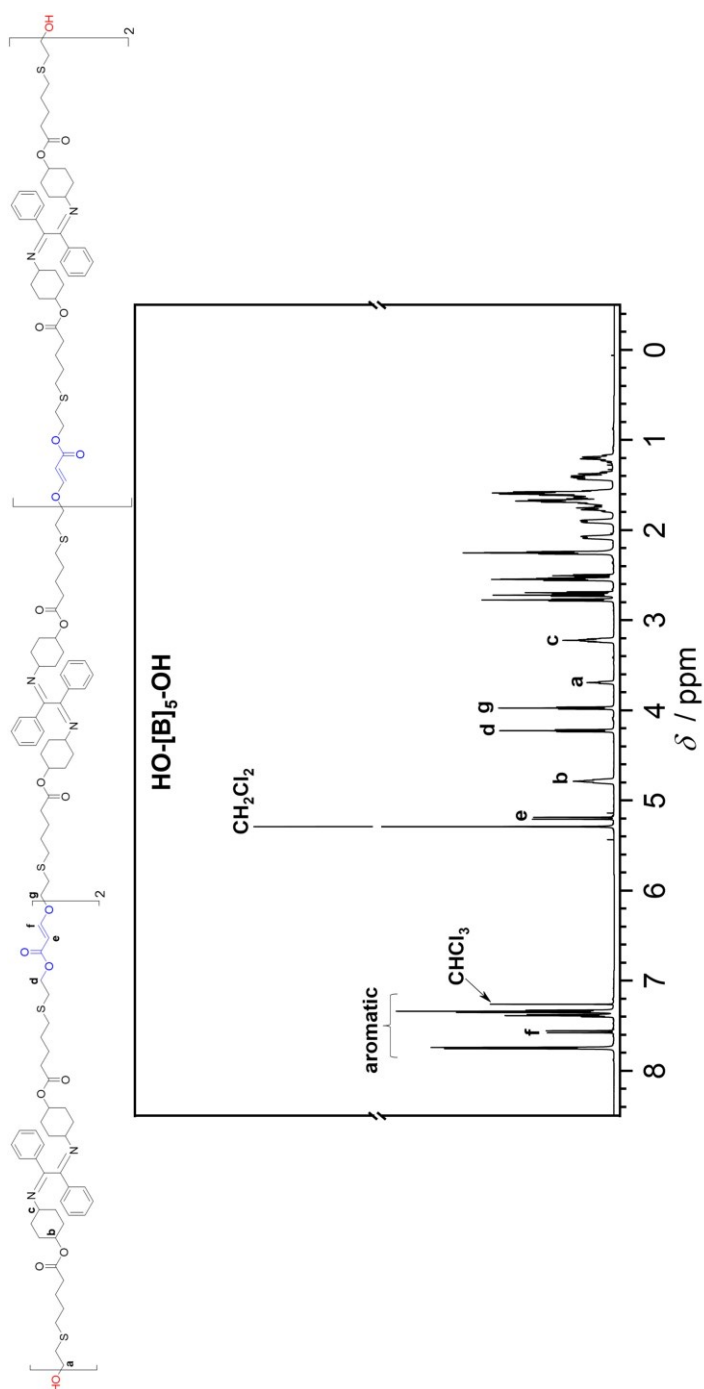
11.4.2.7. HO-[B]₅-OH

Figure S4.22. ¹H NMR (600 MHz, 32 scans) spectrum of HO-[B]₅-OH in CDCl₃.

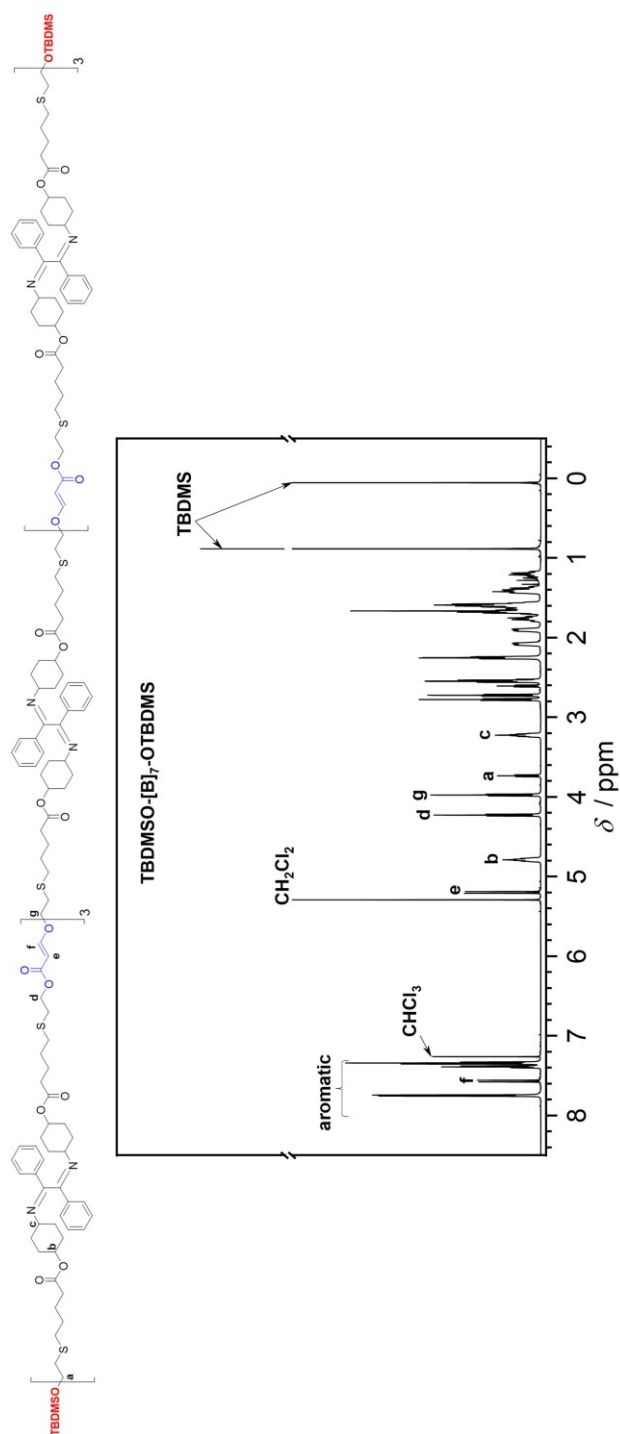
11.4.2.8. TBDMSO-[B]₇-OTBDMS

Figure S4.23. ¹H NMR (600 MHz, 32 scans) spectrum of TBDMSO-[B]₇-OTBDMS in CDCl₃.

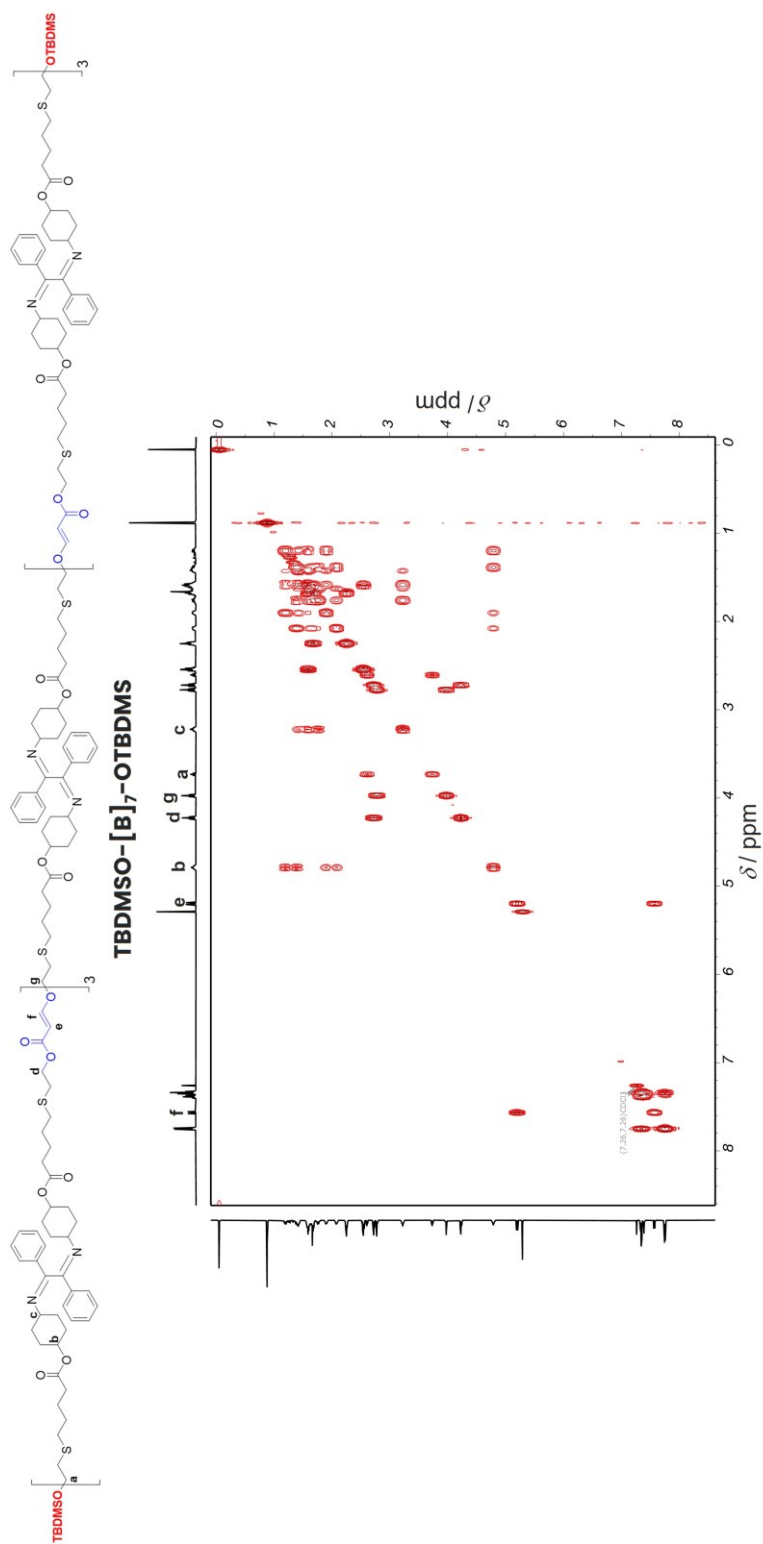


Figure S4.24. COSY NMR spectrum of **TBDMO-[B]₇-OTBDMO** in CDCl_3 .

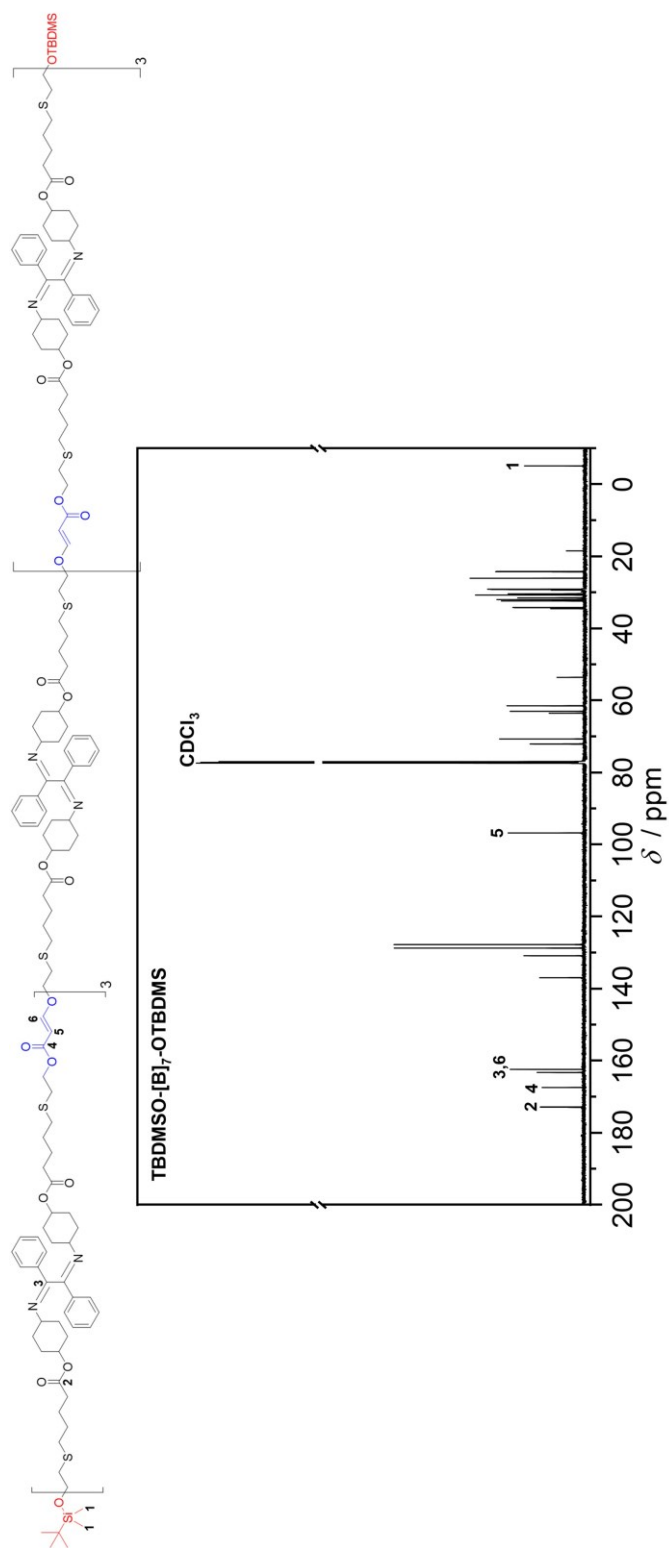


Figure S4.25. Carbon-Proton Decoupled ¹³C NMR (151 MHz) spectrum of **TBDMSO-[B]₇-OTBDMS** in CDCl₃.

HO-[B]₇-OH

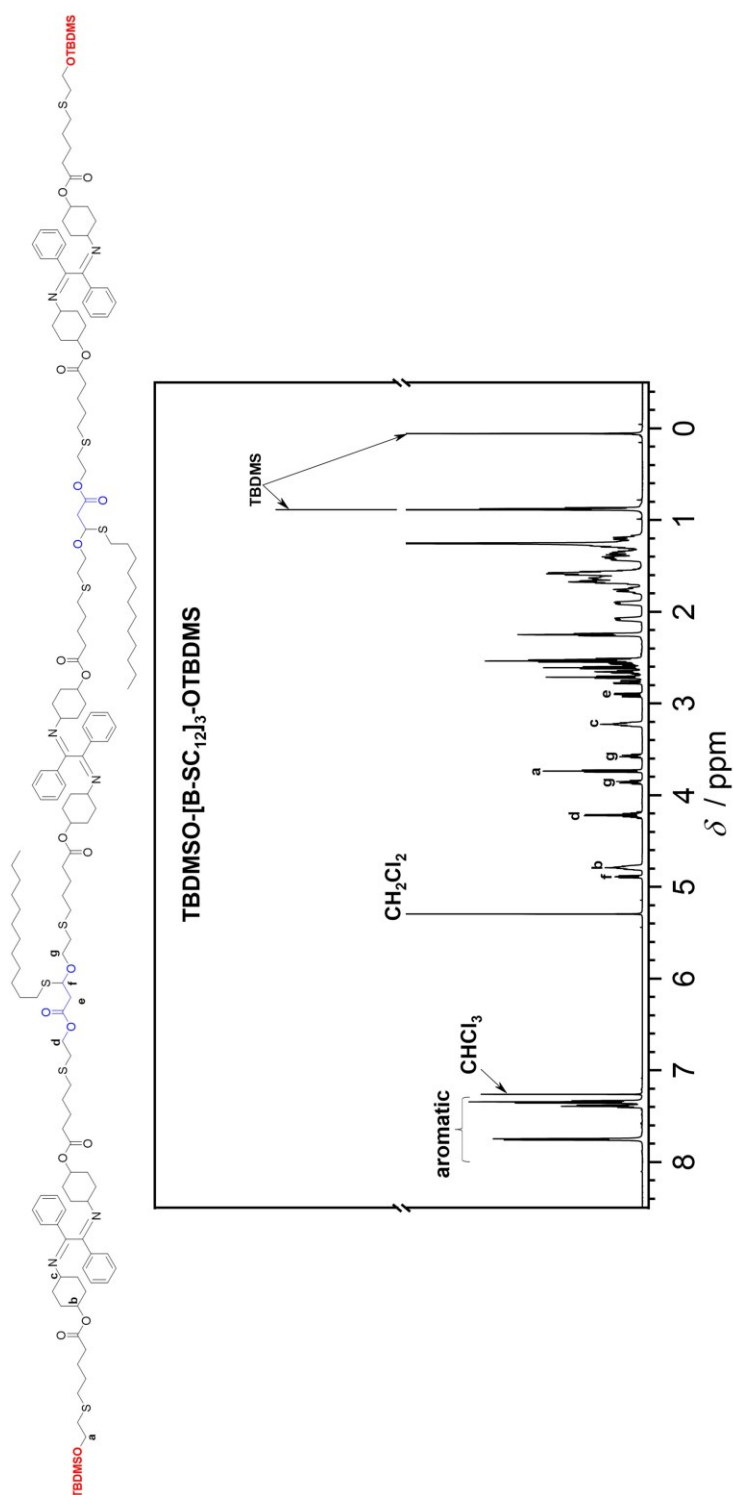
11.4.2.9. TBDMSO-[B-SC₁₂]₃-OTBDMS

Figure S4.27. ¹H NMR (600 MHz, 32 scans) spectrum of TBDMSO-[B-SC₁₂]₃-OTBDMS in CDCl₃.

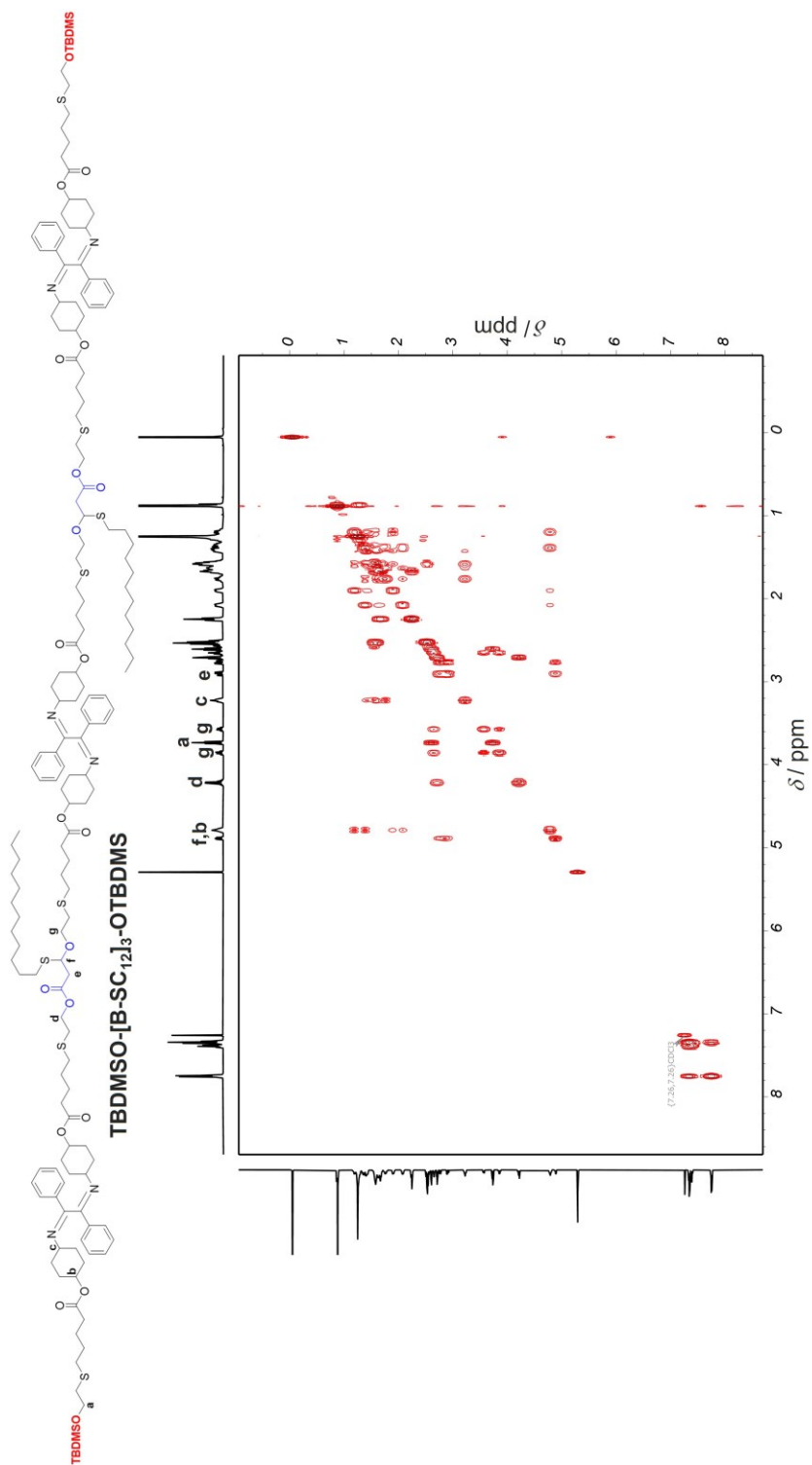


Figure S4.28. COSY NMR spectrum of **TBDMSO-[B-SC₁₂]₃-OTBDMS** in CDCl₃.

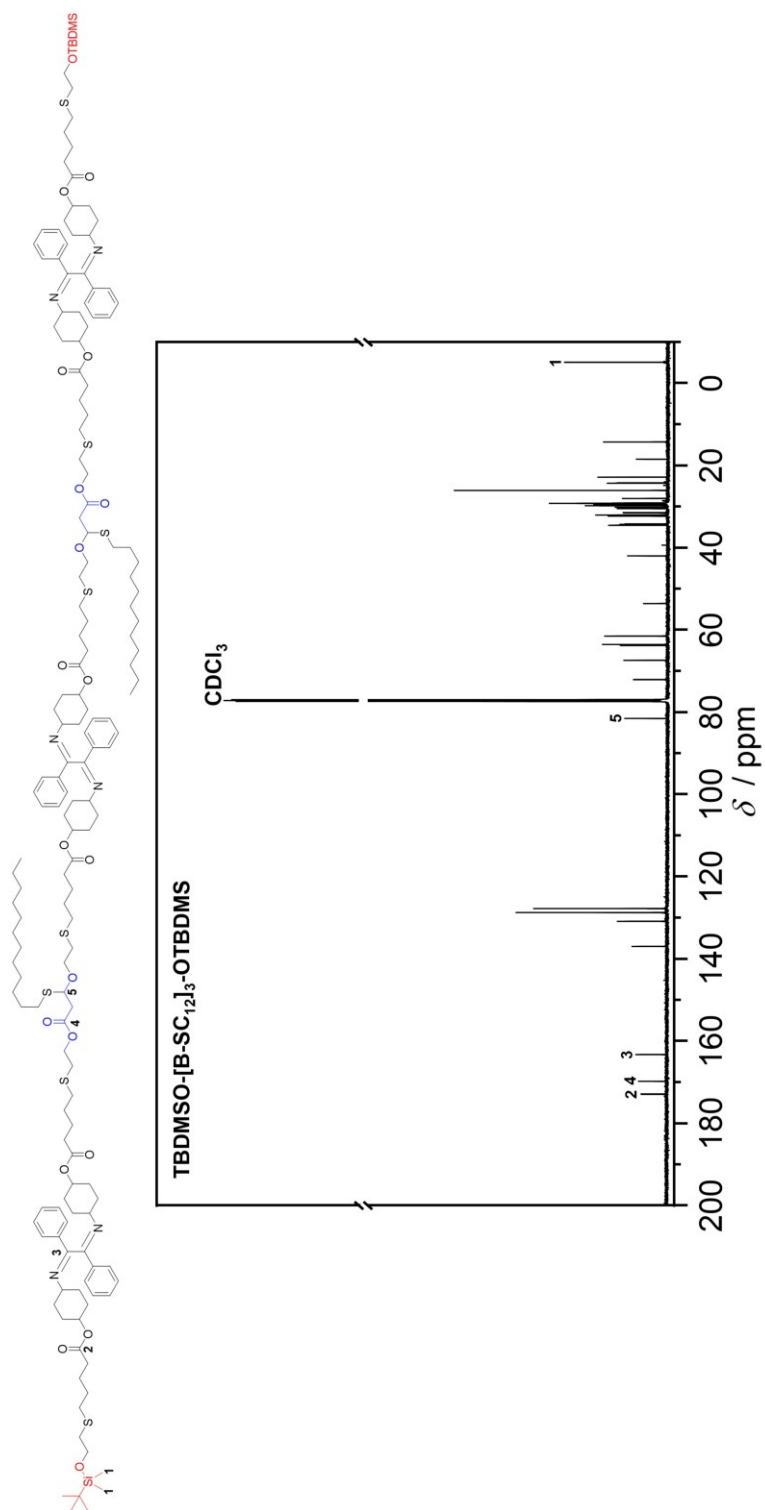


Figure S4.29. Carbon-Proton Decoupled ¹³C NMR (151 MHz) spectrum of **TBDMSO-[B-SC₁₂]₃-OTBDMS** in CDCl₃.

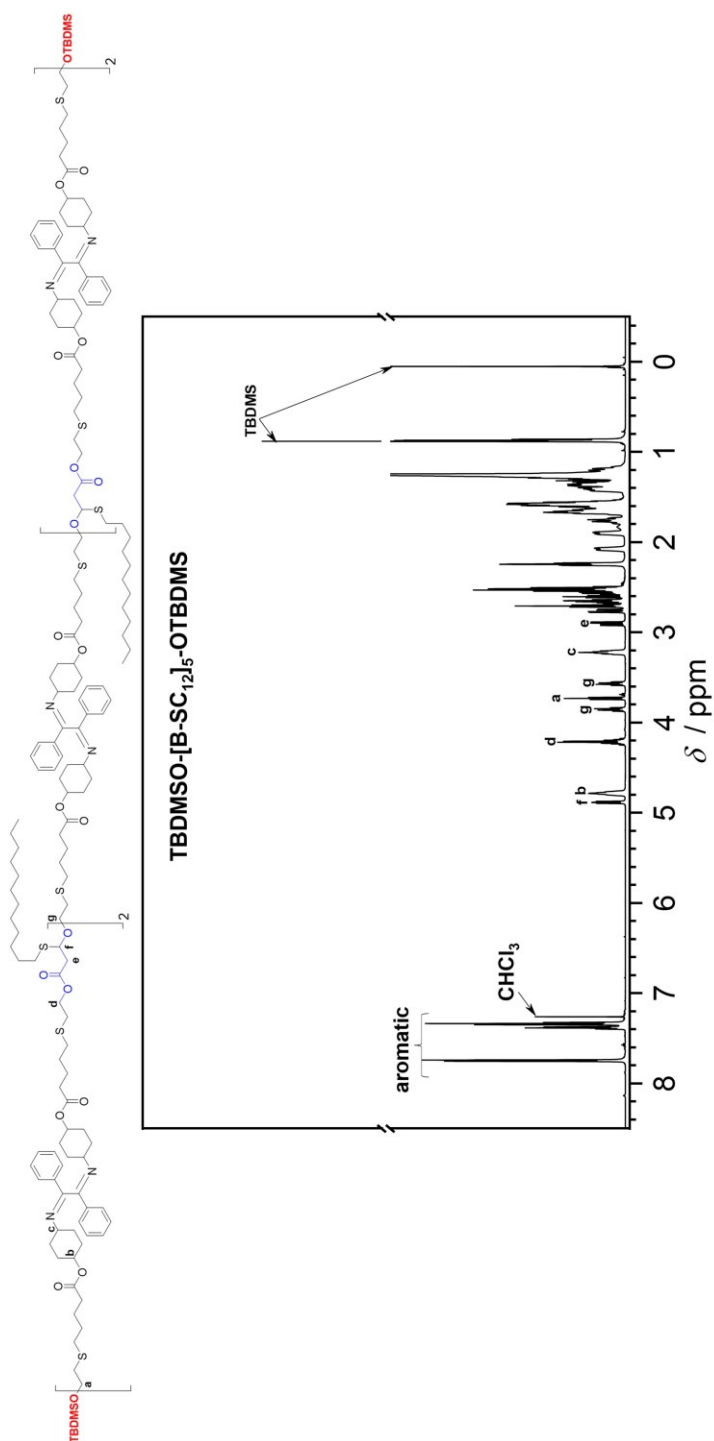
11.4.2.10. TBDMSO-[B-SC₁₂]₅-OTBDMS

Figure S4.30. ¹H NMR (600 MHz, 32 scans) spectrum of TBDMSO-[B-SC₁₂]₅-OTBDMS in CDCl₃.

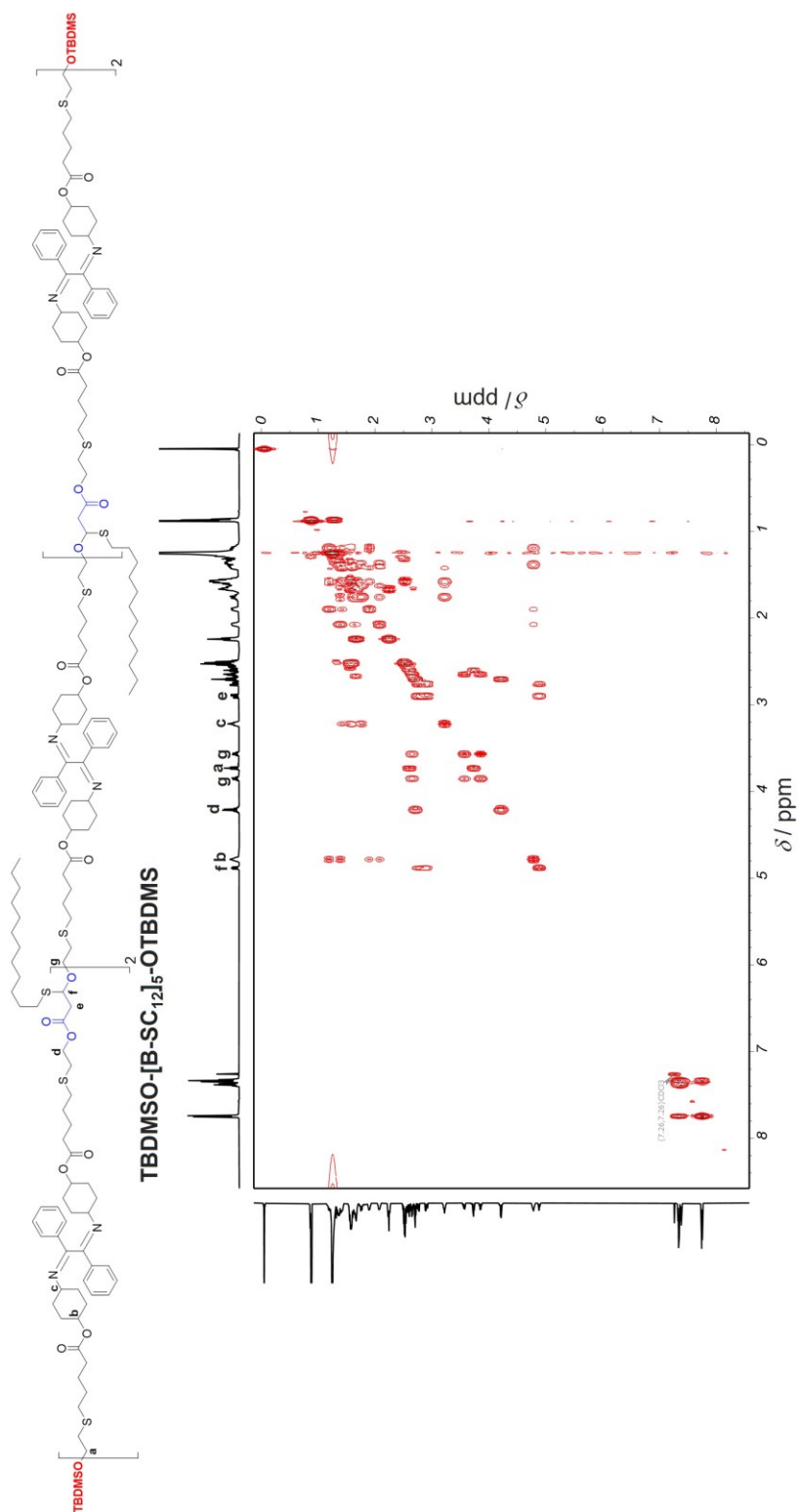


Figure S4.31. COSY NMR spectrum of **TBDMSO-[B-SC₁₂]₅-OTBDMS** in CDCl₃.

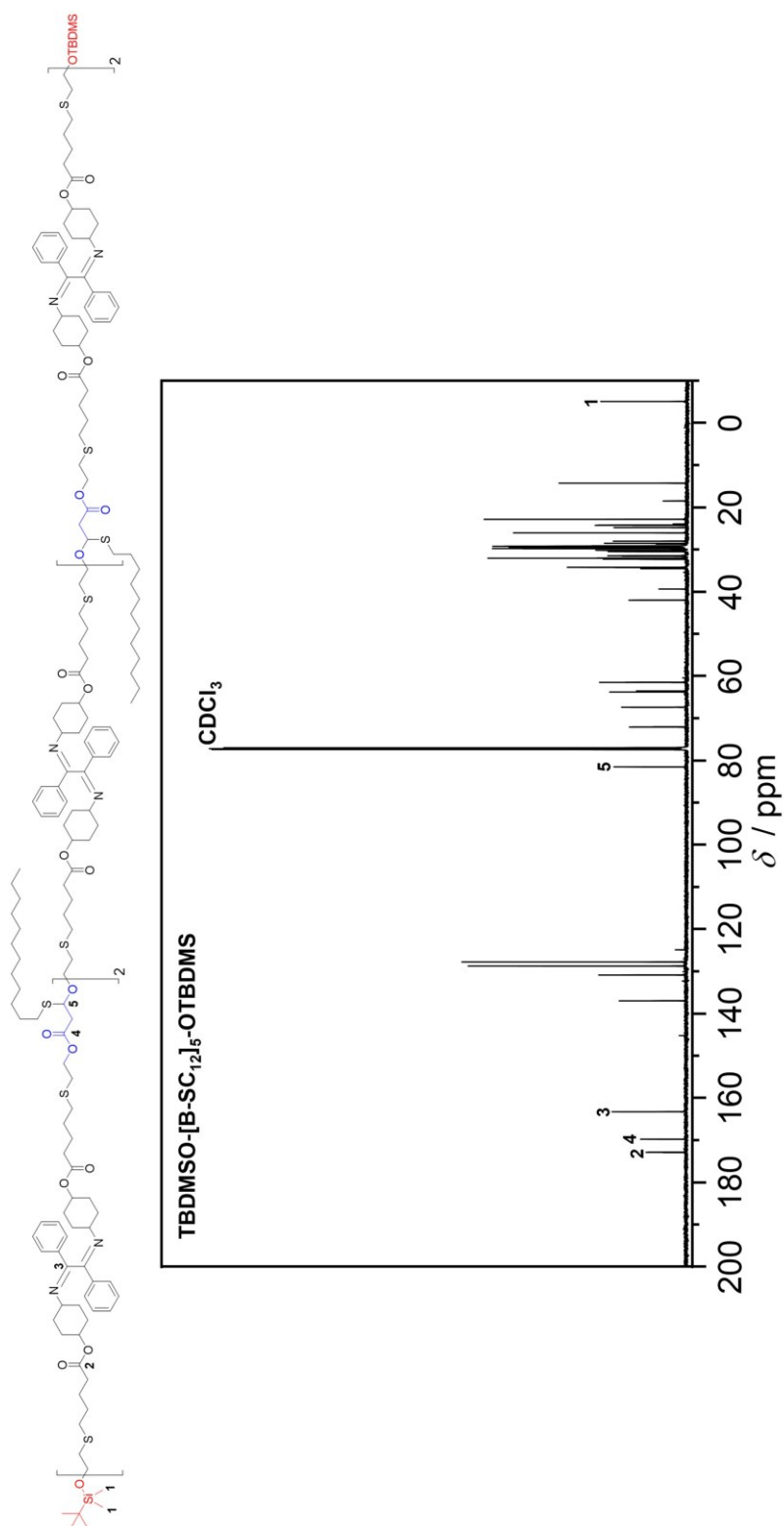


Figure S4.32. Carbon-Proton Decoupled ¹³C NMR (151 MHz) spectrum of **TBDMSO-[B-SC₁₂]₅-OTBDMS** in CDCl₃.

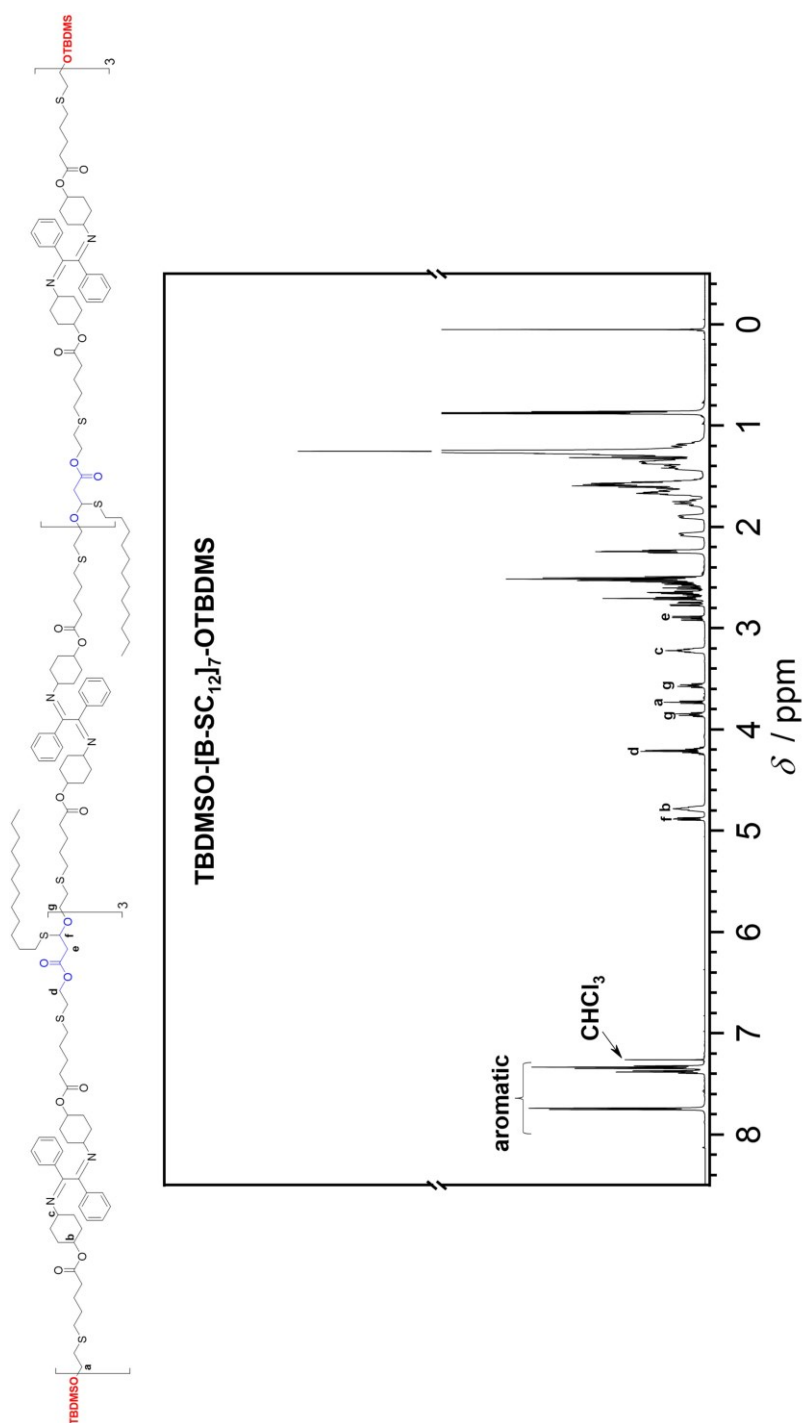
11.4.2.11. TBDMSO-[B-SC₁₂]₇-OTBDMS

Figure S4.33. ¹H NMR (600 MHz, 32 scans) spectrum of TBDMSO-[B-SC₁₂]₇-OTBDMS in CDCl₃.

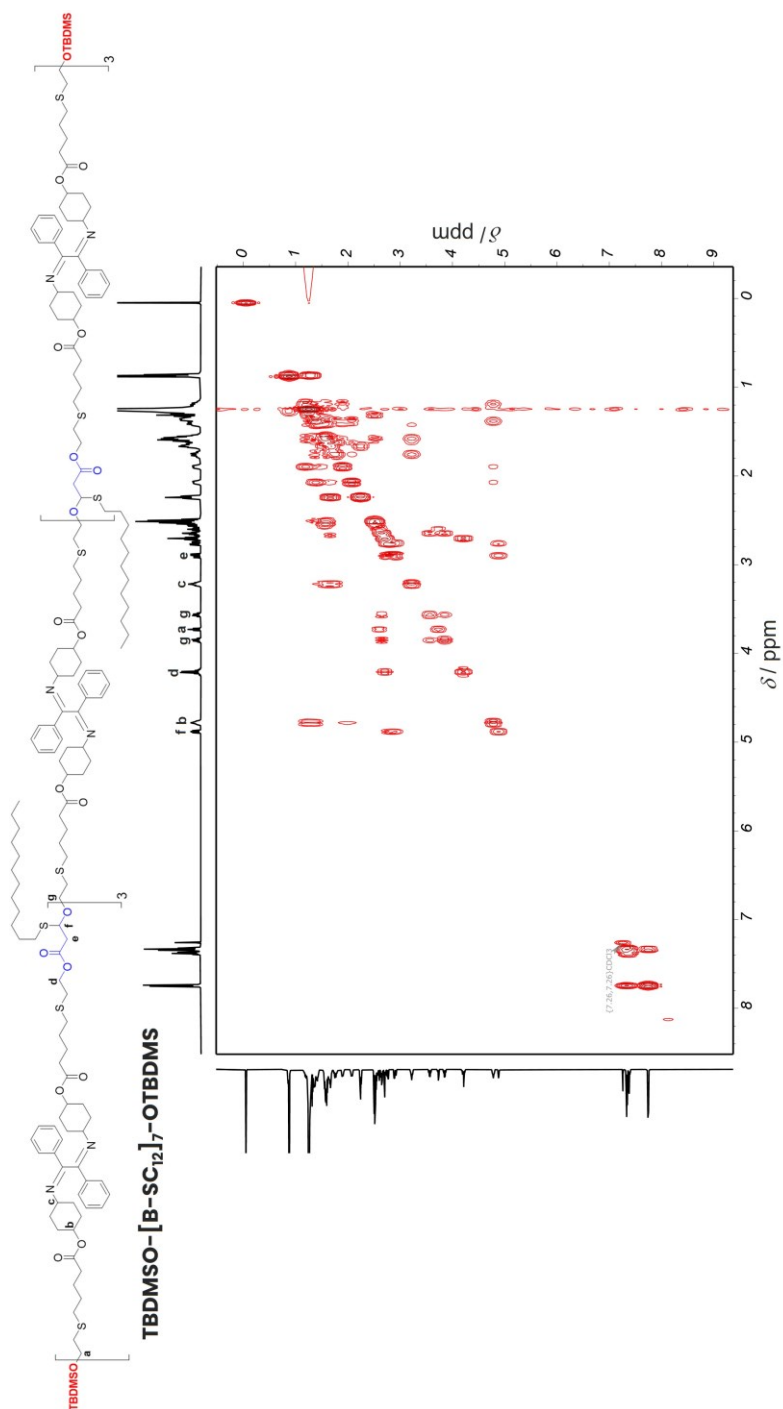


Figure S4.34. COSY NMR spectrum of **TBDMSO-[B-SC₁₂]₇-OTBDMS** in CDCl₃.

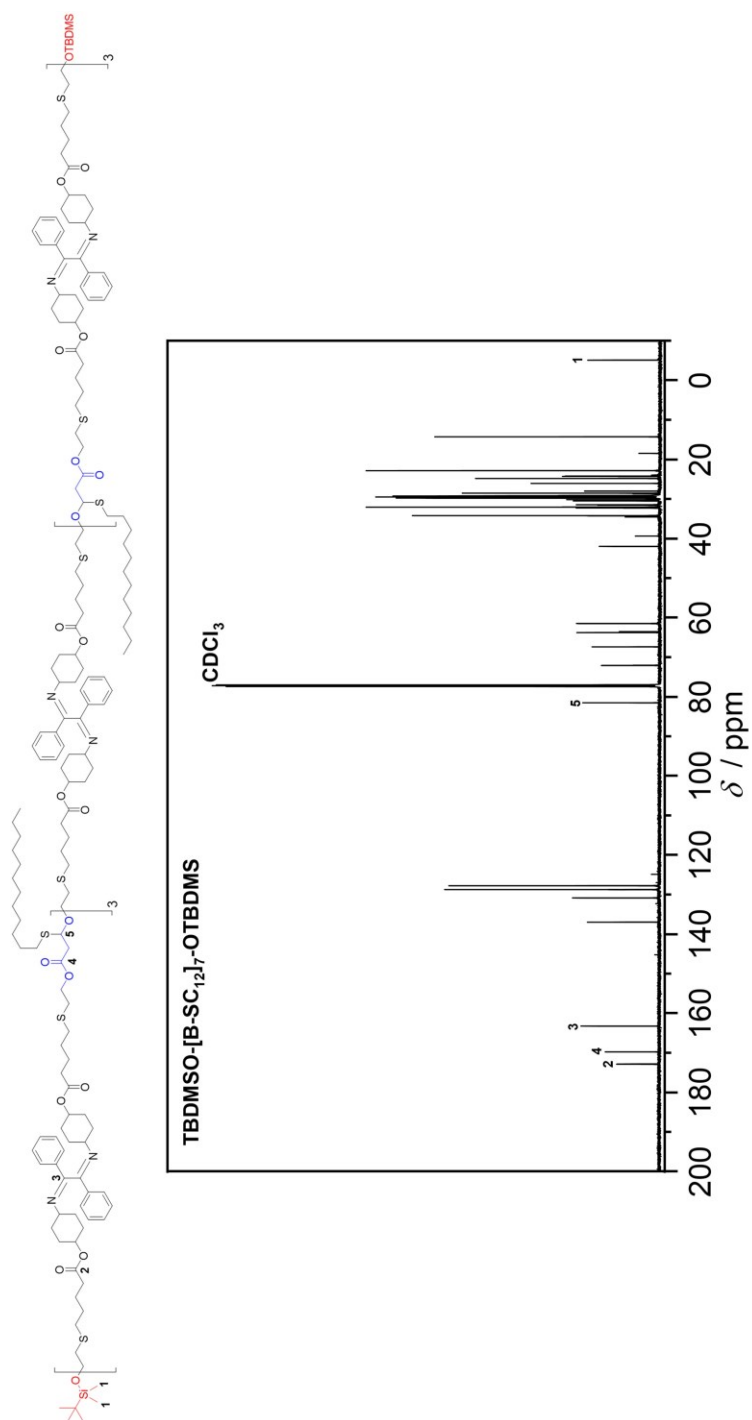


Figure S4.35. Carbon-Proton Decoupled ¹³C NMR (151 MHz) spectrum of **TBDMSO-[B-SC₁₂]₇-OTBDMS** in CDCl₃.

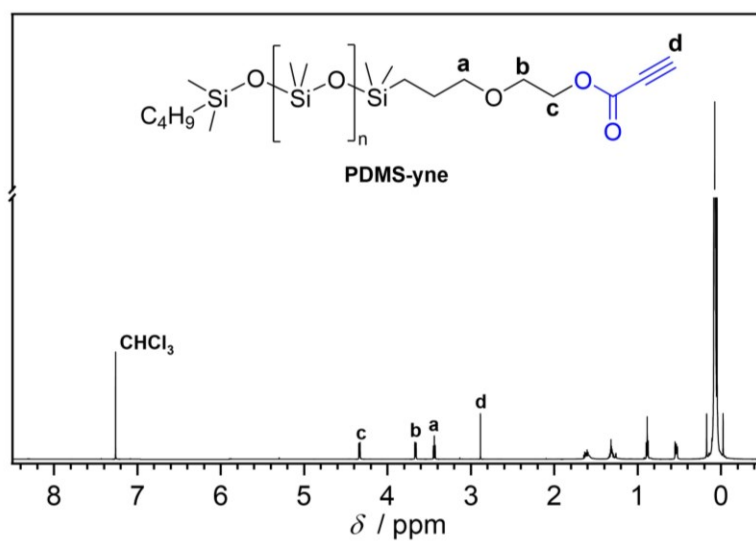
11.4.2.12. PDMS-yne

Figure S4.36. ^1H NMR (600 MHz, 32 scans) spectrum of **PDMS-yne** in CDCl_3 .

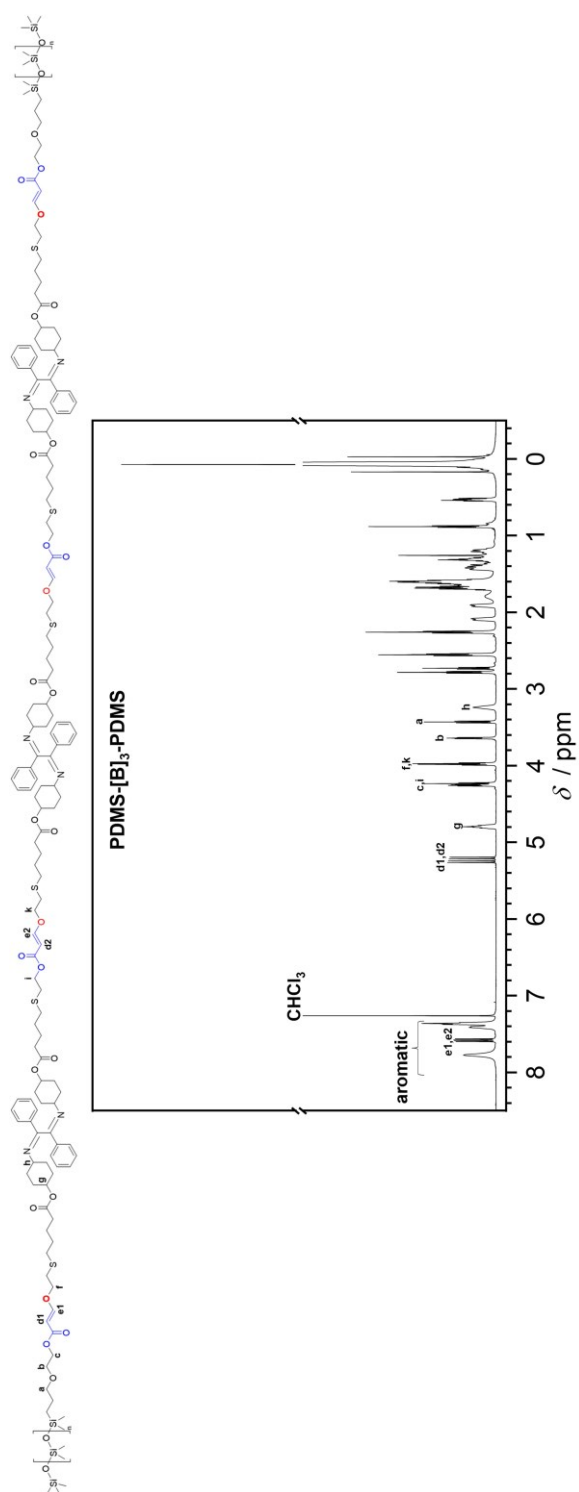
11.4.2.13. PDMS-[B]₃-PDMS

Figure S4.37. ¹H NMR (600 MHz, 32 scans) spectrum of **PDMS-[B]₃-PDMS** in CDCl₃.

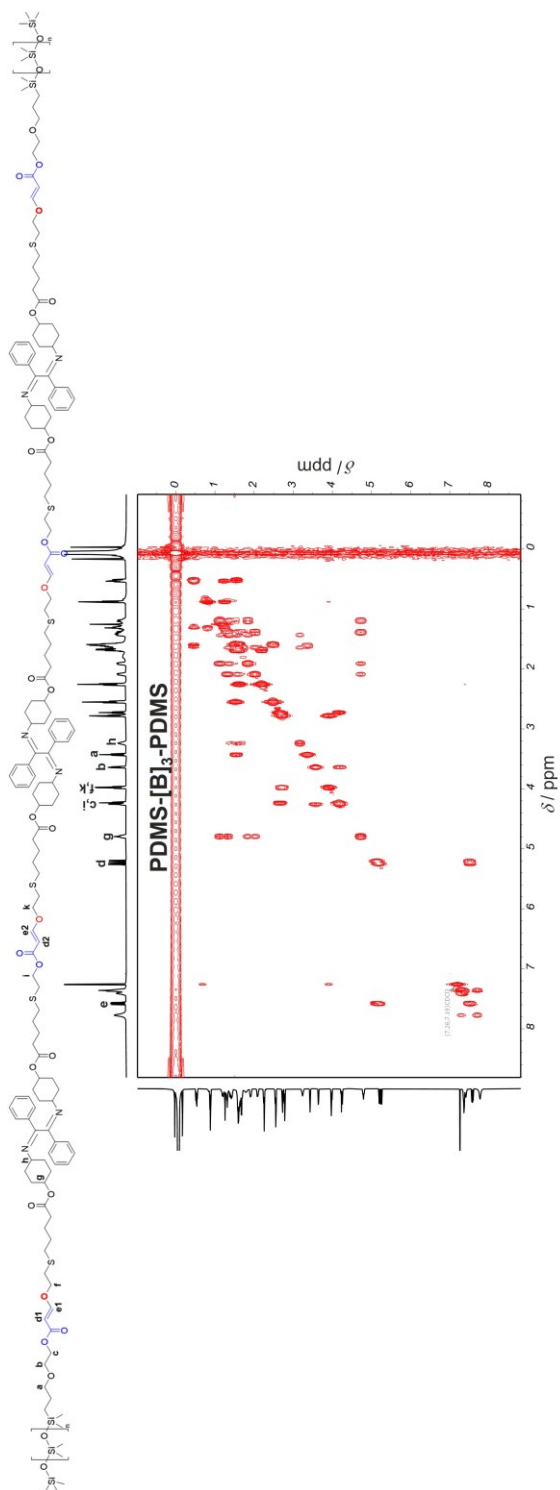


Figure S4.38. COSY NMR spectrum of **PDMS-[B]₃-PDMS** in CDCl₃.

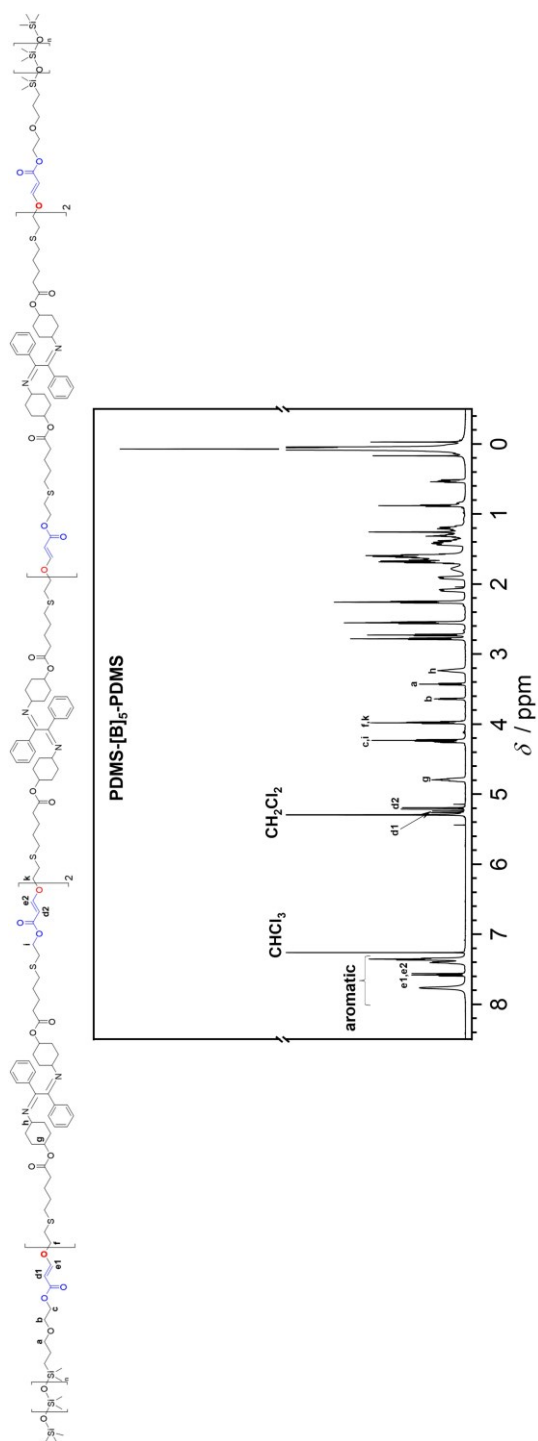
11.4.2.14. PDMS-[B]₅-PDMS

Figure S4.39. ¹H NMR (600 MHz, 32 scans) spectrum of PDMS-[B]₅-PDMS in CDCl₃.

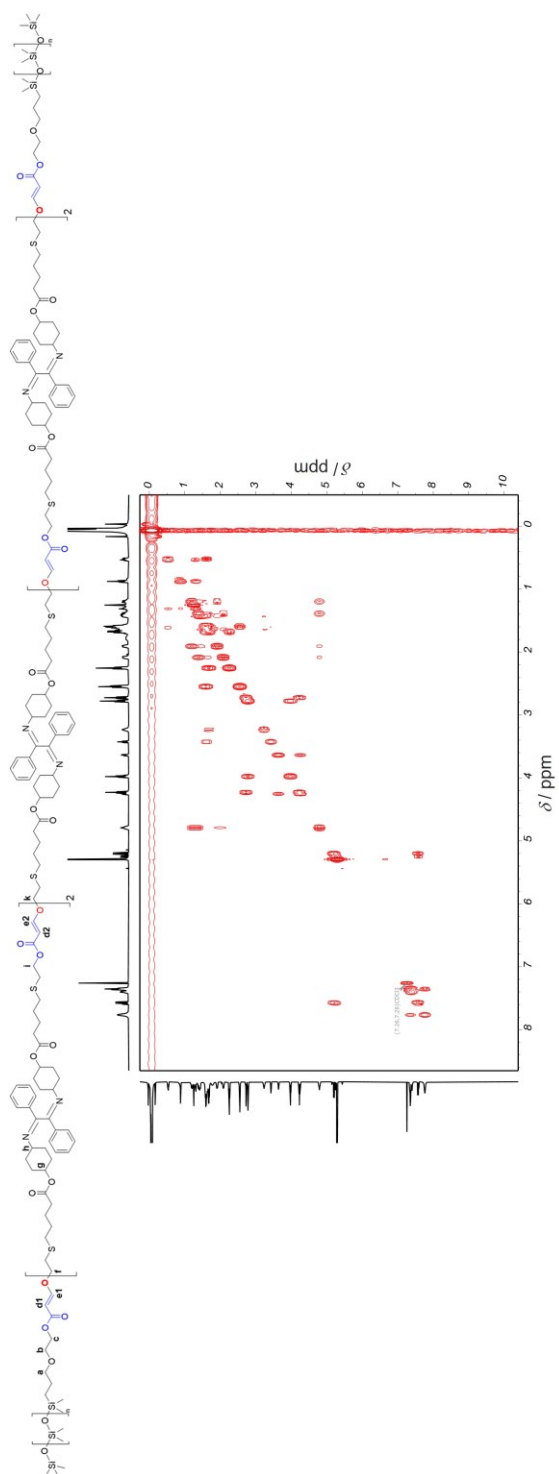


Figure S4.40. COSY NMR spectrum of PDMS-[B]₅-PDMS in CDCl₃.

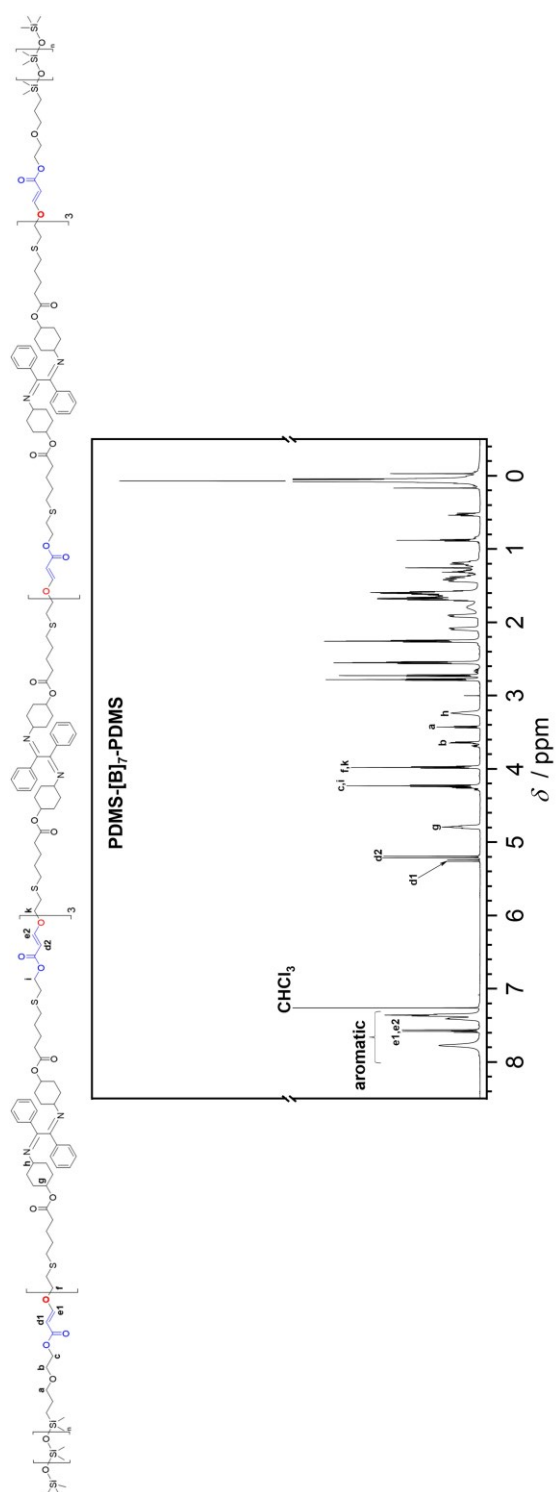
11.4.2.15. PDMS-[B]₇-PDMS

Figure S4.41. ¹H NMR (600 MHz, 32 scans) spectrum of PDMS-[B]₇-PDMS in CDCl₃.

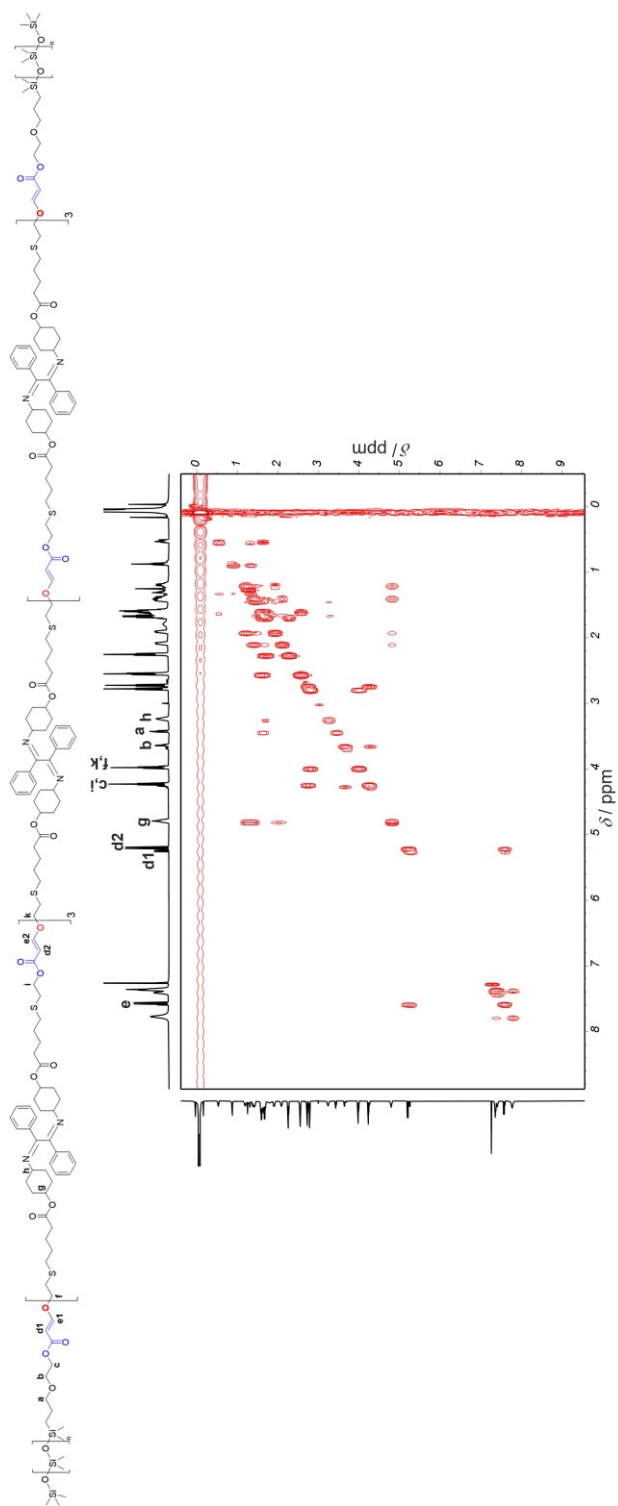


Figure S4.42. COSY NMR spectrum of PDMS-[B]₇-PDMS in CDCl₃.

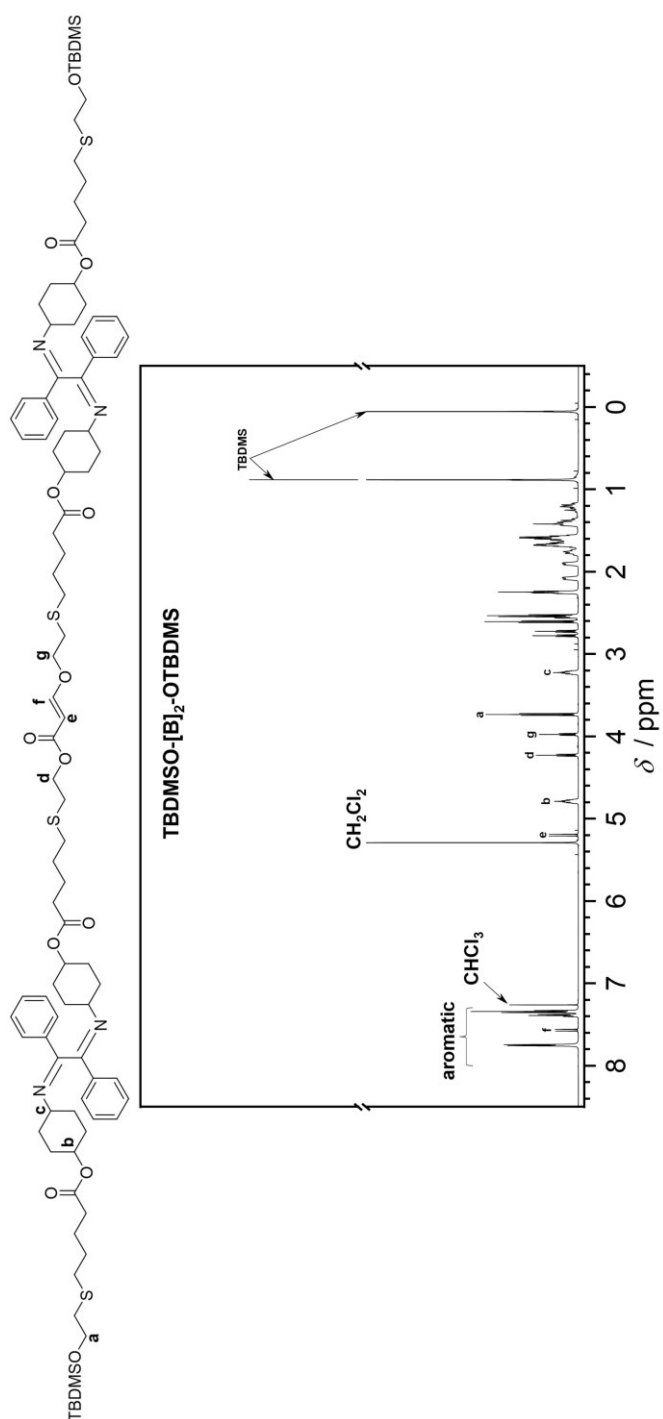
11.4.2.16. TBDMSO-[B]₂-OTBDMS

Figure S4.43. ¹H NMR (600 MHz, 32 scans) spectrum of **TBDMSO-[B]₂-OTBDMS** in CDCl₃.

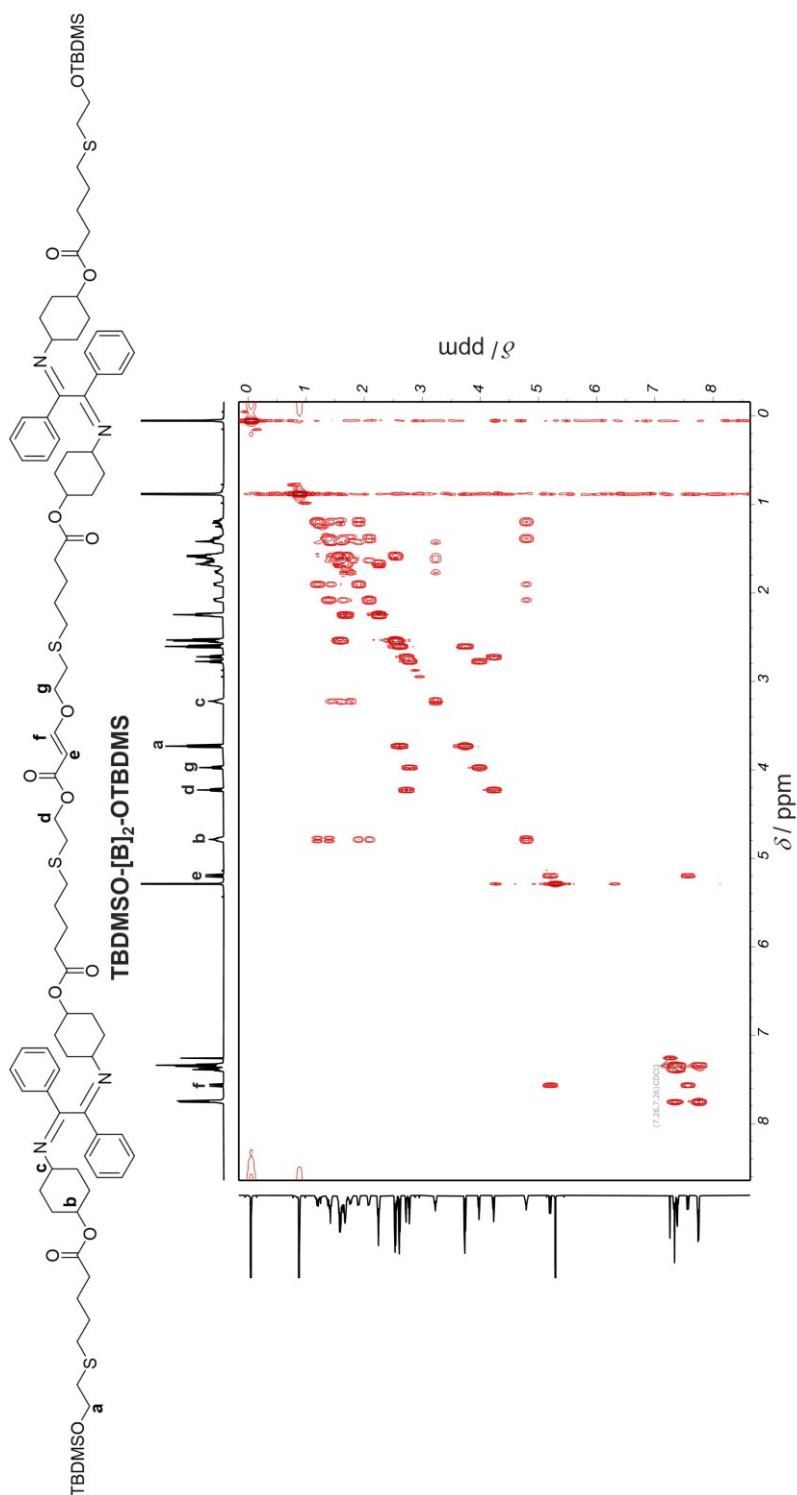


Figure S4.44. COSY NMR spectrum of **TBDMSO-[B]₂-OTBDMS** in CDCl₃.

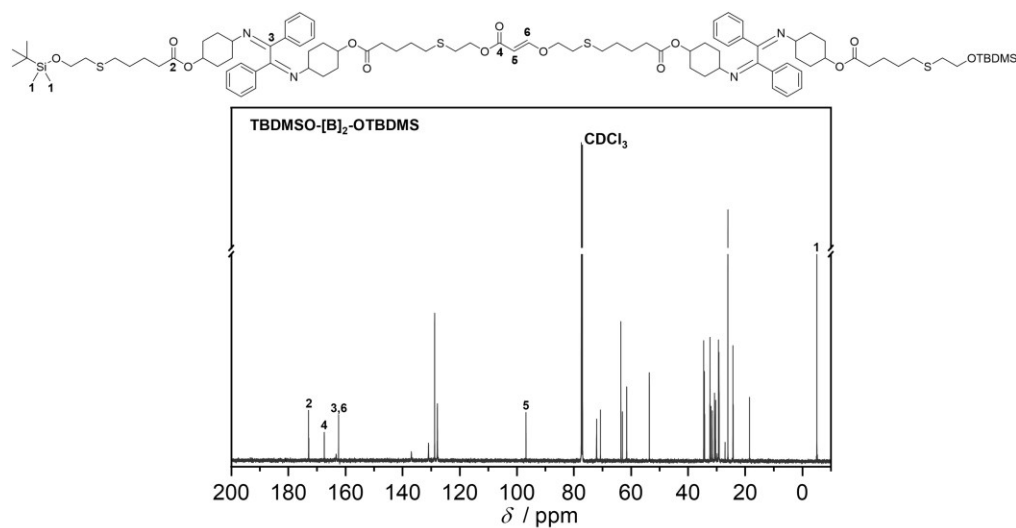


Figure S4.45. Carbon-Proton Decoupled ¹³C NMR (151 MHz) spectrum of TBDMSO-[B]₂-OTBDMS in CDCl₃.

11.4.2.17. HO-[B]₂-OH

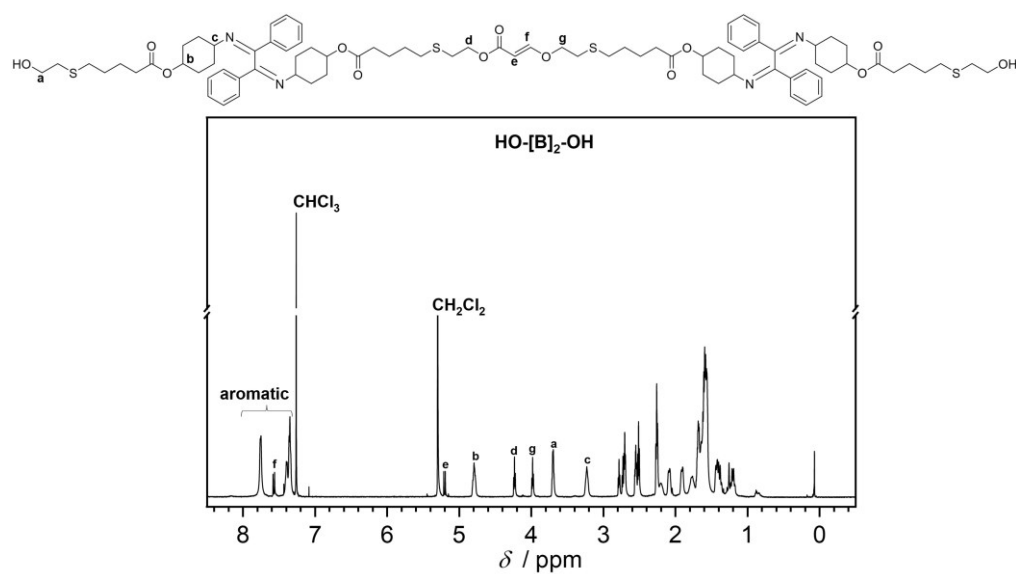


Figure S4.46. ¹H NMR (600 MHz, 32 scans) spectrum of HO-[B]₂-OH in CDCl₃.

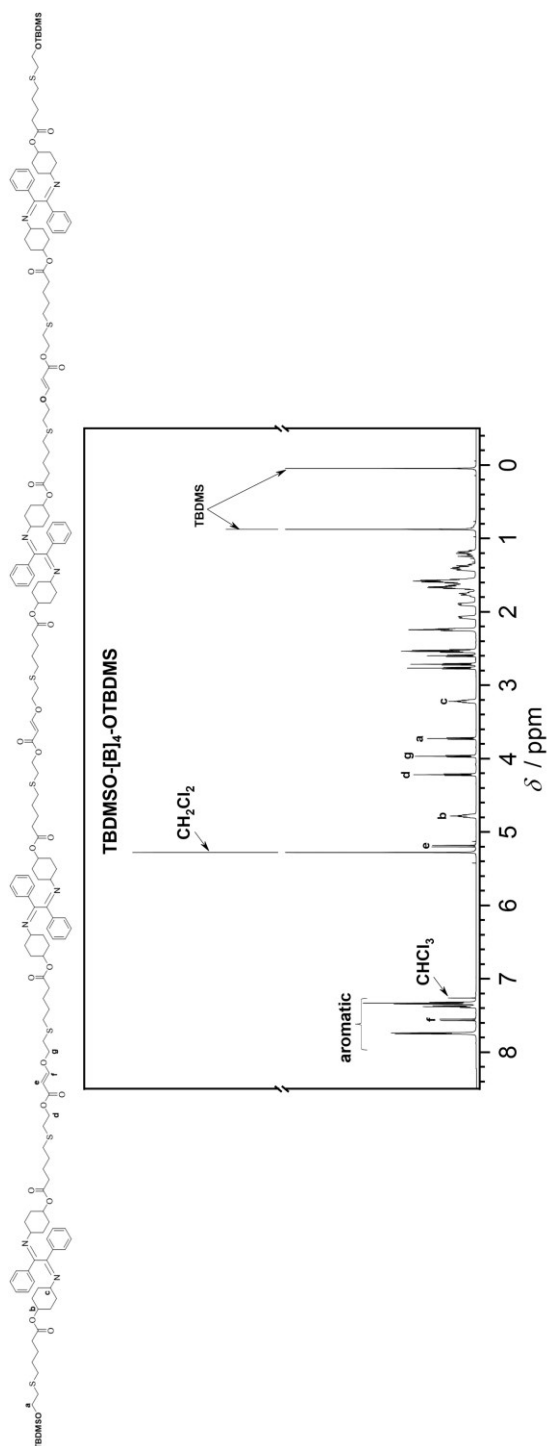
11.4.2.18. TBDMSO-[B]₄-OTBDMS

Figure S4.47. ¹H NMR (600 MHz, 32 scans) spectrum of TBDMSO-[B]₄-OTBDMS in CDCl₃

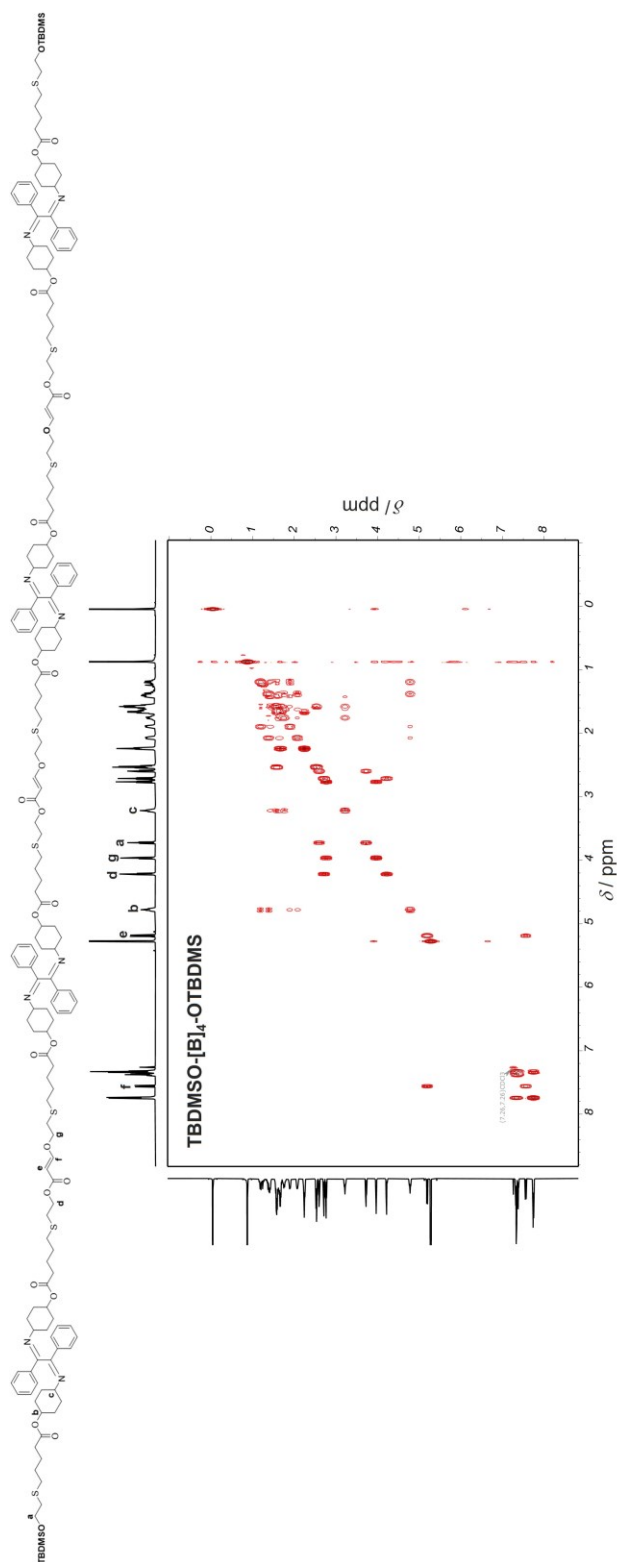


Figure S4.48. COSY NMR spectrum of **TBDMSO-[B]₄-OTBDMS** in CDCl₃.

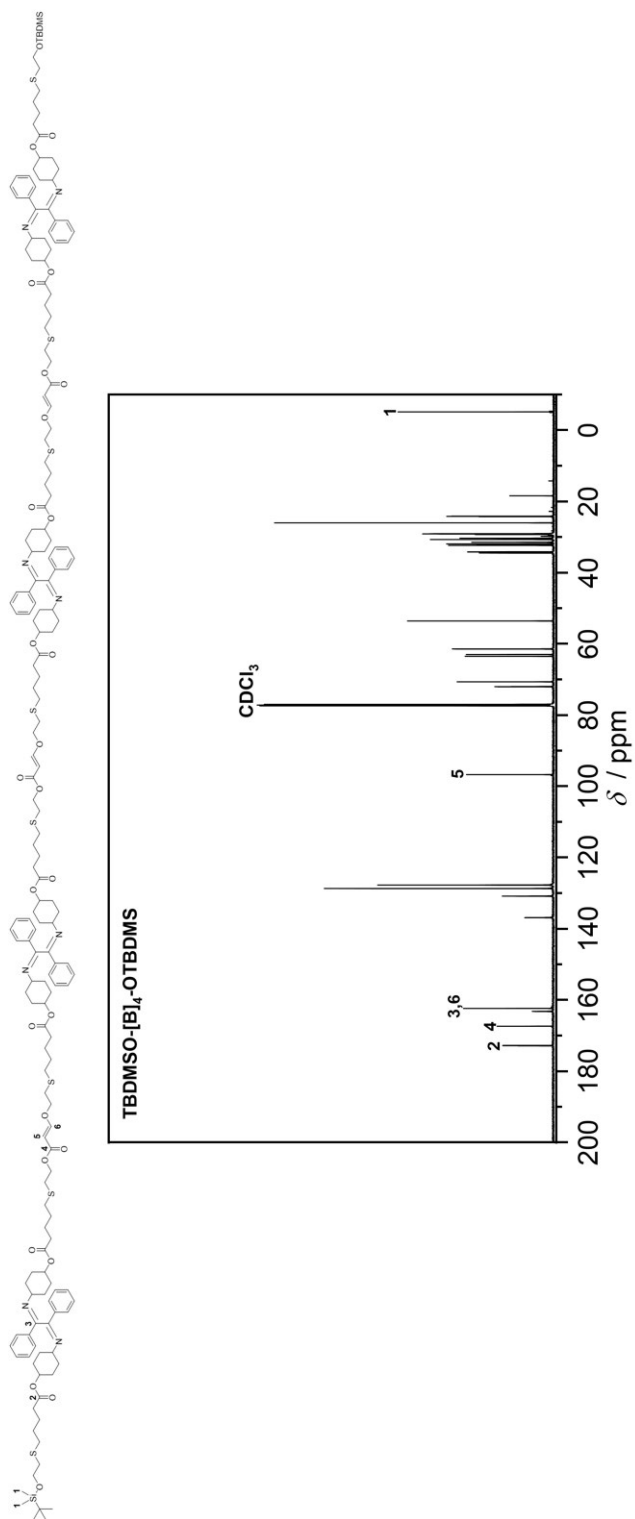


Figure S4.49. Carbon-Proton Decoupled ¹³C NMR (151 MHz) spectrum of **TBDMSO-[B]₄-OTBDMS** in CDCl₃.

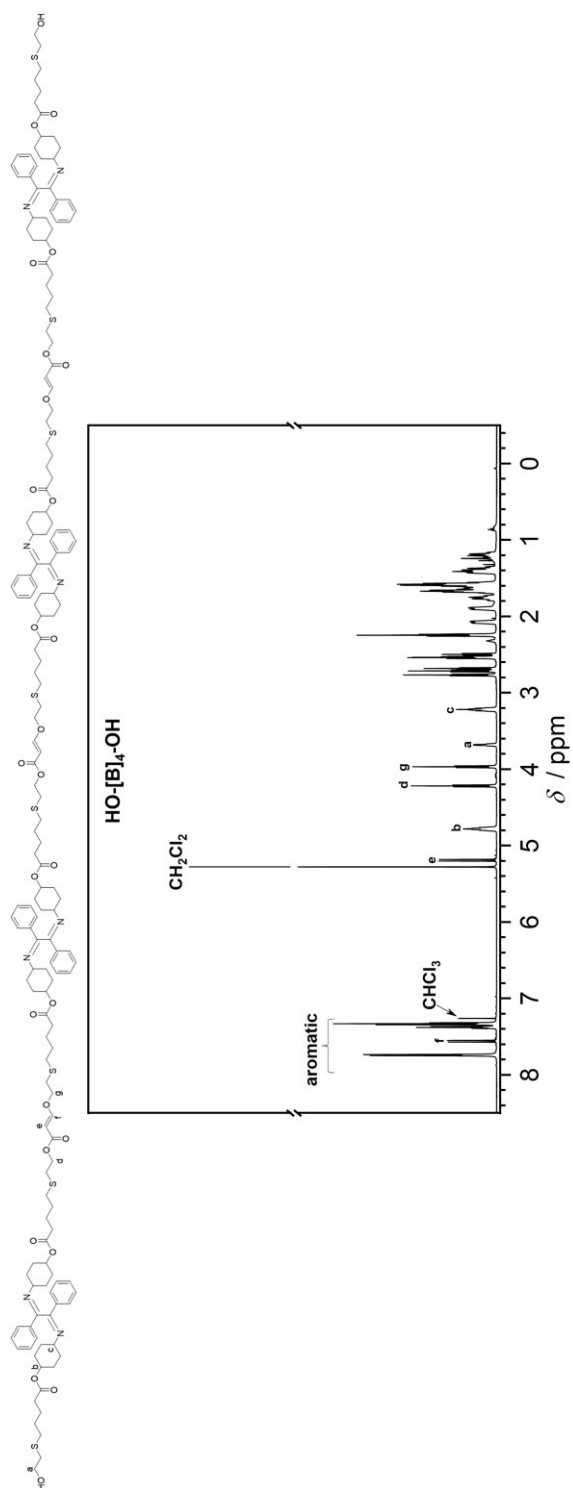
11.4.2.19. HO-[B]₄-OH

Figure S4.50. ¹H NMR (600 MHz, 32 scans) spectrum of HO-[B]₄-OH in CDCl₃

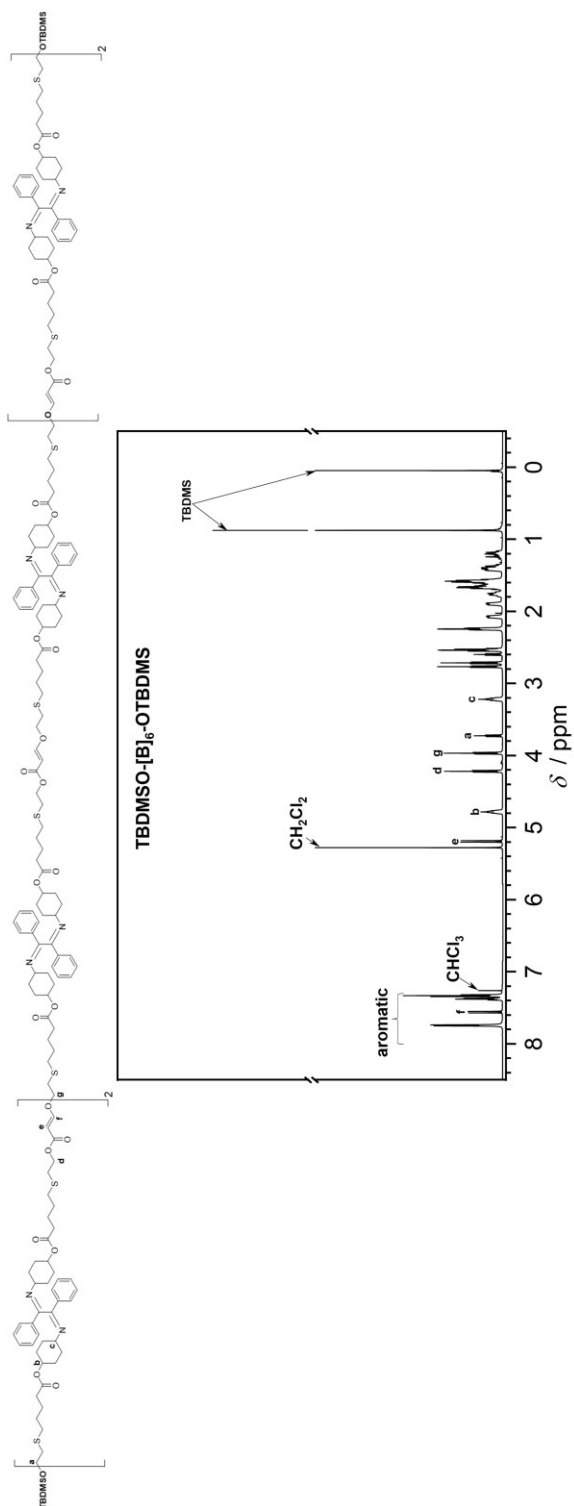
11.4.2.20. TBDMSO-[B]₆-OTBDMS

Figure S4.51. ¹H NMR (600 MHz, 32 scans) spectrum of TBDMSO-[B]₆-OTBDMS in CDCl₃

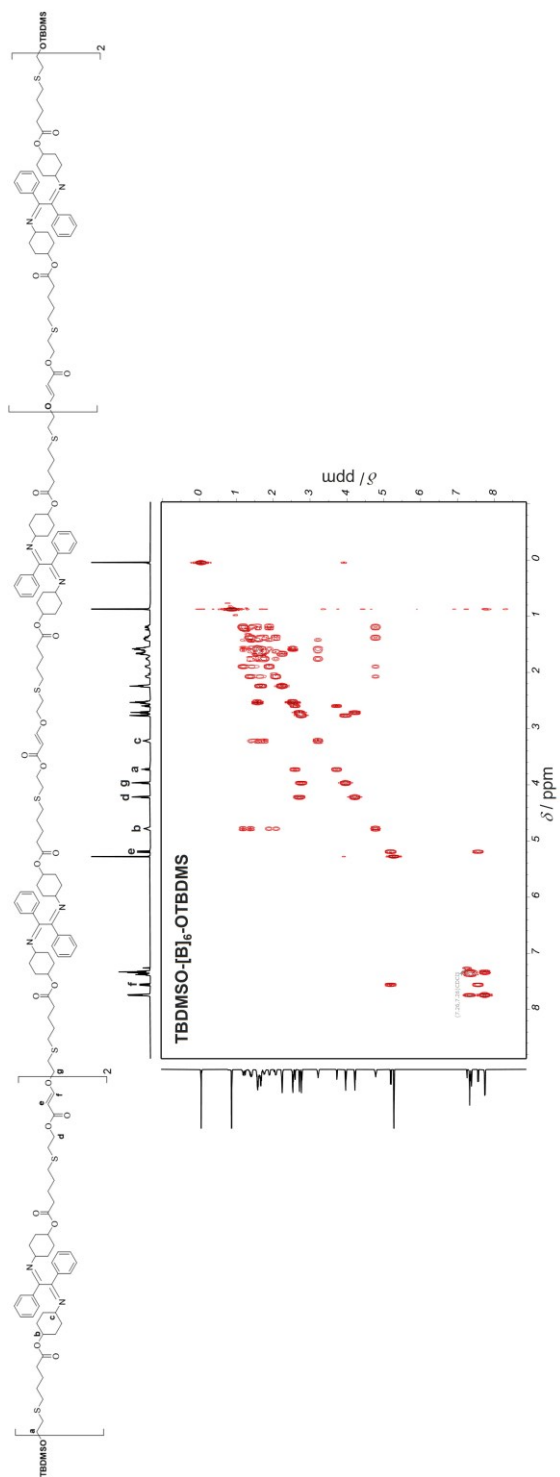


Figure S4.52. COSY NMR spectrum of TBDMSO-[B]₆-OTBDMS in CDCl₃.

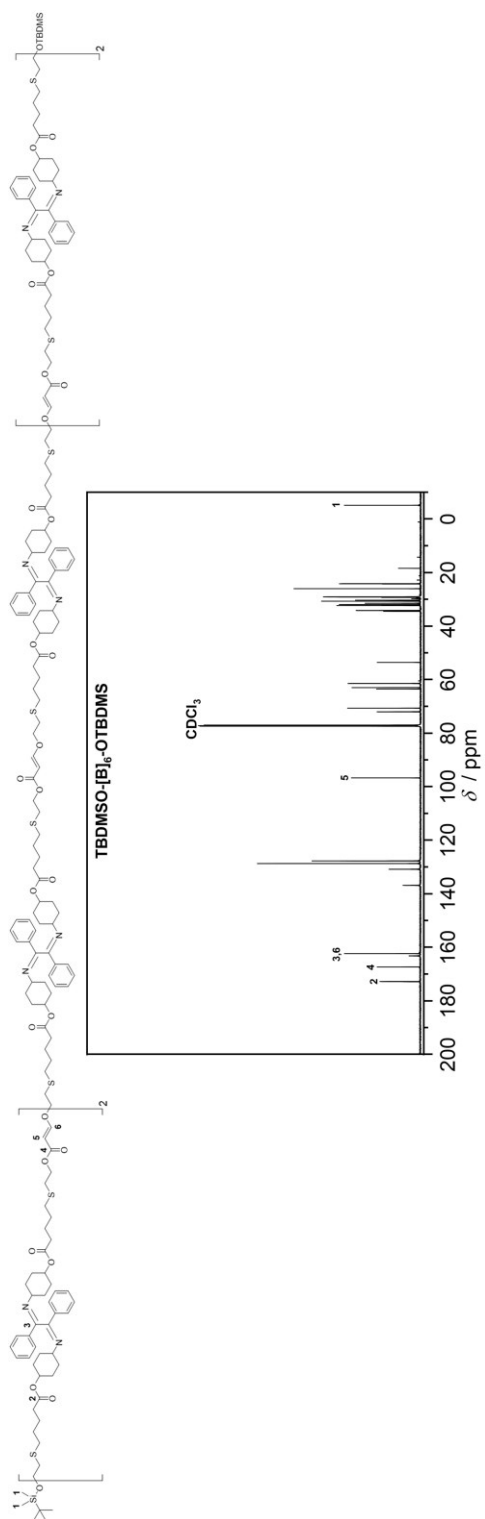


Figure S4.53. Carbon-Proton Decoupled ¹³C NMR (151 MHz) spectrum of **TBDMSO-[B]₆-OTBDMS** in CDCl₃.

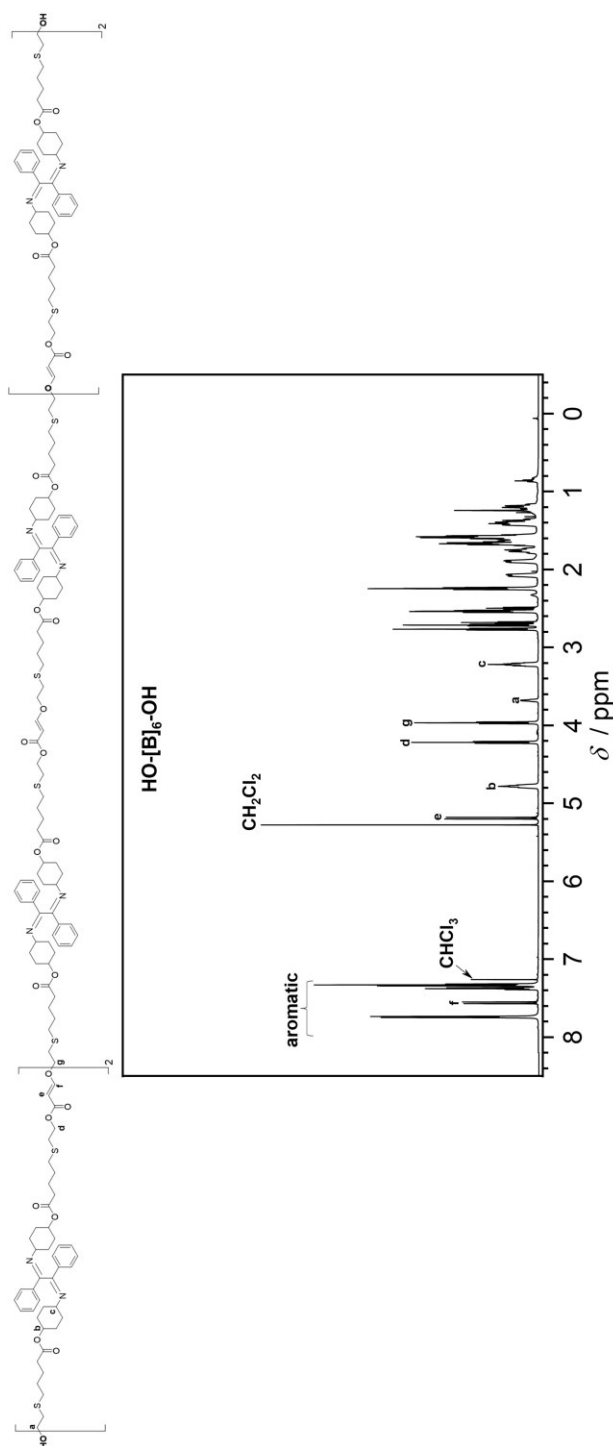
11.4.2.21. HO-[B]₆-OH

Figure S4.54. ¹H NMR (600 MHz, 32 scans) spectrum of HO-[B]₆-OH in CDCl₃.

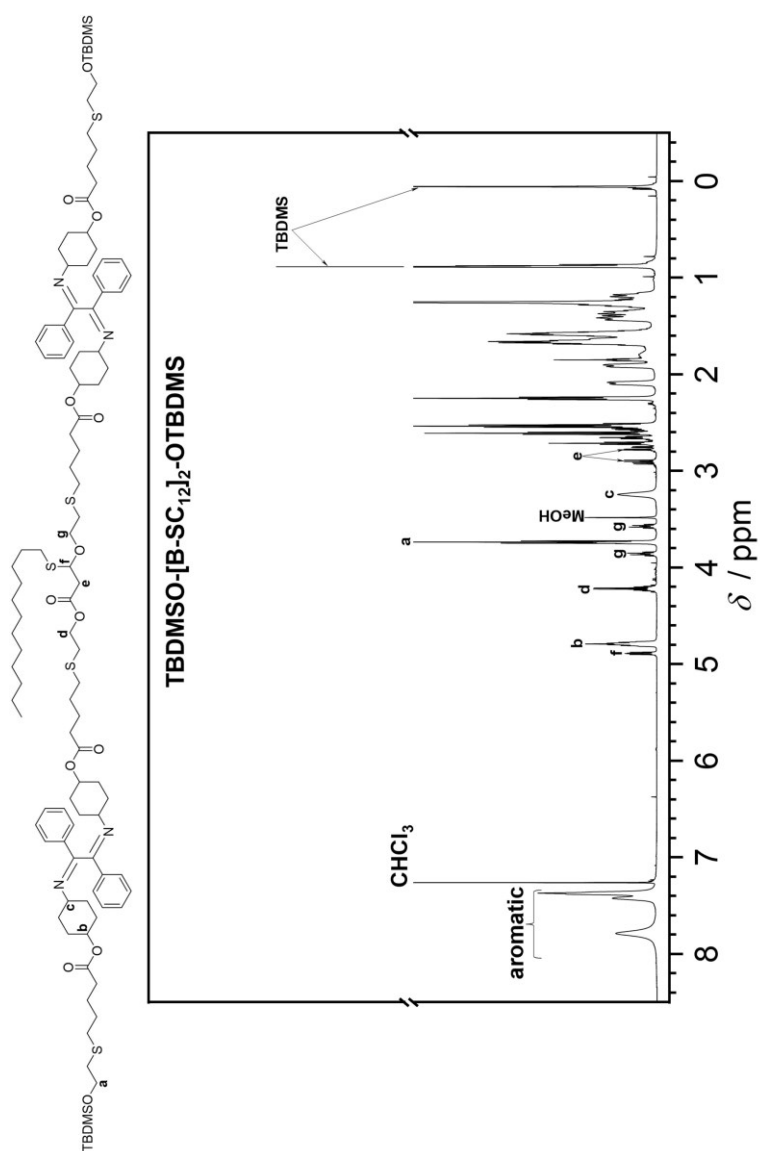
11.4.2.22. TBDMSO-[B-SC₁₂]₂-OTBDMS

Figure S4.55. ¹H NMR (600 MHz, 32 scans) spectrum of **TBDMSO-[B-SC₁₂]₂-OTBDMS** in CDCl₃.

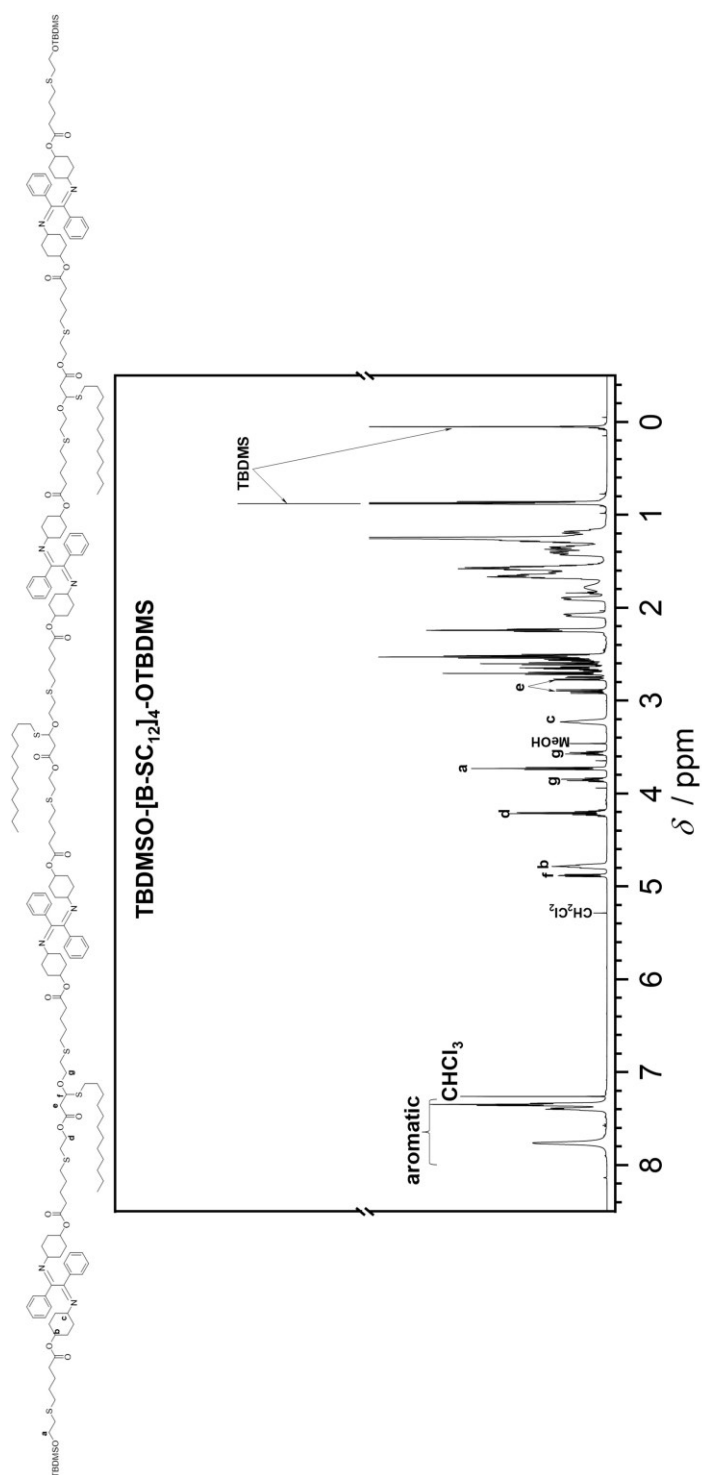
11.4.2.23. TBDMSO-[B-SC₁₂]₄-OTBDMS

Figure S4.56. ¹H NMR (600 MHz, 32 scans) spectrum of **TBDMSO-[B-SC₁₂]₄-OTBDMS** in CDCl₃.

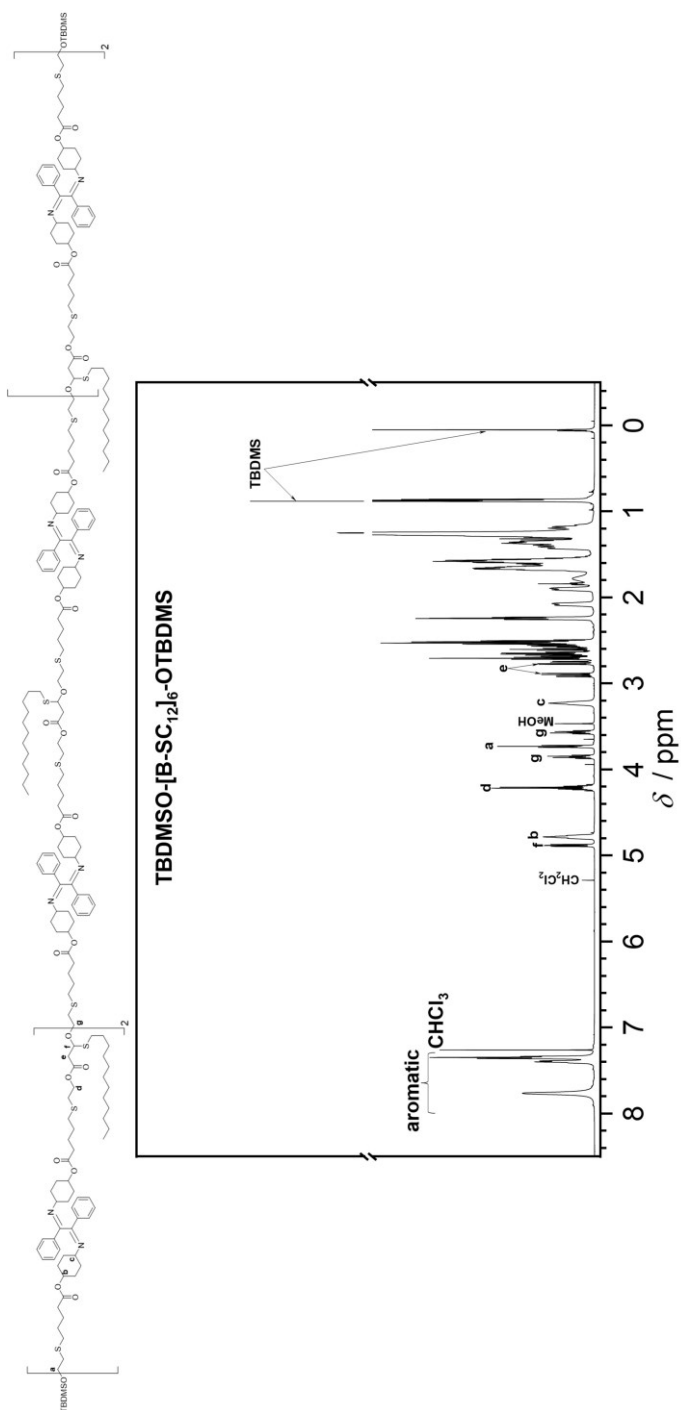
11.4.2.24. TBDMSO-[B-SC₁₂]₆-OTBDMS

Figure S4.57. ¹H NMR (600 MHz, 32 scans) spectrum of TBDMSO-[B-SC₁₂]₆-OTBDMS in CDCl₃.

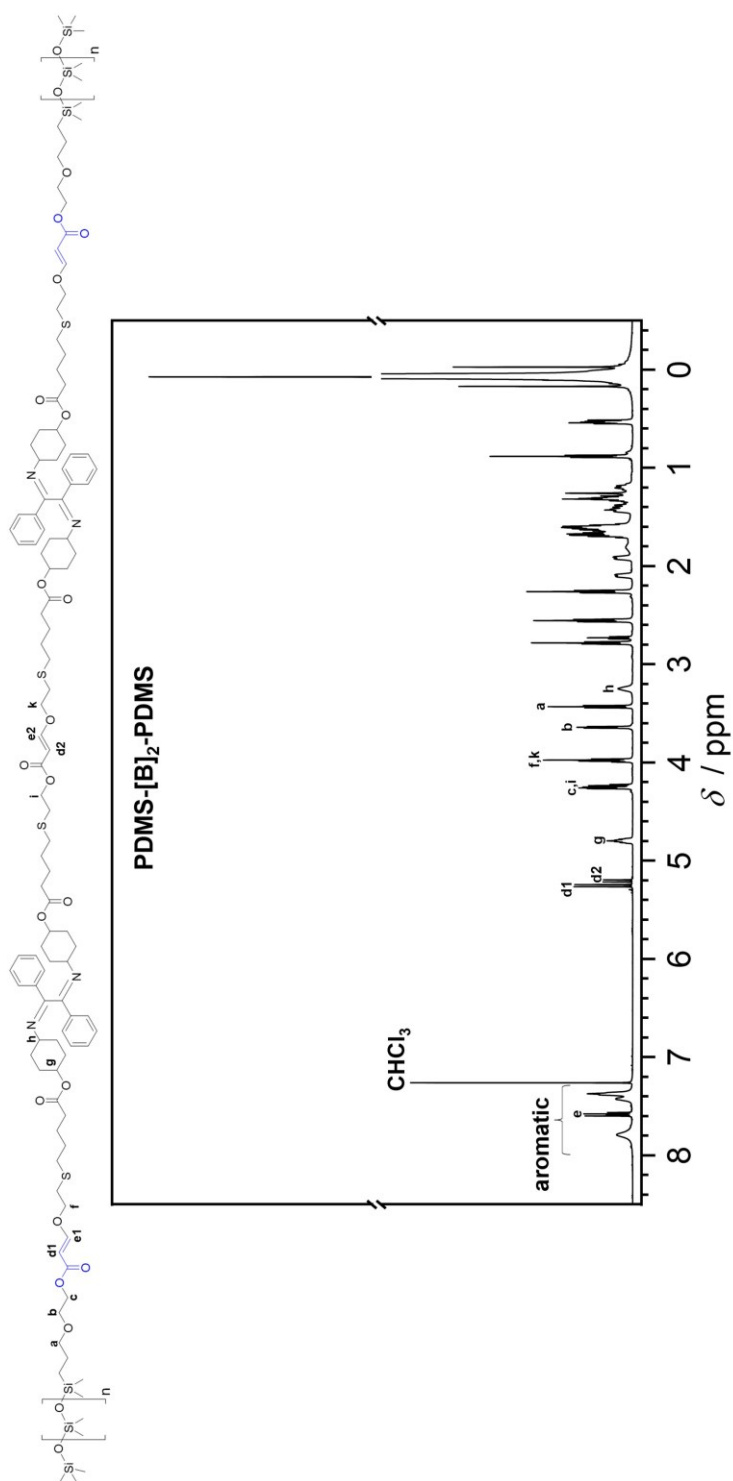
11.4.2.25. PDMS-[B]₂-PDMS

Figure S4.58. ¹H NMR (600 MHz, 32 scans) spectrum of PDMS-[B]₂-PDMS in CDCl₃.

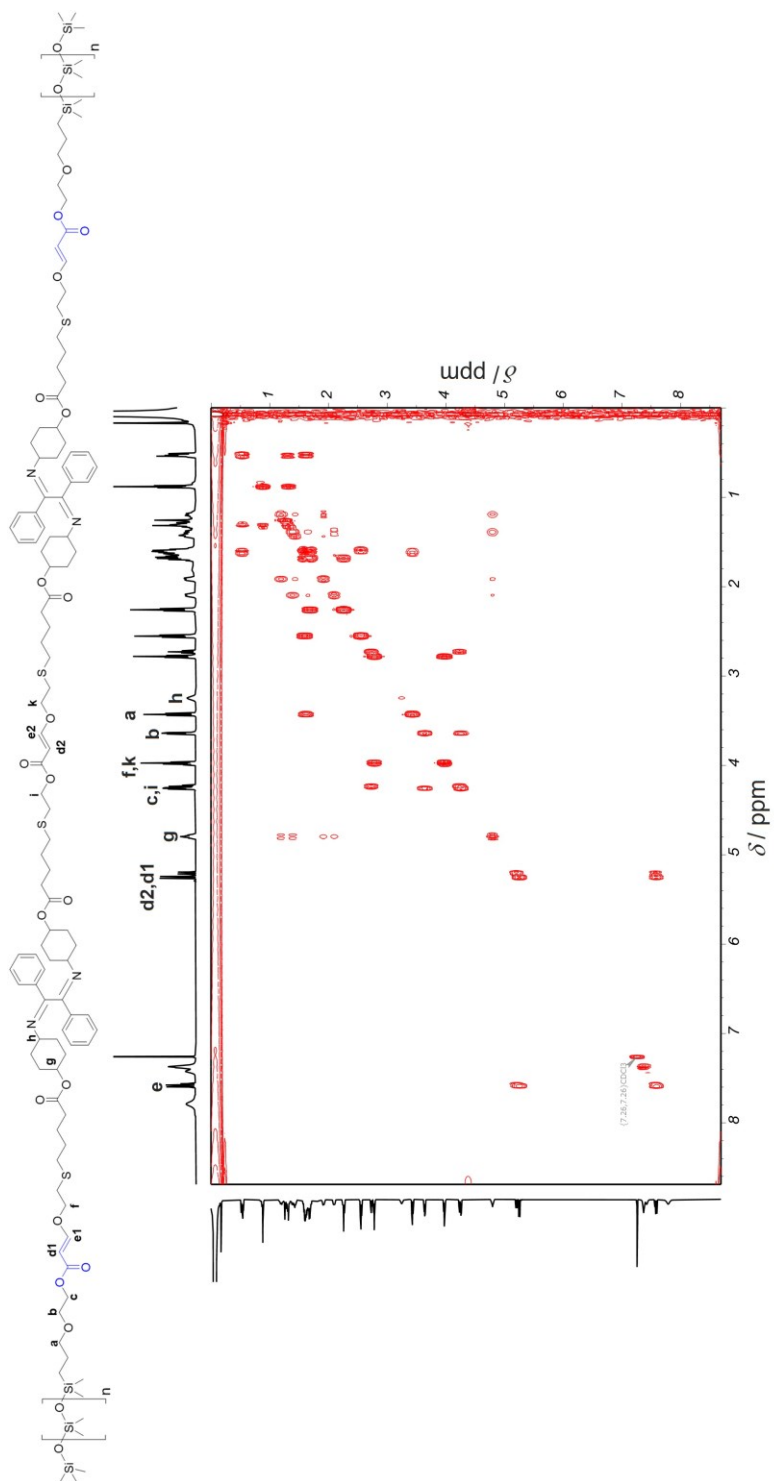


Figure S4.59. COSY NMR spectrum of **PDMS-[B]₂-PDMS** in CDCl_3 .

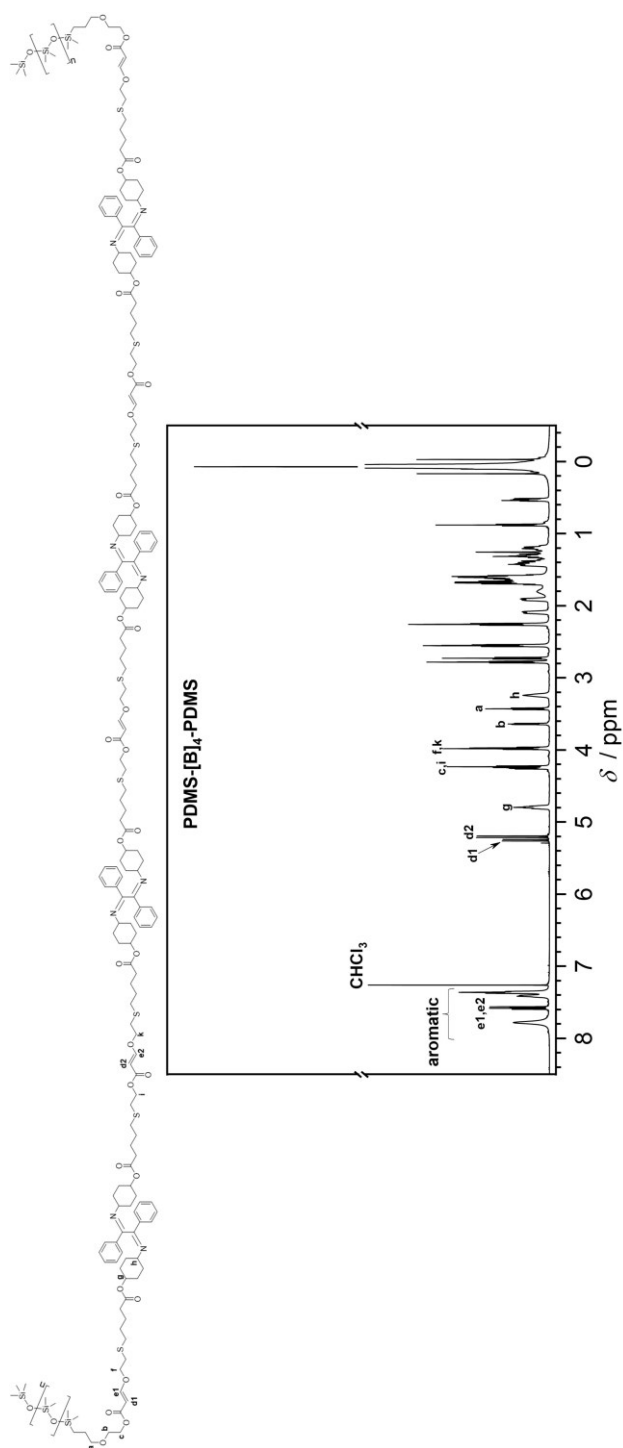
11.4.2.26. PDMS-[B]₄-PDMS

Figure S4.60. ¹H NMR (600 MHz, 32 scans) spectrum of PDMS-[B]₄-PDMS in CDCl₃.

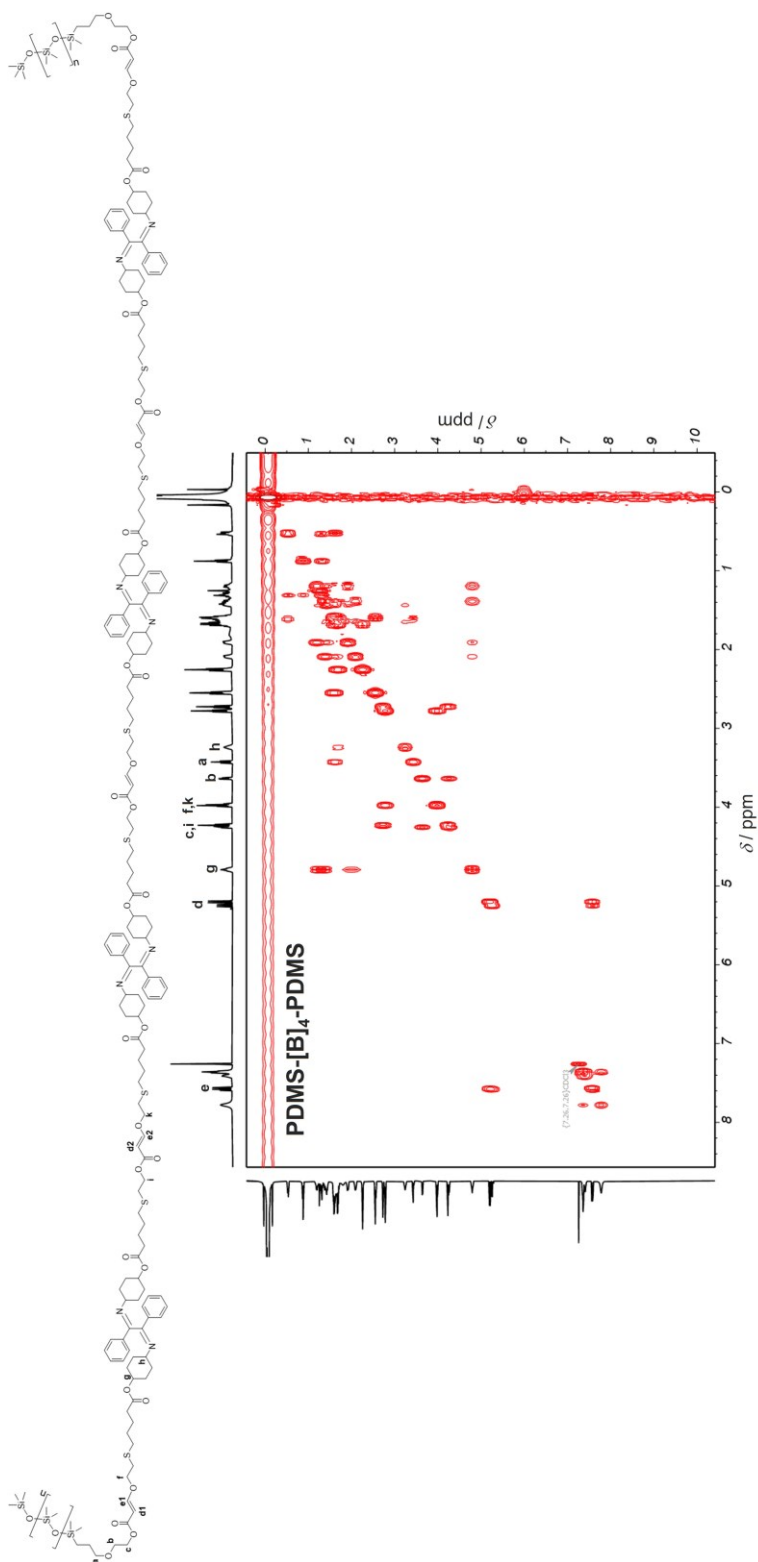


Figure S4.61. COSY NMR spectrum of **PDMS-[B]₄-PDMS** in CDCl₃.

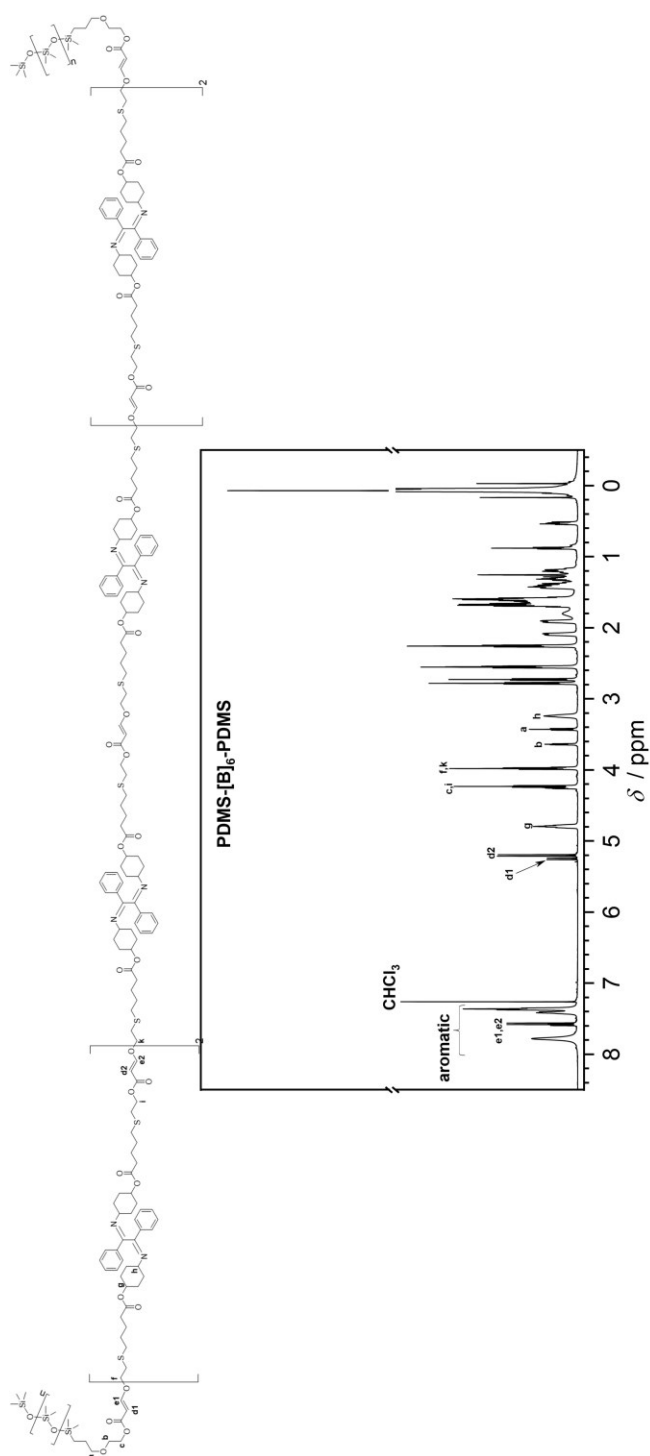
11.4.2.27. PDMS-[B]₆-PDMS

Figure S4.62. ¹H NMR (600 MHz, 32 scans) spectrum of **PDMS-[B]₆-PDMS** in CDCl₃.

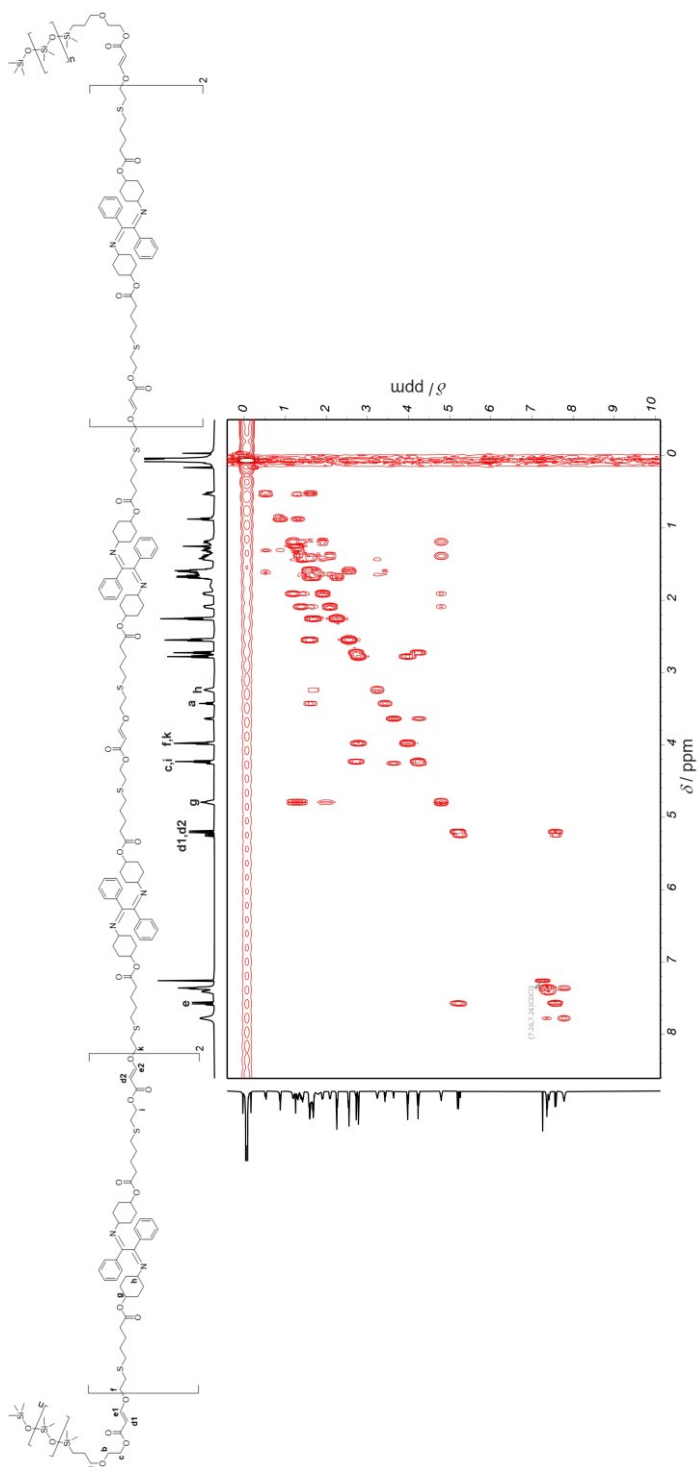


Figure S4.63. COSY NMR spectrum of PDMS-[B]₆-PDMS in CDCl₃.

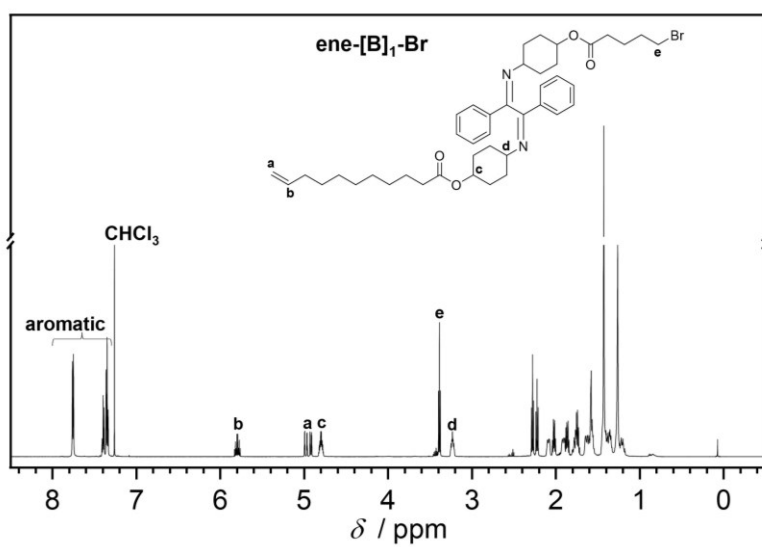
11.4.2.28. ene-[B]₁-Br

Figure S4.64. ¹H NMR (600 MHz, 32 scans) spectrum of ene-[B]₁-Br in CDCl₃.

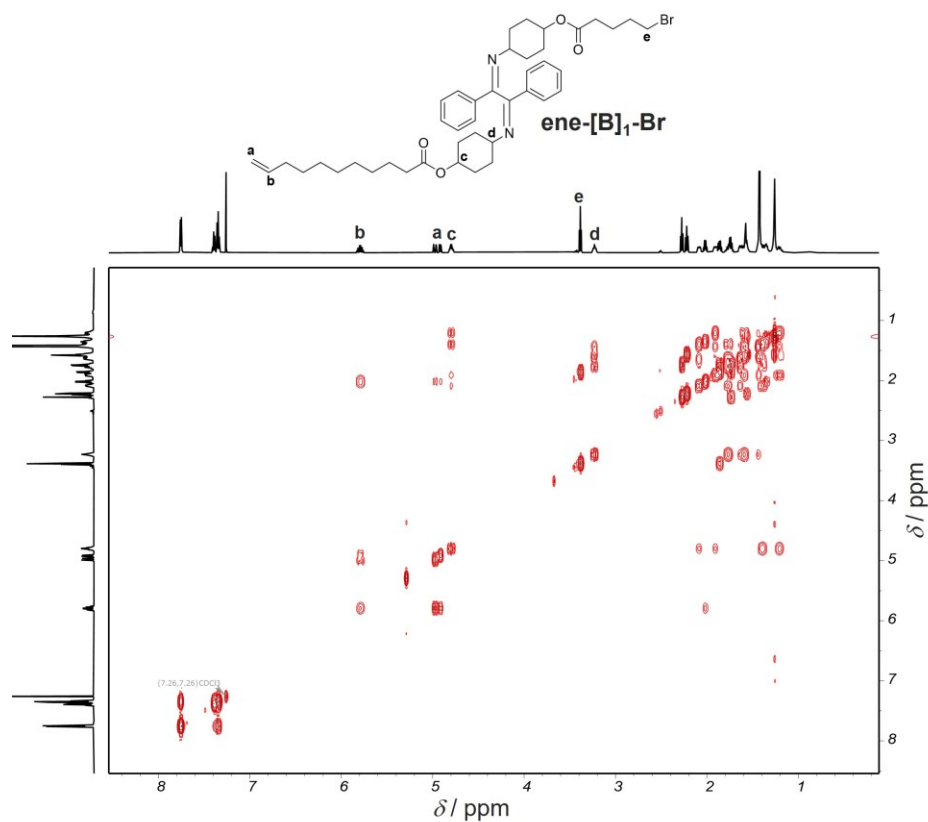


Figure S4.65. COSY NMR spectrum of ene-[B]₁-Br in CDCl₃.

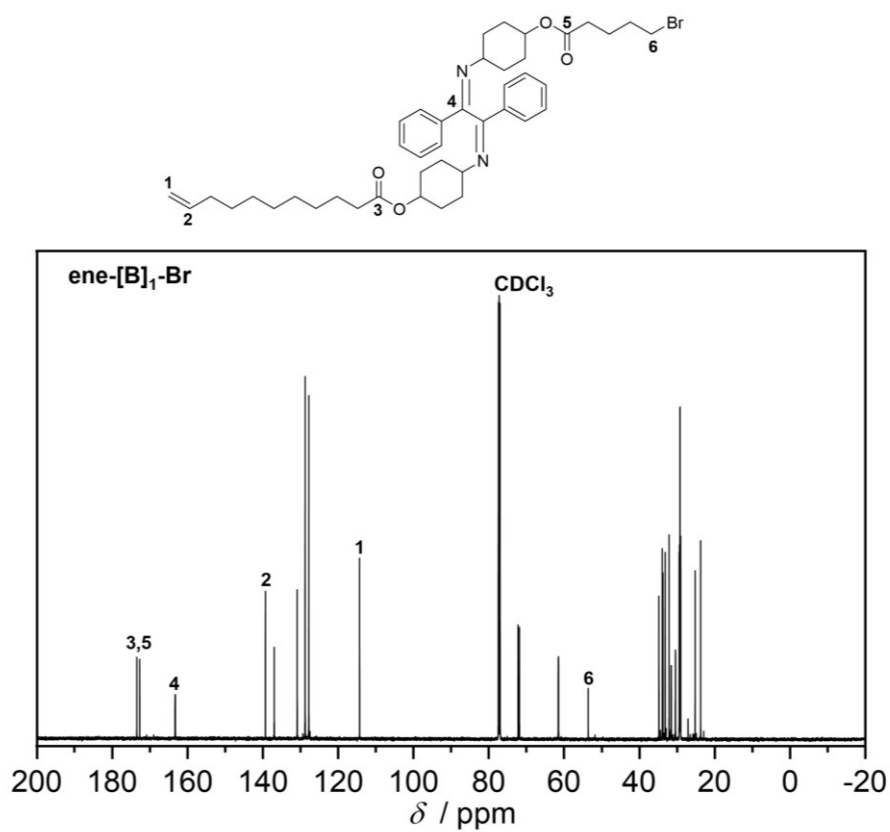


Figure S4.66. Carbon-Proton Decoupled ¹³C NMR (151 MHz) spectrum of **ene-[B]₁-Br** in CDCl₃.

11.4.2.29. ene-[B]₁-OH

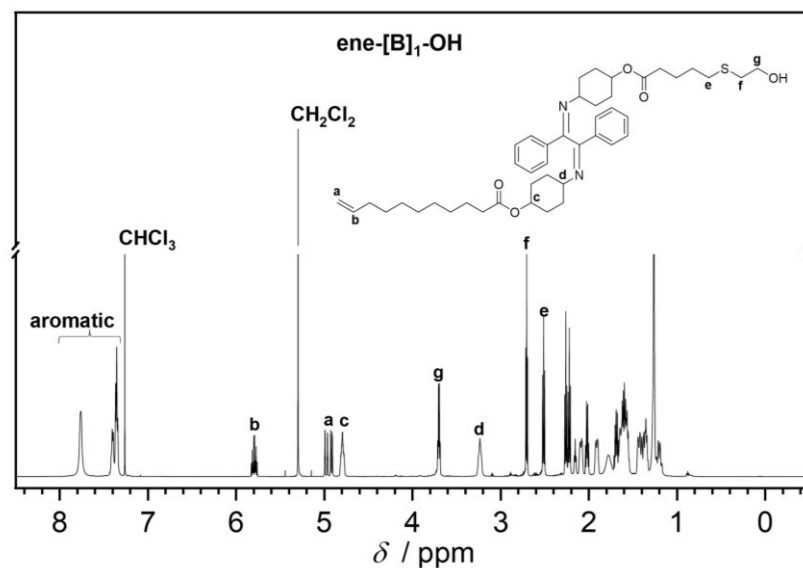


Figure S4.67. ¹H NMR (600 MHz, 32 scans) spectrum of **ene-[B]₁-OH** in CDCl₃.

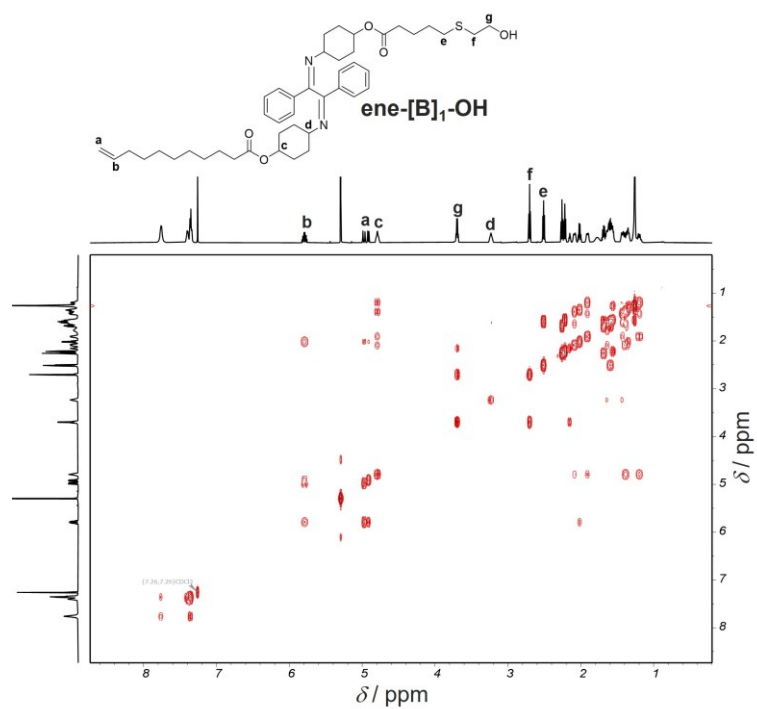
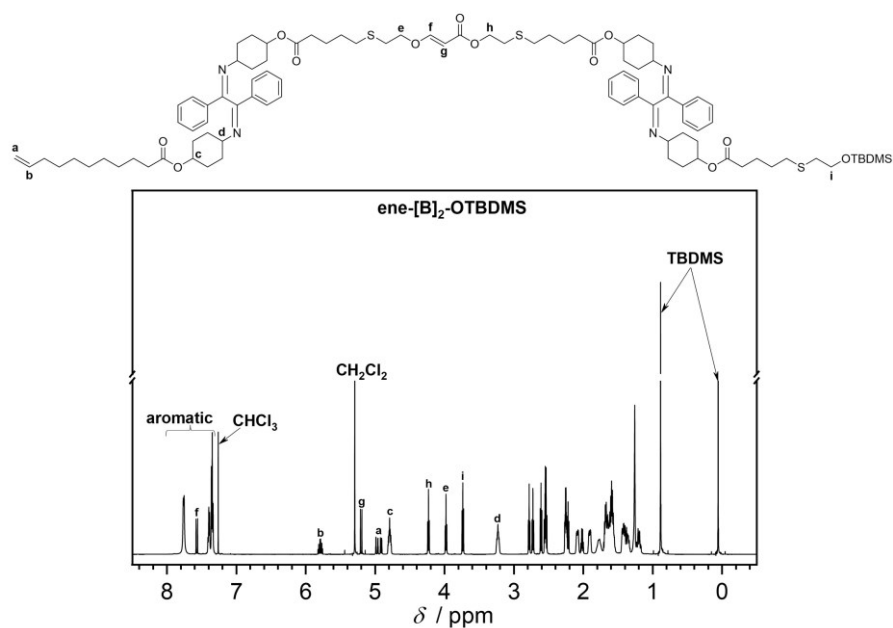
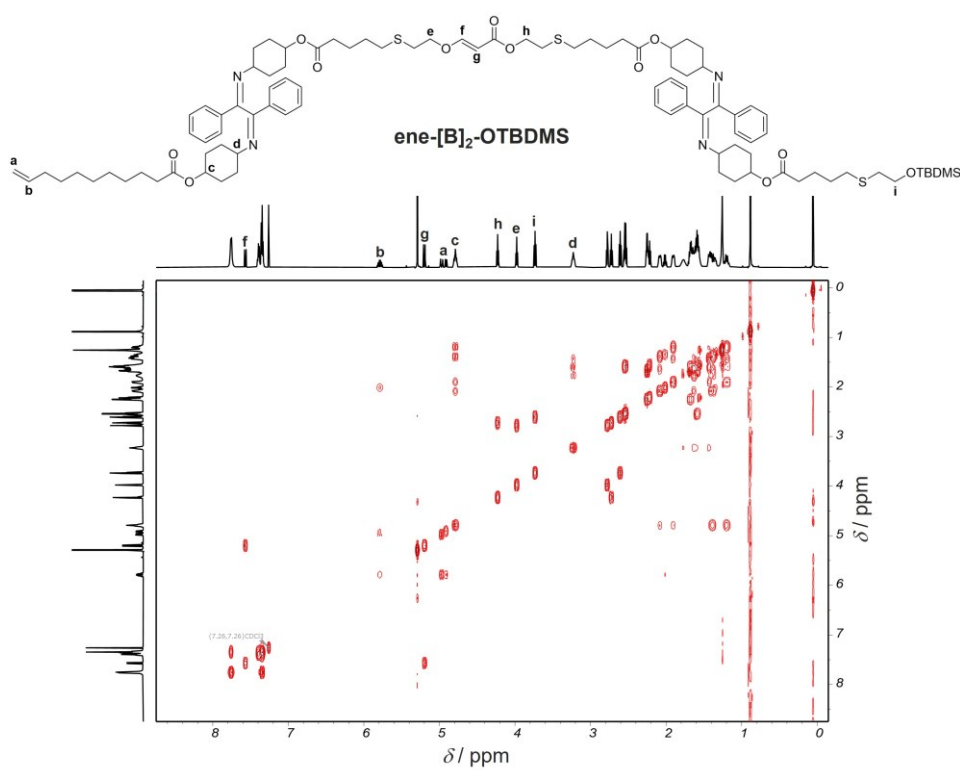


Figure S4.68. COSY NMR spectrum of **ene-[B]₁-OH** in CDCl_3 .

11.4.2.30. ene-[B]₂-OTBDMSFigure S4.69. ¹H NMR (600 MHz, 32 scans) spectrum of ene-[B]₂-OTBDMS in CDCl₃.Figure S4.70. COSY NMR spectrum of ene-[B]₂-OTBDMS in CDCl₃.

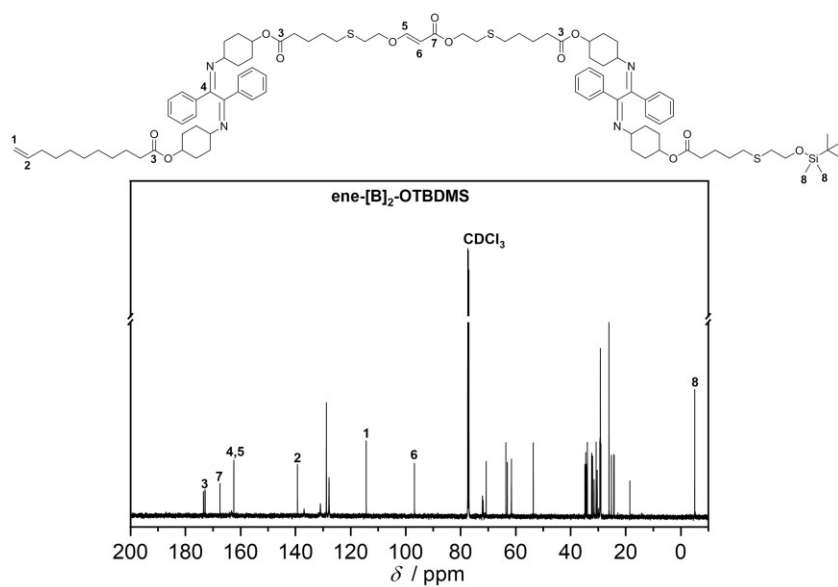


Figure S4.71. Carbon-Proton Decoupled ¹³C NMR (151 MHz) spectrum of **ene-[B]₂-OTBDMS** in CDCl₃.

11.4.2.31. ene-[B]₂-OH

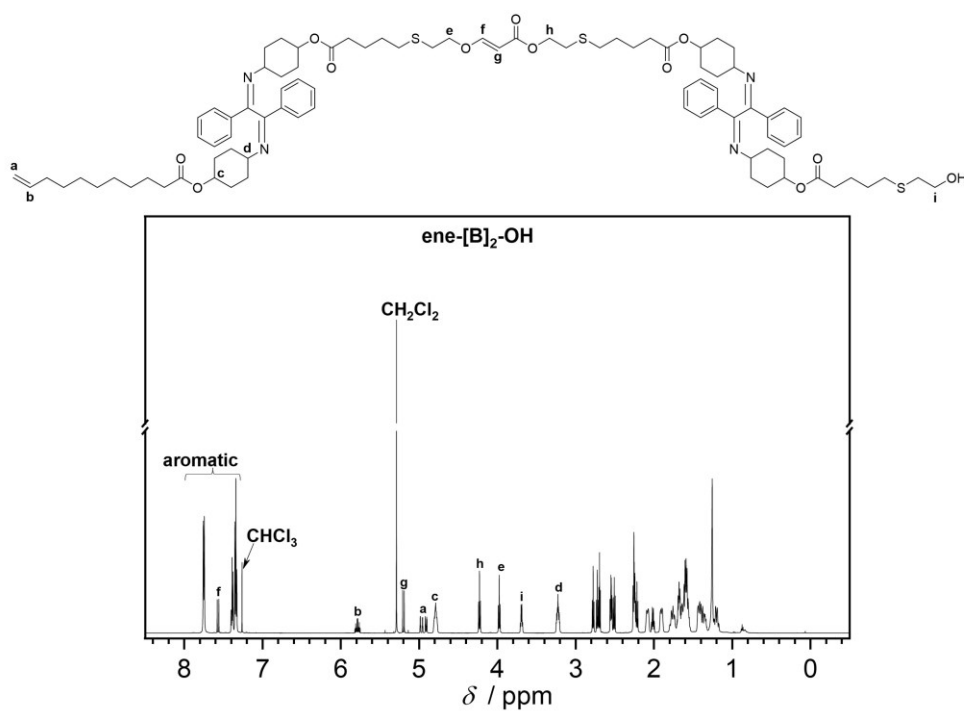


Figure S4.72. ¹H NMR (600 MHz, 32 scans) spectrum of **ene-[B]₂-OH** in CDCl₃.

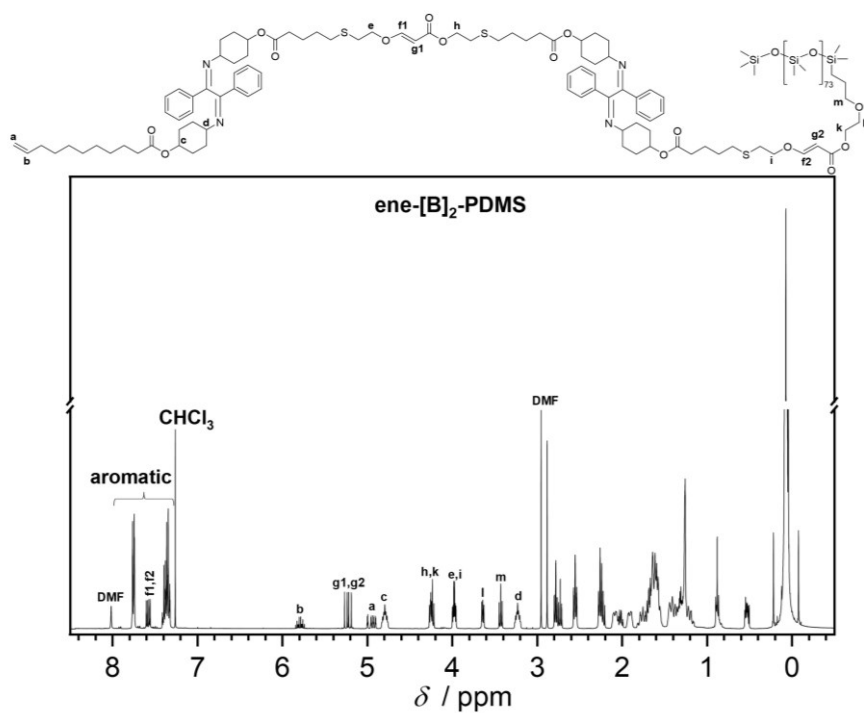
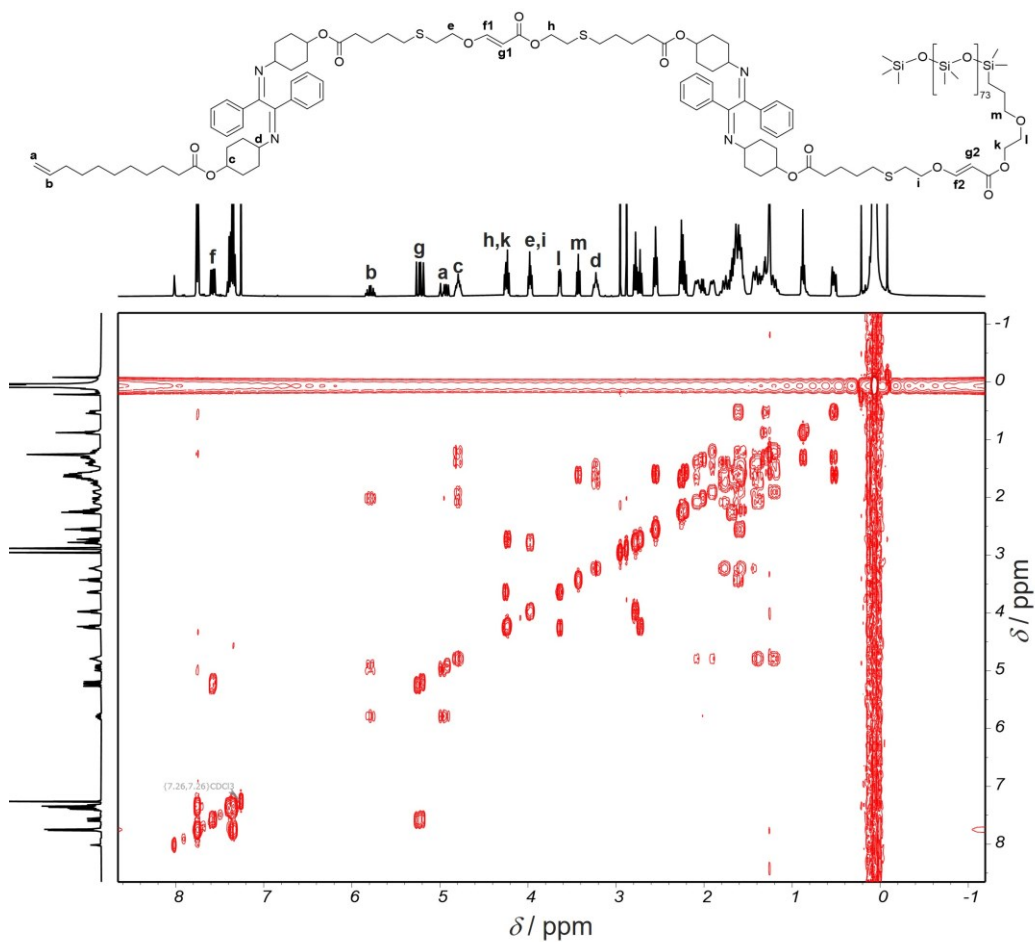
11.4.2.32. ene-[B]₂-PDMSFigure S4.73. ¹H NMR (600 MHz, 32 scans) spectrum of ene-[B]₂-PDMS in CDCl₃.

Figure S4.74. COSY NMR spectrum of *ene*-[B]₂-PDMS in CDCl₃.

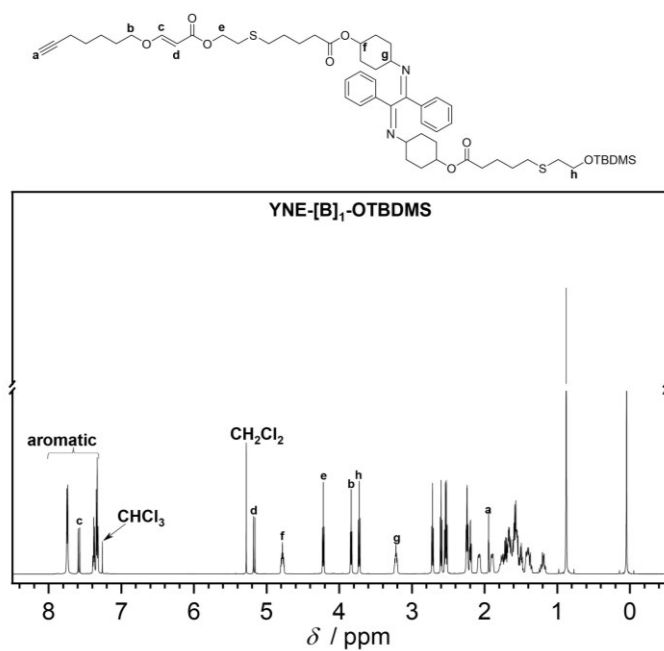
11.4.2.33. YNE-[B]₁-OTBDMS

Figure S4.75. ¹H NMR (600 MHz, 32 scans) spectrum of YNE-[B]₁-OTBDMS in CDCl₃.

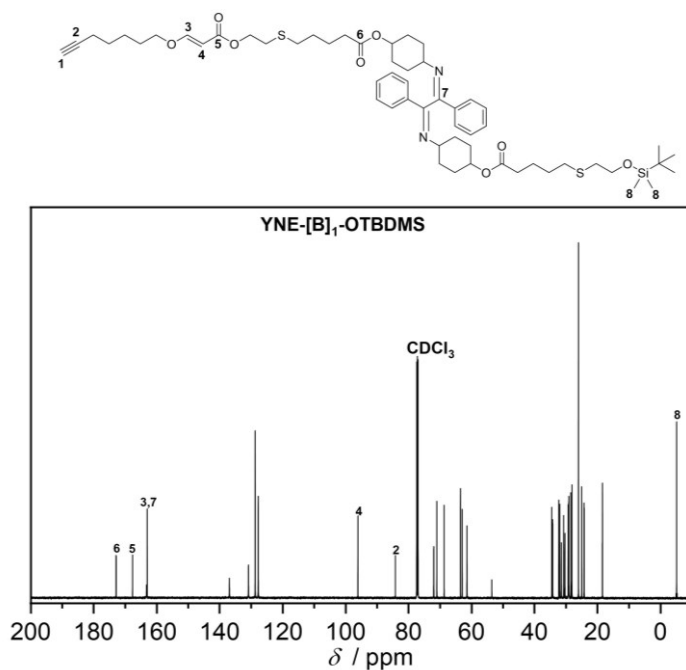


Figure S4.76. Carbon-Proton Decoupled ¹³C NMR (151 MHz) spectrum of YNE-[B]₁-OTBDMS in CDCl₃.

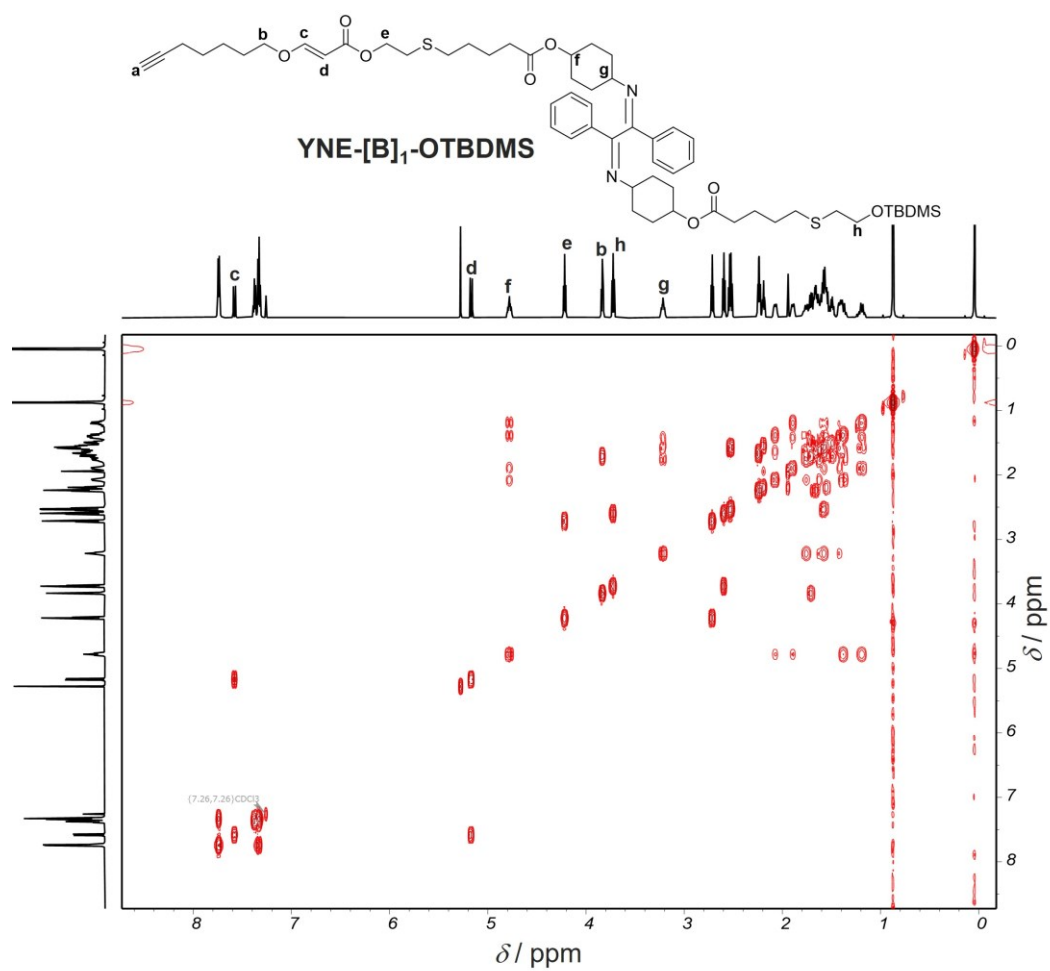


Figure S4.77. COSY NMR spectrum of **YNE-[B]₁-OTBDMS** in CDCl₃.

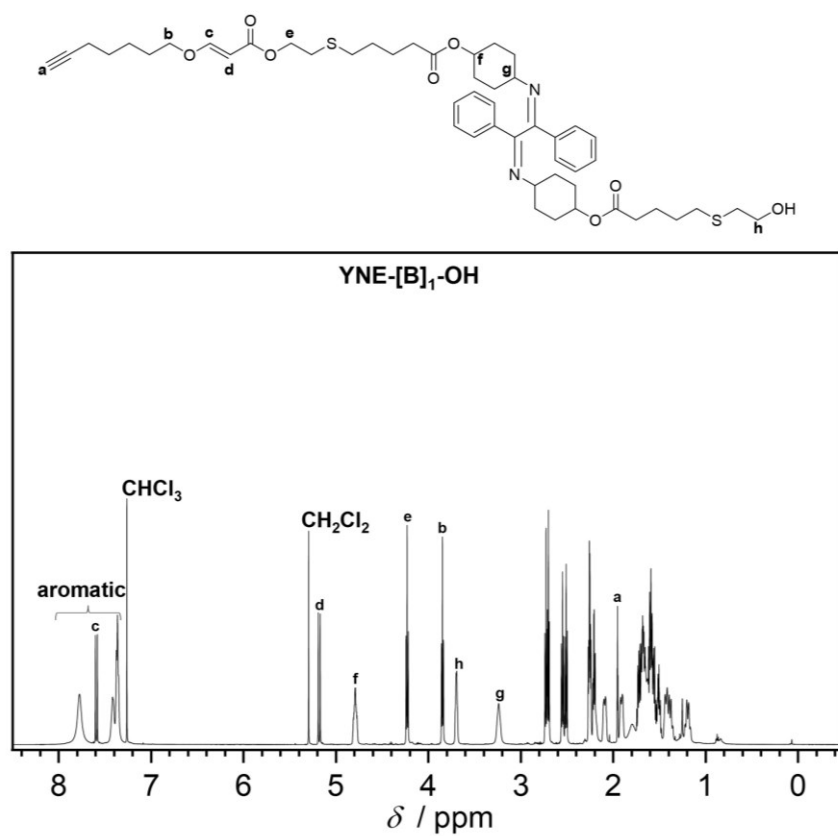


Figure S4.78. ¹H NMR (600 MHz, 32 scans) spectrum of **YNE-[B]₁-OH** in CDCl₃.

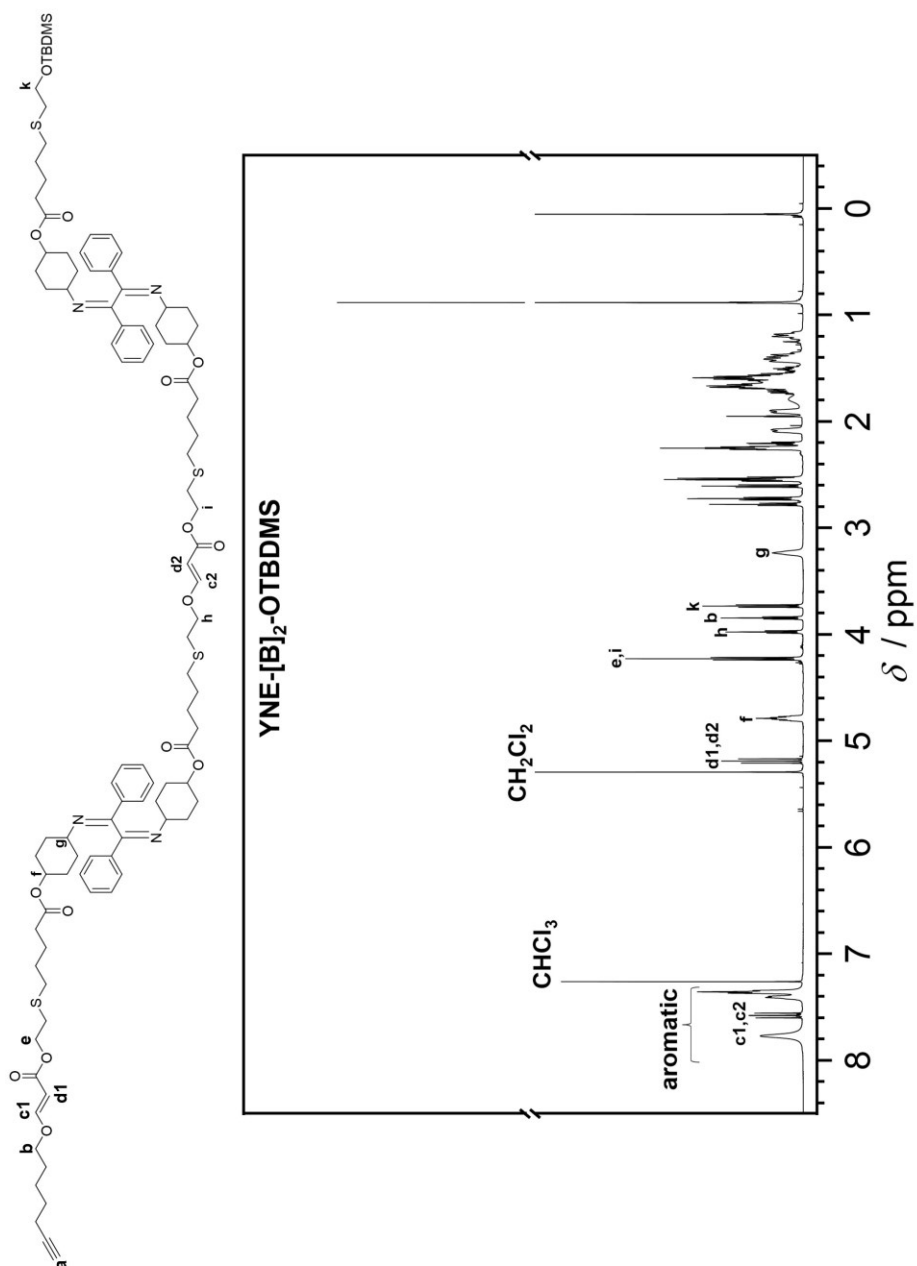
11.4.2.34. YNE-[B]₂-OTBDMS

Figure S4.79. ¹H NMR (600 MHz, 32 scans) spectrum of YNE-[B]₂-OTBDMS in CDCl₃.

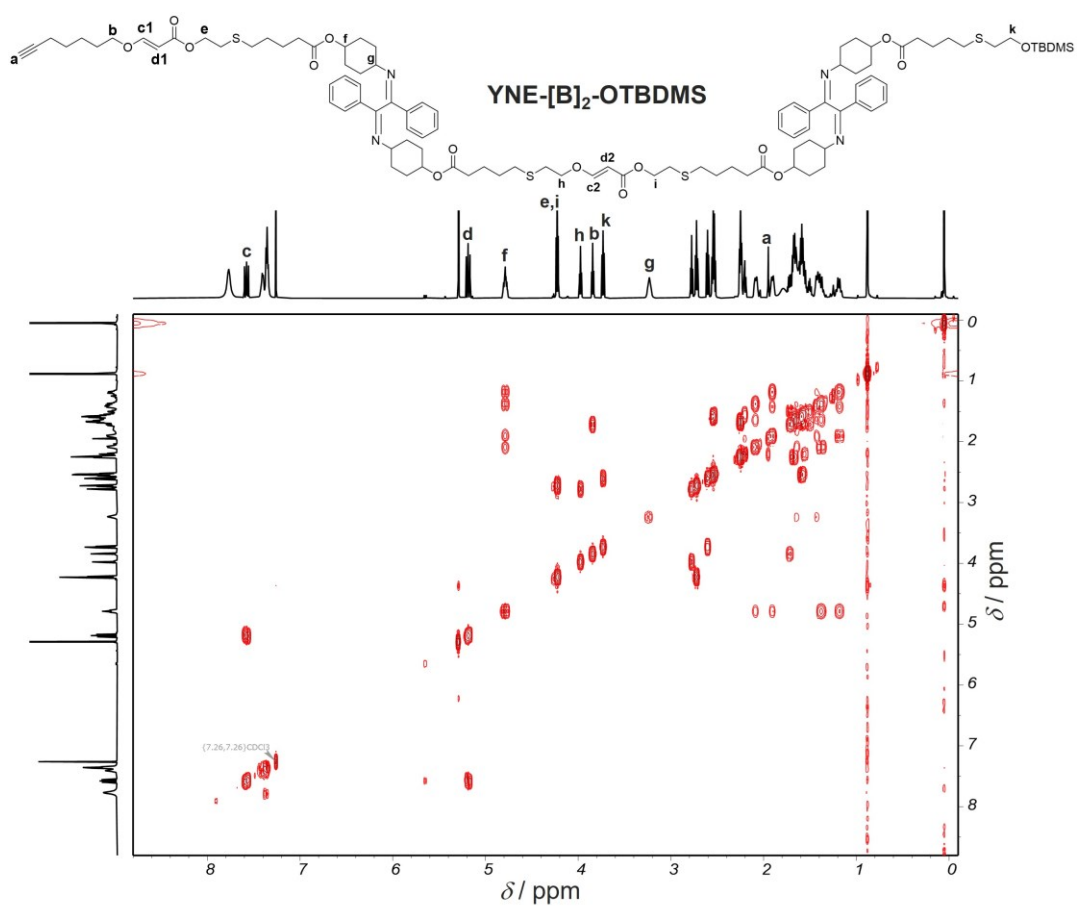


Figure S4.80. COSY NMR spectrum of **YNE-[B]₂-OTBDMS** in CDCl₃.

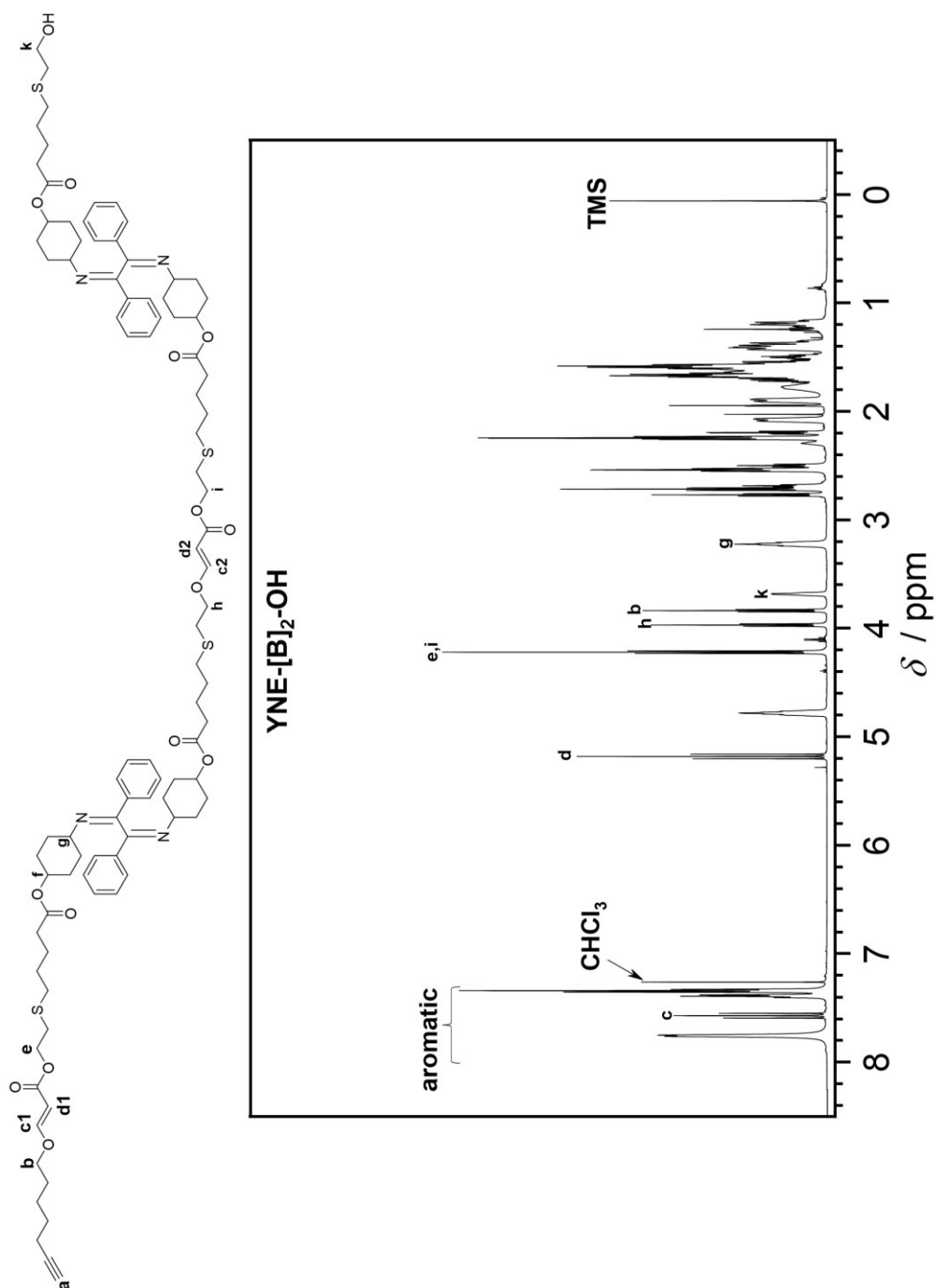
11.4.2.35. YNE-[B]₂-OH

Figure S4.81. ¹H NMR (600 MHz, 32 scans) spectrum of YNE-[B]₂-OH in CDCl₃.

YNE-[B]₂-PDMS

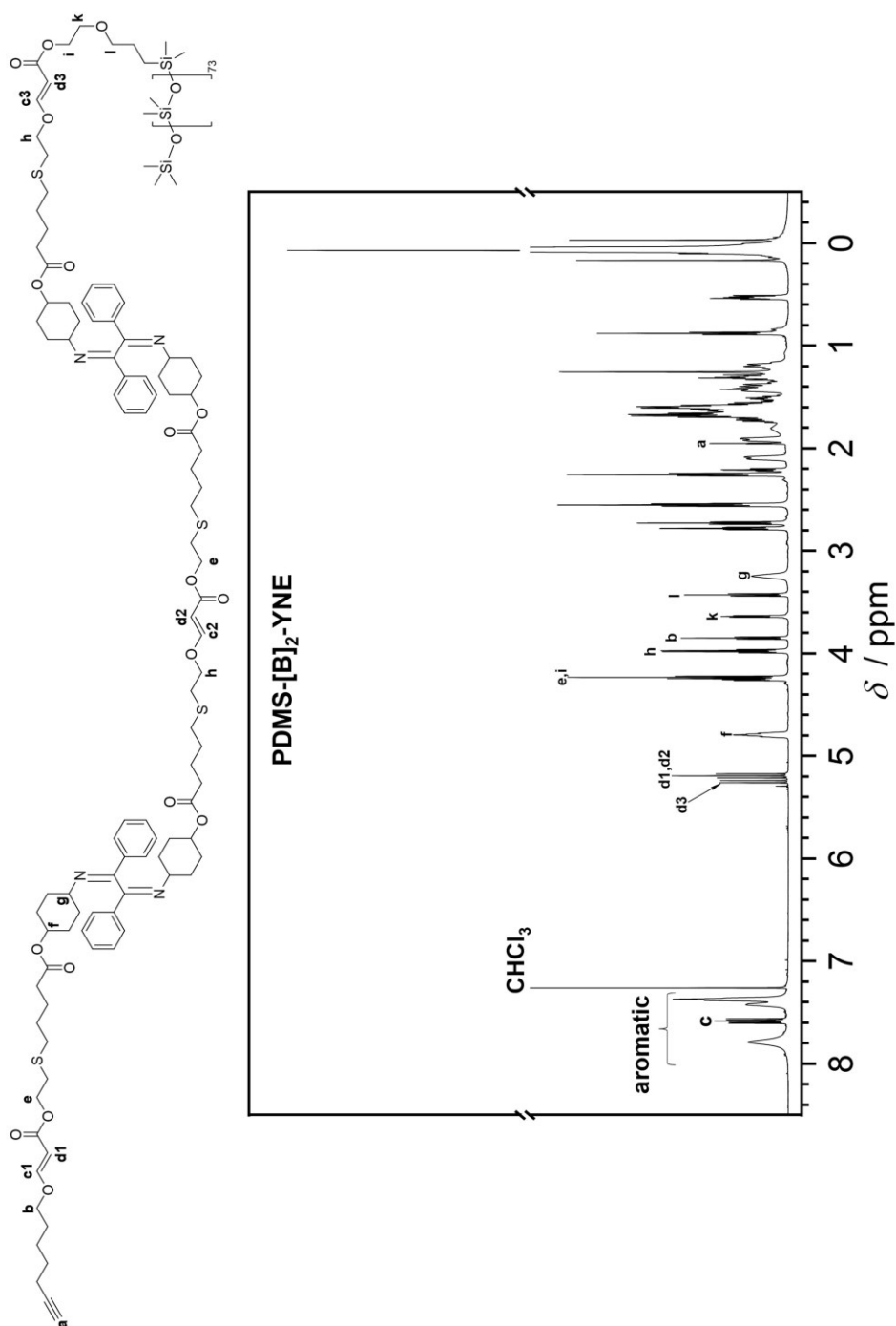


Figure S4.82. ¹H NMR (600 MHz, 32 scans) spectrum of **PDMS-[B]₂-YNE** in CDCl₃.

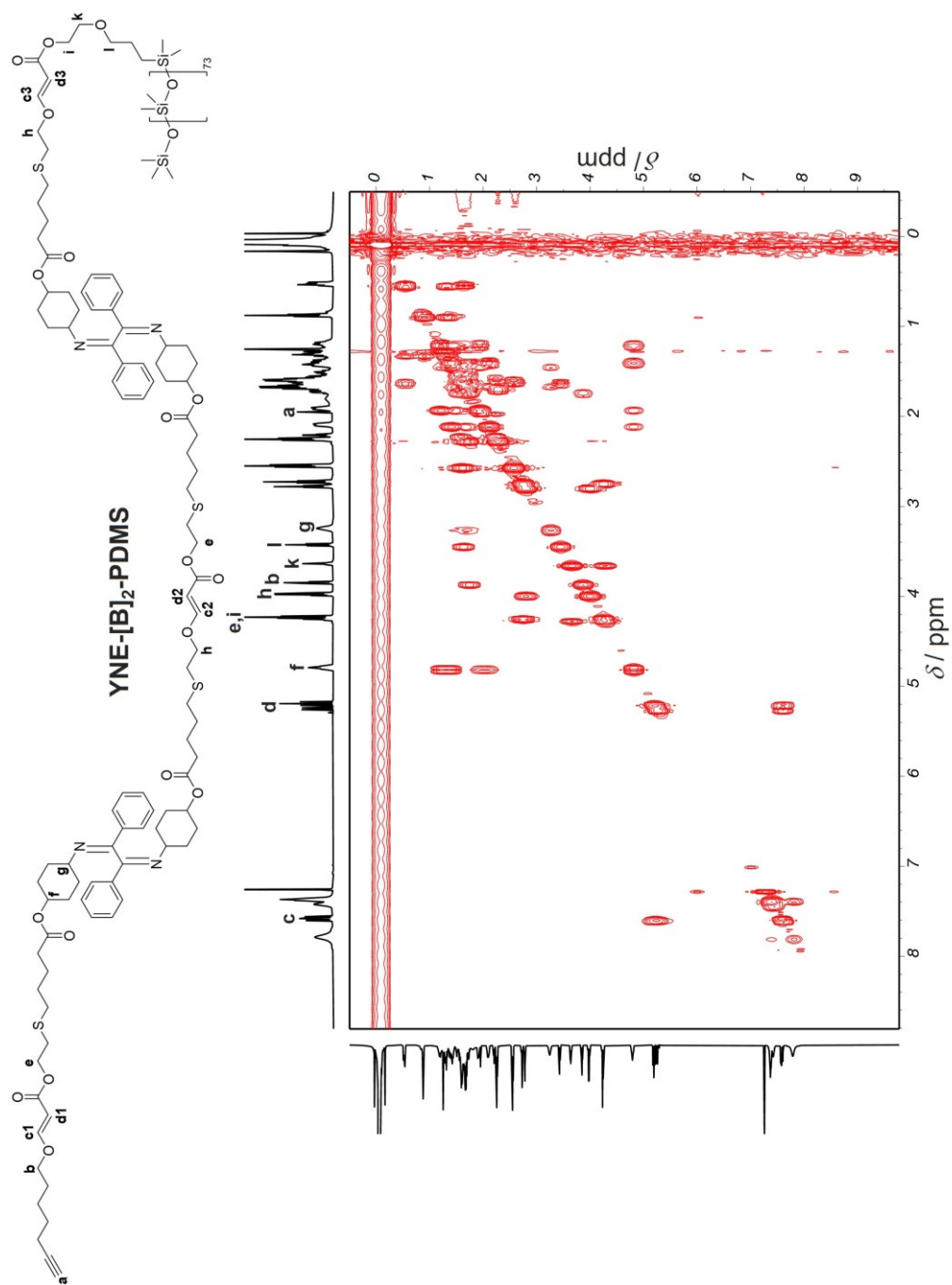


Figure S4.83. COSY NMR spectrum of **YNE-[B]₂-PDMS** in CDCl_3 .

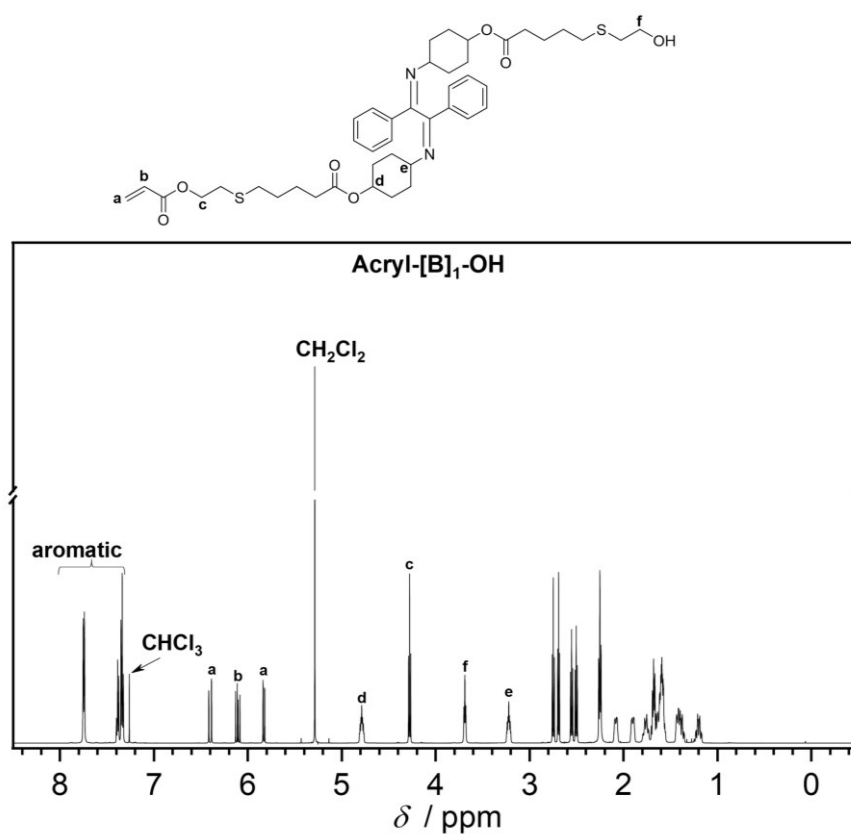
11.4.2.36. Acryl-[B]₁-OH

Figure S4.84. ¹H NMR (600 MHz, 32 scans) spectrum of acryl-[B]₁-OH in CDCl₃.

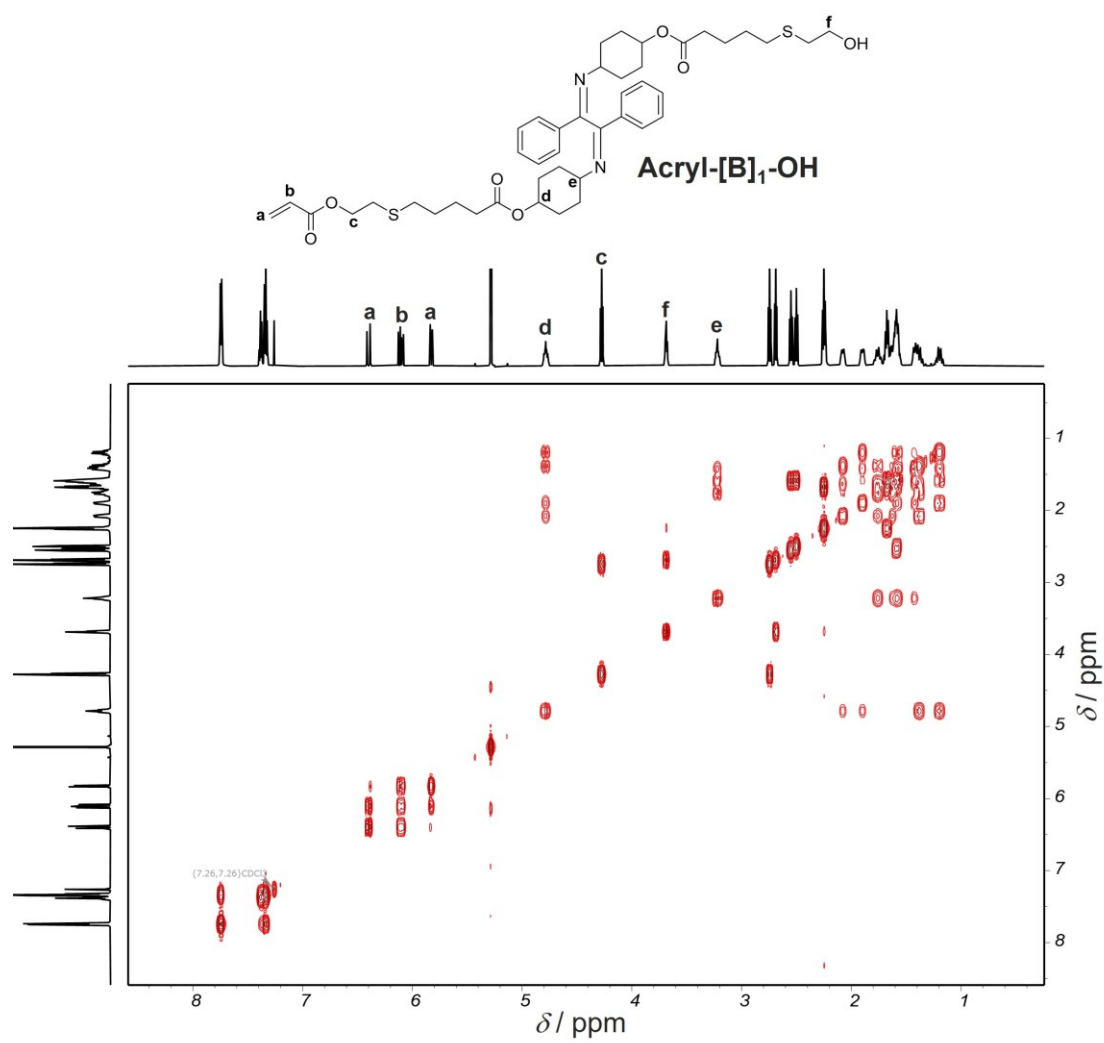


Figure S4.85. COSY NMR spectrum of **acryl-[B]₁-OH** in CDCl₃.

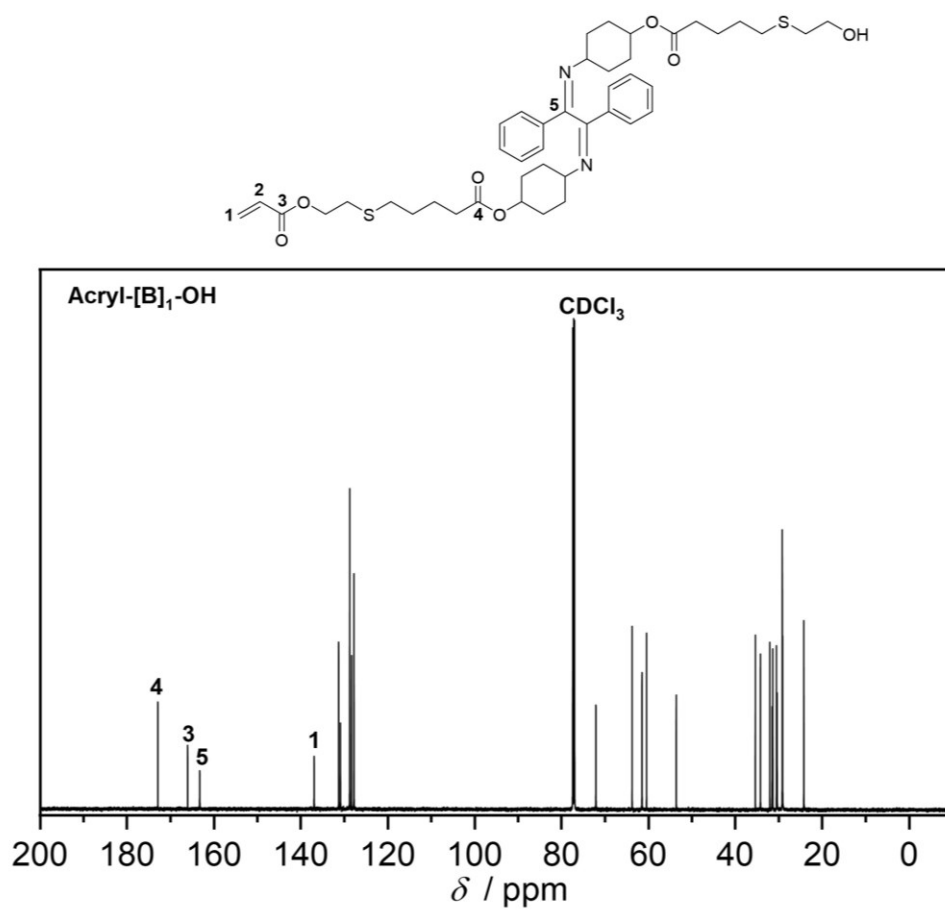


Figure S4.86. Carbon-Proton Decoupled ¹³C NMR (151 MHz) spectrum of **acryl-[B]₁-OH** in CDCl₃.

11.4.2.37. Acryl-[B]₂-OTBDMS

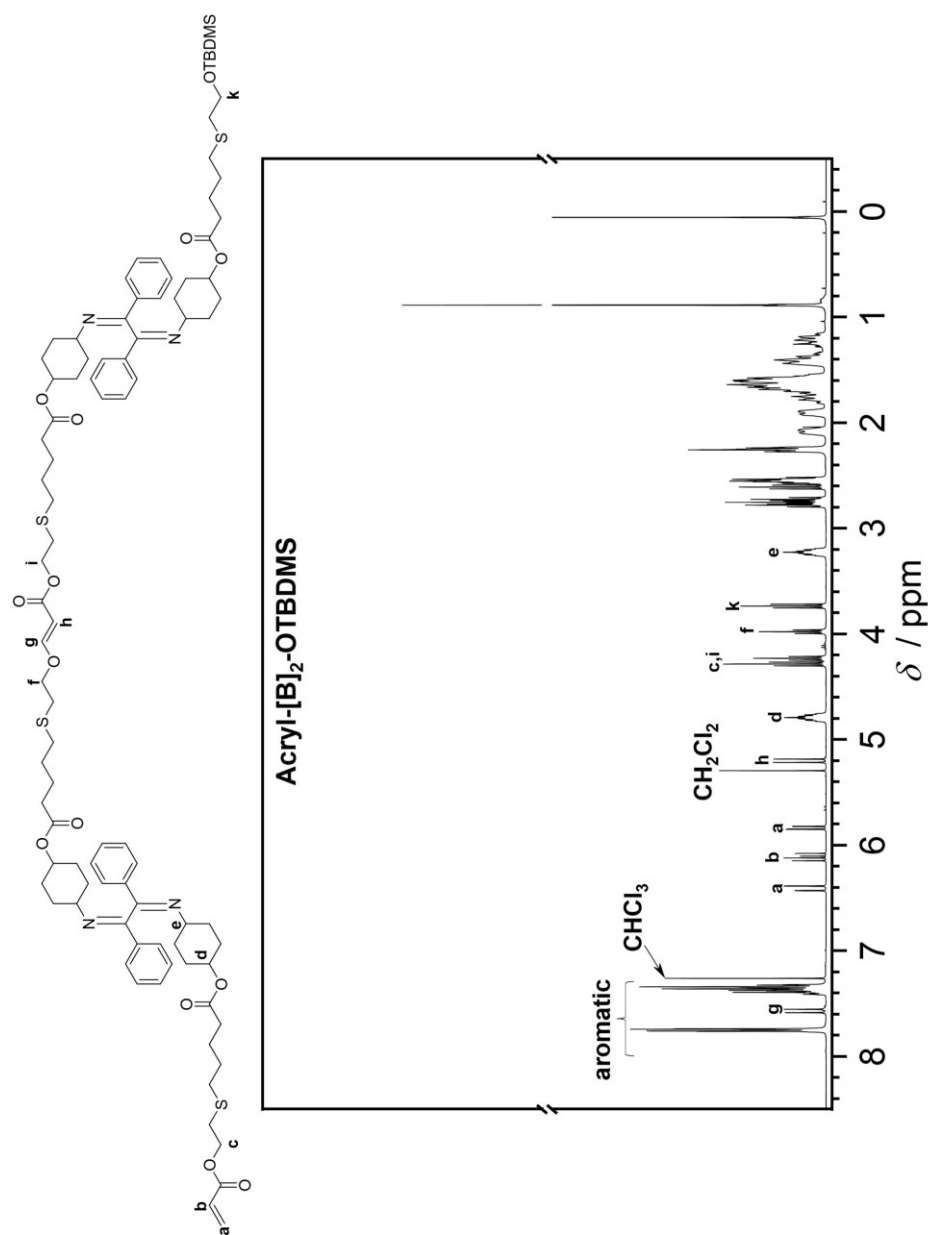


Figure S4.87. ^1H NMR (600 MHz, 32 scans) spectrum of acryl-[B]₂-OTBDMS in CDCl_3 .

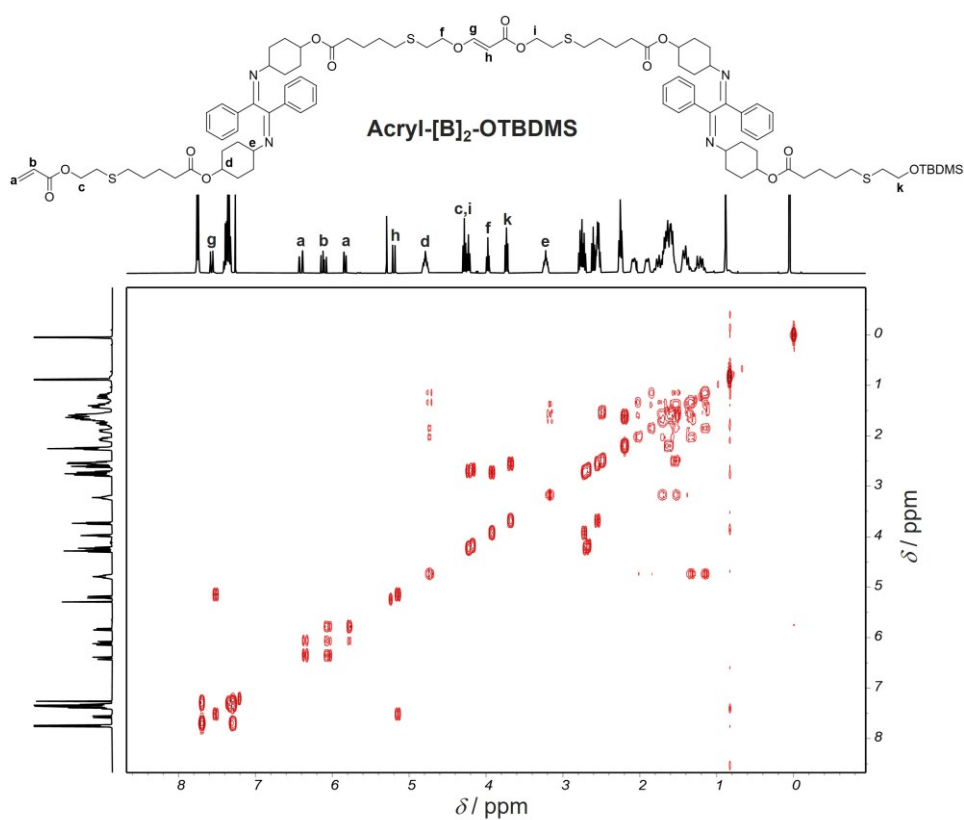


Figure S4.88. COSY NMR spectrum of *acryl-[B]₂-OTBDMS* in CDCl_3 .

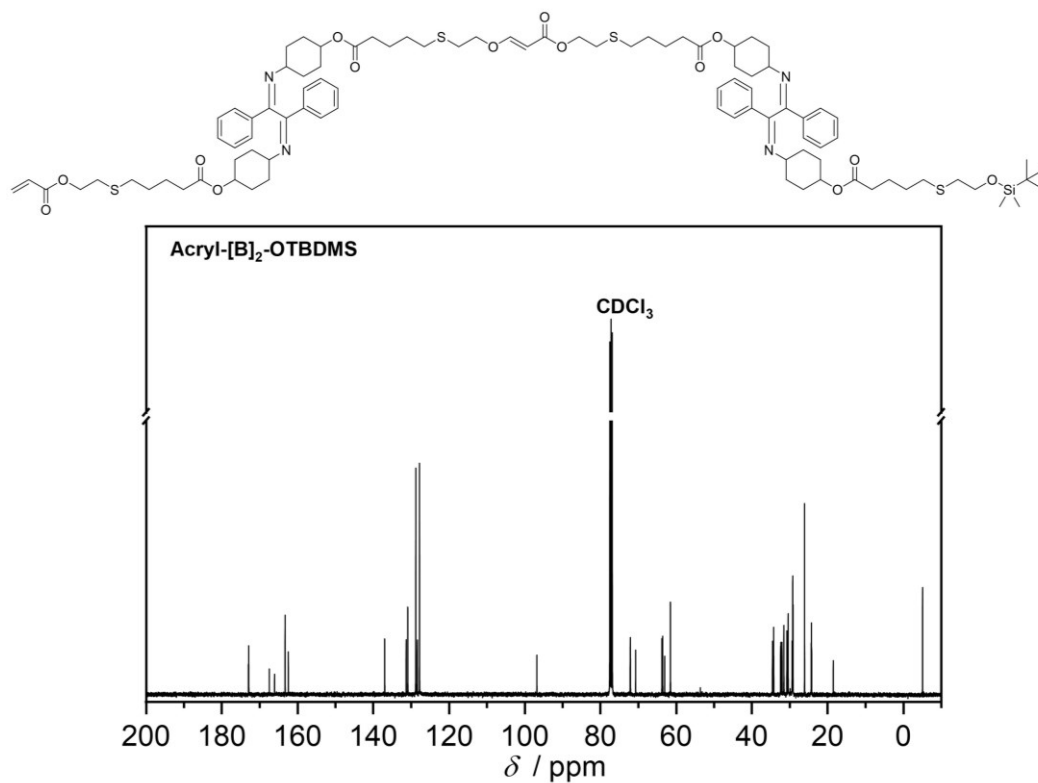


Figure S4.89. Carbon-Proton Decoupled ^{13}C NMR (151 MHz) spectrum of *acryl-[B]₂-OTBDMS* in CDCl_3 .

11.5. Information for Chapter 5

11.5.1. Deconvolution of UV-vis spectra

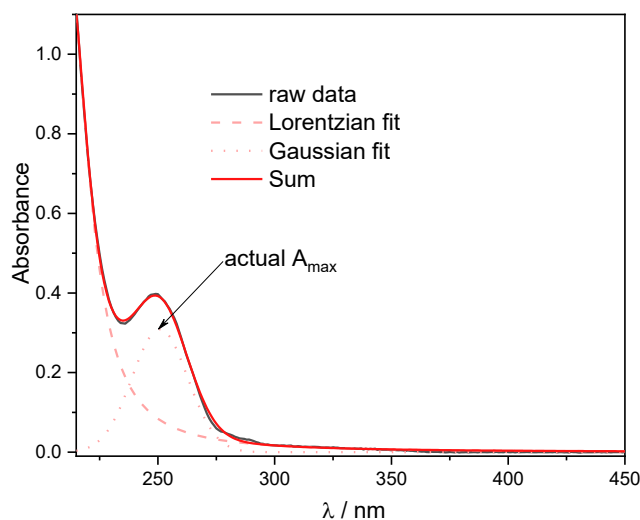


Figure S5.1. Deconvolution of UV-vis spectrum of α -bisimine core for the determination of isomerization conversion

The spectral background was fitted using the Lorentzian equation with simplification:

$$A_{\lambda_1} = \frac{I_1}{4 \left(\frac{\lambda_1 - \lambda_{0,1}}{w_1} \right)^2 + 1}$$

Where:

A_{λ_1} : absorbance at wavelength λ_1 ; I_1 : scaling intensity; λ_1 : wavelength (nm); $\lambda_{0,1}$: wavelength at peak absorbance; w_1 : absorption band width.

The absorption band arising from the chromophore was fitted using the Gaussian equation:

$$A_{\lambda_2} = I_2 e^{-\frac{1}{2} \left(\frac{\lambda_2 - \lambda_{0,2}}{w_2} \right)^2}$$

Where:

A_{λ_2} : absorbance at wavelength λ_2 ; I_2 : scaling intensity; λ_2 : wavelength (nm); $\lambda_{0,2}$: wavelength at peak absorbance; w_2 : absorption band width.

The absorbance values in the Lorentzian fit and Gaussian fit were derived using the Solver function integrated in Microsoft Excel with the following constraints:

$$175 \leq \lambda_1 \leq 225 \text{ (nm)}$$

$$225 \leq \lambda_2 \leq 275 \text{ (nm)}$$

$$\lambda_1 \geq 1$$

The quality of the fit was assessed by the Residual Sum of Squares (RSS) of the fit equations and the raw data. In most cases, RSS is lower than 0.1 (in few cases, RSS is smaller than 0.25). We are aware that many subpeaks may contribute to the absorption band of the chromophore. However, given that the maximum absorption peak decreases upon irradiation and the peak also recovers during thermal back isomerization with insignificant shift, the fitting using only one Gaussian curve is sufficient to allow the reliable determination of conversion of the isomerization process.

11.5.2. Synthesis protocol

11.5.2.1. Synthesis of polymer **P**₁, **P**₂, **P**₅

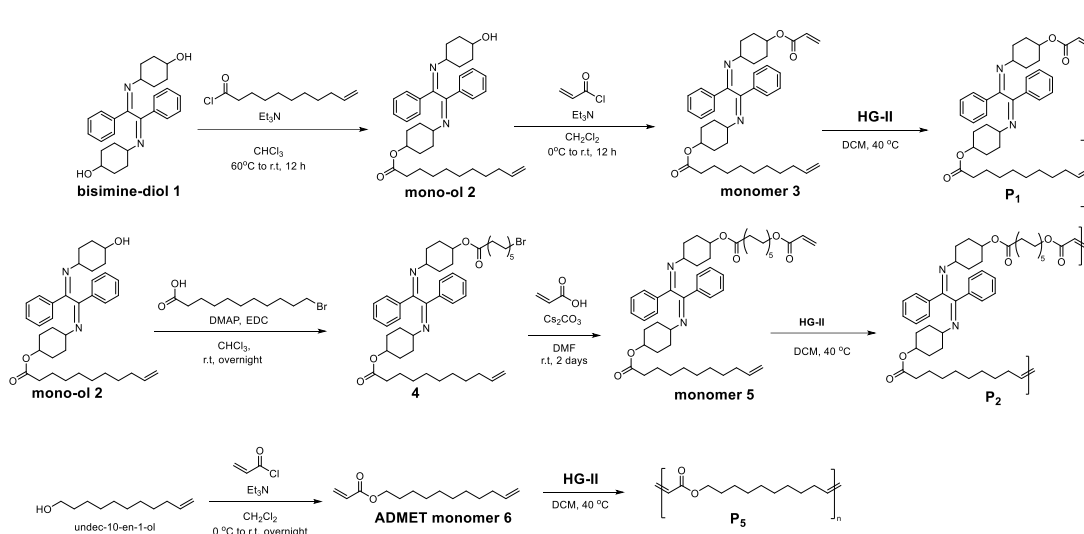


Figure S5.2. Synthesis route for polymer **P**₁, **P**₂ and **P**₅.

Synthesis of compound **1**, **2**, **3** was reported in Chapter 3.¹⁸⁸

Synthesis of compound **4**

α -bisimine mono-ol **2** (2.0 g, 3.5 mmol, 1.0 eq), 11-bromoundecanoic acid (1.0 g, 3.9 mmol, 1.1 eq), and DMAP (57 mg, 0.46 mmol, 12 mol%) were dissolved in CHCl_3 (5.0 mL) at ambient temperature. Subsequently, EDC (772 mg, 4.0 mmol, 1.2 eq) was added to the solution. The reaction was stopped after 18 h. The solvent was removed under reduced pressure and redissolved in ethyl acetate. After filtration, the organic phase was washed with water and brine (3 times) and concentrated. The residue was purified by flash column chromatography ($\text{EtOAc}:\text{H} = 1:9$, v/v), yielding the product as pale-yellow sticky oil (1.8 g, 65 % yield).

¹H NMR (600 MHz, CDCl_3) δ 7.74 – 7.60 (m, 4H), 7.32 – 7.18 (m, 6H), 5.76 – 5.63 (m, 1H), 4.95 – 4.76 (m, 2H), 4.78 – 4.64 (m, 2H), 3.27 (t, $J = 6.9$ Hz, 2H), 3.23 – 3.11 (m, 2H), 2.13 (t, $J = 7.5$ Hz, 4H), 2.06 – 1.96 (m, 2H), 1.95 – 1.89 (m, 2H), 1.86 – 1.79 (m, 2H), 1.76 – 1.65 (m, 4H), 1.60 – 1.43 (m, 8H), 1.40 – 1.23 (m, 10H), 1.23 – 1.07 (m, 18H). **¹³C NMR** (151 MHz, CDCl_3) δ 173.00 (1C), 172.98 (1C), 162.91 (2C, imine), 138.89 (1C, alkene), 136.73 (2C, aromatic) 130.57 (2C, aromatic), 128.46 (4C, aromatic), 127.53 (4C, aromatic), 114.12 (1C,

alkene), 71.54 (2C), 61.23 (2C), 34.50 (2C), 33.69 (1C), 33.67 (1C), 32.69 (1zC), 31.28 (2C), 30.16 (2C), 29.23 (2C), 29.19 (1C), 29.15 (1C), 29.07 (2C), 28.93 (2C), 28.91 (2C), 28.75 (1C), 28.60 (1C), 28.02 (1C), 26.82 (2C), 24.93 (1C), 24.91 (1C). **LC-MS**: calculated m/z for $C_{48}H_{70}BrN_2O_4^+$ $[M+H]^+$ = 819.4493, found: 819.4492.

Synthesis of monomer 5

Acrylic acid (264 mg, 3.7 mmol, 2.0 eq) and compound **4** (1.50 g, 1.83 mmol, 1.0 eq) were dissolved in DMF (18 mL). Subsequently, Cs_2CO_3 (717 mg, 2.2 eq) was added to the solution. The reaction was stopped after 2 days. The mixture was extracted with ethyl acetate and water (3 times). The organic phase was then concentrated and purified by flash column chromatography (EtOAc : H = 4 : 96, v/v) to obtain a sticky oil as product (1.1 g, 74 % yield).

1H NMR (600 MHz, $CDCl_3$) δ 7.78 – 7.72 (m, 4H), 7.42 – 7.30 (m, 6H), 6.39 (dd, J = 17.4, 1.5 Hz, 1H), 6.12 (dd, J = 17.3, 10.3 Hz, 1H), 5.83 – 5.75 (m, 2H), 5.02 – 4.88 (m, 2H), 4.84 – 4.74 (m, 2H), 4.14 (t, J = 6.7 Hz, 2H), 3.30 – 3.16 (m, 2H), 2.22 (t, J = 7.5 Hz, 4H), 2.12 – 2.05 (m, 2H), 2.05 – 1.99 (m, 2H), 1.94 – 1.88 (m, 2H), 1.82 – 1.71 (m, 2H), 1.69 – 1.52 (m, 10H), 1.47 – 1.16 (m, 28H). **^{13}C NMR** (151 MHz, $CDCl_3$) δ 173.31 (2C), 166.32 (1C), 163.13 (2C, imine), 139.14 (1C, alkene), 136.86 (2C, aromatic), 130.75 (2C, aromatic), 130.43 (1C, C=C acrylate), 128.70 (1C, C=C acrylate), 128.63 (4C, aromatic), 127.67 (4C, aromatic), 114.21 (1C, alkene), 71.73 (2C), 64.70 (2C), 61.41 (1C), 34.68 (2C), 33.80 (2C), 31.43 (2C), 30.30 (2C), 29.44 (2C), 29.35 (1C), 29.29 (1C), 29.23 (1C), 29.22 (1C), 29.20 (1C), 29.10 (1C), 29.08 (2C), 29.05 (2C), 28.89 (1C), 28.64 (1C), 25.93 (1C), 25.07 (2C). **LC-MS**: calculated m/z for $C_{51}H_{73}N_2O_6^+$ $[M+H]^+$ = 809.5464, found: 809.5462.

Synthesis of monomer 6

10-undecen-1-ol (1.2 mL, 5.87 mmol, 1.0 eq) and triethyl amine (0.98 mL, 1.2 eq) were dissolved in dry CH_2Cl_2 (6.0 mL), followed by dropwise addition of acryloyl chloride (0.57 mL, 1.2 eq) in dry CH_2Cl_2 (2.0 mL) at 0 °C. The temperature was maintained for 1 h before reaching ambient temperature. The reaction was conducted for 12 h. Upon completion, the reaction mixture was diluted in ethyl acetate and washed with water and brine (3 times). The organic phase was dried over $MgSO_4$, concentrated, and purified by flash column chromatography (EtOAc:H = 1:9, v/v), yielding 800 mg colorless oil as product (61 % yield).

1H NMR (600 MHz, $CDCl_3$) δ 6.39 (dd, J = 17.3, 1.5 Hz, 1H), 6.12 (dd, J = 17.4, 10.5 Hz, 1H), 5.85 – 5.76 (m, 2H), 5.04 – 4.88 (m, 2H), 4.14 (t, J = 6.8 Hz, 2H), 2.10 – 1.97 (m, 2H), 1.66 (dd, J = 8.2, 6.7 Hz, 2H), 1.42 – 1.21 (m, 12H). **^{13}C NMR** (151 MHz, $CDCl_3$) δ 166.48 (1C), 139.33 (1C), 130.53 (1C), 128.80 (1C), 114.27 (1C), 64.84 (1C), 33.93 (1C), 29.58 (1C), 29.52 (1C), 29.36 (1C), 29.22 (1C), 29.05 (1C), 28.75 (1C), 26.05 (1C). **Direct-Injection MS**: calculated m/z for $C_{14}H_{24}NaO_2^+$ $[M+Na]^+$ = 247.1674, found 247.1669.

Synthesis of **P₁** and **P₂**

Polymer **P₁** and **P₂** were synthesized from monomer **3** and **5**, respectively. The reaction conditions were kept the same for both monomers. In a typical experiment, monomer **3** (500 mg, 0.80 mmol) was dissolved in dry DCM (1.0 mL) and the reaction flask was sealed with a rubber septum (with a needle on top). Subsequently, Hoveyda-Grubbs 2nd generation (**HG-II**) catalyst (15 mg, 3.0 mol%) was added and the solution was heated to 40 °C. After 24 h, the solution was diluted with DCM (2.0 mL) and ethyl vinyl ether (in excess) was added. The solution was kept stirring for 30 min at 40 °C. Precipitation in cold methanol yielded solid polymers (isolation yield ~ 80-90 %).

Synthesis of polymer **P₅**

Polymer **P₅** was synthesized in a similar fashion as polymer **P₁** and **P₂**. The molar concentration of monomer **6** was 3.0 M and 1 mol% of **HG-II** catalyst was added. The polymerization was run overnight. Ethyl vinyl ether was added to quench the catalyst and the crude was precipitate in cold MeOH to yield white solid polymer (isolation yield ~ 90%).

11.5.2.2. Modification of polymer **P₁**, **P₂**

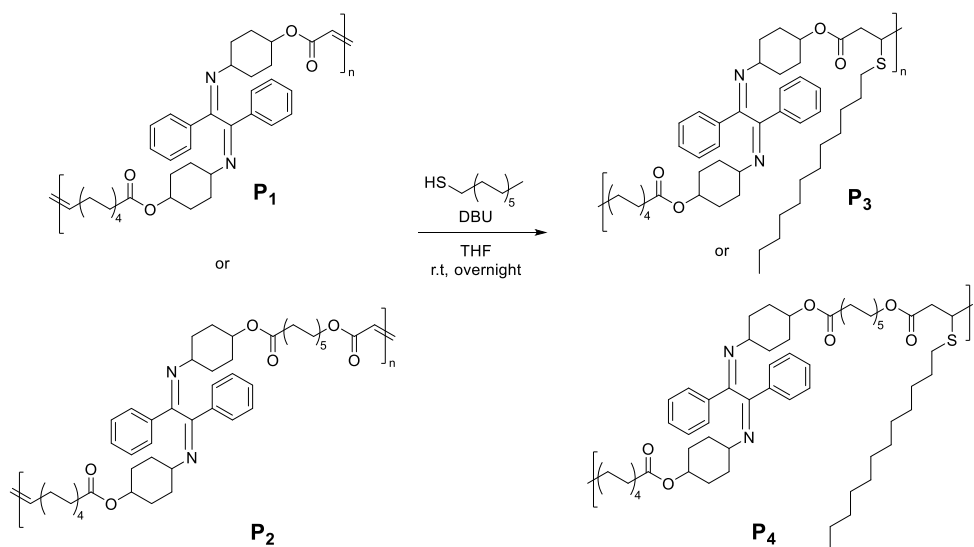


Figure S5.3. Thiol-Michael modification of polymer **P₁**, **P₂** with 1-dodecanethiol.

Polymer **P₁** and **P₂** were modified under identical conditions, affording polymers **P₃** and **P₄**, respectively. In a typical experiment, polymer **P₁** (200 mg, 0.334 mmol of internal acrylate double bonds, 1.0 eq) and 1-dodecanethiol (161 mL, 0.67 mmol, 2.0 eq) were dissolved in THF. DBU (10 mL, 20 mol% to thiol) was subsequently added to the solution. The conversion was monitored by ¹H NMR spectroscopy. Upon completion, the reaction solution was diluted in THF and passed through a short column of (basic aluminium oxide and silica gel). Subsequently, the crude was precipitated in cold methanol to obtain the product (isolation yield ~ 80%).

11.5.3. SEC traces

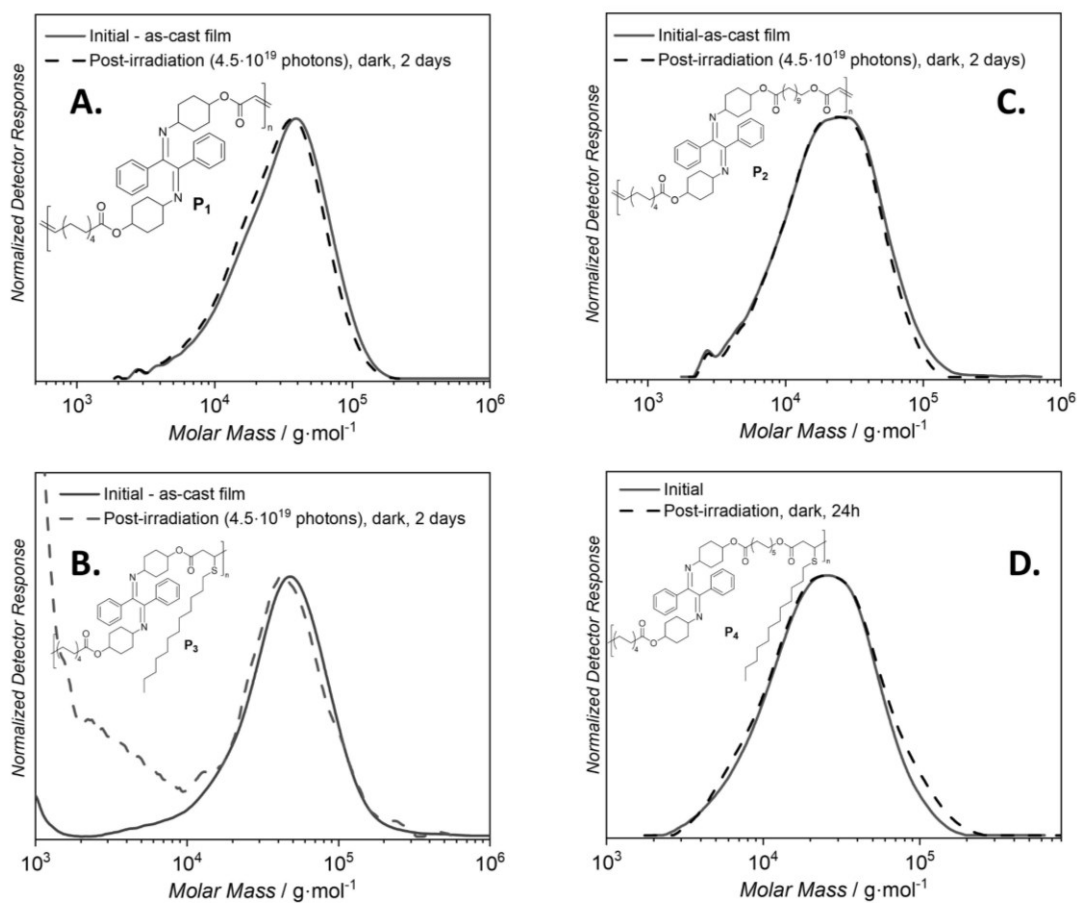


Figure S5.5. THF-SEC traces of pristine and post-310nm irradiated polymer films of P_1 - P_4 .

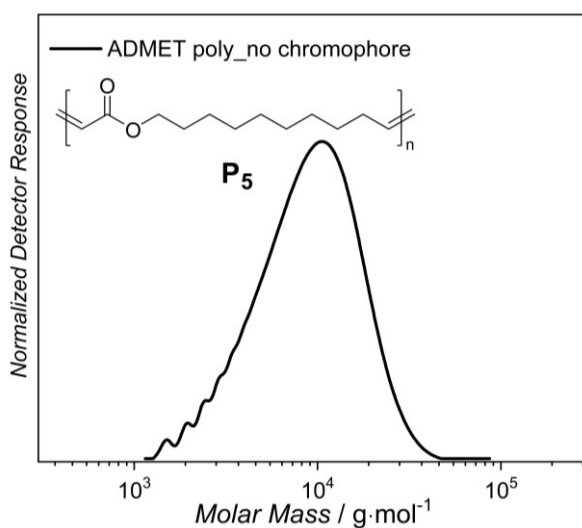


Figure S5.6. THF-SEC trace of non-chromophore polymer P_5 .

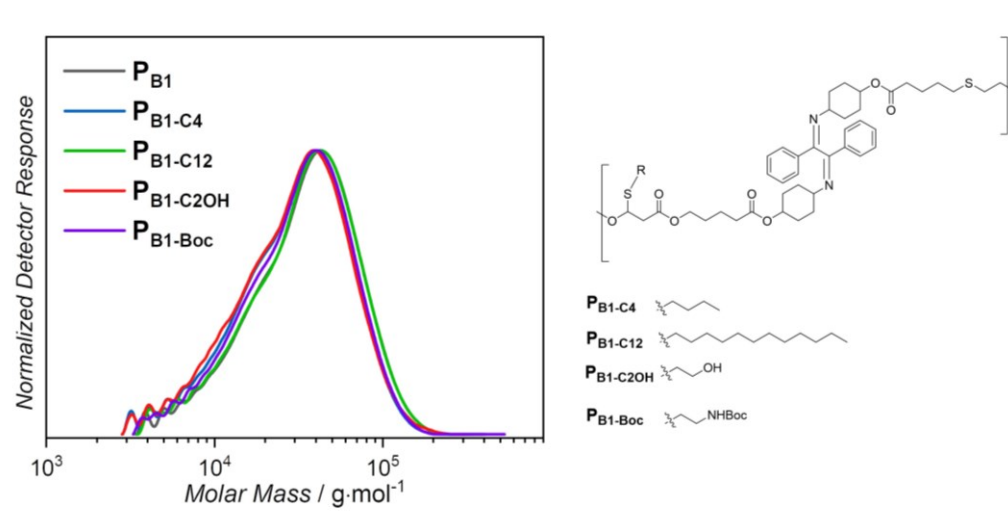


Figure S5.7. THF-SEC traces of parent polymer (P_{B1}) and the derived polymers. In this case, polymer P_{B1} was synthesized in large scale (800 mg) under optimized condition (0.4 M in DCM, 20 mol% DABCO, 2 hours).

11.5.4. TGA thermograms

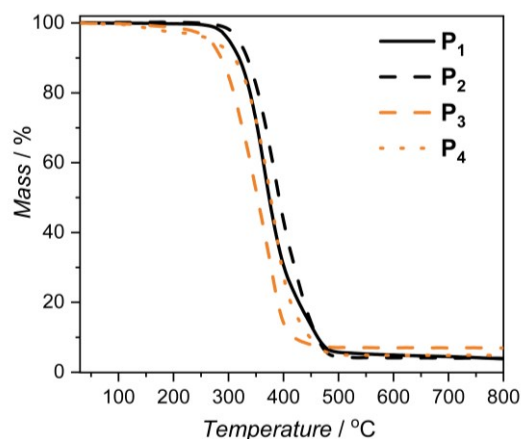


Figure S5.8. TGA thermograms of polymer P_1 - P_4 . $T_{d,5\%}$ (Temperature at which 5% mass of polymer is lost): P_1 (301 $^{\circ}\text{C}$), P_2 (317 $^{\circ}\text{C}$), P_3 (265 $^{\circ}\text{C}$), P_4 (270 $^{\circ}\text{C}$).

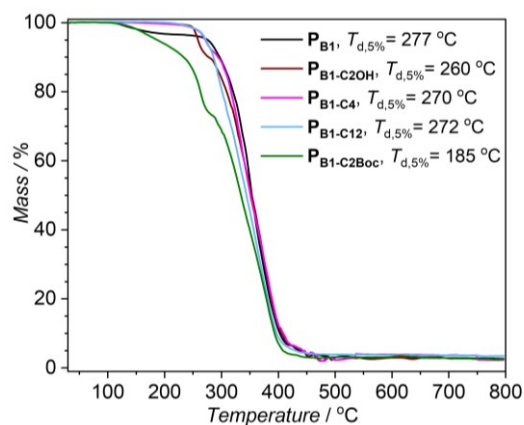


Figure S5.9. TGA thermogram of parent polymer (P_{B1}) and its thiol-Michael-modified derivatives. $T_{d,5\%}$ (Temperature at which 5% mass of polymer is lost) is 277 $^{\circ}\text{C}$ for P_{B1} , 260 $^{\circ}\text{C}$ for $P_{B1-C2OH}$, 270 $^{\circ}\text{C}$ for P_{B1-C4} , 272 $^{\circ}\text{C}$ for P_{B1-C12} , 185 $^{\circ}\text{C}$ for $P_{B1-C2Boc}$.

11.5.1. UV-vis spectrum of P₅

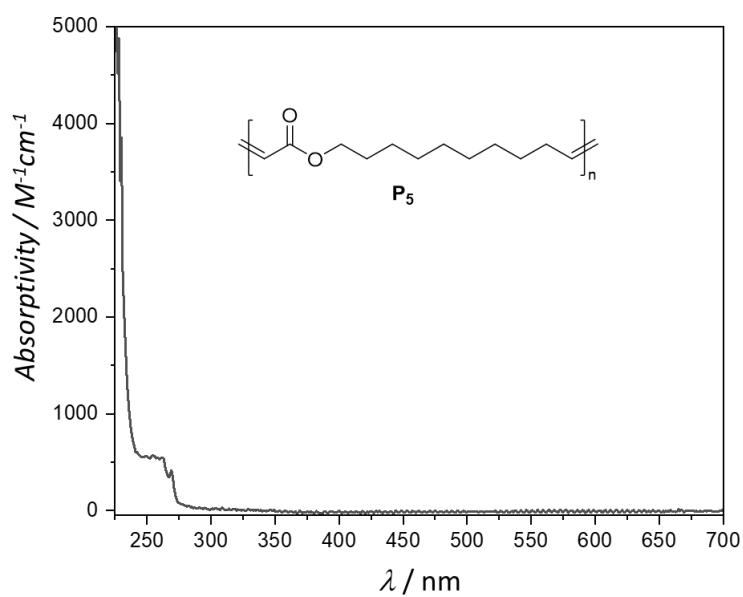


Figure S5.10. UV-vis absorption spectrum of polymer P₅ in THF.

11.5.2. NMR spectra

11.5.2.1. Polymer P₁

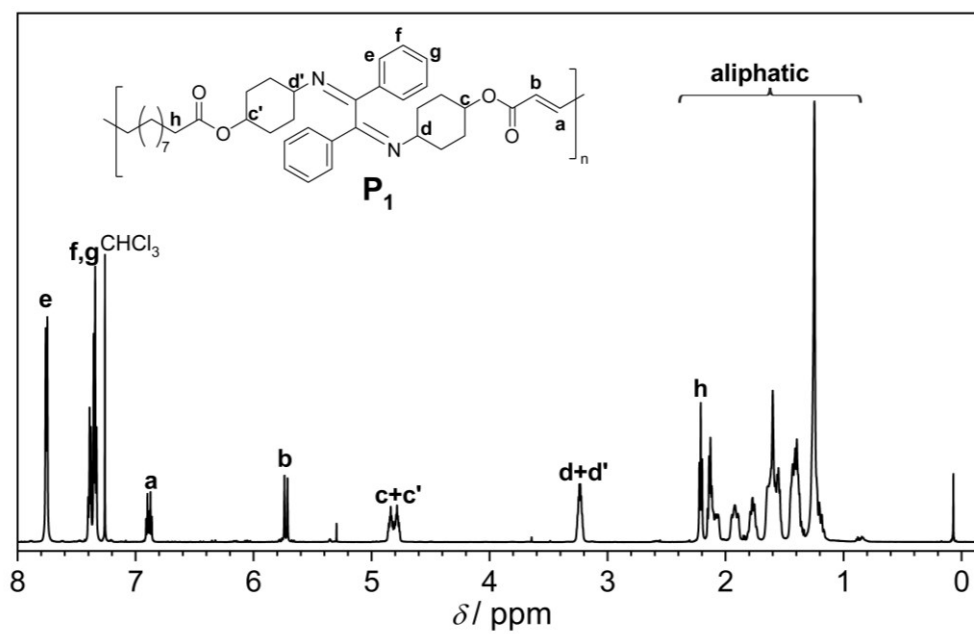


Figure S5.11. ¹H NMR spectrum (600 MHz, 32 scans) of P₁ in CDCl₃

11.5.2.2. Polymer P₂

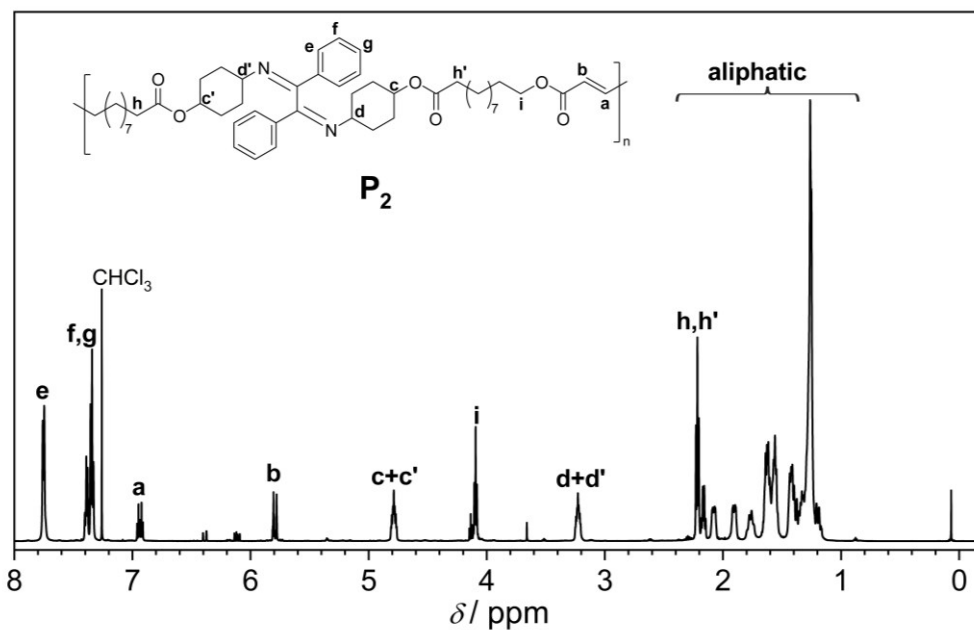


Figure S5.12. ¹H NMR spectrum (600 MHz, 32 scans) of P₂ in CDCl₃

11.5.2.3. Polymer P₃

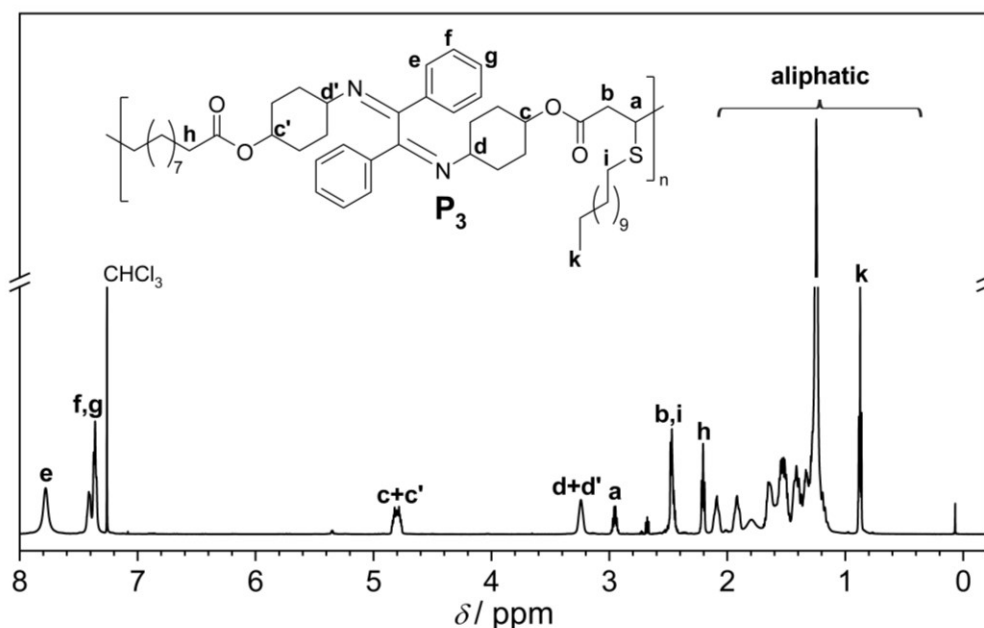


Figure S5.13. ¹H NMR spectrum (600 MHz, 32 scans) of P₃ in CDCl₃.

11.5.2.4. Polymer P₄

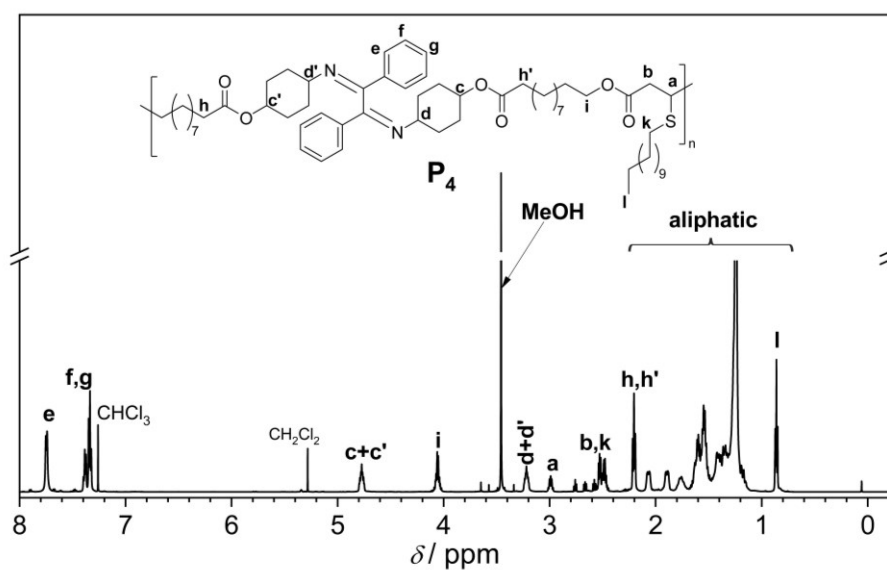


Figure S5.14. ¹H NMR spectrum (600 MHz, 32 scans) of P₄ in CDCl₃.

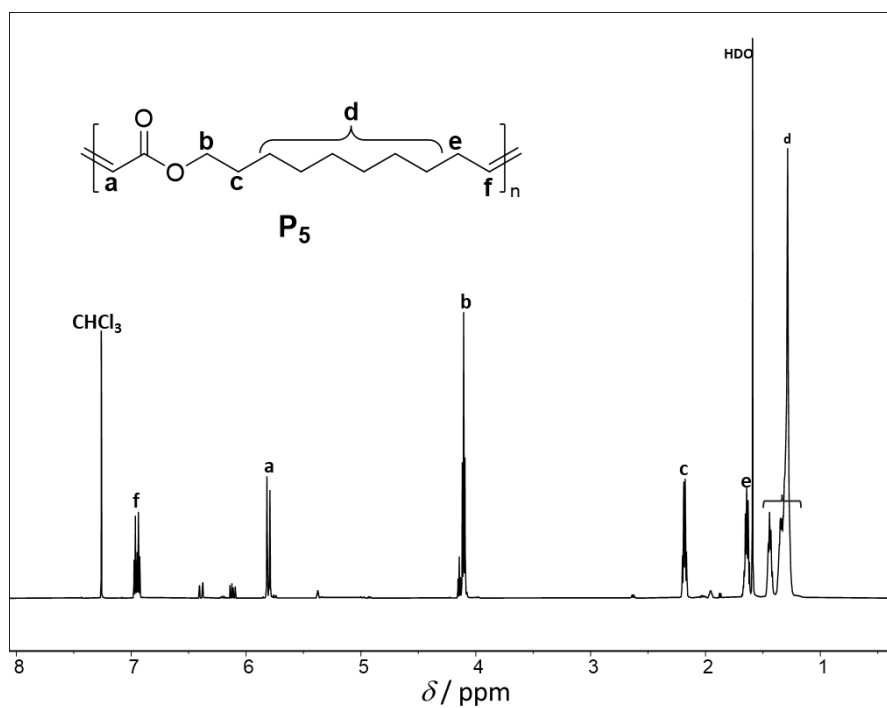


Figure S5.15. ¹H NMR spectrum of polymer P₅ in CDCl₃.

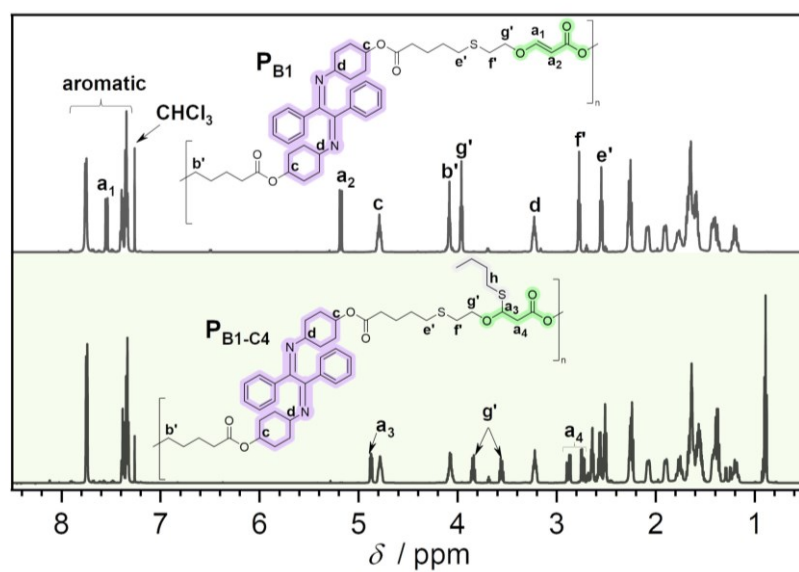
11.5.2.5. Polymer P_{B1-C4} 

Figure S5.16. Stacked ^1H NMR spectra (600 MHz, 32 scans) of P_{B1-C4} and P_{B1} in CDCl_3 .

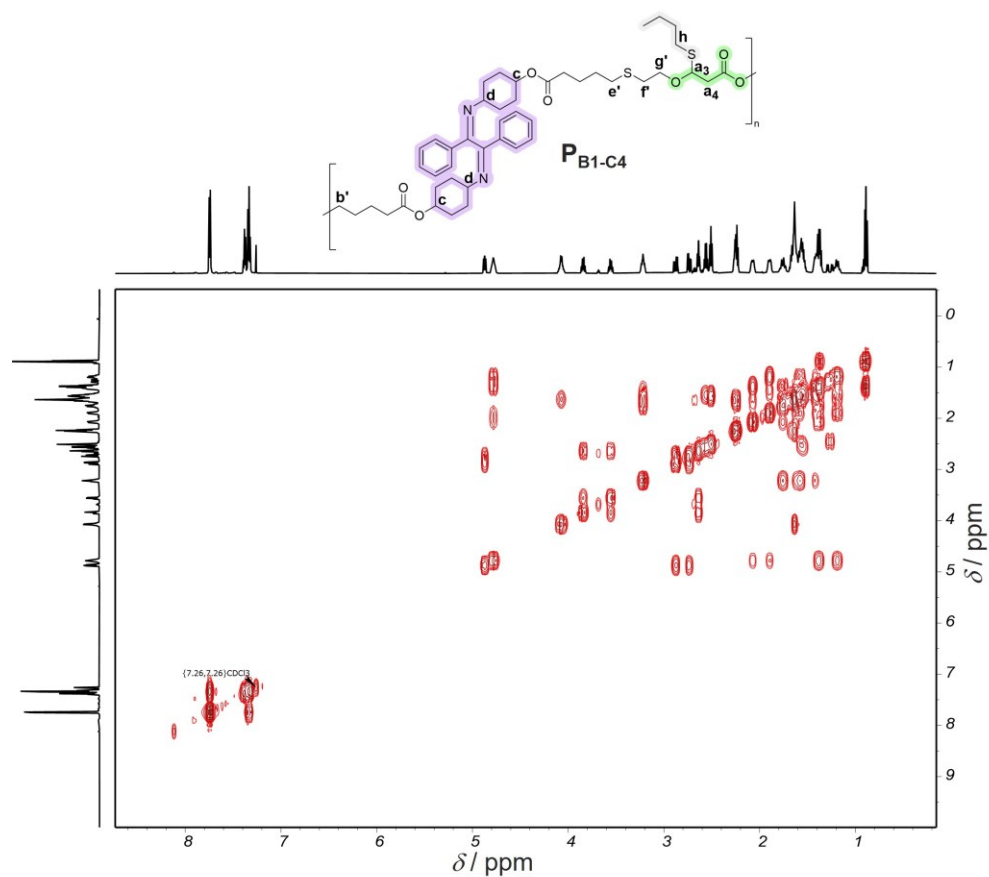


Figure S5.17. COSY NMR spectrum of P_{B1-C4} in CDCl_3 .

11.5.2.6. Polymer P_{B1-C12}

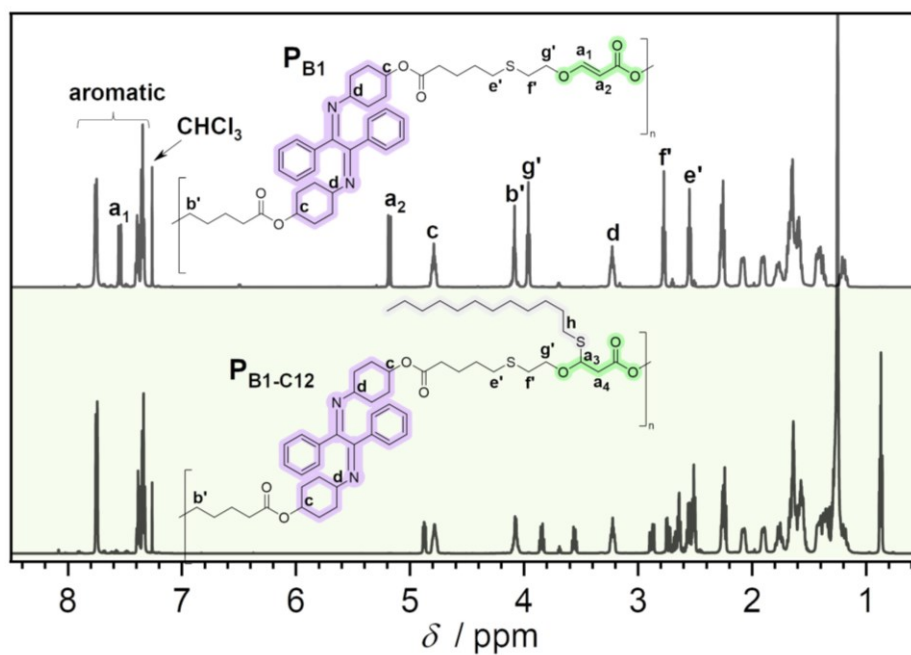


Figure S5.18. Stacked ^1H NMR spectra (600 MHz, 32 scans) of P_{B1-C12} and P_{B1} in CDCl_3 .

11.5.2.7. Polymer $P_{B1-C2OH}$

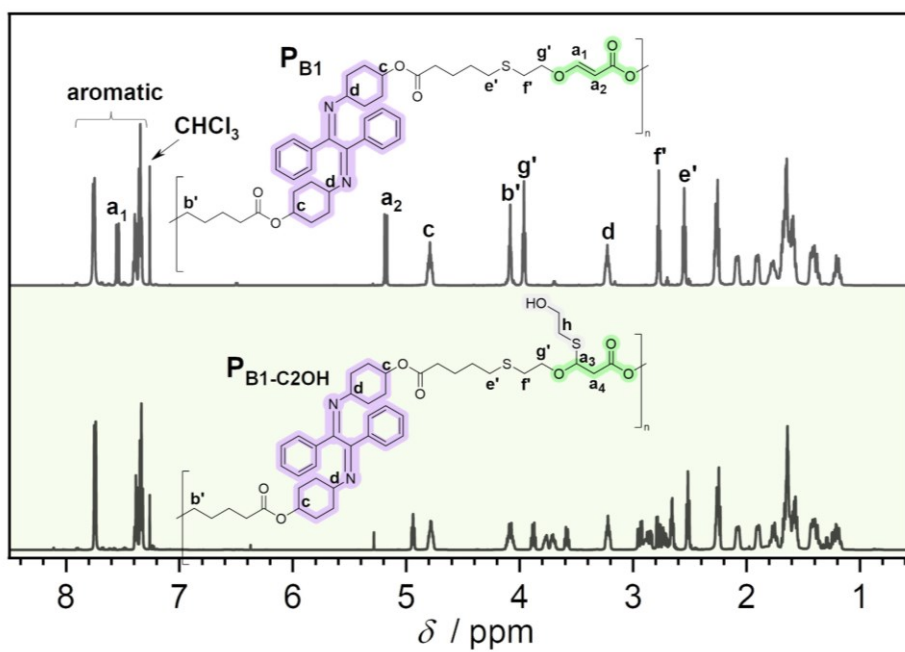


Figure S5.19. Stacked ^1H NMR spectra (600 MHz, 32 scans) of $P_{B1-C2OH}$ and P_{B1} in CDCl_3 .

11.5.2.8. Polymer $P_{B1-C2Boc}$

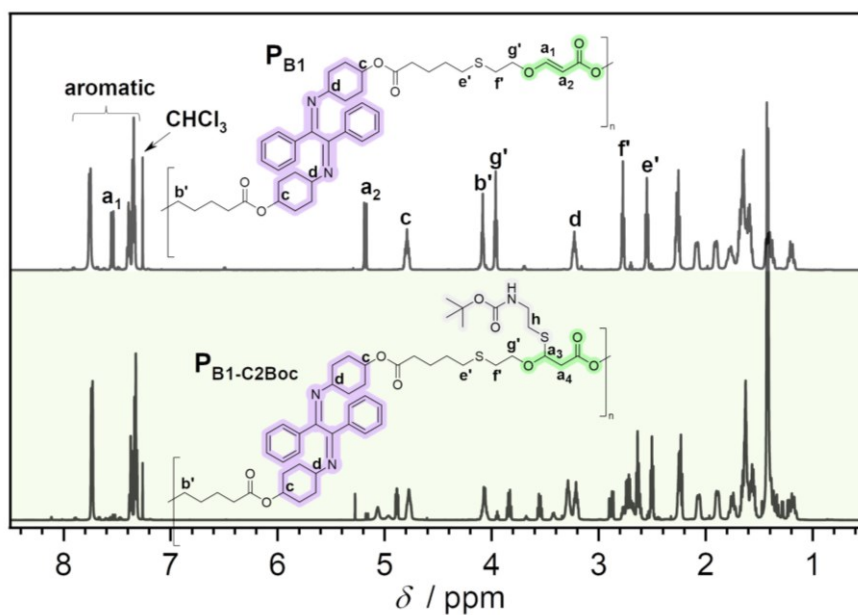


Figure S5.20. Stacked ^1H NMR spectra (600 MHz, 32 scans) of $P_{B1-C2Boc}$ and P_{B1} in CDCl_3 .

11.5.2.9. Polymer P_{B1-TMS}

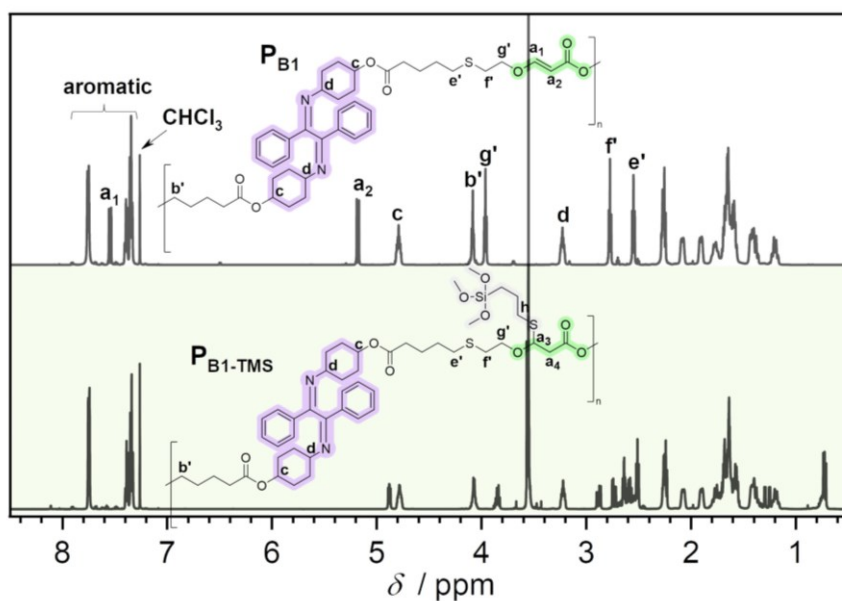


Figure S5.21. Stacked ^1H NMR spectra (600 MHz, 32 scans) of P_{B1-TMS} and P_{B1} in CDCl_3 .

11.6. Information for Chapter 6

Synthesis of oligomers and polymers has already been reported in chapter 4 and 5. The details for instruments and characterization can be found in section 11.1.

11.7. Information for chapter 7

11.7.1. Sample preparation for DSC measurement

Solutions of polymer P_{h1} and P_{h2} of $1.0 \text{ g}\cdot\text{L}^{-1}$ in dichloromethane (DCM) were filled into 24 mL glass vials and irradiated with 400-nm LEDs for approximately 4 h. The conversions were determined via ^1H NMR spectroscopy. Upon reaching the desired conversion, the irradiated solutions were concentrated to $100 \text{ g}\cdot\text{L}^{-1}$ at ambient temperature. The unirradiated samples were prepared in the same manner ($100 \text{ g}\cdot\text{L}^{-1}$). Four polymer solutions (two pristine and two irradiated) were drop-cast separately into four DSC pans with known weights. Subsequently, the pans were transferred to a vacuum oven at 25°C and the vacuum was maintained for 3 days prior to DSC measurement. The masses of the deposited polymers were kept close to each other (approximately $7.25 \text{ mg} - 7.59 \text{ mg}$).

11.7.2. Action plot experiment

For the action plot, the wavelength-dependent conversion was monitored by ^1H NMR spectroscopy. A stock solution of the homopolymer (**Z**)- P_{h1} in DCM ($0.5 \text{ g}\cdot\text{L}^{-1}$) was prepared. The solution was filled in laser vials (0.6 mL each) and the solvent was allowed to evaporated overnight, yielding homologous samples with equable amounts of polymer. After the solvent was evaporated, the polymer residue was dissolved in toluene- d_8 (0.6 mL). The wavelength was varied between 320 and 430 nm, where three samples were measured per wavelength. 0.2 mL of each solution was filled into a Hella Analytics quartz high precision cell cuvette ($10 \text{ mm} \times 10 \text{ mm}$), irradiated separately and then combined for ^1H NMR spectroscopy measurements. The photoisomerization conversion was determined based on the comparison of integrals of resonances corresponding to the (*Z*)- and (*E*)-isomers. The reported values are the average of three separate experiments.

11.7.3. Irradiation study of P_{h1} and P_{h2}

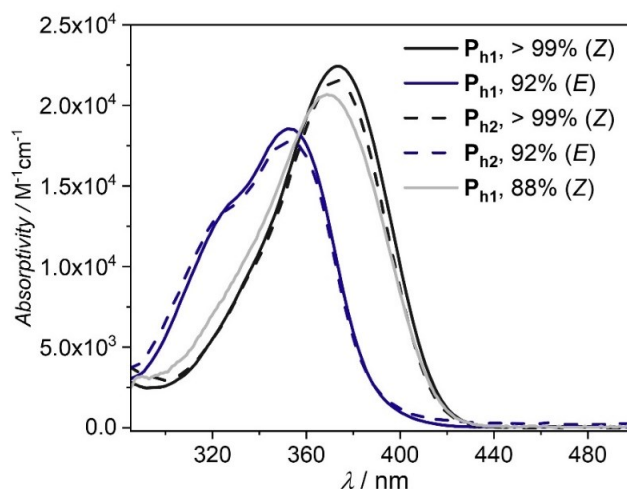


Figure S7.1. Molar absorptivity of polymer P_{h1} and P_{h2} in toluene solution at 25°C .

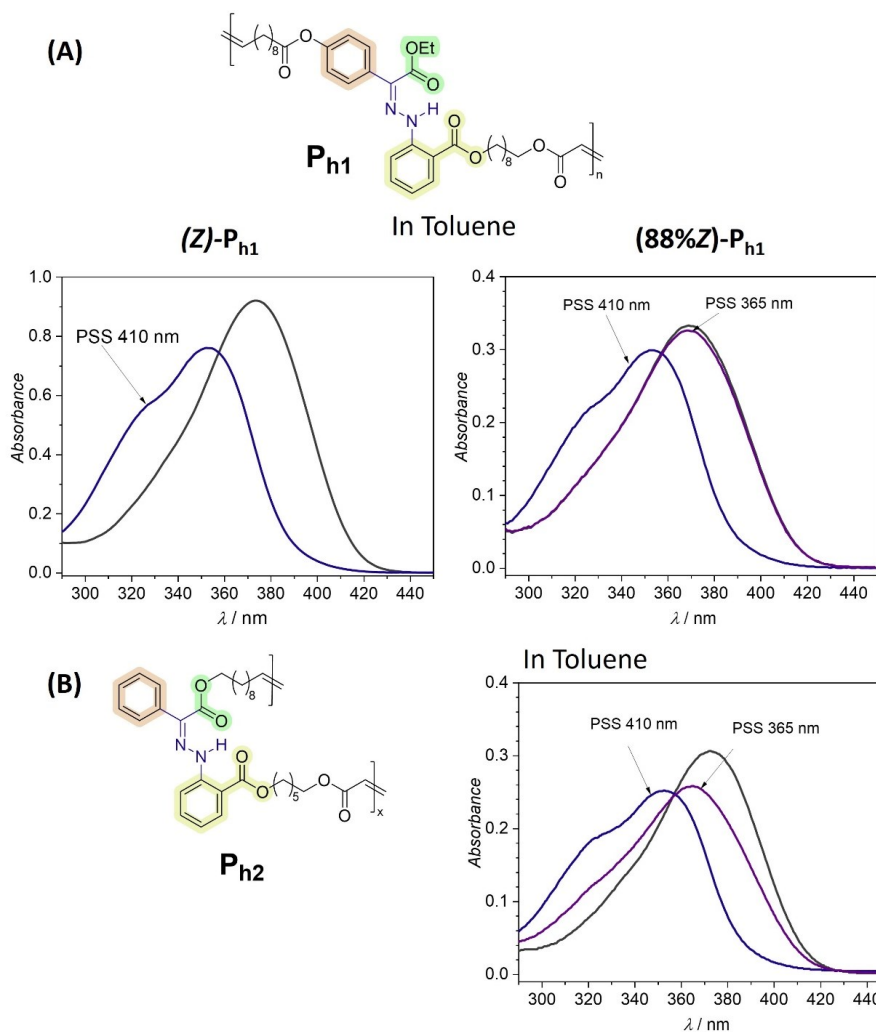


Figure S7.2. Irradiation experiment of polymer **Ph_{h1}** (A) and **Ph_{h2}** (B) solution in toluene solvent monitored by UV-vis spectroscopy at 25 °C. $[\text{photoswitch}] = (1.2\text{--}4.0) \cdot 10^{-5} \text{ M}$.

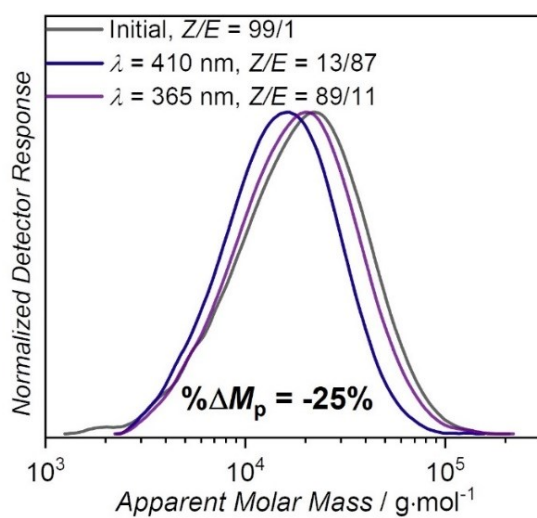


Figure S7.3. DMAc SEC traces recorded for pristine (Z)-**Ph_{h1}** and the corresponding irradiated polymer. The conversion was determined by ^1H NMR spectroscopy. For SEC measurements, the samples were blow-dried to remove the solvent (toluene) and redissolved in DMAc.

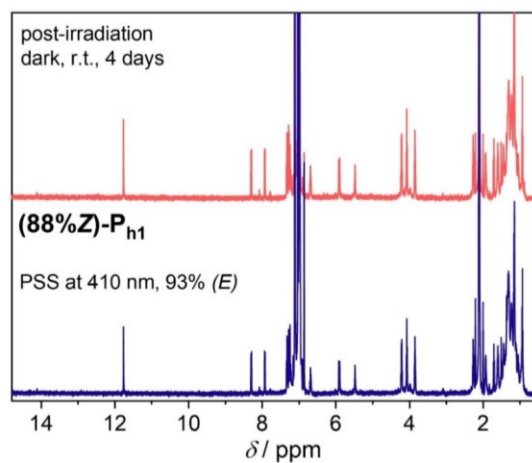


Figure S7.4. ^1H NMR (600 MHz) spectra of **(88%Z)- P_{h1}** in toluene- d_8 under 410-nm irradiation, followed by darkness at r.t for 4 days.

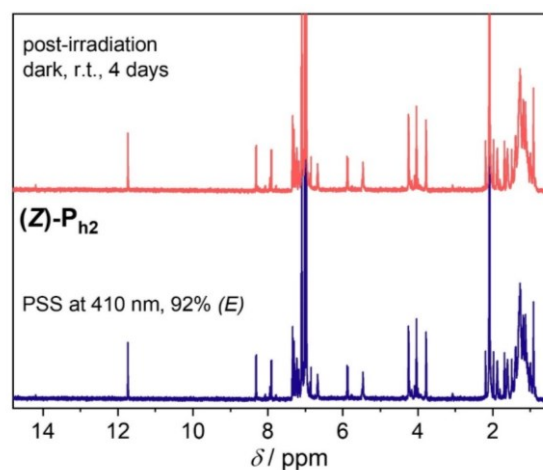


Figure S7.5. ^1H NMR (600 MHz) spectra of **(Z)- P_{h2}** in toluene- d_8 under 410-nm irradiation, followed by darkness at r.t for 4 days.

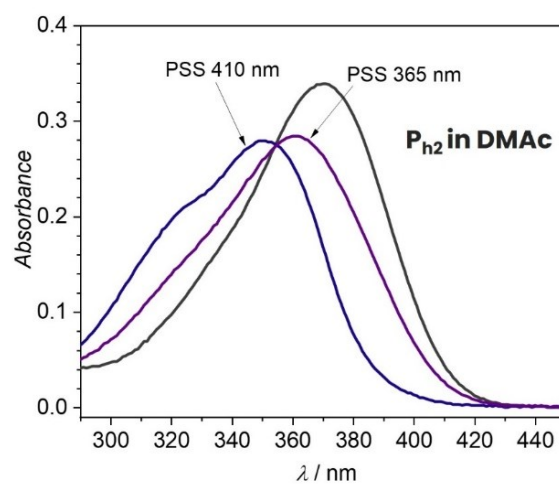


Figure S7.6. Irradiation of polymer P_{h2} solution in DMAc solvent monitored by UV-vis spectroscopy at 25 °C. $[\text{photoswitch}] = 1.5 \cdot 10^{-5} \text{ M}$.

11.7.4. TGA thermograms

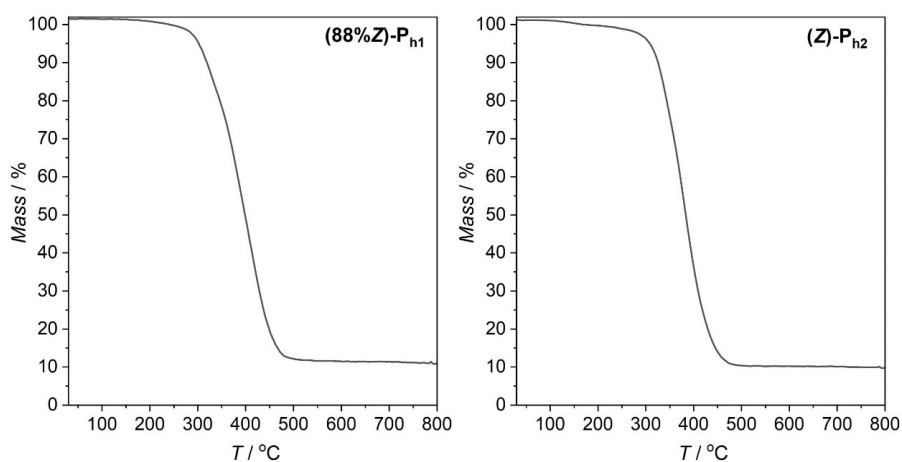


Figure S7.7. TGA thermograms of P_{h1} (A) and P_{h2} (B). Conditions: heating from 30 °C to 800 °C, at 20 °C·min⁻¹, under N₂ atmosphere.

11.7.5. Photoswitching cycle

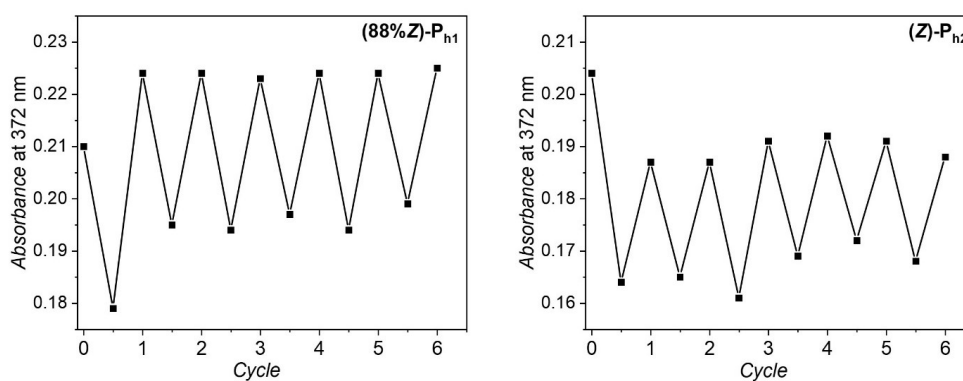
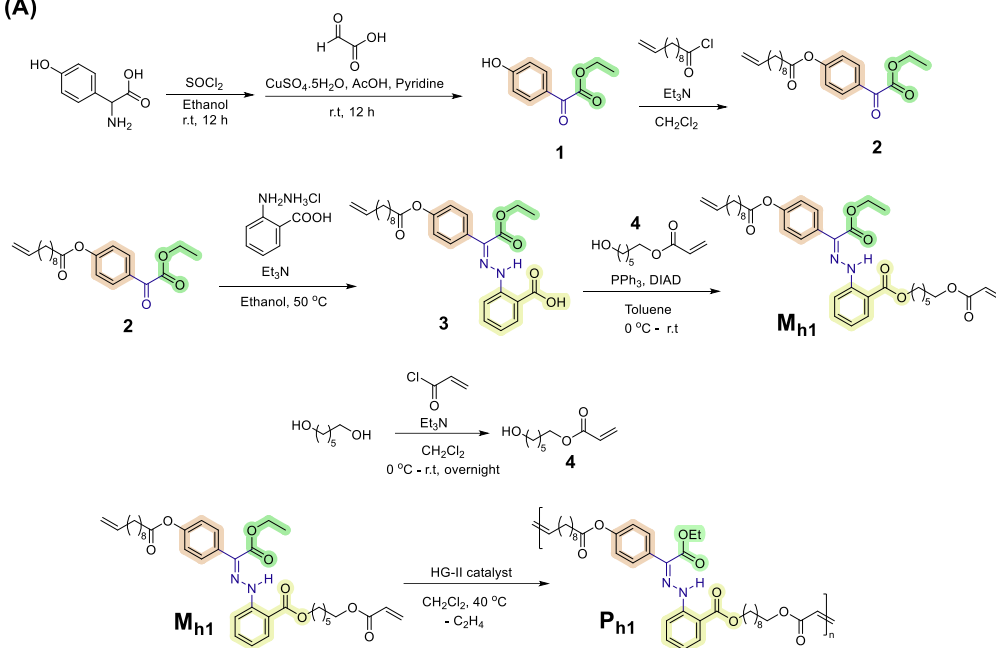


Figure S7.8. Solution photoisomerization cycles of (88%Z)-P_{h1} (left) and (Z)-P_{h2} (right). $c = (1.1\text{--}1.4) \cdot 10^{-5}$ M in toluene at 25 °C; Forward photoisomerization was triggered by irradiating with $\lambda = 410$ nm ($6.0 \cdot 10^{17}$ photons, $P = 4.5$ mW $\pm 13\%$); Back photoisomerization was performed at $\lambda = 310$ nm ($2.1 \cdot 10^{18}$ photons, $P = 5.5$ mW $\pm 6.0\%$).

11.7.6. Synthesis protocol

11.7.6.1. Synthesis of P_{h1} and P_{h2} and precursors

(A)



(B)

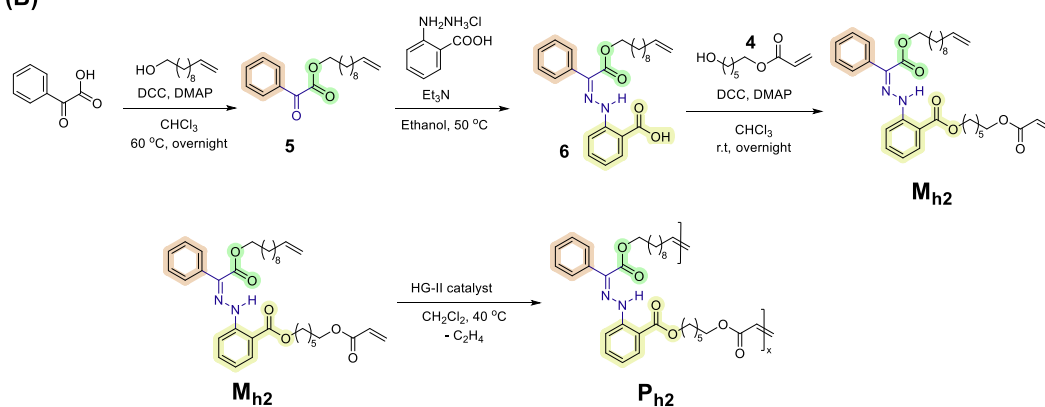
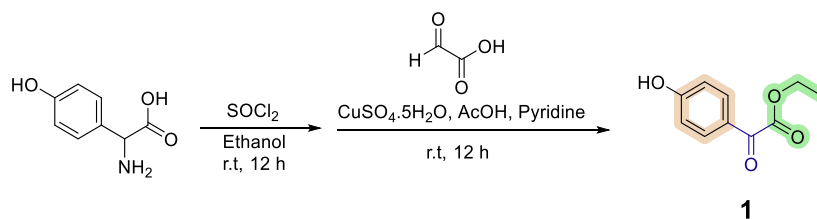


Figure S7.9. Synthesis route to monomers M_{h1} (A) and M_{h2} (B) and the respective polymers, i.e., P_{h1} (A) and P_{h2} (B).

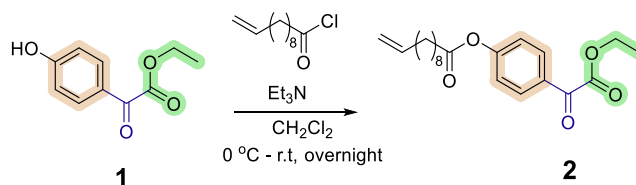
Synthesis of compound 1



D-4-hydroxyphenylglycine (2.50 g, 14.96 mmol, 1.00 eq) was suspended in ethanol (50 mL) before thionyl chloride (3.30 g, 27.57 mmol, 1.80 eq) was added dropwise at ambient temperature, and the reaction mixture was stirred overnight. Subsequently, the solvent was removed under reduced pressure and the residue was washed twice with ice cold diethyl ether to yield *D*-4-Hydroxyphenylglycine ethyl ester as a white solid. The crude product was used in the next step without any further purification. The crude product was dissolved in a solution of glyoxylic acid (17.0 mL), pyridine (3.4 mL) and acetic acid (0.5 mL). After 10 min of stirring, copper (II) sulfate pentahydrate (3.70 g, 23.28 mmol, 1.55 eq) was added and the mixture was stirred overnight at ambient temperature. Water (250 mL) was added to the crude mixture and the aqueous phase was extracted with CH₂Cl₂ (5 x 50 mL). The organic layers were combined and washed with brine and dried over Na₂SO₄. The solvent was removed under reduced pressure and the crude product was purified via flash column chromatography (silica gel, EtOAc/c-Hexane, v/v, from 1/10 to 1/6). The solvent was removed, and the product was dried under reduced pressure at 40 °C. Compound **1** was isolated as a pale-yellow solid (1.70 g, 8.75 mmol, 58 %). The ¹H and ¹³C NMR spectra are in agreement with the literature.¹¹⁷

¹H-NMR (600 MHz, CDCl₃): δ / ppm = 7.98 – 7.93 (m, 2H), 6.96 – 6.89 (m, 2H), 6.84 – 5.70 (m, 1H, Ar-OH), 4.43 (q, 2H), 1.41 (t, 3H). **¹³C-NMR** (151 MHz, CDCl₃): δ / ppm = 185.04 (1C), 164.25 (1C), 162.09 (1C), 133.04 (2C), 125.43 (1C), 115.95 (2C), 62.38 (1C), 14.11 (1C).

Synthesis of compound 2

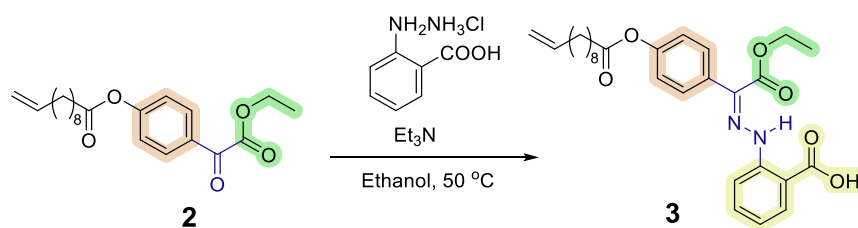


Compound **1** (2.00 g, 10.30 mmol, 1.00 eq) was dissolved in dry CH₂Cl₂ (100 mL) and triethyl amine (1.23 g, 1.70 mL, 10.30 mmol, 1.20 eq) was added. The mixture was purged with argon for 1 h and cooled to 0 °C. Subsequently, 10-undecenoyl chloride (2.35 g, 2.50 mL, 11.60 mmol, 1.10 eq) was added dropwise. The reaction mixture was allowed to warm to ambient temperature and stirred overnight. The organic phase was washed with water (3 x 100 mL) and brine (100 mL) and dried over Na₂SO₄. The solvent was removed under reduced pressure and the crude product was purified via flash column chromatography (silica gel, EtOH/c-

Hexane = 1/20 to 1/10). After the solvent was removed under reduced pressure, the product **2** was obtained as a pale-yellow oil (3.25 g, 9.01 mmol, 88 %).

¹H-NMR (600 MHz, CDCl₃): δ /ppm = 8.04 – 7.95 (m, 2H), 7.21 – 7.12 (m, 2H), 5.74 (m, 1H), 4.96 – 4.89 (m, 1H), 4.86 (m, 1H), 4.38 (q, 2H), 2.51 (t, 2H), 1.98 (m, 2H), 1.69 (p, 2H), 1.39 – 1.20 (m, 14H). **¹³C-NMR** (151 MHz, CDCl₃): δ /ppm = 185.00 (1C), 171.46 (1C), 163.51 (1C), 155.90 (1C), 139.14 (1C), 131.81 (2C), 129.96 (1C), 122.19 (2C), 114.20 (1C), 62.44 (C16), 34.40 (C10), 33.78 (C3), 28.88 (C4), 24.78 (C6), 14.11 (1C). **LC-MS**: calculated m/z for C₂₁H₂₉O₅⁺ [M+H]⁺ = 361.2010, found 361.2012.

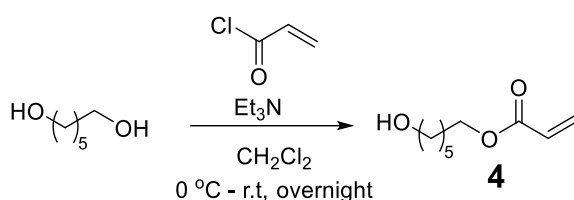
Synthesis of Compound 3



2-Hydrazinobenzoic acid hydrochloride (0.575 g, 3.05 mmol, 1.10 eq) and triethyl amine (0.336 g, 0.463 mL, 3.32 mmol, 1.20 eq) were dissolved in ethanol (40 mL). Subsequently, compound **2** (1.00 g, 2.77 mmol, 1.00 eq) was added and the mixture was stirred for an additional 4 h at 50 °C. The solvent was removed under reduced pressure and the crude product was purified via flash column chromatography (silica gel, DCM/MeOH = 20/1 → 10/1). The solvent was removed, and the product was dried under reduced pressure at 40 °C. The isomeric mixture of **3** was further purified by flash column chromatography (DCM:MeOH 20:1) to obtain the pure isomer as a yellow solid (0.636 g, 1.29 mmol, 47%).

¹H-NMR (600 MHz, CD₂Cl₂): δ /ppm = 13.67 (s, 1H), 8.04 (dd, 1H), 7.92 (dd, 1H), 7.73 – 7.67 (m, 2H), 7.55 (m, 1H), 7.12 – 7.06 (m, 2H), 6.99 (m, 1H), 5.82 (m, 2H), 5.00 (m, 1H), 4.97 (m, 1H), 4.91 (m, 2H), 4.42 (q, 2H), 2.56 (t, 2H), 2.35 (t, 3H), 1.77 – 1.69 (m, 2H), 1.62 (q, 3H), 1.46 – 1.24 (m, 29H). **¹³C-NMR** (151 MHz, CD₂Cl₂): δ /ppm = 178.72 (1C), 172.27 (1C), 162.30 (1C), 150.74 (-C=N-), 146.55 (1C), 139.29 (1C), 135.24 (1C), 134.00 (1C), 131.74 (1C), 131.24 (1C), 129.61 (2C), 121.19 (2C), 120.54 (1C), 114.60 (1C), 113.83 (1C), 61.58 (1C), 34.30 (1C), 33.78 (1C), 29.29 (3C), 24.88 (1C), 24.68 (2C), 13.99 (1C). **LC-MS**: calculated m/z for C₂₈H₃₃N₂O₆⁻ [M-H]⁻ = 493.2333, found 493.2344.

Synthesis of compound **4** (6-Hydroxyhexyl acrylate)

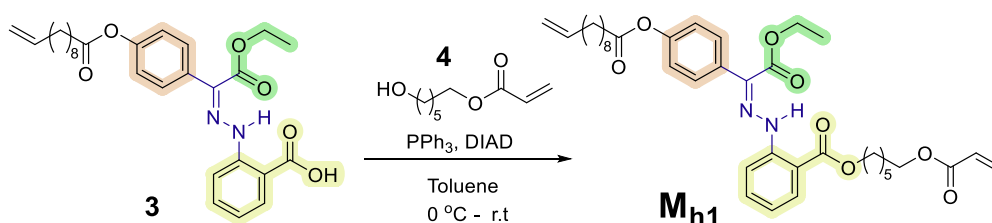


1,6-Hexanediol (25.0 g, 211 mmol, 1 eq.) was dissolved in dry DCM (20 mL) before acryloyl chloride (9.50 g, 8.50 mL, 105 mmol, 0.50 eq.) was added dropwise at 0 °C. The mixture was allowed to warm to ambient temperature and stirred overnight. The solvent was removed under reduced pressure and the crude product was purified by flash column chromatography (silica gel, EtOAc/c-Hexane, 1/10 → 1/1). The product was isolated as a colorless liquid (5.20 g, 30 mmol, 18%). ¹H and ¹³C NMR spectra are in agreement with the literature.²⁹⁷

¹H-NMR (600 MHz, CDCl₃): δ (ppm) = 6.33 (dd, 1H), 6.05 (dd, 1H), 5.75 (dd, 1H), 4.12 – 4.02 (m, 3H), 3.57 (t, 2H), 1.66 – 1.58 (m, 2H), 1.55 – 1.47 (m, 2H), 1.39 – 1.29 (m, 4H).

¹³C-NMR (151 MHz, CDCl₃): δ (ppm) 166.49 (1C, -C=O), 130.66 (1C, CH=CH₂), 128.72 (1C, -CH=CH₂), 64.66 (1C), 62.94 (1C), 32.73 (1C), 28.73 (1C), 25.87 (1C), 25.52 (1C).

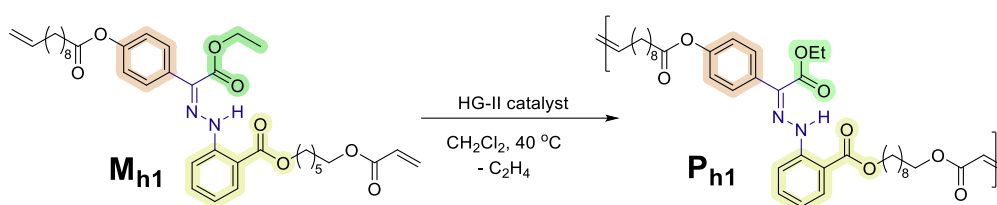
Synthesis of monomer **M_{h1}**



Compound **3** (*E/Z* mixture) (0.636 g, 1.29 mmol, 1.00 eq) was dissolved in toluene and triphenylphosphine (PPh₃) (0.407 g, 1.55 mmol, 1.20) and 6-hydroxyhexyl acrylate (compound **4**) (0.334 g, 1.94 mmol, 1.5 eq) were added to the mixture. The mixture was cooled to 0 °C and diisopropyl azodicarboxylate (DIAD) (0.313 g, 0.32 mL, 1.55 mmol, 1.20 eq) was added dropwise. The reaction mixture was allowed to warm to ambient temperature and stirred overnight. Subsequently, the solvent was removed under reduced pressure and purified via flash column chromatography (silica gel, c-Hex/EtOAc/DCM = 96:3:1 to 73:20:7) affording the *Z*- and *E*-isomers separately. The solvent was evaporated and the product (**M_{h1}**, (*Z*)- isomer) was dried under reduced pressure at 40 °C. The (*Z*)-monomer (380 mg, 0.586 mmol, 45%) and the (*E*)-monomer (23 mg, 0.035 mmol, 3%) were isolated as pale-yellow solids.

¹H-NMR (600 MHz, CD₂Cl₂): δ /ppm = 13.76 (s, 1H), 7.93 (dd, 1H), 7.84 (dd, 1H), 7.66 – 7.61 (m, 2H), 7.46–7.41 (m, 1H), 7.04 – 6.99 (m, 2H), 6.90 (ddd, 1H), 6.27 (dd, 1H), 6.03 (dd, 1H), 5.80 – 5.69 (m, 2H), 4.92 (ddt, 1H), 4.84 (ddt, 1H), 4.35 (q, 2H), 4.29 (t, 2H), 4.07 (t, 2H), 2.49 (t, 2H), 1.97 (tdd, 2H), 1.78 – 1.59 (m, 4H), 1.48 – 1.12 (m, 19H). **¹³C-NMR** (151 MHz, CD₂Cl₂): δ (ppm) = 172.25 (1C), 167.23 (1C), 166.06 (1C), 162.36 (1C), 150.64 (1C), 145.98 (1C), 139.29 (1C), 134.27 (1C), 134.18 (1C), 130.92 (1C), 130.59 (1C), 130.09 (1C), 129.64 (2C), 128.65 (1C), 121.15 (2C), 120.50 (1C), 114.52 (1C), 113.83 (1C), 112.98 (1C), 65.04 (1C), 64.42 (1C), 61.50 (1C), 34.29 (1C), 33.78 (1C), 29.29 (1C), 29.21 (1C), 29.06 (1C), 28.93 (1C), 28.58 (1C), 28.55 (1C), 26.91 (1C), 25.77 (1C), 25.69 (1C), 24.89 (1C), 13.99 (1C). **LC-MS**: calculated m/z for C₃₇H₄₉N₂O₈⁺ [M+H]⁺ = 649.3483, found 649.3482.

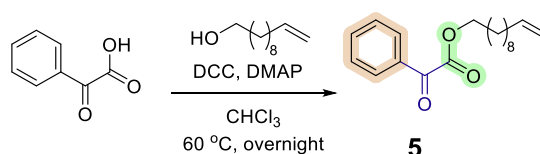
Synthesis of polymer P_{h1}



Monomer (**Z**)-**M_{h1}** or (**88%Z**)-**M_{h1}** (80 mg, 0.12 mmol, 1 eq.) was added to a crimp vial and the vial was purged with argon for 2 h, before the monomer was dissolved in dry DCM (0.2 mL, 0.8 M). The Hoveyda-Grubbs catalyst 2nd Generation (HG-II) (1.6 mg, 2 mol%) was added and a needle was placed in the septum of the crimp vial to allow the gas that is produced to escape. The reaction mixture was stirred at 40 °C for 12 h. A sample was withdrawn from the crude reaction mixture and the conversion was examined via NMR spectroscopy. Ethyl vinyl ether (0.1 mL) was added to the reaction mixture to quench the catalyst and the mixture was stirred for an additional 30 min at 40 °C. The polymer was precipitated from ice cold methanol (50 mL) and collected via centrifugation and dried under reduced pressure at 40 °C overnight.

¹H-NMR (600 MHz, CD₂Cl₂): δ / ppm = 13.76 (s, 1H), 7.92 (d, 1H), 7.84 (d, 1H), 7.63 (d, 2H), 7.43 (t, 1H), 7.01 (d, 2H), 6.93 – 6.79 (m, 2H), 5.73 (d, 1H), 4.35 (q, 2H), 4.28 (t, 2H), 4.03 (t, 2H), 2.48 (t, 2H), 1.93 (q, 2H), 1.74 (p, 2H), 1.66 (t, 2H), 1.60 (d, 2H), 1.48 – 1.12 (m, 17H).

Synthesis of compound 5

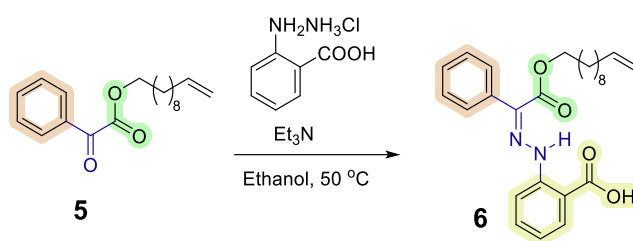


A mixture of benzoylformic acid (1.50 g, 10 mmol, 1 eq), 10-undecen-1-ol (2.2 mL, 11 mmol, 1.1 eq) and DMAP (1.24 g, 2.0 mmol, 0.2 eq) was stirred in chloroform (60 mL) at 60 °C. After 10 minutes of stirring, DCC (2.17 g, 10.5 mmol, 1.05 eq) was added to the mixture and the reaction was run overnight. Upon completion, the solid was filtered out and the solvent was removed under reduced pressure at 40 °C. The residue was purified by flash column

chromatography (EtOAc / Cyclohexane, 1/9, v/v) to yield 1.8 g (60% yield) pale yellow oil as a product (compound **5**).

¹H-NMR (600 MHz, CDCl₃): δ / ppm = 8.00 (d, 2H), 7.66 (t, 1H), 7.52 (t, 2H), 5.86 – 5.76 (m, 1H), 5.01 – 4.90 (m, 2H), 4.38 (t, 2H), 2.04 (q, 2H), 1.83 – 1.70 (m, 4H), 1.40 – 1.21 (m, 10H). **¹³C-NMR** (151 MHz, CDCl₃) δ / ppm = 186.62 (1C, C=O), 164.13 (1C, -COO-), 139.30 (1C, -CH=CH₂), 135.00 (1C, aromatic), 132.64 (1C, aromatic), 130.14 (2C, aromatic), 129.02 (2C, aromatic), 114.27 (1C, -CH=CH₂), 66.52 (1C), 33.91 (1C), 29.52 (1C), 29.48 (1C), 29.26 (1C), 29.20 (1C), 29.02 (1C), 28.58 (1C), 25.90 (1C). **ESI-MS**: calculated m/z for C₁₉H₂₆NaO₃⁺ [M+Na]⁺ = 325.1780, found 325.1781.

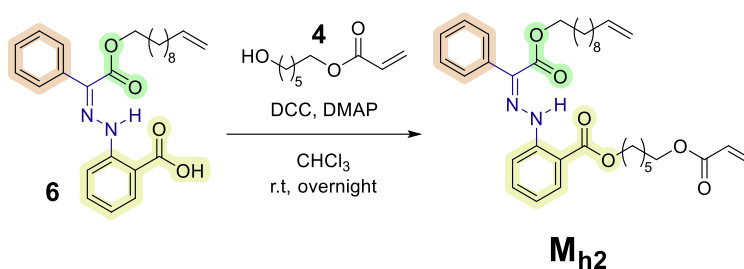
Synthesis of compound **6**



2-Hydrazinobenzoic acid hydrochloride (1.12 g, 5.95 mmol, 1.0 eq) and triethylamine (0.83 mL, 1.0 eq) were mixed in ethanol (60 mL), followed by addition of compound **5** (1.80 g, 5.95 mmol, 1.0 eq). The reaction mixture was heated to 50 °C. After 4 hours of reaction, the solvent was removed under reduced pressure at 40 °C and the residue was extracted with dichloromethane (3 x 30 mL), dried over Na₂SO₄, and purified by flash column chromatography (EtOAc/c-Hexane/MeOH, 3/6/1, v/v). The product was obtained as a yellow solid (420 mg, 30% yield).

¹H NMR (600 MHz, CDCl₃) δ / ppm = 13.84 (s, 1H), 8.11 – 8.06 (m, 1H), 7.97 – 7.93 (m, 1H), 7.68 (d, 2H), 7.52 (t, 1H), 7.41 – 7.37 (m, 2H), 7.35 (t, 1H), 7.00 – 6.94 (m, 1H), 5.85 – 5.76 (m, 1H), 4.96 (dd, 2H), 4.35 (t, 2H), 2.07 – 2.00 (m, 2H), 1.77 – 1.70 (m, 4H), 1.42 – 1.15 (m, 10H). **¹³C NMR** (151 MHz, CDCl₃) δ / ppm = 171.33 (1C), 162.75 (1C), 146.72 (1C), 139.33 (1C), 136.65 (1C), 134.99 (1C), 131.99 (1C), 131.88 (1C), 128.72 (2C), 128.08 (1C), 128.03 (2C), 120.54 (1C), 114.75 (1C), 114.27 (1C), 112.27 (1C), 65.49 (1C), 33.93 (1C), 29.58 (1C), 29.49 (1C), 29.29 (1C), 29.23 (1C), 29.05 (1C), 28.63 (1C), 25.63 (1C). **LC-MS**: calculated m/z for C₂₆H₃₁N₂O₄⁻ [M-H]⁻ = 435.2289, found 435.2290.

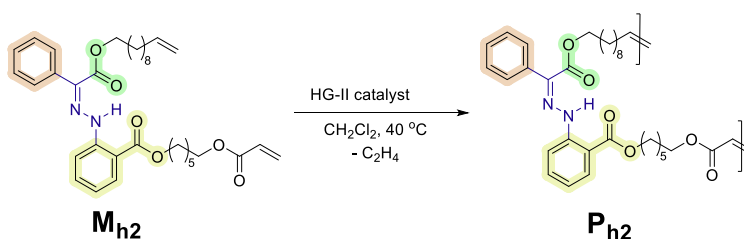
Synthesis of monomer **M_{h2}**



Compound **6** (280 mg, 0.64 mmol, 1.0 eq) and compound **4** (133 mg, 0.77 mmol, 1.2 eq) were stirred with DMAP (15.7 mg, 0.128 mmol, 0.2 eq) in chloroform at 40 °C for 10 min. Subsequently, DCC (133.6 mg, 0.65 mmol, 1.01 eq) was added to the reaction mixture. The reaction was stopped after 18 h. The solvent was removed under reduced pressure and the residue was purified by flash column chromatography (EtOAc/c-Hexane, 1/9, v/v) to yield 300 mg yellow oil as a product (79% yield).

¹H NMR (600 MHz, CDCl₃) δ / ppm = 13.97 (s, 1H), 8.00 (d, 1H), 7.95 (d, 1H), 7.68 (d, 2H), 7.51 (t, 1H), 7.40 (t, 2H), 7.35 (t, 1H), 6.96 (t, 1H), 6.40 (dd, 1H), 6.12 (dd, 1H), 5.86 – 5.77 (m, 2H), 4.96 (dd, 2H), 4.43 – 4.35 (m, 4H), 4.20 – 4.15 (m, 2H), 2.04 (q, 2H), 1.87 – 1.79 (m, 2H), 1.77 – 1.69 (m, 4H), 1.54 – 1.44 (m, 4H), 1.40 – 1.23 (m, 12H). **¹³C NMR** (151 MHz, CDCl₃) δ / ppm = 167.39 (1C, carbonyl), 166.32 (1C, carbonyl), 162.79 (1C, carbonyl), 146.15 (1C, C=N-), 139.21 (1C), 136.62 (1C), 134.33 (1C), 131.43 (1C), 130.94 (1C), 130.55 (1C), 128.69 (2C), 128.58 (1C), 127.90 (1C), 127.87 (2C), 120.44 (1C), 114.72 (1C), 114.16 (1C), 112.83 (1C), 65.54 (1C), 65.03 (1C), 64.51 (1C), 33.81 (1C), 29.44 (1C), 29.37 (1C), 29.15 (1C), 29.11 (1C), 28.93 (1C), 28.62 (1C), 28.57 (1C), 28.46 (1C), 25.98 (1C), 25.81 (1C), 25.73 (1C). **LC-MS**: calculated m/z for C₃₅H₄₇N₂O₆⁺ [M+H]⁺ = 591.3429, found 591.3437.

Synthesis of polymer **P_{h2}**



Polymer **P_{h2}** was synthesized in the same manner as polymer **P_{h1}**. Monomer (**Z**)-**M_{h2}** (230 mg, 0.39 mmol, 1 eq.) was added to a crimp vial and the vial was purged with argon for 2 h, before the monomer was dissolved in dry DCM (0.5 mL, 0.8 M). Hoveyda-Grubbs catalyst 2nd Generation (**HG-II**) (4.9 mg, 2 mol%) was added and a needle was placed in the septum of the crimp vial to allow the gas that is produced to be released. The reaction mixture was stirred at 40 °C for 12 h. A sample was withdrawn from the crude reaction mixture and the conversion was determined via NMR spectroscopy. Ethyl vinyl ether (0.1 mL) was added to the reaction mixture to quench the catalyst and the mixture was stirred again for 30 min at 40 °C. The

resulting polymer was purified by precipitation in ice cold methanol (50 mL) and collected via centrifugation and dried under reduced pressure at 40 °C overnight.

11.7.6.2. Synthesis of hydrazone oligomers via hydroxyl-yne and TBAF deprotection

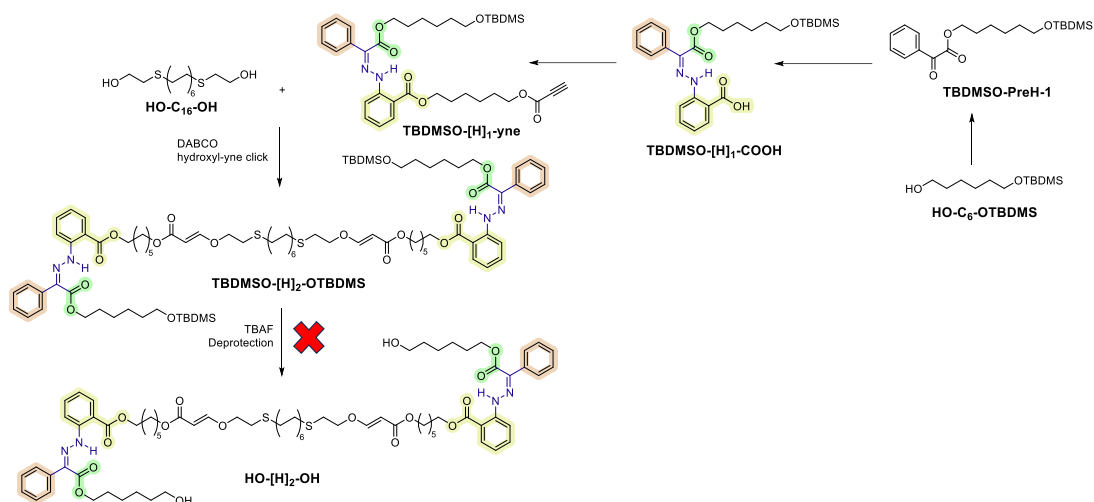
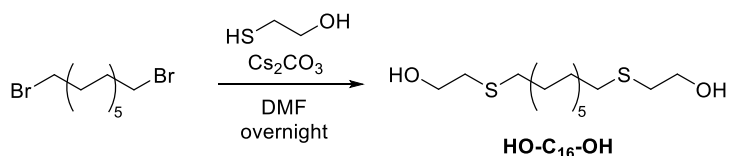


Figure S7.10. Synthesis of hydrazone-based oligomers via hydroxyl-yne click and TBAF deprotection.

Synthesis of HO-C₁₆-OH

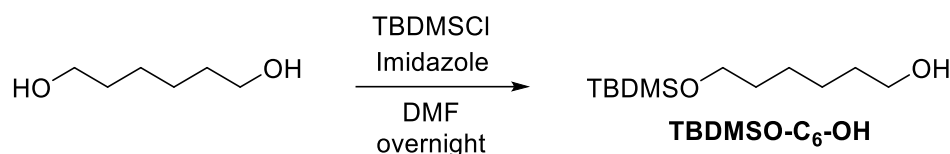


1,12-Dibromododecane (2000 mg, 6.10 mmol, 1.0 eq) was dissolved in 24 mL DMF, followed by injection of 2-mercaptoethanol (1.28 mL, 18.3 mmol, 3.0 eq). After this, cesium carbonate (Cs_2CO_3 , 2980 mg, 9.14 mmol, 1.5 eq) was poured into the solution. The reaction was stirred at room temperature overnight. Upon completion, the reaction mixture was diluted with 150 mL ethyl acetate (EtOAc) and extracted with water and brine (3 times) to removed salts and DMF. The EtOAc phase was then dried over with sodium sulfate (Na_2SO_4), filtered, and removed under reduced pressure. The residue was purified by washing with diethyl ether (Et_2O). The precipitate was filtered out and dried at 40 °C overnight to afford the product as white flakes (1500 mg, 76% purification yield).

^1H NMR (400 MHz, CDCl_3) δ 3.71 (t, J = 6.0 Hz, 4H), 2.72 (t, J = 6.0 Hz, 4H), 2.55 – 2.47 (m, 4H), 1.57 (ddt, J = 8.3, 7.3, 6.3 Hz, 4H), 1.40 – 1.19 (m, 16H). **^{13}C NMR** (101 MHz, CDCl_3) δ 60.30 (2C), 35.44 (2C), 31.76 (2C), 29.87 (2C), 29.63 (2C), 29.58 (2C), 29.31 (2C), 28.95 (2C).

LC-MS: calculated m/z for $\text{C}_{16}\text{H}_{35}\text{O}_2\text{S}_2^+$ $[\text{M}+\text{H}]^+ = 323.2073$, found 323.2079.

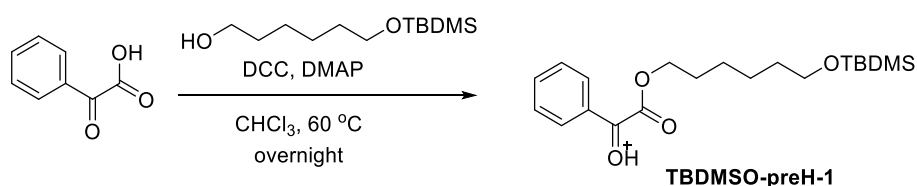
Synthesis of HO-C₆-OTBDMS



1,6-Hexanediol (5000 mg, 42.3 mmol, 1.0 eq) and imidazole (5760 mg, 84.6 mmol, 2.0 eq) were dissolved in dry DMF at room temperature. tert-Butyldimethylsilyl chloride (TBDMSCl, 6377 mg, 42.3 mmol, 1.0 eq) was then added and the reaction mixture was stirred overnight. Upon completion, the mixture was diluted with 200 mL EtOAc and extracted with water and brine (3 times). The organic phase was dried over Na₂SO₄, filtered and evaporated under reduced pressure. The residue was purified by flash column chromatography with EtOAc/Cy as the eluent (from 100% Cy to 20% Cy). The product was obtained as an oil (2900 mg, ~30% yield).

¹H NMR (600 MHz, CDCl₃) δ 3.66 – 3.52 (m, 4H), 1.60 – 1.47 (m, 4H), 1.40 – 1.30 (m, 4H), 0.88 (s, 9H), 0.03 (s, 6H). **¹³C NMR** (151 MHz, CDCl₃) δ 63.30, 63.03, 32.92, 32.89, 27.04, 27.03, 26.09, 26.08, 25.75, 25.67, -5.15. **LC-MS**: calculated m/z for C₁₂H₂₉O₂Si⁺ [M+H]⁺ = 233.1932, found 233.1930.

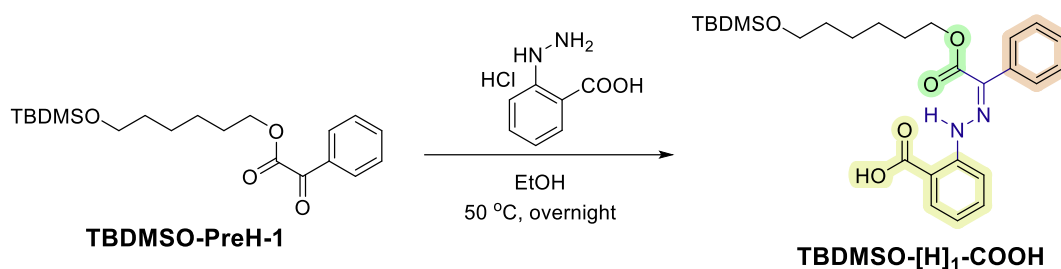
Synthesis of TBDMSO-PreH-1



Phenylglyoxylic acid (1000 mg, 6.67 mmol, 1.0 eq), **TBDMSO-C₁₆-OH** (1700 mg, 7.33 mmol, 1.1 eq) and DMAP (81.4 mg, 10 mol%) were dissolved in 27 mL CHCl₃. Upon addition of DCC (1512 mg, 7.33 mmol, 1.1 eq), the mixture was heated to 60 °C and stirred overnight. Upon completion, the solid was filtered out and the organic phase was enriched at reduced pressure. The residue was purified by flash column chromatography (EtOAc/Cy, 5/95, v/v), affording the product as an oil (~ 1900 mg, ~ 80% yield).

¹H NMR (600 MHz, CDCl₃) δ 8.02 – 7.98 (m, 2H), 7.66 (ddt, J = 8.7, 7.2, 1.3 Hz, 1H), 7.54 – 7.48 (m, 2H), 4.38 (t, J = 6.8 Hz, 2H), 3.60 (t, J = 6.5 Hz, 2H), 1.79 (dq, J = 8.0, 6.8 Hz, 2H), 1.56 – 1.50 (m, 2H), 1.46 – 1.37 (m, 4H), 0.88 (s, 9H), 0.04 (s, 6H). **¹³C NMR** (151 MHz, CDCl₃) δ 186.58, 164.11, 135.00, 132.64, 130.14, 129.02, 66.43, 63.14, 35.06, 32.76, 28.61, 27.04, 26.09, 25.75, 25.59, 25.56, 18.48. **LC-MS**: calculated m/z for C₂₀H₃₃O₄Si⁺ [M+H]⁺ = 365.2143, found 365.2141.

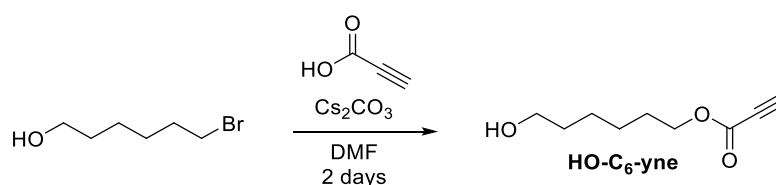
Synthesis of TBDMSO-[H]₁-COOH



TBDMSO-PreH-1 (1500 mg, 4.11 mmol, 1.0 eq) was dissolved in 80 mL EtOH with a few drops of acetic acid. Following that, 2-hydrazinobenzoic acid hydrochloride (780 mg, 1.0 eq) was added to the solution. The reaction was stirred at 50 °C overnight. Upon completion, the solvent was partly removed and the enriched mixture was extracted with EtOAc (2 times), dried over Na₂SO₄ and concentrated. The product (~ 600 mg, 30% yield) was obtained after flash column chromatography (EtOAc/Cy, 95% Cy to 20% Cy).

¹H NMR (600 MHz, CDCl₃) δ 13.66 (s, 1H), 8.10 (dd, J = 8.0, 1.6 Hz, 1H), 7.96 (dd, J = 8.6, 1.1 Hz, 1H), 7.75 – 7.66 (m, 2H), 7.55 (dddd, J = 9.2, 7.1, 1.6, 0.6 Hz, 1H), 7.40 (tt, J = 6.7, 1.0 Hz, 2H), 7.38 – 7.33 (m, 1H), 6.98 (ddd, J = 8.1, 7.1, 1.2 Hz, 1H), 4.42 (t, J = 6.7 Hz, 2H), 3.62 (t, J = 6.5 Hz, 2H), 1.81 – 1.75 (m, 2H), 1.57 – 1.50 (m, 2H), 1.46 – 1.35 (m, 4H), 0.90 (s, 9H), 0.06 (s, 6H). **¹³C NMR** (151 MHz, CDCl₃) δ 171.90, 162.71, 146.88, 136.43, 135.33, 132.47, 131.94, 128.57, 128.18, 128.06, 120.42, 114.79, 111.60, 65.53, 63.33, 32.68, 28.57, 26.09, 25.84, 25.46, 18.48, -5.15. **LC-MS**: calculated m/z for C₂₇H₃₇N₂O₅Si [M-H]⁻ = 497.2477, found 497.2479.

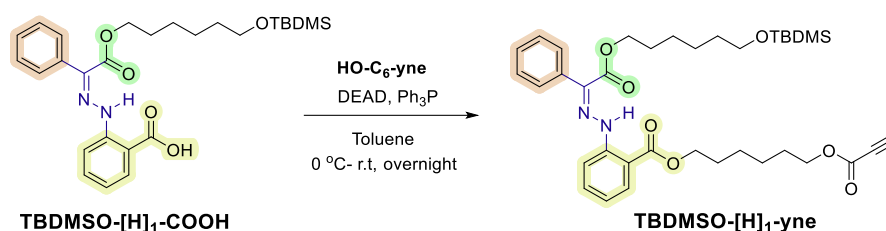
Synthesis of HO-C₆-yne



Propiolic acid (2.0 mL, 3.0 eq) and 6-bromo-1-hexanol (2000 mg, 11.0 mmol, 1.0 eq) were dissolved in 45 mL dry DMF. Cesium carbonate (5400 mg, 16.5 mmol, 1.5 eq) was added and the mixture was stirred for 2 days at room temperature. Upon completion, the mixture was diluted with EtOAc, followed by water/brine workup. The organic phase was dried over Na₂SO₄, filtered, and concentrated under reduced pressure. The residue was further purified via flash column chromatography (EtOAc/Cy, 95% Cy to 30% Cy), affording the product as an oil (1600 mg, 85% yield).

¹H NMR (400 MHz, CDCl₃) δ 4.18 (t, J = 6.7 Hz, 2H), 3.62 (t, J = 6.5 Hz, 2H), 2.89 (s, 1H), 1.68 (pd, J = 6.8, 4.0 Hz, 2H), 1.62 – 1.50 (m, 2H), 1.43 – 1.32 (m, 4H). **¹³C NMR** (101 MHz, CDCl₃) δ 152.94, 74.84, 74.71, 66.42, 62.80, 32.61, 28.38, 25.67, 25.42. **LC-MS**: calculated m/z for C₉H₁₅O₃⁺ [M+ H]⁺ = 171.1016, found 171.0992.

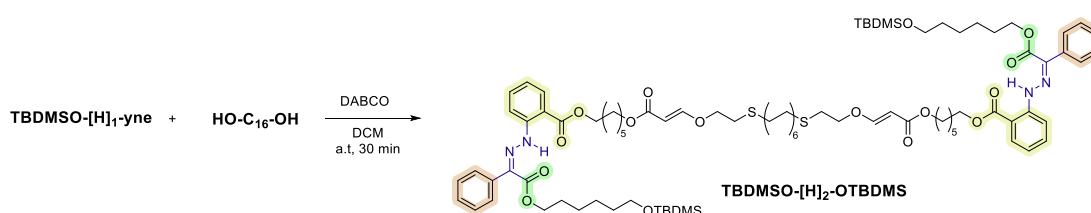
Synthesis of TBDMSO-[H]₁-yne



The solution of **TBDMSO-[H]₁-COOH** (500 mg, 1.0 mmol, 1.0 eq), **HO-C₆-yne** (187 mg, 1.1 mmol, 1.1 eq) and triphenyl phosphine (Ph₃P, 290 mg, 1.1 mmol, 1.1 eq) in 2 mL toluene was cooled to 0 °C. Following that, diisopropyl azodicarboxylate (DIAD, 217 μL, 1.1 eq) was injected to the solution at 0 °C and the reaction mixture was stirred overnight. Upon completion, most of toluene was removed under reduced pressure and the residue was purified by flash column chromatography (Toluene/DCM, 90/10, v/v). The product was obtained as a yellow oil (~450 mg, 70% yield).

¹H NMR (600 MHz, CDCl₃) δ 13.97 (s, 1H), 8.00 (dd, J = 8.0, 1.6 Hz, 1H), 7.95 (dd, J = 8.5, 1.1 Hz, 1H), 7.72 – 7.65 (m, 2H), 7.52 – 7.48 (m, 1H), 7.41 – 7.37 (m, 2H), 7.36 – 7.33 (m, 1H), 6.96 (ddd, J = 8.1, 7.1, 1.2 Hz, 1H), 4.39 (dt, J = 13.4, 6.7 Hz, 4H), 4.21 (t, J = 6.6 Hz, 2H), 3.59 (t, J = 6.5 Hz, 2H), 2.87 (s, 1H), 1.81 (dt, J = 8.1, 6.5 Hz, 2H), 1.74 (ddt, J = 14.8, 8.0, 6.6 Hz, 4H), 1.55 – 1.45 (m, 6H), 1.42 – 1.33 (m, 4H), 0.89 (s, 9H), 0.04 (s, 6H). **¹³C NMR** (151 MHz, CDCl₃) δ 167.50, 162.89, 152.93, 146.27, 136.73, 134.47, 131.54, 131.06, 128.81, 128.03, 128.00, 120.58, 114.85, 112.93, 74.84, 74.67, 66.38, 65.58, 65.09, 63.20, 32.85, 28.70, 28.62, 28.39, 26.11, 25.98, 25.86, 25.68, 25.57, -5.13. **LC-MS**: calculated m/z for C₃₆H₅₀N₂NaO₇Si⁺ [M+ Na]⁺ = 673.3285, found 673.3272.

Synthesis of TBDMSO-[H]₂-OTBDMS



TBDMSO-[H]₁-yne (300 mg, 0.46 mmol, 2.1 eq) and **HO-C₁₆-OH** (71 mg, 0.22 mmol, 1.0 eq) were fully dissolved in 1.5 mL DCM/CHCl₃ mixture (70/30, v/v) at 40 °C. The solution was let to cool down to room temperature before DABCO base (10 mg, 20 mol% of OH-functional group) was added. The reaction was stirred for 30 min and then immediately purified by flash column chromatography (DCM/EtOAc, 90/10, v/v) to afford the product as a sticky yellow oil (340 mg, 95% purification yield).

¹H NMR (600 MHz, CDCl₃) δ 13.97 (s, 2H), 7.99 (dd, J = 8.0, 1.6 Hz, 2H), 7.94 (dd, J = 8.6, 1.2 Hz, 2H), 7.70 – 7.66 (m, 4H), 7.58 (d, J = 12.6 Hz, 2H), 7.50 (dddd, J = 8.7, 7.2, 1.6, 0.7 Hz, 2H), 7.42 – 7.36 (m, 4H), 7.36 – 7.32 (m, 2H), 6.96 (ddd, J = 8.2, 7.1, 1.2 Hz, 2H), 5.21 (d,

$J = 12.7$ Hz, 2H), 4.38 (dt, $J = 11.2, 6.7$ Hz, 8H), 4.12 (t, $J = 6.6$ Hz, 4H), 3.98 (t, $J = 6.8$ Hz, 4H), 3.59 (t, $J = 6.5$ Hz, 4H), 2.79 (t, $J = 6.8$ Hz, 4H), 2.64 – 2.52 (m, 4H), 1.86 – 1.79 (m, 4H), 1.73 (dt, $J = 8.0, 6.7$ Hz, 4H), 1.69 (p, $J = 6.8$ Hz, 4H), 1.60 – 1.55 (m, 4H), 1.54 – 1.43 (m, 12H), 1.40 – 1.33 (m, 12H), 1.31 – 1.23 (m, 12H), 0.89 (s, 18H), 0.04 (s, 12H). ^{13}C NMR (151 MHz, CDCl_3) δ 167.82, 167.50, 162.88, 162.02, 146.26, 136.73, 134.44, 131.51, 131.06, 128.81, 128.01, 127.99, 120.57, 114.83, 112.95, 97.07, 70.59, 65.58, 65.17, 63.99, 63.19, 32.84, 30.75, 29.81, 29.69, 29.63, 29.35, 28.94, 28.84, 28.75, 28.61, 26.11, 25.98, 25.95, 25.88, 25.57, 18.49, -5.13.

11.7.6.3. Synthesis of hydrazone-based oligomers via hydroxyl-yne click and metathesis

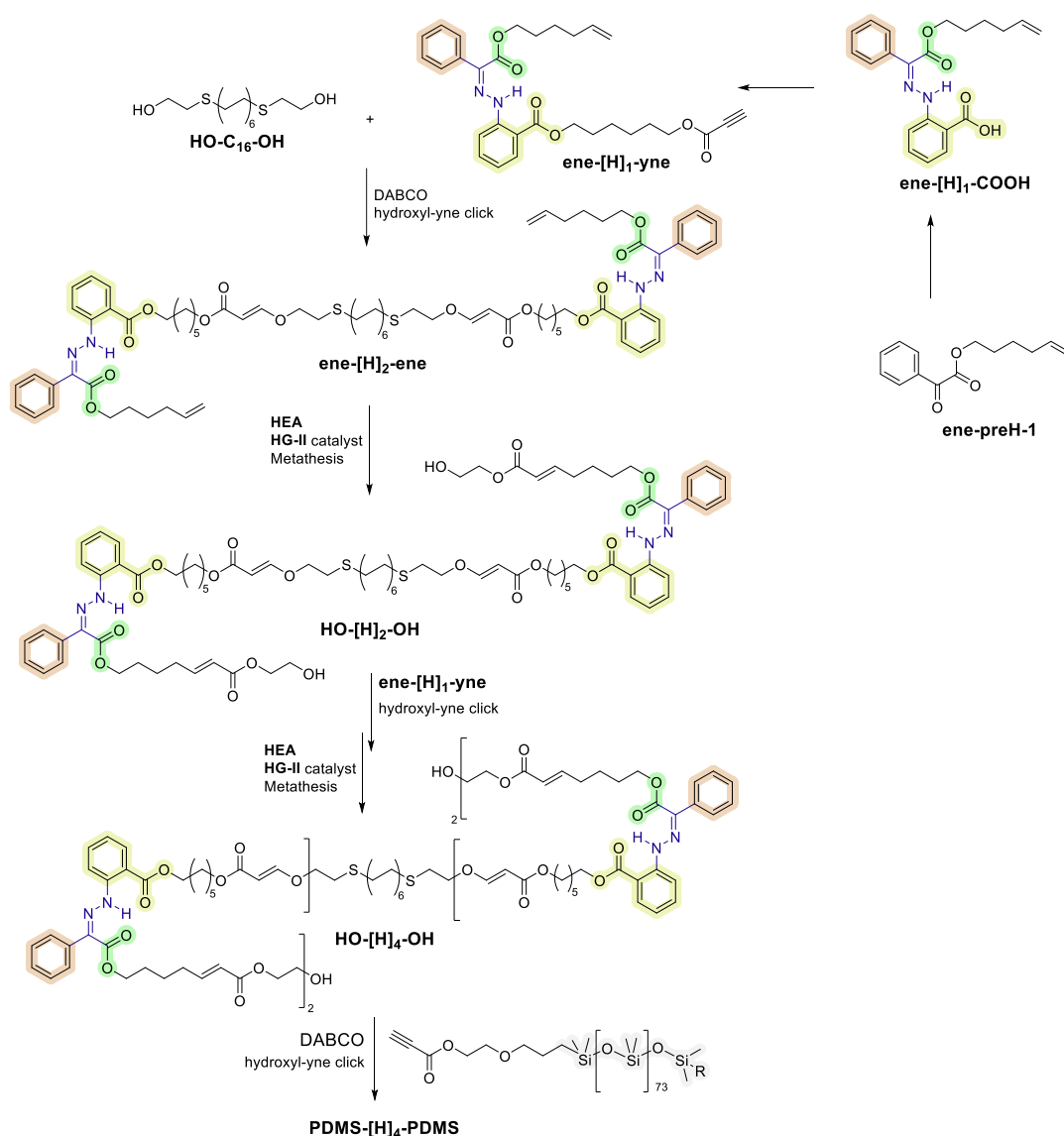
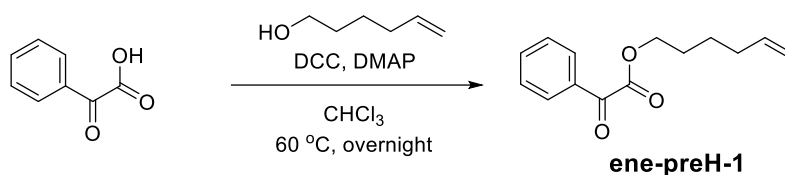


Figure S7.11. Synthesis route for hydrazone-based oligomers and block copolymers via hydroxyl-yne click reaction and cross metathesis.

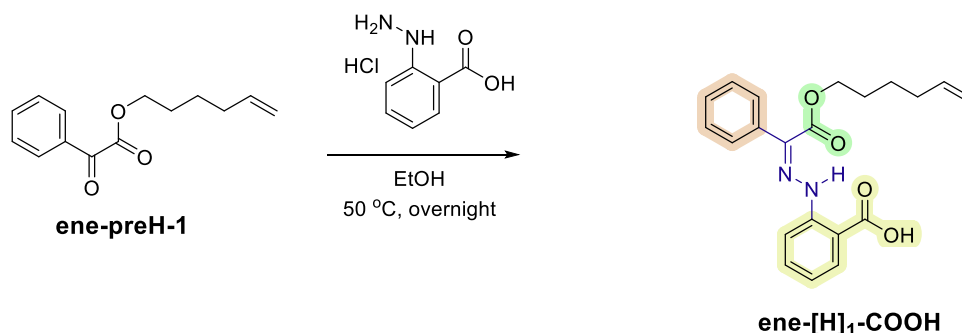
Synthesis of ene-preH-1



Benzoyl formic acid (5000 mg, 33.3 mmol, 1.0 eq), 5-hexen-1-ol (3663 mg, 36.6 mmol, 1.1 eq) and DMAP (407 mg, 10 mol%) were dissolved in 140 mL CHCl_3 at 60 °C. Following that, DCC (7560 mg, 36.6 mmol, 1.1 eq) was added to the mixture and the reaction was stirred overnight. Upon completion, the solid was filtered out and the solution was concentrated under reduced pressure. The residue was purified by flash column chromatography (EtOAc/Cy, 5/95, v/v), affording the product as an oil (6950 mg, 90% yield).

$^1\text{H NMR}$ (600 MHz, CDCl_3) δ 8.01 – 7.98 (m, 2H), 7.65 (ddt, J = 7.7, 7.1, 1.3 Hz, 1H), 7.52 – 7.49 (m, 2H), 5.78 (ddt, J = 16.9, 10.2, 6.7 Hz, 1H), 5.05 – 4.94 (m, 2H), 4.39 (t, J = 6.7 Hz, 2H), 2.15 – 2.06 (m, 2H), 1.83 – 1.75 (m, 2H), 1.52 (tt, J = 9.9, 6.5 Hz, 2H). $^{13}\text{C NMR}$ (151 MHz, CDCl_3) δ 186.53, 164.06, 138.13, 135.01, 132.59, 130.11, 129.00, 115.19, 66.24, 35.03, 33.25, 27.97, 25.56, 25.12. **LC-MS**: calculated m/z for $\text{C}_{14}\text{H}_{17}\text{O}_3^+$ $[\text{M}+\text{H}]^+ = 233.1173$, found 233.1172.

Synthesis of ene-[H]₁-COOH

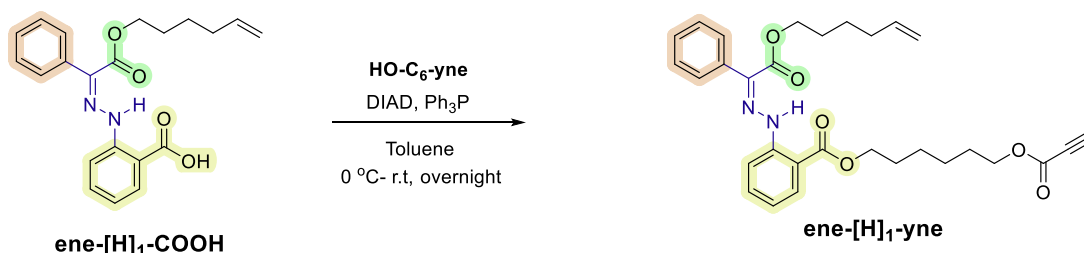


ene-preH-1 (5000 mg, 21.5 mmol, 1.0 eq) was dissolved in 220 mL EtOH with a few drops of acetic acid. Following that, 2-hydrazinobenzoic acid hydrochloride (4060 mg, 1.0 eq) was added to the solution. The reaction was stirred at 50 °C overnight. Upon completion, the solvent was partly removed and the enriched mixture was extracted with EtOAc and water/brine (2 times), dried over Na_2SO_4 and concentrated. The product (3200 mg, 40% yield) was obtained after precipitation in cold methanol and dried in the vacuum at 40 °C overnight.

$^1\text{H NMR}$ (400 MHz, CDCl_3) δ 13.74 (s, 1H), 8.11 (dd, J = 8.0, 1.6 Hz, 1H), 7.97 (dd, J = 8.5, 1.1 Hz, 1H), 7.70 (dd, J = 8.2, 1.6 Hz, 2H), 7.56 (dddd, J = 8.7, 7.2, 1.6, 0.6 Hz, 1H), 7.45 – 7.33 (m, 2H), 6.99 (ddd, J = 8.1, 7.1, 1.2 Hz, 1H), 5.79 (ddt, J = 16.9, 10.2, 6.6 Hz, 1H), 5.10 – 4.92 (m, 2H), 4.42 (t, J = 6.7 Hz, 2H), 2.14 – 2.07 (m, 2H), 1.83 – 1.74 (m, 2H), 1.51 (tt, J = 9.9, 6.4 Hz, 2H). $^{13}\text{C NMR}$ (101 MHz, CDCl_3) δ 172.10, 162.76, 146.92, 138.35, 136.47, 135.51,

132.38, 132.02, 128.69, 128.23, 128.09, 120.56, 115.08, 114.89, 111.42, 65.47, 33.30, 28.07, 25.35. **LC-MS**: calculated m/z for $C_{21}H_{21}N_2O_4^-$ $[M-H]^-$ = 365.1506, found 365.1505.

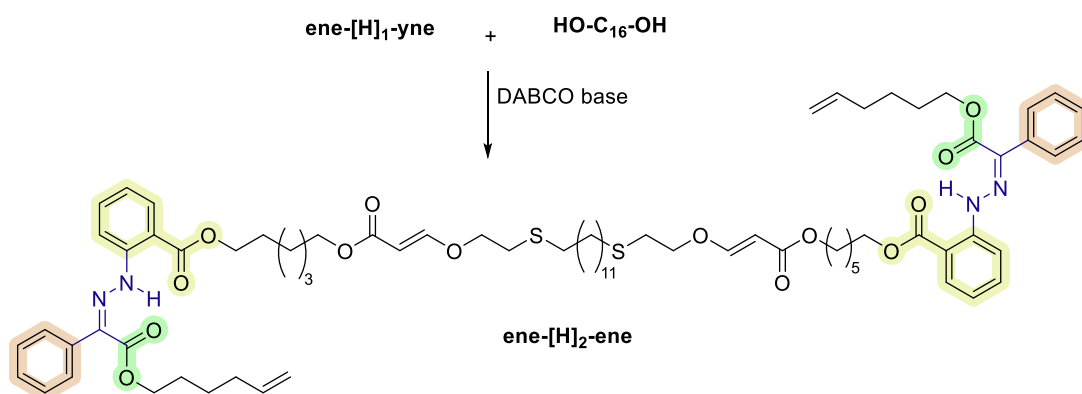
Synthesis of ene-[H]₁-yne



The solution of **ene-[H]₁-COOH** (2000 mg, 5.46 mmol, 1.0 eq), **HO-C₆-yne** (1021 mg, 1.1 mmol, 1.1 eq) and triphenyl phosphine (Ph_3P , 1575 mg, 1.1 mmol, 1.1 eq) in 11 mL toluene was cooled to 0 °C. Following that, diisopropyl azodicarboxylate (DIAD, 1.2 mL, 1.1 eq) was injected to the solution at 0 °C and the reaction mixture was stirred overnight. Upon completion, most of toluene was removed under reduced pressure and the residue was purified by flash column chromatography (Toluene/DCM, 90/10, v/v). The product was obtained as a yellow oil (~1700 mg, 60% yield).

¹H NMR (400 MHz, CDCl_3) δ 13.96 (s, 1H), 8.00 (dd, J = 8.1, 1.6 Hz, 1H), 7.95 (dd, J = 8.6, 1.2 Hz, 1H), 7.71 – 7.66 (m, 2H), 7.50 (dddd, J = 8.7, 7.1, 1.6, 0.6 Hz, 1H), 7.43 – 7.32 (m, 3H), 6.96 (ddd, J = 8.2, 7.1, 1.2 Hz, 1H), 5.78 (ddt, J = 16.9, 10.2, 6.6 Hz, 1H), 5.06 – 4.92 (m, 2H), 4.40 (td, J = 6.6, 4.1 Hz, 4H), 4.21 (t, J = 6.6 Hz, 2H), 2.87 (s, 1H), 2.13 – 2.05 (m, 2H), 1.86 – 1.68 (m, 6H), 1.53 – 1.43 (m, 6H). **¹³C NMR** (101 MHz, CDCl_3) δ 167.49, 162.86, 152.92, 146.24, 138.36, 136.70, 134.47, 131.49, 131.05, 128.80, 128.03, 128.00, 120.59, 115.05, 114.84, 112.92, 74.87, 74.68, 66.37, 65.41, 65.08, 33.30, 28.69, 28.37, 28.00, 25.85, 25.67, 25.37. **LC-MS**: calculated m/z for $C_{30}H_{34}N_2NaO_6^+$ $[M+Na]^+$ = 541.2315, found 541.2304.

Synthesis of ene-[H]₂-ene

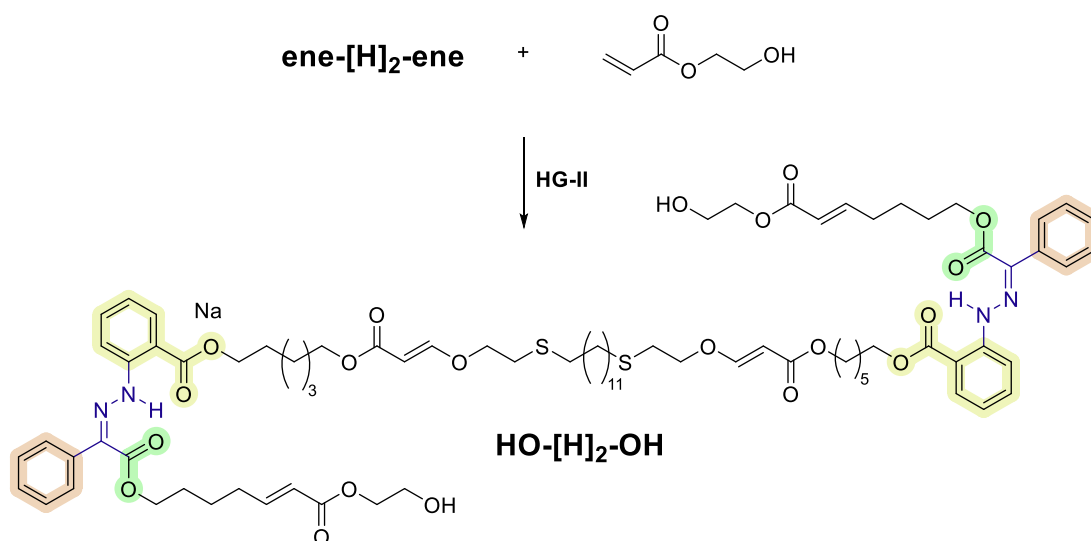


ene-[H]₁-yne (500 mg, 0.97 mmol, 2.1 eq) and **HO-C₁₆-OH** (146 mg, 0.46 mmol, 1.0 eq) were fully dissolved in 2.5 mL DCM/ CHCl_3 mixture (70/30, v/v) at 40 °C. The solution was let to cool down to room temperature before DABCO base (20 mg, 20 mol% of OH-functional group) was

added. The reaction was stirred for 30 min and then immediately purified by flash column chromatography (DCM/EtOAc, 90/10, v/v) to afford the product as a sticky yellow oil (580 mg, 93% purification yield).

^1H NMR (600 MHz, CDCl_3) δ 13.96 (s, 2H), 8.00 (dd, J = 8.0, 1.6 Hz, 2H), 7.94 (dd, J = 8.6, 1.2 Hz, 2H), 7.71 – 7.65 (m, 4H), 7.58 (d, J = 12.6 Hz, 2H), 7.50 (dddd, J = 8.7, 7.2, 1.6, 0.6 Hz, 2H), 7.42 – 7.37 (m, 4H), 7.36 – 7.32 (m, 2H), 6.96 (ddd, J = 8.2, 7.1, 1.2 Hz, 2H), 5.78 (ddt, J = 16.9, 10.2, 6.7 Hz, 2H), 5.22 (d, J = 12.6 Hz, 2H), 5.03 – 4.95 (m, 4H), 4.39 (td, J = 6.7, 4.5 Hz, 8H), 4.12 (t, J = 6.7 Hz, 4H), 3.98 (t, J = 6.8 Hz, 4H), 2.79 (t, J = 6.8 Hz, 4H), 2.55 (t, J = 7.4 Hz, 4H), 2.08 (tdd, J = 6.6, 4.5, 3.3 Hz, 4H), 1.81 (dq, J = 8.4, 6.7 Hz, 4H), 1.78 – 1.73 (m, 4H), 1.69 (p, J = 6.8 Hz, 4H), 1.57 (p, J = 7.4 Hz, 4H), 1.53 – 1.45 (m, 12H), 1.39 – 1.33 (m, 4H), 1.30 – 1.24 (m, 12H). **^{13}C NMR** (151 MHz, CDCl_3) δ 167.82, 167.51, 162.86, 162.02, 146.24, 138.36, 136.71, 134.44, 131.48, 131.06, 128.80, 128.00, 120.58, 115.05, 114.83, 112.96, 97.06, 70.60, 65.41, 65.18, 63.98, 33.30, 32.84, 30.74, 29.81, 29.68, 29.63, 29.35, 28.94, 28.84, 28.74, 28.00, 25.94, 25.87, 25.38. **SEC-MS**: calculated m/z for $\text{C}_{76}\text{H}_{102}\text{N}_4\text{NaO}_{14}\text{S}_2^+$ $[\text{M}+\text{Na}]^+ = 1381.6732, 1382.6765, 1383.6799, 1384.6832$; found: 1381.6735, 1387.6766, 1383.6779, 1384.6794.

Synthesis HO-[H]₂-OH

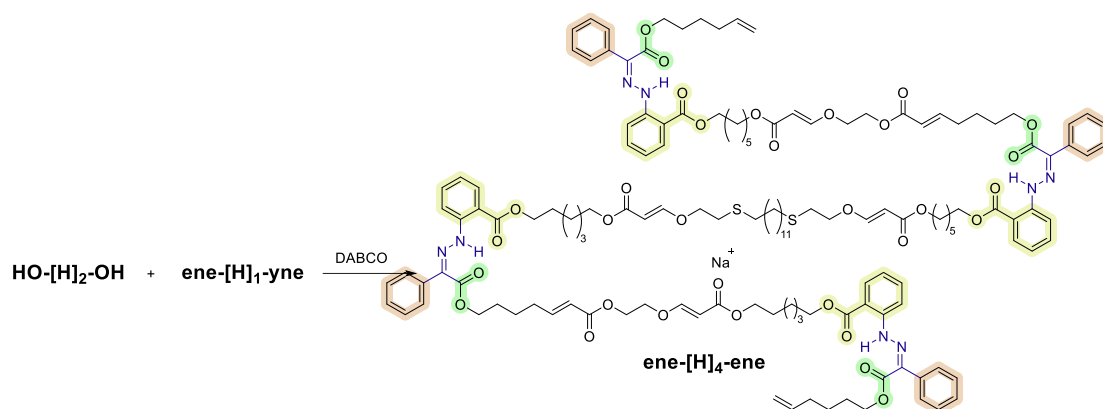


2-hydroxyethyl acrylate (0.63 mL, 15 eq) and ene-[H]₂-ene (500 mg, 0.37 mmol, 1.0 eq) were fully dissolved in 1.0 mL anhydrous DCM. Following this, Hoveyda-Grubbs 2nd generation (**HG-II**, 12 mg, 5.0 mol%) catalyst was added, and the reaction container was quickly submerged in an oil bath preheated to 40 °C. The reaction was carried out for 1 h, after which a ^1H NMR spectrum was recorded to determine the conversion. Upon completion, ethyl vinyl ether (0.05 mL) was injected into the reaction. After 10 minutes, the crude reaction mixture was diluted in EtOAc, extracted with water and brine (3 times). The organic phase was concentrated under reduced pressure. The residue was purified by flash column chromatography

(DCM/EtOAc/MeOH, 90/9/1 to 1/99/2, v/v), affording the product as a sticky yellow oil (495 mg, 88% yield).

¹H NMR (600 MHz, CDCl₃) δ 13.94 (s, 2H), 7.99 (d, J = 8.0 Hz, 2H), 7.93 (d, J = 8.5 Hz, 2H), 7.66 (d, J = 7.5 Hz, 4H), 7.57 (d, J = 12.6 Hz, 2H), 7.49 (t, J = 7.9 Hz, 2H), 7.38 (t, J = 7.4 Hz, 4H), 7.34 (t, J = 7.3 Hz, 2H), 7.01 – 6.91 (m, 4H), 5.84 (d, J = 15.6 Hz, 2H), 5.21 (d, J = 12.6 Hz, 2H), 4.38 (t, J = 6.6 Hz, 8H), 4.29 – 4.23 (m, 4H), 4.11 (t, J = 6.7 Hz, 4H), 3.97 (t, J = 6.8 Hz, 4H), 3.84 (t, J = 4.6 Hz, 4H), 2.78 (t, J = 6.8 Hz, 4H), 2.54 (t, J = 7.5 Hz, 4H), 2.23 (q, J = 7.3 Hz, 4H), 1.78 (dp, J = 22.4, 6.8 Hz, 8H), 1.68 (p, J = 6.9 Hz, 4H), 1.56 (h, J = 7.4 Hz, 8H), 1.46 (dp, J = 22.0, 7.4 Hz, 8H), 1.35 (p, J = 6.9 Hz, 4H), 1.29 – 1.23 (m, 12H). **¹³C NMR** (151 MHz, CDCl₃) δ 167.82, 167.47, 166.84, 162.70, 162.01, 149.38, 146.12, 136.59, 134.42, 131.25, 131.01, 128.71, 128.03, 127.98, 121.32, 120.61, 114.78, 112.92, 96.98, 70.56, 66.07, 65.13, 64.96, 63.94, 61.36, 32.77, 31.71, 30.68, 29.74, 29.61, 29.56, 29.27, 28.87, 28.76, 28.67, 28.00, 25.87, 25.80, 24.53.

Synthesis of ene-[H]₄-ene

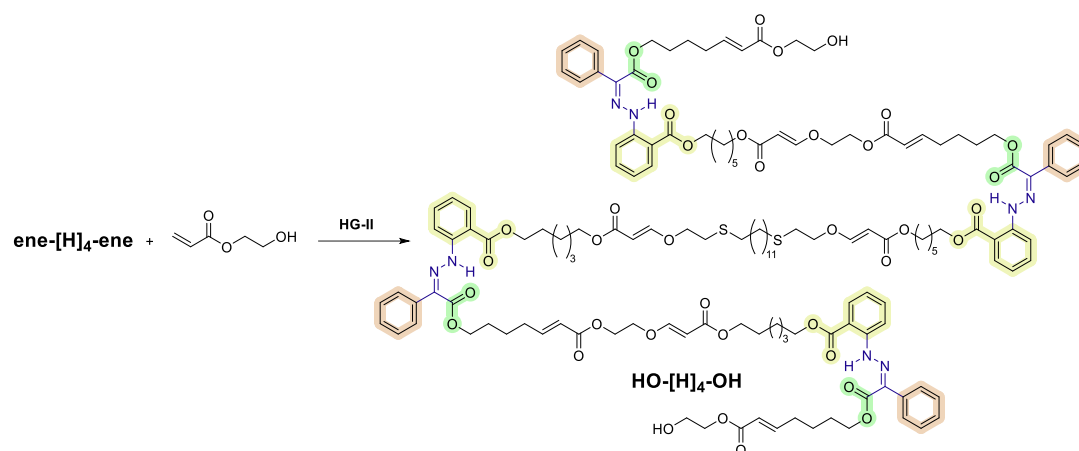


ene-[H]₁-yne (283 mg, 0.55 mmol, 2.1 eq) and **HO-[H]₄-OH** (400 mg, 0.26 mmol, 1.0 eq) were fully dissolved in 1.1 mL DCM. Following that, DABCO base (12 mg, 20 mol% of OH-functional group) was added. The reaction was stirred for 30 min and then immediately purified by flash column chromatography (DCM/EtOAc, 80/20, v/v) to afford the product as a sticky yellow oil (630 mg, 95% purification yield).

¹H NMR (600 MHz, CDCl₃) δ 13.97 (s, 2H), 13.96 (s, 2H), 7.99 (dt, J = 8.1, 1.6 Hz, 4H), 7.95 – 7.91 (m, 4H), 7.69 – 7.63 (m, 8H), 7.59 (d, J = 10.0 Hz, 2H), 7.57 (d, J = 9.9 Hz, 2H), 7.49 (ddt, J = 8.5, 6.8, 1.8 Hz, 4H), 7.40 – 7.36 (m, 8H), 7.36 – 7.32 (m, 4H), 7.00 – 6.92 (m, 6H), 5.83 (dt, J = 15.7, 1.6 Hz, 2H), 5.80 – 5.74 (m, 2H), 5.23 (d, J = 9.7 Hz, 2H), 5.21 (d, J = 9.6 Hz, 2H), 5.02 – 4.94 (m, 4H), 4.38 (td, J = 6.6, 3.7 Hz, 20H), 4.15 – 4.09 (m, 8H), 4.06 – 4.03 (m, 4H), 3.98 (t, J = 6.8 Hz, 4H), 2.79 (t, J = 6.8 Hz, 4H), 2.57 – 2.52 (m, 4H), 2.23 (qd, J = 7.2, 1.6 Hz, 4H), 2.10 – 2.05 (m, 4H), 1.84 – 1.78 (m, 8H), 1.75 (dt, J = 14.5, 7.0 Hz, 8H), 1.71 – 1.65 (m, 8H), 1.56 (ddt, J = 10.5, 7.7, 5.1 Hz, 8H), 1.53 – 1.39 (m, 18H), 1.39 – 1.32 (m, 6H),

1.25 (t, $J = 7.2$ Hz, 12H). **^{13}C NMR** (151 MHz, CDCl_3) δ 167.80, 167.64, 167.51, 167.49, 166.19, 162.84, 162.74, 162.01, 161.94, 149.79, 146.22, 146.18, 138.34, 136.69, 136.65, 134.45, 134.43, 131.47, 131.27, 131.04, 128.78, 128.07, 128.02, 127.99, 121.08, 120.66, 120.57, 115.03, 114.84, 114.82, 112.97, 112.94, 97.29, 97.04, 70.58, 68.75, 65.39, 65.18, 65.15, 65.00, 64.01, 63.96, 62.01, 33.28, 32.82, 31.80, 30.73, 29.79, 29.67, 29.61, 29.33, 28.92, 28.82, 28.81, 28.78, 28.72, 28.05, 27.98, 25.94, 25.92, 25.85, 25.36, 24.57, 21.16. **SEC-MS**: calculated m/z for $\text{C}_{142}\text{H}_{178}\text{N}_8\text{NaO}_{32}\text{S}_2^+$ $[\text{M}+\text{Na}]^+ = 2595.1915$ (100.0%), 2596.1948 (76.3%), 2594.1881 (65.1%), 2597.1982 (38.5%), 2598.2015 (14.5%), found: 2595.1863, 1596.1887, 2594.1826, 2597.1904, 2598.1921.

Synthesis of HO-[H]₄-OH

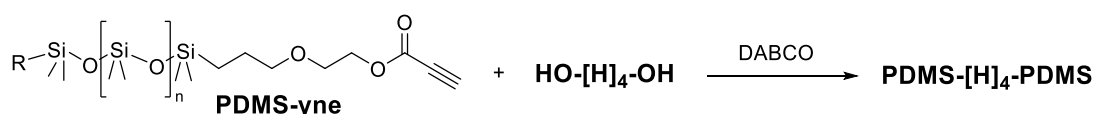


2-hydroxyethyl acrylate (0.37 mL, 15 eq) and **ene-[H]₄-ene** (550 mg, 0.21 mmol, 1.0 eq) were fully dissolved in 0.5 mL anhydrous DCM. Following this, Hoveyda-Grubbs 2nd generation (**HG-II**, 7.0 mg, 5.0 mol%) catalyst was added, and the reaction container was quickly submerged in an oil bath preheated to 40 °C. The reaction was carried out for 1 h, after which a ^1H NMR spectrum was recorded to determine the conversion. Upon completion, ethyl vinyl ether (0.05 mL) was injected into the reaction. After 10 minutes, the crude reaction mixture was diluted in EtOAc, extracted with water and brine (3 times). The organic phase was concentrated under reduced pressure. The residue was purified by flash column chromatography (DCM/EtOAc/MeOH, 90/9/1 to 1/99/2, v/v), affording the product as a sticky yellow oil (500 mg, 85% yield).

^1H NMR (600 MHz, CDCl_3) δ 13.97 (s, 2H), 13.95 (s, 2H), 7.99 (dq, $J = 8.0, 2.0$ Hz, 4H), 7.96 – 7.91 (m, 4H), 7.69 – 7.63 (m, 8H), 7.58 (dd, $J = 12.7, 9.9$ Hz, 4H), 7.49 (ddd, $J = 8.7, 7.1, 1.6$ Hz, 4H), 7.39 (tdd, $J = 5.9, 2.6, 1.5$ Hz, 8H), 7.36 – 7.32 (m, 4H), 7.00 – 6.92 (m, 8H), 5.84 (ddt, $J = 15.6, 11.7, 1.6$ Hz, 4H), 5.25 – 5.19 (m, 4H), 4.42 – 4.35 (m, 20H), 4.28 – 4.25 (m, 4H), 4.12 (t, $J = 6.7$ Hz, 8H), 4.05 (dd, $J = 5.6, 3.7$ Hz, 4H), 3.98 (t, $J = 6.8$ Hz, 4H), 3.86 – 3.82 (m, 4H), 2.79 (t, $J = 6.8$ Hz, 4H), 2.54 (t, $J = 7.4$ Hz, 4H), 2.23 (qdd, $J = 7.2, 4.0, 1.5$ Hz, 8H), 1.84 – 1.73 (m, 18H), 1.71 – 1.65 (m, 8H), 1.56 (ddt, $J = 10.5, 7.8, 4.3$ Hz, 12H), 1.52 – 1.42 (m, 16H), 1.36 (dq, $J = 12.6, 6.5$ Hz, 4H), 1.30 – 1.22 (m, 12H). **^{13}C NMR** (151 MHz,

CDCl₃) δ 167.82, 167.67, 167.51, 166.88, 166.21, 162.74, 162.02, 161.96, 149.81, 149.43, 146.17, 136.64, 134.46, 131.29, 131.26, 131.05, 128.76, 128.02, 121.35, 121.06, 120.66, 114.83, 112.96, 97.28, 97.04, 70.58, 68.76, 66.12, 65.17, 65.00, 64.01, 63.97, 62.01, 61.46, 53.55, 32.82, 31.79, 31.75, 30.73, 29.79, 29.66, 29.61, 29.33, 28.92, 28.81, 28.80, 28.71, 28.04, 25.93, 25.91, 25.85, 25.83, 24.57. **SEC-MS:** calculated m/z for C₁₄₈H₁₈₆N₈Na₂O₃₈S₂²⁺ [M+Na]⁺ = 1397.1064 (100.0%), 1397.6081 (79.5%), 1396.6047 (62.5%), 1398.1097 (41.8%), 1398.6114 (16.4%), found: 1397.1051, 1397.6064, 1396.6035, 1398.1075, 1398.6085. Note that this is only for the target product. Other species with higher m/z are also observed, but not listed here.

Synthesis of PDMS-[H]₄-PDMS



PDMS-yne (reported in chapter 4) (200 mg, 2.2 eq) and **HO-[H]₄-OH** (50 mg, 0.018 mmol, 1.0 eq) were dissolved in 0.9 mL anhydrous DCM. Following that, DABCO (0.82 mg, 20 mol% of the OH-group) was added to the solution. The reaction was stopped after 30 min and purified immediately by flash column chromatography (DCM/EtOAc, 99/1 to 50/50, v/v), affording the product (~ 100 mg, ~50% yield).

11.7.7. NMR spectra

11.7.7.1. Compound 1

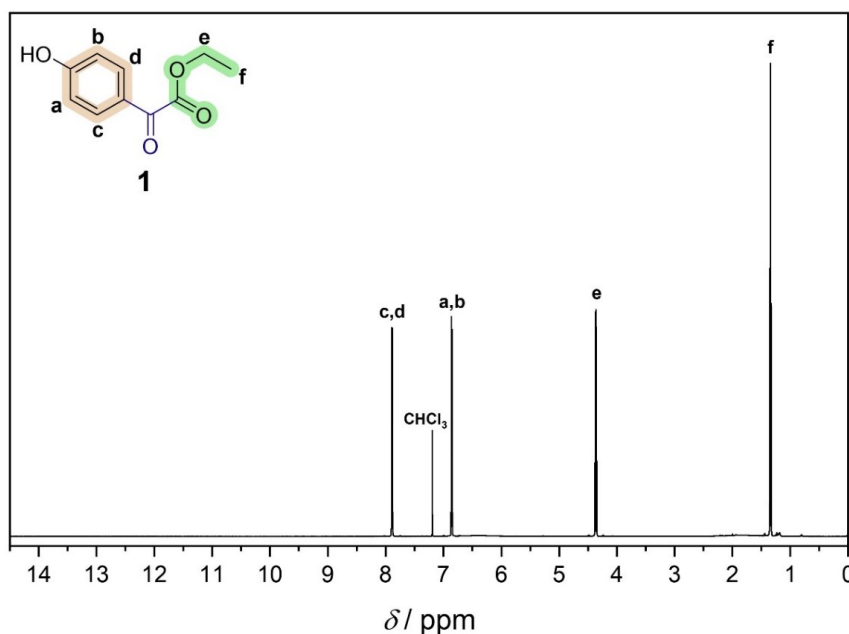


Figure S7.12. ¹H NMR (600 MHz, 16 scans) spectrum of compound **1** in CDCl₃.

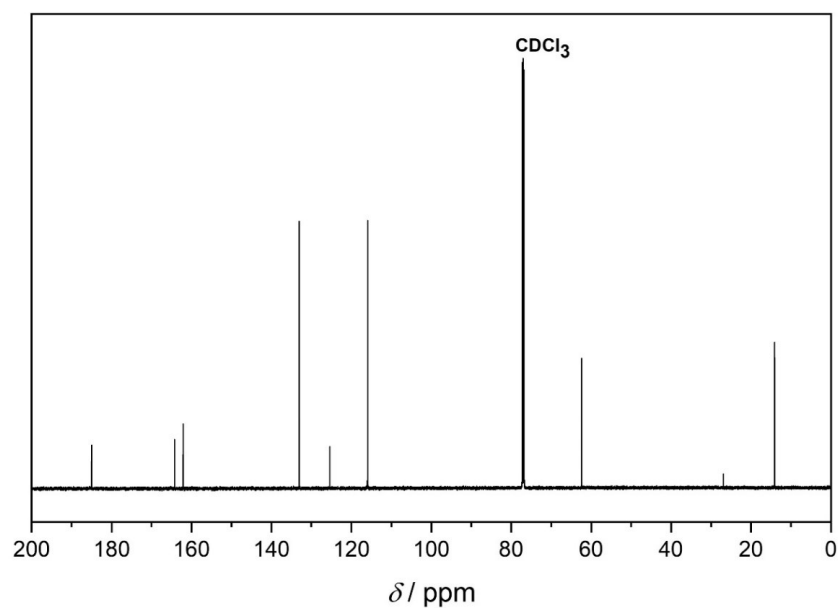


Figure S7.13. ^{13}C NMR (151 MHz, 1024 scans) spectrum of compound **1** in CDCl_3 .

11.7.7.2. Compound 2

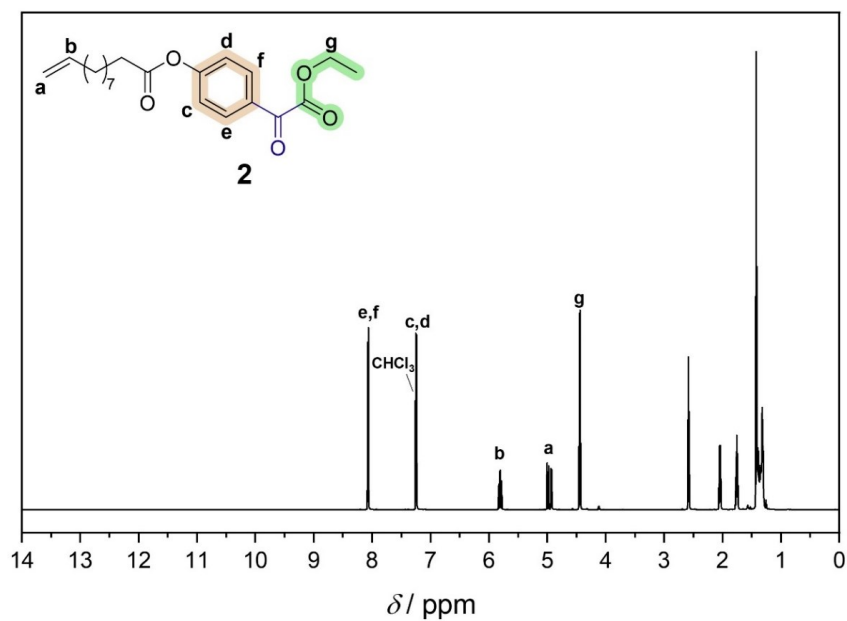


Figure S7.14. ^1H NMR (600 MHz, 16 scans) spectrum of compound **2** in CDCl_3 .

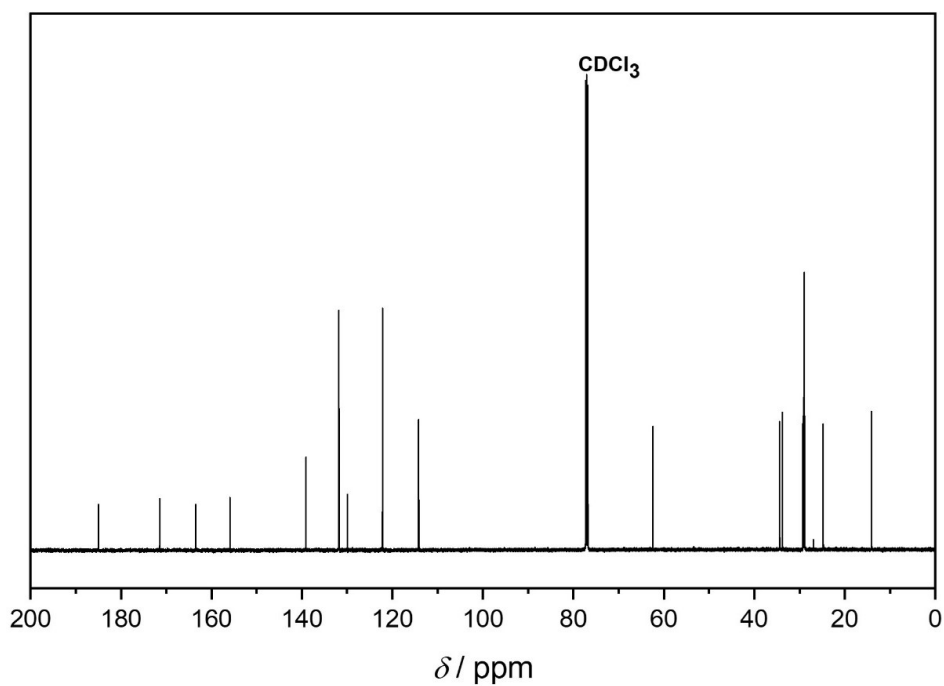


Figure S7.15. ^{13}C NMR (151 MHz, 1024 scans) spectrum of compound **2** in CDCl_3 .

11.7.7.3. Compound 3

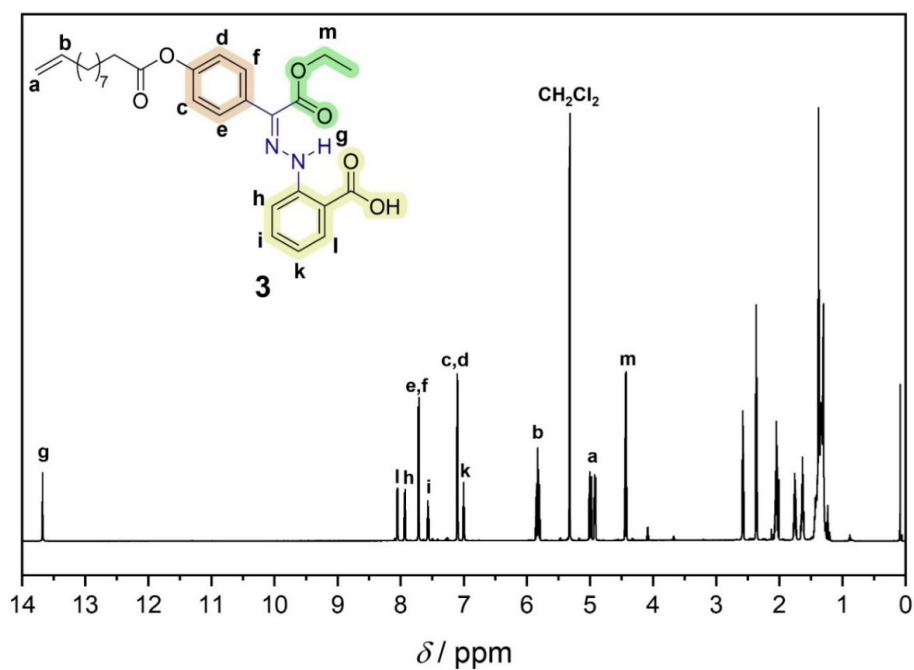


Figure S7.16. ^1H NMR (600 MHz, 16 scans) spectrum of compound **3** in CD_2Cl_2 .

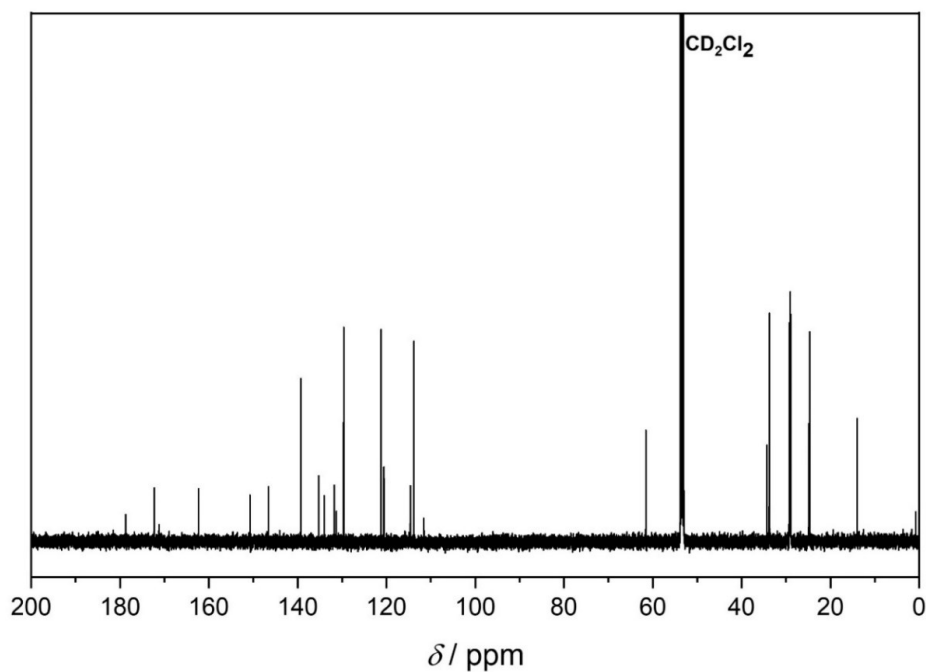


Figure S7.17. ^{13}C NMR (151 MHz, 1024 scans) spectrum of compound **3** in CD_2Cl_2 .

11.7.7.4. Compound 4

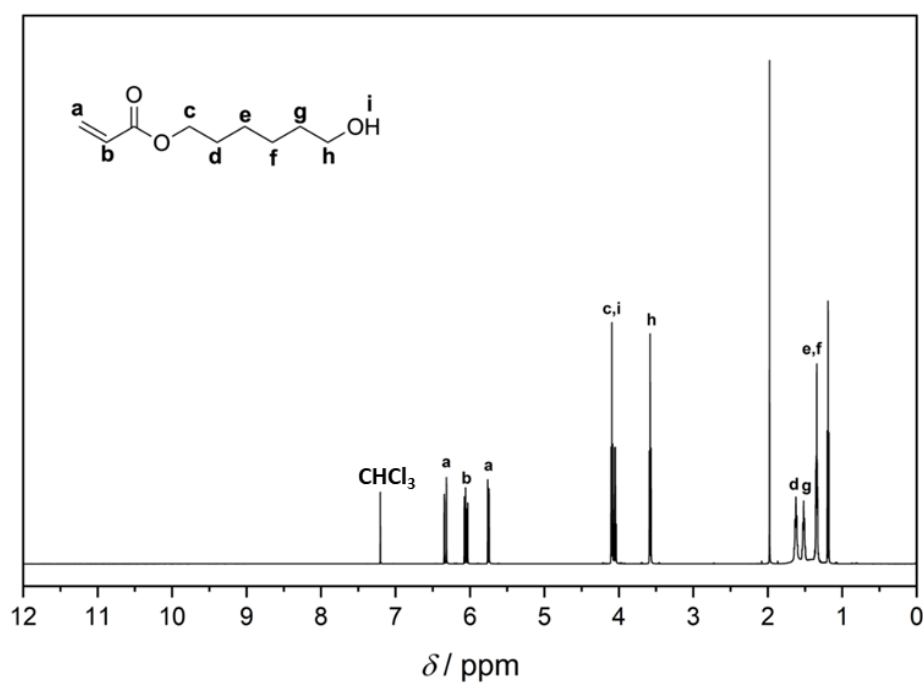


Figure S7.18. ^1H NMR (600 MHz, 16 scans) spectrum of compound **4** in CDCl_3 .

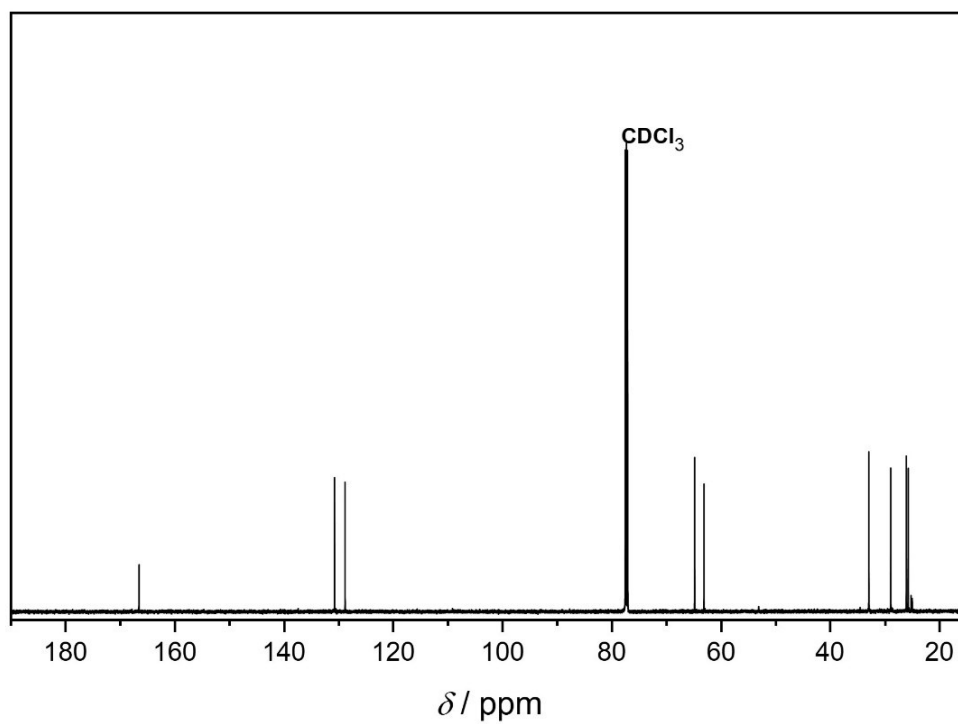


Figure S7.19. ^{13}C NMR (151 MHz, 1024 scans) spectrum of compound **4** in CDCl_3 .

11.7.7.5. Monomer M_{h1}

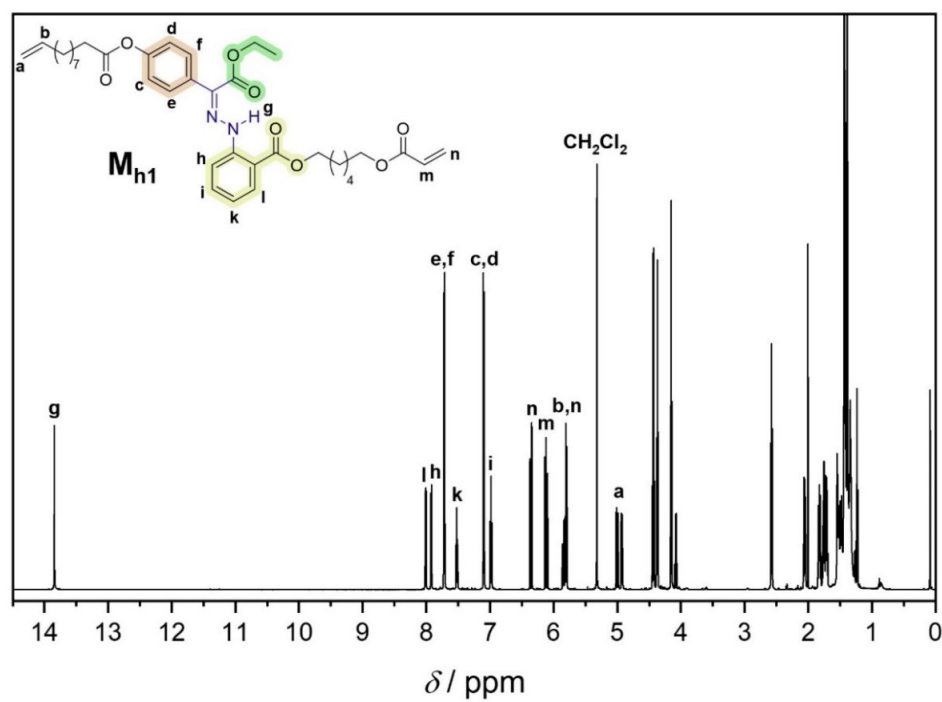


Figure S7.20. ^1H NMR (600 MHz, 16 scans) spectrum of monomer M_{h1} in CD_2Cl_2 .

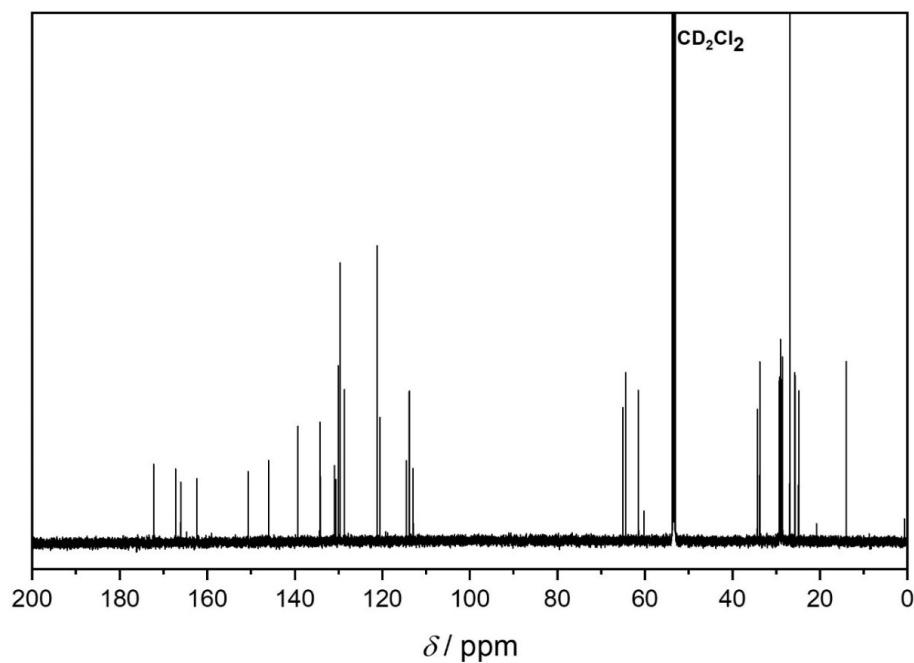


Figure S7.21. ^{13}C NMR (151 MHz, 1024 scans) spectrum of monomer \mathbf{M}_{h1} in CD_2Cl_2 .

11.7.7.6. Polymer \mathbf{P}_{h1}

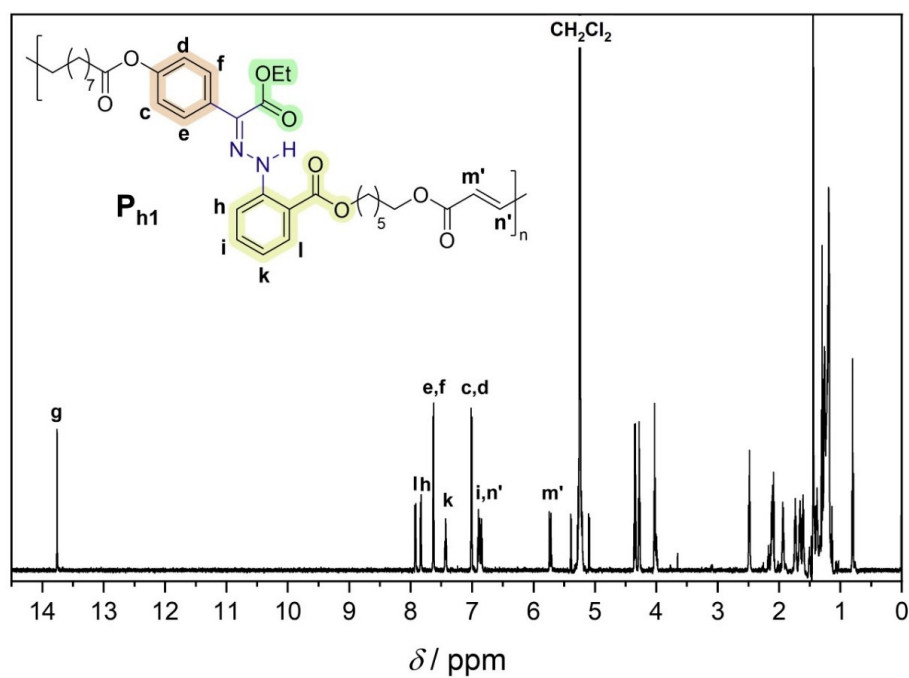


Figure S7.22. ^1H NMR (600 MHz, 32 scans) spectrum of polymer $(\mathbf{Z})\text{-P}_{h1}$ in CD_2Cl_2 .

11.7.7.7. Compound 5

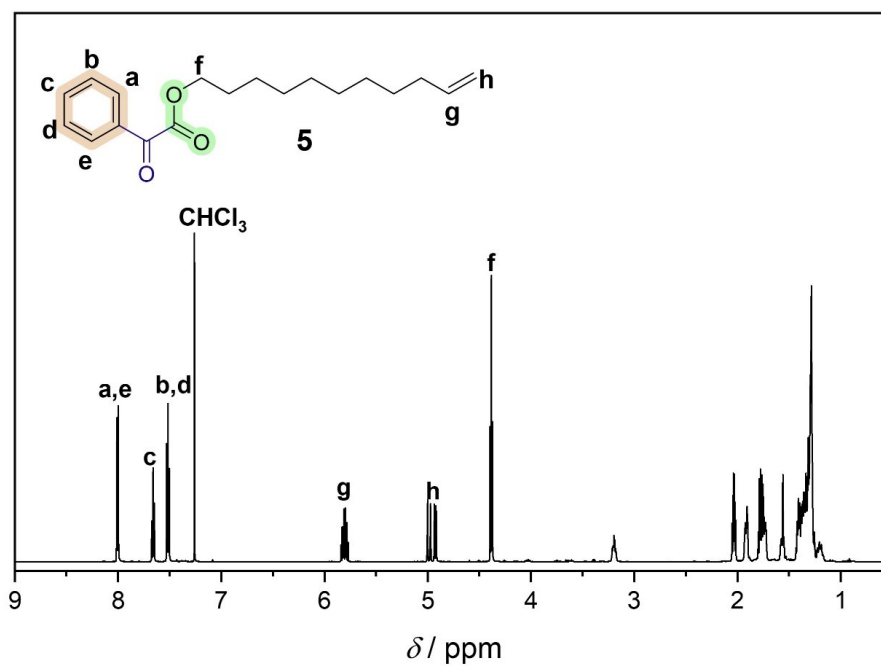


Figure S7.23. ¹H NMR (600 MHz, 16 scans) spectrum of compound 5 in CDCl₃.

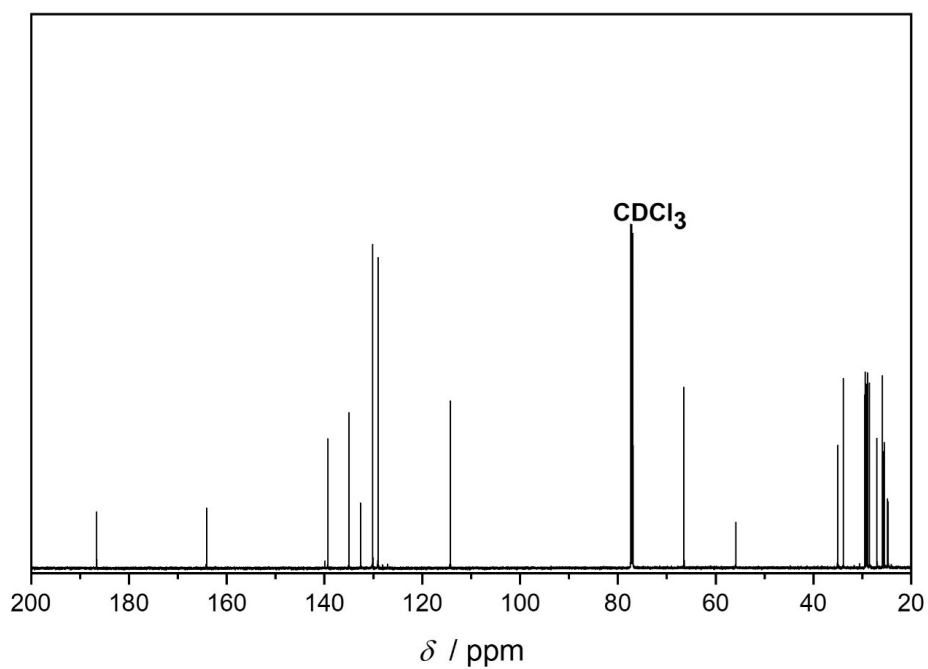


Figure S7.24. ¹³C NMR (151 MHz, 1024 scans) spectrum of compound 5 in CDCl₃.

11.7.7.8. Compound 6

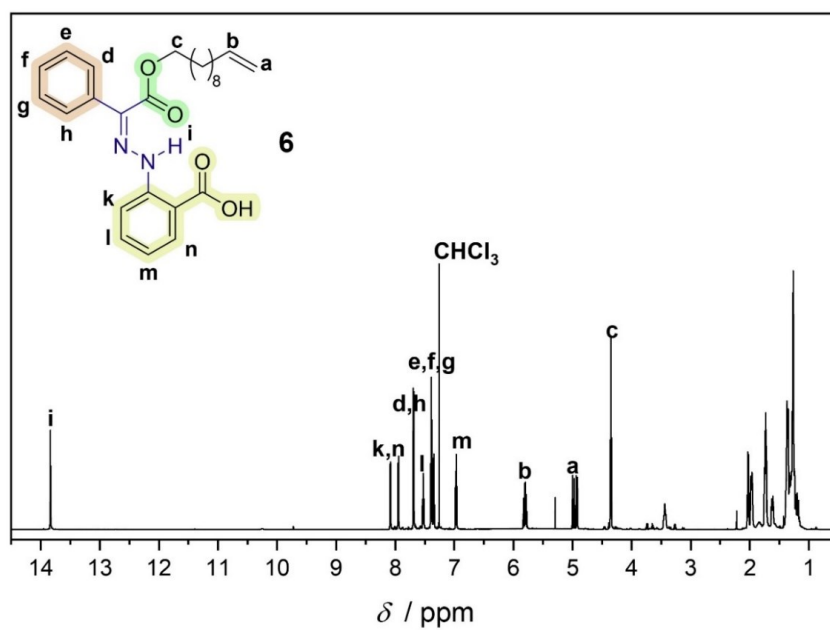


Figure S7.25. ^1H NMR (600 MHz, 16 scans) spectrum of compound 6 in CDCl_3 .

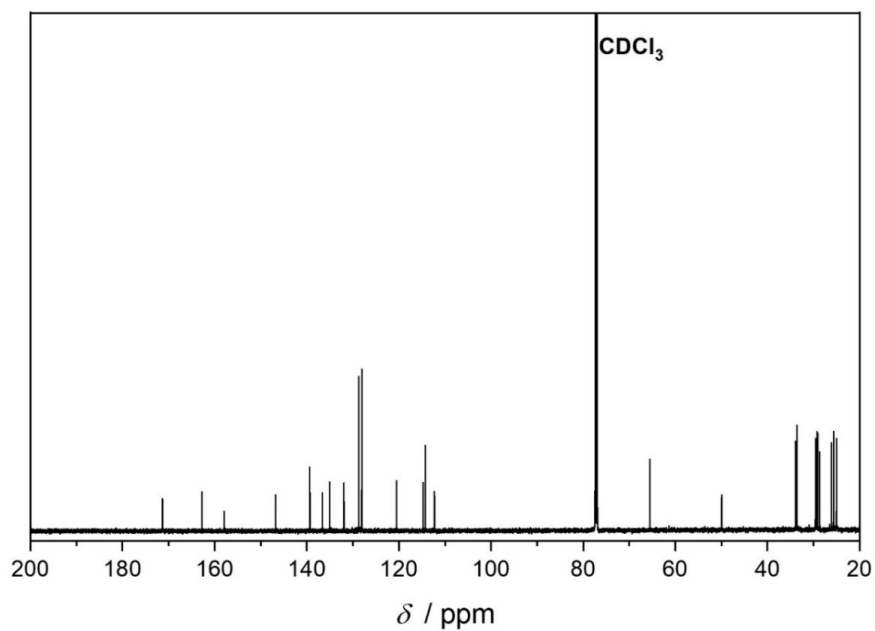


Figure S7.26. ^{13}C NMR (151 MHz, 1024 scans) spectrum of compound 6 in CDCl_3 .

11.7.7.9. Monomer M_{h2}

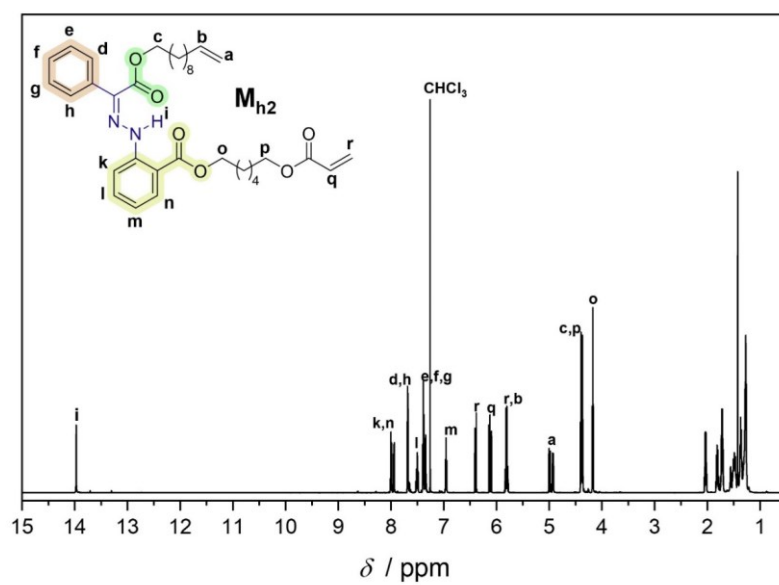


Figure S7.27. ^1H NMR (600 MHz, 16 scans) spectrum of monomer M_{h2} in CDCl_3 .

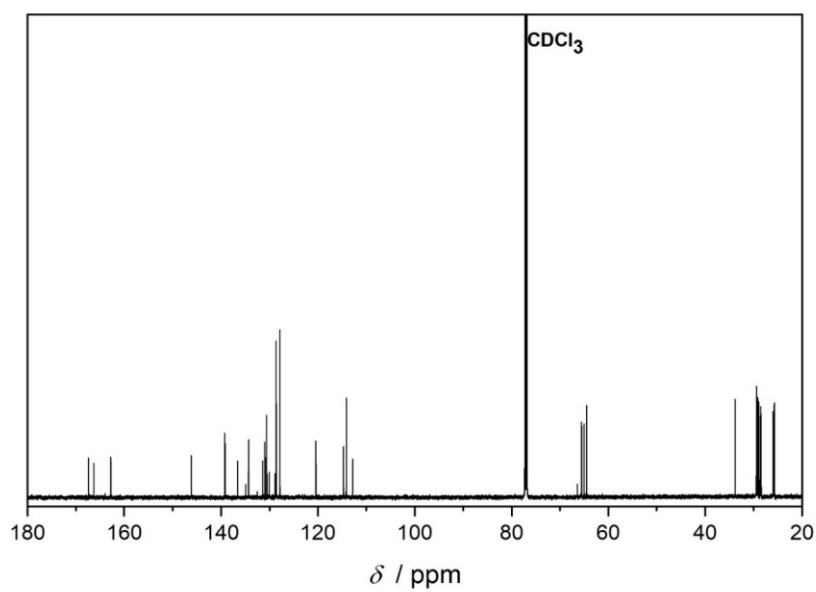


Figure S7.28. ^{13}C NMR (151 MHz, 1024 scans) spectrum of monomer M_{h2} in CDCl_3 .

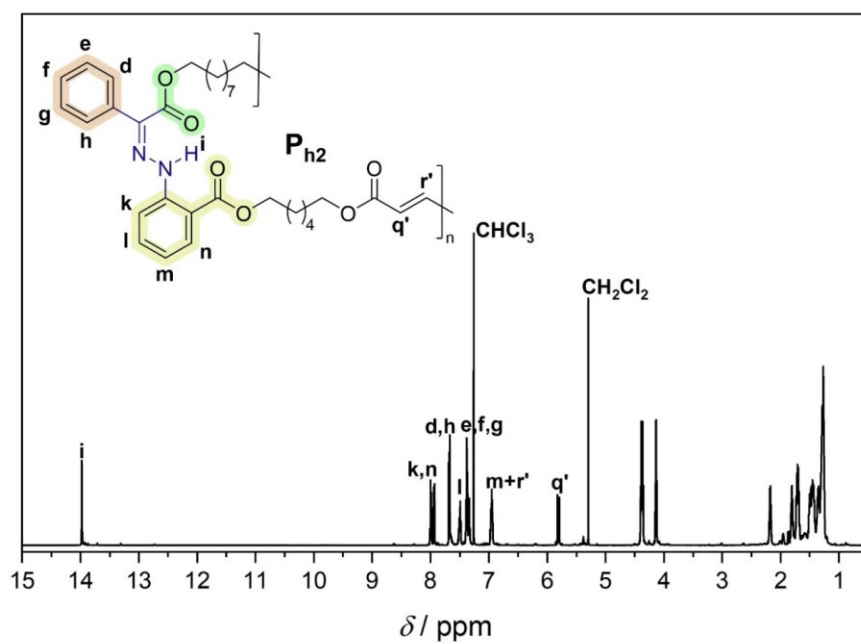
11.7.7.10. Polymer P_{h2} 

Figure S7.29. ^1H NMR (600 MHz, 32 scans) spectrum of polymer $(Z)\text{-}P_{h2}$ CDCl_3 .

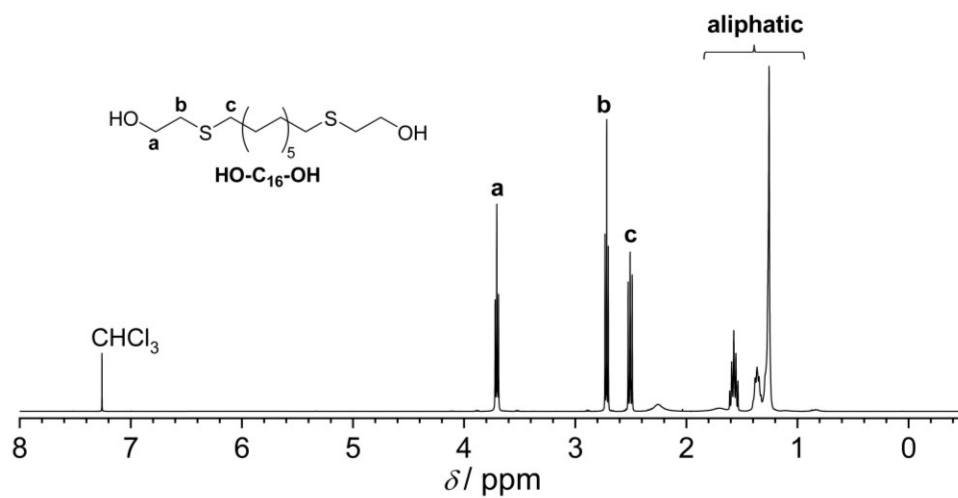
11.7.7.11. $\text{HO-C}_{16}\text{-OH}$ 

Figure S7.30. ^1H NMR spectrum of $\text{HO-C}_{16}\text{-OH}$ in CDCl_3 .

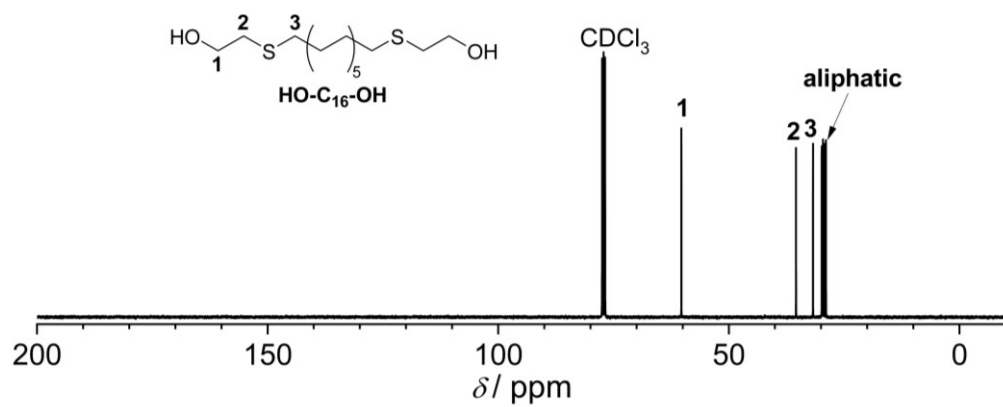


Figure S7.31. ^{13}C NMR spectrum of $\text{HO-C}_{16}\text{-OH}$ in CDCl_3 .

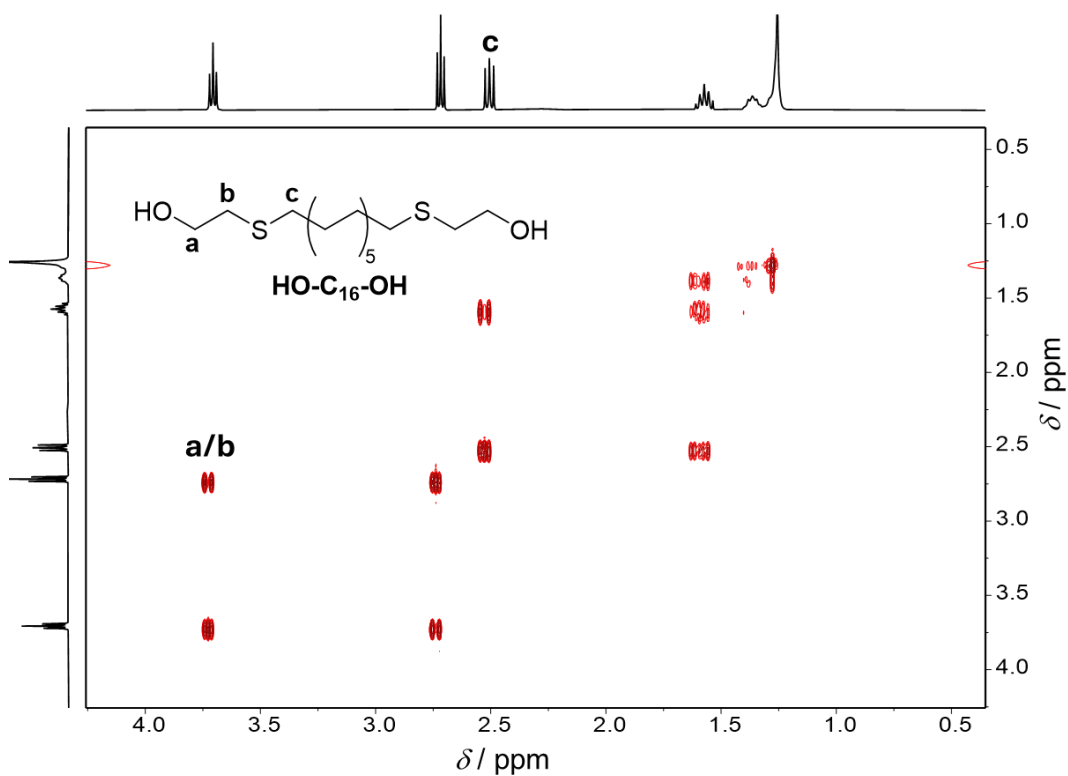
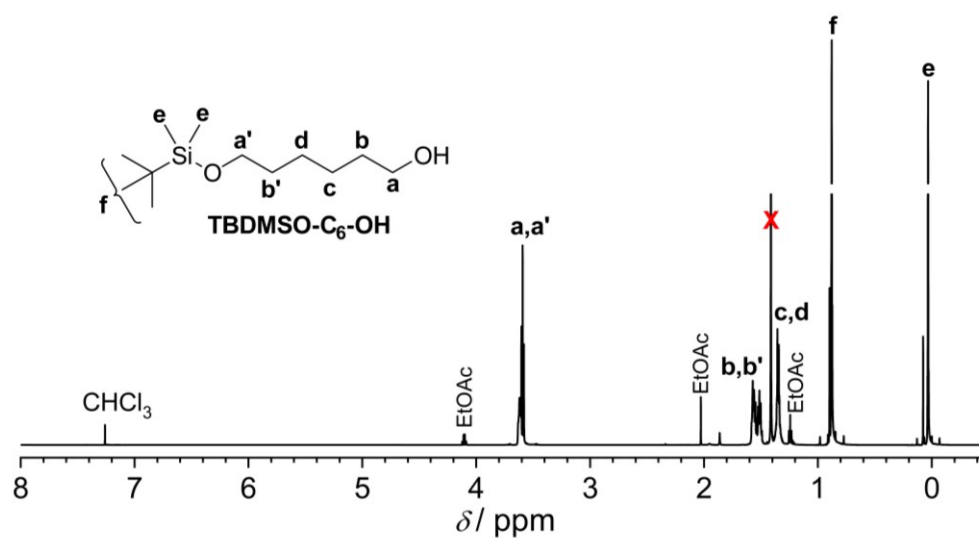
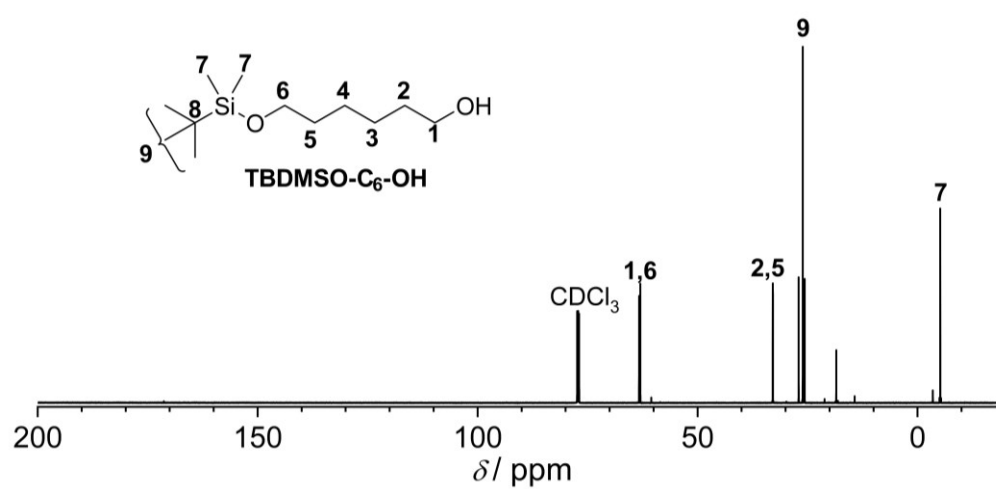
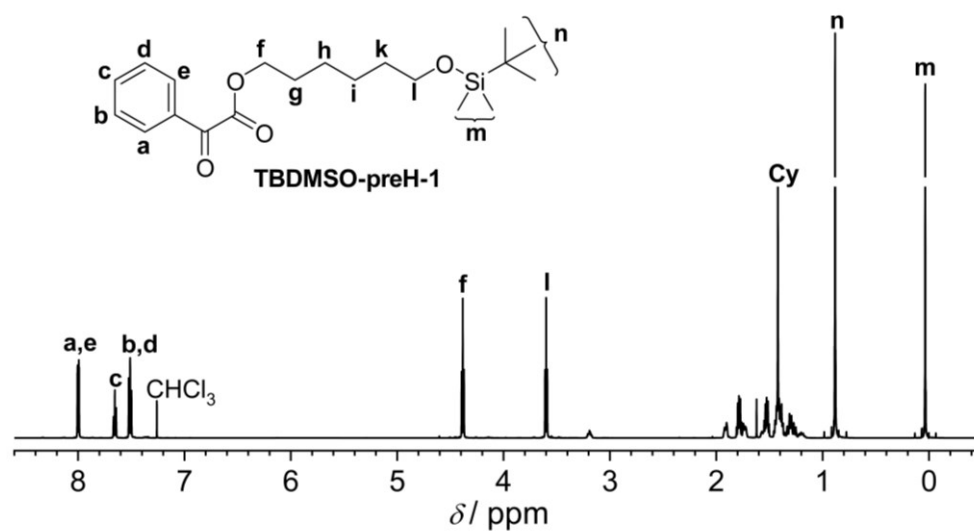
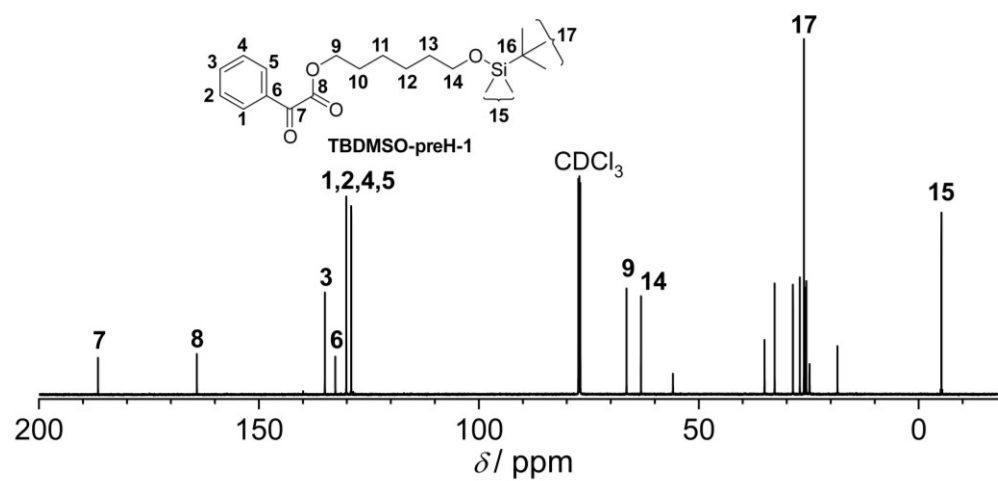


Figure S7.32. COSY NMR spectrum of $\text{HO-C}_{16}\text{-OH}$ in CDCl_3 .

11.7.7.12. TBDMSO-C₆-OHFigure S7.33. ¹H NMR spectrum of TBDMSO-C₆-OH in CDCl₃.Figure S7.34. ¹³C NMR spectrum of TBDMSO-C₆-OH in CDCl₃.

11.7.7.13. TBDMSO-preH-1

Figure S7.35. ^1H NMR spectrum of TBDMSO-preH-1 in CDCl_3 .Figure S7.36. ^{13}C NMR spectrum of TBDMSO-preH-1 in CDCl_3 .

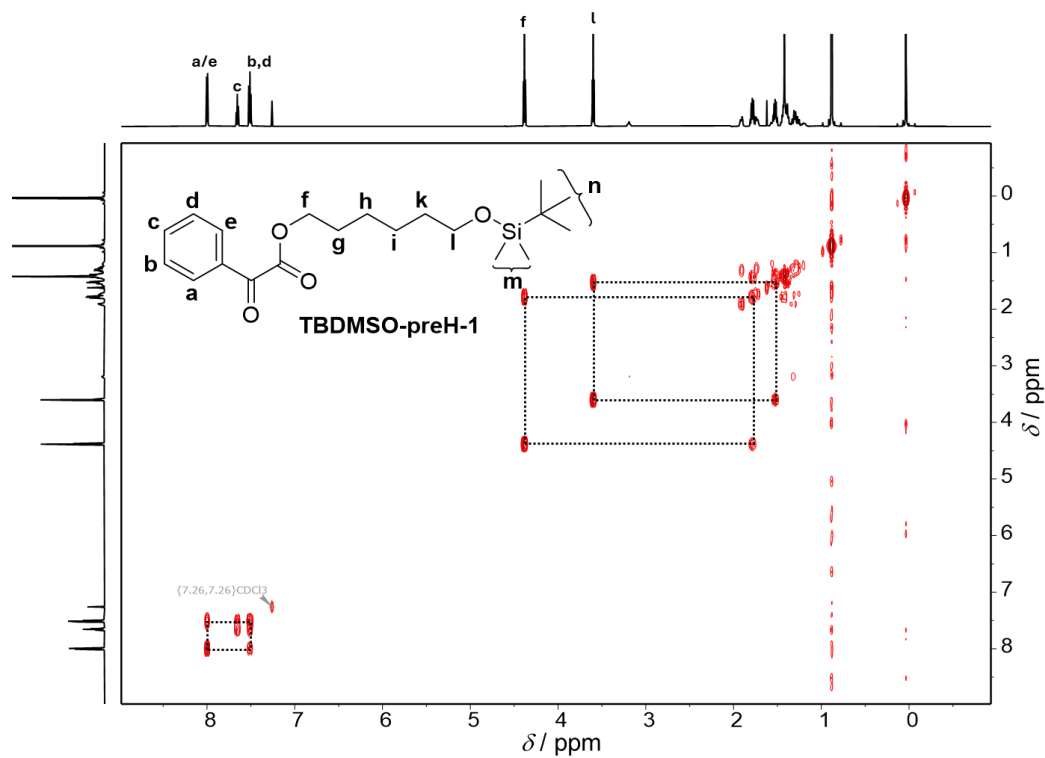


Figure S7.37. COSY NMR spectrum of **TBDMSO-preH-1** in CDCl₃.

11.7.7.14. TBDMSO-[H]₁-COOH

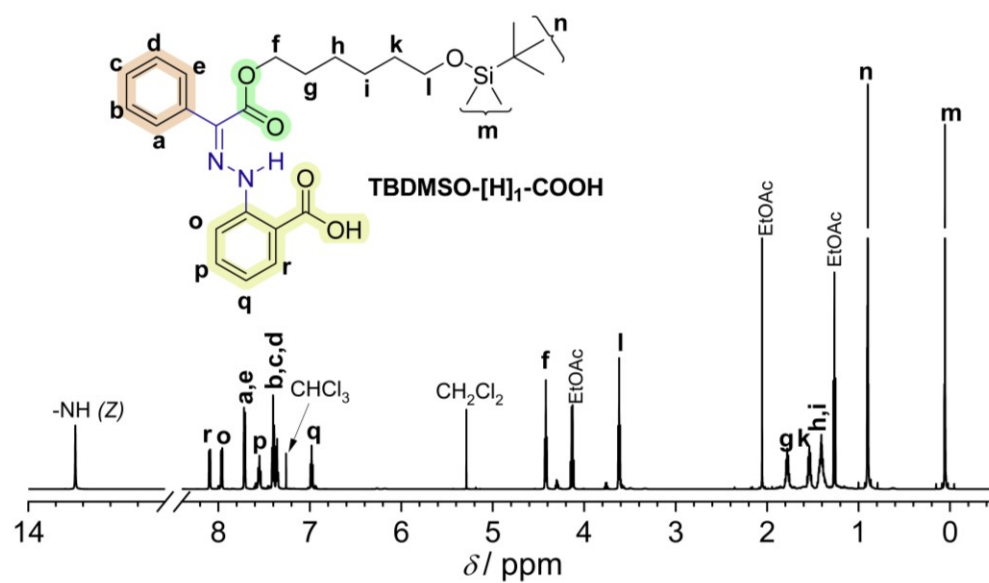


Figure S7.38. ¹H NMR spectrum of **TBDMSO-[H]₁-COOH** in CDCl₃.

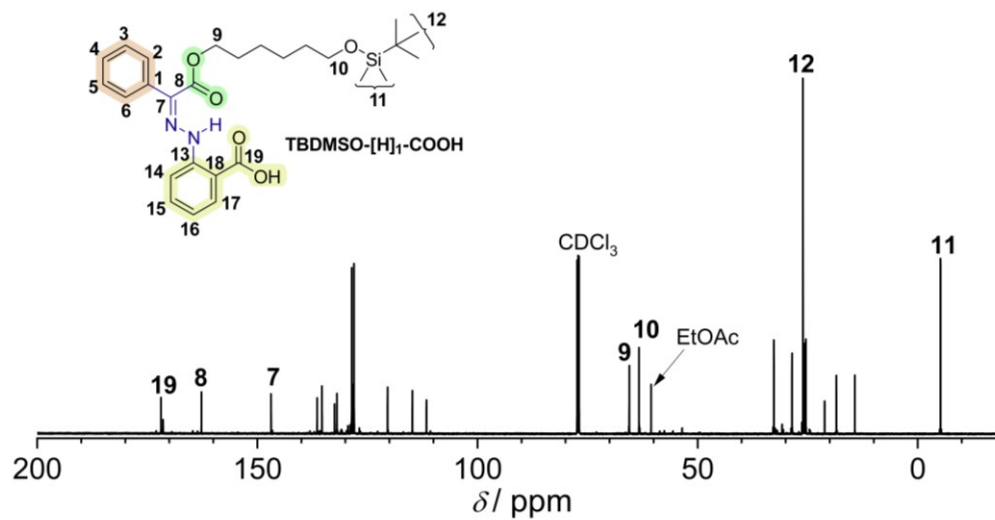


Figure S7.39. ^{13}C NMR spectrum of $\text{TBDMSO}-[\text{H}]_1\text{-COOH}$ in CDCl_3 .

11.7.7.15. HO-C₆-yne

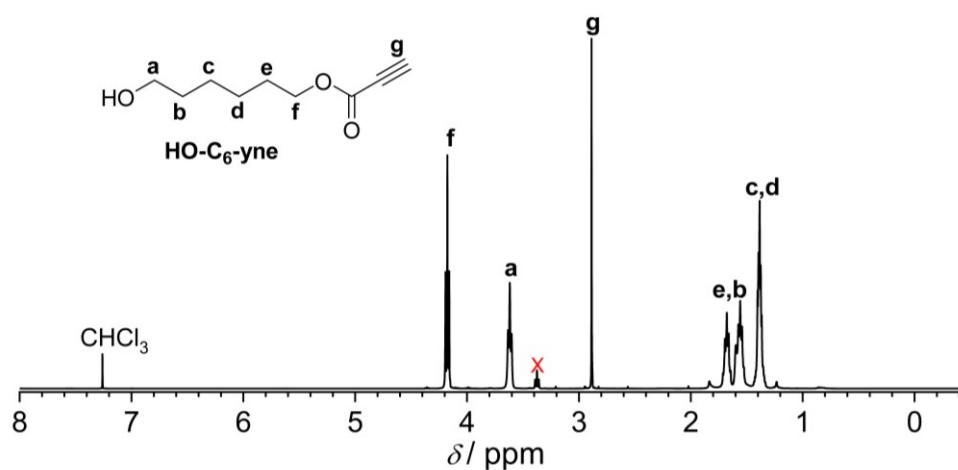


Figure S7.40. ^1H NMR spectrum of $\text{HO-C}_6\text{-yne}$ in CDCl_3 .

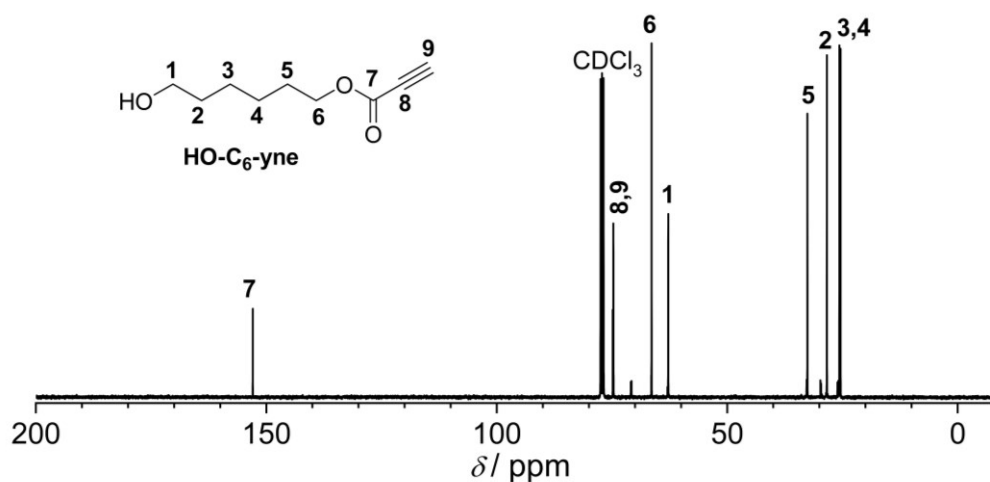
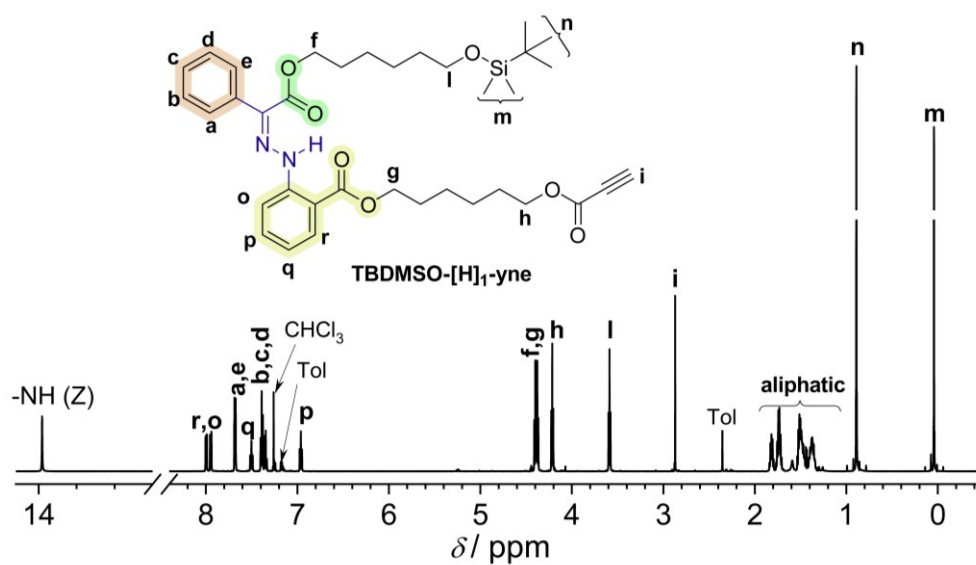
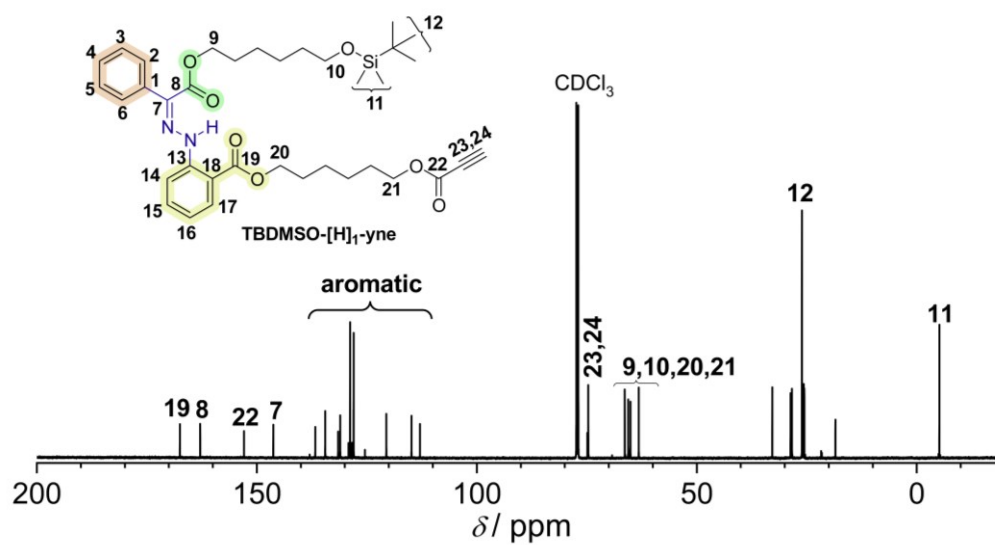
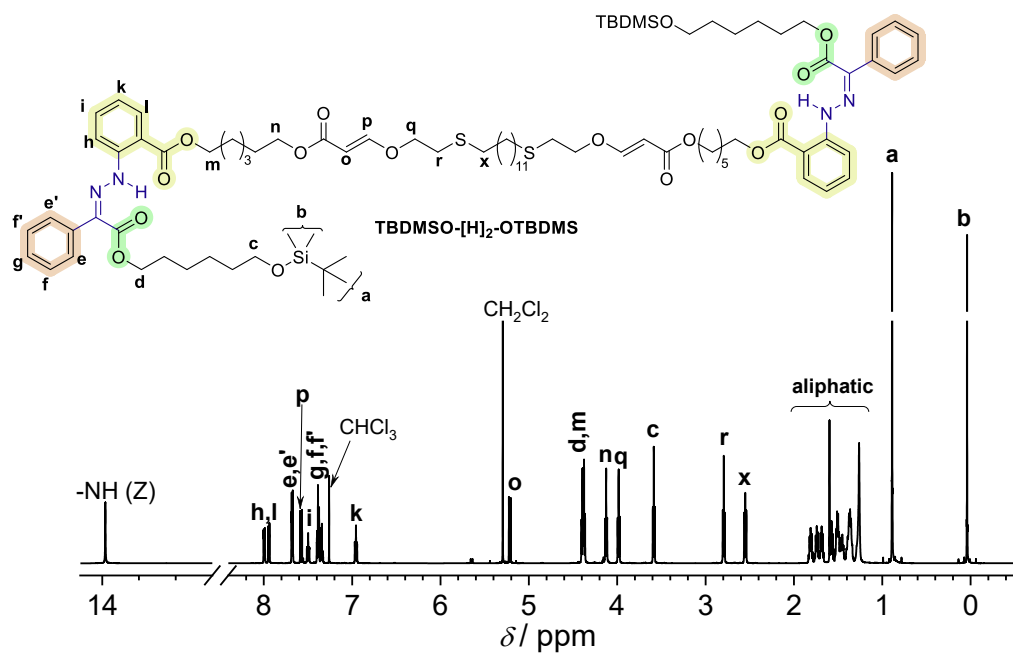
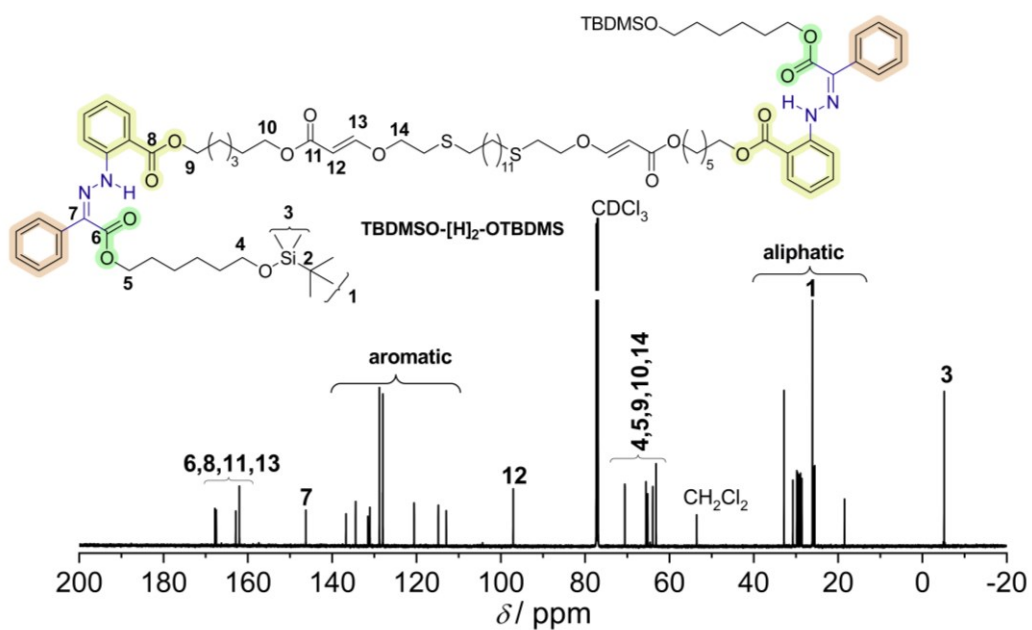
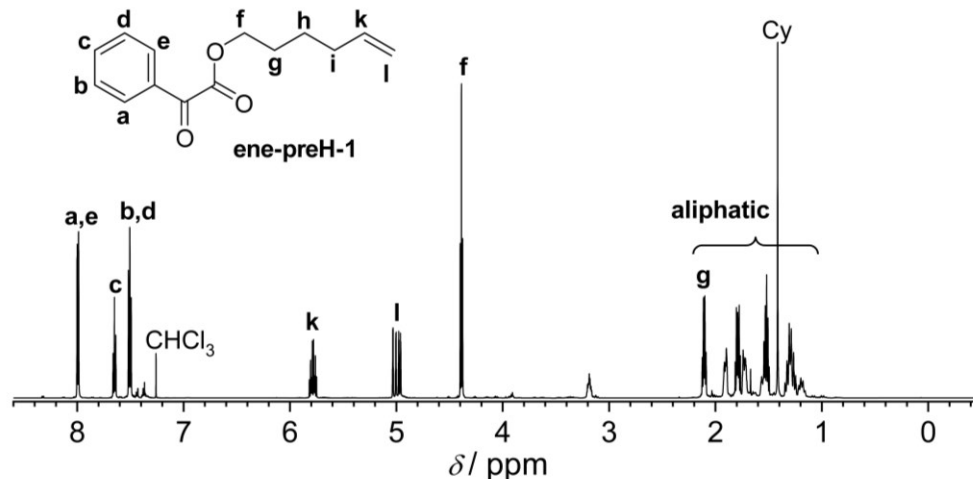
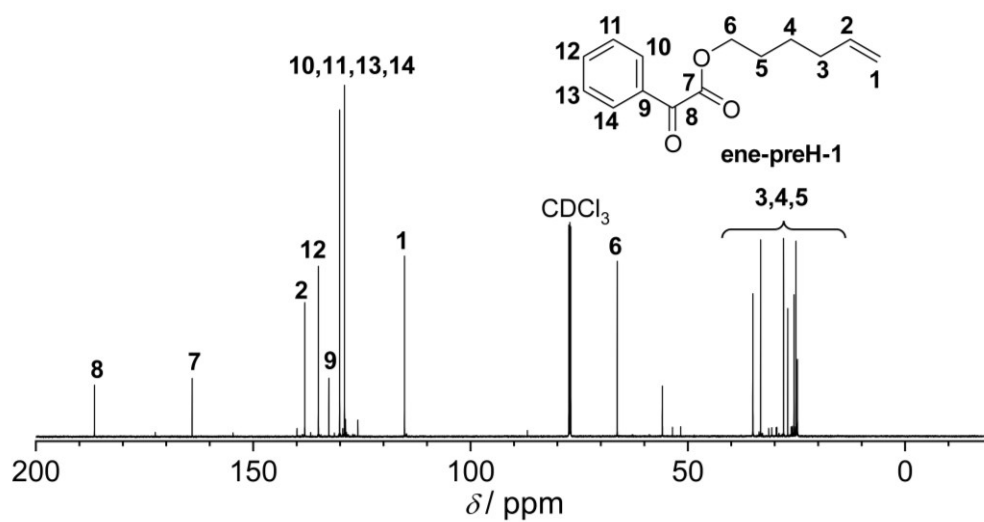


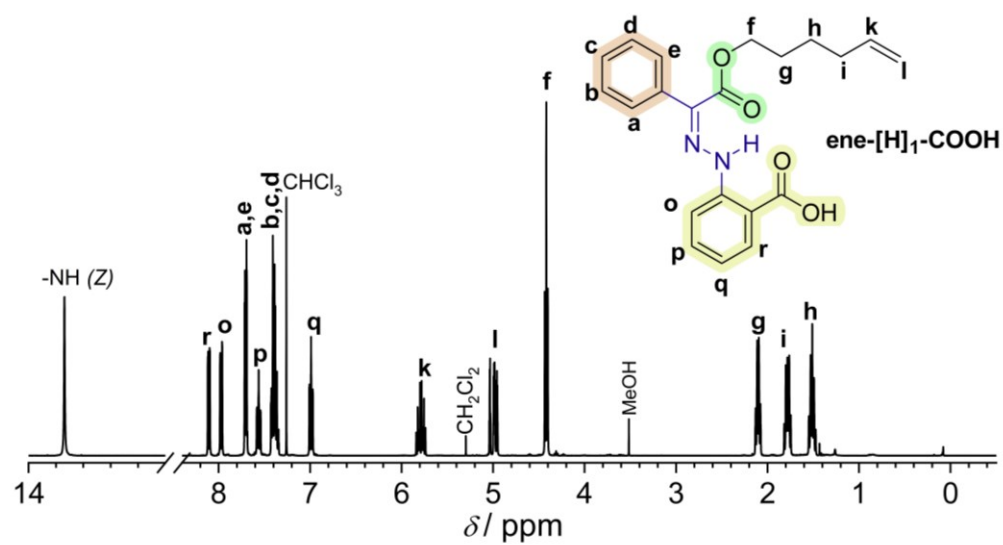
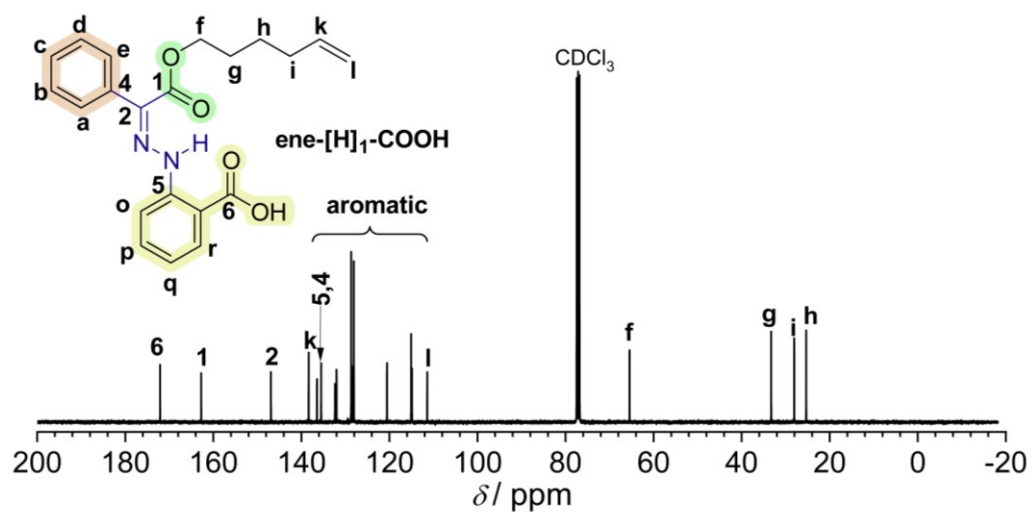
Figure S7.41. ^{13}C NMR spectrum of $\text{HO-C}_6\text{-yne}$ in CDCl_3 .

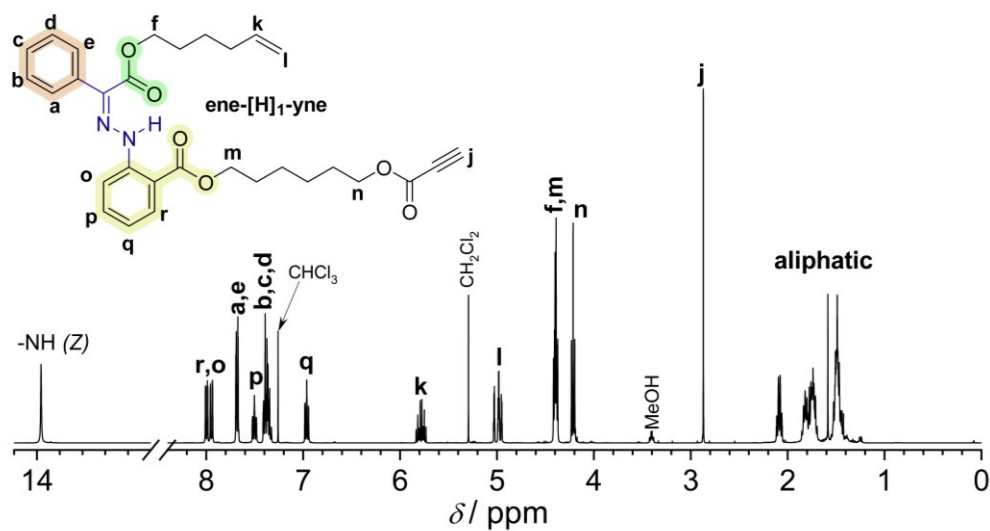
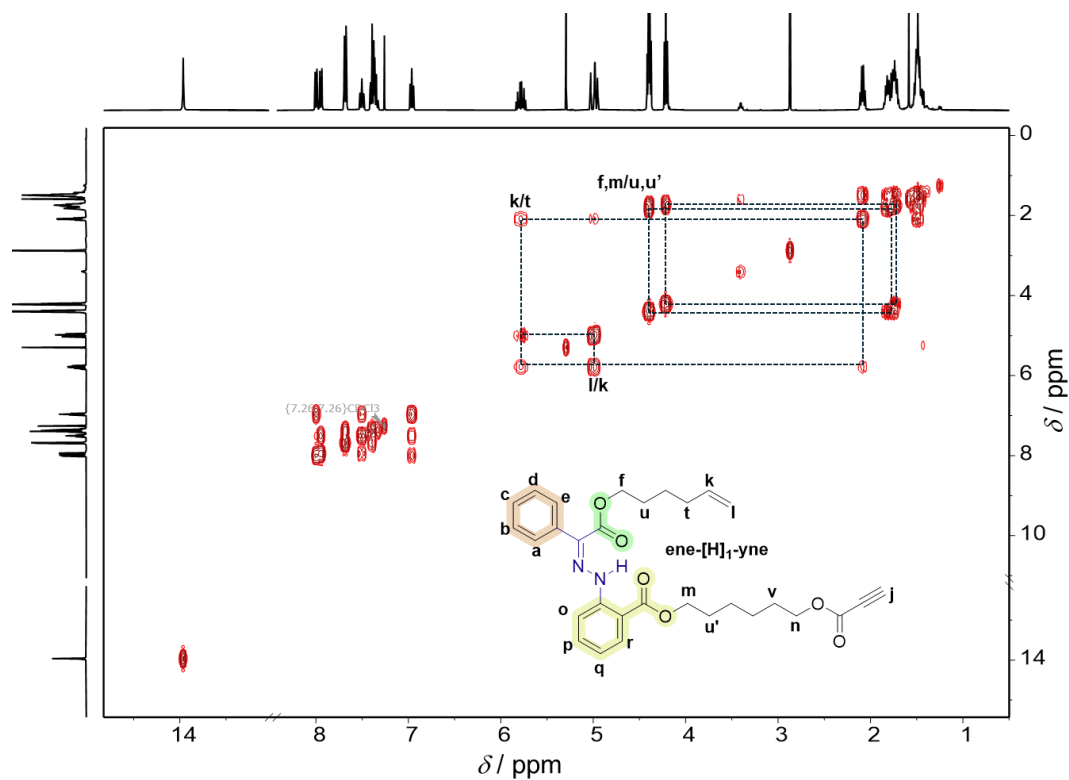
11.7.7.16. TBDMSO- $[H]_1$ -yneFigure S7.42. 1H NMR spectrum of TBDMSO- $[H]_1$ -yne in $CDCl_3$.Figure S7.43. ^{13}C NMR spectrum of TBDMSO- $[H]_1$ -yne in $CDCl_3$.

11.7.7.17. TBDMSO- $[\text{H}]_2$ -OTBDMSFigure S7.44. ^1H NMR spectrum of TBDMSO- $[\text{H}]_2$ -OTBDMS in CDCl_3 .Figure S7.45. ^{13}C NMR spectrum of TBDMSO- $[\text{H}]_2$ -OTBDMS in CDCl_3 .

11.7.7.18. ene-preH-1

Figure S7.46. ^1H NMR spectrum of **ene-preH-1** in CDCl_3 .Figure S7.47. ^{13}C NMR spectrum of **ene-preH-1** in CDCl_3 .

11.7.7.19. ene-[H]₁-COOHFigure S7.48. ¹H NMR spectrum of ene-[H]₁-COOH in CDCl₃.Figure S7.49. ¹³C NMR spectrum of ene-[H]₁-COOH in CDCl₃.

11.7.7.20. ene-[H]₁-yneFigure S7.50. ¹H NMR spectrum of ene-[H]₁-yne in CDCl₃.Figure S7.51. COSY NMR spectrum of ene-[H]₁-yne in CDCl₃.

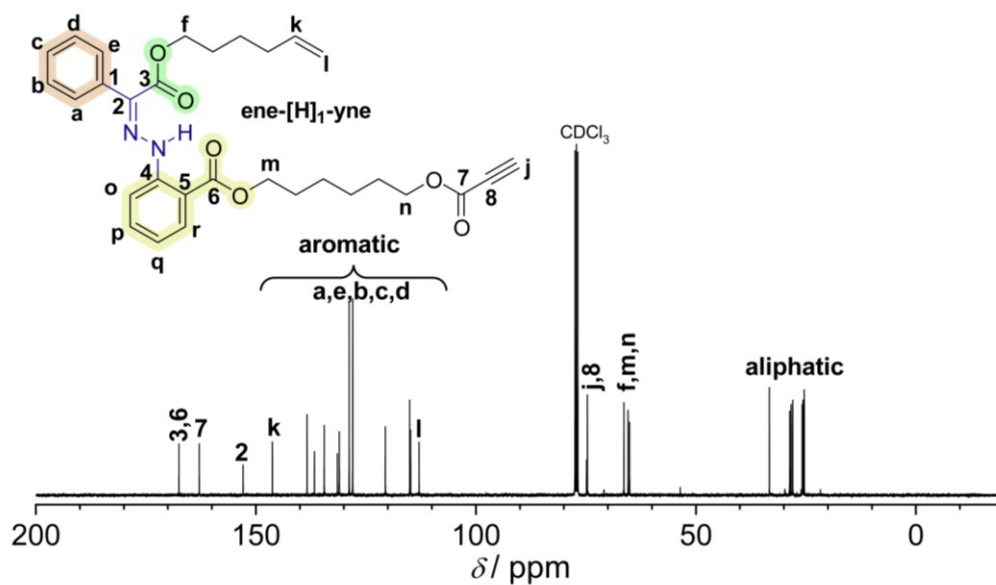


Figure S7.52. ¹³C NMR spectrum of **ene-[H]₁-yne** in CDCl₃.

11.7.7.21. ene-[H]₂-ene

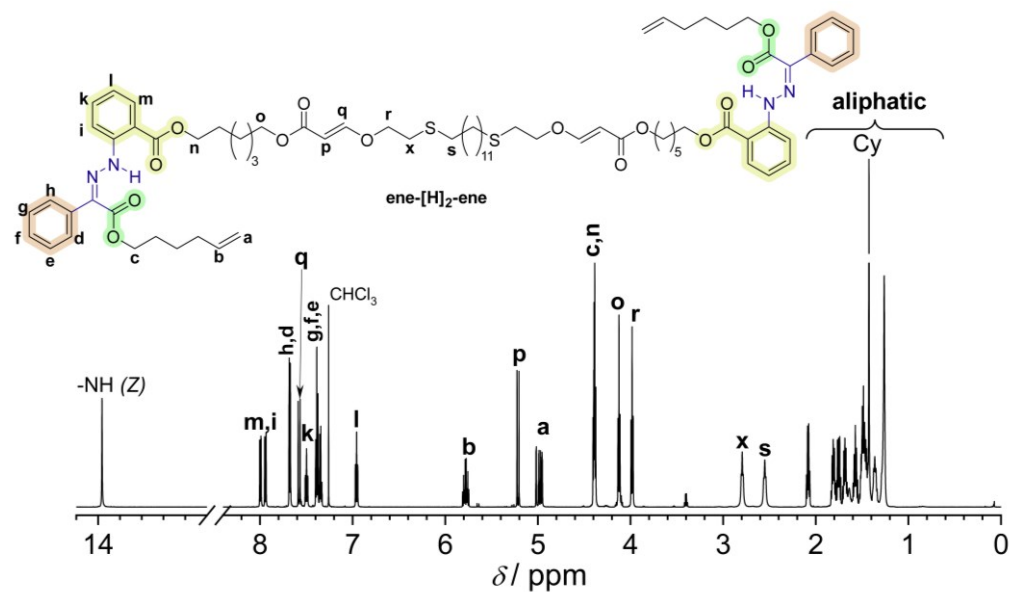


Figure S7.53. ¹H NMR spectrum of **ene-[H]₂-ene** in CDCl₃.

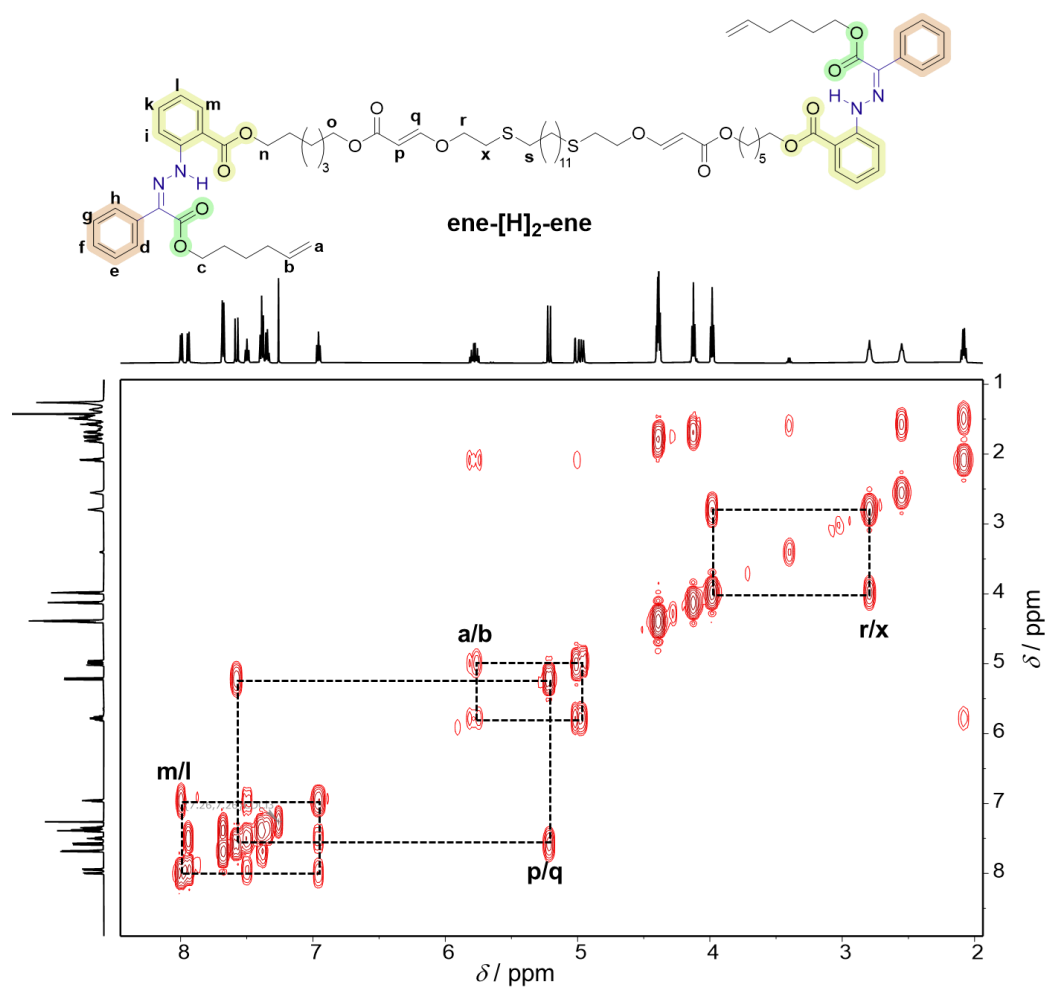


Figure S7.54. Sectional COSY NMR spectrum of **ene-[H]₂-ene** in CDCl₃.

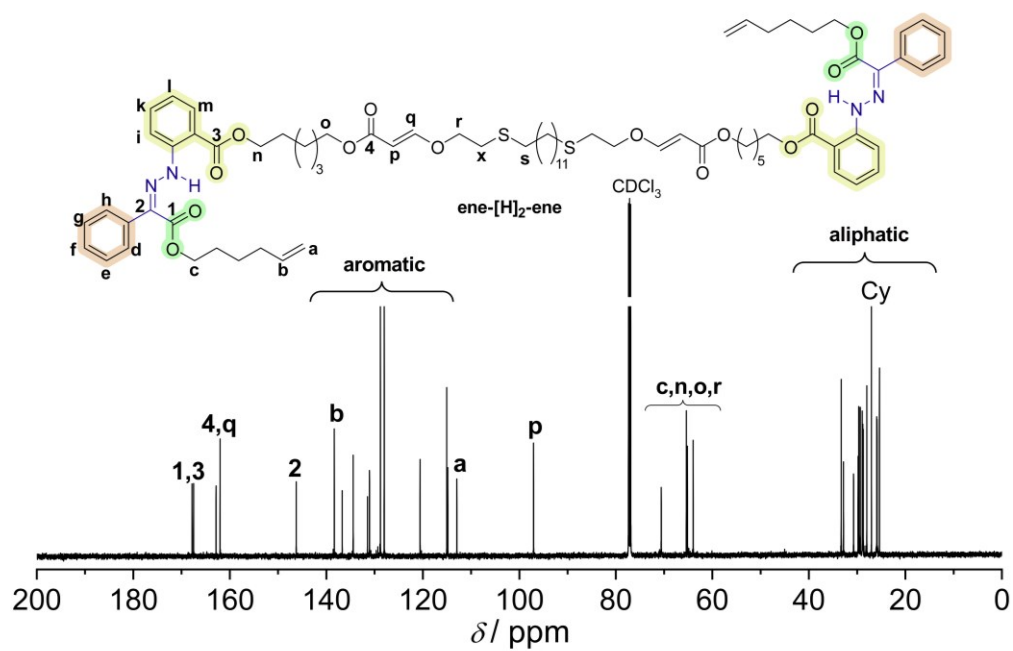


Figure S7.55. ¹³C NMR spectrum of *ene*-[H]₂-*ene* in CDCl₃.

11.7.7.22. HO-[H]₂-OH

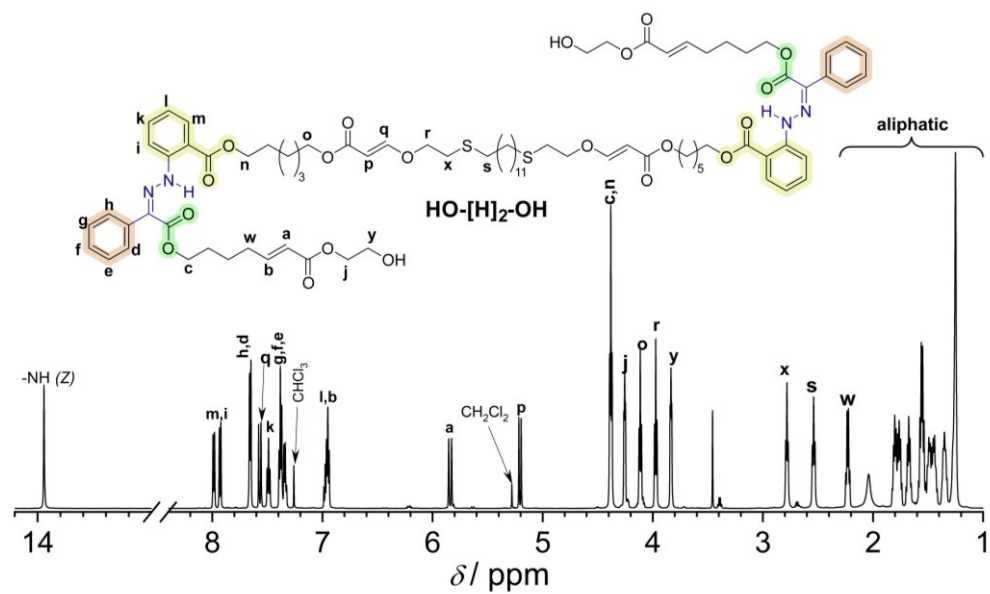


Figure S7.56. ¹H NMR spectrum of *HO*-[H]₂-*OH* in CDCl₃.

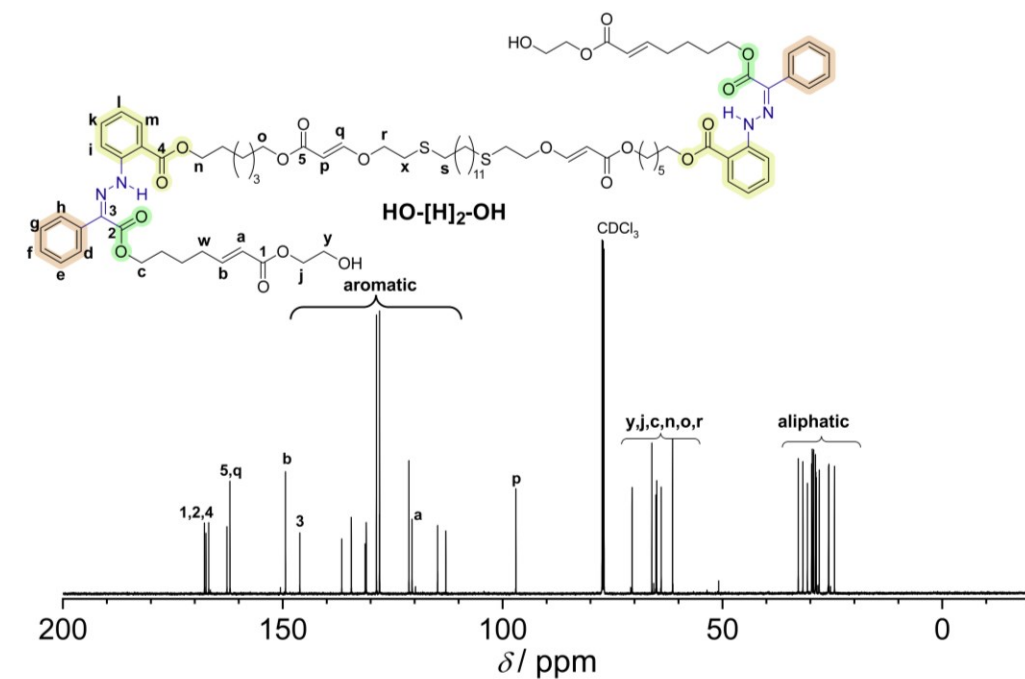


Figure S7.57. ^{13}C NMR spectrum of **HO-[H]₂-OH** in CDCl_3 .

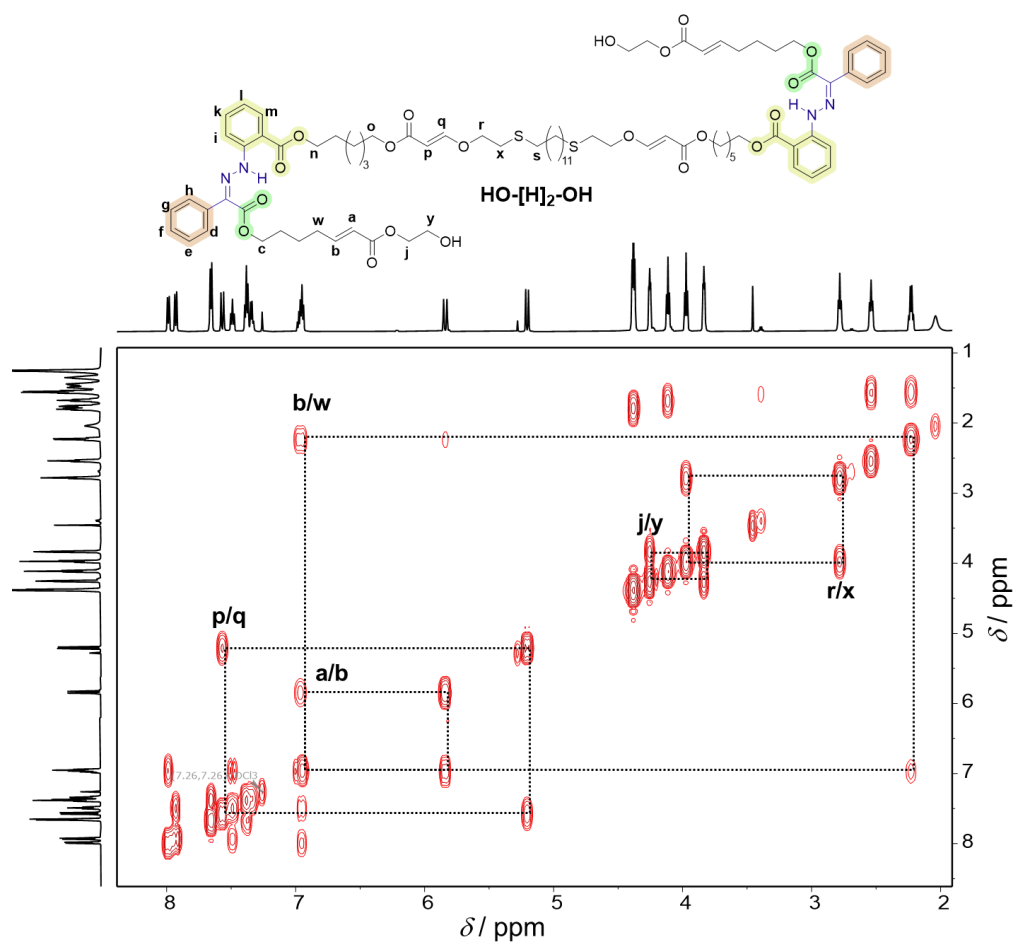
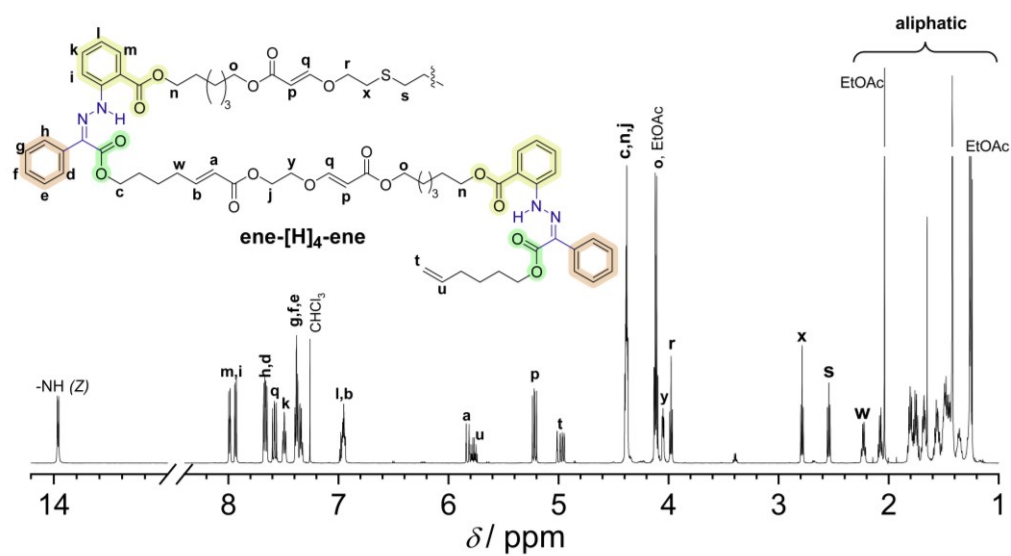
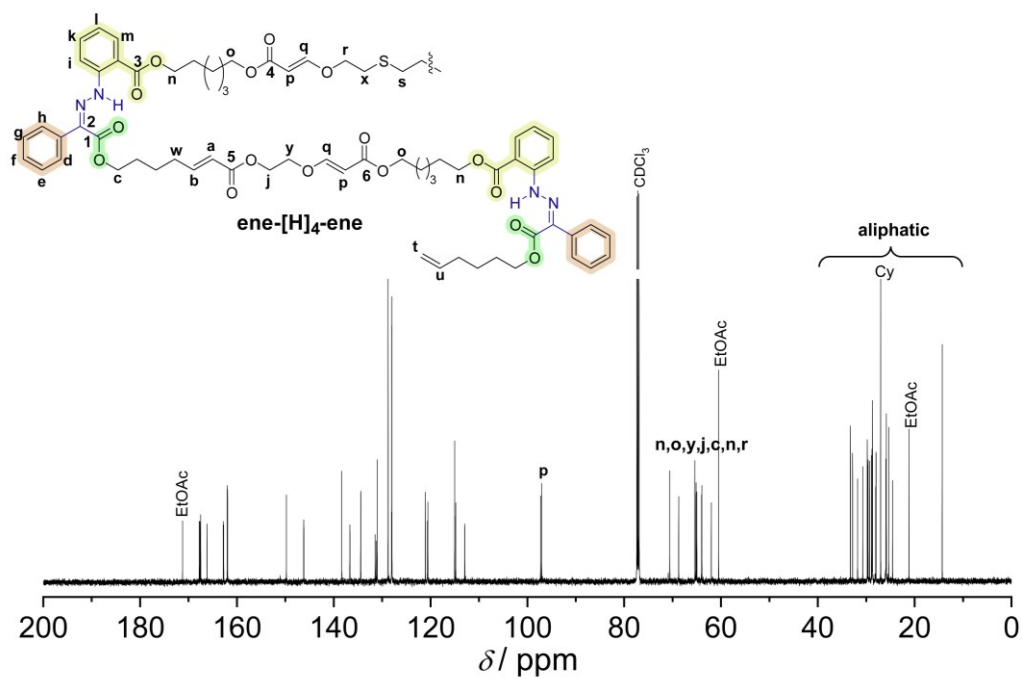


Figure S7.58. COSY NMR spectrum of **HO-[H]₂-OH** in CDCl_3 .

11.7.7.23. ene-[H]₄-eneFigure S7.59. ¹H NMR spectrum of **ene-[H]₄-ene** in CDCl₃.Figure S7.60. ¹³C NMR spectrum of **ene-[H]₄-ene** in CDCl₃.

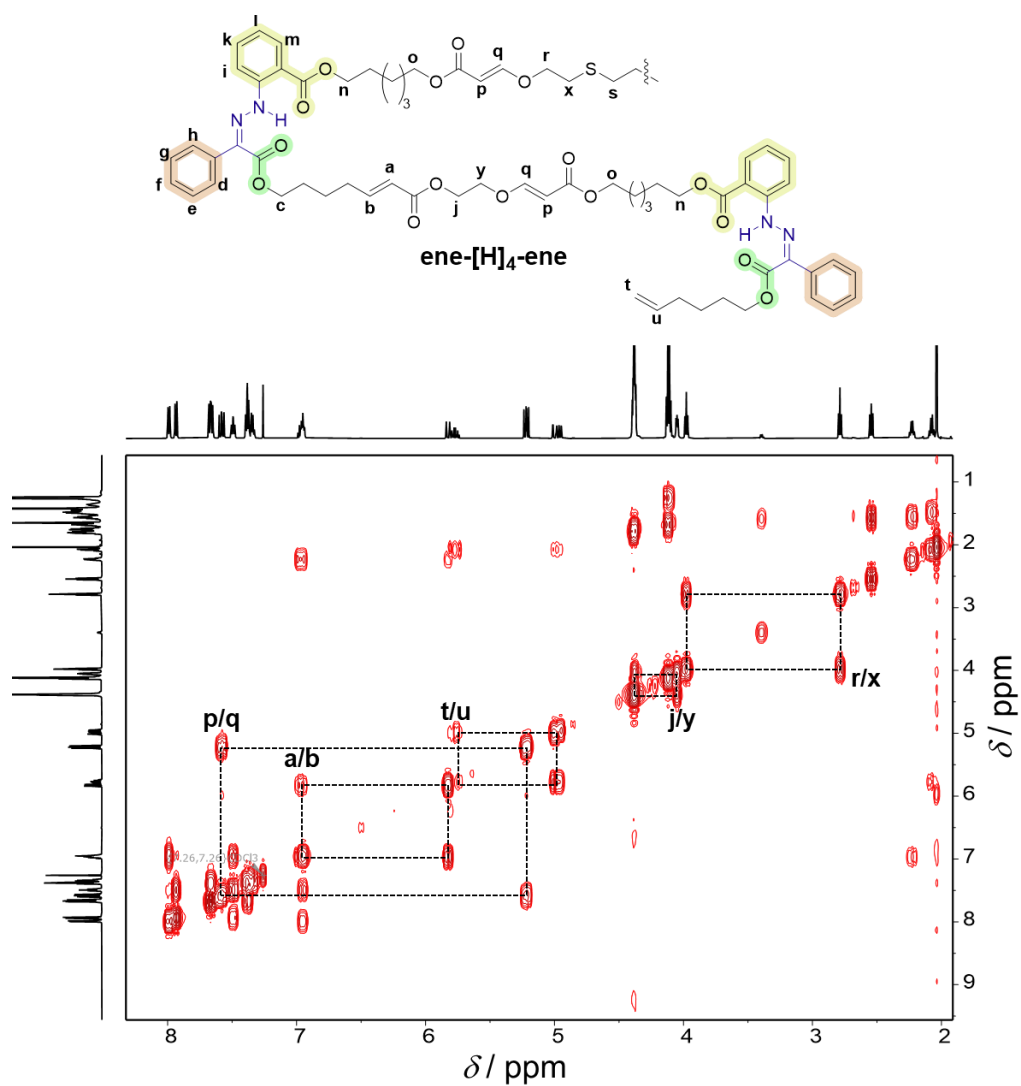
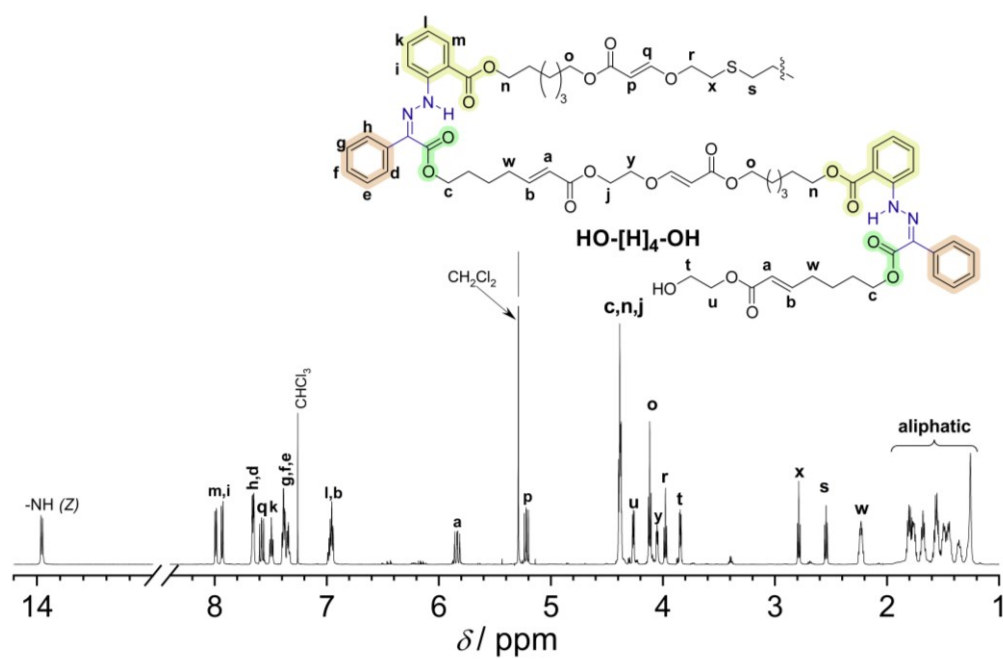
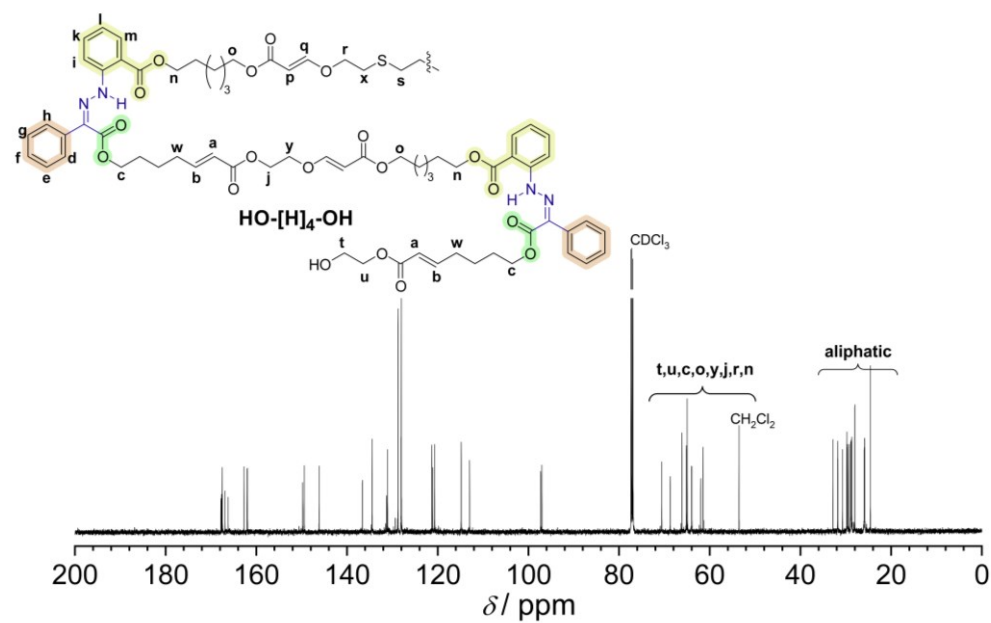


Figure S7.61. COSY NMR spectrum of **ene-[H]₄-ene** in CDCl_3 .

11.7.7.24. HO-[H]₄-OHFigure S7.62. ¹H NMR spectrum of HO-[H]₄-OH in CDCl₃.Figure S7.63. ¹³C NMR spectrum of HO-[H]₄-OH in CDCl₃.

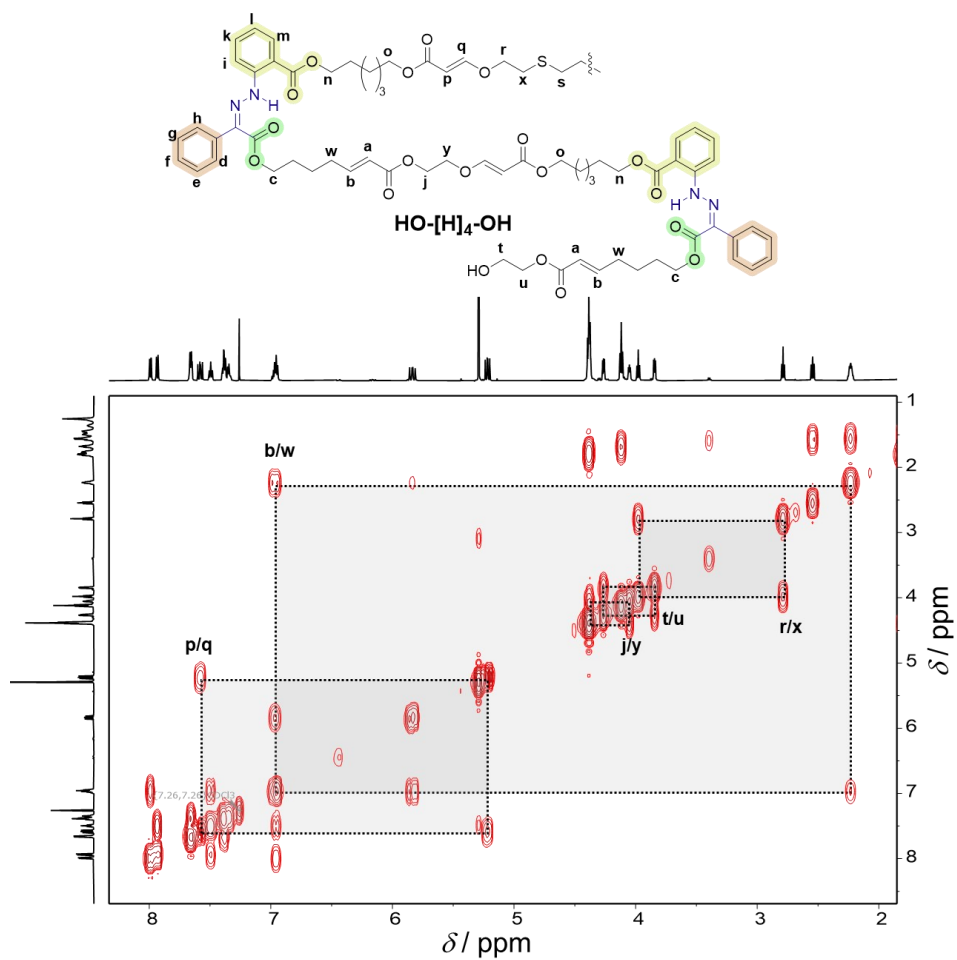
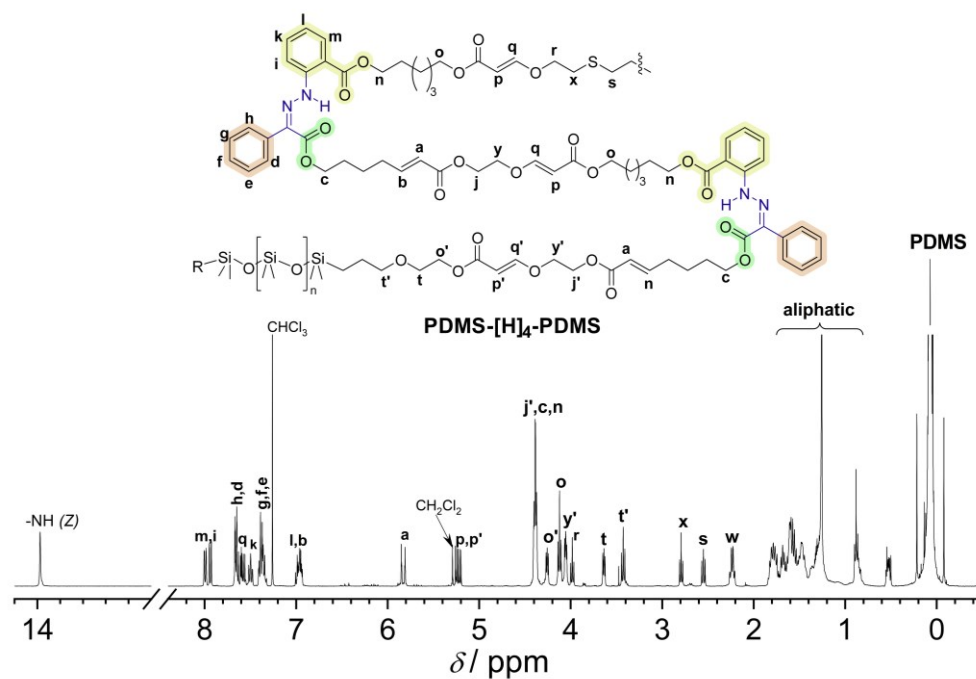


Figure S7.64. COSY NMR spectrum of $\text{HO-[H]}_4\text{-OH}$ in CDCl_3 .

11.7.7.25. PDMS-[H]₄-PDMSFigure S7.65. ¹H NMR spectrum of PDMS-[H]₄-PDMS in CDCl₃.

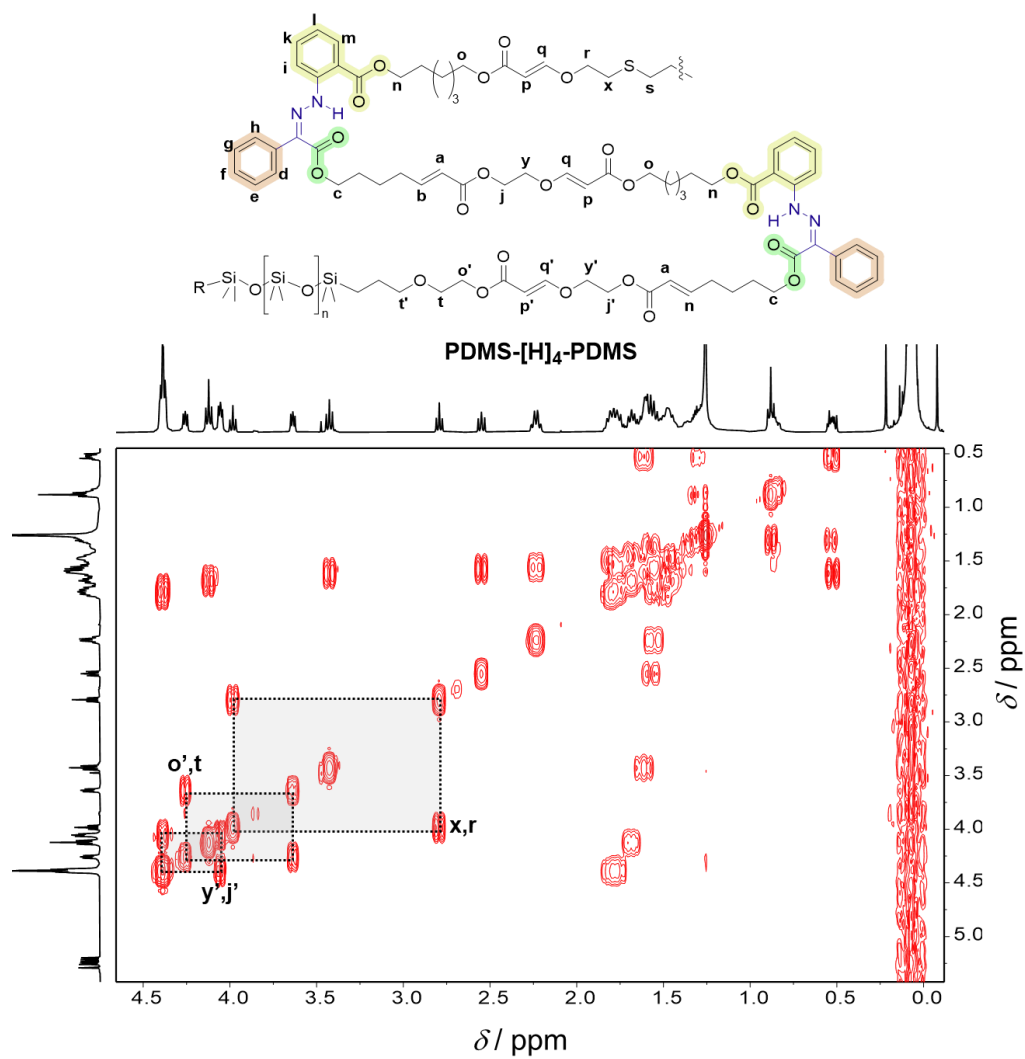


Figure S7.66. Sectional COSY NMR spectrum of **PDMS-[H]₄-PDMS** in CDCl₃.

11.8. Information for Chapter 8

11.8.1. Photochromism study on main-chain polymers in DMAc and Toluene

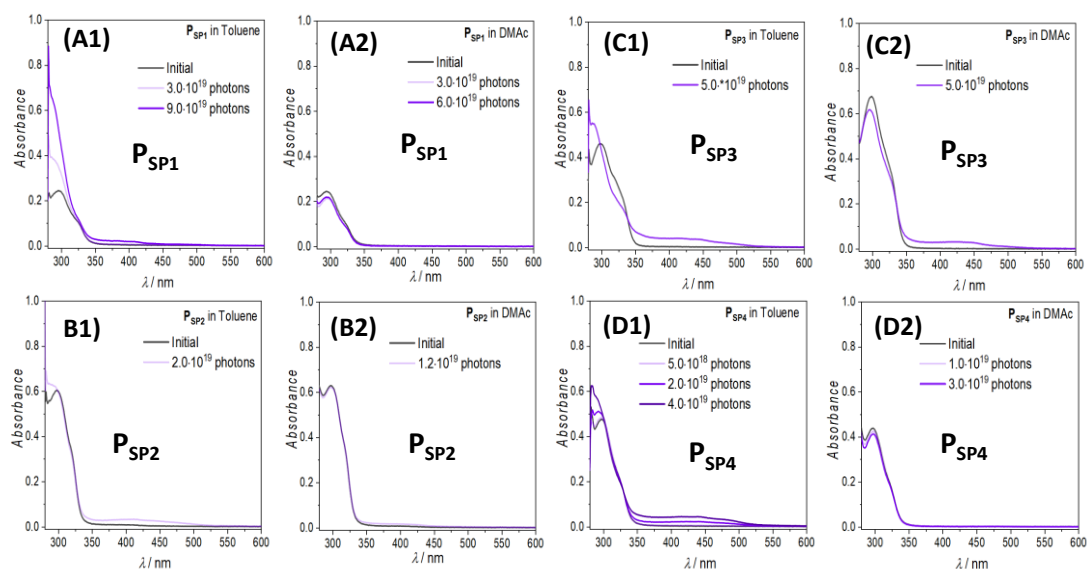


Figure S8.1. UV-vis spectra recorded for P_{SP1} , P_{SP2} , P_{SP3} and P_{SP4} before and after 330 nm irradiation in either toluene or DMAc solvent. Molar concentrations are between 50 and 150 μM .

11.8.2. Halochromism investigated by NMR and SEC

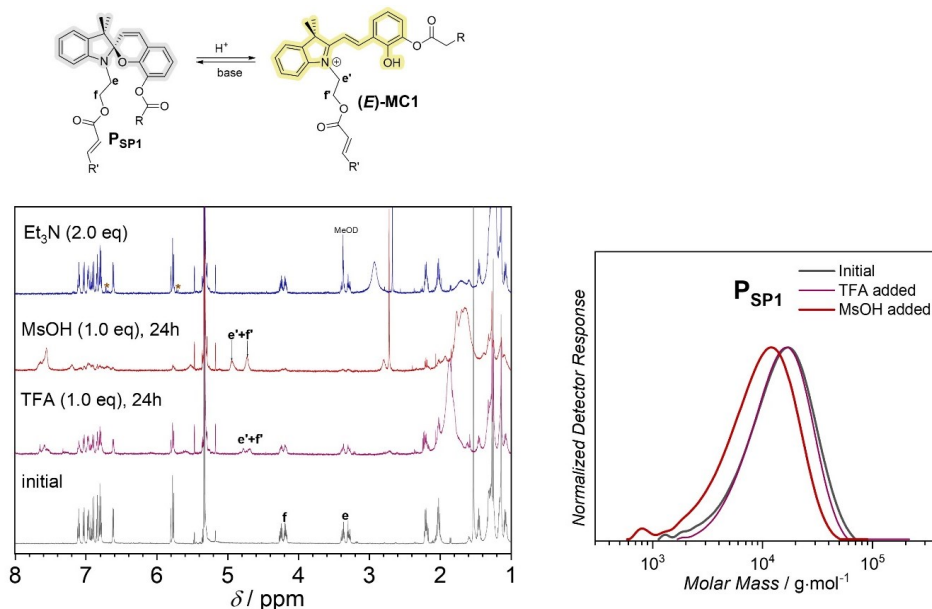


Figure S8.2. ^1H NMR spectra (left) and DMAc-SEC traces (right) of P_{SP1} solution before and after addition of TFA (1.0 eq) and MsOH (1.0 eq). The MsOH-added solution was subsequently quenched with 2.0 eq Et_3N . As can be seen in the NMR spectrum of the Et_3N -quenched polymer solution (top, blue), a small degree of degradation (most likely hydrolysis) was observed (signals marked with an asterisk). The breakage of one bond in the main-chain can cause significant shift in the SEC traces. In addition, side reactions arising from the internal acrylate C-C double bonds (e.g., [2+2]-cyclization) and the damage of the chromophore can be excluded as there is no change in the corresponding resonances of the acrylate C-C double bonds and the chromophore in the Et_3N -quenched polymer solution and the pristine solution.

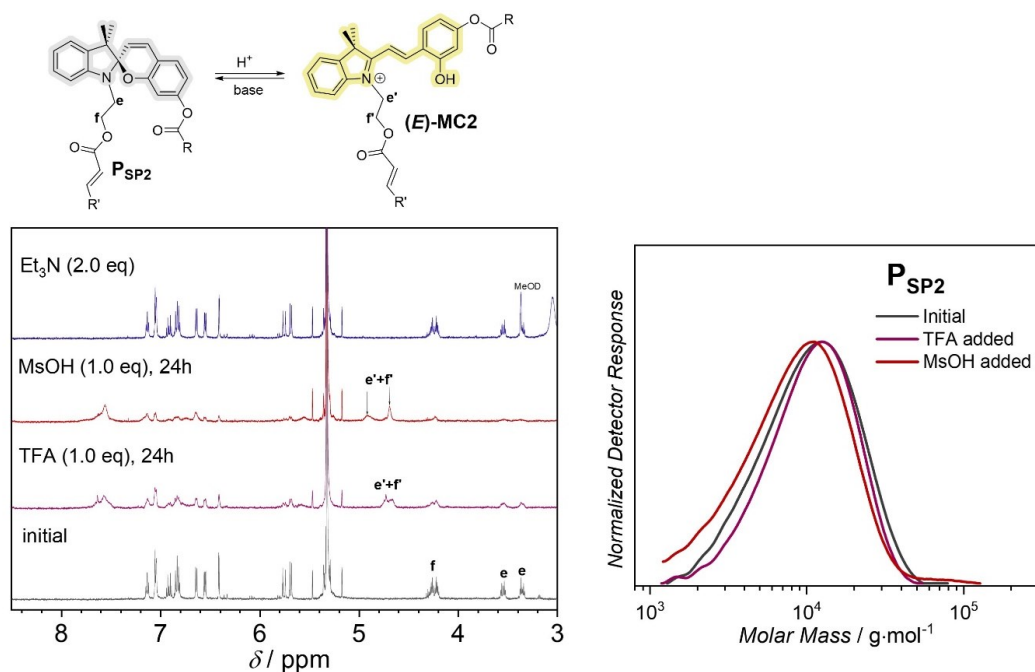


Figure S8.3. 1H NMR spectra (left) and DMac-SEC traces (right) of P_{SP2} solution before and after addition of TFA (1.0 eq) and MsOH (1.0 eq). The MsOH-added solution was subsequently quenched with 2.0 eq Et₃N. Insignificant damage was shown in the NMR spectrum of the Et₃N-quenched polymer solution and the corresponding SEC traces.

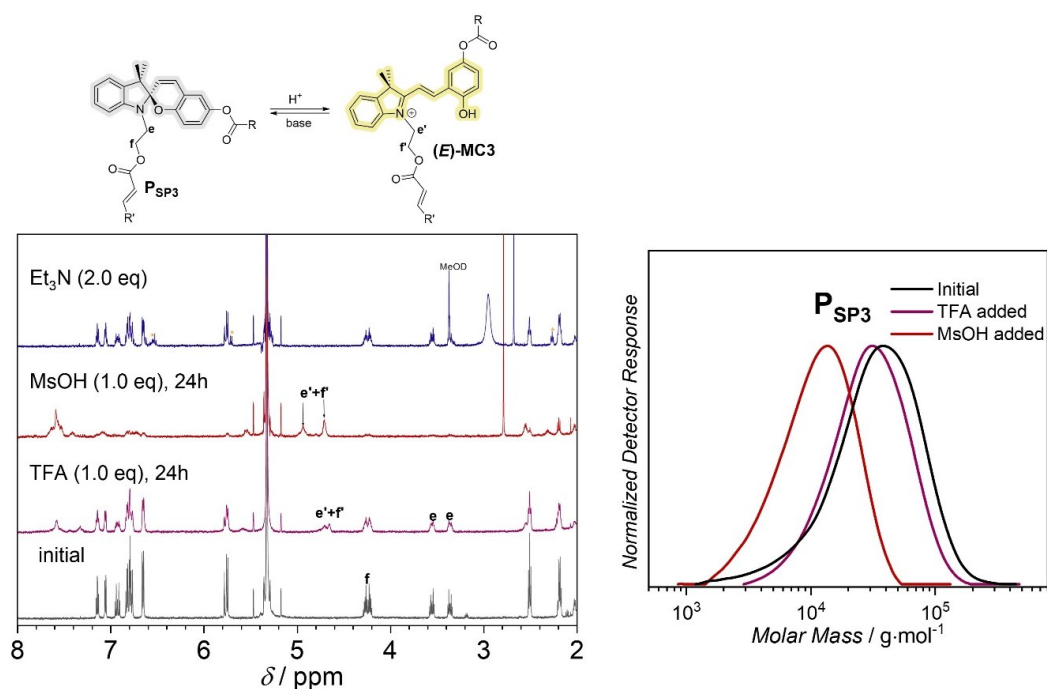


Figure S8.4. 1H NMR spectra (left) and DMac-SEC traces (right) of P_{SP3} solution before and after addition of TFA (1.0 eq) and MsOH (1.0 eq). The MsOH-added solution was subsequently quenched with 2.0 eq Et₃N. Significant degradation (due to hydrolysis of ester bonds) was observed in the MsOH-added solution. The NMR spectrum of the MsOH-added solution quenched with Et₃N (top, blue) also indicates significant degradation (resonances marked with an asterisk). The chromophore and the internal acrylate C-C double bonds remain intact as shown in the NMR spectrum (top, blue).

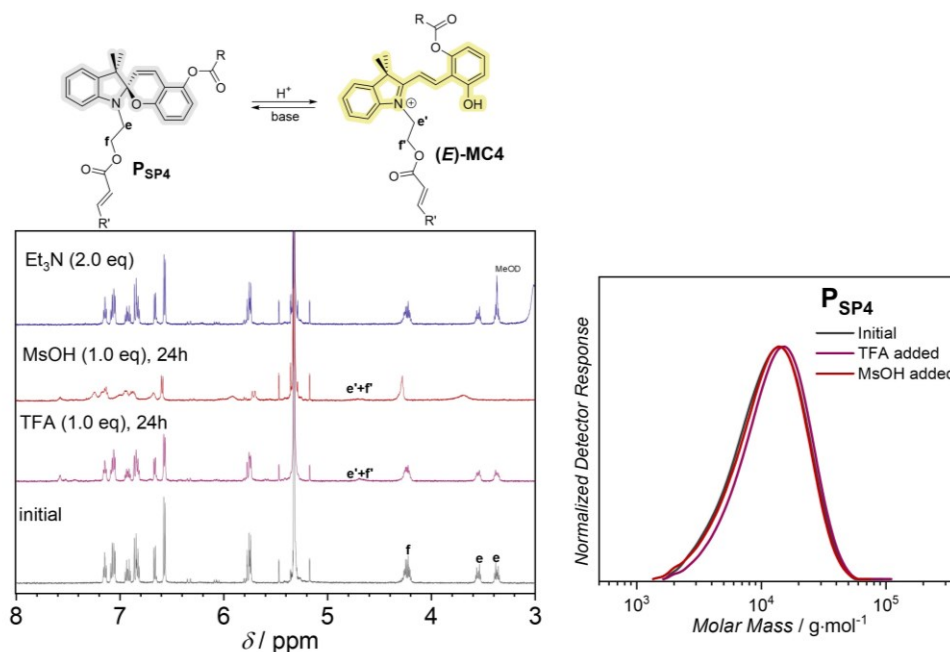


Figure S8.5. 1H NMR spectra (left) and DMac-SEC traces (right) of P_{SP4} solution before and after addition of TFA (1.0 eq) and MsOH (1.0 eq). The MsOH-added solution was subsequently quenched with 2.0 eq Et₃N. Both NMR spectrum and SEC traces confirm the resistance of the polymer solution against hydrolysis induced upon MsOH addition.

11.8.3. UV-vis spectra of P_{SP2} film

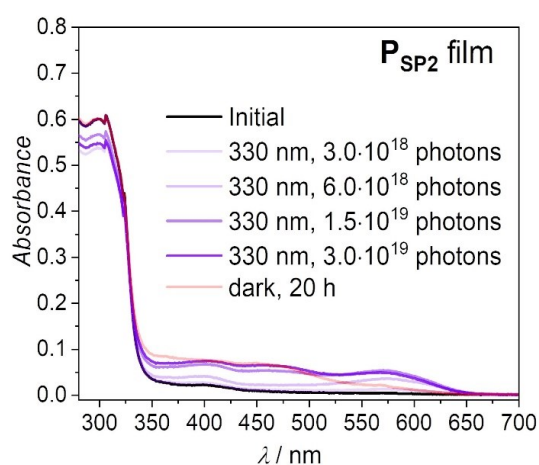


Figure S8.6. UV-vis spectra of P_{SP2} polymer film on a quartz slide before and after 330 nm irradiation. The film was generated by spin-coating of the P_{SP2} solution (60 mg·mL⁻¹) in toluene and subsequently dried at reduced vacuum for 24h before the irradiation experiment (330 nm irradiation, $P = 6.5 \text{ mW} \pm 6.5\%$).

11.8.4. Dynamic Light Scattering (DLS) spectra

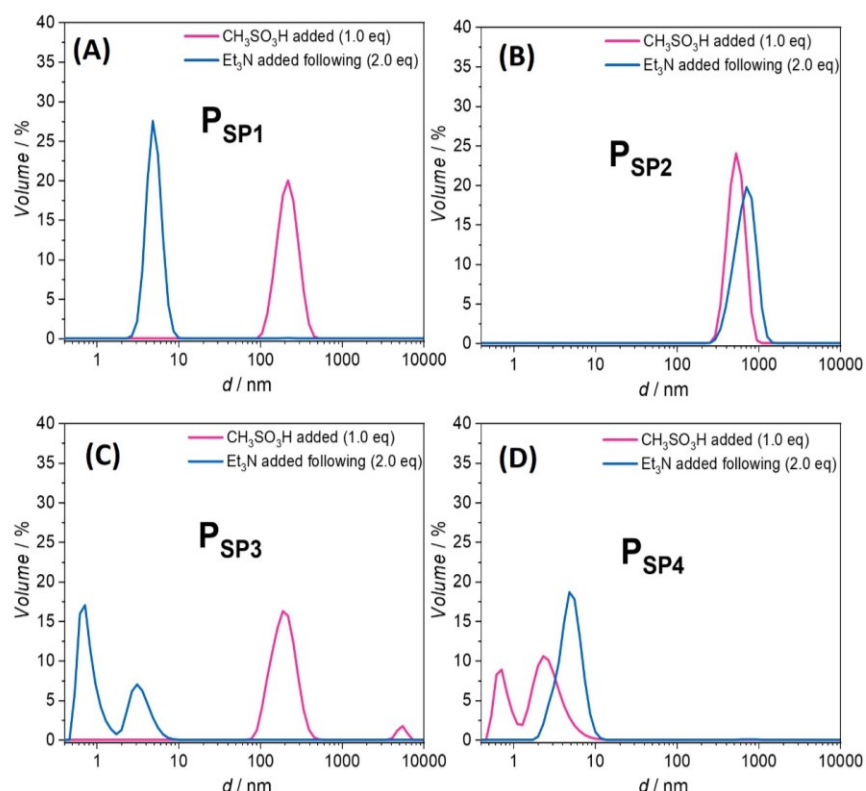


Figure S8.7. DLS size distribution (Volume%) recorded for four polymers after addition of MsOH (1.0 eq) acid in DCM at 25 °C. The polymer solutions were kept in the dark overnight before the measurement.

11.8.5. Synthesis Protocol

11.8.5.1. Synthesis of spiropyran main-chain homopolymers

Synthesis of P_{SP1}

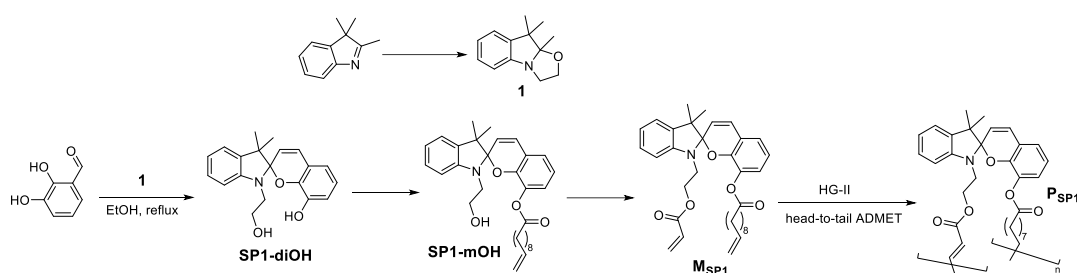


Figure S8.8. Synthesis route for M_{SP1} and P_{SP1} .

Synthesis of compound 1

A solution of 2,3,3-trimethylindolenine (5.0 g, 31.4 mmol, 1.0 eq) and 2-bromoethanol (4.9 mL, 47.1 mmol, 1.2 eq) in 40 mL acetonitrile (ACN) was refluxed overnight. Upon completion, the solvent was removed under reduced pressure and a solution of KOH (120 mL, 0.32 M) was added to the residue. After stirring for approximately 30 minutes, the mixture was extracted with DCM and brine. The organic phase was dried over Na_2SO_4 , followed by evaporation,

yielding compound **1** as purple oil. The product was used for the next reaction without further purification. The ^1H NMR spectrum of the compound matches with the literature spectrum.²⁹⁸

^1H NMR (600 MHz, CDCl_3) δ 7.13 (td, $J = 7.7, 1.3$ Hz, 1H), 7.07 (d, $J = 7.4$ Hz, 1H), 6.92 (t, $J = 7.4$ Hz, 1H), 6.76 (d, $J = 7.8$ Hz, 1H), 3.87 – 3.81 (m, 1H), 3.76 – 3.69 (m, 1H), 3.62 – 3.54 (m, 1H), 3.54 – 3.48 (m, 1H), 1.43 (s, 3H), 1.39 (s, 3H), 1.18 (s, 3H). **LC-MS**: calculated m/z for $\text{C}_{13}\text{H}_{18}\text{NO}^+$ $[\text{M}+\text{H}]^+ = 204.1383$, found 204.1385.

Synthesis of **SP1-diOH**

Compound **1** (1500 mg, 7.4 mmol, 1.0 eq) and 2,3-dihydroxybenzaldehyde (1020 mg, 7.4 mol, 1.0 eq) was added to 15 mL ethanol and the resulting mixture was refluxed overnight. The solvent was subsequently removed under reduced pressure. The product was obtained by crystallization in $\text{ACN}:\text{H}_2\text{O}$ (7/3, v/v) as gray solid (1400 mg, 60% yield).

^1H NMR (600 MHz, CDCl_3) δ 7.16 (td, $J = 7.7, 1.3$ Hz, 1H), 7.08 (dd, $J = 7.2, 1.3$ Hz, 1H), 6.88 – 6.83 (m, 2H), 6.79 (dd, $J = 8.0, 1.6$ Hz, 1H), 6.75 (t, $J = 7.7$ Hz, 1H), 6.66 – 6.62 (m, 2H), 5.71 (d, $J = 10.3$ Hz, 1H), 3.79 (ddd, $J = 11.0, 7.3, 5.1$ Hz, 1H), 3.70 (dt, $J = 11.1, 5.5$ Hz, 1H), 3.50 (ddd, $J = 14.8, 7.4, 5.7$ Hz, 1H), 3.31 (dt, $J = 14.9, 5.2$ Hz, 1H), 1.30 (s, 3H), 1.18 (s, 3H). **^{13}C NMR** (151 MHz, CDCl_3) δ 147.34, 143.42, 140.53, 136.36, 129.79, 127.85, 122.09, 120.93, 120.76, 119.75, 119.67, 118.88, 118.31, 116.03, 106.96, 105.74, 61.15, 52.30, 46.02, 20.01. **LC-MS**: calculated m/z for $\text{C}_{20}\text{H}_{22}\text{NO}_3^+$ $[\text{M}+\text{H}]^+ = 324.1595$, found 324.1596.

Synthesis of **SP1-mOH**

SP1-diOH (1000 mg, 3.09 mmol, 1.0 eq) was dissolved in 15 mL CHCl_3 at 50 °C, followed by triethylamine (Et_3N) (0.43 mL, 3.09 mmol, 1.0 eq). 10-undecenoyl chloride (0.66 mL, 3.09 mmol, 1.0 eq) was added slowly to the mixture. After 18 h, the mixture was washed with water and brine and the organic phase was dried over Na_2SO_4 . The crude product was purified by flash column chromatography (Cy/EtOAc , 7/3, v/v). The product was obtained as an oil (822 mg, 55% yield).

^1H NMR (600 MHz, CDCl_3) δ 7.10 (t, $J = 7.7$ Hz, 1H), 7.04 (d, $J = 7.2$ Hz, 1H), 6.94 (dd, $J = 7.5, 1.6$ Hz, 1H), 6.89 (d, $J = 10.3$ Hz, 1H), 6.86 (dd, $J = 8.0, 1.6$ Hz, 1H), 6.83 – 6.78 (m, 2H), 6.60 (d, $J = 7.7$ Hz, 1H), 5.88 – 5.79 (m, 1H), 5.74 (d, $J = 10.3$ Hz, 1H), 5.01 (d, $J = 17.0$ Hz, 1H), 4.95 (d, $J = 10.2$ Hz, 1H), 3.77 – 3.65 (m, 2H), 3.42 – 3.34 (m, 1H), 3.33 – 3.26 (m, 1H), 2.06 (ddt, $J = 17.9, 13.0, 9.3$ Hz, 4H), 1.39 (q, $J = 7.6$ Hz, 2H), 1.32 – 1.21 (m, 7H), 1.20 – 1.12 (m, 7H), 1.08 (q, $J = 6.8$ Hz, 2H). **LC-MS**: calculated m/z for $\text{C}_{31}\text{H}_{40}\text{NO}_4^+$ $[\text{M}+\text{H}]^+ = 490.2952$, found 490.2962.

Synthesis of **M_{SP1}**

To a solution of **SP1-mOH** (800 mg, 1.63 mmol, 1.0 eq) and Et_3N (0.25 mL, 1.82 mmol, 1.12 eq) in DCM (2.5 mL), acryloyl chloride (0.15 mL, 1.80 mmol, 1.1 eq) was slowly added at 0 °C. After 18 h, the reaction mixture was washed with water and brine, and the organic phase was

dried over Na_2SO_4 . Pure product was obtained by flash column chromatography (Cy/EtOAc, 9/1, v/v) as an oil (700 mg, 79% yield).

^1H NMR (600 MHz, CDCl_3) δ 7.11 (t, J = 7.7 Hz, 1H), 7.03 (dd, J = 7.2, 1.2 Hz, 1H), 6.94 (dd, J = 7.5, 1.6 Hz, 1H), 6.89 – 6.84 (m, 2H), 6.83 – 6.78 (m, 2H), 6.62 (d, J = 7.7 Hz, 1H), 6.37 (dd, J = 17.4, 1.4 Hz, 1H), 6.08 (dd, J = 17.3, 10.5 Hz, 1H), 5.87 – 5.82 (m, 1H), 5.81 (dd, J = 10.5, 1.5 Hz, 1H), 5.75 (d, J = 10.3 Hz, 1H), 5.01 (dd, J = 17.2, 1.6 Hz, 1H), 4.95 (dd, J = 10.2, 1.0 Hz, 1H), 4.27 (t, J = 6.3 Hz, 2H), 3.46 – 3.40 (m, 1H), 3.38 – 3.32 (m, 1H), 2.09 – 1.99 (m, 4H), 1.39 (q, J = 7.6 Hz, 2H), 1.34 – 1.20 (m, 7H), 1.19 – 1.11 (m, 7H), 1.10 – 1.03 (m, 2H). **^{13}C NMR** (151 MHz, CDCl_3) δ 171.81, 166.13, 147.14, 145.04, 139.34, 138.04, 136.51, 130.97, 129.47, 128.50, 127.53, 126.96, 124.20, 123.01, 121.53, 119.89, 119.85, 119.51, 119.39, 63.00, 51.73, 42.51, 34.11, 33.96, 33.88, 33.87, 29.43, 29.23, 29.21, 29.07, 29.03, 25.96, 24.66, 19.67. **LC-MS**: calculated m/z for $\text{C}_{34}\text{H}_{42}\text{NO}_5^+$ $[\text{M}+\text{H}]^+ = 544.3058$, found 544.3068.

Synthesis of P_{SP1}

Monomer M_{SP1} (200 mg, 0.37 mmol) was dissolved in CH_2Cl_2 in a crimp vial. The solution was heated to 40 °C upon addition of Hoveyda-Grubbs 2nd generation (**HG-II**) (4.6 mg, 2 mol%) and a needle was pierced into the septum to allow the ethylene gas generated from the reaction to escape. After 18 h, ethyl vinyl ether (0.02 mL) was injected into the mixture and the solution was stirred for 30 min. The polymer was precipitated in methanol and collected via centrifugation and dried under vacuum at 40 °C.

Synthesis of P_{SP2}

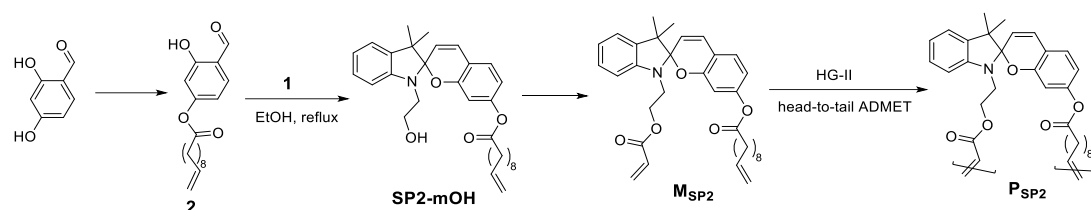


Figure S8.9. Synthesis route for monomer M_{SP2} and polymer P_{SP2} .

Synthesis of compound 2

2,4-Dihydroxybenzaldehyde (2 000 mg, 14.48 mmol, 1.0 eq), 10-undecenoic acid (2668 mg, 14.48 mmol, 1.0 eq) and DMAP (354 mg, 2.9 mol, 0.2 eq) were dissolved in CHCl_3 at 50 °C. DCC (3017 mg, 14.6 mmol, 1.05 eq) was added in portion to the reaction mixture. The reaction was stirred overnight at 50 °C. After 18 h, the precipitate was filtered out and the residue was purified by flash column chromatography (cyclohexane:ethyl acetate, 95-80/5-20, v/v), yielding the product as an oil (2 500 mg, 56% yield).

^1H NMR (600 MHz, CDCl_3) δ 11.21 (s, 1H), 9.85 (s, 1H), 7.56 (d, J = 8.4 Hz, 1H), 6.78 (dd, J = 8.4, 2.1 Hz, 1H), 6.74 (d, J = 2.1 Hz, 1H), 5.81 (ddt, J = 17.0, 10.2, 6.7 Hz, 1H), 5.00 (ddt, J = 17.1, 2.2, 1.6 Hz, 1H), 4.93 (ddt, J = 10.2, 2.3, 1.2 Hz, 1H), 2.56 (t, J = 7.5 Hz, 2H), 2.08 – 2.02 (m, 2H), 1.78 – 1.71 (m, 2H), 1.41 – 1.29 (m, 10H). **^{13}C NMR** (151 MHz, CDCl_3) δ 195.59,

171.38, 163.28, 157.60, 139.30, 135.04, 118.74, 114.33, 114.07, 110.82, 34.54, 33.91, 29.40, 29.30, 29.17, 29.15, 29.02, 27.06, 24.91. **LC-MS**: calculated m/z for $C_{18}H_{23}O_4^-$ $[M-H]^-$ = 303.1601, found 303.1601.

Synthesis of SP2-mOH

Compound **1** (1255 mg, 4.90 mol, 1.0 eq) and compound **2** (1500 mg, 4.90 mmol, 1.0 eq) were dissolved in ethanol (10 mL) and the solution was refluxed overnight. The solvent was subsequently removed, and the product (1500 mg, 62% yield) was obtained by column chromatography (cyclohexane/ethyl acetate, 95-50/50, v/v).

1H NMR (600 MHz, $CDCl_3$) δ 7.16 (td, J = 7.7, 1.3 Hz, 1H), 7.07 (dd, J = 7.2, 1.3 Hz, 1H), 7.02 (d, J = 8.2 Hz, 1H), 6.86 (td, J = 7.4, 0.9 Hz, 1H), 6.82 (dd, J = 10.3, 0.7 Hz, 1H), 6.63 (d, J = 7.8 Hz, 1H), 6.57 (dd, J = 8.2, 2.2 Hz, 1H), 6.45 (dd, J = 2.2, 0.7 Hz, 1H), 5.80 (ddt, J = 16.9, 10.2, 6.7 Hz, 1H), 5.66 (d, J = 10.2 Hz, 1H), 5.01 – 4.96 (m, 1H), 4.92 (ddt, J = 10.2, 2.3, 1.2 Hz, 1H), 3.75 (ddt, J = 35.3, 11.1, 6.0 Hz, 2H), 3.49 (ddd, J = 14.9, 7.4, 5.3 Hz, 1H), 3.31 (dt, J = 15.0, 5.1 Hz, 1H), 2.48 (t, J = 7.5 Hz, 2H), 2.06 – 2.01 (m, 2H), 1.69 (p, J = 7.5 Hz, 2H), 1.40 – 1.34 (m, 4H), 1.30 (d, J = 5.7 Hz, 9H), 1.17 (s, 3H). **^{13}C NMR** (151 MHz, $CDCl_3$) δ 172.13, 154.78, 151.87, 147.46, 139.32, 136.52, 129.04, 127.72, 127.36, 121.97, 119.60, 119.15, 116.55, 114.29, 113.77, 108.83, 106.84, 105.10, 61.06, 52.39, 46.26, 34.50, 33.91, 29.39, 29.32, 29.18, 29.15, 29.01, 26.02, 25.04, 20.40. **LC-MS**: calculated m/z for $C_{31}H_{40}NO_4^+$ $[M+H]^+$ = 490.2951, found 490.2952.

Synthesis of M_{SP2}

To a solution of **SP2-mOH** (600 mg, 1.22 mmol, 1.0 eq) and Et_3N (0.22 mL, 1.37 mmol, 1.12 eq) in DCM (2.5 mL) acryloyl chloride (0.11 mL, 1.37 mmol, 1.12 eq) was slowly added at 0 °C. After 18 h, the reaction mixture was washed with water and brine, and the organic phase was dried over Na_2SO_4 . Pure product was obtained by flash column chromatography (cyclohexane/ethyl acetate, 9/1, v/v) as an oil (400 mg, 60% yield).

1H NMR (600 MHz, $CDCl_3$) δ 7.17 (td, J = 7.7, 1.3 Hz, 1H), 7.07 (dd, J = 7.2, 1.3 Hz, 1H), 7.02 (d, J = 8.2 Hz, 1H), 6.85 (td, J = 7.4, 0.9 Hz, 1H), 6.82 (d, J = 10.3 Hz, 1H), 6.66 (d, J = 7.8 Hz, 1H), 6.56 (dd, J = 8.2, 2.2 Hz, 1H), 6.45 – 6.44 (m, 1H), 6.38 (dd, J = 17.3, 1.4 Hz, 1H), 6.08 (dd, J = 17.4, 10.5 Hz, 1H), 5.84 – 5.77 (m, 2H), 5.67 (d, J = 10.2 Hz, 1H), 4.99 (dq, J = 17.1, 1.7 Hz, 1H), 4.92 (ddt, J = 10.2, 2.3, 1.2 Hz, 1H), 4.31 (t, J = 6.4 Hz, 2H), 3.57 (dt, J = 15.1, 6.7 Hz, 1H), 3.40 (dt, J = 15.1, 6.1 Hz, 1H), 2.48 (t, J = 7.5 Hz, 2H), 2.05 – 2.01 (m, 2H), 1.70 (p, J = 7.5 Hz, 2H), 1.40 – 1.34 (m, 4H), 1.33 – 1.22 (m, 9H), 1.14 (s, 3H). **^{13}C NMR** (151 MHz, $CDCl_3$) δ 172.13, 166.14, 154.95, 151.85, 147.21, 139.30, 136.40, 131.09, 129.02, 128.41, 127.72, 127.31, 121.86, 119.50, 119.05, 116.42, 114.28, 113.60, 108.82, 106.60, 104.93, 62.90, 52.35, 42.57, 34.49, 33.91, 29.38, 29.31, 29.17, 29.15, 29.01, 25.99, 25.04, 20.15. **LC-MS**: calculated m/z for $C_{34}H_{42}NO_5^+$ $[M+H]^+$ = 544.3058, found 544.3057.

Synthesis of P_{SP2}

Monomer M_{SP2} (200 mg, 0.37 mol) was dissolved in 1,2-dichlorobenzene (DCB) in a vial which can be attached to the vacuum pump. After HG-II catalyst (4.6 mg, 2 mol%) was added, the mixture was heated to 50 °C at 200 mbar. After 2 h, the pressure was reduced to 100 mbar for 1 h, after which the pressure was further reduced to 50 mbar for 30 minutes. The total reaction time was 3.5 h. Upon completion, ethyl vinyl ether (0.05 mL) was added, and the solution was stirred at ambient pressure for 30 minutes. The polymer was precipitated twice in MeOH and collected via centrifugation and dried under vacuum at 40 °C.

Synthesis of P_{SP3}

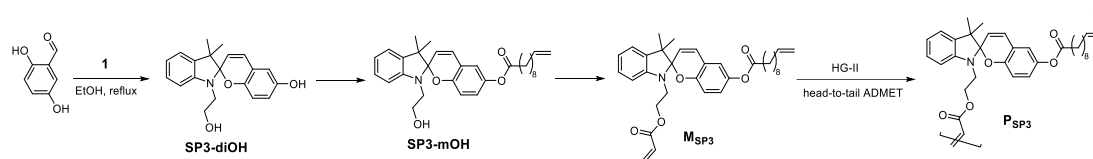


Figure S8.10. Synthesis route for M_{SP3} and P_{SP3} .

Synthesis of $SP3\text{-diOH}$

Compound **1** (1800 mg, 8.82 mmol, 1.0 eq) and 2,5-dihydroxybenzaldehyde (1217 mg, 8.82 mol, 1.0 eq) were added to 18 mL ethanol and the resulting mixture was refluxed overnight. The solvent was subsequently removed under reduced pressure. The product was obtained by crystallization in ACN:H₂O (7/3, v/v) as gray solid (1000 mg, 35% yield). ¹H NMR spectrum matches with the literature spectrum.²³⁸

¹H NMR (600 MHz, CDCl₃) δ 7.15 (td, J = 7.7, 1.3 Hz, 1H), 7.07 (dd, J = 7.3, 1.3 Hz, 1H), 6.84 (td, J = 7.4, 0.9 Hz, 1H), 6.71 (d, J = 10.2 Hz, 1H), 6.60 (d, J = 7.8 Hz, 1H), 6.55 – 6.51 (m, 3H), 5.66 (d, J = 10.2 Hz, 1H), 3.80 (ddd, J = 11.2, 6.2, 4.8 Hz, 1H), 3.73 (ddd, J = 11.2, 6.6, 4.5 Hz, 1H), 3.54 (ddd, J = 15.1, 6.7, 4.9 Hz, 1H), 3.37 (ddd, J = 15.0, 6.2, 4.5 Hz, 1H), 1.29 (s, 3H), 1.14 (s, 3H). **LC-MS**: calculated m/z for C₂₀H₂₂NO₃⁺ [M+H]⁺ = 324.1595, found 324.1587.

Synthesis of $SP3\text{-mOH}$

SP3-diOH (500 mg, 1.54 mmol, 1.0 eq) was dissolved in 18 mL CHCl₃ at 50 °C, followed by triethylamine (Et₃N) (0.22 mL, 1.54 mmol, 1.0 eq). 10-undecenoyl chloride (0.33 mL, 1.54 mmol, 1.0 eq) was slowly added to the mixture. After 18 h, the mixture was washed with water and brine, and the organic phase was dried over Na₂SO₄. The crude product was purified by flash column chromatography (cyclohexane/ethyl acetate, 7/3, v/v). The product was obtained as an oil (490 mg, 65% yield).

¹H NMR (600 MHz, CDCl₃) δ 7.16 (td, J = 7.7, 1.3 Hz, 1H), 7.09 – 7.07 (m, 1H), 6.86 (t, J = 7.4 Hz, 1H), 6.78 (tt, J = 5.0, 2.5 Hz, 3H), 6.70 – 6.66 (m, 1H), 6.64 (d, J = 7.8 Hz, 1H), 5.81 (ddt, J = 16.9, 10.2, 6.7 Hz, 1H), 5.72 (d, J = 10.2 Hz, 1H), 5.02 – 4.97 (m, 1H), 4.93 (ddt, J = 10.2, 2.3, 1.3 Hz, 1H), 3.79 – 3.71 (m, 2H), 3.53 – 3.46 (m, 1H), 3.37 – 3.28 (m, 1H), 2.52 (s, 2H),

2.08 – 2.02 (m, 2H), 1.73 (p, $J = 7.5$ Hz, 2H), 1.41 – 1.36 (m, 4H), 1.36 – 1.28 (m, 9H), 1.17 (s, 3H). **LC-MS**: calculated m/z for $C_{31}H_{40}NO_4^+$ $[M+H]^+ = 490.2952$, found 490.2946.

Synthesis of M_{SP3}

To a solution of **SP3-mOH** (500 mg, 1.02 mmol, 1.0 eq) and Et_3N (0.17 mL, 1.23 mmol, 1.2 eq) acryloyl chloride (0.10 mL, 1.23 mmol, 1.2 eq) was slowly added at 0 °C. After 18 h, the reaction mixture was washed with water and brine, and the organic phase was dried over Na_2SO_4 . Pure product was obtained by flash column chromatography (cyclohexane/ethyl acetate, 9/1, v/v) as an oil (500 mg, 80% yield).

1H NMR (600 MHz, $CDCl_3$) δ 7.17 (t, $J = 7.5$ Hz, 1H), 7.07 (d, $J = 7.2$ Hz, 1H), 6.86 (t, $J = 7.4$ Hz, 1H), 6.81 – 6.74 (m, 3H), 6.66 (d, $J = 8.1$ Hz, 2H), 6.38 (d, $J = 17.3$ Hz, 1H), 6.07 (dd, $J = 17.4, 10.4$ Hz, 1H), 5.85 – 5.78 (m, 2H), 5.72 (d, $J = 10.1$ Hz, 1H), 5.00 (d, $J = 16.8$ Hz, 1H), 4.94 (d, $J = 9.8$ Hz, 1H), 4.30 (t, $J = 6.3$ Hz, 2H), 3.61 – 3.55 (m, 1H), 3.40 (dt, $J = 15.0, 6.1$ Hz, 1H), 2.52 (t, $J = 7.4$ Hz, 2H), 2.05 (td, $J = 8.7, 4.2$ Hz, 2H), 1.73 (q, $J = 7.5$ Hz, 2H), 1.42 – 1.28 (m, 13H), 1.14 (s, 3H). **^{13}C NMR** (151 MHz, $CDCl_3$) δ 172.79, 166.13, 151.66, 147.21, 143.83, 139.29, 136.39, 131.10, 129.09, 128.39, 127.74, 122.66, 121.88, 120.53, 119.52, 119.47, 118.88, 115.75, 114.31, 106.58, 104.75, 62.90, 52.44, 42.55, 34.45, 33.91, 29.41, 29.33, 29.21, 29.18, 29.02, 25.96, 25.09, 20.22. **LC-MS**: calculated m/z for $C_{34}H_{42}NO_5^+$ $[M+H]^+ = 544.3058$, found 544.3053.

Synthesis of P_{SP3}

Monomer M_{SP3} (200 mg, 0.37 mol) was dissolved in CH_2Cl_2 in a crimp vial. The solution was heated to 40 °C upon addition of Hoveyda-Grubbs 2nd generation (**HG-II**) (4.6 mg, 2 mol%) and a needle was pierced into the septum to allow the ethylene gas generated from the reaction to escape. After 18 h, ethyl vinyl ether (0.02 mL) was injected into the mixture and the solution was stirred for 30 min. The polymer was precipitated in methanol and collected via centrifugation and dried under vacuum at 40 °C.

Synthesis of P_{SP4}

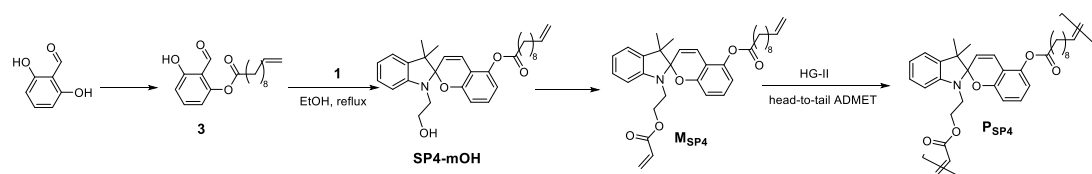


Figure S8.11. Synthesis route for M_{SP4} and P_{SP4} .

Synthesis of compound 3

2,6-dihydroxybenzaldehyde (1500 mg, 10.86 mmol, 1.0 eq), 10-undecenoic acid (2 000 mg, 10.86 mmol, 1.0 eq) and DMAP (265 mg, 2.17 mol, 0.2 eq) was dissolved in $CHCl_3$ at 50 °C. DCC (2260 mg, 10.97 mmol, 1.01 eq) and added in portions to the reaction mixture. The reaction was stirred overnight at 50 °C. After 18 h, the precipitate was filtered off and the

residue was purified by flash column chromatography (cyclohexane/ethyl acetate, 95-80/5-20, v/v), yielding the product as an oil (1700 mg, 51% yield).

¹H NMR (600 MHz, CDCl₃) δ 11.21 (s, 1H), 9.85 (s, 1H), 7.56 (d, J = 8.4 Hz, 1H), 6.78 (dd, J = 8.4, 2.1 Hz, 1H), 6.74 (d, J = 2.1 Hz, 1H), 5.81 (ddt, J = 17.0, 10.2, 6.7 Hz, 1H), 5.00 (ddt, J = 17.1, 2.2, 1.6 Hz, 1H), 4.93 (ddt, J = 10.2, 2.3, 1.2 Hz, 1H), 2.56 (t, J = 7.5 Hz, 2H), 2.08 – 2.02 (m, 2H), 1.78 – 1.71 (m, 2H), 1.41 – 1.29 (m, 10H). **¹³C NMR** (151 MHz, CDCl₃) δ 195.59, 171.38, 163.28, 157.60, 139.30, 135.04, 118.74, 114.33, 114.07, 110.82, 34.54, 33.91, 29.40, 29.30, 29.17, 29.15, 29.02, 24.91. **LC-MS**: calculated m/z for C₁₈H₂₅O₄⁺ [M+H]⁺ = 303.1601, found 303.1602.

Synthesis of SP4-mOH

Compound **1** (1 000 mg, 4.93 mmol, 1.0 eq) and compound **3** (1 700 mg, 4.93 mmol, 1.0 eq) was dissolved in ethanol (10 mL) and the solution was refluxed overnight. The solvent was subsequently removed and the product (1 600 mg, 66% yield) was obtained by column chromatography (cyclohexane/ethyl acetate, 95-50/50, v/v).

¹H NMR (600 MHz, CDCl₃) δ 7.17 (td, J = 7.7, 1.3 Hz, 1H), 7.10 – 7.05 (m, 2H), 6.88 – 6.83 (m, 2H), 6.64 (d, J = 7.8 Hz, 1H), 6.60 (ddd, J = 8.1, 2.8, 0.9 Hz, 2H), 5.83 (ddt, J = 17.0, 10.2, 6.7 Hz, 1H), 5.73 (d, J = 10.4 Hz, 1H), 5.01 (ddd, J = 17.1, 2.1, 1.5 Hz, 1H), 4.95 (ddt, J = 10.2, 2.3, 1.3 Hz, 1H), 3.77 (ddd, J = 11.2, 7.2, 5.0 Hz, 1H), 3.72 (dt, J = 11.2, 5.5 Hz, 1H), 3.50 (ddd, J = 14.9, 7.3, 5.5 Hz, 1H), 3.32 (dt, J = 15.0, 5.2 Hz, 1H), 2.62 (t, J = 7.6 Hz, 2H), 2.14 – 2.02 (m, 2H), 1.80 (p, J = 7.6 Hz, 2H), 1.42 – 1.28 (m, 13H), 1.17 (s, 3H). **¹³C NMR** (151 MHz, CDCl₃) δ 172.11, 154.84, 147.38, 146.80, 139.26, 136.43, 129.69, 127.75, 123.38, 121.96, 120.41, 119.57, 114.33, 113.95, 112.92, 112.08, 106.79, 104.63, 60.99, 52.43, 46.19, 34.41, 33.92, 29.43, 29.34, 29.30, 29.19, 29.03, 25.99, 25.14, 20.40. **LC-MS**: calculated m/z for C₃₁H₄₀NO₄⁺ [M+H]⁺ = 490.2952, found 490.2949.

Synthesis of M_{SP4}

To a solution of **SP4-mOH** (600 mg, 1.22 mmol, 1.0 eq) and Et₃N (0.22 mL, 1.31 eq) acryloyl chloride (0.13 mL, 1.60 mmol, 1.30 eq) was slowly added at 0 °C. After 18 h, the reaction mixture was washed with water and brine, and the organic phase was dried over Na₂SO₄. Pure product was obtained by flash column chromatography (cyclohexane/ethyl acetate, 9/1, v/v) as an oil (450 mg, 68% yield).

¹H NMR (600 MHz, CDCl₃) δ 7.18 (td, J = 7.7, 1.3 Hz, 1H), 7.09 – 7.04 (m, 2H), 6.90 – 6.82 (m, 2H), 6.68 (d, J = 7.8 Hz, 1H), 6.58 (d, J = 8.2 Hz, 2H), 6.37 (dd, J = 17.4, 1.4 Hz, 1H), 6.07 (dd, J = 17.4, 10.5 Hz, 1H), 5.89 – 5.78 (m, 2H), 5.72 (d, J = 10.4 Hz, 1H), 5.01 (dq, J = 17.1, 1.7 Hz, 1H), 4.94 (ddt, J = 10.2, 2.3, 1.2 Hz, 1H), 4.30 (t, J = 6.4 Hz, 2H), 3.60 (dt, J = 13.9, 6.6 Hz, 1H), 3.41 (dt, J = 15.1, 6.2 Hz, 1H), 2.62 (t, J = 7.6 Hz, 2H), 2.10 – 2.03 (m, 2H), 1.80 (p, J = 7.6 Hz, 2H), 1.51 – 1.32 (m, 12H), 1.29 (s, 3H), 1.13 (s, 1H). **¹³C NMR** (151 MHz, CDCl₃) δ 172.05, 166.14, 155.04, 147.22, 146.77, 139.27, 136.34, 131.08, 129.64, 128.39, 127.74, 123.39, 121.89, 120.35, 119.51, 114.34, 113.78, 112.92, 111.86, 106.64, 104.63, 62.91, 52.52,

42.52, 34.42, 33.92, 29.43, 29.34, 29.30, 29.19, 29.03, 25.88, 25.15, 20.17. **LC-MS**: calculated m/z for $C_{34}H_{42}NO_5^+$ $[M+H]^+ = 544.3058$, found 544.3062.

Synthesis of P_{SP4}

Monomer M_{SP4} (100 mg, 0.183 mol) was dissolved in CH_2Cl_2 in a crimp vial. The solution was heated to 40 °C upon addition of Hoveyda-Grubbs 2nd generation (**HG-II**) (2.3 mg, 2 mol%) and a needle was pierced into the septum to allow the ethylene gas generated from the reaction to escape. After 18 h, ethyl vinyl ether (0.02 mL) was injected into the mixture and the solution was stirred for 30 min. The polymer was precipitated in methanol and collected via centrifugation and dried under vacuum at 40 °C.

11.8.5.2. Synthesis of spiropyran oligomers

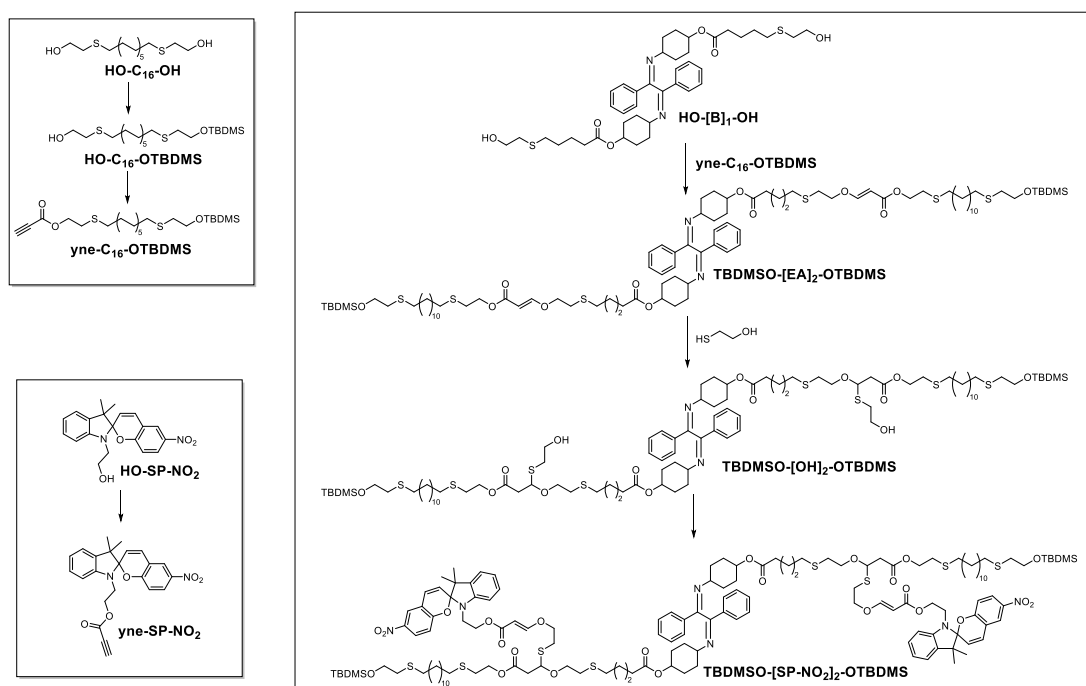
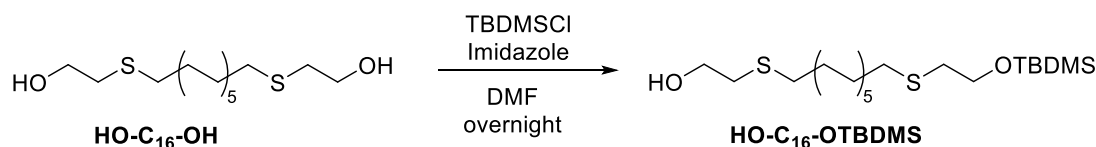


Figure S8.12. Synthesis of spiropyran-based oligomers.

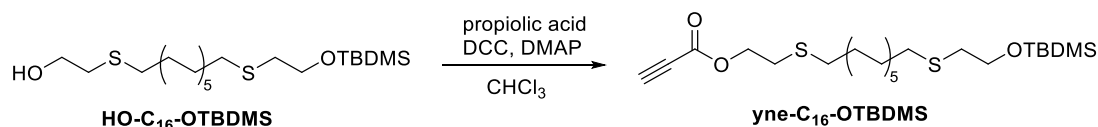
Synthesis of **HO-C₁₆-OTBDMS**



HO-C₁₆-OH (2000 mg, 6.2 mmol, 1 eq) and imidazole (843 mg, 12.4 mmol, 2.0 eq) were dissolved in 25 mL DMF at room temperature. Following this, **TBDMSCl** (933 mg, 6.2 mmol, 1.0 eq) was added to the solution and the reaction was run overnight. Upon completion, the mixture was diluted with 150 mL EtOAc and extracted with water and brine. The organic phase was dried over Na_2SO_4 , filtered and concentrated under reduced pressure. The residue was purified by flash column chromatography (EtOAc/Cy, 2/98 to 80/20, v/v), affording the product as an oil (1100 mg, 40% yield).

^1H NMR (400 MHz, CDCl_3) δ 3.75 (t, J = 7.1 Hz, 2H), 3.71 (t, J = 5.9 Hz, 2H), 2.73 (t, J = 5.9 Hz, 2H), 2.63 (dd, J = 7.6, 6.9 Hz, 2H), 2.53 (ddd, J = 10.9, 8.0, 6.9 Hz, 4H), 1.63 – 1.53 (m, 4H), 1.42 – 1.32 (m, 4H), 1.31 – 1.23 (m, 12H), 0.90 (s, 9H), 0.07 (s, 6H). **^{13}C NMR** (101 MHz, CDCl_3) δ 63.61, 60.27, 35.50, 34.52, 32.81, 31.76, 30.06, 29.90, 29.69, 29.64, 29.38, 29.35, 29.02, 28.99, 26.07, -5.10.

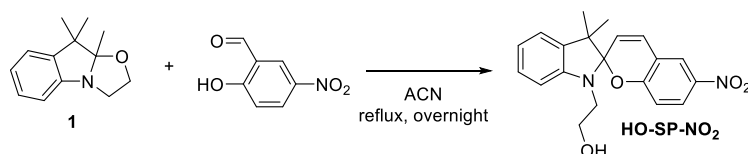
Synthesis of yne- C_{16} -OTBDMS



HO- C_{16} -OTBDMS (2000 mg, 4.6 mmol, 1.0 eq) and propiolic acid (342 μL , 1.2 eq) were dissolved in 5 mL CHCl_3 . Following that, DCC (1135 mg, 5.5 mmol, 1.2 eq) and DMAP (56 mg, 0.1 eq) were prepared separately in 4 mL CHCl_3 , and the resulting mixture was added slowly over 10 minutes to the previous solution. The reaction was stopped after 4 hours. The crude was purified by flash column chromatography (EtOAc/Cy , 10/90, v/v), affording the product (1450 mg, 72% yield).

^1H NMR (400 MHz, CDCl_3) δ 4.32 (t, J = 7.1 Hz, 2H), 3.75 (t, J = 7.2 Hz, 2H), 2.90 (s, 1H), 2.77 (t, J = 7.1 Hz, 2H), 2.62 (t, J = 7.3 Hz, 2H), 2.54 (q, J = 7.4 Hz, 4H), 1.57 (dddd, J = 14.9, 8.3, 7.1, 4.6 Hz, 4H), 1.39 – 1.33 (m, 4H), 1.32 – 1.20 (m, 12H), 0.89 (s, 9H), 0.06 (s, 6H). **^{13}C NMR** (101 MHz, CDCl_3) δ 152.54, 75.20, 74.59, 65.32, 63.59, 35.05, 34.50, 32.79, 32.56, 30.08, 30.04, 29.77, 29.68, 29.64, 29.62, 29.37, 29.32, 29.00, 28.92, 27.04, 26.05, -5.12. LC-MS: **LC-MS**: calculated m/z for $\text{C}_{25}\text{H}_{49}\text{O}_3\text{S}_2\text{Si}^+ [\text{M}+\text{H}]^+ = 489.2887$, found 489.2881.

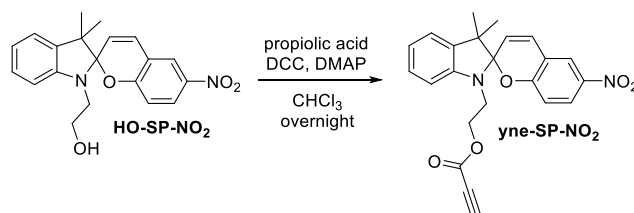
Synthesis of HO-SP- NO_2



Compound **1** (1500 mg, 7.4 mmol, 1.0 eq) and 2-hydroxy-5-nitrobenzaldehyde (1233 mg, 7.4 mol, 1.0 eq) was added to 15 mL ethanol and the resulting mixture was refluxed overnight. Upon completion, the reaction was cooled down to room temperature and the purple precipitate was collected by filtration, washed with cold ethanol and dried in vacuum at 40 $^\circ\text{C}$. The product was received as purple solid (1850 mg, ~65% yield). The ^1H NMR spectrum matches with the reported.²⁹⁹

^1H NMR (600 MHz, CDCl_3) δ 8.04 – 7.96 (m, 2H), 7.19 (td, J = 7.7, 1.3 Hz, 1H), 7.10 (dd, J = 7.3, 1.3 Hz, 1H), 6.93 – 6.87 (m, 2H), 6.76 (d, J = 8.9 Hz, 1H), 6.67 (d, J = 7.8 Hz, 1H), 5.88 (d, J = 10.3 Hz, 1H), 3.81 (ddd, J = 11.1, 7.4, 5.0 Hz, 1H), 3.76 – 3.68 (m, 1H), 3.46 (ddd, J = 14.9, 7.4, 5.6 Hz, 1H), 3.33 (dt, J = 15.0, 5.2 Hz, 1H), 1.29 (s, 3H), 1.19 (s, 3H).

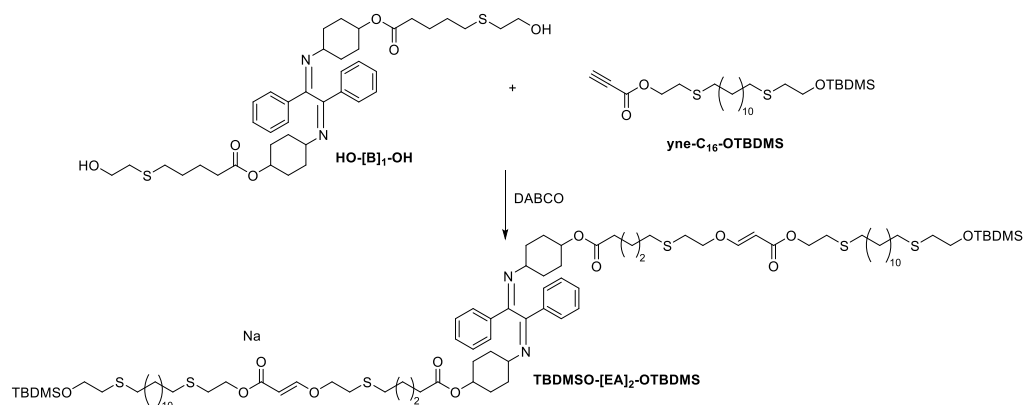
Synthesis of yne-SP-NO₂



HO-SP-NO₂ (500 mg, 1.4 mmol, 1.0 eq) and propiolic acid (106 μ L, 1.2 eq) were dissolved in 1.5 mL CHCl₃. Following that, DCC (351 mg, 1.7 mmol, 1.2 eq) and DMAP (17.3 mg, 0.1 eq) were prepared separately in 2 mL CHCl₃, and the resulting mixture was added slowly over 5 minutes to the previous solution. The reaction was stopped after 4 hours. The crude was purified by flash column chromatography (EtOAc/Cy, 10/90, v/v), affording the product (280 mg, 45% yield).

¹H NMR (400 MHz, CDCl₃) δ 8.04 – 7.99 (m, 2H), 7.21 (td, J = 7.7, 1.3 Hz, 1H), 7.10 (dd, J = 7.3, 1.3 Hz, 1H), 6.96 – 6.89 (m, 2H), 6.78 – 6.72 (m, 1H), 6.65 (dt, J = 7.9, 0.7 Hz, 1H), 5.90 (d, J = 10.4 Hz, 1H), 4.35 (ddd, J = 6.4, 5.7, 1.8 Hz, 2H), 3.57 (dt, J = 15.3, 6.6 Hz, 1H), 3.44 (dt, J = 15.3, 5.7 Hz, 1H), 2.89 (s, 1H), 1.29 (s, 3H), 1.18 (s, 3H). **¹³C NMR** (101 MHz, CDCl₃) δ 159.38, 152.49, 146.42, 141.25, 135.86, 128.55, 127.99, 126.09, 122.02, 121.75, 120.23, 118.52, 115.66, 106.70, 106.52, 75.40, 74.40, 63.88, 52.92, 42.27, 25.93, 19.95. **LC-MS**: calculated m/z for C₂₃H₂₁N₂O₅⁺ [M+H]⁺ = 405.1445, found 405.1444.

Synthesis TBDMSO-[EA]₂-OTBDMS

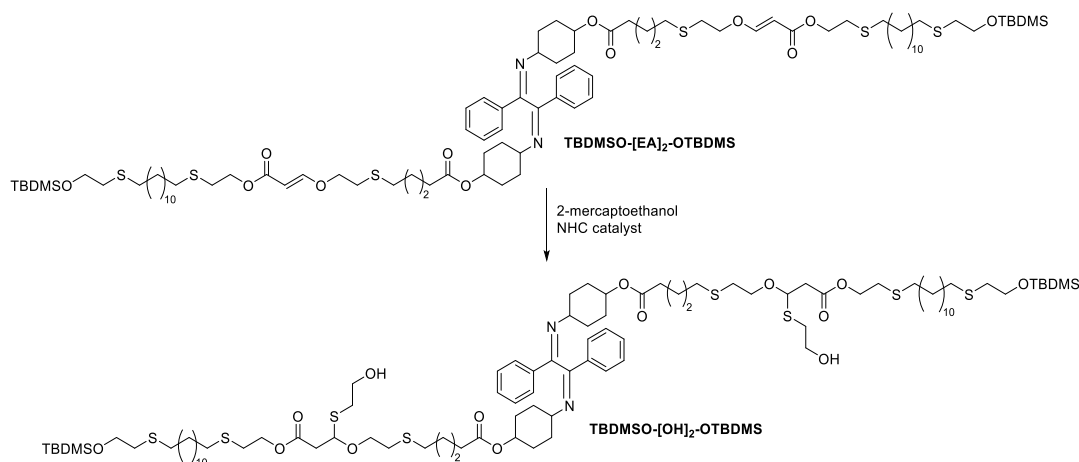


yne-C₁₆-OTBDMS (283 mg, 0.58 mmol, 2.1 eq) and **HO-[B]₁-OH** (200 mg, 0.28 mmol, 1.0 eq) were fully dissolved in 1.2 mL DCM. Following that, DABCO base (12 mg, 20 mol% of OH-functional group) was added. The reaction was stirred for 30 min and then immediately purified by flash column chromatography (DCM/EtOAc, 90/10, v/v) to afford the product (440 mg, 94% purification yield).

¹H NMR (400 MHz, CDCl₃) δ 7.78 – 7.71 (m, 4H), 7.57 (d, J = 12.6 Hz, 2H), 7.42 – 7.30 (m, 6H), 5.21 (d, J = 12.6 Hz, 2H), 4.79 (tt, J = 10.1, 4.2 Hz, 2H), 4.25 (t, J = 7.0 Hz, 4H), 3.98 (t, J = 6.7 Hz, 4H), 3.75 (dd, J = 7.6, 6.9 Hz, 4H), 3.22 (ddt, J = 13.6, 9.2, 3.9 Hz, 2H), 2.76 (dt, J

= 14.1, 6.9 Hz, 8H), 2.63 (dd, J = 7.6, 6.8 Hz, 4H), 2.54 (td, J = 7.4, 5.6 Hz, 12H), 2.25 (t, J = 7.2 Hz, 4H), 2.11 – 2.03 (m, 2H), 1.95 – 1.86 (m, 2H), 1.82 – 1.52 (m, 22H), 1.46 – 1.32 (m, 12H), 1.26 (d, J = 3.6 Hz, 26H), 0.89 (s, 18H), 0.06 (s, 12H). **^{13}C NMR** (101 MHz, CDCl_3) δ 172.82, 167.43, 163.25, 162.36, 136.93, 130.85, 128.73, 127.75, 96.80, 72.09, 70.66, 63.59, 63.14, 61.46, 34.50, 34.17, 32.79, 32.51, 32.38, 31.51, 30.74, 30.73, 30.38, 30.05, 29.83, 29.69, 29.65, 29.38, 29.36, 29.17, 29.08, 29.01, 28.98, 26.06, 24.17, 18.47, -5.12. **SEC-MS**: calculated m/z for $\text{C}_{90}\text{H}_{152}\text{N}_2\text{NaO}_{12}\text{S}_6\text{Si}_2^+$ $[\text{M}+\text{H}]^+$ = 1723.9106, found 1723.9115.

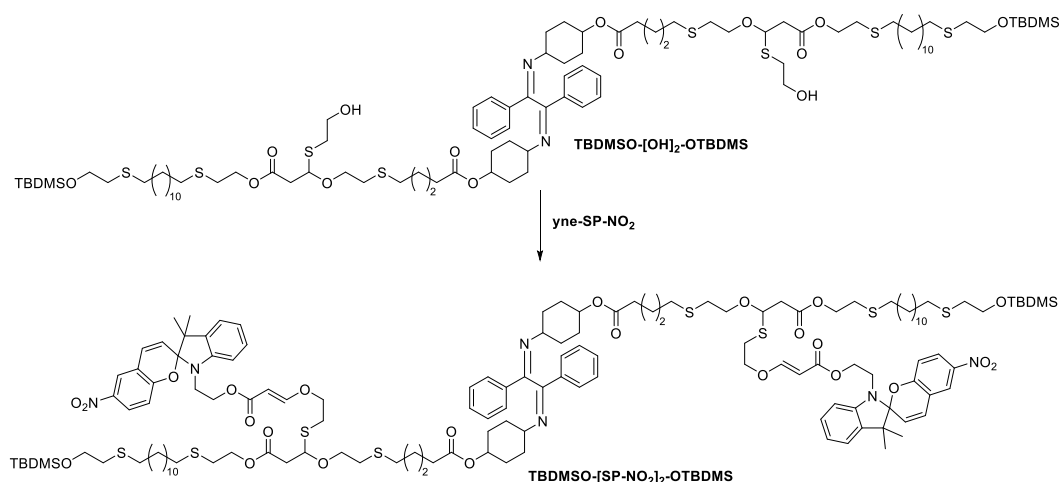
Synthesis TBDMSO-[OH] $_2$ -OTBDMS



TBDMSO-[EA] $_2$ -OTBDMS (100 mg, 0.06 mmol, 1.0 eq) and 2-mercaptothiol (82.4 μL , 20 eq) were dissolved in 0.15 mL THF. The NHC catalyst, 1,3-bis(2,6-diisopropylphenyl)imidazol-2-ylidene, (4.6 mg, 0.2 eq) was subsequently added. A crude NMR was recorded after 4 h of reaction to determine the conversion (close to 100% conversion). Upon completion, the reaction mixture was diluted in DCM and washed with saturated NaHCO_3 solution (2 times) and water/brine (2 times). The residue was concentrated and then precipitated in methanol to obtain pure product (~ 100 mg, 92% yield).

^1H NMR (600 MHz, CDCl_3) δ 7.76 – 7.72 (m, 4H), 7.41 – 7.37 (m, 2H), 7.34 (ddd, J = 8.3, 6.9, 1.2 Hz, 4H), 4.96 (dd, J = 7.7, 6.2 Hz, 2H), 4.78 (tt, J = 10.2, 4.2 Hz, 2H), 4.24 (qt, J = 11.1, 7.0 Hz, 4H), 3.90 (dt, J = 9.7, 6.8 Hz, 2H), 3.79 (ddd, J = 11.1, 6.3, 4.7 Hz, 2H), 3.76 – 3.69 (m, 6H), 3.61 (dt, J = 9.7, 6.5 Hz, 2H), 3.22 (tt, J = 9.7, 3.9 Hz, 2H), 2.98 (dd, J = 15.6, 7.7 Hz, 2H), 2.88 (ddd, J = 14.2, 7.3, 4.6 Hz, 2H), 2.78 – 2.70 (m, 6H), 2.67 (td, J = 6.8, 2.4 Hz, 4H), 2.64 – 2.60 (m, 4H), 2.55 – 2.51 (m, 12H), 2.25 (t, J = 7.3 Hz, 4H), 2.11 – 2.05 (m, 2H), 1.94 – 1.87 (m, 2H), 1.76 (tdd, J = 13.1, 9.6, 3.6 Hz, 2H), 1.70 – 1.64 (m, 4H), 1.64 – 1.53 (m, 14), 1.46 – 1.15 (m, 42H), 0.89 (s, 18H), 0.06 (s, 12H). **^{13}C NMR** (151 MHz, CDCl_3) δ 172.95, 169.70, 163.25, 136.93, 130.85, 128.73, 127.75, 81.34, 72.09, 67.71, 63.98, 63.59, 62.46, 61.46, 41.56, 34.50, 34.21, 32.79, 32.50, 32.27, 31.89, 31.36, 30.51, 30.04, 29.80, 29.69, 29.64, 29.37, 29.36, 29.17, 29.15, 29.11, 29.00, 28.97, 26.05, 24.23, 18.47, -5.12. **SEC-MS**: calculated m/z for $\text{C}_{94}\text{H}_{164}\text{KN}_2\text{O}_{14}\text{S}_8\text{Si}_2^+$ $[\text{M}+\text{K}]^+$ = 1896.9157, found 1896.9358.

Synthesis of TBDMSO-[SP-NO₂]₂-OTBDMS



yne-SP-NO₂ (43 mg, 0.11 mmol, 2.2 eq) and **TBDMSO-[OH]₂-OTBDMS** (90 mg, 0.05 mmol, 1.0 eq) were fully dissolved in 0.2 mL DCM. Following that, DABCO base (2 mg, 20 mol% of OH-functional group) was added. The reaction was stirred for 30 min and then immediately purified by flash column chromatography (DCM/EtOAc, 90/10, v/v) to afford the product (120 mg, 94% purification yield).

¹H NMR (600 MHz, CDCl₃) δ 8.00 (d, J = 8.5 Hz, 4H), 7.77 – 7.72 (m, 4H), 7.50 (d, J = 12.6 Hz, 2H), 7.40 – 7.36 (m, 2H), 7.35 – 7.31 (m, 4H), 7.19 (td, J = 7.6, 1.3 Hz, 2H), 7.08 (dd, J = 7.2, 1.2 Hz, 2H), 6.91 (d, J = 10.4 Hz, 2H), 6.88 (td, J = 7.4, 0.9 Hz, 2H), 6.74 (d, J = 8.5 Hz, 2H), 6.68 (d, J = 7.8 Hz, 2H), 5.86 (d, J = 10.3 Hz, 2H), 5.12 (d, J = 12.6 Hz, 2H), 4.95 (dd, J = 8.1, 5.8 Hz, 2H), 4.78 (tt, J = 10.2, 4.2 Hz, 2H), 4.24 (tt, J = 6.9, 4.4 Hz, 8H), 4.01 – 3.92 (m, 4H), 3.85 (dt, J = 9.8, 6.7 Hz, 2H), 3.75 (t, J = 7.2 Hz, 4H), 3.59 (dt, J = 9.7, 6.4 Hz, 2H), 3.52 (dt, J = 15.2, 6.6 Hz, 2H), 3.40 (dt, J = 15.1, 6.1 Hz, 2H), 3.22 (dq, J = 9.8, 4.7 Hz, 2H), 2.95 – 2.82 (m, 6H), 2.77 (dd, J = 15.5, 5.7 Hz, 2H), 2.73 (t, J = 7.0 Hz, 4H), 2.66 (t, J = 6.6 Hz, 4H), 2.63 (t, J = 7.2 Hz, 4H), 2.55 – 2.49 (m, 12H), 2.24 (t, J = 7.4 Hz, 4H), 2.11 – 2.04 (m, 2H), 1.93 – 1.86 (m, 2H), 1.80 – 1.72 (m, 2H), 1.70 – 1.60 (m, 8H), 1.60 – 1.53 (m, 14H), 1.45 – 1.13 (m, 48H), 0.89 (s, 18H), 0.07 (s, 12H). **¹³C NMR** (151 MHz, CDCl₃) δ 172.84, 169.39, 167.33, 163.23, 162.32, 159.54, 146.78, 141.17, 136.93, 135.81, 130.84, 128.72, 128.44, 127.97, 127.74, 126.06, 122.88, 121.91, 121.89, 119.97, 118.56, 115.68, 106.84, 106.58, 96.78, 81.51, 72.05, 70.73, 67.58, 63.95, 63.58, 61.99, 61.44, 53.55, 52.96, 42.62, 41.87, 34.49, 34.18, 32.78, 32.48, 32.33, 31.44, 30.51, 30.03, 29.80, 29.69, 29.64, 29.37, 29.13, 28.99, 28.97, 26.50, 26.04, 26.01, 24.22, 21.16, 19.95, 18.46, -5.13. **SEC-MS**: calculated m/z for C₁₄₀H₂₀₄KN₆O₂₄S₈Si₂⁺ [M+K]⁺ = 2705.1897, 2706.1930, 2704.1863, 2707.1964, 2708.1888, 2706.1821, found 2705.2166, 2706.2178, 2704.2139, 2707.2180, 2708.2188.

11.8.5.3. Synthesis of Spiropyran-based block copolymer

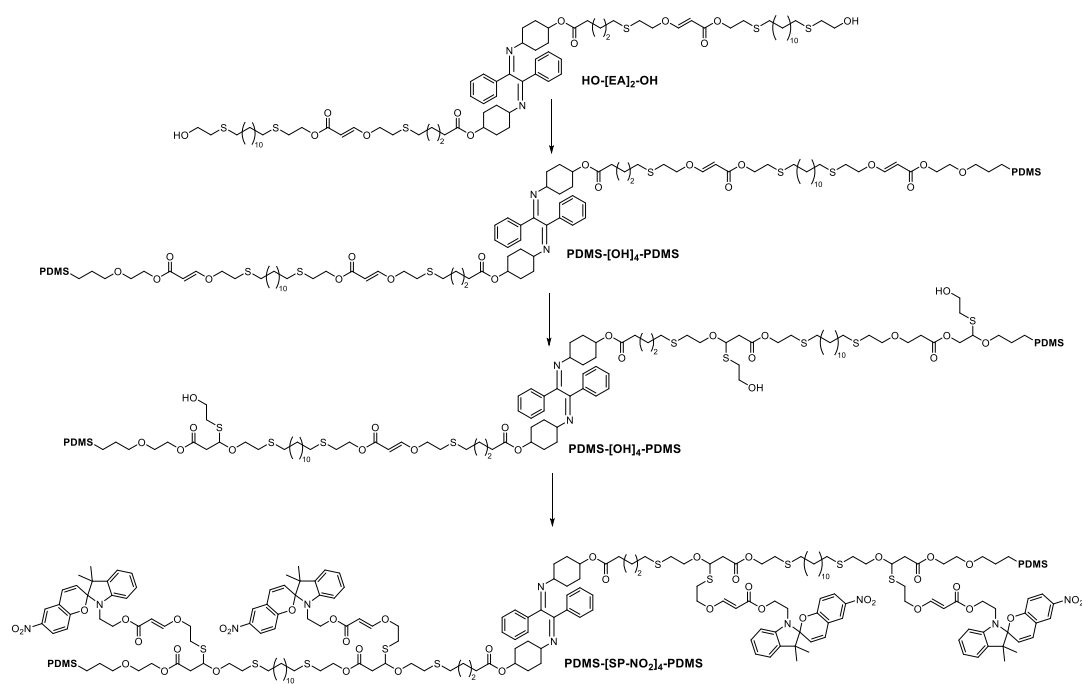
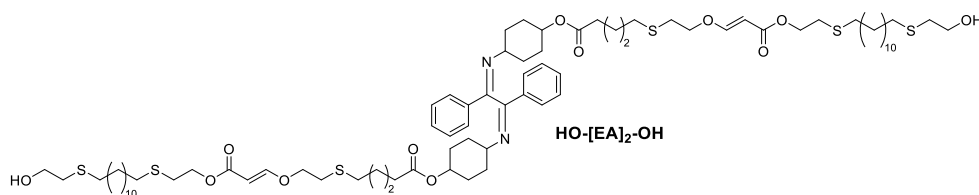


Figure S8.13. Synthesis of block copolymers from PDMS and spiropyran.

Synthesis of HO-[EA]₂-OH



TBAF 1M solution in THF (1.76 mL, 15 eq) was added to **TBDMSO-[EA]₂-OTBDMS** (200 mg, 0.12 mmol, 1.0 eq) and the resulting solution was stirred at ambient temperature for 30 minutes. The reaction mixture was subsequently diluted in DCM and extracted with water (2 times). The organic phase was then dried with Na₂SO₄ and concentrated at reduced pressure. The residue was purified via flash column chromatography (DCM:EtOAc, 100% DCM to 50% DCM), yielding the product (160 mg, 92% purification yield).

¹H NMR (600 MHz, CDCl₃) δ 7.76 – 7.70 (m, 4H), 7.56 (d, J = 12.6 Hz, 2H), 7.39 – 7.35 (m, 2H), 7.35 – 7.30 (m, 4H), 5.19 (d, J = 12.6 Hz, 2H), 4.77 (tt, J = 10.2, 4.2 Hz, 2H), 4.23 (t, J = 7.0 Hz, 4H), 3.96 (t, J = 6.7 Hz, 4H), 3.69 (q, J = 6.0 Hz, 4H), 3.21 (tt, J = 9.7, 3.9 Hz, 2H), 2.76 (t, J = 6.7 Hz, 4H), 2.73 (t, J = 7.0 Hz, 4H), 2.70 (t, J = 6.0 Hz, 4H), 2.53 (t, J = 7.4 Hz, 8H), 2.51 – 2.47 (m, 4H), 2.24 (t, J = 7.3 Hz, 4H), 2.10 – 2.03 (m, 2H), 1.92 – 1.86 (m, 2H), 1.75 (tdd, J = 13.1, 9.6, 3.6 Hz, 2H), 1.70 – 1.63 (m, 4H), 1.63 – 1.53 (m, 16H), 1.45 – 1.31 (m, 12H), 1.30 – 1.13 (m, 26H). **LC-MS**: calculated m/z for C₇₈H₁₂₄N₂NaO₁₂S₆⁺ [M+Na]⁺ = 1495.7371, found 1495.7367.

Synthesis of PDMS-[EA]₄-PDMS

PDMS-yne (M_n = 5000 g·mol⁻¹, reported in chapter 4) (299 mg, 0.06 mmol, 2.2 eq) and **HO-[EA]₂-OH** (40 mg, 0.027 mmol, 1.0 eq) were dissolved in 1.5 mL anhydrous DCM. Following that, DABCO (1.0 mg, 20 mol% of the OH-group) was added to the solution. The reaction was stopped after 45 min and purified immediately by flash column chromatography (DCM/EtOAc, 99/1 to 50/50, v/v), affording the product (270 mg, 87% yield). Synthesis of PDMS-[OH]₄-PDMS

Synthesis of PDMS-[OH]₄-PDMS

PDMS-[EA]₄-PDMS (100 mg, 0.034 mmol of ether acrylate, 1.0 eq) and 2-mercaptothiol (25 μ L, 10 eq) were dissolved in 0.15 mL THF. The NHC catalyst, 1,3-bis(2,6-diisopropylphenyl)imidazol-2-ylidene, (2.7 mg, 0.2 eq of ether acrylate) was subsequently added. A crude NMR was recorded after 4 h of reaction to determine the conversion (close to 100% conversion). Upon completion, the reaction mixture was diluted in DCM and washed with saturated NaHCO₃ solution (2 times). The residue was purified by flash column chromatography (DCM/EtOAc, 99/1 to 50/50, v/v) (90 mg, 87% yield).

Synthesis of PDMS-[SP-NO₂]₄-PDMS

PDMS-[OH]₄-PDMS (80 mg, 0.027 mmol of hydroxy, 1.0 eq) and **yne-SP-NO₂** (12 mg, 0.03 mmol, 1.1 eq) were fully dissolved in 0.3 mL DCM. Following that, DABCO base (1.2 mg, 20 mol% of OH-functional group) was added. The reaction was stirred for 30 min and then immediately purified by flash column chromatography (DCM/EtOAc, 90/10, v/v) to afford the product (82 mg, 90% purification yield).

11.8.6. NMR spectra

11.8.6.1. Compound 1

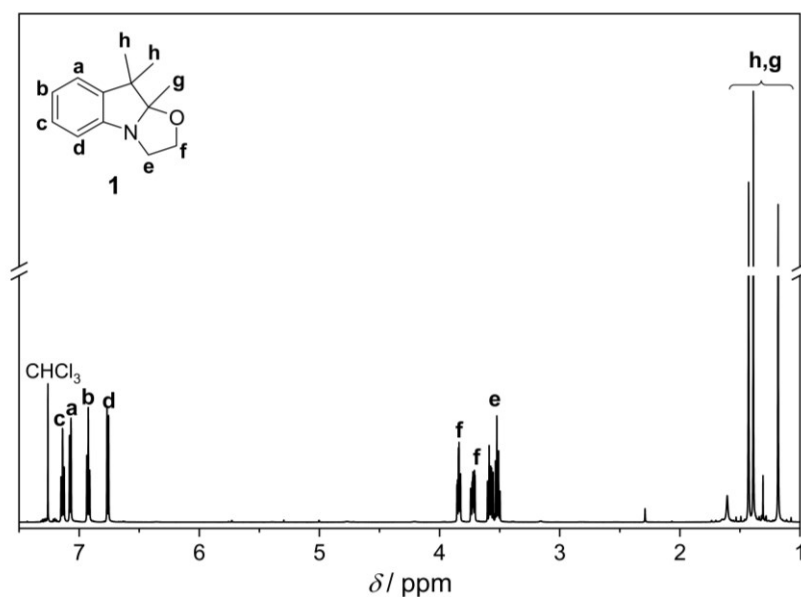


Figure S8.14. ¹H NMR spectrum (600 MHz, 16 scans) of compound **1** recorded in CDCl₃.

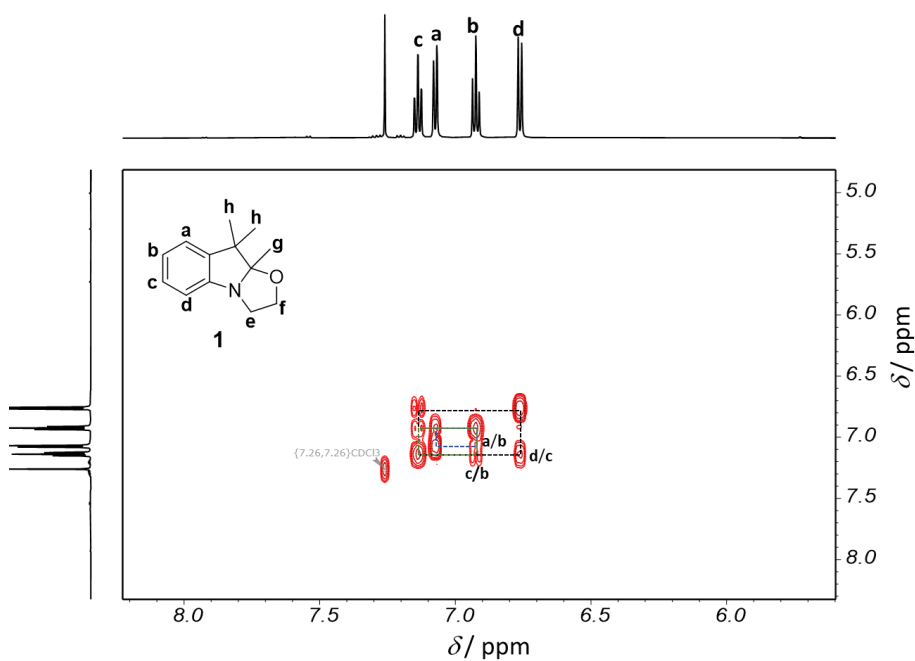


Figure S8.15. Sectional COSY spectrum of compound **1** recorded in CDCl_3 .

11.8.6.2. SP1-diOH

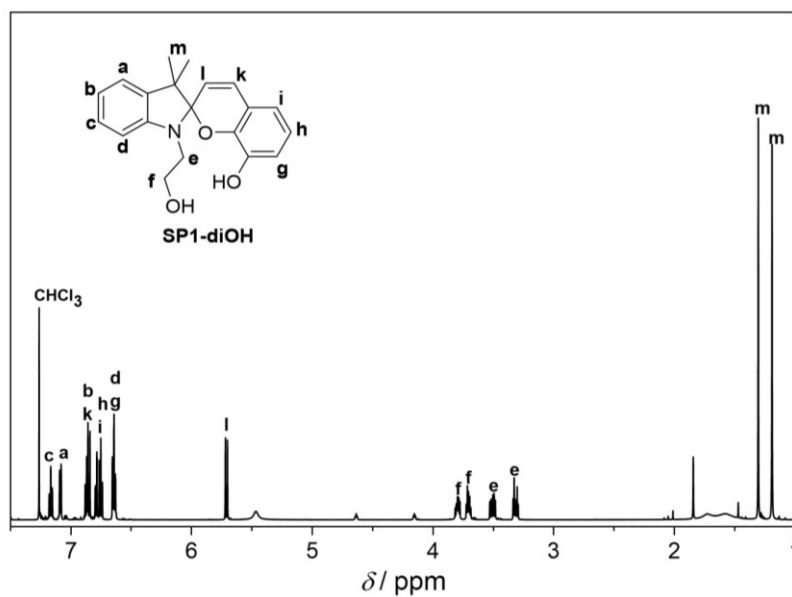


Figure S8.16. ^1H NMR spectrum (600 MHz, 16 scans) of **SP1-diOH** recorded in CDCl_3 .

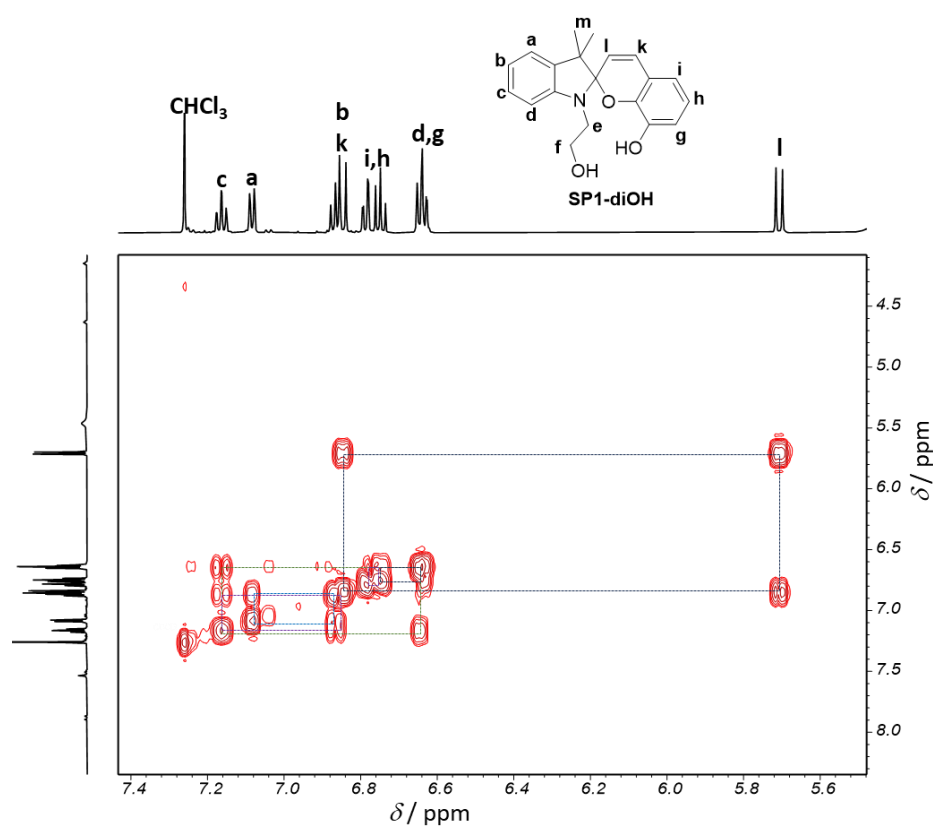


Figure S8.17. Sectional COSY spectrum of compound **SP1-diOH** recorded in CDCl_3 .

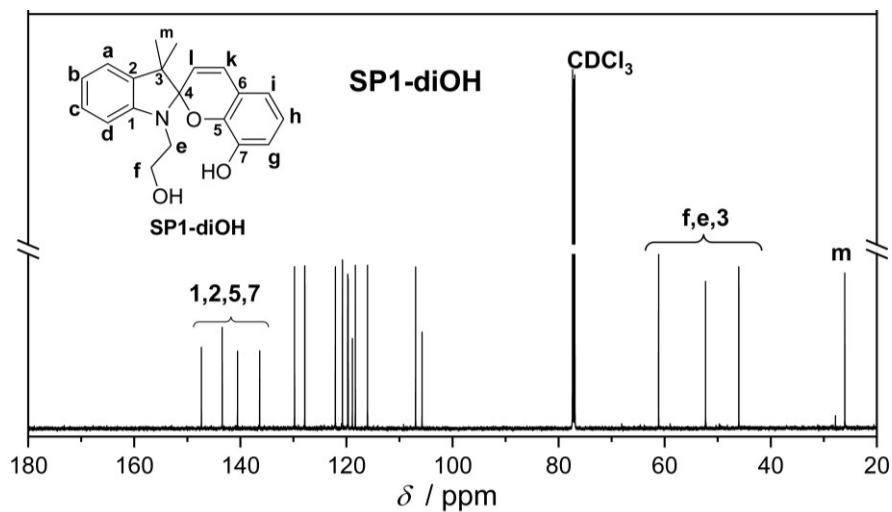


Figure S8.18. ^{13}C (151 MHz) NMR spectrum of **SP1-diOH** in CDCl_3 .

11.8.6.3. SP1-mOH

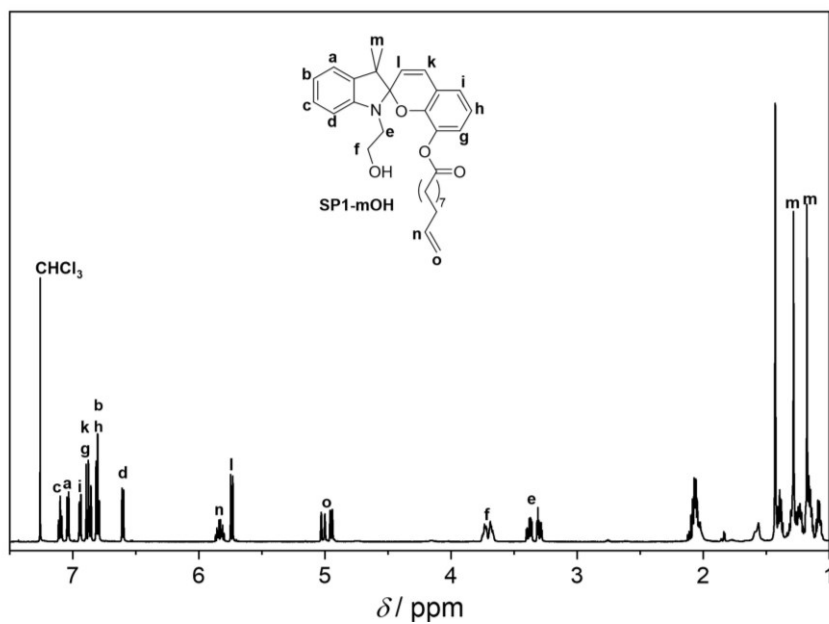


Figure S8.19. ^1H NMR spectrum (600 MHz, 16 scans) of **SP1-mOH** recorded in CDCl_3 .

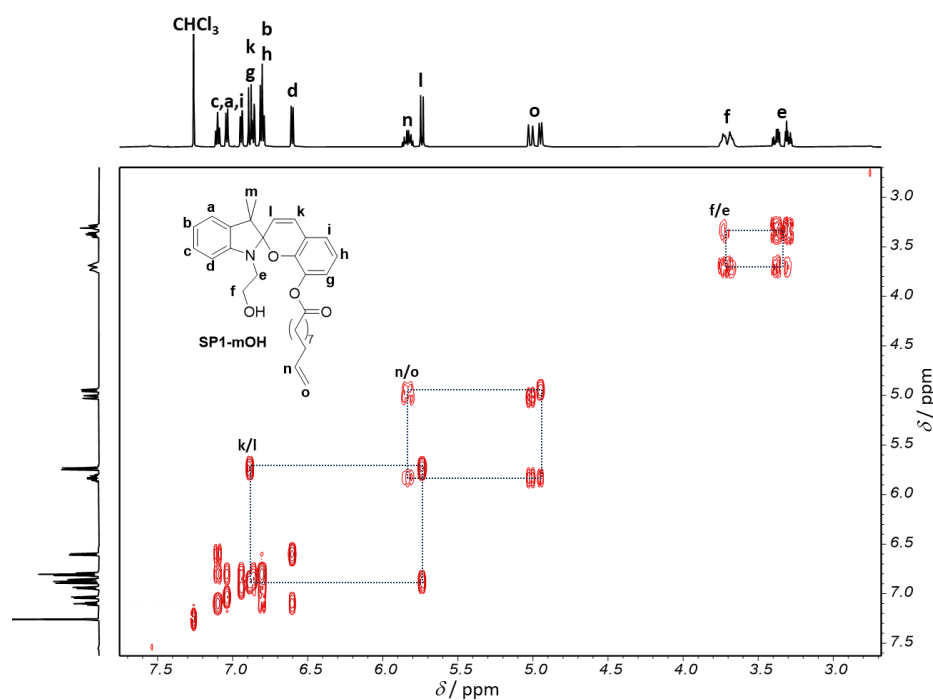


Figure S8.20. COSY sectional spectrum of compound **SP1-mOH** recorded in CDCl_3 .

11.8.6.4. **M_{SP1}**

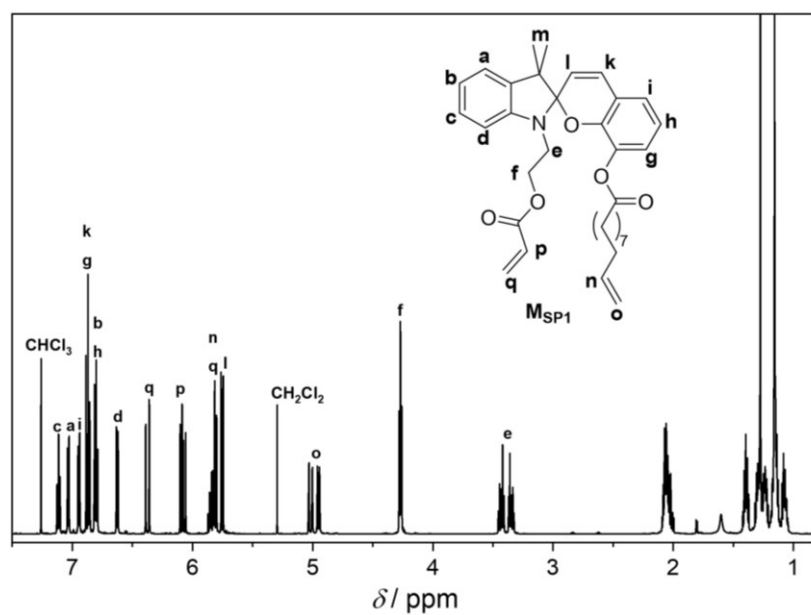


Figure S8.21. ^1H NMR spectrum (600 MHz, 16 scans) of **M_{SP1}** recorded in CDCl_3 .

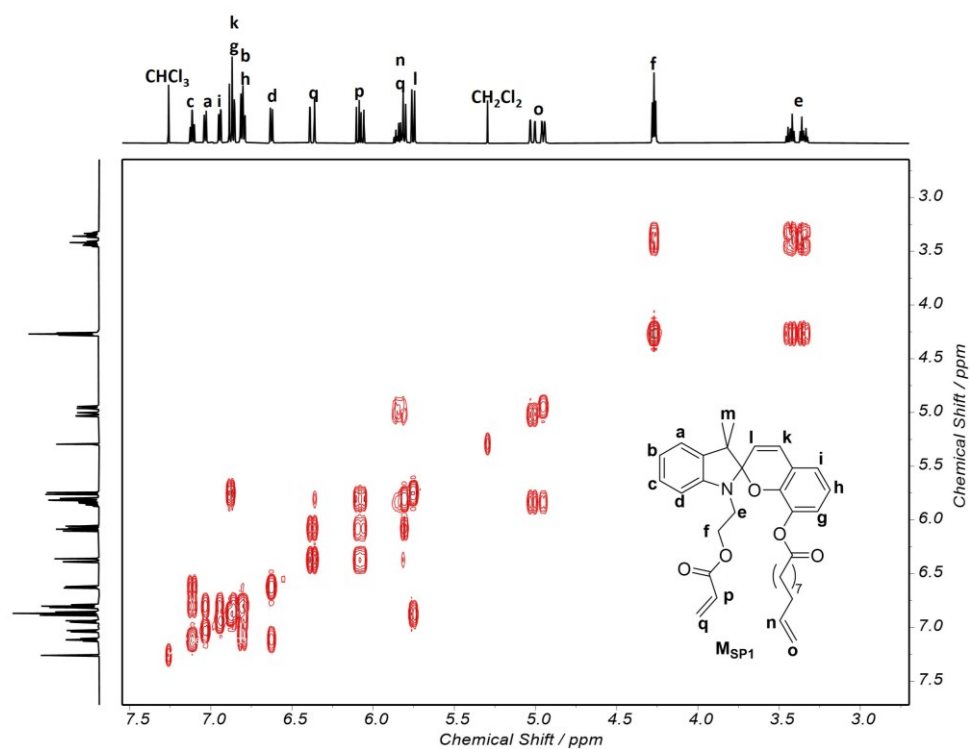


Figure S8.22. COSY sectional spectrum of compound M_{SP1} recorded in $CDCl_3$.

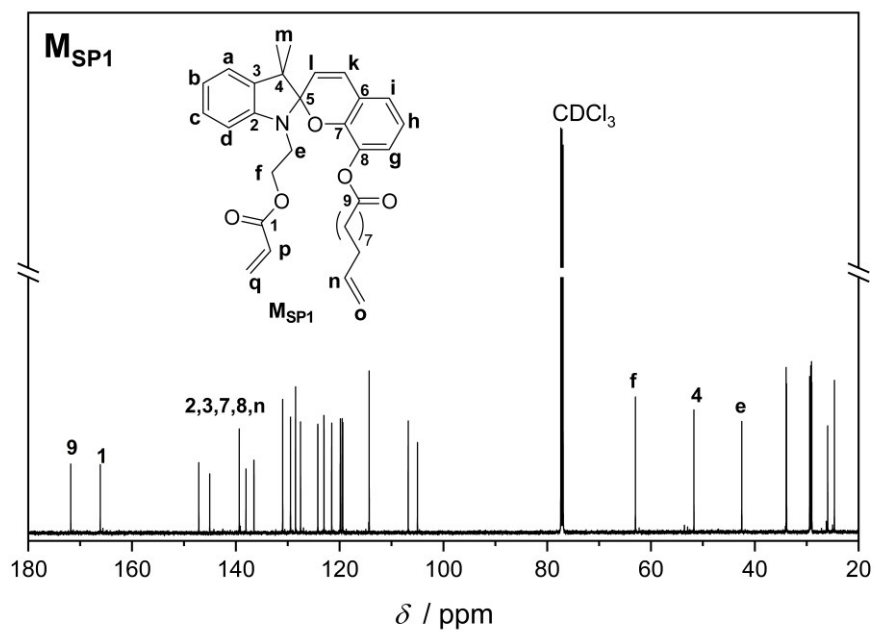


Figure S8.23. ^{13}C (151 MHz) NMR spectrum of M_{SP1} in $CDCl_3$.

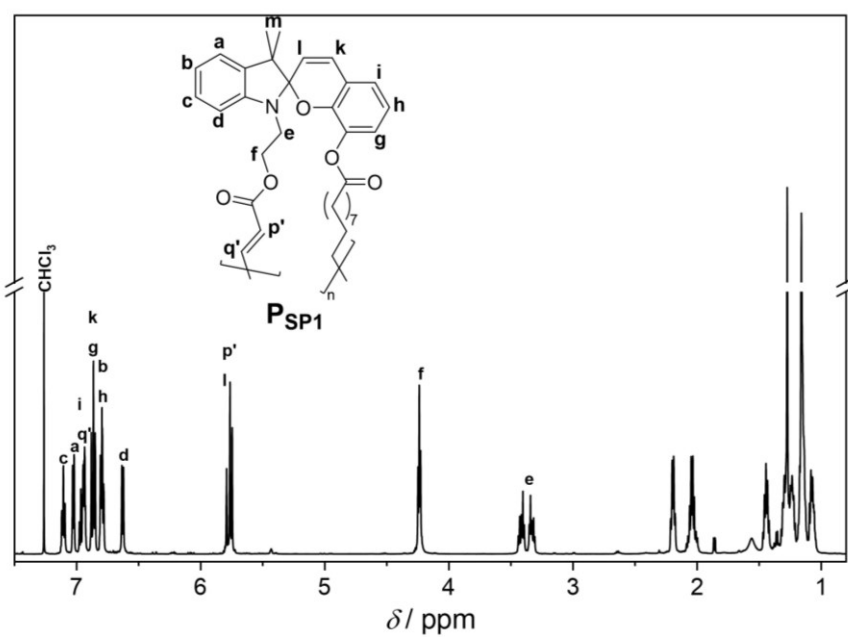
11.8.6.5. P_{SP1} 

Figure S8.24. ^1H NMR spectrum (600 MHz, 32 scans) of P_{SP1} recorded in CDCl_3 .

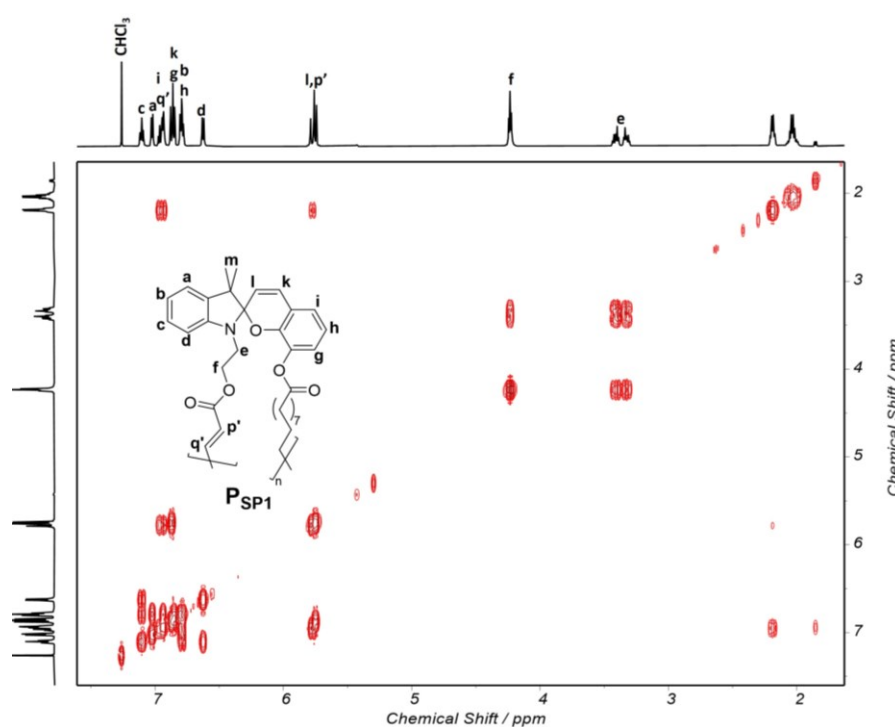


Figure S8.25. COSY sectional spectrum of compound P_{SP1} recorded in CDCl_3 .

11.8.6.6. Compound 2

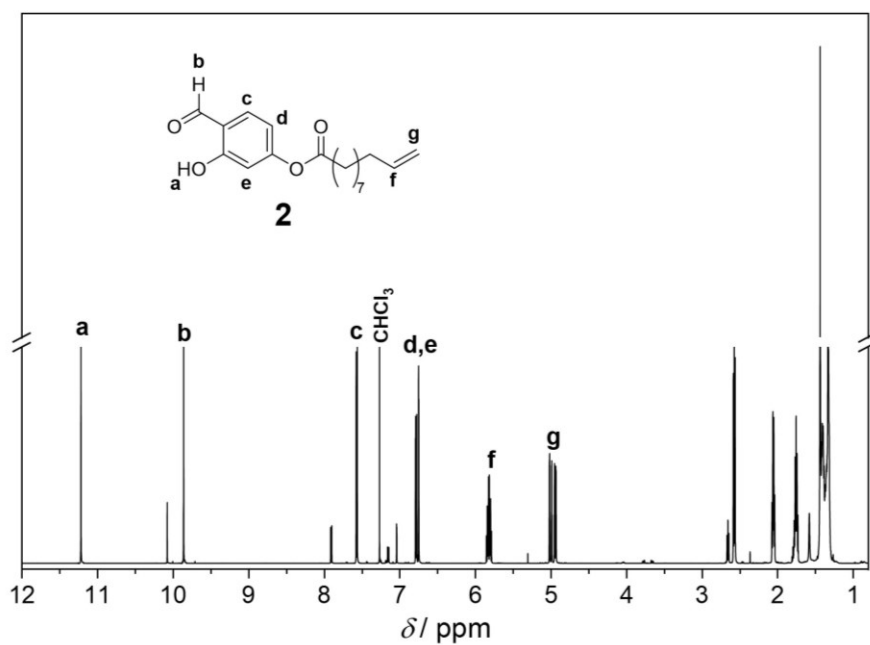


Figure S8.26. ^1H NMR spectrum (600 MHz, 16 scans) of compound **2** recorded in CDCl_3 .

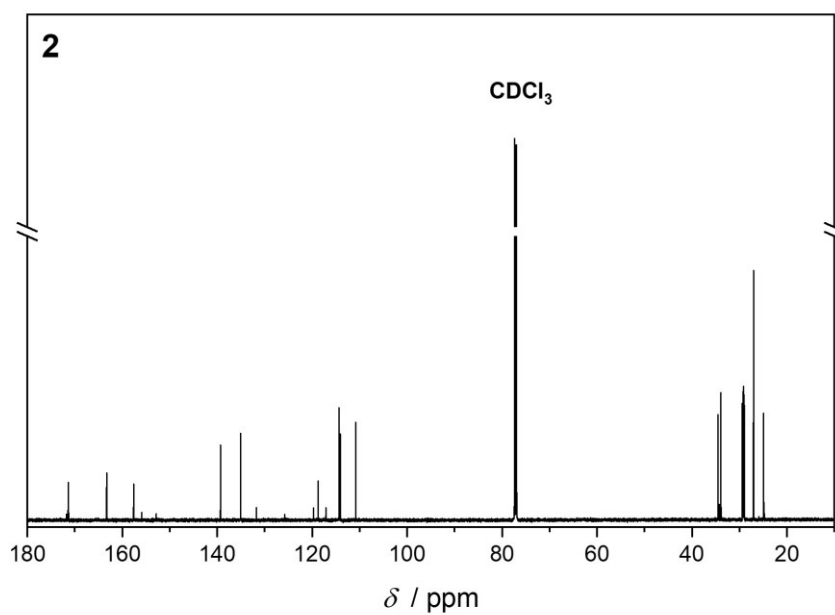


Figure S8.27. ^{13}C (151 MHz) NMR spectrum of compound **2** in CDCl_3 .

11.8.6.7. SP2-mOH

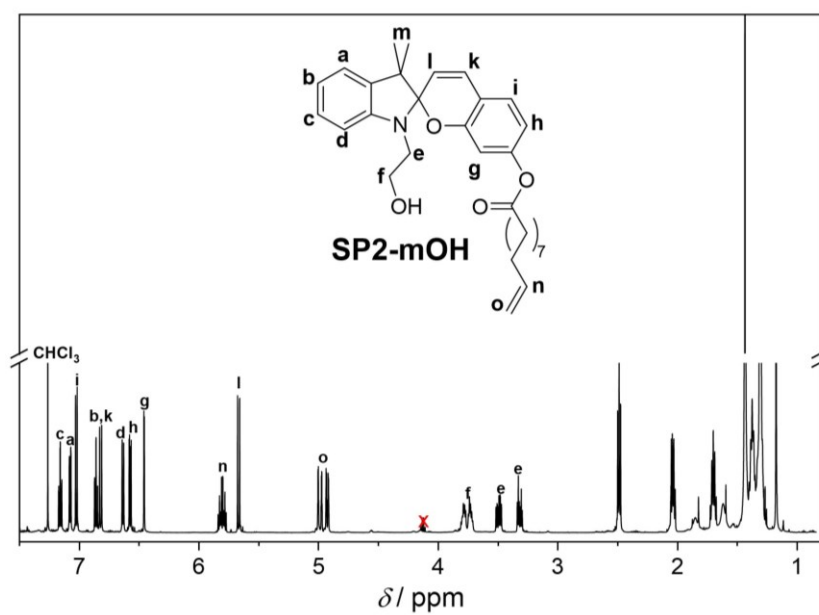


Figure S8.28. ^1H NMR spectrum (600 MHz, 16 scans) of **SP2-mOH** recorded in CDCl_3 .

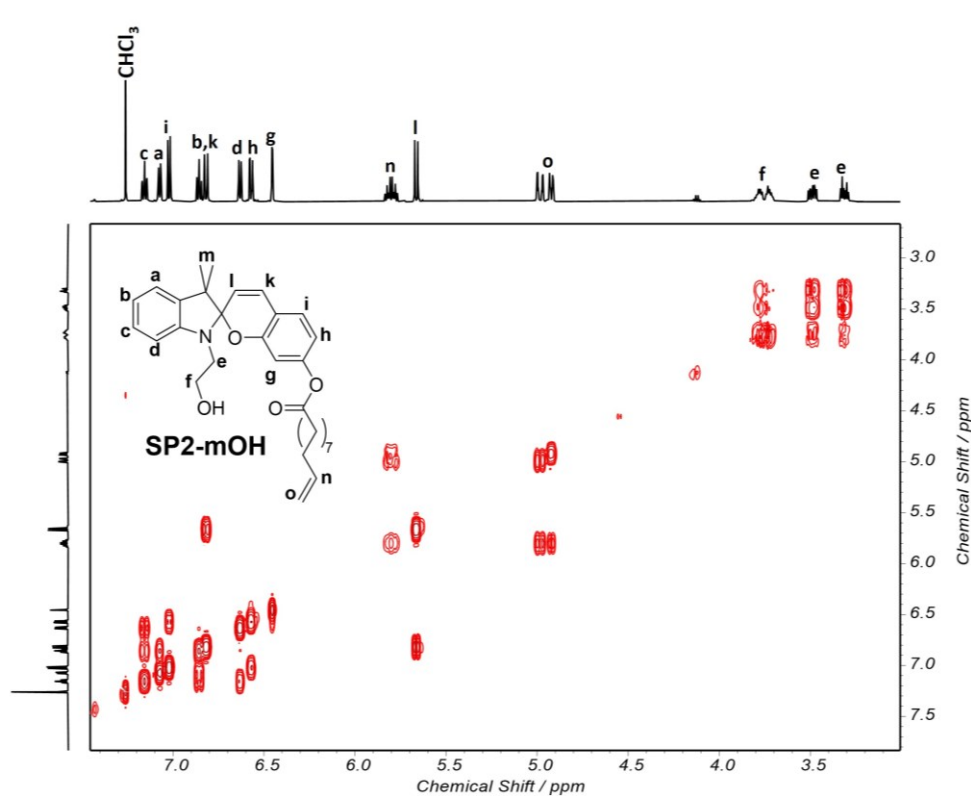


Figure S8.29. COSY sectional spectrum of compound **SP2-mOH** recorded in CDCl_3 .

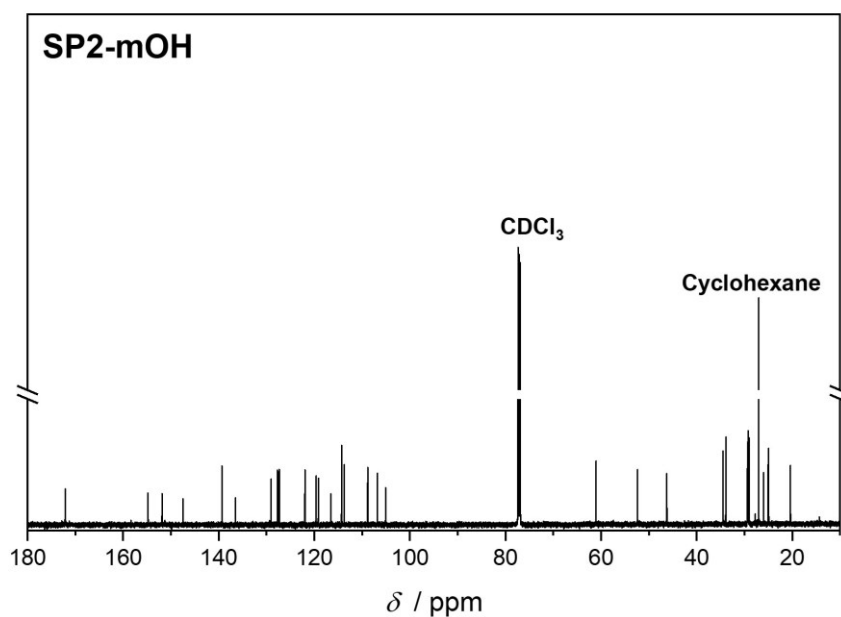


Figure S8.30. ¹³C (151 MHz) NMR spectrum of **SP2-mOH** in CDCl₃.

11.8.6.8. **M_{SP2}**

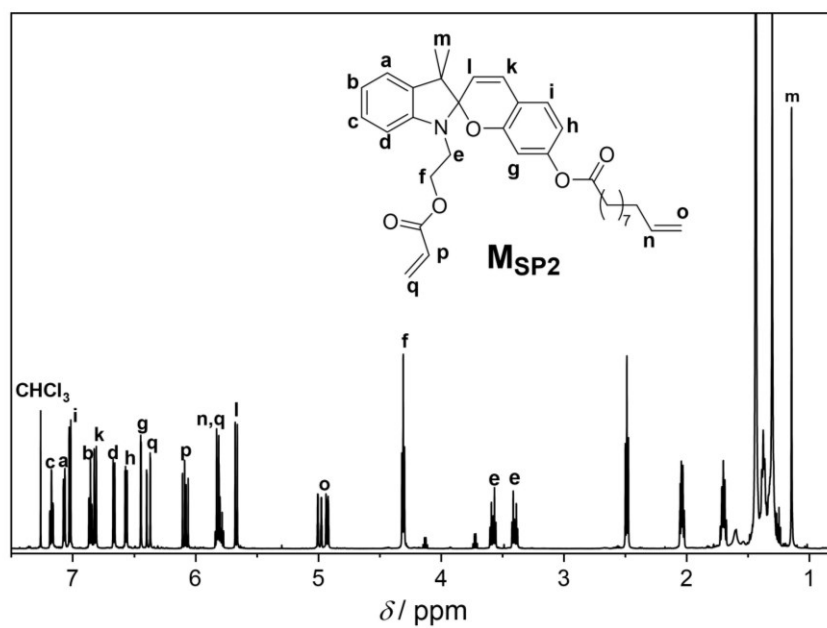


Figure S8.31. ¹H NMR spectrum (600 MHz, 16 scans) of **M_{SP2}** recorded in CDCl₃.

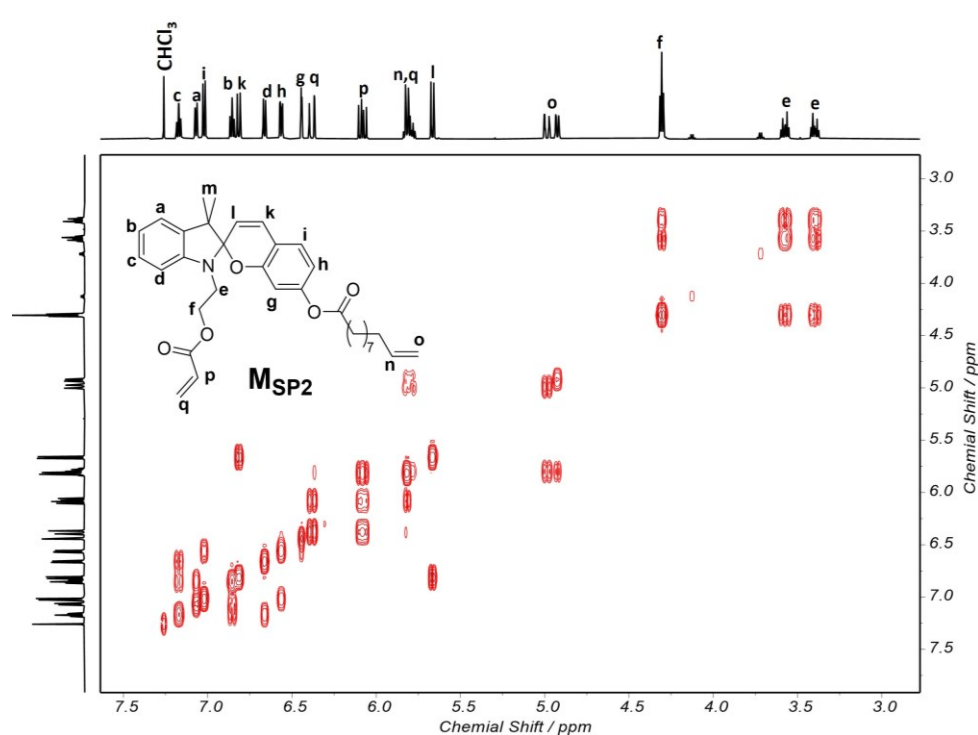


Figure S8.32. COSY sectional spectrum of compound M_{SP2} recorded in $CDCl_3$.

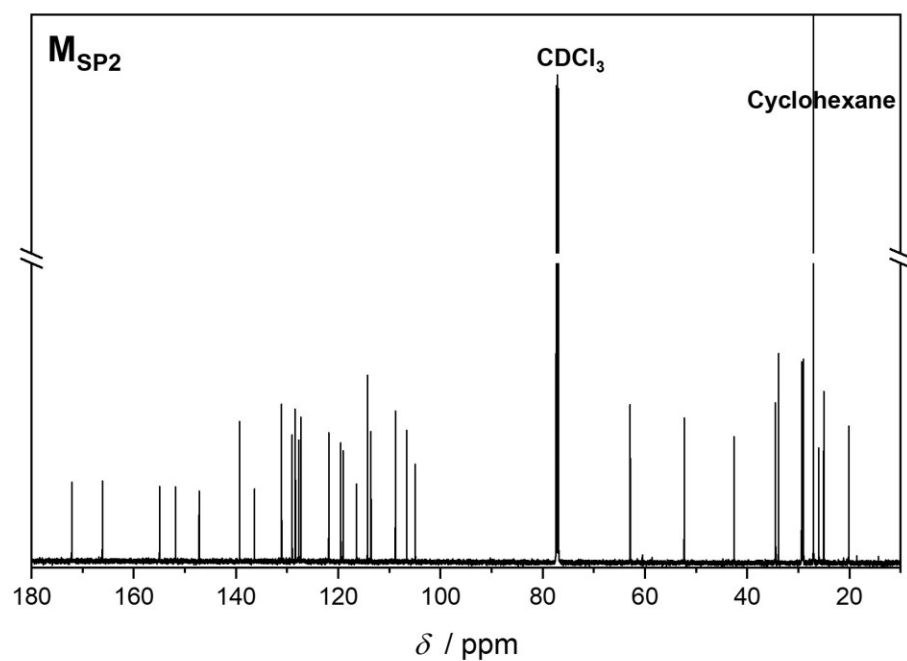


Figure S8.33. ^{13}C (151 MHz) NMR spectrum of M_{SP2} in $CDCl_3$.

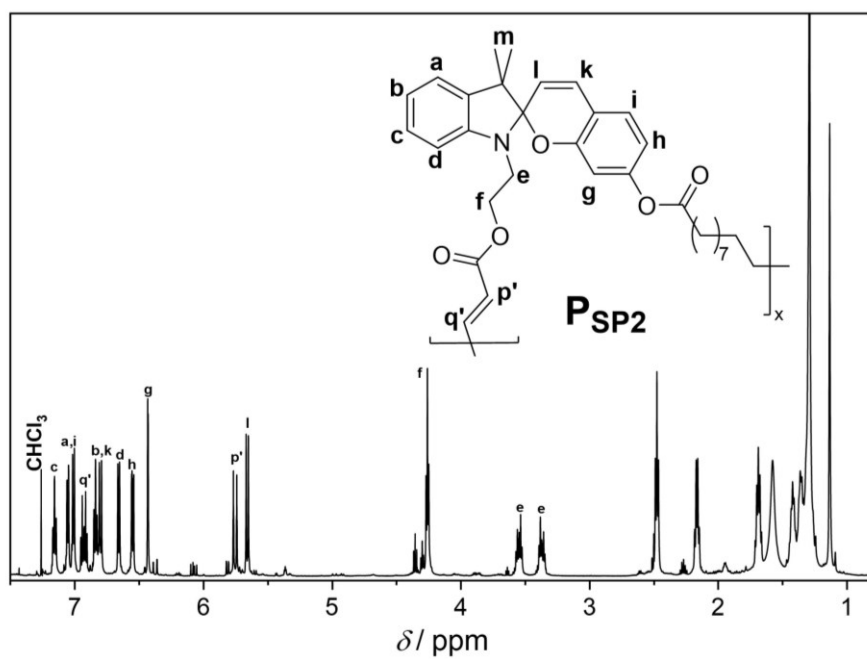
11.8.6.9. P_{SP2} 

Figure S8.34. ^1H NMR spectrum (600 MHz, 32 scans) of P_{SP2} recorded in CDCl_3 .

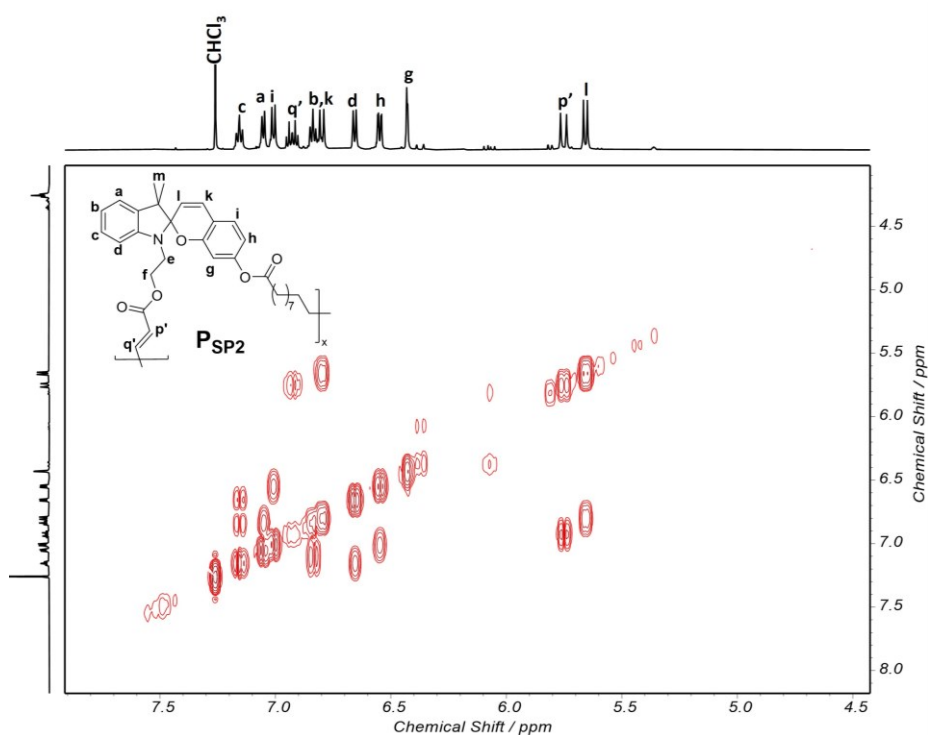


Figure S8.35. COSY sectional spectrum of compound P_{SP2} recorded in CDCl_3 .

11.8.6.10. SP3-diOH

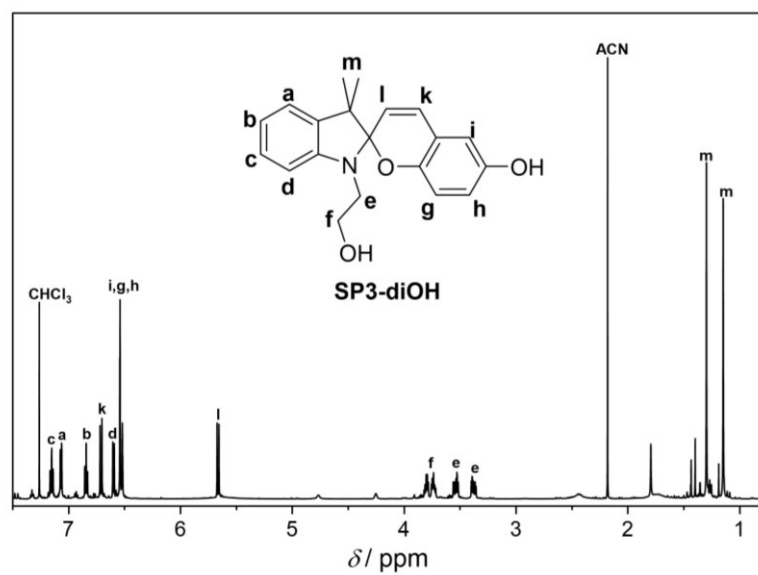


Figure S8.36. ^1H NMR spectrum (600 MHz, 16 scans) of **SP3-diOH** recorded in CDCl_3 .

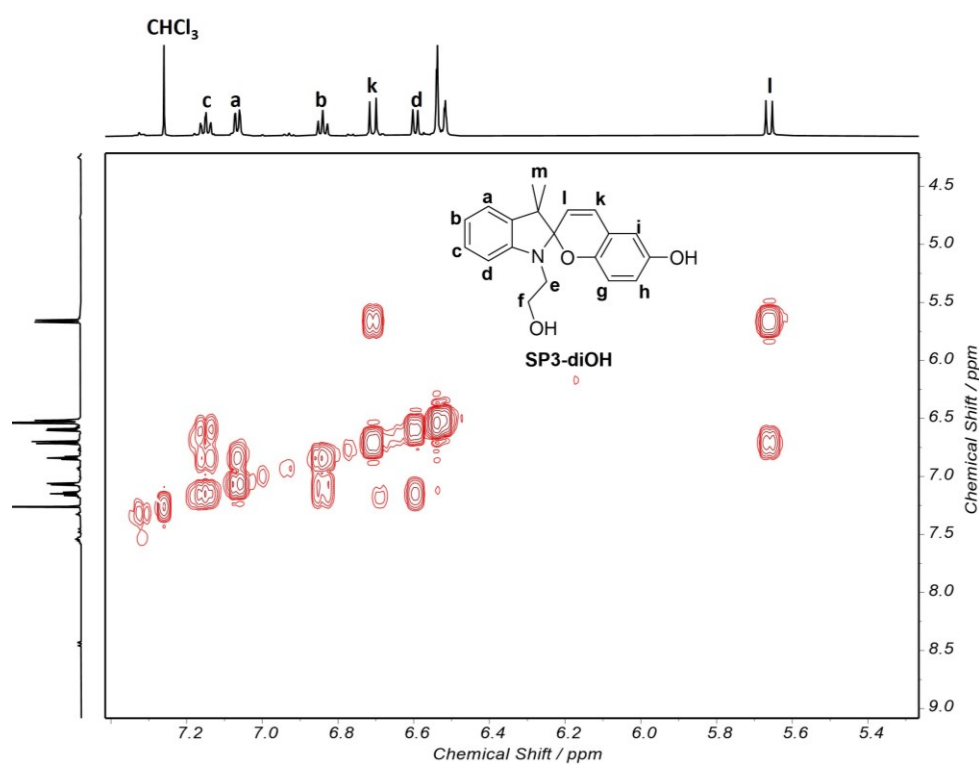


Figure S8.37. COSY sectional spectrum of compound **SP3-diOH** recorded in CDCl_3 .

11.8.6.11. SP3-mOH

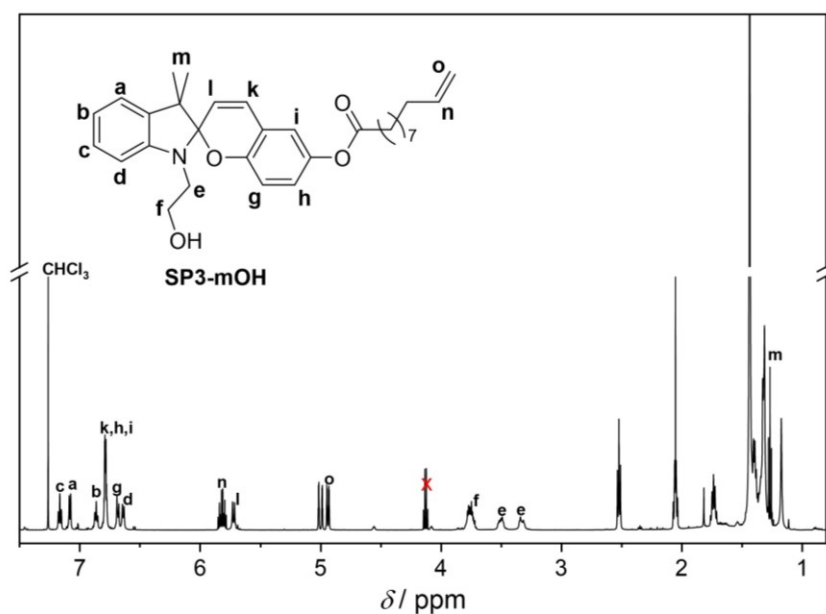


Figure S8.38. ^1H NMR spectrum (600 MHz, 16 scans) of **SP3-mOH** recorded in CDCl_3 .

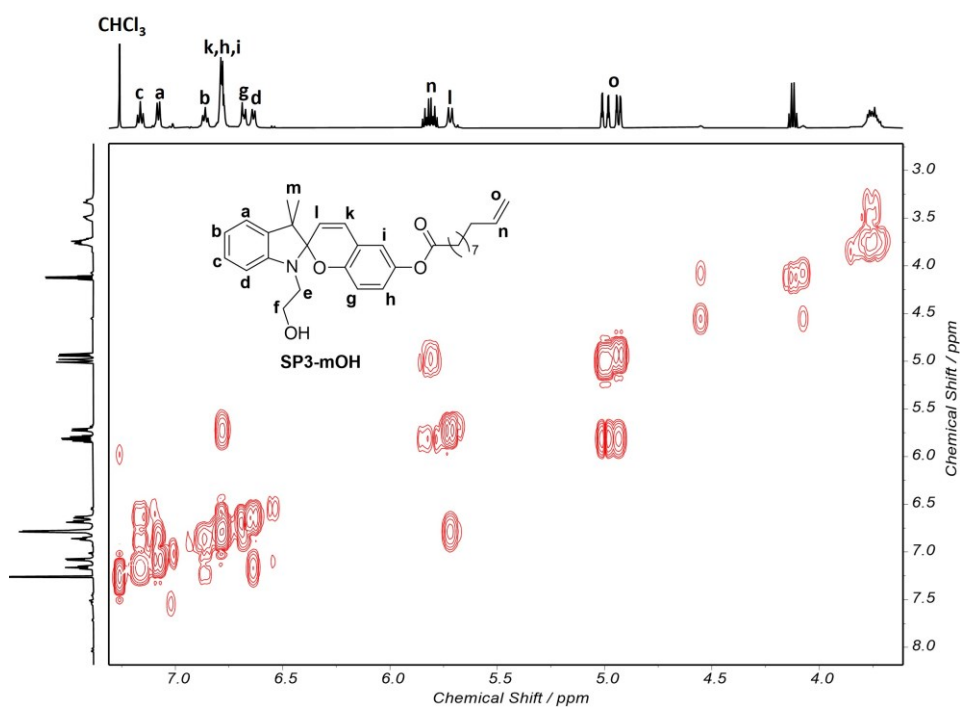


Figure S8.39. COSY sectional spectrum of compound **SP3-mOH** recorded in CDCl_3 .

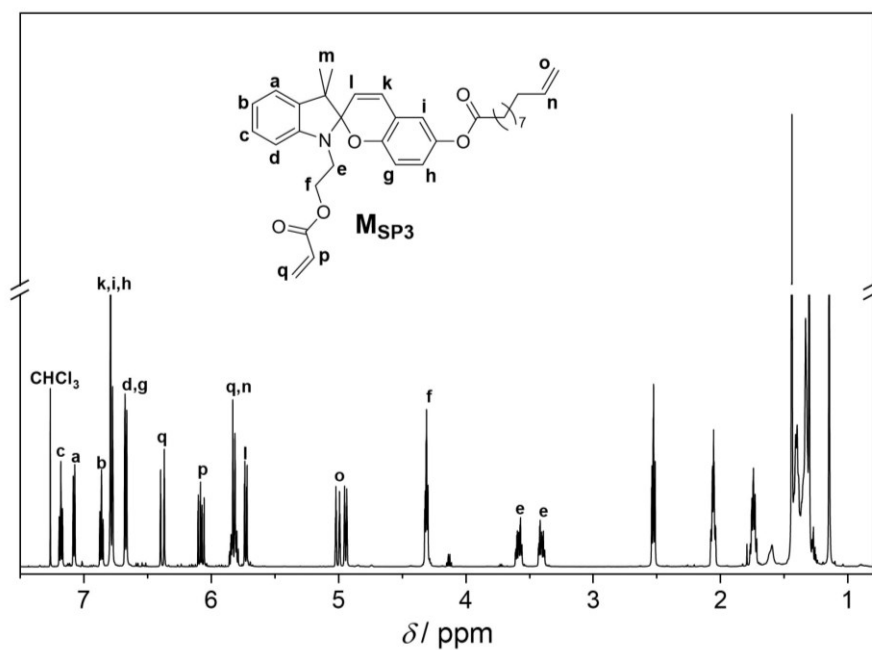
11.8.6.12. M_{SP3} 

Figure S8.40. 1H NMR spectrum (600 MHz, 16 scans) of M_{SP3} recorded in $CDCl_3$.

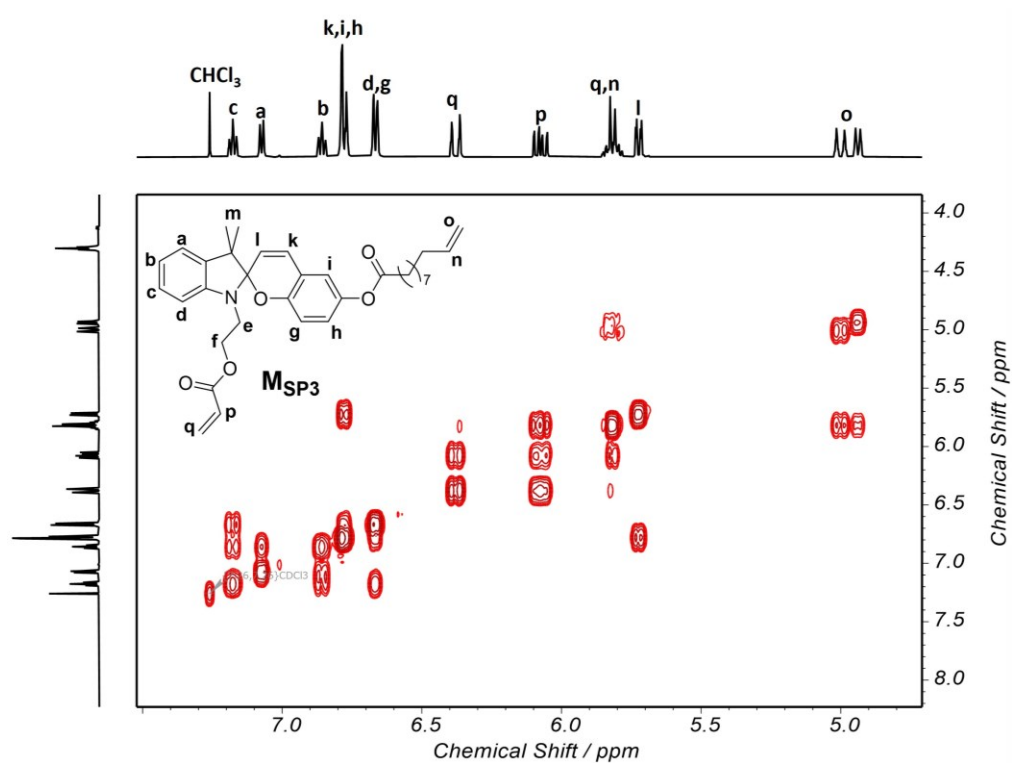


Figure S8.41. COSY sectional spectrum of compound M_{SP3} recorded in $CDCl_3$.

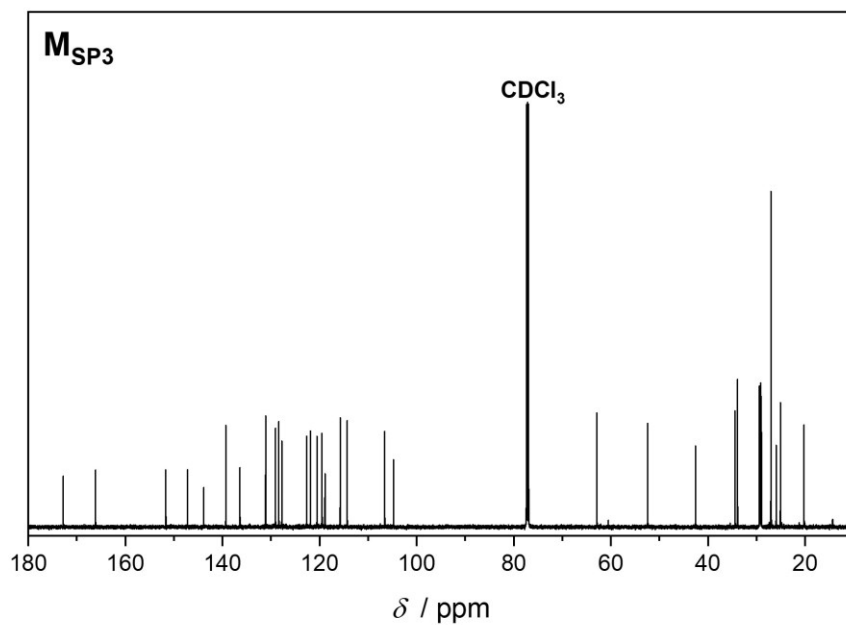


Figure S8.42. ¹³C (151 MHz) NMR spectrum of **M_{SP3}** in CDCl₃.

11.8.6.13. **P_{SP3}**

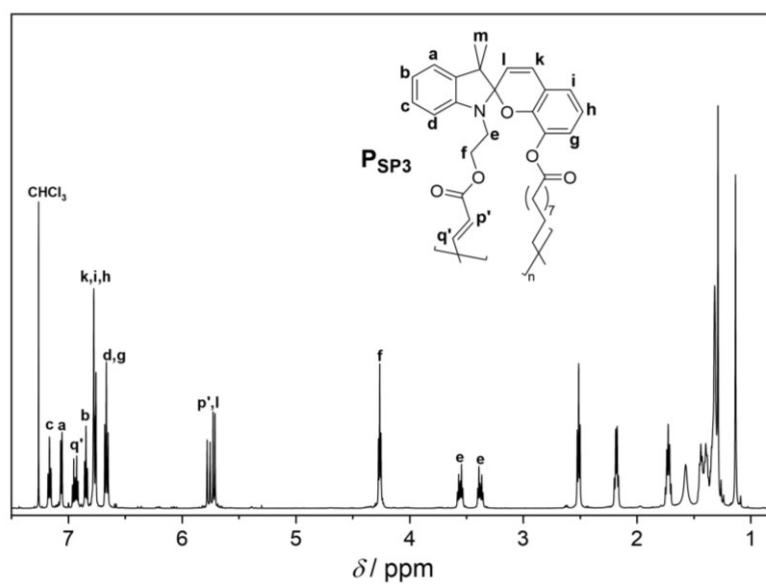


Figure S8.43. ¹H NMR spectrum (600 MHz, 32 scans) of **P_{SP3}** recorded in CDCl₃.

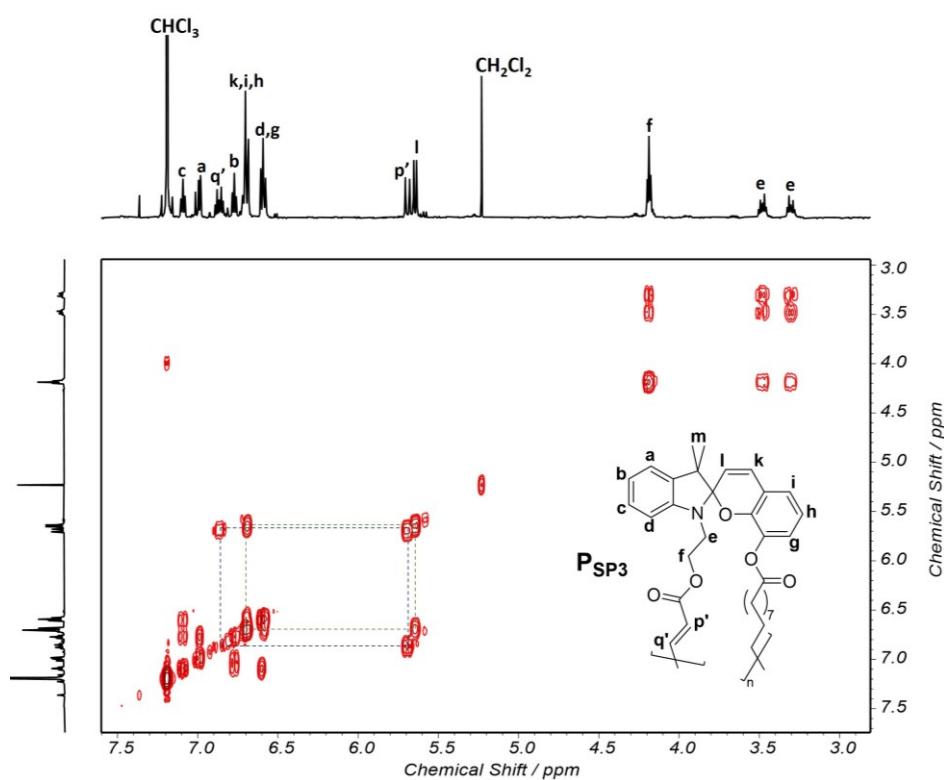


Figure S8.44. COSY sectional spectrum of compound P_{SP3} recorded in $CDCl_3$.

11.8.6.14. Compound 3

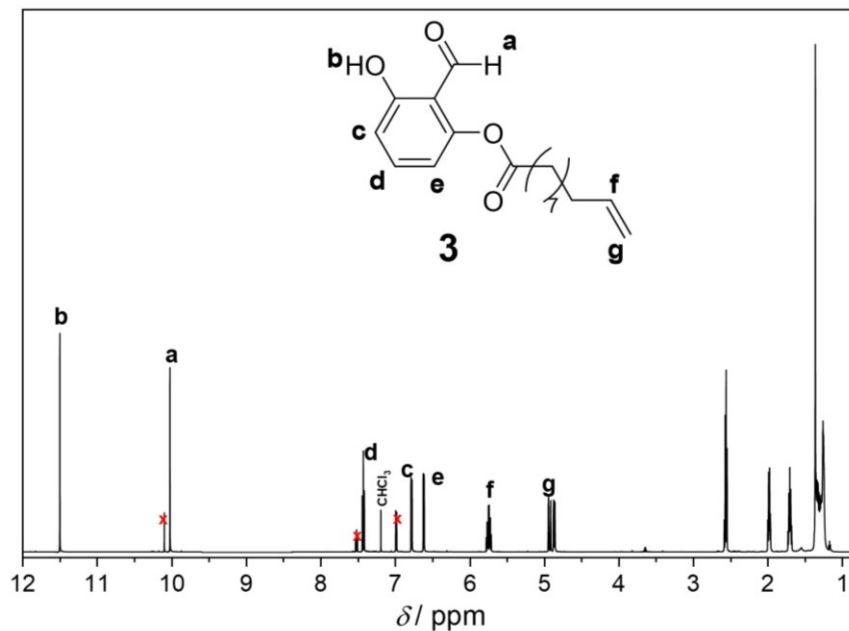


Figure S8.45. 1H NMR spectrum (600 MHz, 16 scans) of compound **3** recorded in $CDCl_3$. By-products are marked with a cross.

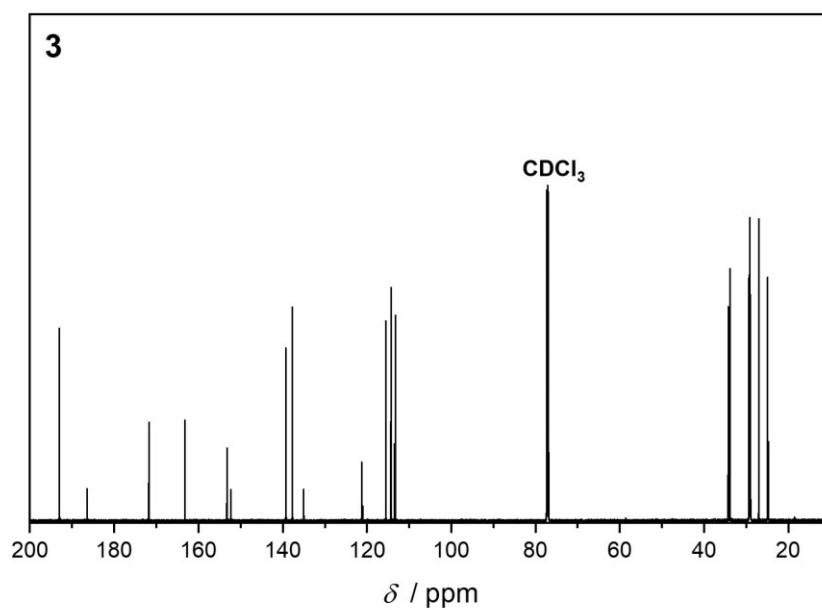


Figure S8.46. ^{13}C (151 MHz) NMR spectrum of compound **3** in CDCl_3 .

11.8.6.15. SP4-mOH

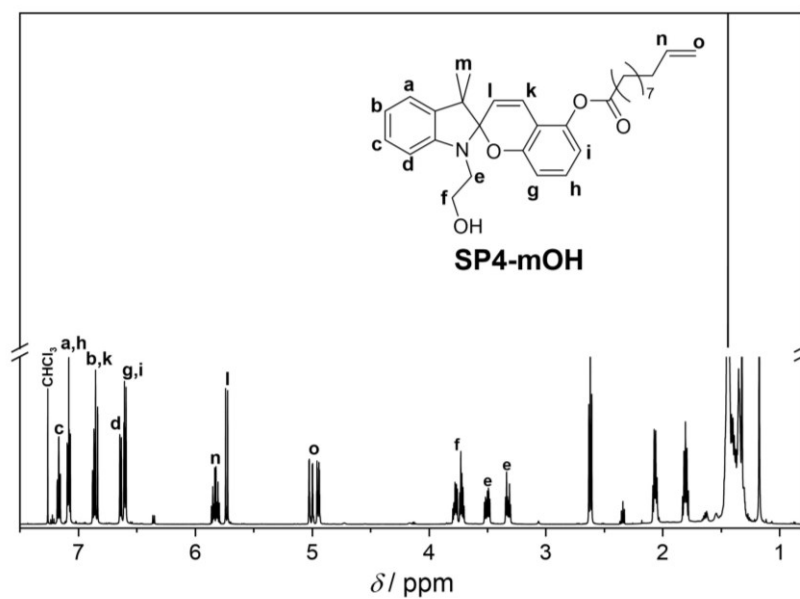


Figure S8.47. ^1H NMR spectrum (600 MHz, 16 scans) of **SP4-mOH** recorded in CDCl_3 .

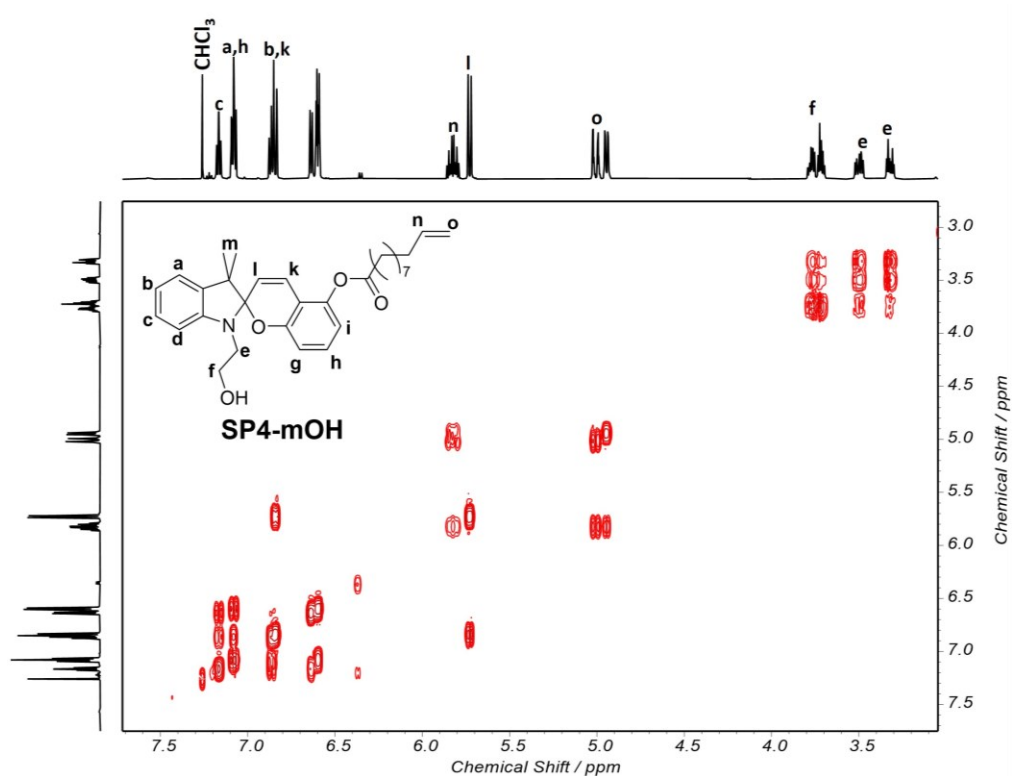


Figure S8.48. COSY sectional spectrum of compound **SP4-mOH** recorded in CDCl_3 .

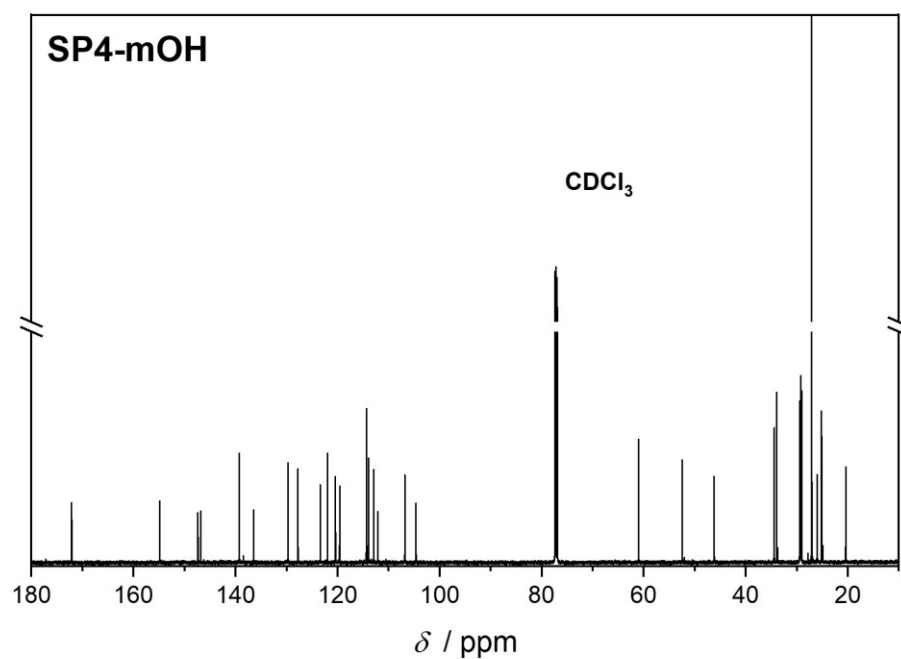


Figure S8.49. ^{13}C (151 MHz) NMR spectrum of **SP4-mOH** in CDCl_3 .

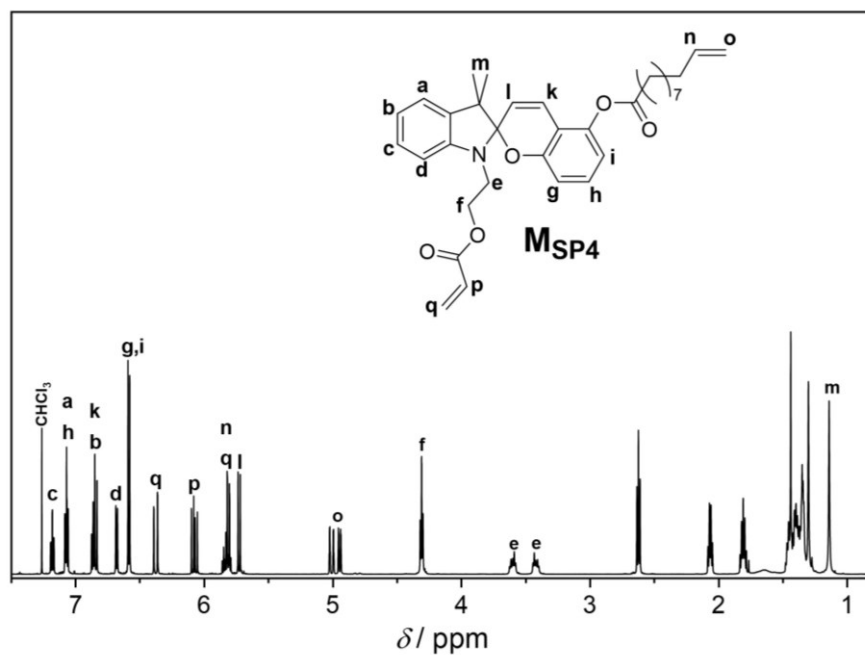
11.8.6.16. M_{SP4} 

Figure S8.50. ^1H NMR spectrum (600 MHz, 16 scans) of M_{SP4} recorded in CDCl_3 .

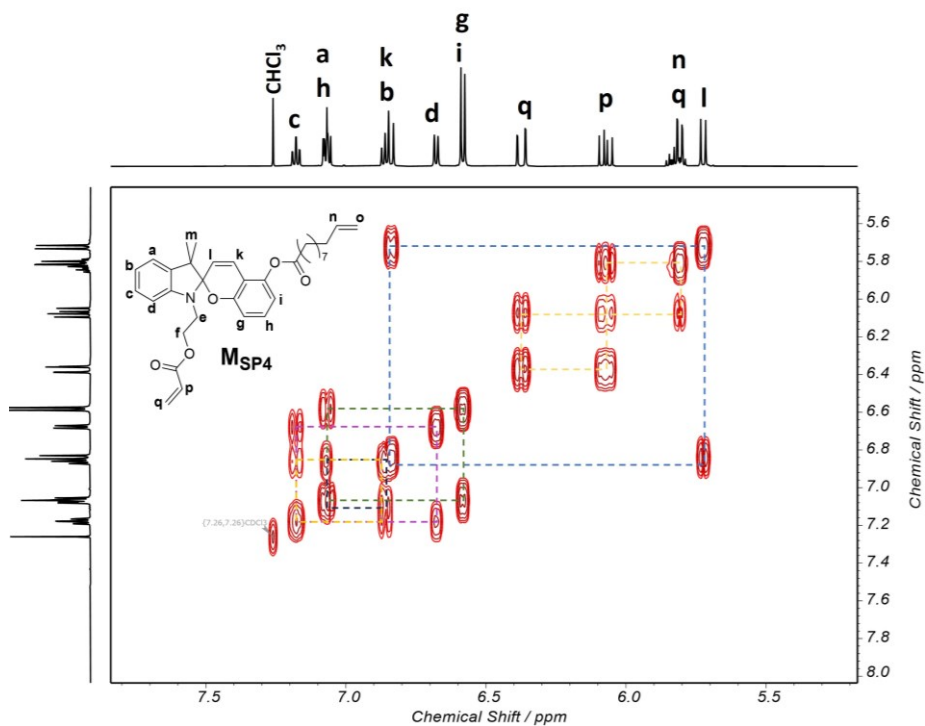


Figure S8.51. COSY sectional spectrum of compound M_{SP4} recorded in CDCl_3 .

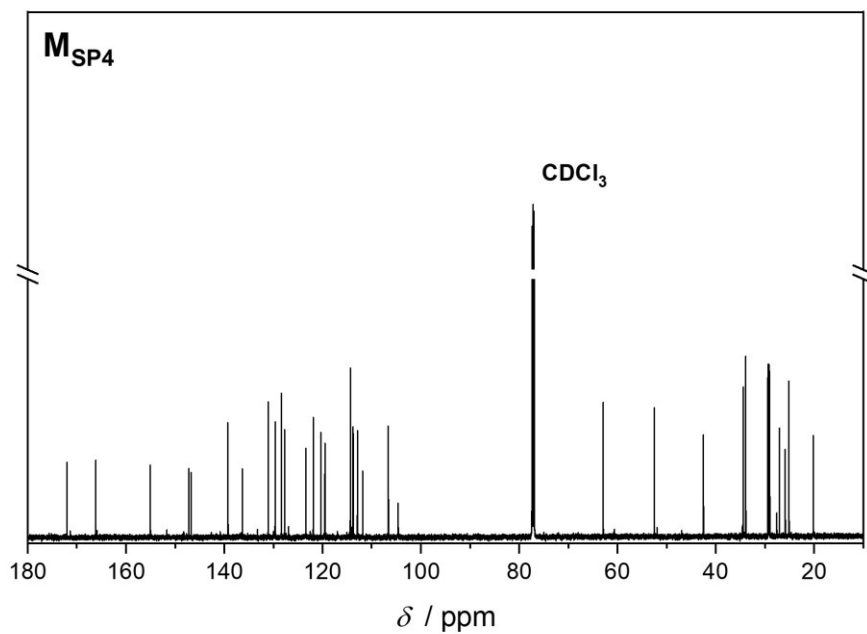


Figure S8.52. ^{13}C (151 MHz) NMR spectrum of **M_{SP4}** in CDCl_3 .

11.8.6.17. **P_{SP4}**

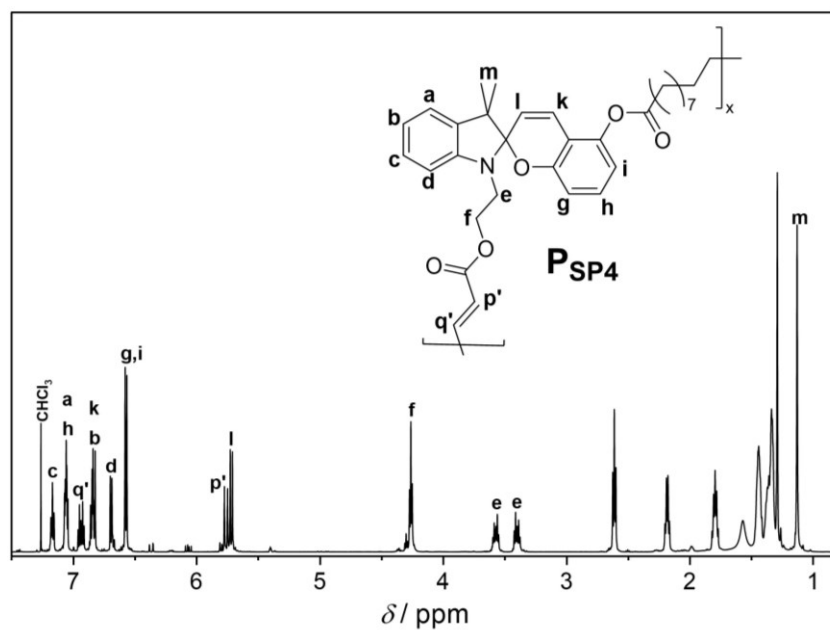


Figure S8.53. ^1H NMR spectrum (600 MHz, 32 scans) of **P_{SP4}** recorded in CDCl_3 .

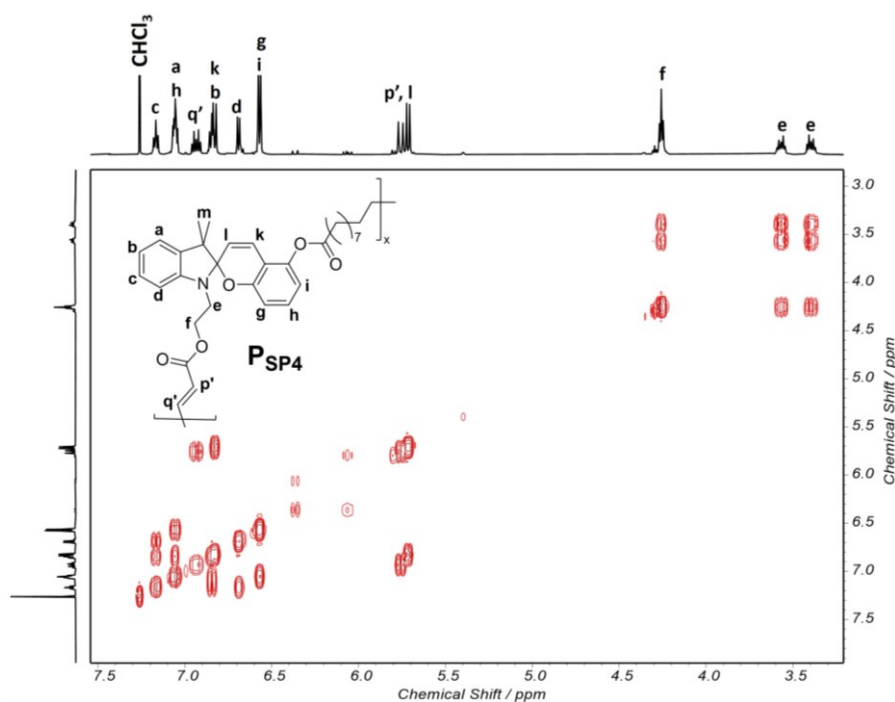


Figure S8.54. COSY sectional spectrum of compound P_{SP4} recorded in $CDCl_3$.

11.8.6.18. HO- C_{16} -OTBDMS

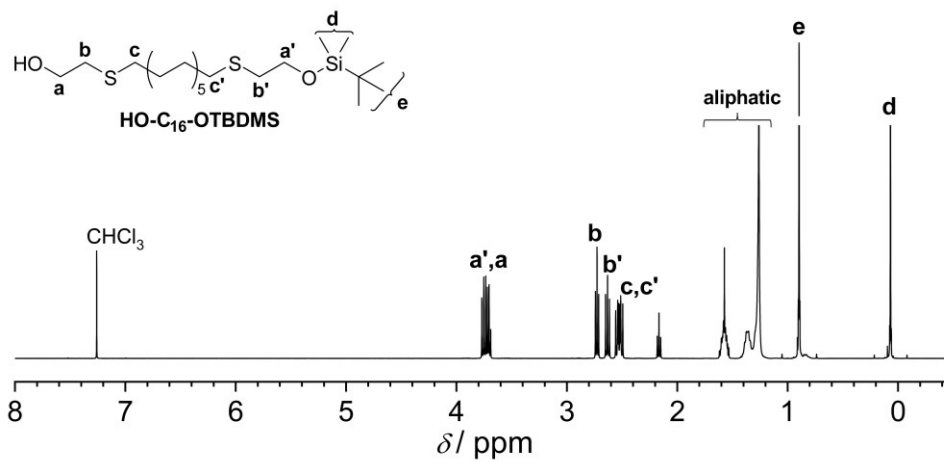


Figure S8.55. 1H NMR spectrum of HO- C_{16} -OTBDMS in $CDCl_3$.

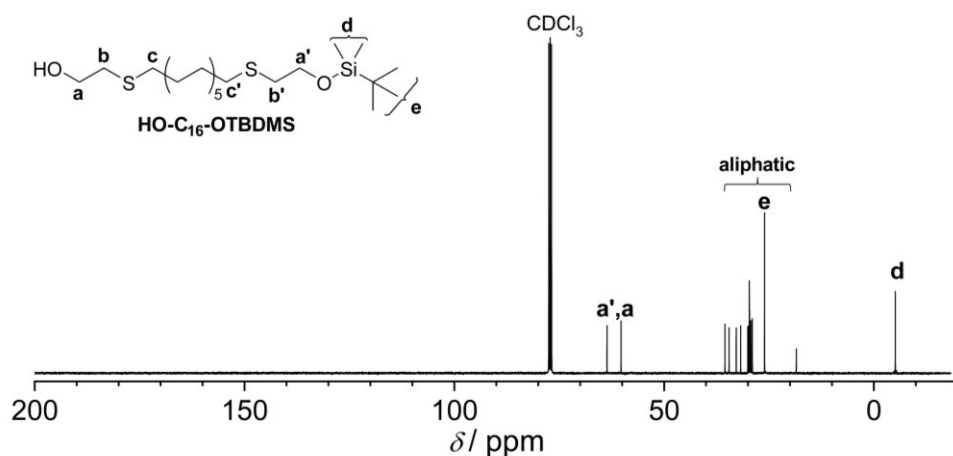


Figure S8.56. ^{13}C NMR spectrum of *HO-C₁₆-OTBDMS* in CDCl_3 .

11.8.6.19. *yne-C₁₆-OTBDMS*

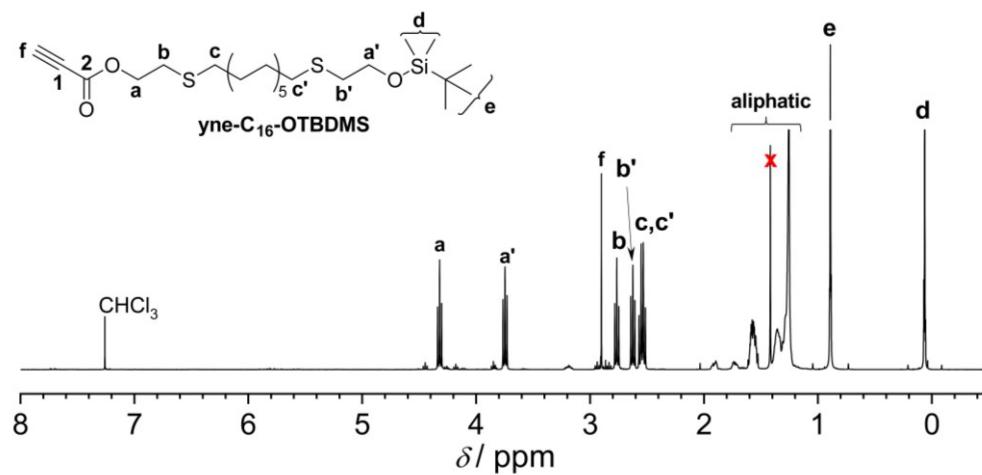


Figure S8.57. ^1H MR spectrum of *yne-C₁₆-OTBDMS* in CDCl_3 .

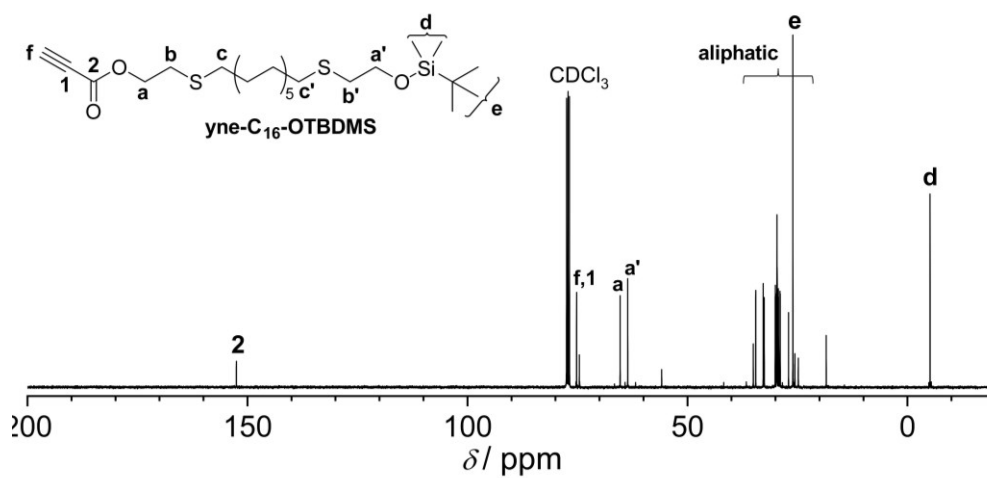
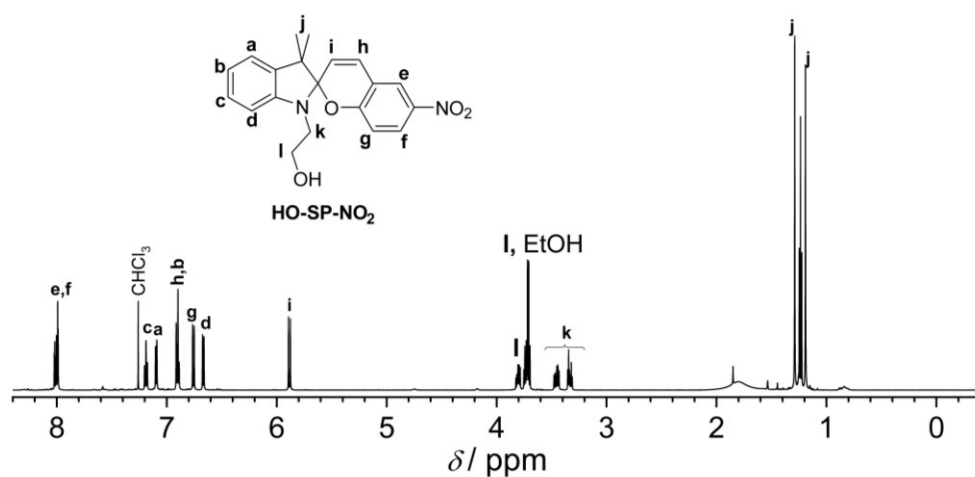
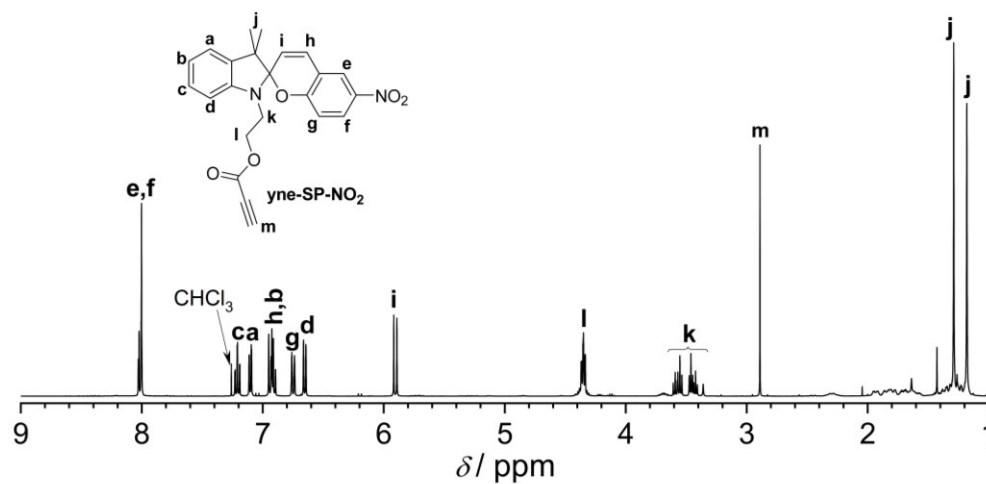


Figure S8.58. ^{13}C NMR spectrum of *yne-C₁₆-OTBDMS* in CDCl_3 .

11.8.6.20. HO-SP-NO₂Figure S8.59. ¹H NMR spectrum of HO-SP-NO₂ in CDCl₃.11.8.6.21. yne-SP-NO₂Figure S8.60. ¹H NMR spectrum of yne-SP-NO₂ in CDCl₃.

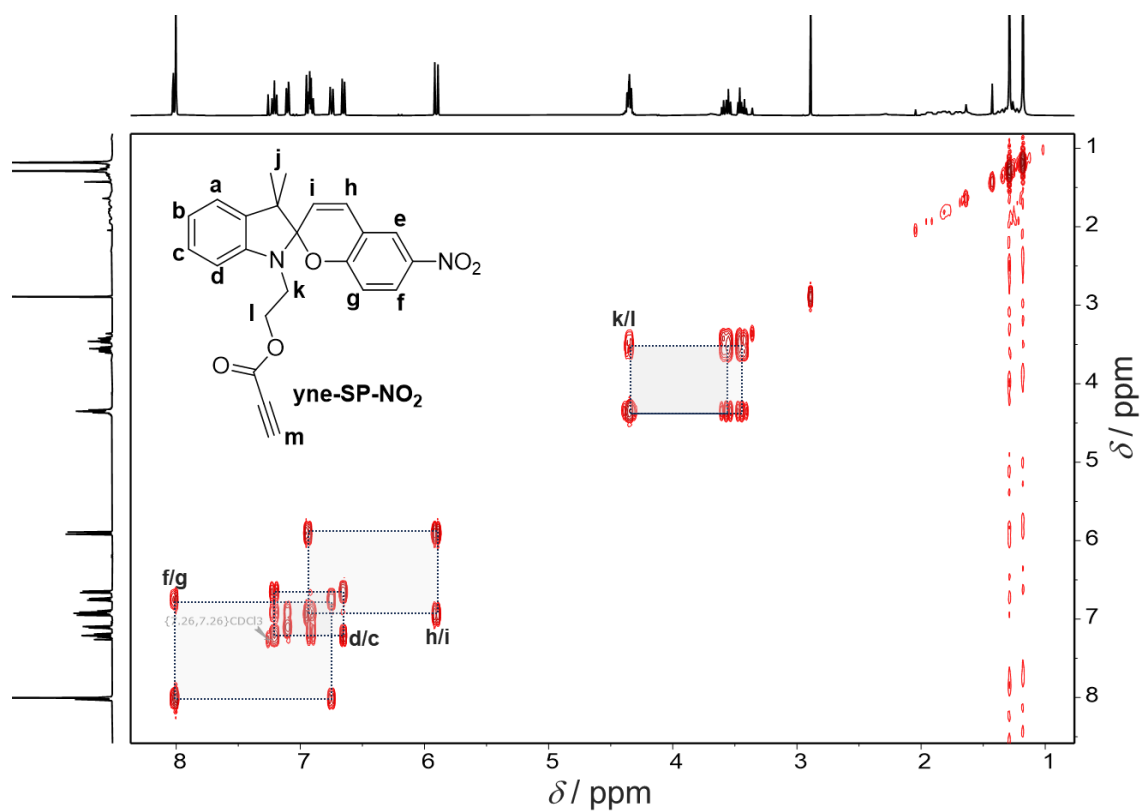


Figure S8.61. COSY spectrum of **yne-SP-NO₂** in CDCl₃.

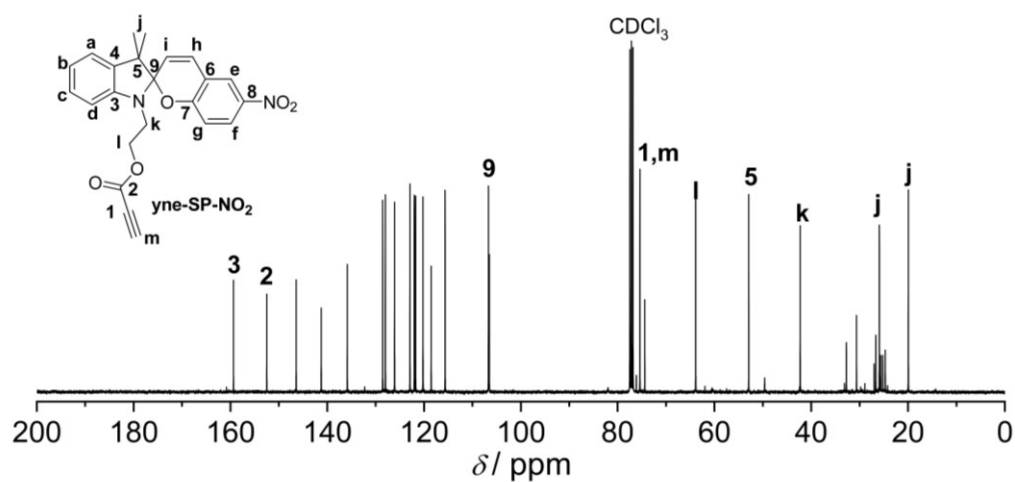
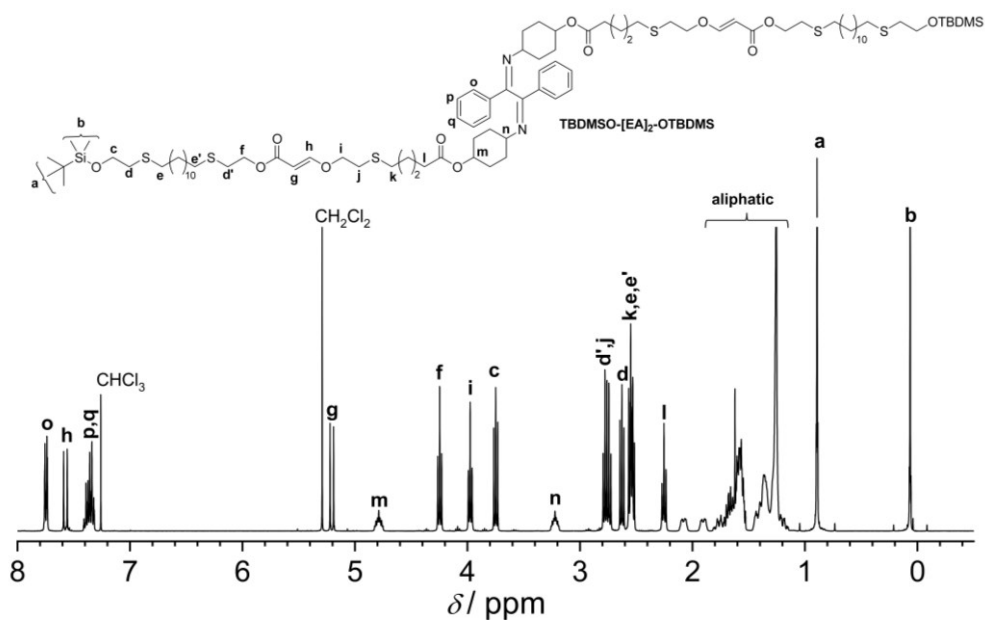
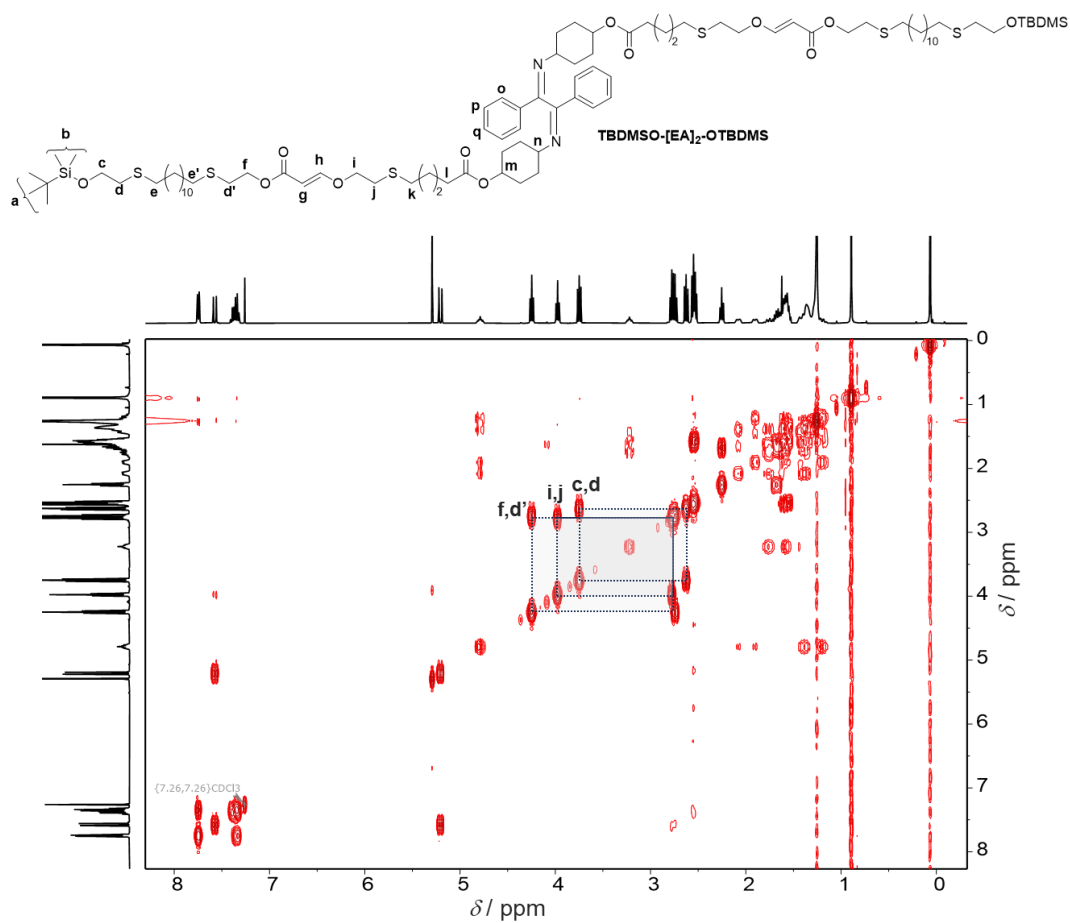
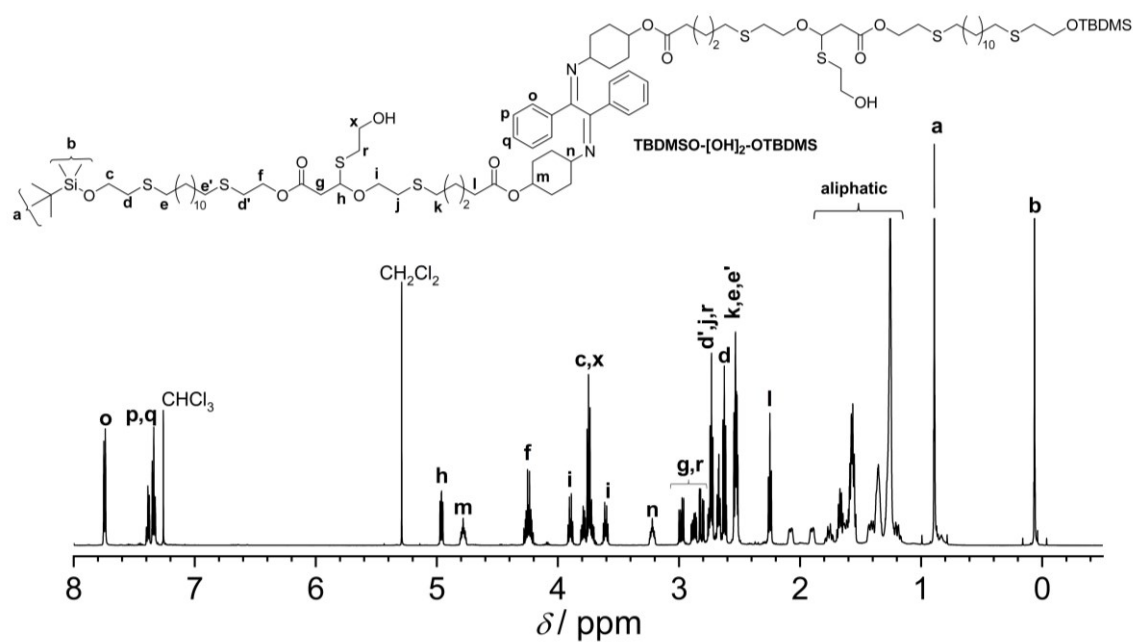


Figure S8.62. ¹³C NMR spectrum of **yne-SP-NO₂** in CDCl₃.

11.8.6.22. TBDMSO-[EA]₂-OTBDMSFigure S8.63. ¹H NMR spectrum of TBDMSO-[EA]₂-OTBDMS in CDCl₃.Figure S8.64. COSY spectrum of TBDMSO-[EA]₂-OTBDMS in CDCl₃.

11.8.6.23. TBDMSO-[OH]₂-OTBDMS



370

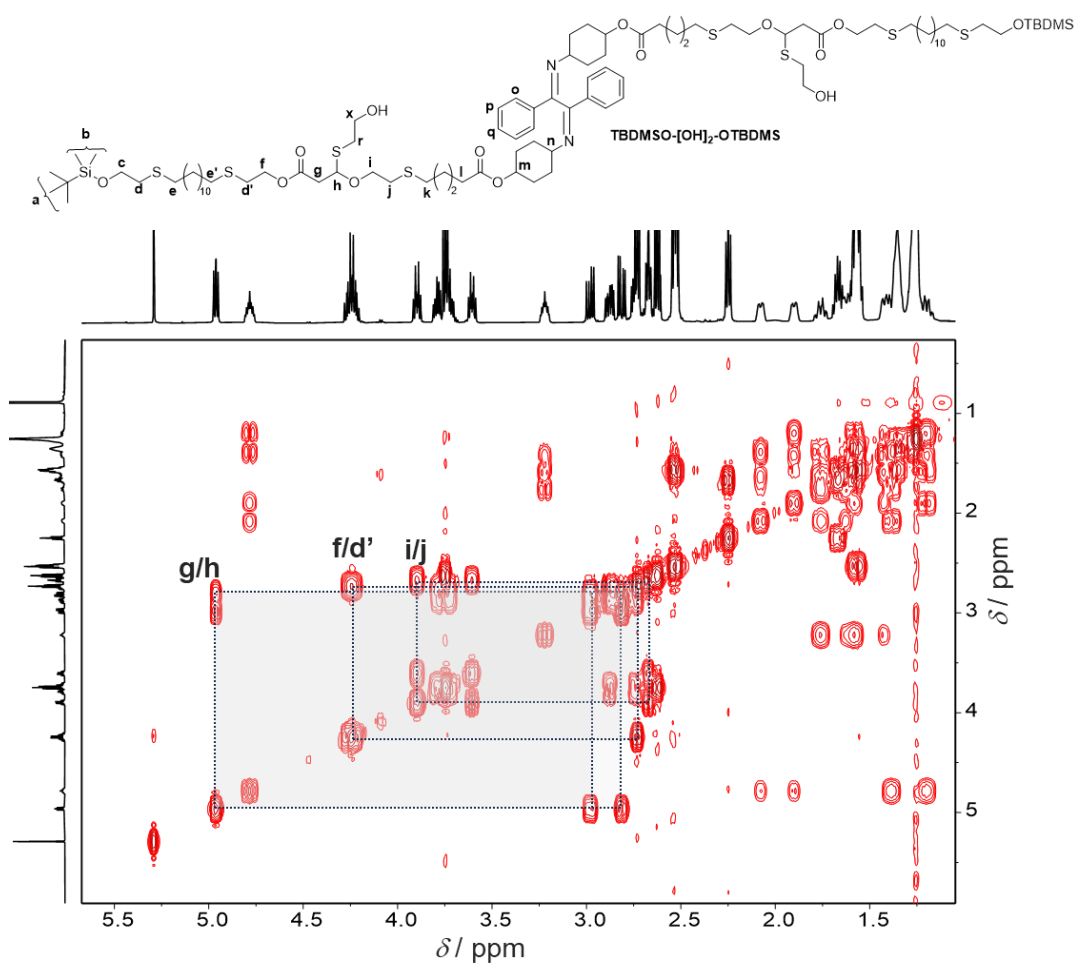


Figure S8.67. COSY sectional spectrum of **TBDMSO-[OH]₂-OTBDMS** in CDCl_3 .

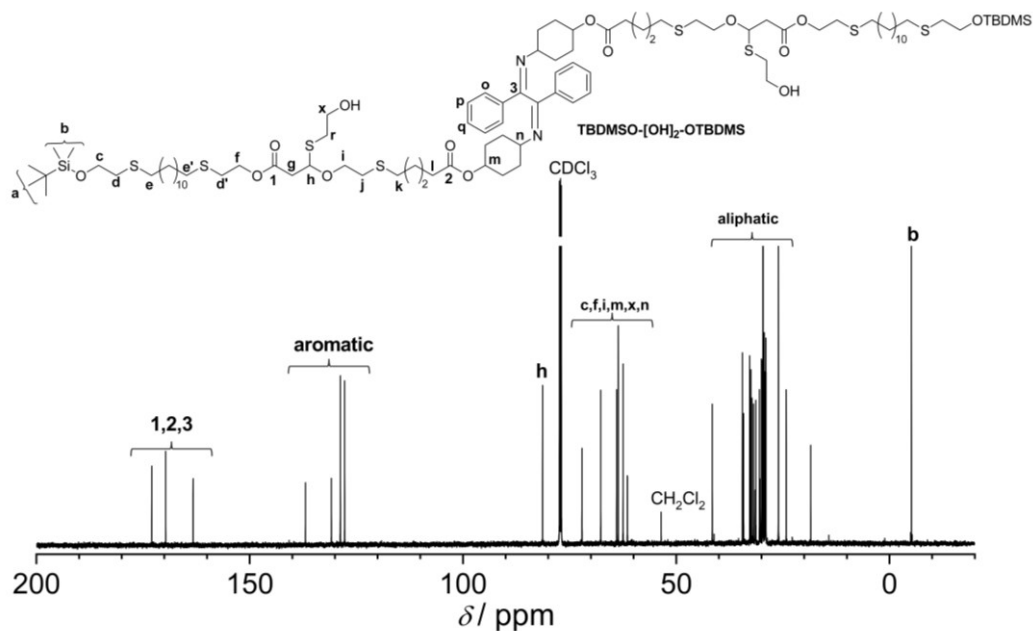
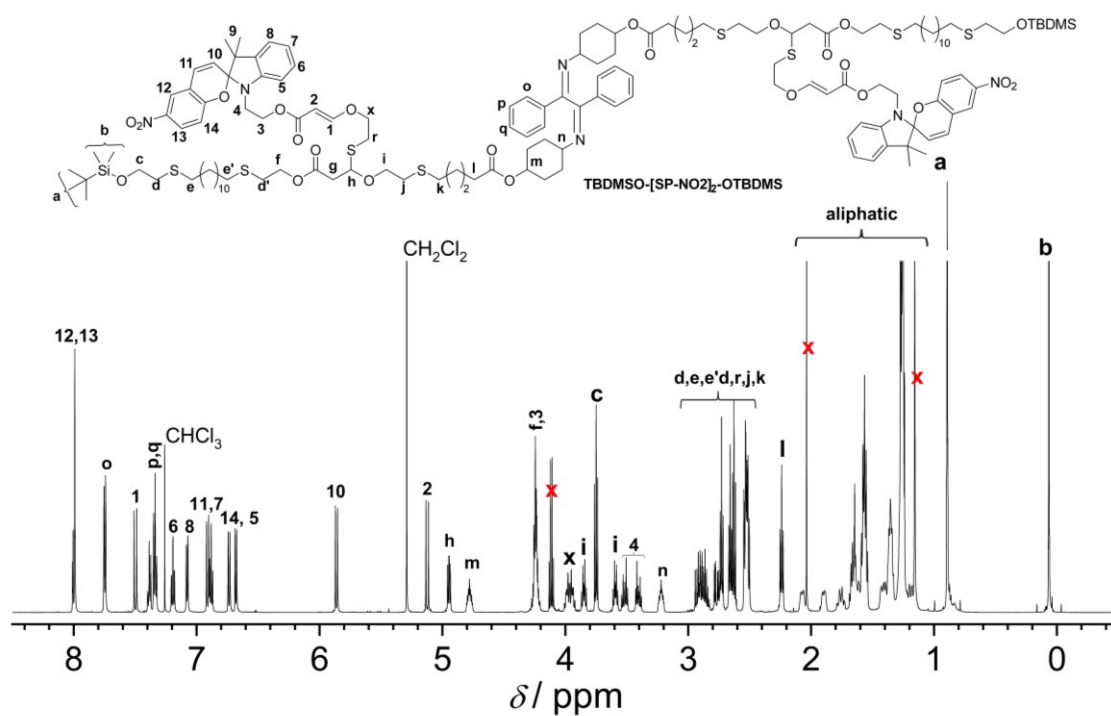
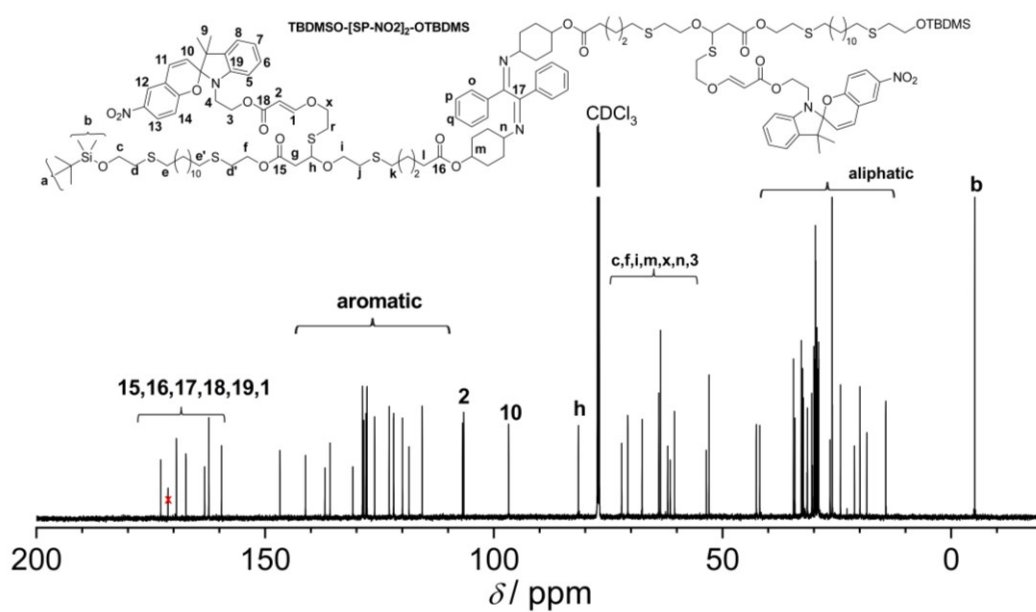


Figure S8.68. ^{13}C NMR spectrum of **TBDMSO-[OH]₂-OTBDMS** in CDCl_3 .

11.8.6.24. TBDMSO-[SP-NO₂]₂-OTBDMSFigure S8.69. ¹H NMR spectrum of TBDMSO-[SP-NO₂]₂-OTBDMS in CDCl₃.Figure S8.70. ¹³C NMR spectrum of TBDMSO-[SP-NO₂]₂-OTBDMS in CDCl₃.

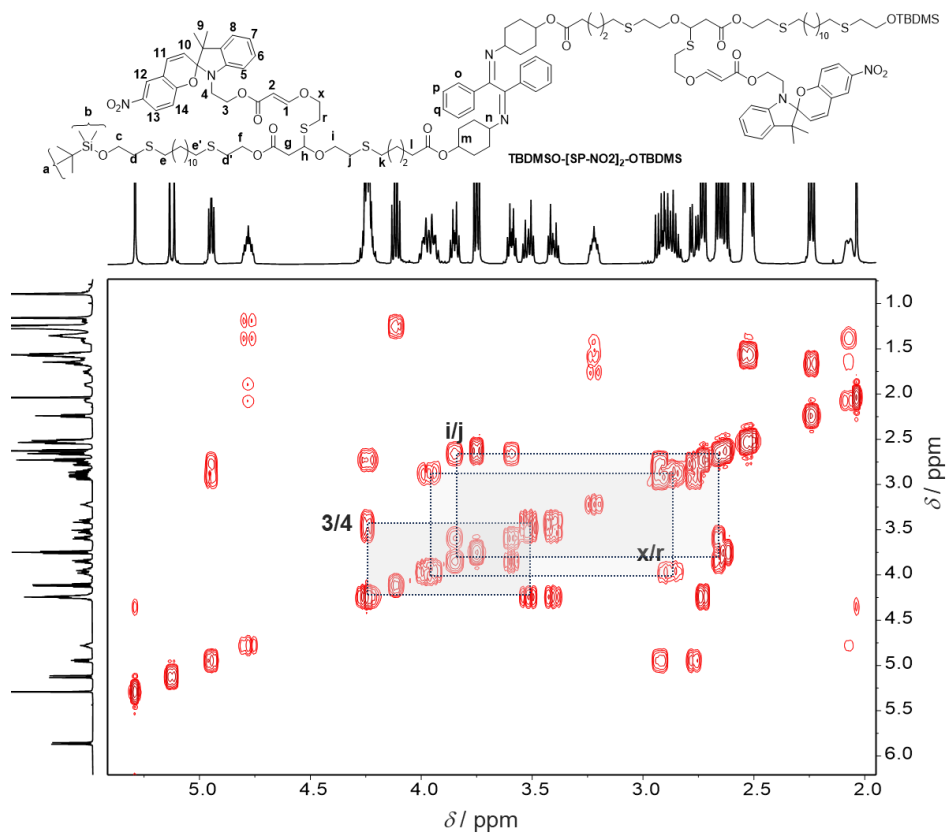


Figure S8.71. COSY NMR spectrum of **TBDMSO-[SP-NO₂]₂-OTBDMS** in CDCl₃.

11.8.6.25. HO-[EA]₂-OH

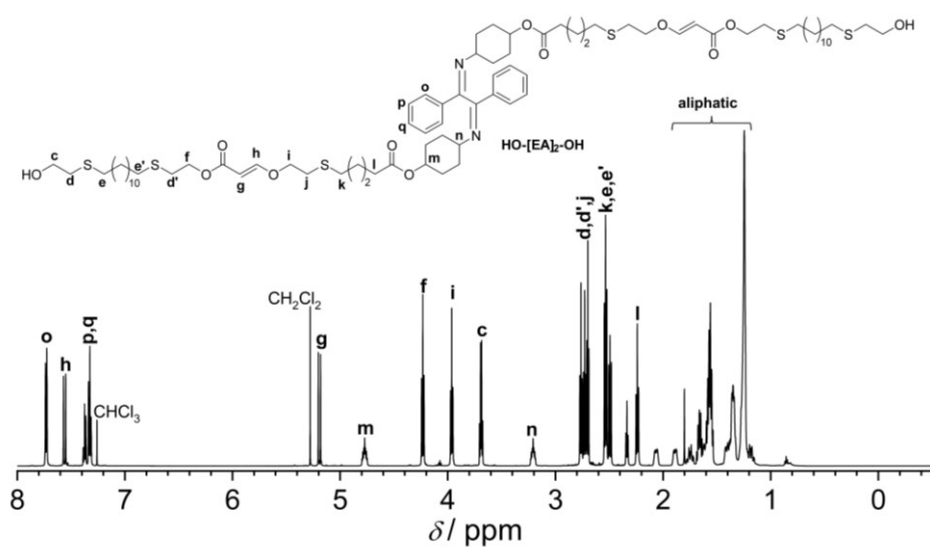


Figure S8.72. ¹H NMR spectrum of **HO-[EA]₂-OH** in CDCl₃.

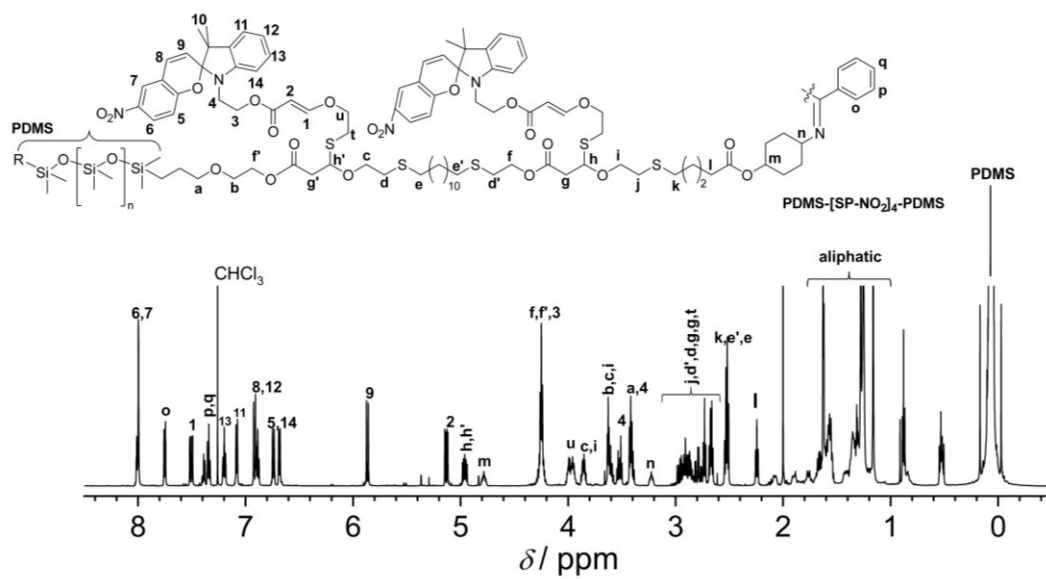
11.8.6.28. PDMS-[SP-NO₂]₄-PDMS

Figure S8.75. ¹H NMR spectrum of PDMS-[SP-NO₂]₄-PDMS in CDCl₃.

11.9. Information for Chapter 9

11.9.1. TEM investigation of BCP periodicity

Depicted below are the TEM micrographs from which the periodicity/domain spacing of the phase separated triBCPs has been extracted via their power spectrum (**Error! Reference source not found.**S9). The morphology is dominated by the surface interaction between the BCPs and the carbon substrate, leading – in combination with thickness variations – to a mix of morphologies that strongly differ from the regular bulk morphologies (body centered cubic (BCC), face centered cubic (FCC), hexagonally packed cylinder (Hex), gyroid (Gyr), and lamella (Lam) and makes a precise determination challenging.³⁰⁰ Where identifiable, the observable thin film phases are indicated.

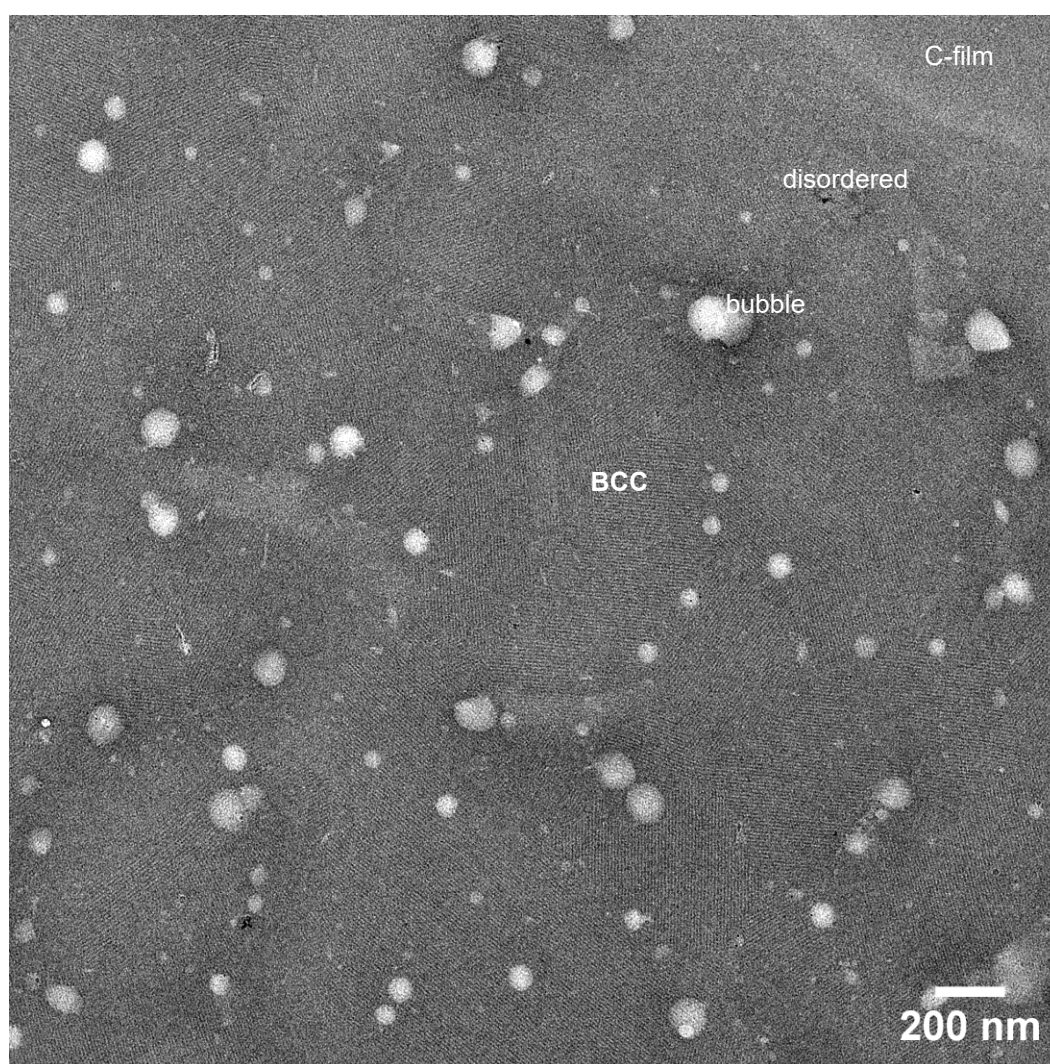


Figure S9.1. TEM micrograph of the triblock copolymer samples **PDMS-[B]₂-PDMS** used to extract the periodicity from the power spectrum in **Figure S9.7**. The bright spots are bubbles resulting from the sample preparation.

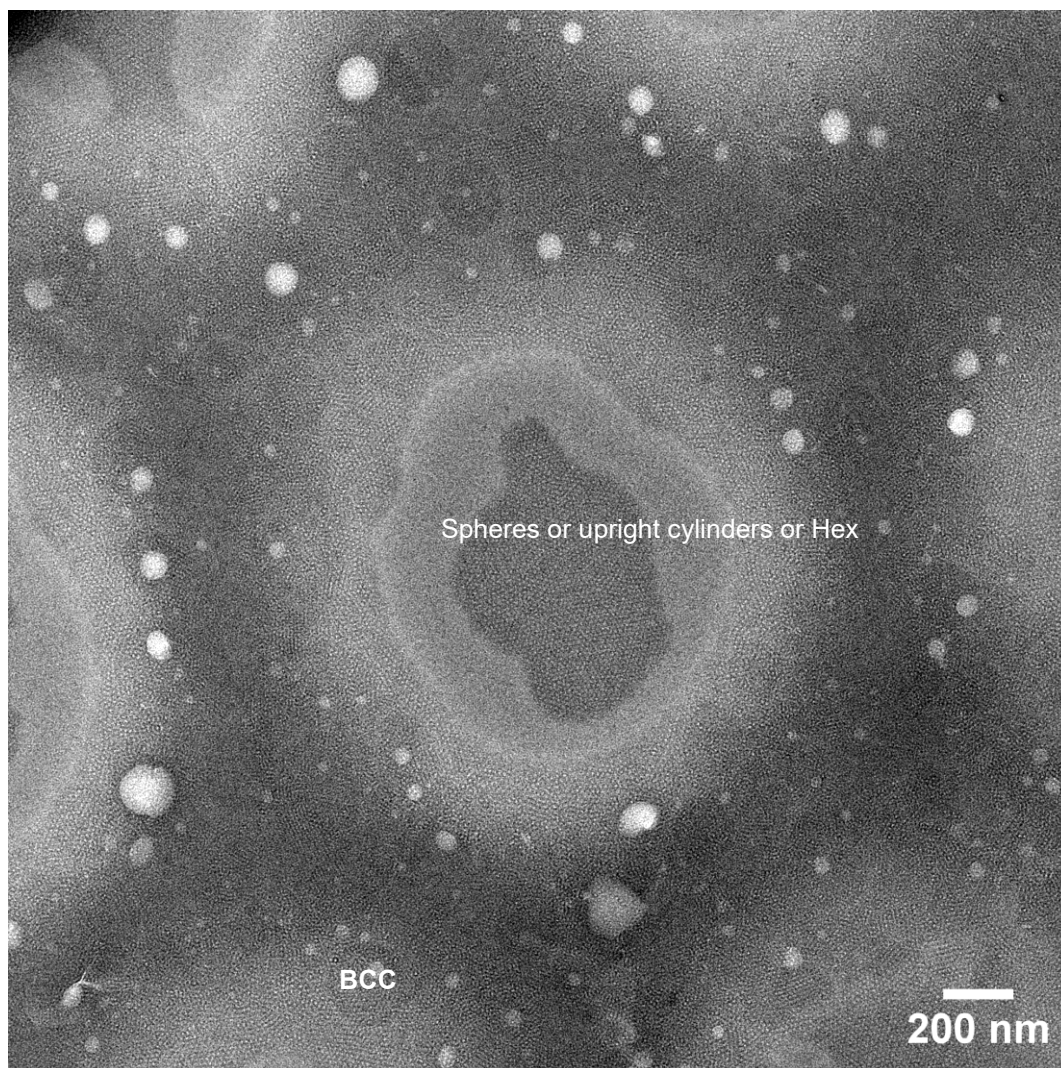


Figure S9.2. TEM micrograph of the triblock copolymer samples **PDMS-[B]₃-PDMS** used to extract the periodicity from the power spectrum in **Figure S9.7**.

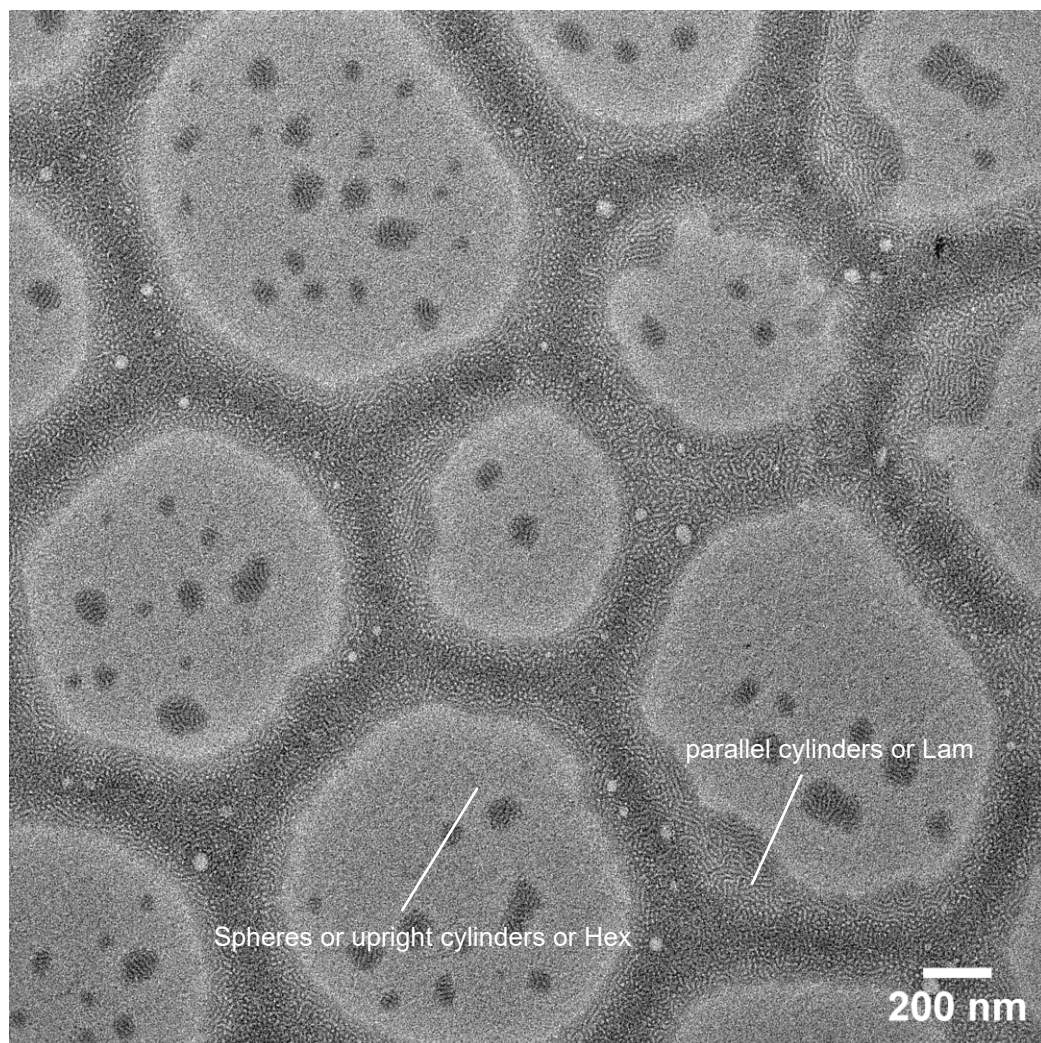


Figure S9.3. TEM micrograph of the triblock copolymer samples **PDMS- $[B]_x$ -PDMS** used to extract the periodicity from the power spectrum in **Figure S9.7**.

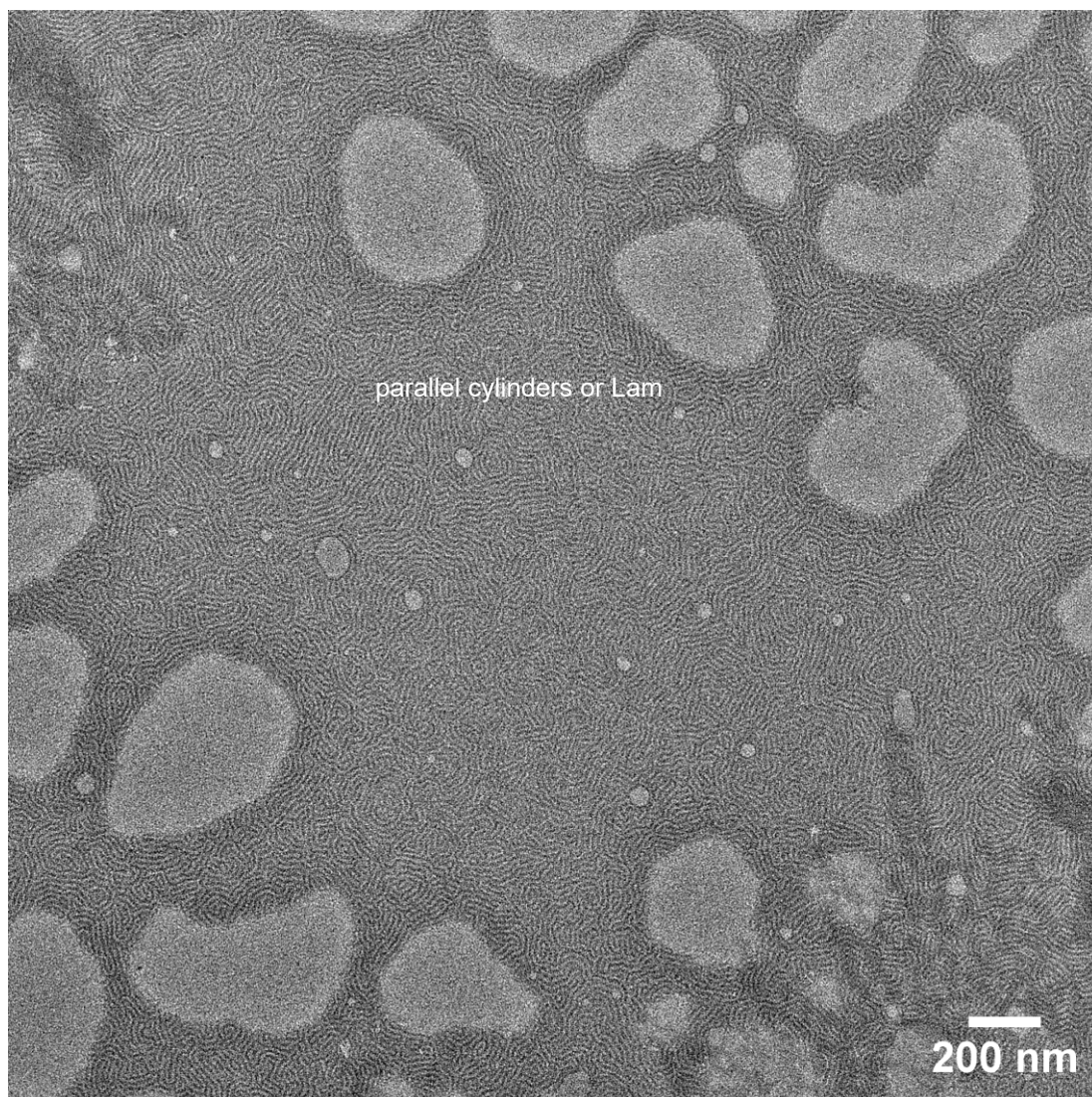


Figure S9.4. TEM micrograph of the triblock copolymer samples **PDMS-[B]₅-PDMS** used to extract the periodicity from the power spectrum in **Figure S9.7**.

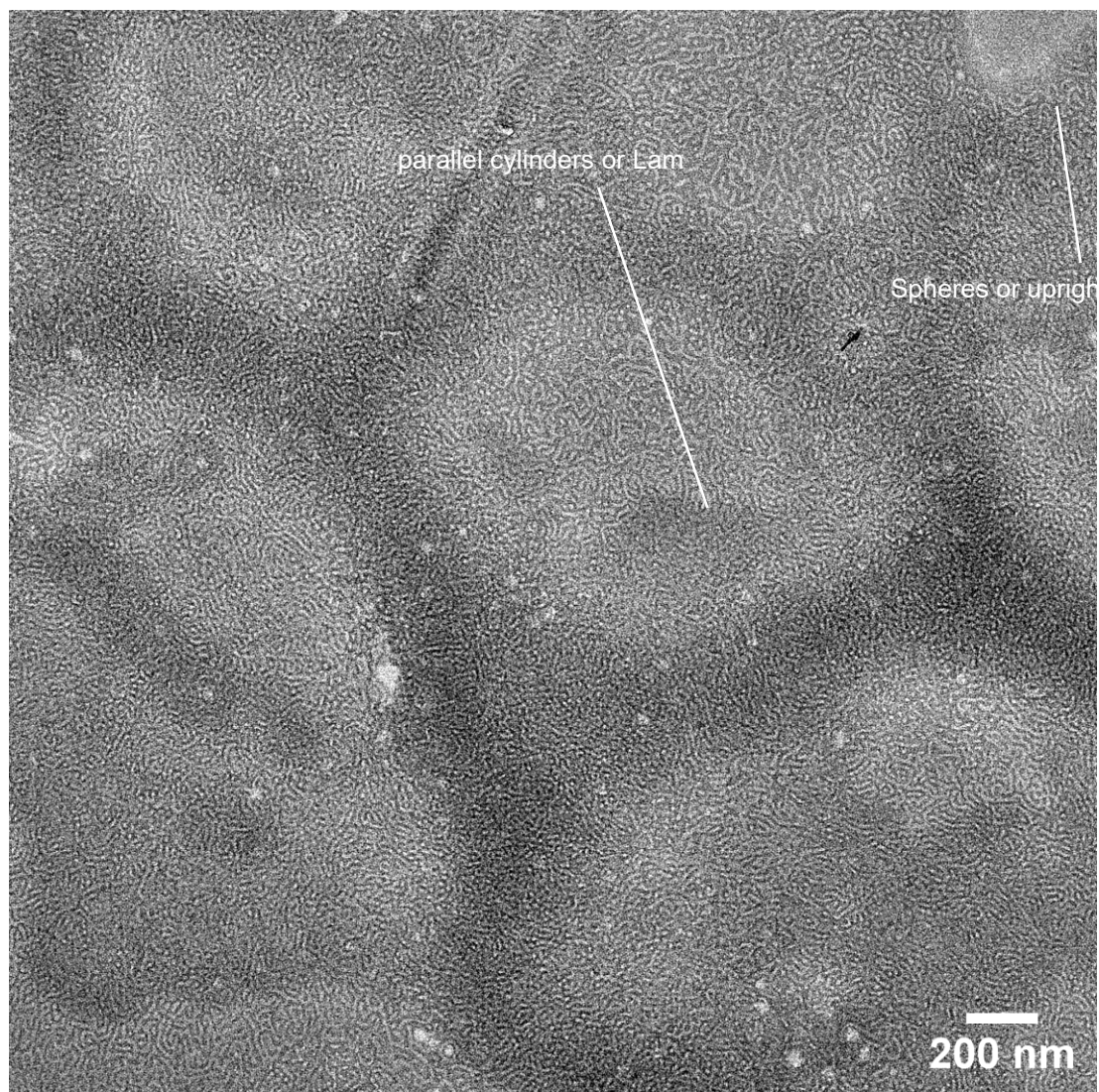


Figure S9.5. TEM micrograph of the triblock copolymer samples **PDMS-[B]₆-PDMS** used to extract the periodicity from the power spectrum in **Figure S9.7**.

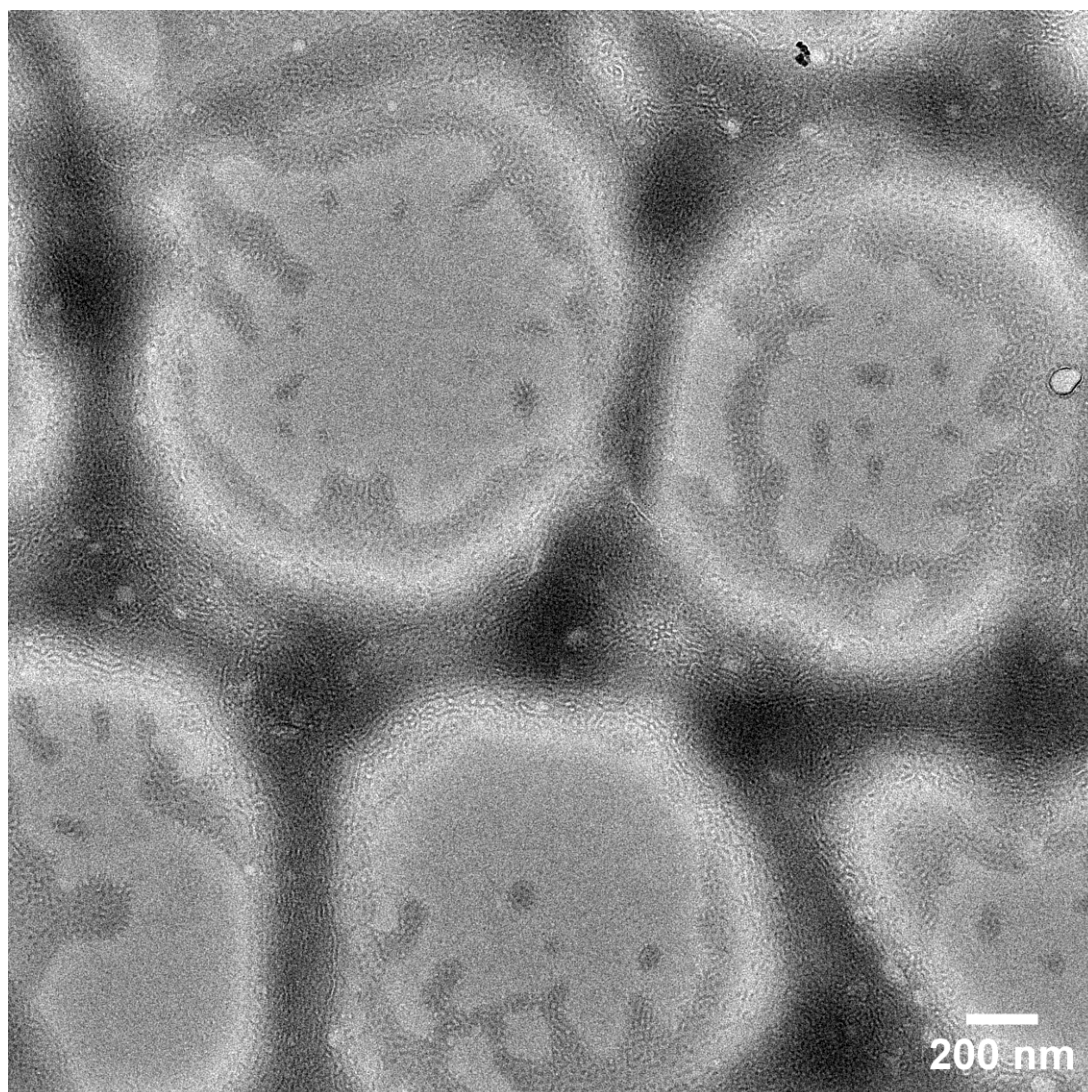


Figure S9.6. TEM micrograph of the triblock copolymer samples **PDMS-[B]₇-PDMS** used to extract the periodicity from the power spectrum in **Figure S9.7**.

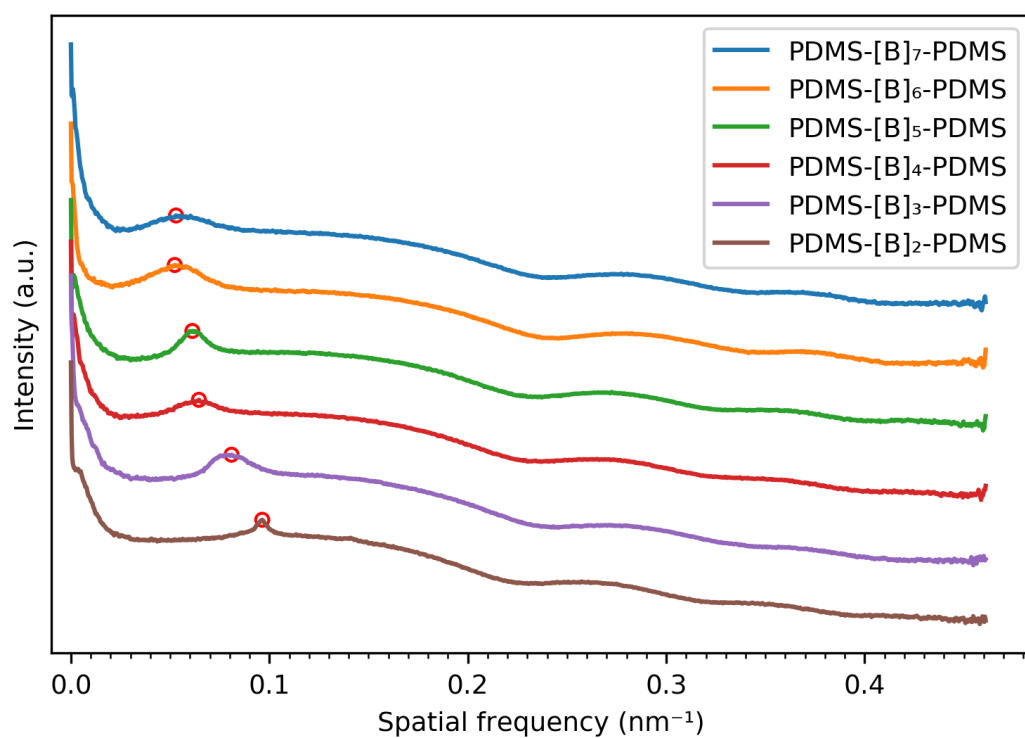


Figure S9.7. Power spectra of the triblock copolymers TEM micrographs. The red circles indicate the peak maxima used to extract the domain spacing of the phase separation.

11.9.2. Spectra and Graphs

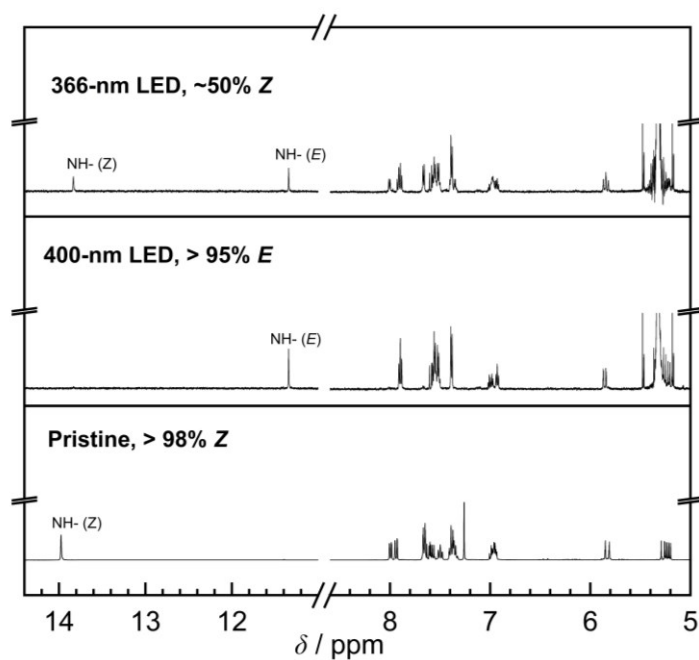


Figure S9.8. Stack sectional ^1H NMR spectra (in CDCl_3 or CD_2Cl_2) of PDMS-[H]₄-PDMS block copolymer before and after irradiation with LEDs. The solution was withdrawn from the same stock solution to ensure the homogeneity of the sample in SAXS measurements.

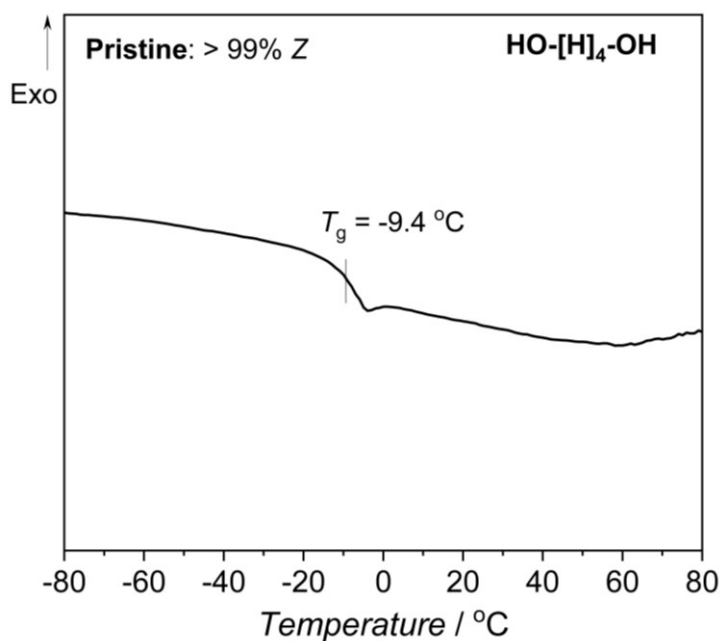


Figure S9.9. DSC thermogram of hydrazone oligomer, HO-[H]₄-OH. The curve was taken from the second heating cycle.

References

1. Yang GG, Choi HJ, Han KH, Kim JH, Lee CW, Jung EI, et al. Block copolymer nanopatterning for nonsemiconductor device applications. *ACS Applied Materials & Interfaces*. **2022**;14(10):12011-37.
2. Morris M. Directed self-assembly of block copolymers for nanocircuitry fabrication. *Microelectronic Engineering*. **2015**;132:207-17.
3. Tang C, Lennon EM, Fredrickson GH, Kramer EJ, Hawker CJ. Evolution of block copolymer lithography to highly ordered square arrays. *Science*. **2008**;322(5900):429-32.
4. Seshimo T, Maeda R, Odashima R, Takenaka Y, Kawana D, Ohmori K, et al. Perpendicularly oriented sub-10-nm block copolymer lamellae by atmospheric thermal annealing for one minute. *Scientific reports*. **2016**;6(1):19481.
5. Jeong G, Yu DM, Mapas JKD, Sun Z, Rzayev J, Russell TP. Realizing 5.4 nm full pitch lamellar microdomains by a solid-state transformation. *Macromolecules*. **2017**;50(18):7148-54.
6. Cao H, Dai L, Liu Y, Li X, Yang Z, Deng H. Methacrylic block copolymers containing liquid crystalline and fluorinated side chains capable of fast formation of 4 nm domains. *Macromolecules*. **2020**;53(20):8757-64.
7. Kwak J, Mishra AK, Lee J, Lee KS, Choi C, Maiti S, et al. Fabrication of sub-3 nm feature size based on block copolymer self-assembly for next-generation nanolithography. *Macromolecules*. **2017**;50(17):6813-8.
8. Hancox E, Derry MJ, Greenall MJ, Huband S, Al-Shok L, Town JS, et al. Heterotelechelic homopolymers mimicking high χ -ultralow N block copolymers with sub-2 nm domain size. *Chemical Science*. **2022**;13(14):4019-28.
9. Maekawa S, Seshimo T, Dazai T, Sato K, Hatakeyama-Sato K, Nabae Y, et al. Chemically tailored block copolymers for highly reliable sub-10-nm patterns by directed self-assembly. *Nature Communications*. **2024**;15(1):5671.
10. Boothby J, Ware T. Dual-responsive, shape-switching bilayers enabled by liquid crystal elastomers. *Soft Matter*. **2017**;13(24):4349-56.
11. Kalva N, Uthaman S, Lee SJ, Lim YJ, Augustine R, Huh KM, et al. Degradable pH-responsive polymer prodrug micelles with aggregation-induced emission for cellular imaging and cancer therapy. *Reactive and Functional Polymers*. **2021**;166:104966.
12. Fang Y, Ni Y, Choi B, Leo SY, Gao J, Ge B, et al. Chromogenic photonic crystals enabled by novel vapor - responsive shape - memory polymers. *Advanced Materials*. **2015**;27(24):3696-704.
13. Göstl R, Senf A, Hecht S. Remote-controlling chemical reactions by light: Towards chemistry with high spatio-temporal resolution. *Chemical Society Reviews*. **2014**;43(6):1982-96.
14. Liu T, Bao B, Li Y, Lin Q, Zhu L. Photo-responsive Polymers based on o-Nitrobenzyl Derivatives: From Structural Design to Applications. *Progress in Polymer Science*. **2023**:101741.
15. Boelke J, Hecht S. Designing molecular photoswitches for soft materials applications. *Advanced Optical Materials*. **2019**;7(16):1900404.
16. Jenkins A, Kratochvíl P, Stepto R, Suter U. Glossary of basic terms in polymer science (IUPAC Recommendations 1996). *Pure and applied chemistry*. **1996**;68(12):2287-311.
17. Feldthusen J, Iván B, Müller AH. Synthesis of linear and star-shaped block copolymers of isobutylene and methacrylates by combination of living cationic and anionic polymerizations. *Macromolecules*. **1998**;31(3):578-85.

18. Kwon Y, Faust R. Synthesis of polyisobutylene-based block copolymers with precisely controlled architecture by living cationic polymerization. *New Synthetic Methods*. **2004**;107-36.
19. Mühlebach A, Gaynor SG, Matyjaszewski K. Synthesis of amphiphilic block copolymers by atom transfer radical polymerization (ATRP). *Macromolecules*. **1998**;31(18):6046-52.
20. Keddie DJ. A guide to the synthesis of block copolymers using reversible-addition fragmentation chain transfer (RAFT) polymerization. *Chemical Society Reviews*. **2014**;43(2):496-505.
21. Banerjee SL, Singha NK. A new class of dual responsive self-healable hydrogels based on a core crosslinked ionic block copolymer micelle prepared via RAFT polymerization and Diels–Alder “click” chemistry. *Soft Matter*. **2017**;13(47):9024-35.
22. Abdellatif MM, Nomura K. Precise synthesis of amphiphilic multiblock copolymers by combination of acyclic diene metathesis (ADMET) polymerization with atom transfer radical polymerization (ATRP) and click chemistry. *ACS Macro Letters*. **2012**;1(3):423-7.
23. Paquet C, Kumacheva E. Nanostructured polymers for photonics. *Materials today*. **2008**;11(4):48-56.
24. Giraud EC, Ghoshal T, Morris MA. Observation of ordered microphase separation of block copolymer micellar thin films under argon-plasma radiation. *Applied Surface Science*. **2021**;561:149800.
25. Bayomi RAH, Aoki T, Sasaki S, Sakurai S. Regular ordering of spherical microdomains in dewetted monolayer islands induced by thermal annealing of spin-coated ultrathin films of a triblock copolymer. *Soft Matter*. **2021**;17(31):7396-407.
26. Zhang C, Vigil DL, Sun D, Bates MW, Loman T, Murphy EA, et al. Emergence of hexagonally close-packed spheres in linear block copolymer melts. *Journal of the American Chemical Society*. **2021**;143(35):14106-14.
27. Han SH, Pryamitsyn V, Bae D, Kwak J, Ganesan V, Kim JK. Highly asymmetric lamellar nanopatterns via block copolymer blends capable of hydrogen bonding. *ACS nano*. **2012**;6(9):7966-72.
28. Shi W, Hamilton AL, Delaney KT, Fredrickson GH, Kramer EJ, Ntaras C, et al. Creating extremely asymmetric lamellar structures via fluctuation-assisted unbinding of miktoarm star block copolymer alloys. *Journal of the American Chemical Society*. **2015**;137(19):6160-3.
29. Leibler L. Theory of Microphase Separation in Block Copolymers. *Macromolecules*. **1980**;13(6):1602-17.
30. Shelton CK, Epps III TH. Block copolymer thin films: Characterizing nanostructure evolution with in situ X-ray and neutron scattering. *Polymer*. **2016**;105:545-61.
31. Hasegawa H, Tanaka H, Hashimoto T, Han CC. SANS and SAXS study of block copolymer/homopolymer mixtures. *Journal of Applied Crystallography*. **1991**;24(5):672-8.
32. Stubenrauch K, Fritz-Popovski G, Ingolić E, Grogger W, Glatter O, Stelzer F, et al. Microphase separation study of amphiphilic ROMP block copolymers by SAXS and TEM. *Macromolecules*. **2007**;40(13):4592-600.
33. McLean RS, Sauer BB. Tapping-mode AFM studies using phase detection for resolution of nanophases in segmented polyurethanes and other block copolymers. *Macromolecules*. **1997**;30(26):8314-7.
34. Rasmont A, Leclère P, Doneux C, Lambin G, Tong JD, Jérôme R, et al. Microphase separation at the surface of block copolymers, as studied with atomic force microscopy. *Colloids and surfaces B: biointerfaces*. **2000**;19(4):381-95.

35. Cochran EW, Garcia-Cervera CJ, Fredrickson GH. Stability of the gyroid phase in diblock copolymers at strong segregation. *Macromolecules*. **2006**;39(7):2449-51.
36. Huang C, Zhu Y, Man X. Block copolymer thin films. *Physics Reports*. **2021**;932:1-36.
37. Zhu S, Li D, Zhan H, Chen S, Peng J. Synergistic Manipulation of Phase Transition between Cocrystallization and Microphase Segregation in Conjugated Triblock Copolymers for Organic Field-Effect Transistors. *Macromolecules*. **2024**;57(5):2067-77.
38. Scherf U, Gutacker A, Koenen N. All-conjugated block copolymers. *Accounts of chemical research*. **2008**;41(9):1086-97.
39. Yager KG, Lai E, Black CT. Self-assembled phases of block copolymer blend thin films. *ACS nano*. **2014**;8(10):10582-8.
40. Choi C, Ahn S, Kim JK. Diverse morphologies of block copolymers by blending with homo (and co) polymers. *ACS Publications*; **2020**. p. 4577-80.
41. Yamaguchi D, Shiratake S, Hashimoto T. Ordered structure in blends of block copolymers. 5. Blends of lamella-forming block copolymers showing both microphase separation involving unique morphological transitions and macrophase separation. *Macromolecules*. **2000**;33(22):8258-68.
42. Tanaka H, Hasegawa H, Hashimoto T. Ordered structure in mixtures of a block copolymer and homopolymers. 1. Solubilization of low molecular weight homopolymers. *Macromolecules*. **1991**;24(1):240-51.
43. Jo G, Ahn H, Park MJ. Simple route for tuning the morphology and conductivity of polymer electrolytes: one end functional group is enough. *ACS Macro Letters*. **2013**;2(11):990-5.
44. Park J, Nam J, Seo M, Li S. Side-Chain Density Driven Morphology Transition in Brush-Linear Diblock Copolymers. *ACS Macro Letters*. **2022**;11(4):468-74.
45. Lin Z, Nabae Y, Hayakawa T. Control of microphase-separated structures by tuning the functional groups and the degree of modification for a single block copolymer. *Polymer Chemistry*. **2023**;14(17):2045-53.
46. Schoberth HG, Olszowka V, Schmidt K, Böker A. Effects of electric fields on block copolymer nanostructures. *Complex Macromolecular Systems I*. **2010**:1-31.
47. Schmidt K, Schoberth HG, Ruppel M, Zettl H, Hänsel H, Weiss TM, et al. Reversible tuning of a block-copolymer nanostructure via electric fields. *Nature materials*. **2008**;7(2):142-5.
48. Choi C, Park J, Vincent Joseph KL, Lee J, Ahn S, Kwak J, et al. Simultaneous fabrication of line and dot dual nanopatterns using miktoarm block copolymer with photocleavable linker. *Nature communications*. **2017**;8(1):1765.
49. Yu H, Iyoda T, Ikeda T. Photoinduced alignment of nanocylinders by supramolecular cooperative motions. *Journal of the American Chemical Society*. **2006**;128(34):11010-1.
50. Zha RH, Vantomme G, Berrocal JA, Gosens R, de Waal B, Meskers S, et al. Photoswitchable nanomaterials based on hierarchically organized siloxane oligomers. *Advanced Functional Materials*. **2018**;28(1):1703952.
51. Douglas P, Burrows HD, Evans RC. Foundations of photochemistry: a background on the interaction between light and molecules. *Applied photochemistry: Springer*; **2013**. p. 1-88.
52. Bléger D, Hecht S. Visible - light - activated molecular switches. *Angewandte Chemie International Edition*. **2015**;54(39):11338-49.
53. Beharry AA, Sadovski O, Woolley GA. Azobenzene photoswitching without ultraviolet light. *Journal of the American Chemical Society*. **2011**;133(49):19684-7.

54. Bléger D, Schwarz J, Brouwer AM, Hecht S. o-Fluoroazobenzenes as readily synthesized photoswitches offering nearly quantitative two-way isomerization with visible light. *Journal of the American Chemical Society*. **2012**;134(51):20597-600.
55. Siewertsen R, Neumann H, Buchheim-Stehn B, Herges R, Nather C, Renth F, et al. Highly efficient reversible Z–E photoisomerization of a bridged azobenzene with visible light through resolved S1 ($n\pi^*$) absorption bands. *Journal of the American Chemical Society*. **2009**;131(43):15594-5.
56. Calbo J, Weston CE, White AJ, Rzepa HS, Contreras-García J, Fuchter MJ. Tuning azoheteroarene photoswitch performance through heteroaryl design. *Journal of the American Chemical Society*. **2017**;139(3):1261-74.
57. Mitscherlich E. Ueber das stickstoffbenzid. *Annalen der Physik*. **1834**;108(15):225-7.
58. Hartley GS. The cis-form of azobenzene. *Nature*. **1937**;140(3537):281-.
59. Norikane Y, Uchida E, Tanaka S, Fujiwara K, Koyama E, Azumi R, et al. Photoinduced crystal-to-liquid phase transitions of azobenzene derivatives and their application in photolithography processes through a solid–liquid patterning. *Organic letters*. **2014**;16(19):5012-5.
60. Eligehausen S, Sarge SM, Öhlschläger G, Cammenga HK. The pseudobinary phase diagram cis-/trans-azobenzene and the cis \rightarrow trans isomerization in various states of aggregation. *Journal of thermal analysis*. **1989**;35:515-26.
61. Griffiths K, Halcovitch NR, Griffin JM. Crystalline azobenzene composites as photochemical phase-change materials. *New Journal of Chemistry*. **2022**;46(9):4057-61.
62. Uchida E, Sakaki K, Nakamura Y, Azumi R, Hirai Y, Akiyama H, et al. Control of the orientation and photoinduced phase transitions of macrocyclic azobenzene. *Chemistry–A European Journal*. **2013**;19(51):17391-7.
63. Ube T, Ikeda T. Photomobile polymer materials with crosslinked liquid - crystalline structures: molecular design, fabrication, and functions. *Angewandte Chemie International Edition*. **2014**;53(39):10290-9.
64. Lameijer LN, Budzak S, Simeth NA, Hansen MJ, Feringa BL, Jacquemin D, et al. General principles for the design of visible - light - responsive photoswitches: tetra - ortho - chloro - azobenzenes. *Angewandte Chemie International Edition*. **2020**;59(48):21663-70.
65. Knie C, Utecht M, Zhao F, Kulla H, Kovalenko S, Brouwer AM, et al. ortho - Fluoroazobenzenes: visible light switches with very long - lived z isomers. *Chemistry–A European Journal*. **2014**;20(50):16492-501.
66. Fang D, Zhang Z-Y, Shangguan Z, He Y, Yu C, Li T. (Hetero) arylazo-1, 2, 3-triazoles: “Clicked” photoswitches for versatile functionalization and electronic decoupling. *Journal of the American Chemical Society*. **2021**;143(36):14502-10.
67. Moore WM, Morgan DD, Stermitz FR. The photochemical conversion of stilbene to phenanthrene. The nature of the intermediate. *Journal of the American Chemical Society*. **1963**;85(6):829-30.
68. Mallory FB, Wood CS, Gordon JT. Photochemistry of stilbenes. III. Some aspects of the mechanism of photocyclization to phenanthrenes. *Journal of the American Chemical Society*. **1964**;86(15):3094-102.
69. Lewis FD, Wu T, Burch EL, Bassani DM, Yang J-S, Schneider S, et al. Hybrid oligonucleotides containing stilbene units. Excimer fluorescence and photodimerization. *Journal of the American Chemical Society*. **1995**;117(34):8785-92.

70. Schraub M, Gray H, Hampp N. Selective [2+ 2]-cycloaddition in methacrylic stilbene polymers without interference from E/Z-Isomerization. *Macromolecules*. **2011**;44(22):8755-62.
71. Xu F, Sheng J, Stindt CN, Crespi S, Danowski W, Hilbers MF, et al. All-visible-light-driven stiff-stilbene photoswitches. *Chemical Science*. **2024**;15(18):6763-9.
72. Imato K, Sasaki A, Ishii A, Hino T, Kaneda N, Ohira K, et al. Sterically hindered stiff-stilbene photoswitch offers large motions, 90% two-way photoisomerization, and high thermal stability. *The Journal of Organic Chemistry*. **2022**;87(23):15762-70.
73. Villarón D, Wezenberg SJ. Stiff - stilbene photoswitches: from fundamental studies to emergent applications. *Angewandte Chemie*. **2020**;132(32):13292-302.
74. Waldeck DH. Photoisomerization dynamics of stilbenes. *Chemical Reviews*. **1991**;91(3):415-36.
75. Oelgemöller M, Frank R, Lemmen P, Lenoir D, Lex J, Inoue Y. Synthesis, structural characterization and photoisomerization of cyclic stilbenes. *Tetrahedron*. **2012**;68(21):4048-56.
76. Koumura N, Zijlstra RW, van Delden RA, Harada N, Feringa BL. Light-driven monodirectional molecular rotor. *Nature*. **1999**;401(6749):152-5.
77. Pollard MM, Meetsma A, Feringa BL. A redesign of light-driven rotary molecular motors. *Organic & biomolecular chemistry*. **2008**;6(3):507-12.
78. Kistemaker JC, Štacko P, Visser J, Feringa BL. Unidirectional rotary motion in achiral molecular motors. *Nature Chemistry*. **2015**;7(11):890-6.
79. Wyman GM. The interaction of excited thioindigo with hydroxylic compounds and its implications on the photostability of indigo. *Journal of the Chemical Society D: Chemical Communications*. **1971**(21):1332-4.
80. Pina J, Sarmiento D, Accoto M, Gentili PL, Vaccaro L, Galvao A, et al. Excited-state proton transfer in indigo. *The Journal of Physical Chemistry B*. **2017**;121(10):2308-18.
81. Weinstein J, Wyman GM. Spectroscopic Studies on Dyes. II. The Structure of N, N'-Dimethylindigo. *Journal of the American Chemical Society*. **1956**;78(16):4007-10.
82. Huang C-Y, Bonasera A, Hristov L, Garmshausen Y, Schmidt BM, Jacquemin D, et al. N, N' -disubstituted indigos as readily available red-light photoswitches with tunable thermal half-lives. *Journal of the American Chemical Society*. **2017**;139(42):15205-11.
83. Huang CY, Hecht S. A blueprint for transforming indigos to photoresponsive molecular tools. *Chemistry—A European Journal*. **2023**;29(43):e202300981.
84. Petermayer C, Dube H. Indigoid photoswitches: visible light responsive molecular tools. *Accounts of chemical research*. **2018**;51(5):1153-63.
85. Walden SL, Nguyen PH, Li H-K, Liu X, Le MT, Xian Jun L, et al. Visible light-induced switching of soft matter materials properties based on thioindigo photoswitches. *Nature Communications*. **2023**;14(1):8298.
86. Pereira RC, Pineiro M, Galvao AM, de Melo JSS. Thioindigo, and sulfonated thioindigo derivatives as solvent polarity dependent fluorescent on-off systems. *Dyes and Pigments*. **2018**;158:259-66.
87. Petermayer C, Thumser S, Kink F, Mayer P, Dube H. Hemiindigo: highly bistable photoswitching at the biooptical window. *Journal of the American Chemical Society*. **2017**;139(42):15060-7.
88. Petermayer C, Dube H. Circular dichroism photoswitching with a twist: axially chiral hemiindigo. *Journal of the American Chemical Society*. **2018**;140(42):13558-61.
89. Cordes T, Schadendorf T, Priewisch B, Rück-Braun K, Zinth W. The Hammett relationship and reactions in the excited electronic state: Hemithioindigo Z/E-photoisomerization. *The Journal of Physical Chemistry A*. **2008**;112(4):581-8.

90. Gernet A, El Rhaz A, Jean L. Easily Accessible Substituted Heterocyclic Hemithioindigos as Bistable Molecular Photoswitches. *Chemistry–A European Journal*. **2023**;29(48):e202301160.
91. Lehn JM. Conjecture: imines as unidirectional photodriven molecular motors—motional and constitutional dynamic devices. *Chemistry–A European Journal*. **2006**;12(23):5910-5.
92. Greb L, Eichhöfer A, Lehn JM. Internal C–C bond rotation in photoisomers of α -bisimines: a light-responsive two-step molecular speed regulator based on double imine photoswitching. *Wiley Online Library*; **2016**.
93. Greb L, Mutlu H, Barner-Kowollik C, Lehn J-M. Photo- and metallo-responsive N-alkyl α -bisimines as orthogonally addressable main-chain functional groups in metathesis polymers. *Journal of the American Chemical Society*. **2016**;138(4):1142-5.
94. Wu J, Kreimendahl L, Tao S, Anhalt O, Greenfield JL. Photoswitchable imines: aryliminopyrazoles quantitatively convert to long-lived Z-isomers with visible light. *Chemical Science*. **2024**;15(11):3872-8.
95. Cozzi PG. Metal–Salen Schiff base complexes in catalysis: practical aspects. *Chemical Society Reviews*. **2004**;33(7):410-21.
96. Gupta K, Sutar AK. Catalytic activities of Schiff base transition metal complexes. *Coordination Chemistry Reviews*. **2008**;252(12-14):1420-50.
97. Belowich ME, Stoddart JF. Dynamic imine chemistry. *Chemical Society Reviews*. **2012**;41(6):2003-24.
98. Greb L, Lehn J-M. Light-driven molecular motors: imines as four-step or two-step unidirectional rotors. *Journal of the American Chemical Society*. **2014**;136(38):13114-7.
99. van Dijken DJ, Kovaříček P, Ihrig SP, Hecht S. Acylhydrazones as widely tunable photoswitches. *Journal of the American Chemical Society*. **2015**;137(47):14982-91.
100. Qian H, Pramanik S, Aprahamian I. Photochromic hydrazone switches with extremely long thermal half-lives. *Journal of the American Chemical Society*. **2017**;139(27):9140-3.
101. Li Q, Qian H, Shao B, Hughes RP, Aprahamian I. Building strain with large macrocycles and using it to tune the thermal half-lives of hydrazone photochromes. *Journal of the American Chemical Society*. **2018**;140(37):11829-35.
102. Tatum LA, Su X, Aprahamian I. Simple hydrazone building blocks for complicated functional materials. *Accounts of Chemical Research*. **2014**;47(7):2141-9.
103. Chaur MN, Collado D, Lehn JM. Configurational and constitutional information storage: multiple dynamics in systems based on pyridyl and acyl hydrazones. *Chemistry–A European Journal*. **2011**;17(1):248-58.
104. Mravec B, Budzak S, Medved' M, Pasteka LF, Slavov C, Sassmannshausen T, et al. Design of High-Performance Pyridine/Quinoline Hydrazone Photoswitches. *The Journal of Organic Chemistry*. **2021**;86(17):11633-46.
105. Qiu Q, Yang S, Gerkman MA, Fu H, Aprahamian I, Han GG. Photon energy storage in strained cyclic hydrazones: emerging molecular solar thermal energy storage compounds. *Journal of the American Chemical Society*. **2022**;144(28):12627-31.
106. Minkin VI. Photo-, thermo-, solvato-, and electrochromic spiroheterocyclic compounds. *Chemical reviews*. **2004**;104(5):2751-76.
107. Rad JK, Balzade Z, Mahdavian AR. Spiropyran-based advanced photoswitchable materials: A fascinating pathway to the future stimuli-responsive devices. *Journal of Photochemistry and Photobiology C: Photochemistry Reviews*. **2022**;51:100487.
108. Klajn R. Spiropyran-based dynamic materials. *Chemical Society Reviews*. **2014**;43(1):148-84.
109. Bletz M, Pfeifer-Fukumura U, Kolb U, Baumann W. Ground- and first-excited-singlet-state electric dipole moments of some photochromic spirobenzopyrans in their

- spiropyran and merocyanine form. *The Journal of Physical Chemistry A*. **2002**;106(10):2232-6.
110. Levitus M, Glasser G, Neher D, Aramendía PF. Direct measurement of the dipole moment of a metastable merocyanine by electromechanical interferometry. *Chemical physics letters*. **1997**;277(1-3):118-24.
111. Whelan J, Abdallah D, Wojtyk J, Buncel E. Micro-environmental fine-tuning of electronic and kinetic properties of photochromic dyes. *Journal of Materials Chemistry*. **2010**;20(27):5727-35.
112. Wimberger L, Prasad SK, Peeks MD, Andréasson J, Schmidt TW, Beves JE. Large, tunable, and reversible pH changes by merocyanine photoacids. *Journal of the American Chemical Society*. **2021**;143(49):20758-68.
113. McCoy CP, Donnelly L, Jones DS, Gorman SP. Synthesis and characterisation of polymerisable photochromic spiropyrans: towards photomechanical biomaterials. *Tetrahedron letters*. **2007**;48(4):657-61.
114. Tian H, Yang S. Recent progresses on diarylethene based photochromic switches. *Chemical Society Reviews*. **2004**;33(2):85-97.
115. Clerc M, Sandlass S, Rifaie-Graham O, Peterson JA, Bruns N, de Alaniz JR, et al. Visible light-responsive materials: the (photo) chemistry and applications of donor-acceptor Stenhouse adducts in polymer science. *Chemical Society Reviews*. **2023**.
116. Wani OM, Verpaalen R, Zeng H, Priimagi A, Schenning AP. An artificial nocturnal flower via humidity - gated photoactuation in liquid crystal networks. *Advanced Materials*. **2019**;31(2):1805985.
117. Ryabchun A, Li Q, Lancia F, Aprahamian I, Katsonis N. Shape-persistent actuators from hydrazone photoswitches. *Journal of the American Chemical Society*. **2019**;141(3):1196-200.
118. Hu J, Li X, Ni Y, Ma S, Yu H. A programmable and biomimetic photo-actuator: a composite of a photo-liquefiable azobenzene derivative and commercial plastic film. *Journal of Materials Chemistry C*. **2018**;6(40):10815-21.
119. Lu X, Guo S, Tong X, Xia H, Zhao Y. Tunable photocontrolled motions using stored strain energy in malleable azobenzene liquid crystalline polymer actuators. *Advanced Materials*. **2017**;29(28):1606467.
120. Ube T, Nakayama R, Ikeda T. Photoinduced motions of thermoplastic polyurethanes containing azobenzene moieties in main chains. *Macromolecules*. **2022**;55(2):413-20.
121. Sun X, Zhang M, Wei J, Yu Y. Multiple shape manipulation of azobenzene-containing polyimide by combining shape memory effect, photofixity, and photodeformation. *ACS Macro Letters*. **2023**;12(7):921-7.
122. Zhou L, Liu Q, Lv X, Gao L, Fang S, Yu H. Photoinduced triple shape memory polyurethane enabled by doping with azobenzene and GO. *Journal of Materials Chemistry C*. **2016**;4(42):9993-7.
123. Lee KM, Koerner H, Vaia RA, Bunning TJ, White TJ. Light-activated shape memory of glassy, azobenzene liquid crystalline polymer networks. *Soft Matter*. **2011**;7(9):4318-24.
124. Ohm C, Brehmer M, Zentel R. Liquid crystalline elastomers as actuators and sensors. *Advanced materials*. **2010**;22(31):3366-87.
125. Abdollahi A, Sahandi-Zangabad K, Roghani-Mamaqani H. Rewritable anticounterfeiting polymer inks based on functionalized stimuli-responsive latex particles containing spiropyran photoswitches: reversible photopatterning and security marking. *ACS applied materials & interfaces*. **2018**;10(45):39279-92.

126. Arjmand F, Mohamadnia Z. Fabrication of a light-responsive polymer nanocomposite containing spiropyran as a sensor for reversible recognition of metal ions. *Polymer Chemistry*. **2022**;13(7):937-45.
127. Cui C, Liu G, Gao H, Wang M, Gao J. Spiropyran-based photo-and thermal-responsive smart polymer with controllable wettability. *Polymer*. **2022**;253:124995.
128. Wagner N, Theato P. Light-induced wettability changes on polymer surfaces. *Polymer*. **2014**;55(16):3436-53.
129. Zhang Z, Chen M, Schneider I, Liu Y, Liang S, Sun S, et al. Long alkyl side chains simultaneously improve mechanical robustness and healing ability of a photoswitchable polymer. *Macromolecules*. **2020**;53(19):8562-9.
130. Han GG, Li H, Grossman JC. Optically-controlled long-term storage and release of thermal energy in phase-change materials. *Nature communications*. **2017**;8(1):1446.
131. Zhang P, Cai F, Wang W, Wang G, Yu H. Light-switchable adhesion of azobenzene-containing siloxane-based tough adhesive. *ACS Applied Polymer Materials*. **2021**;3(5):2325-9.
132. Yang S, Harris JD, Lambai A, Jeliaskov LL, Mohanty G, Zeng H, et al. Multistage reversible T_g photomodulation and hardening of hydrazone-containing polymers. *Journal of the American Chemical Society*. **2021**;143(40):16348-53.
133. Castiglioni F, Danowski W, Perego J, Leung FK-C, Sozzani P, Bracco S, et al. Modulation of porosity in a solid material enabled by bulk photoisomerization of an overcrowded alkene. *Nature Chemistry*. **2020**;12(7):595-602.
134. Wagener KB, Boncella J, Nel J. Acyclic diene metathesis (ADMET) polymerization. *Macromolecules*. **1991**;24(10):2649-57.
135. Trnka TM, Grubbs RH. The development of L₂X₂Ru CHR olefin metathesis catalysts: an organometallic success story. *Accounts of Chemical Research*. **2001**;34(1):18-29.
136. Mutlu H, de Espinosa LM, Meier MA. Acyclic diene metathesis: a versatile tool for the construction of defined polymer architectures. *Chemical Society Reviews*. **2011**;40(3):1404-45.
137. Lucero JM, Romero Z, Moreno A, Huber DL, Simocko C. ADMET polymerization in affordable, commercially available, high boiling solvents. *SN Applied Sciences*. **2020**;2:1-8.
138. Fokou PA, Meier MA. Use of a renewable and degradable monomer to study the temperature-dependent olefin isomerization during ADMET polymerizations. *Journal of the American Chemical Society*. **2009**;131(5):1664-5.
139. Fokou PA, Meier MA. Studying and suppressing olefin isomerization side reactions during ADMET polymerizations. *Macromolecular rapid communications*. **2010**;31(4):368-73.
140. Schulz MD, Wagener KB. Solvent effects in alternating ADMET polymerization. *ACS Macro Letters*. **2012**;1(4):449-51.
141. de Espinosa LM, Meier MA. Synthesis of star-and block-copolymers using ADMET: head-to-tail selectivity during step-growth polymerization. *Chemical Communications*. **2011**;47(6):1908-10.
142. Smith JA, Brzezinska KR, Valenti DJ, Wagener KB. Precisely controlled methyl branching in polyethylene via acyclic diene metathesis (ADMET) polymerization. *Macromolecules*. **2000**;33(10):3781-94.
143. Pribyl J, Wagener KB, Rojas G. ADMET polymers: synthesis, structure elucidation, and function. *Materials Chemistry Frontiers*. **2021**;5(1):14-43.
144. Ding L, Xu M, Wang J, Liao Y, Qiu J. Controlled synthesis of azobenzene functionalized homo and copolymers via direct acyclic diene metathesis polymerization. *Polymer*. **2014**;55(7):1681-7.

145. Ding L, Li Y, Cang H, Li J, Wang C, Song W. Controlled synthesis of azobenzene-containing block copolymers both in the main-and side-chain from SET-LRP polymers via ADMET polymerization. *Polymer*. **2020**;190:122229.
146. Krishnan BP, Xue L, Xiong X, Cui J. Photoinduced strain - assisted synthesis of a stiff - stilbene polymer by ring - opening metathesis polymerization. *Chemistry – A European Journal*. **2020**;26(65):14828-32.
147. Nomura K, Abdellatif MM. Precise synthesis of polymers containing functional end groups by living ring-opening metathesis polymerization (ROMP): Efficient tools for synthesis of block/graft copolymers. *Polymer*. **2010**;51(9):1861-81.
148. Su JK, Jin Z, Zhang R, Lu G, Liu P, Xia Y. Tuning the Reactivity of Cyclopropenes from Living Ring - Opening Metathesis Polymerization (ROMP) to Single - Addition and Alternating ROMP. *Angewandte Chemie International Edition*. **2019**;58(49):17771-6.
149. Lu P, Kensy VK, Tritt RL, Seidenkranz DT, Boydston AJ. Metal-free ring-opening metathesis polymerization: from concept to creation. *Accounts of Chemical Research*. **2020**;53(10):2325-35.
150. Ogawa KA, Goetz AE, Boydston AJ. Metal-free ring-opening metathesis polymerization. *Journal of the American Chemical Society*. **2015**;137(4):1400-3.
151. Goetz AE, Pascual LM, Dunford DG, Ogawa KA, Knorr Jr DB, Boydston AJ. Expanded functionality of polymers prepared using metal-free ring-opening metathesis polymerization. *ACS Macro Letters*. **2016**;5(5):579-82.
152. Tardy A, Nicolas J, Gimes D, Lefay C, Guillaneuf Y. Radical ring-opening polymerization: Scope, limitations, and application to (bio) degradable materials. *Chemical reviews*. **2017**;117(3):1319-406.
153. Huang H, Sun B, Huang Y, Niu J. Radical cascade-triggered controlled ring-opening polymerization of macrocyclic monomers. *Journal of the American Chemical Society*. **2018**;140(33):10402-6.
154. Evans RA, Moad G, Rizzardo E, Thang SH. New free-radical ring-opening acrylate monomers. *Macromolecules*. **1994**;27(26):7935-7.
155. Paulusse JM, Amir RJ, Evans RA, Hawker CJ. Free radical polymers with tunable and selective bio-and chemical degradability. *Journal of the American Chemical Society*. **2009**;131(28):9805-12.
156. Sbordonc F, Veskova J, Richardson B, Do PT, Micallef A, Frisch H. Embedding Peptides into Synthetic Polymers: Radical Ring-Opening Copolymerization of Cyclic Peptides. *Journal of the American Chemical Society*. **2023**;145(11):6221-9.
157. Do PT, Poad BL, Frisch H. Programming photodegradability into vinylic polymers via radical ring - opening polymerization. *Angewandte Chemie*. **2023**;135(6):e202213511.
158. Worch JC, Stubbs CJ, Price MJ, Dove AP. Click nucleophilic conjugate additions to activated alkynes: exploring thiol-yne, amino-yne, and hydroxyl-yne reactions from (bio) organic to polymer chemistry. *Chemical Reviews*. **2021**;121(12):6744-76.
159. Fu X, Qin A, Tang BZ. X - yne click polymerization. *Aggregate*. **2023**;4(5):e350.
160. Fu X, Qin A, Tang BZ. Dynamic covalent polymers generated from X - yne click polymerization. *Journal of Polymer Science*. **2024**;62(5):787-98.
161. Si H, Wang K, Song B, Qin A, Tang BZ. Organobase-catalysed hydroxyl-yne click polymerization. *Polymer Chemistry*. **2020**;11(14):2568-75.
162. Ritter VC, McDonald SM, Dobrynin AV, Craig SL, Becker ML. Mechanochromism and Strain - Induced Crystallization in Thiol - yne - Derived Stereoelastomers. *Advanced Materials*. **2023**;35(41):2302163.

163. Akar E, Luleburgaz S, Gunay US, Kumbaraci V, Tunca U, Durmaz H. Amino-yne reaction: An exquisite method for polymer-polymer conjugation and post-polymerization modification. *European Polymer Journal*. **2023**;199:112470.
164. Mao G, Wang J, Clingman SR, Ober CK, Chen JT, Thomas EL. Molecular design, synthesis, and characterization of liquid crystal- coil diblock copolymers with azobenzene side groups. *Macromolecules*. **1997**;30(9):2556-67.
165. Wang G, Tong X, Zhao Y. Preparation of azobenzene-containing amphiphilic diblock copolymers for light-responsive micellar aggregates. *Macromolecules*. **2004**;37(24):8911-7.
166. Frenz C, Fuchs A, Schmidt HW, Theissen U, Haarer D. Diblock Copolymers with Azobenzene Side - Groups and Polystyrene Matrix: Synthesis, Characterization and Photoaddressing. *Macromolecular Chemistry and Physics*. **2004**;205(9):1246-58.
167. Yoshida T, Doi M, Kanaoka S, Aoshima S. Polymer surface modification using diblock copolymers containing azobenzene. *Journal of Polymer Science Part A: Polymer Chemistry*. **2005**;43(22):5704-9.
168. Yu H, Shishido A, Iyoda T, Ikeda T. Novel wormlike nanostructures self - assembled in a well defined liquid crystalline diblock copolymer with azobenzene moieties. *Macromolecular rapid communications*. **2007**;28(8):927-31.
169. Wang Y, Zhang M, Moers C, Chen S, Xu H, Wang Z, et al. Block copolymer aggregates with photo-responsive switches: towards a controllable supramolecular container. *Polymer*. **2009**;50(20):4821-8.
170. Del Barrio J, Oriol L, Alcala R, Sanchez C. Azobenzene-containing linear-dendritic diblock copolymers by click chemistry: Synthesis, characterization, morphological study, and photoinduction of optical anisotropy. *Macromolecules*. **2009**;42(15):5752-60.
171. Feng Z, Lin L, Yan Z, Yu Y. Dual responsive block copolymer micelles functionalized by NIPAM and azobenzene. *Macromolecular rapid communications*. **2010**;31(7):640-4.
172. Yan B, Tong X, Ayotte P, Zhao Y. Light-responsive block copolymer vesicles based on a photo-softening effect. *Soft Matter*. **2011**;7(21):10001-9.
173. Xiang Y, Xue X, Zhu J, Zhang Z, Zhang W, Zhou N, et al. Fluorescence behavior of an azobenzene-containing amphiphilic diblock copolymer. *Polymer Chemistry*. **2010**;1(9):1453-8.
174. Spiridon MC, Demazy N, Brochon C, Cloutet E, Hadziioannou G, Aissou K, et al. Optical alignment of Si-containing nanodomains formed by photoresponsive amorphous block copolymer thin films. *Macromolecules*. **2020**;53(1):68-77.
175. Audia B, Bugakov MA, Boiko NI, Pagliusi P, Cipparrone G, Shibaev VP. Photopatterning of Azobenzene - Containing Liquid Crystalline Triblock Copolymers: Light - Induced Anisotropy and Photostabilization. *Macromolecular Rapid Communications*. **2020**;41(20):2000384.
176. Cai F, Song T, Yang B, Lv X, Zhang L, Yu H. Enhancement of solar thermal fuel by microphase separation and nanoconfinement of a block copolymer. *Chemistry of Materials*. **2021**;33(24):9750-9.
177. Sun S, Yuan C, Xie Z, Xu W-C, Zhang Q, Wu S. Photoresponsive nanostructures of azobenzene-containing block copolymers at solid surfaces. *Polymer Chemistry*. **2022**;13(3):411-9.
178. Xue X, Zhu J, Zhang Z, Cheng Z, Tu Y, Zhu X. Synthesis and characterization of azobenzene-functionalized poly (styrene)-b-poly (vinyl acetate) via the combination of RAFT and “click” chemistry. *Polymer*. **2010**;51(14):3083-90.

179. Qu T, Hu X, Zhou Z, Liu Y, Wang J, Hu F, et al. Morphology Control of Perpendicularly Oriented Lamellar Films from Azobenzene-Containing Block Copolymers with Different Spacer Lengths. *The Journal of Physical Chemistry C*. **2023**;127(7):3882-9.
180. Deng Z, Sun Y, Chen A. Light - Triggered Reversible Swelling of Azobenzene - Containing Block Copolymer Worms via Confined Deformation Prepared by Polymerization - Induced Self - Assembly. *Macromolecular Rapid Communications*. **2024**;2400372.
181. Truong NP, Jones GR, Bradford KG, Konkolewicz D, Anastasaki A. A comparison of RAFT and ATRP methods for controlled radical polymerization. *Nature Reviews Chemistry*. **2021**;5(12):859-69.
182. Do PT, Poad BL, Frisch H. Programming Photodegradability into Vinylic Polymers via Radical Ring - Opening Polymerization. *Angewandte Chemie International Edition*. **2023**;62(6):e202213511.
183. Xu X, Zhou N, Zhu J, Tu Y, Zhang Z, Cheng Z, et al. The First Example of Main - Chain Cyclic Azobenzene Polymers. *Macromolecular rapid communications*. **2010**;31(20):1791-7.
184. Fang L, Zhang H, Li Z, Zhang Y, Zhang Y, Zhang H. Synthesis of reactive azobenzene main-chain liquid crystalline polymers via Michael addition polymerization and photomechanical effects of their supramolecular hydrogen-bonded fibers. *Macromolecules*. **2013**;46(19):7650-60.
185. Ding L, Zhang L, Yang D, Huang W, Xie M, Zhang Y. New azo-chromophore-containing multiblock poly (butadiene) s synthesized by the combination of ring-opening metathesis polymerization and click chemistry. *Polymer*. **2010**;51(6):1285-92.
186. Wang V, Kim J, Kim J, Lee SW, Kim KT. On-demand shape transformation of polymer vesicles via site-specific isomerization of hydrazone photoswitches in monodisperse hydrophobic oligomers. *Polymer Chemistry*. **2021**;12(35):5027-36.
187. Apebende EA, Dubois L, Bruns N. Light-responsive block copolymers with a spiropyran located at the block junction. *European Polymer Journal*. **2019**;119:83-93.
188. Thai LD, Guimaraes TR, Spann S, Goldmann AS, Golberg D, Mutlu H, et al. Photoswitchable block copolymers based on main chain α -bisimines. *Polymer Chemistry*. **2022**;13(39):5625-35.
189. Matyjaszewski K, Davis K, Patten TE, Wei M. Observation and analysis of a slow termination process in the atom transfer radical polymerization of styrene. *Tetrahedron*. **1997**;53(45):15321-9.
190. Jakubowski W, Kirci - Denizli B, Gil RR, Matyjaszewski K. Polystyrene with improved chain - end functionality and higher molecular weight by ARGET ATRP. *Macromolecular Chemistry and Physics*. **2008**;209(1):32-9.
191. Mather BD, Viswanathan K, Miller KM, Long TE. Michael addition reactions in macromolecular design for emerging technologies. *Progress in Polymer Science*. **2006**;31(5):487-531.
192. Li W, Wang J. Lewis base catalyzed aerobic oxidative intermolecular azide-zwitterion cycloaddition. *Angewandte Chemie International Edition*. **2014**;53(51):14186-90.
193. Thai LD, Guimaraes TR, Chambers LC, Kammerer JA, Golberg D, Mutlu H, et al. Molecular photoswitching of main-chain α -bisimines in solid-state polymers. *Journal of the American Chemical Society*. **2023**;145(27):14748-55.
194. Daglar O, Gunay US, Hizal G, Tunca U, Durmaz H. Extremely rapid polythioether synthesis in the presence of TBD. *Macromolecules*. **2019**;52(9):3558-72.

195. Thai LD, Kammerer JA, Théato P, Mutlu H, Barner-Kowollik C. Access to main-chain photoswitching polymers via hydroxyl-yne click polymerization. *ACS Macro Letters*. **2024**;13(6):681-7.
196. Song B, Lu D, Qin A, Tang BZ. Combining hydroxyl-yne and thiol-ene click reactions to facilitate access to sequence-defined macromolecules for high-density data storage. *Journal of the American Chemical Society*. **2021**;144(4):1672-80.
197. Jiang Q, Zhang H, Jiang Q, Zhang S, Guan S, Huang W, et al. Hydroxyl-yne click polymerization: a facile strategy toward poly(vinyl amino ether ester)s with color-tunable luminescence. *Polymer Chemistry*. **2023**;14(11):1232-40.
198. Lynd NA, Meuler AJ, Hillmyer MA. Polydispersity and block copolymer self-assembly. *Progress in Polymer Science*. **2008**;33(9):875-93.
199. Oschmann B, Lawrence J, Schulze MW, Ren JM, Anastasaki A, Luo Y, et al. Effects of tailored dispersity on the self-assembly of dimethylsiloxane-methyl methacrylate block co-oligomers. *ACS Macro Letters*. **2017**;6(7):668-73.
200. Cooke DM, Shi A-C. Effects of polydispersity on phase behavior of diblock copolymers. *Macromolecules*. **2006**;39(19):6661-71.
201. Trinh TT, Laure C, Lutz JF. Synthesis of monodisperse sequence-defined polymers using protecting-group-free iterative strategies. *Macromolecular Chemistry and Physics*. **2015**;216(14):1498-506.
202. Shi Q, Zhang Z, Liu S. Precision Sequence-Defined Polymers: From Sequencing to Biological Functions. *Angewandte Chemie International Edition*. **2024**;63(6):e202313370.
203. Lutz J-F. The future of sequence-defined polymers. *European Polymer Journal*. **2023**;112465.
204. Zhu Y, Tao Y. Sequence-controlled and sequence-defined polypeptoids via the Ugi reaction: synthesis and sequence-driven properties. *Polymer Chemistry*. **2021**;12(34):4895-902.
205. Martens S, Landuyt A, Espeel P, Devreese B, Dawyndt P, Du Prez F. Multifunctional sequence-defined macromolecules for chemical data storage. *Nature Communications*. **2018**;9(1):4451.
206. Cannon SJ, Blechert S. Recent developments in olefin cross-metathesis. *Angewandte Chemie International Edition*. **2003**;42(17):1900-23.
207. Meldal M. Polymer “clicking” by CuAAC reactions. *Macromolecular Rapid Communications*. **2008**;29(12-13):1016-51.
208. Nakatani R, Takano H, Chandra A, Yoshimura Y, Wang L, Suzuki Y, et al. Perpendicular orientation control without interfacial treatment of RAFT-synthesized high- χ block copolymer thin films with sub-10 nm features prepared via thermal annealing. *ACS applied materials & interfaces*. **2017**;9(37):31266-78.
209. Nunns A, Gwyther J, Manners I. Inorganic block copolymer lithography. *Polymer*. **2013**;54(4):1269-84.
210. Fekete S, Beck A, Veuthey J-L, Guilleme D. Theory and practice of size exclusion chromatography for the analysis of protein aggregates. *Journal of pharmaceutical and biomedical analysis*. **2014**;101:161-73.
211. Popovici S-T, Kok WT, Schoenmakers PJ. Band broadening in size-exclusion chromatography of polydisperse samples. *Journal of Chromatography A*. **2004**;1060(1-2):237-52.
212. Williams DE, Martin CR, Dolgoplova EA, Swifton A, Godfrey DC, Ejegbawo OA, et al. Flipping the switch: fast photoisomerization in a confined environment. *Journal of the American Chemical Society*. **2018**;140(24):7611-22.

213. Varghese S, Das S. Role of molecular packing in determining solid-state optical properties of π -conjugated materials. *The Journal of Physical Chemistry Letters*. **2011**;2(8):863-73.
214. Sun F, Wang D. Toward real-world applications: promoting fast and efficient photoswitching in the solid state. *Journal of Materials Chemistry C*. **2022**;10(37):13700-16.
215. Weis P, Wang D, Wu S. Visible-light-responsive azopolymers with inhibited π - π stacking enable fully reversible photopatterning. *Macromolecules*. **2016**;49(17):6368-73.
216. Wu Z, Pan K, Mo S, Wang B, Zhao X, Yin M. Tetraphenylethene-induced free volumes for the isomerization of spiropyran toward multifunctional materials in the solid state. *ACS Applied Materials & Interfaces*. **2018**;10(36):30879-86.
217. Xiong X, Sun F, Gao A, Wang Z, Duan Y, Yao Z, et al. Ester matters? Promoting photoisomerization of donor-acceptor Stenhouse adducts in the solid state and “burn after reading” encryption. *Chemical Engineering Journal*. **2022**;450:138090.
218. Izumi A, Teraguchi M, Nomura R, Masuda T. Synthesis of poly (p-phenylene)-based photoresponsive conjugated polymers having azobenzene units in the main chain. *Macromolecules*. **2000**;33(15):5347-52.
219. Wang J, Jiang Q, Hao X, Yan H, Peng H, Xiong B, et al. Reversible photo-responsive gel-sol transitions of robust organogels based on an azobenzene-containing main-chain liquid crystalline polymer. *RSC Advances*. **2020**;10(7):3726-33.
220. Rad JK, Balzade Z, Mahdavian AR. Spiropyran-based advanced photoswitchable materials: A fascinating pathway to the future stimuli-responsive devices. *Journal of Photochemistry and Photobiology C: Photochemistry Reviews*. **2022**:100487.
221. Cai F, Yang B, Lv X, Feng W, Yu H. Mechanically mutable polymer enabled by light. *Science Advances*. **2022**;8(34):eabo1626.
222. Perera K, Wu W, You L, Elman JF, Wang Z, Wang X, et al. Absorption Coefficient and Optical Contrast Modulation through Side Chain Engineering of Electrochromic Polymers. *Macromolecules*. **2023**;56(2):480-9.
223. Hempel E, Huth H, Beiner M. Interrelation between side chain crystallization and dynamic glass transitions in higher poly (n-alkyl methacrylates). *Thermochimica Acta*. **2003**;403(1):105-14.
224. Reimschuessel H. On the glass transition temperature of comblike polymers: Effects of side chain length and backbone chain structure. *Journal of Polymer Science: Polymer Chemistry Edition*. **1979**;17(8):2447-57.
225. Li Z, Wu F, Lv H, Yang D, Chen Z, Zhao X, et al. Side - Chain Engineering for Enhancing the Thermal Stability of Polymer Solar Cells. *Advanced Materials*. **2015**;27(43):6999-7003.
226. Cao Z, Galuska L, Qian Z, Zhang S, Huang L, Prine N, et al. The effect of side-chain branch position on the thermal properties of poly (3-alkylthiophenes). *Polymer Chemistry*. **2020**;11(2):517-26.
227. Luo X, Xie S, Liu J, Hu H, Jiang J, Huang W, et al. The relationship between the degree of branching and glass transition temperature of branched polyethylene: experiment and simulation. *Polymer Chemistry*. **2014**;5(4):1305-12.
228. Khalyavina A, Häußler L, Lederer A. Effect of the degree of branching on the glass transition temperature of polyesters. *Polymer*. **2012**;53(5):1049-53.
229. Mamunya Y, Iurzhenko M. Polymer Chemistry, 2007, 587 pages, Paul C. Hiemenz, Timothy P. Lodge, 1574447793, 9781574447798, CRC PressINC, 2007. *Journal of Polymer Science Part A-1, Polymer Chemistry*. **1972**;10(3).

230. Irshadeen IM, Walden SL, Wegener M, Truong VX, Frisch H, Blinco JP, et al. Action plots in action: in-depth insights into photochemical reactivity. *Journal of the American Chemical Society*. **2021**;143(50):21113-26.
231. Xiong Z, Zhang J, Sun JZ, Zhang H, Tang BZ. Excited-State Odd–Even Effect in Through-Space Interactions. *Journal of the American Chemical Society*. **2023**;145(38):21104-13.
232. Tao F, Bernasek SL. Understanding odd–even effects in organic self-assembled monolayers. *Chemical reviews*. **2007**;107(5):1408-53.
233. Roviello A, Sirigu A. Odd - even effects in polymeric liquid crystals. *Die Makromolekulare Chemie*. **1982**;183(4):895-904.
234. Baghbanzadeh M, Simeone FC, Bowers CM, Liao K-C, Thuo M, Baghbanzadeh M, et al. Odd–even effects in charge transport across n-alkanethiolate-based sams. *Journal of the American Chemical Society*. **2014**;136(48):16919-25.
235. Baeyer A. Ueber regelmässigkeiten im schmelzpunkt homologer verbindungen. *Berichte der deutschen chemischen Gesellschaft*. **1877**;10(2):1286-8.
236. Zhang X, Zuo X, Ortmann P, Mecking S, Alamo RG. Crystallization of long-spaced precision polyacetals I: melting and recrystallization of rapidly formed crystallites. *Macromolecules*. **2019**;52(13):4934-48.
237. Voisin E, Johan Foster E, Rakotomalala M, Williams VE. Effects of symmetry on the stability of columnar liquid crystals. *Chemistry of Materials*. **2009**;21(14):3251-61.
238. Lin Y, Barbee MH, Chang C-C, Craig SL. Regiochemical effects on mechanophore activation in bulk materials. *Journal of the American Chemical Society*. **2018**;140(46):15969-75.
239. Landge SM, Tkatchouk E, Benítez D, Lanfranchi DA, Elhabiri M, Goddard III WA, et al. Isomerization mechanism in hydrazone-based rotary switches: lateral shift, rotation, or tautomerization? *Journal of the American Chemical Society*. **2011**;133(25):9812-23.
240. Thai LD, Fanelli J, Munaweera R, O'Mara ML, Barner - Kowollik C, Mutlu H. Main - chain Macromolecular Hydrazone Photoswitches. *Angewandte Chemie International Edition*. **2024**;63(4):e202315887.
241. Abd El-Wahab H. The synthesis and characterization of the hydrazone ligand and its metal complexes and their performance in epoxy formulation surface coatings. *Progress in Organic Coatings*. **2015**;89:106-13.
242. Kumar RR, Ramesh R, Matecki JG. Synthesis and structure of arene ruthenium (II) benzhydrazone complexes: Antiproliferative activity, apoptosis induction and cell cycle analysis. *Journal of Organometallic Chemistry*. **2018**;862:95-104.
243. Appiah C, Woltersdorf G, Pérez-Camargo RA, Müller AJ, Binder WH. Crystallization behavior of precision polymers containing azobenzene defects. *European Polymer Journal*. **2017**;97:299-307.
244. Handbook P. ; Brandrup, J., Immergut, EH, Grulke, EA, Eds. *Wiley: New York*; **1999**.
245. Lu Y-X, Tournilhac F, Leibler L, Guan Z. Making insoluble polymer networks malleable via olefin metathesis. *Journal of the American Chemical Society*. **2012**;134(20):8424-7.
246. Lu Y-X, Guan Z. Olefin metathesis for effective polymer healing via dynamic exchange of strong carbon–carbon double bonds. *Journal of the American Chemical Society*. **2012**;134(34):14226-31.
247. Otsuka H, Muta T, Sakada M, Maeda T, Takahara A. Scrambling reaction between polymers prepared by step-growth and chain-growth polymerizations: macromolecular cross-metathesis between 1, 4-polybutadiene and olefin-containing polyester. *Chemical communications*. **2009**(9):1073-5.

248. Voorter PJ, McKay A, Dai J, Paravagna O, Cameron NR, Junkers T. Solvent - Independent Molecular Weight Determination of Polymers Based on a Truly Universal Calibration. *Angewandte Chemie International Edition*. **2022**;61(5):e202114536.
249. Guo X, Laryea E, Wilhelm M, Luy B, Nirschl H, Guthausen G. Diffusion in Polymer Solutions: Molecular Weight Distribution by PFG - NMR and Relation to SEC. *Macromolecular Chemistry and Physics*. **2017**;218(1):1600440.
250. Kortekaas L, Browne WR. The evolution of spiropyran: fundamentals and progress of an extraordinarily versatile photochrome. *Chemical Society Reviews*. **2019**;48(12):3406-24.
251. Li M, Zhang Q, Zhou Y-N, Zhu S. Let spiropyran help polymers feel force! *Progress in Polymer Science*. **2018**;79:26-39.
252. Jaycox GD. Stimuli - responsive polymers. VIII. Polyesters and poly (ester amides) containing azobenzene and chiral binaphthylene segments: Highly adaptive materials endowed with light - , heat - , and solvent - regulated optical rotatory power. *Journal of Polymer Science Part A: Polymer Chemistry*. **2006**;44(1):207-18.
253. Min P, Li Y, Wang L, Song W, Ding L. The shackling photoisomerization effect on self-assembly of azobenzene-containing side-chain homopolymers. *Polymer*. **2022**;258:125301.
254. Wei M, Gao Y, Li X, Serpe MJ. Stimuli-responsive polymers and their applications. *Polymer Chemistry*. **2017**;8(1):127-43.
255. Schattling P, Jochum FD, Theato P. Multi-stimuli responsive polymers—the all-in-one talents. *Polymer Chemistry*. **2014**;5(1):25-36.
256. Schulz-Senft M, Gates PJ, Sönnichsen FD, Staubitz A. Diversely halogenated spiropyrans-Useful synthetic building blocks for a versatile class of molecular switches. *Dyes and Pigments*. **2017**;136:292-301.
257. Görner H. Photochromism of nitrospiropyrans: effects of structure, solvent and temperature. *Physical Chemistry Chemical Physics*. **2001**;3(3):416-23.
258. Day JH. Thermochromism. *Chemical Reviews*. **1963**;63(1):65-80.
259. Kempe F, Metzler L, Brügger O, Buchheit H, Walter M, Komber H, et al. Substituent - controlled energetics and barriers of mechanochromic spiropyran - functionalized poly (ϵ - caprolactone). *Macromolecular Chemistry and Physics*. **2023**;224(1):2200254.
260. Kellmann A, Tfibel F, Pottier E, Guglielmetti R, Samat A, Rajzmann M. Effect of nitro substituents on the photochromism of some spiro [indoline-naphthopyrans] under laser excitation. *Journal of Photochemistry and Photobiology A: Chemistry*. **1993**;76(1-2):77-82.
261. Sakuragi M, Aoki K, Tamaki T, Ichimura K. The role of triplet state of nitrospiropyran in their photochromic reaction. *Bulletin of the Chemical Society of Japan*. **1990**;63(1):74-9.
262. Thai LD, Kammerer JA, Mutlu H, Barner-Kowollik C. Photo-and halochromism of spiropyran-based main-chain polymers. *Chemical Science*. **2024**;15(10):3687-97.
263. Pantsyrnyi V, Gal'bershtam M. Preparation of spiropyrans from 3-formylsalicylic acid derivatives. *Chemistry of Heterocyclic Compounds*. **1971**;7(1):134-5.
264. Mavila S, Diesendruck CE, Linde S, Amir L, Shikler R, Lemcoff NG. Polycyclooctadiene complexes of rhodium (I): direct access to organometallic nanoparticles. *Angewandte Chemie International Edition*. **2013**;22(52):5767-70.
265. Thai LD, Fanelli J, Munaweera R, O'Mara M, Barner-Kowollik C, Mutlu H. Main-chain macromolecular hydrazone photoswitches. *Angewandte Chemie (International ed in English)*.e202315887.

266. Wojtyk JT, Wasey A, Xiao N-N, Kazmaier PM, Hoz S, Yu C, et al. Elucidating the mechanisms of acidochromic spiropyran-merocyanine interconversion. *The Journal of Physical Chemistry A*. **2007**;111(13):2511-6.
267. Ganesan R, Remacle F. Stabilization of merocyanine by protonation, charge, and external electric fields and effects on the isomerization of spiropyran: a computational study. *Theoretical Chemistry in Belgium: A Topical Collection from Theoretical Chemistry Accounts*. **2014**:167-79.
268. Kortekaas L, Chen J, Jacquemin D, Browne W. Proton-stabilized photochemically reversible E/Z isomerization of spiropyran. *The Journal of Physical Chemistry B*. **2018**;122(24):6423-30.
269. Keum S-R, Lee K-B, Kazmaier PM, Buncel E. A novel method for measurement of the merocyanine-spiropyran interconversion in non-activated 1, 3, 3-trimethylspiro-(2H-1-benzopyran-2, 2' -indoline) derivatives. *Tetrahedron Letters*. **1994**;35(7):1015-8.
270. Shiozaki H. Molecular orbital calculations for acid induced ring opening reaction of spiropyran. *Dyes and Pigments*. **1997**;33(3):229-37.
271. Murugan NA, Chakrabarti S, Ågren H. Solvent dependence of structure, charge distribution, and absorption spectrum in the photochromic merocyanine- spiropyran pair. *The Journal of Physical Chemistry B*. **2011**;115(14):4025-32.
272. Piard J. Influence of the solvent on the thermal back reaction of one spiropyran. *Journal of Chemical Education*. **2014**;91(12):2105-11.
273. Tian W, Tian J. An insight into the solvent effect on photo-, solvato-chromism of spiropyran through the perspective of intermolecular interactions. *Dyes and Pigments*. **2014**;105:66-74.
274. Weber S. Stabilization of the merocyanine form of photochromic compounds in fluoro alcohols is due to a hydrogen bond. *Chemical Communications*. **1998**(24):2685-6.
275. Zhang J-J, Duan X-H, Wu Y, Yang J-C, Guo L-N. Transition-metal free C-C bond cleavage/borylation of cycloketone oxime esters. *Chemical Science*. **2019**;10(1):161-6.
276. Li Y, Cheng K, Lu X, Sun J. A Facile and Efficient Approach to N - Protected - β - Sulfinyl - enamines via C - Sulfinylation of Enamides and Enecarbamates. *Advanced Synthesis & Catalysis*. **2010**;352(11 - 12):1876-80.
277. Guo K, Chen Y. Lewis acid and base triggered molecular switch. *Journal of Materials Chemistry*. **2009**;19(32):5790-3.
278. Allerhand A, Von Rague Schleyer P. A survey of CH groups as proton donors in hydrogen bonding. *Journal of the American Chemical Society*. **1963**;85(12):1715-23.
279. Sommer M, Komber H. Spiropyran main - chain conjugated polymers. *Macromolecular Rapid Communications*. **2013**;34(1):57-62.
280. Komber H, Müllers S, Lombeck F, Held A, Walter M, Sommer M. Soluble and stable alternating main-chain merocyanine copolymers through quantitative spiropyran-merocyanine conversion. *Polymer Chemistry*. **2014**;5(2):443-53.
281. Ferreira P, Moncelsi G, Aragay G, Ballester P. Hydrogen - bonded dimeric capsules with appended spiropyran units: towards controlled cargo release. *Chemistry- A European Journal*. **2021**;27(49):12675-85.
282. Goldburt E, Shvartsman F, Fishman S, Krongauz V. Intramolecular interactions in photochromic spiropyran-merocyanine polymers. *Macromolecules*. **1984**;17(6):1225-30.
283. Lide DR. CRC Handbook of Chemistry and Physics: CRC press; **2004**.
284. Guthrie JP. Hydrolysis of esters of oxy acids: p K a values for strong acids; Brønsted relationship for attack of water at methyl; free energies of hydrolysis of esters

- of oxy acids; and a linear relationship between free energy of hydrolysis and p K a holding over a range of 20 p K units. *Canadian Journal of Chemistry*. **1978**;56(17):2342-54.
285. Genovese ME, Colusso E, Colombo M, Martucci A, Athanassiou A, Fragouli D. Acidochromic fibrous polymer composites for rapid gas detection. *Journal of Materials Chemistry A*. **2017**;5(1):339-48.
286. Onai Y, Mamiya M, Kiyokawa T, Okuwa K, Kobayashi M, Shinohara H, et al. Colored merocyanine aggregates: long-lived crystals of large size (10-100. μ m) and deaggregation of small aggregates in solutions. *The Journal of Physical Chemistry*. **1993**;97(37):9499-505.
287. Chibisov AK, Görner H. Photoprocesses in spiropyran-derived merocyanines. *The Journal of Physical Chemistry A*. **1997**;101(24):4305-12.
288. Hamley IW, Castelletto V. Small-angle scattering of block copolymers: in the melt, solution and crystal states. *Progress in polymer science*. **2004**;29(9):909-48.
289. Gronheid R, Nealey P. Directed Self-assembly of Block Co-polymers for Nano-manufacturing: *Woodhead Publishing*; **2015**.
290. Dollase T, Spiess HW, Gottlieb M, Yerushalmi-Rozen R. Crystallization of PDMS: The effect of physical and chemical crosslinks. *Europhysics Letters*. **2002**;60(3):390.
291. Jeon S, Lee S, Kim J, Eim S, Lee W, Nam WH, et al. Two-dimensional directed lamellar assembly in silicon-and fluorine-containing block copolymer with identical surface energies. *NPG Asia Materials*. **2023**;15(1):68.
292. Hwang S, Ober C, Perutz S, Iyengar D, Schneggenburger L, Kramer E. Block copolymers with low surface energy segments: siloxane-and perfluoroalkane-modified blocks. *Polymer*. **1995**;36(6):1321-5.
293. Jeon S, Jun T, Jeon HI, Ahn H, Lee S, Lee B, et al. Various Low-Symmetry Phases in High- χ and Conformationally Asymmetric PDMS-b-PTFEA Copolymers. *Macromolecules*. **2021**;54(20):9351-60.
294. Gruending T, Guilhaus M, Barner-Kowollik C. Fast and accurate determination of absolute individual molecular weight distributions from mixtures of polymers via size exclusion chromatography– electrospray ionization mass spectrometry. *Macromolecules*. **2009**;42(17):6366-74.
295. Kammerer JA, Duan X, Neubrech F, Schröder RR, Liu N, Pfannmöller M. Stabilizing γ - MgH₂ at nanotwins in mechanically constrained nanoparticles. *Advanced Materials*. **2021**;33(11):2008259.
296. Droumaguet B. Multifunctional giant amphiphiles via simultaneous copper (I)-catalyzed azide–alkyne cycloaddition and living radical polymerization. *Chemical Communications*. **2012**;48(10):1586-8.
297. Wang L, Zhu K, Cao W, Sun C, Lu C, Xu H. ROS-triggered degradation of selenide-containing polymers based on selenoxide elimination. *Polymer Chemistry*. **2019**;10(16):2039-46.
298. Müller P, Müller R, Hammer L, Barner-Kowollik C, Wegener M, Blasco E. STED-inspired laser lithography based on photoswitchable spirothiopyran moieties. *Chemistry of Materials*. **2019**;31(6):1966-72.
299. Zhu M-Q, Chen T, Zhang G-F, Li C, Gong W-L, Chen Z-Q, et al. Spiropyran-based biodegradable polymer all-optical transistors integrate the switching and modulation of visible light frequency. *Chemical Communications*. **2014**;50(20):2664-6.
300. Knoll A, Horvat A, Lyakhova K, Krausch G, Sevink G, Zvelindovsky A, et al. Phase behavior in thin films of cylinder-forming block copolymers. *Physical Review Letters*. **2002**;89(3):035501.

Curriculum Vitae (CV)

M. Sc. Linh Duy Thai

Sex: Male

Nationality: Vietnamese

Education

07.2021-11.2024 **Cotutelle PhD Degree: Photo- and Polymer Chemistry**

Queensland University of Technology (QUT) – Australia

Karlsruhe Institute of Technology (KIT) – Germany

Dissertation title: “*Photoswitchable Macromolecules: The Foundation of Photodynamic Block Copolymer Lithography*”

Keywords: photoswitches, hydrazone, α -bisimine, spiropyran, main-chain, click chemistry, hydroxyl-yne click, thiol-Michael click, ADMET polymerization, ARGET ATRP, sequence-defined, block copolymer, nanostructures

Principal Supervisor: DProf. Dr. Christopher Barner-Kowollik

Associate Supervisor: DProf. Dr. Dmitri Golberg

External Supervisor: Junior Prof. Dr. Hatice Mutlu

09.2018-09.2020 **Joint Master’s Degree: Surface, Electro-, Radiation, and Photo-Chemistry**

SERP+ program: <https://www.master-serp.eu/>

Paris-Saclay University – France

University of Porto – Portugal

Thesis title: “*Study of New Trifluoromethylation Reactions under Photoredox Catalysis*”

Keywords: photoredox, trifluoromethylation, α,β -unsaturated carbonyl

Supervisor: Dr. Guillaume Dagousset

Thesis title: "Synthesis of Poly(2-(dichlorotriazinyl)oxyethyl methacrylate)-random-poly(stearyl acrylate) Crosslinked by Thiol Crosslinkers Towards Self-Healing Materials"

Keywords: photo-ATRP, self-healing, disulfide bonds

Supervisors: Assoc. Prof. Dr. Le Thu Thi Nguyen, Assoc. Prof. Dr. Ha Tran Nguyen

Publications

- | | | |
|-------------|-----|---|
| | [8] | <i>Sequence-Defined Main-Chain Photoswitchable Macromolecules with Odd-Even Effect Controlled Properties</i> |
| | | Thai, L. D.; Kammerer, J. A.; Golberg, D.; Mutlu, H.; Barner-Kowollik, C. <i>Chem</i> 2024 , in press. |
| | [7] | <i>Access to Main-chain Photoswitching Polymers via Hydroxyl-yne Click Polymerization</i> |
| 2024 | | Thai, L. D.; Kammerer, J. A.; Théato, P.; Mutlu, H.; Barner-Kowollik, C. <i>ACS Macro Lett.</i> 2024 , 13, 681-687. |
| | [6] | <i>Photo- and Halochromism of Spiropyran-based Main-chain Polymers</i> |
| | | Thai, L. D.; Kammerer, J. A.; Mutlu, H.; Barner-Kowollik, C. <i>Chem. Sci.</i> 2024 , 3687-3697. |
| | [5] | <i>Main-chain Macromolecular Hydrazone Photoswitches</i> |
| | | Thai, L. D.; Fanelli, J.; Munaweera, R.; O'Mara, M. L.; Barner-Kowollik, C.; Mutlu, H. <i>Angew. Chem. Int. Ed.</i> 2024 , e202315887. |
| 2023 | [4] | <i>Molecular Photoswitching of Main-chain α-bisimines in Solid-State Polymers</i> |
| | | Thai, L. D.; Guimarães, T. R.; Chambers, L. C.; Kammerer, J. A.; Golberg, D.; Mutlu, H.; Barner-Kowollik, C. <i>J. Am. Chem. Soc.</i> 2023 , 145, 1478-14755. |
| | [3] | <i>Photoswitchable Block Copolymers Based on Main Chain α-Bisimines</i> |
| | | Thai, L. D.; Guimarães, T. R.; Spann, S.; Goldmann, A. S.; Golberg, D.; Mutlu, H.; Barner-Kowollik, C. <i>Polym. Chem.</i> 2022 , 13, 5625-5635. |
| 2022 | [2] | <i>Remote Radical Trifluoromethylation: A Unified Approach to the Selective Synthesis of γ-Trifluoromethyl α,β-Unsaturated Carbonyl Compounds</i> |
| | | Briand, M.; Thai, L.D.; Bourdreux, F.; Vanthuyne, N.; Moreau, X.; Magnier, E.; Anselmi, E.; Dagousset, G. <i>Org. Lett.</i> 2022 , 24, 9375–9380. |

- 2019** [1] *Synthesis of a Novel Fluorescent Cyanide Chemosensor Based on Photoswitching Poly(pyrene-1-ylmethyl-methacrylate-random-methylmethacrylate-random-methacrylate spirooxazine)*
Tran, H.M.; Nguyen, T.H.; Nguyen, V.Q.; Tran, P.H.; **Thai, L.D.**; Truong, T.T.; Nguyen, L.T.T.; Nguyen, H.T. *Macromol.*, **2019**, 27, 25–32.
-

Conferences

- 07.2024** The 50th World Polymer Congress, IUPAC MACRO (oral presentation)
02.2024 The 38th Australasian Polymer Symposium (38APS) (oral presentation)
11.2023 Queensland Annual Chemistry Symposium (QACS) 2023 (best oral presentation award)